



An experimental study of free-surface dynamics and internal motions in fully aerated hydraulic jumps

Author:

Montano Luna, Laura

Publication Date:

2019

DOI:

<https://doi.org/10.26190/unsworks/21593>

License:

<https://creativecommons.org/licenses/by-nc-nd/3.0/au/>

Link to license to see what you are allowed to do with this resource.

Downloaded from <http://hdl.handle.net/1959.4/64908> in <https://unsworks.unsw.edu.au> on 2024-05-04

An experimental study of free-surface dynamics and internal motions in fully aerated hydraulic jumps

Laura Montano

A thesis in fulfilment of the requirements for the degree of
DOCTOR OF PHILOSOPHY



School of Civil and Environmental Engineering

Faculty of Engineering

UNSW Sydney

August 2019

Thesis/Dissertation Sheet

Surname/Family Name	: Montano
Given Name/s	: Laura
Abbreviation for degree as give in the University calendar	: PhD
Faculty	: Faculty of Engineering
School	: School of Civil and Environmental Engineering
Thesis Title	: An experimental study of free-surface dynamics and internal motions in fully aerated hydraulic jumps

Abstract 350 words maximum:

Hydraulic jumps occur at the sudden transition from supercritical to subcritical flows. They are characterised by three-dimensional motions, instabilities and strong flow aeration. Due to the large energy dissipation capacity, hydraulic jumps are widely used in energy dissipators downstream of flow conveyance structures. The complexity of hydraulic jumps has fascinated researchers for centuries and numerous experimental studies provided important insights into the hydraulic jump phenomenon. However, the energy dissipation processes associated with complex three-dimensional motions and interactions of entrained air with the flow turbulence are still poorly understood due to limitations in experimental techniques. Herein, novel technologies were applied in the present study to enhance the current understanding of free-surface dynamics and three-dimensional motions inside fully aerated hydraulic jumps.

Extensive experiments were conducted at the UNSW Water Research Laboratory in large-scale open channel flow facilities for fully and partially developed inflow conditions upstream of the hydraulic jumps. Distributions of air-water flow properties were measured with state-of-the-art double-tip conductivity probes identifying a strong effect of the inflow conditions on the flow aeration resulting in larger void fractions and bubble count rates for fully developed inflow conditions. World-first use of LIDAR technology in fully aerated hydraulics jumps provided the most detailed information of time-varying free-surface features and jump toe movements to date. The results highlighted the strong effect of the jump toe oscillations on the free-surface fluctuations, characteristic frequencies and turbulent scales. Unique measurements of internal three-dimensional motions in hydraulic jumps were conducted with a submerged sphere connected to a six-axis load cell. The results provided the first direct measurements of transverse and vertical motions inside hydraulic jumps highlighting the strong three-dimensionality of the internal motions and the need to consider flow processes in all directions to better understand the complex dynamics of hydraulic jumps. The combination of the new experimental results provided the most detailed picture of the dissipative flow processes inside hydraulic jumps to date. The study demonstrated that the use of advanced instrumentation can provide new insights into complex hydraulic phenomena such as hydraulic jumps.

Declaration relating to disposition of project thesis/dissertation

I hereby grant to the University of New South Wales or its agents the right to archive and to make available my thesis or dissertation in whole or in part in the University libraries in all forms of media, now or here after known, subject to the provisions of the Copyright Act 1968. I retain all property rights, such as patent rights. I also retain the right to use in future works (such as articles or books) all or part of this thesis or dissertation.

I also authorise University Microfilms to use the 350 word abstract of my thesis in Dissertation Abstracts International (this is applicable to doctoral theses only).

Signature:	Witness Signature:	Date: <u>20/08/2019</u>
------------------	--------------------------	-------------------------

The University recognises that there may be exceptional circumstances requiring restrictions on copying or conditions on use. Requests for restriction for a period of up to 2 years must be made in writing. Requests for a longer period of restriction may be considered in exceptional circumstances and require the approval of the Dean of Graduate Research.

FOR OFFICE USE ONLY	Date of completion of requirements for Award:	
----------------------------	---	--

Originality Statement

'I hereby declare that this submission is my own work and to the best of my knowledge it contains no materials previously published or written by another person, or substantial proportions of material which have been accepted for the award of any other degree or diploma at UNSW or any other educational institution, except where due acknowledgement is made in the thesis. Any contribution made to the research by others, with whom I have worked at UNSW or elsewhere, is explicitly acknowledged in the thesis. I also declare that the intellectual content of this thesis is the product of my own work, except to the extent that assistance from others in the project's design and conception or in style, presentation and linguistic expression is acknowledged.'

Laura Montano
August 2019

Copyright Statement

I hereby grant the University of New South Wales or its agents the right to archive and to make available my thesis or dissertation in whole or part in the University libraries in all forms of media, now or here after known, subject to the provisions of the Copyright Act 1968. I retain all proprietary rights, such as patent rights. I also retain the right to use in future works (such as articles or books) all or part of this thesis or dissertation.

I also authorise University Microfilms to use the 350 word abstract of my thesis in Dissertation Abstract International (this is applicable to doctoral theses only).

I have either used no substantial portions of copyright material in my thesis or I have obtained permission to use copyright material; where permission has not been granted I have applied/will apply for a partial restriction of the digital copy of my thesis or dissertation.'

Laura Montano
August 2019

Authenticity Statement

'I certify that the Library deposit digital copy is a direct equivalent of the final officially approved version of my thesis. No emendation of content has occurred and if there are any minor variations in formatting, they are the result of the conversion to digital format.'

Laura Montano

August 2019

Inclusion of Publications Statement

UNSW is supportive of candidates publishing their research results during their candidature as detailed in the UNSW Thesis Examination Procedure.

Publications can be used in their thesis in lieu of a Chapter if:

- The student contributed greater than 50% of the content in the publication and is the “primary author”, i.e., the student was responsible primarily for the planning, execution and preparation of the work for publication
- The student has approval to include the publication in their thesis in lieu of a Chapter from their supervisor and Postgraduate Coordinator.
- The publication is not subject to any obligations or contractual agreements with a third party that would constrain its inclusion in the thesis

Please indicate whether this thesis contains published material or not.

- This thesis contains no publications, either published or submitted for publication.*
- Some of the work described in this thesis has been published and it has been documented in the relevant Chapters with acknowledgement.*
- This thesis has publications (either published or submitted for publication) incorporated into it in lieu of a chapter and the details are presented below.*

CANDIDATE’S DECLARATION

I declare that:

- I have complied with the Thesis Examination Procedure
- where I have used a publication in lieu of a Chapter, the listed publication(s) below meet(s) the requirements to be included in the thesis.

Name:	Signature:	Date (dd/mm/yyyy):
Laura Montano		20/08/2019

ABSTRACT

Hydraulic jumps occur at the sudden transition from supercritical to subcritical flows. They are characterised by three-dimensional motions, instabilities and strong flow aeration. Due to the large energy dissipation capacity, hydraulic jumps are widely used in energy dissipators downstream of flow conveyance structures. The complexity of hydraulic jumps has fascinated researchers for centuries and numerous experimental studies provided important insights into the hydraulic jump phenomenon. However, the energy dissipation processes associated with complex three-dimensional motions and interactions of entrained air with the flow turbulence are still poorly understood due to limitations in experimental techniques. Herein, novel technologies were applied in the present study to enhance the current understanding of free-surface dynamics and three-dimensional motions inside fully aerated hydraulic jumps.

Extensive experiments were conducted at the UNSW Water Research Laboratory in large-scale open channel flow facilities for fully and partially developed inflow conditions upstream of the hydraulic jumps. Distributions of air-water flow properties were measured with state-of-the-art double-tip conductivity probes identifying a strong effect of the inflow conditions on the flow aeration resulting in larger void fractions and bubble count rates for fully developed inflow conditions. World-first use of LIDAR technology in fully aerated hydraulics jumps provided the most detailed information of time-varying free-surface features and jump toe movements to date. The results highlighted the strong effect of the jump toe oscillations on the free-surface fluctuations, characteristic frequencies and turbulent scales. Unique measurements of internal three-dimensional motions in hydraulic jumps were conducted with a submerged sphere connected to a six-axis load cell. The results provided the first direct measurements of transverse and vertical motions inside hydraulic jumps highlighting the strong three-dimensionality of the internal motions and the need to consider flow processes in all directions to better understand the complex dynamics of hydraulic jumps. The combination of the new experimental results provided the most detailed picture of the dissipative flow processes inside hydraulic jumps to date. The study demonstrated that the use of advanced instrumentation can provide new insights into complex hydraulic phenomena such as hydraulic jumps.

ACKNOWLEDGMENTS

This dissertation is a result of a challenging but rewarding journey of more than three years in a foreign country, over 14,000 km from my family, and a daily learning process. Many things were left behind when I decided to follow this academic dream, but I am here today full of gratitude for all the people involved in the achievement of this personal milestone.

First of all, I want to thank God for this opportunity. I was continuously witness of His greatness, His promises and His love. Secondly, I would like to express my sincere gratitude to my supervisors Dr. Stefan Felder and Hon. A/Prof. Ron Cox for their guidance and support along this journey. I was honoured to work with both of them. I would like to offer my special appreciation to Dr. Stefan Felder for the time, the advice and the continuous encouragement. I believe that he is one of the most dedicated supervisors and I had the pleasure to be one of his students. I also would like to express my gratitude to Hon. A/Prof. Ron Cox for his continuous support and for sharing his wide experience and knowledge. I was very fortunate to be guided by one of the most experienced water experts in Australia.

I would also like to thank the Water Research Laboratory (WRL) family. Everyone has been welcoming and encouraging. I am so grateful of being part of one of the world's leading water laboratories. I give special thanks to Rob Jenkins and Larry Paice for all their technical support, patience and their willingness to help me during my experimental journey. I would also extend my gratitude to Grace and Coral for always being aware of my progress and my achievements. A big thank you to all past and present WRL PhD students. It has been a pleasure to be part of such a diverse group, for sharing your language, culture and slang. I am happy to see the success of the ones who have already been awarded doctorates and I wish the best for the ones who are on the path to achieve that. I extend my gratitude to my PhD friends at WRC. I also want to express my gratitude to my undergraduate students Rui Li and Hanwen Cui. I wish the best in their PhD journey. Lastly, I want to thank my Colombian family in Australia: my lovely chorus and my "Uniandes" friends. You were an oasis in a foreign land.

Finally, I would like to especially thank my family. Gracias a mis padres Humberto y Dylia, a mi hermana Natalia, a mis sobrinos Sarita y Nico. Ustedes han sido el motor para continuar en este proceso. A ustedes les dedico este gran logro y anhelo retribuirles todo el amor y el apoyo que me han brindado. Este gran logro también se lo dedico a Mamá Isabel. A pesar de que no puedo celebrar este logro presencialmente, al cielo elevo este gran paso y espero celebrarlo algún día a su lado. Y finalmente le dedico la culminación de este doctorado a mi compañero de viaje, de vida y de sueños. Jaysson, gracias por apoyarme durante estos años, gracias por tus consejos, tu paciencia y tu amor. Gracias por nuestras largas conversaciones "técnicas" y siempre tener la palabra indicada para encontrar la solución a mis problemas. Es gracias a ti que hoy puedo culminar este camino, y estoy lista para que juntos sigamos conquistando nuevos sueños.

RELEVANT PUBLICATIONS

Peer-reviewed journal manuscripts

Montano, L., and Felder, S. 2019. ‘An experimental study of air-water flows in hydraulic jumps on flat slopes’, *Journal of Hydraulic Research* (in print, accepted for publication on 20/9/2019)

Montano, L., and Felder, S. 2019 ‘LIDAR observations of free-surface time and length scales in hydraulic jumps’, *Journal of Hydraulic Engineering* (in print, accepted for publication on 14/8/2019)

Montano, L., Li, R., and Felder, S. 2018. ‘Continuous measurements of time-varying free-surface profiles in aerated hydraulic jumps with a LIDAR’, *Experimental Thermal and Fluid Science*, vol. 93, pp. 379 – 397.

Peer-reviewed conference manuscripts

Montano, L., and Felder, S. 2019, ‘Measuring internal forces in a hydraulic jump with a load cell’, in *Proc., 38th IAHR World Congress*, Panama City, Panama, 10 pages.

Li, R., **Montano, L.**, Splinter, K., and Felder, S. 2019, ‘Opportunities of LIDAR measurements in air-water flows’, in *Proc., 38th IAHR World Congress*, Panama City, Panama, 10 pages.

Montano, L., and Felder, S. 2018, ‘LIDAR measurements of free-surface profiles and turbulent scales in a hydraulic jump’, in *Proc., 7th IAHR International Symposium on Hydraulic Structures*, Aachen, Germany, 10 pages.

Montano, L., and Felder, S. 2018, ‘Effect of inflow conditions on the air-water flow properties in hydraulic jumps’, in *Proc., 21st Australasian in Fluid Mechanics Conference*, Australasian Fluid Mechanics Conference, Adelaide, Australia, 4 pages.

Montano, L., and Felder, S. 2017, ‘Air-water flow properties in hydraulic jumps on a positive slope’, In *37th IAHR World Congress*, Kuala Lumpur, Malaysia, 10 pages.

Li, R., **Montano, L.**, and Felder, S. 2017, ‘LIDAR measurements of free-surface characteristics in a hydraulic jump’, In *13th Hydraulics in Water Engineering Conference*, Sydney, Australia, 8 pages.

Montano, L., and Felder, S. 2017, ‘Measurements of air-water flow properties in hydraulic jumps in a sloping channel’, In *13th Hydraulics in Water Engineering Conference*, Sydney, Australia, 9 pages.

TABLE OF CONTENTS

ABSTRACT	VII
ACKNOWLEDGEMENTS	VIII
RELEVANT PUBLICATIONS	IX
TABLE OF CONTENTS	XI
LIST OF FIGURES	XV
LIST OF TABLES	XXI
LIST OF SYMBOLS	XXII
LIST OF ABBREVIATIONS	XXVI
1. INTRODUCTION	1
2. LITERATURE REVIEW	10
2.1. A BRIEF TIMELINE OF HYDRAULIC JUMP RESEARCH	11
2.2. HYDRAULIC JUMP CONCEPTS	14
2.3. ENERGY DISSIPATION PROCESSES IN HYDRAULIC JUMPS	16
2.4. AIR-WATER FLOW PROPERTIES IN HYDRAULIC JUMPS	19
2.5. FREE-SURFACE FLUCTUATIONS AND JUMP TOE OSCILLATIONS	26
2.6. FORCES AND PRESSURE MEASUREMENTS IN HYDRAULIC JUMPS	30
2.6. 1. FORCE MEASUREMENTS IN HYDRAULIC JUMPS	31
2.6. 2. PRESSURE MEASUREMENTS IN HYDRAULIC JUMPS	33
2.7. SCALE EFFECTS	34
2.8. THESIS OVERVIEW AND OBJECTIVES	39
3. EXPERIMENTAL CONFIGURATION AND METHODOLOGY	42
3.1. EXPERIMENTAL FACILITY	43
3.2. INSTRUMENTATION	44
3.2. 1. AIR-WATER FLOW PROPERTIES	44
3.2. 2. FREE-SURFACE FLUCTUATIONS AND JUMP TOE OSCILLATIONS	47
3.2. 3. FORCES AND SUBMERGED SPHERE INSIDE HYDRAULIC JUMP	49
3.2. 4. INFLOW DEPTHS	52
3.2. 3. INFLOW CONDITIONS	52
3.3. POST-PROCESSING OF RAW DATA	54
3.3. 1. AIR-WATER FLOW PROPERTIES	54
3.3. 2. FREE-SURFACE FLUCTUATIONS AND JUMP TOE OSCILLATIONS	57
3.3. 3. FORCES	64
3.4. DATA VALIDATION, LIMITATIONS AND UNCERTAINTIES	68
3.4. 1. FLOW DISCHARGE	69
3.4. 2. AIR-WATER FLOW PROPERTIES	69
3.4. 3. FREE-SURFACE FLUCTUATIONS AND JUMP TOE OSCILLATIONS	70
	xi

3.4. 4. FORCES	72
3.5. FLOW CONDITIONS	75
4. AIR-WATER FLOW PROPERTIES	77
4.1. INTRODUCTION	78
4.2. VISUAL OBSERVATIONS OF AIR-WATER FLOW PATTERNS	79
4.3. EFFECT OF INFLOW CONDITIONS ON AIR-WATER FLOW PROPERTY DISTRIBUTIONS IN HYDRAULIC JUMPS	82
4.3. 1. FLOW PROPERTIES UPSTREAM OF HYDRAULIC JUMPS	82
4.3. 2. FLOW PATTERNS	84
4.3. 3. VOID FRACTION	85
4.3. 4. BUBBLE COUNT RATE	87
4.3. 5. INTERFACIAL VELOCITY	88
4.3. 6. AIR-BUBBLE CHORD TIMES	89
4.3. 7. AUTO- AND CROSS-CORRELATION TIME SCALES	92
4.4. EFFECT OF INFLOW CONDITIONS ON THE DECAY IN CHARACTERISTIC AIR-WATER FLOW PARAMETERS	93
4.4. 1. DECAY IN THE VOID FRACTION	93
4.4. 2. DECAY IN THE BUBBLE COUNT RATE	96
4.4. 3. CHARACTERISTIC ELEVATIONS	97
4.4. 2. DECAY IN THE INTERFACIAL VELOCITY	99
4.4. 2. DECAY IN THE CHORD TIME	99
4.5. SCALE EFFECTS	100
4.6. SUMMARY	102
5. FREE-SURFACE CHARACTERISTICS AND JUMP TOE OSCILLATIONS	105
5.1. INTRODUCTION	106
5.2. TIME-AVERAGED FREE-SURFACE PROFILES	107
5.3. HYDRAULIC JUMP LENGTH	112
5.4. FREE-SURFACE FLUCTUATIONS	114
5.5. JUMP TOE OSCILLATIONS	118
5.6. CHARACTERISTIC FREQUENCIES OF THE FREE-SURFACE	123
5.6. 1. MODE 1	123
5.6. 2. MODE 2	126
5.6. 3. FREE-SURFACE FREQUENCY REGIONS	128
5.7. AUTO-CORRELATION TIME SCALES	129
5.8. CROSS-CORRELATION TIME SCALES	135
5.9. INTEGRAL LENGTH SCALES	136
5.10. SCALE EFFECTS	142
5.11. SUMMARY	146
6. INTERNAL FORCES IN HYDRAULIC JUMPS	149
6.1. INTRODUCTION	150
6.2. TIME-AVERAGED FORCES	152
6.3. FORCE FLUCTUATIONS	156

6.4. CHARACTERISTIC FREQUENCIES	159
6.5. AUTO-CORRELATION TIME SCALES	163
6.6. DECAY IN THE INTERNAL FORCE PARAMETERS	164
6.7. EFFECT OF INFLOW CONDITIONS	169
6.8. SCALE EFFECTS	173
6.9. SUMMARY	177
7. DISCUSSION	180
7.1. INTRODUCTION	181
7.2. TIME-AVERAGED PROPERTIES IN HYDRAULIC JUMPS	183
7.3. FLUCTUATIONS IN HYDRAULIC JUMPS	187
7.4. CHARACTERISTIC FREQUENCIES IN HYDRAULIC JUMPS	189
7.5. AUTO-CORRELATION TIME SCALES ALONG HYDRAULIC JUMPS	190
7.6. EFFECT OF INFLOW CONDITIONS	192
7.7. SCALE EFFECTS	194
7.8. DESIGN CONSIDERATIONS	195
8. CONCLUSIONS AND FUTURE RESEARCH	198
9. REFERENCES	203
APPENDICES	222
A. INFLOW CONDITIONS	223
A. 1. AIR-WATER FLOW PROPERTIES	223
B. SENSITIVITY ANALYSIS	227
B. 1. INTRODUCTION	227
B. 2. AIR-WATER FLOW PROPERTIES	228
B. 3. FREE-SURFACE FEATURES	232
B. 4. INTERNAL FORCES	236
C. FILTERING TECHNIQUES	243
C. 1. INTRODUCTION	243
C. 2. LIDAR	243
C. 3. LOAD CELL	247
D. AIR-WATER FLOW PROPERTIES: DECAY AIR-WATER FLOW PARAMETERS	253
D. 1. INTRODUCTION	253
D. 2. VOID FRACTION	253
D. 3. BUBBLE COUNT RATE	256
D. 4. INTERFACIAL VELOCITY	258
E. AIR-WATER FLOW PROPERTIES: SCALE EFFECTS	260
E. 1. INTRODUCTION	260
E. 2. VOID FRACTION	260
E. 3. BUBBLE COUNT RATE	261
E. 4. INTERFACIAL VELOCITY	262
E. 5. CHORD TIME	263
E. 6. AUTO- AND CROSS-CORRELATION TIME SCALES	264

F. AIR-WATER FLOW PROPERTIES: HYDRAULIC JUMPS ON SLOPED CHANNELS	266
F. 1. INTRODUCTION	267
F. 2. EXPERIMENTAL CONFIGURATION	268
F. 3. FLOW PATTERNS	270
F. 4. VOID FRACTION	276
F. 5. BUBBLE COUNT RATE	279
F. 6. INTERFACIAL VELOCITY	281
F. 7. CHORD SIZES	284
F. 8. AUTO- AND CROSS-CORRELATION TIME SCALES	285
F. 9. DISCUSSION	286
F. 10. CONCLUSION	287
G. FREE-SURFACE: TURBULENT SCALES	289
H. INTERNAL FORCES: DEFINITION STRUCTURAL DESIGN	305
I. INTERNAL FORCES	313
I. 1. INTRODUCTION	313
I. 2. STREAMWISE FORCES	313
I. 3. TRANSVERSE FORCES	322
I. 4. VERTICAL FORCES	328

LIST OF FIGURES

FIGURE 1-1. ALYZIA ANCIENT GREEK DAM. SPILLWAY IN OPERATION AND GENERATION OF HYDRAULIC JUMPS (KOUTSOYIANNIS ET AL. 2008).....	2
FIGURE 1-2. HYDRAULIC JUMP AS ENERGY DISSIPATER:	4
FIGURE 1-3. CHARACTERISTICS OF A TYPICAL HYDRAULIC JUMP ($Fr_l = 5.1$, $Re = 8.3 \times 10^4$); FLOW FROM LEFT TO RIGHT.....	5
FIGURE 1-4. STILLING BASIN OF HINZE DAM, QUEENSLAND, AUSTRALIA (COURTESY OF DR. STEFAN FELDER).....	7
FIGURE 2-1. CHRONOLOGICAL SUMMARY OF HYDRAULIC JUMP RESEARCH ACCORDING TO HAGER (1992).....	13
FIGURE 2-2. CLASSICAL HYDRAULIC JUMP SCHEME.....	14
FIGURE 2-3. CONCEPTUAL SKETCH OF VOID FRACTION DISTRIBUTIONS AND VOID FRACTION PARAMETERS IN HYDRAULIC JUMPS ($Fr_l = 8.5$, $Re = 7.5 \times 10^4$, $x/d_l = 8$ – PARTIALLY DEVELOPED INFLOW CONDITIONS).....	20
FIGURE 2-4. TYPICAL BUBBLE COUNT RATE DISTRIBUTION AND BUBBLE COUNT RATE PARAMETERS IN HYDRAULIC JUMP ($Fr_l = 7.0$, $Re = 1.2 \times 10^4$, $x/d_l = 8$ – PARTIALLY DEVELOPED INFLOW CONDITIONS).....	21
FIGURE 2-5. INTERFACIAL VELOCITY DISTRIBUTIONS AND CHARACTERISTIC PARAMETERS IN HYDRAULIC JUMPS; COMPARISON WALL JET THEORY ($Fr_l = 8.0$, $Re = 1.2 \times 10^5$, $x/d_l = 8$ – FULLY DEVELOPED INFLOW CONDITIONS).....	22
FIGURE 2-6. DYNAMICAL PRESSURE DISTRIBUTION (P_d) ON THE UPSTREAM FACE OF A BAFFLE BLOCK. ADAPTED FROM OHTSU ET AL. (1991).....	32
FIGURE 3-1. PHOTO OF THE EXPERIMENTAL SETUP OF HYDRAULIC JUMPS DOWNSTREAM OF A SLUICE GATE.....	43
FIGURE 3-2. EXPERIMENTAL SETUP OF HYDRAULIC JUMPS DOWNSTREAM OF A SLUICE GATE (NOT TO SCALE).....	44
FIGURE 3-3. DATA ACQUISITION DIAGRAM OF THE CONDUCTIVITY PROBE.....	45
FIGURE 3-4. WRL DOUBLE-TIP CONDUCTIVITY PROBE.....	45
FIGURE 3-5. EFFECT OF SAMPLING DURATION ON THE VOID FRACTION AND BUBBLE COUNT RATE MEASUREMENTS FOR HYDRAULIC JUMPS DOWNSTREAM OF THE SLUICE GATE WITH $Fr_l = 8.8$ AND $Re = 8.8 \times 10^4$	46
FIGURE 3-6. LABORATORY SETUP OF LIDAR EXPERIMENTS IN HYDRAULIC JUMPS DOWNSTREAM OF A SLOPED CHANNEL. RED ARROWS: LASER BEAMS; BLUE ARROWS: TRANSFORMATION OF LASER BEAMS INCLUDING REFLECTION, REFRACTION OR ABSORPTION.....	48
FIGURE 3-7. PHOTOS OF THE EXPERIMENTAL SETUP INCLUDING LIDAR POSITIONING WITH TYPICAL HYDRAULIC JUMP DOWNSTREAM OF THE SLUICE GATE (EXPERIMENT E_FD: $Fr_l = 8.5$, $Re = 7.5 \times 10^4$).....	48
FIGURE 3-8. DATA ACQUISITION DIAGRAM OF THE LIDAR.....	49
FIGURE 3-9. SIX-AXIS LOAD CELL M3813B. ADAPTED FROM DATA SHEET INFORMATION FROM SUNRISE INSTRUMENTS® (2018).....	49
FIGURE 3-10. DATA ACQUISITION DIAGRAM OF THE LOAD CELL.....	50

FIGURE 3-11. MEASUREMENT OF THREE-DIMENSIONAL INTERNAL FORCES IN HYDRAULIC JUMPS WITH A LOAD CELL.....	51
FIGURE 3-12. POINTER GAUGE MEASUREMENTS DOWNSTREAM OF THE SLUICE GATE ($Q = 0.048 \text{ m}^3/\text{s}$, $h_0 = 0.027 \text{ m}$).....	52
FIGURE 3-13. PITOT TUBE MEASUREMENTS IN FULLY DEVELOPED FLOWS DOWNSTREAM OF THE SLUICE GATE; NOTE THE FREE-SURFACE ROUGHNESS IN THE HIGH-VELOCITY FLOWS ($Q = 0.059 \text{ m}^3/\text{s}$, $h_0 = 0.03 \text{ m}$).....	53
FIGURE 3-14. TYPICAL CONDUCTIVITY PROBE RAW DATA SIGNAL OBTAINED WITH ONE TIP AND CORRESPONDING INSTANTENEOUS VOID FRACTION C	55
FIGURE 3-15. FLOW CHART OF THE POST-PROCESSING OF THE LIDAR DATA.....	58
FIGURE 3-16. EXAMPLE OF RAW FREE-SURFACE DATA AND JUMP TOE SELECTION AT NINE DIFFERENT TIME STEPS. TIME STEPS BETWEEN GRAPHS: 35 HZ (EXPERIMENT I_FD: $Fr_l = 3.8$, $Re = 9.5 \times 10^4$	60
FIGURE 3-17. CORRELATION FUNCTIONS OF THE RAW LIDAR SIGNAL OF A DRY CHANNEL BED	62
FIGURE 3-18. TEMPORAL VARIATION OF 20 FREE-SURFACE PROFILES WITH 1 S TIME STEPS; COMPARISON OF MODES 1 AND 2. MEDIAN PROFILES IN RED (CONFIGURATION II, EXPERIMENT CHJ_S2.1: $Fr_l = 4.6$, $Re = 1 \times 10^5$	64
FIGURE 3-19. LOAD CELL POST-PROCESSING FLOW CHART OF BASIC FORCE PARAMETERS.....	66
FIGURE 3-20. VERTICAL FORCE DIAGRAM AND DEFINITION OF RELEVANT FORCES.....	67
FIGURE 3-21. ESTIMATION OF THE LOCAL TIME-AVERAGED VOID FRACTION; EXAMPLE OF VOID FRACTION DATA FOR EXPERIMENT H: $Fr_l = 3.8$, $Re = 6.2 \times 10^4$, $x/d_l = 3$ - FULLY DEVELOPED INFLOW CONDITIONS.....	68
FIGURE 3-22. LOCATION OF THE MEAN JUMP TOE POSITION IN SELECTED HYDRAULIC JUMPS.....	69
FIGURE 3-23. DISCHARGE FLUCTUATIONS DURING ACCURACY TEST OF FLOW RATES.....	69
FIGURE 3-24. SENSITIVITY ANALYSIS OF THE PROBABILITY MASS FUNCTION OF THE RAW AND HIGH-PASS FILTERED SIGNAL OF THE LIDAR MEASUREMENTS OF THE CHANNEL BED.....	71
FIGURE 3-25. EXAMPLES OF RAW FORCE SIGNALS FOR DRY CONDITION.....	73
FIGURE 3-26. VALIDATION OF THE SIX-AXIS LOAD CELL PERFORMANCE IN DRY CONDITIONS.....	74
FIGURE 3-27. VALIDATION OF FORCE MEASUREMENTS WITH THE SIX-AXIS LOAD CELL IN UNIFORM FLOW CONDITIONS.....	75
FIGURE 4-1. AERATION FEATURES IN THE HYDRAULIC JUMP.....	80
FIGURE 4-2. FLOW PATTERNS IN HYDRAULIC JUMPS IN THE PRESENT STUDY.....	81
FIGURE 4-3. FREE-SURFACE PROFILES IN THE SUPERCRITICAL REGION DOWNSTREAM OF A SLUICE GATE. COMPARISON OF FLOW DEPTH MEASUREMENTS WITH POINTER GAUGE (PG) AND CONDUCTIVITY PROBE (CP).....	83
FIGURE 4-4. VELOCITY DISTRIBUTIONS AT SEVERAL CROSS-SECTIONS DOWNSTREAM OF THE SLUICE GATE. COMPARISON OF ESTIMATED BOUNDARY LAYER THICKNESS AND EQUATION 4.2.....	84
FIGURE 4-5. INFLOW CONDITIONS UPSTREAM OF HYDRAULIC JUMPS. EXPERIMENT E: $Fr_l = 8.5$, $Re = 7.5 \times 10^4$	84
FIGURE 4-6. COMPARISON IN THE FLOW PATTERNS BETWEEN HYDRAULIC JUMPS WITH FULLY AND PARTIALLY DEVELOPED INFLOW CONDITIONS.....	85

FIGURE 4-7. COMPARISON OF VOID FRACTION DISTRIBUTIONS FOR FULLY (FD) AND PARTIALLY (PD) DEVELOPED INFLOW CONDITIONS AT SEVERAL CROSS SECTIONS ALONG THE HYDRAULIC JUMP: EXPERIMENT B: $Fr_l = 5.1$, $Re = 6.2 \times 10^4$. COMPARISON WITH THE ADVECTIVE DIFFUSION EQUATION FOR AIR BUBBLES IN HYDRAULIC JUMPS (EQUATIONS 2.7A AND 2.7B: DOTTED LINE = FULLY DEVELOPED INFLOW CONDITIONS; DASHED LINES = PARTIALLY DEVELOPED INFLOW CONDITIONS)..... 86

FIGURE 4-8. COMPARISON OF BUBBLE COUNT RATE DISTRIBUTIONS FOR A HYDRAULIC JUMP WITH FULLY (FD) AND PARTIALLY (PD) DEVELOPED INFLOW CONDITIONS: EXPERIMENT F: $Fr_l = 8.4$, $Re = 1.2 \times 10^5$ 87

FIGURE 4-9. COMPARISON OF THE INTERFACIAL VELOCITY DISTRIBUTIONS FOR FULLY (FD) AND PARTIALLY (PD) DEVELOPED INFLOW CONDITIONS AT DIFFERENT CROSS-SECTIONS ALONG THE HYDRAULIC JUMP: EXPERIMENT F: $Fr_l = 8.0$, $Re = 1.2 \times 10^5$ 89

FIGURE 4-10. DISTRIBUTION OF TIME-AVERAGED BUBBLE CHORD TIMES FOR HYDRAULIC JUMPS WITH FULLY (FD) AND PARTIALLY (PD) DEVELOPED INFLOW CONDITIONS: EXPERIMENT E: $Fr_l = 8.5$, $Re = 7.5 \times 10^4$. DOTTED LINES REPRESENT THE CROSS-SECTION POSITION AND DASHED LINES INDICATE THE BUBBLE COUNT RATE DISTRIBUTIONS..... 90

FIGURE 4-11. PDF OF THE AIR BUBBLE CHORD TIMES FOR $y = Y_{Fmax,SR}$ AT DIFFERENT CROSS-SECTIONS ALONG THE HYDRAULIC JUMP FOR FULLY (FD) AND PARTIALLY (PD) DEVELOPED INFLOW CONDITIONS..... 91

FIGURE 4-12. DISTRIBUTIONS OF AIR-WATER AUTO- AND CROSS-CORRELATION TIME SCALES FOR HYDRAULIC JUMPS WITH FULLY (FD) AND PARTIALLY (PD) DEVELOPED INFLOW CONDITIONS. DASHED LINES = $Y_{Fmax,SR}$, AND DOTTED-DASHED LINES = Y_{Cmin} 93

FIGURE 4-13. COMPARISON ON THE DECAY OF CHARACTERISTIC VOID FRACTION PARAMETERS FOR HYDRAULIC JUMPS WITH FULLY (FD) AND PARTIALLY (PD) DEVELOPED INFLOW CONDITIONS..... 95

FIGURE 4-14. COMPARISON IN CHARACTERISTIC VOID FRACTION PARAMETERS IN HYDRAULICS JUMPS WITH FULLY (FD) AND PARTIALLY (PD) DEVELOPED INFLOW CONDITIONS 95

FIGURE 4-15. COMPARISON OF THE DECAY IN DIMENSIONLESS DIFFUSIVITY FOR HYDRAULIC JUMPS WITH FULLY AND PARTIALLY DEVELOPED INFLOW CONDITIONS..... 96

FIGURE 4-16. COMPARISON OF THE DECAY IN CHARACTERISTIC BUBBLE COUNT RATE PARAMETERS FOR HYDRAULIC JUMPS WITH FULLY (FD) AND PARTIALLY (PD) DEVELOPED INFLOW CONDITIONS..... 97

FIGURE 4-17. COMPARISON OF CHARACTERISTIC ELEVATIONS FOR HYDRAULIC JUMPS WITH FULLY (FD) AND PARTIALLY (PD) DEVELOPED INFLOW CONDITIONS..... 98

FIGURE 4-18. MAXIMUM INTERFACIAL VELOCITY DECAY FOR HYDRAULIC JUMPS WITH FULLY (FD) AND PARTIALLY (PD) DEVELOPED INFLOW CONDITIONS..... 99

FIGURE 4-19. MODE OF THE CHORD TIME DISTRIBUTION FOR $y = Y_{FMAX,SR}$ FOR HYDRAULIC JUMPS WITH FULLY (FD) AND PARTIALLY (PD) DEVELOPED INFLOW CONDITIONS..... 100

FIGURE 4-20. COMPARATIVE ANALYSIS OF SCALE EFFECTS IN THE AIR-WATER FLOW PROPERTIES FOR HYDRAULIC JUMPS WITH FULLY DEVELOPED INFLOW CONDITIONS (FD) USING A FROUDE SIMILITUDE..... 101

FIGURE 4-21. COMPILATION OF THE AIR-WATER FLOW PARAMETERS IN HYDRAULIC JUMPS WITH FULLY DEVELOPED INFLOW CONDITIONS..... 103

FIGURE 5-1. PHOTOS OF FREE-SURFACE PROFILES IN A HYDRAULIC JUMP WITH TIME STEPS OF 0.1 s, EXPERIMENT E: $Fr_l = 8.5$, $Re = 7.5 \times 10^4$, FULLY DEVELOPED INFLOW CONDITIONS. FLOW FROM RIGHT TO LEFT..... 106

FIGURE 5-2. TYPICAL BASIC FREE-SURFACE CHARACTERISTICS IN A HYDRAULIC JUMP MEASURED WITH A LIDAR AND COMPARISON WITH PREVIOUS LITERATURE. EXPERIMENT C: $Fr_l = 7.0$, $Re = 6.2 \times 10^4$, FULLY DEVELOPED INFLOW CONDITIONS. P: PIEZOMETER, PG: POINTER GAUGE, ADM: ACOUSTIC DISPLACEMENT METER..... 109

FIGURE 5-3. TIME-AVERAGED FREE-SURFACE PROFILES OF HYDRAULIC JUMPS IN THE PRESENT STUDY WITH FREE-JUMP TOE MOVEMENT (MODE 1) AND FULLY (FD) AND PARTIALLY (PD) DEVELOPED INFLOW CONDITIONS AND COMPARISON WITH PREVIOUS LITERATURE WITH PARTIALLY AND UNDEVELOPED INFLOW CONDITIONS (WG: WIRE GAUGE, PG: POINTER GAUGE, ADM: ACOUSTIC DISPLACEMENT METER).....	111
FIGURE 5-4. CONJUGATE DEPTH RATIO AND SHEAR STRESS AS FUNCTION OF THE FROUDE NUMBER IN HYDRAULIC JUMPS WITH FULLY (FD) AND PARTIALLY (PD) DEVELOPED INFLOW CONDITIONS.....	112
FIGURE 5-5. COMPARISON OF JUMP LENGTH IN THE PRESENT STUDY WITH PREVIOUS OBSERVATIONS OF JUMP AND ROLLER LENGTHS AND WITH THE SEMI-EMPIRICAL EQUATION OF HAGER ET AL. (1990).....	113
FIGURE 5-6. TIME-AVERAGED FREE-SURFACE PROFILES MEASURED WITH THE LIDAR IN HYDRAULIC JUMPS WITH FULLY (FD) AND PARTIALLY (PD) DEVELOPED INFLOW CONDITIONS.....	114
FIGURE 5-7. FREE-SURFACE FLUCTUATIONS OF HYDRAULIC JUMPS WITH FULLY (FD) AND PARTIALLY (PD) DEVELOPED INFLOW CONDITIONS AND COMPARISON WITH PREVIOUS LITERATURE (WG: WIRE GAUGE, ADM: ACOUSTIC DISPLACEMENT METER).....	116
FIGURE 5-8. MAXIMUM FREE-SURFACE FLUCTUATIONS FOR DIFFERENT INFLOW FROUDE NUMBERS; COMPARISON OF PRESENT DATA FOR MODES 1 AND 2 AND FULLY (FD) AND PARTIALLY (PD) DEVELOPED INFLOW CONDITIONS WITH PREVIOUS DATA AND EQUATION 5.2.....	117
FIGURE 5-9. RAW DATA OF JUMP TOE OSCILLATIONS MEASURED WITH THE LIDAR.....	119
FIGURE 5-10. BOX AND WHISKER PLOT OF JUMP TOE OSCILLATIONS. LOWER AND HIGHER WHISKERS PRESENT MINIMUM AND MAXIMUM OSCILLATIONS, LOWER AND HIGHER EXTERNAL LINES PRESENT THE 25 TH AND 75 TH PERCENTILES; RED MIDDLE LINE REPRESENTS THE MEDIAN.....	120
FIGURE 5-11. JUMP TOE OSCILLATIONS AS FUNCTION OF INFLOW FROUDE NUMBER FOR HYDRAULIC JUMPS WITH FULLY (FD) AND PARTIALLY (PD) DEVELOPED INFLOW CONDITIONS; COMPARISON OF PRESENT RESULTS WITH PREVIOUS OBSERVATIONS AND EQUATION 5.3.....	122
FIGURE 5-12. COMPARISON OF THE JUMP TOE CHARACTERISTIC FREQUENCIES BETWEEN HYDRAULIC JUMPS WITH FULLY (FD) AND PARTIALLY (PD) DEVELOPED INFLOW CONDITIONS.....	123
FIGURE 5-13. FFT ANALYSIS AND CHARACTERISTIC FREQUENCIES FOR A HYDRAULIC JUMP WITH FREE MOVING JUMP TOE (MODE 1), EXPERIMENT C: $Fr_l = 7.0$, $Re = 6.2 \times 10^4$, FULLY DEVELOPED INFLOW CONDITIONS.....	124
FIGURE 5-14. CHARACTERISTIC FREQUENCIES IN HYDRAULIC JUMPS WITH FREE-MOVING JUMP TOE (MODE 1) AND FULLY (FD) AND PARTIALLY (PD) DEVELOPED INFLOW CONDITIONS. RED SYMBOLS: DOMINANT FREQUENCY; BLUE SYMBOLS: SECONDARY FREQUENCY; GREEN SYMBOLS: TWO DOMINANT FREQUENCIES. BLACK LINE: MEAN FLOW DEPTH d/d_l	125
FIGURE 5-15. CHARACTERISTIC FREQUENCIES FOR HYDRAULIC JUMPS WITH FULLY (FD) AND PARTIALLY (PD) DEVELOPED INFLOW CONDITIONS AS FUNCTION OF THE FROUDE NUMBER.....	126
FIGURE 5-16. FFT ANALYSIS AND CHARACTERISTIC FREQUENCIES FOR A HYDRAULIC JUMP WITH FIXED JUMP TOE (MODE 2), EXPERIMENT C: $Fr_l = 7.0$, $Re = 6.2 \times 10^4$, FULLY DEVELOPED INFLOW CONDITIONS..	127
FIGURE 5-17. CHARACTERISTIC FREQUENCIES FOR HYDRAULIC JUMPS WITH FULLY DEVELOPED INFLOW CONDITIONS WITH FIXED JUMP TOE (MODE 2). RED SYMBOLS: DOMINANT FREQUENCY; BLUE SYMBOLS: SECONDARY FREQUENCY; GREEN SYMBOLS: TWO DOMINANT FREQUENCIES. BLACK LINE: MEAN FLOW DEPTH d/d_l	128
FIGURE 5-18. CHARACTERISTIC FREE-SURFACE FREQUENCY REGIONS IN HYDRAULIC JUMPS.....	129
FIGURE 5-19. FREE-SURFACE AUTO-CORRELATION TIME SCALES ALONG HYDRAULIC JUMPS WITH FULLY (FD) AND PARTIALLY (PD) DEVELOPED INFLOW CONDITIONS.....	131
FIGURE 5-20. FREE-SURFACE AUTO-CORRELATION TIME SCALES ALONG HYDRAULIC JUMPS WITH FULLY	132

(FD) AND PARTIALLY (PD) DEVELOPED INFLOW CONDITIONS FOR MODE 1.....

FIGURE 5-21. FREE-SURFACE AUTO-CORRELATION TIME SCALES ALONG HYDRAULIC JUMPS WITH FULLY (FD) AND PARTIALLY (PD) DEVELOPED INFLOW CONDITIONS FOR MODE 2..... 133

FIGURE 5-22. FREE-SURFACE AUTO-CORRELATION TIME SCALES FOR HYDRAULIC JUMPS WITH FULLY (FD) AND PARTIALLY (PD) DEVELOPED INFLOW CONDITIONS..... 134

FIGURE 5-23. DIMENSIONLESS CROSS-CORRELATION INTEGRAL FREE-SURFACE TIME SCALES IN HYDRAULIC JUMPS WITH FULLY (FD) AND PARTIALLY (PD) DEVELOPED INFLOW CONDITIONS FOR MODE 1. EXPERIMENT C ($Fr_l = 7.0$, $Re = 6.2 \times 10^4$)..... 136

FIGURE 5-24. MAXIMUM CROSS-CORRELATION COEFFICIENTS ALONG A HYDRAULIC JUMP..... 137

FIGURE 5-25. MAXIMUM CROSS-CORRELATION COEFFICIENTS IN HYDRAULIC JUMPS WITH FULLY (FD) AND PARTIALLY (PD) DEVELOPED INFLOW CONDITIONS AS FUNCTION OF THE NORMALIZED DIMENSIONLESS SEPARATION DISTANCE; COMPARISON WITH EQUATION 5.5 AND ADM DATA AND EMPIRICAL EQUATION OF CHACHEREAU AND CHANSON (2011B)..... 138

FIGURE 5-26. INTEGRAL FREE-SURFACE LENGTH SCALES ALONG HYDRAULIC JUMPS WITH FULLY (FD) AND PARTIALLY (PD) DEVELOPED INFLOW CONDITIONS..... 140

FIGURE 5-27. INTEGRAL FREE-SURFACE LENGTH SCALES ALONG HYDRAULIC JUMPS WITH FULLY DEVELOPED INFLOW CONDITIONS (FD) FOR MODE 2..... 141

FIGURE 5-28. MAXIMUM INTEGRAL FREE-SURFACE LENGTH SCALES AS FUNCTION OF THE INFLOW FROUDE NUMBER IN HYDRAULIC JUMPS WITH FULLY (FD) AND PARTIALLY (PD) DEVELOPED INFLOW CONDITIONS; COMPARISON WITH EQUATION 5.6 FOR MODE 2..... 142

FIGURE 5-29. SCALE EFFECTS IN FREE-SURFACE FEATURES IN HYDRAULIC JUMPS WITH FULLY (FD) AND PARTIALLY (PD) DEVELOPED INFLOW CONDITIONS..... 144

FIGURE 5-30. SCALE EFFECTS IN FREE-SURFACE TURBULENT SCALES IN HYDRAULIC JUMPS WITH FULLY (FD) AND PARTIALLY (PD) DEVELOPED INFLOW CONDITIONS..... 145

FIGURE 5-31. COMPILATION OF THE FREE-SURFACE PARAMETERS IN THE HYDRAULIC JUMP – MODE 1 (EXPERIMENT I: $Fr_l = 3.8$, $Re = 9.5 \times 10^5$ FULLY DEVELOPED INFLOW CONDITIONS)..... 147

FIGURE 6-1. TRAJECTORY OF THE INSTANTANEOUS FORCES UPON A SUBMERGED SPHERE INSIDE A HYDRAULIC JUMP (EXPERIMENT F: $Fr_l = 8.0$, $Re = 1.2 \times 10^5$, $x/d_l = 20$, $y/d_l = 2.1$, FULLY DEVELOPED INFLOW CONDITIONS)..... 150

FIGURE 6-2. VERTICAL MEASUREMENT POSITIONS AT FIVE DIFFERENT CROSS-SECTIONS ALONG THE HYDRAULIC JUMP. EXPERIMENT E: $Fr_l = 8.5$, $Re = 7.5 \times 10^4$, PARTIALLY DEVELOPED INFLOW CONDITIONS 151

FIGURE 6-3. DISTRIBUTION OF THE TIME-AVERAGED FORCES AT DIFFERENT CROSS-SECTIONS ALONG A HYDRAULIC JUMP (EXPERIMENT F: $Fr_l = 8.0$, $Re = 1.2 \times 10^5$, FULLY DEVELOPED INFLOW CONDITIONS)..... 154

FIGURE 6-4. TWO-DIMENSIONAL DISTRIBUTION OF THE TIME-AVERAGED FORCES IN HYDRAULIC JUMPS IN THE CHANNEL CENTRELINE: EXPERIMENT A: $Fr_l = 5.1$, $Re = 8.3 \times 10^4$ – FULLY DEVELOPED INFLOW CONDITIONS..... 156

FIGURE 6-5. COMPARISON OF DISTRIBUTIONS OF FORCE FLUCTUATIONS IN x , y AND z -DIRECTIONS ALONG SELECTED HYDRAULIC JUMPS..... 157

FIGURE 6-6. CONTOUR PLOTS OF THE FORCE FLUCTUATIONS IN A HYDRAULIC JUMP. EXPERIMENT F: $Fr_l = 8.0$, $Re = 1.2 \times 10^5$ – FULLY DEVELOPED INFLOW CONDITIONS..... 159

FIGURE 6-7. DISTRIBUTIONS OF THE CHARACTERISTIC FREQUENCIES OF THE MOTIONS OF THE SUBMERGED SPHERE INSIDE THE HYDRAULIC JUMP. EXPERIMENT A: $Fr_l = 5.1$, $Re = 8.3 \times 10^5$ – FULLY DEVELOPED..... 160

FIGURE 6-8. STROUHAL NUMBER OF THE CROSS-SECTIONAL AVERAGED DOMINANT FREQUENCIES AS A FUNCTION OF Fr_l 161

FIGURE 6-9. DISTRIBUTION OF THE STROUHAL NUMBER OF THE STREAMWISE DOMINANT FREQUENCIES ESTIMATED BASED UPON THE SPHERE DIAMETER AND THE INTERFACIAL VELOCITY.....	162
FIGURE 6-10. COMPARISON OF THE STREAMWISE, TRANSVERSE AND VERTICAL AUTO-CORRELATION TIME SCALES OF THE FORCES ON A SUBMERGED SPHERE IN A HYDRAULIC JUMP. EXPERIMENT B: $Fr_l = 5.1, Re = 6.2 \times 10^4$ – FULLY DEVELOPED.....	164
FIGURE 6-11. DECAY OF FORCE PARAMETERS ALONG HYDRAULIC JUMPS WITH FULLY DEVELOPED INFLOW CONDITIONS (FD).....	167
FIGURE 6-12. DECAY OF FREQUENCY PARAMETERS ALONG HYDRAULIC JUMPS WITH FULLY DEVELOPED INFLOW CONDITIONS (FD). DASHED LINES = COMPARISON WITH EQUATIONS 6.6 AND 6.7.....	168
FIGURE 6-13. COMPARISON OF THE TIME-AVERAGED FORCES BETWEEN HYDRAULIC JUMPS WITH FULLY (FD) AND PARTIALLY (PD) DEVELOPED INFLOW CONDITIONS.....	170
FIGURE 6-14. COMPARISON OF THE MAXIMUM FORCE FLUCTUATIONS FOR HYDRAULIC JUMPS WITH FULLY (FD) AND PARTIALLY (PD) DEVELOPED INFLOW CONDITIONS.....	171
FIGURE 6-15. COMPARISON OF THE DIMENSIONLESS DOMINANT FREQUENCY FOR HYDRAULIC JUMPS WITH FULLY (FD) AND PARTIALLY (PD) DEVELOPED INFLOW CONDITIONS.....	172
FIGURE 6-16. SCALE EFFECTS IN THE FORCE PARAMETERS IN HYDRAULIC JUMPS WITH FULLY DEVELOPED INFLOW CONDITIONS.....	176
FIGURE 6-17. COMPILATION OF THE INTERNAL FORCES MEASURED OVER A SPHERE IN A HYDRAULIC JUMP WITH FULLY DEVELOPED INFLOW CONDITIONS (EXPERIMENT E: $Fr_l = 8.2, Re = 7.5 \times 10^4$, FULLY DEVELOPED INFLOW CONDITIONS).....	178
FIGURE 7-1. SUMMARY OF CHARACTERISTIC AIR-WATER FLOW AND FORCE PARAMETERS FOR ALL HYDRAULIC JUMPS WITH FULLY DEVELOPED INFLOW CONDITIONS; DEFINITION OF HYDRAULIC JUMP REGIONS.....	183
FIGURE 7-2. CONTOUR PLOTS OF TIME-AVERAGED AIR-WATER FLOW PROPERTIES AND FORCE PARAMETERS IN HYDRAULIC JUMPS WITH FULLY DEVELOPED INFLOW CONDITIONS. WJSR: WALL JET SHEAR REGION; ASR: ADVECTIVE SHEAR REGION; RR: RECIRCULATION REGION.....	186
FIGURE 7-3. SUMMARY OF THE TIME-AVERAGED PROPERTIES IN A HYDRAULIC JUMP WITH FULLY DEVELOPED INFLOW CONDITIONS (EXPERIMENT F: $Fr_l = 8.0, Re = 1.2 \times 10^5$).....	187
FIGURE 7-4. SIMILARITY IN FLUCTUATIONS ALONG HYDRAULIC JUMPS WITH FULLY DEVELOPED INFLOW CONDITIONS.....	188
FIGURE 7-5 CHARACTERISTIC FREQUENCIES OF THE MOTIONS IN HYDRAULIC JUMPS WITH FULLY DEVELOPED INFLOW CONDITIONS (EXPERIMENT B: $Fr_l = 5.1, Re = 6.2 \times 10^4$).....	190
FIGURE 7-6 AUTO-CORRELATION TIME SCALES IN A HYDRAULIC JUMP WITH FULLY DEVELOPED INFLOW CONDITIONS (EXPERIMENT F: $Fr_l = 8.0, Re = 1.2 \times 10^5$).....	191
FIGURE 7-7 CONCEPTUAL SKETCH OF THE EFFECTS OF THE INFLOW CONDITIONS ON THE FLOW FEATURES OF HYDRAULIC JUMPS WITH PARTIALLY AND FULLY DEVELOPED INFLOW CONDITIONS; FIGURES ADAPTED AND EXTENDED FROM TAKAHASHI AND OHTSU (2017).....	194

LIST OF TABLES

TABLE 1-1. HYDRAULIC JUMP TYPES IN HORIZONTAL CHANNELS BASED UPON INFLOW FROUDE NUMBER (CHOW 1973; PETERKA 1984; HAGER 1992; CHANSON 2004).....	5
TABLE 2-1. EXPERIMENTAL STUDIES OF INTERNAL ENERGETIC PROCESSES IN HYDRAULIC JUMPS.....	17
TABLE 2-2. RESEARCH OF AIR-WATER FLOW PROPERTIES IN HYDRAULIC JUMPS ON SMOOTH HORIZONTAL CHANNEL BED.....	22
TABLE 2-3. INSTRUMENTATION TO MEASURE THE AIR-WATER PROPERTIES IN HYDRAULIC JUMPS.....	25
TABLE 2-4. EXPERIMENTAL STUDIES OF FREE-SURFACE CHARACTERISTICS IN HYDRAULIC JUMPS.....	29
TABLE 2-5. MEASUREMENT OF FORCES AND PRESSURES IN HYDRAULIC JUMPS.....	30
TABLE 2-6. HYDRAULIC JUMPS PARAMETERS IN RECTANGULAR CHANNELS CONSIDERED IN THE PRESENT STUDY.....	35
TABLE 2-7. INVESTIGATION OF SCALE EFFECTS IN HYDRAULIC JUMPS.....	36
TABLE 2-8. SUMMARY OF SCALE EFFECTS IN TERMS OF FROUDE SIMILITUDE IN HYDRAULIC JUMPS BASED ON PREVIOUS LITERATURE (CHANSON 2006; 2007a, MURZYN AND CHANSON 2008; CHANSON AND GUALTIERI 2008; CHANSON AND CHACHEREAU 2013; WANG 2014; FELDER AND CHANSON 2016a, 2018).....	38
TABLE 2-9. THESIS OUTLINE.....	40
TABLE 3-1. RANGE OF VARIATION OF BASIC AIR-WATER FLOW PROPERTIES IN HYDRAULIC JUMPS MEASURED WITH A CONDUCTIVITY PROBE	70
TABLE 3-2. EXPERIMENTAL FLOW CONDITIONS IN THE PRESENT STUDY.....	76
TABLE 4-1. EXPERIMENTAL FLOW CONDITIONS FOR MEASUREMENTS OF AIR-WATER FLOW PROPERTIES..	78
TABLE 4-2. EMPIRICAL EQUATIONS OF THE DECAY IN CHARACTERISTIC VOID FRACTION PARAMETERS...	94
TABLE 4-3. SUMMARY TABLE OF THE EFFECT OF THE INFLOW CONDITIONS AND SCALE EFFECTS IN THE AERATION FEATURES IN HYDRAULIC JUMPS.....	103
TABLE 5-1. EXPERIMENTAL FLOW CONDITIONS FOR LIDAR MEASUREMENTS OF THE FREE-SURFACE.....	107
TABLE 5-2. JUMP TOE OSCILLATIONS IN FULLY AND PARTIALLY DEVELOPED HYDRAULIC JUMPS MEASURED WITH THE LIDAR.....	121
TABLE 5-3. SUMMARY TABLE OF THE EFFECT OF THE INFLOW CONDITIONS AND SCALE EFFECTS ON THE FREE-SURFACE PARAMETERS OF HYDRAULIC JUMPS.....	148
TABLE 6-1. EXPERIMENTAL FLOW CONDITIONS FOR MEASUREMENTS OF INTERNAL MOTIONS IN HYDRAULIC JUMPS USING A SUBMERGED SPHERE.....	152
TABLE 6-2. SUMMARY TABLE OF THE EFFECT OF THE INFLOW CONDITIONS AND SCALE EFFECTS IN THE INTERNAL MOTIONS IN THE HYDRAULIC JUMP.....	178
TABLE 7-1. SCALE EFFECTS IN FULLY DEVELOPED HYDRAULIC JUMPS.....	194
TABLE 7-2. LEVEL OF AERATION, FORCES AND FLUCTUATIONS BASED UPON THE LOCATION OF INTEREST IN THE HYDRAULIC JUMP.....	197

LIST OF SYMBOLS

Symbol	Description	Units
A	Area of an object exposed to the fluid	m ²
A_1	Cross-sectional area upstream of the hydraulic jump	m ²
A_2	Cross-sectional area downstream of the hydraulic jump	m ²
C	Local time-averaged void fraction	-
C_{avg}	Local time-averaged void fraction around the sphere	-
C_d	Drag coefficient	-
C_{max}	Maximum void fraction in a cross-section	-
C_{mean}	Mean void fraction in a cross-section ($C_{mean} = \frac{1}{Y_{90}} \int_{y=0}^{y=Y_{90}} C \times dy$)	-
C_{min}	Minimum void fraction in a cross-section	-
c	Instantaneous void fraction	-
D_t	Air bubble diffusivity coefficient	m/s ²
$D^\#$	Dimensionless diffusivity coefficient in the shear region	-
D^*	Dimensionless diffusivity coefficient in the recirculation region	-
d	Flow depth	m
d'	Free-surface fluctuations	m
d_1	Conjugate flow depth upstream of the hydraulic jump	m
d_{90}	Equivalent clear-water flow depth with an upper integration limit of Y_{90}	m
d_{95}	Equivalent clear-water flow depth with an upper integration limit of Y_{95}	m
d_{98}	Equivalent clear-water flow depth with an upper integration limit of Y_{98}	m
d_{max}'	Maximum free-surface fluctuations	m
d_2	Conjugate flow depth downstream of the hydraulic jump	m
F	Bubble count rate	Hz
$F_{buoyancy}$	Buoyancy force	N
F_D	Drag force	N
$F_{Dx,measured}$	Measured streamwise drag force	N
$F_{Dx,theory}$	Theoretical streamwise drag force	N
F_{Dy}	Vertical drag force	N
F_{maxSR}	Maximum bubble count rate peak in the shear region	Hz
F_{maxRR}	Maximum bubble count rate peak in the recirculation region	Hz
$F_{w/s}$	Total incoming force upstream the hydraulic jump ($F_{w/s} = F_l + \rho d_l V_l$)	N
F_x	Time-averaged streamwise force	N
F_x'	Streamwise force fluctuations	N
F_{x_zero}	Initial recording of the time-averaged streamwise force without any load	N
f_x	Instantaneous streamwise force	N
f_{x_HJ}	Instantaneous streamwise force before subtracting F_{x_zero}	N
F_y	Time-averaged vertical force	N
F_y'	Vertical force fluctuations	N
F_{y_zero}	Initial recording of the time-averaged vertical force without any load	N
f_y	Instantaneous vertical force	N
f_{y_HJ}	Instantaneous vertical force before subtracting F_{y_zero}	N

F_z	Time-averaged transverse force	N
F_z'	Transverse force fluctuations	N
F_{z_zero}	Initial recording of the time-averaged transverse force without any load	N
f_z	Instantaneous transverse force	N
f_{z_HJ}	Instantaneous transverse force before subtracting F_{z_zero}	N
F_1	Hydrostatic force upstream of the hydraulic jump	N
F_2	Hydrostatic force downstream of the hydraulic jump	N
F_τ	Shear force	N
Fr_0	Froude number at the sluice gate position	-
Fr_1	Inflow Froude number	-
$freq_{toe}$	Characteristic jump toe frequency	Hz
$freq_{fs(dom)}$	Dominant free-surface frequency	Hz
$freq_{fs(sec)}$	Secondary free-surface frequency	Hz
$freq_{F_x,dom}$	Dominant frequency of the streamwise forces	Hz
$freq_{F_z,dom}$	Dominant frequency of the transverse forces	Hz
$freq_{F_y,dom}$	Dominant frequency of the vertical forces	Hz
$freq_p$	Characteristic frequency of pressure fluctuations	Hz
g	Gravitational acceleration	m/s ²
H_1	Total head upstream of the hydraulic jump	m
H_2	Total head downstream of the hydraulic jump	m
h_{bp}	Baffle block height	m
h_0	Sluice gate opening	m
k_s	Roughness height	m
L	Length of the channel	m
L_{fs}	Streamwise free-surface integral length scales	m
L_{fs_max}	Maximum free-surface length scales	m
L_j	Hydraulic jump length	m
L_r	Roller length	m
M_x	Longitudinal Momentum	Nm
M_y	Vertical Momentum	Nm
M_z	Transverse Momentum	Nm
Mo	Morton number	-
N	Total number of samples	-
N_{CP}	Power law exponent of the velocity distribution	-
p'	Pressure fluctuations	Pa
P_d	Dynamic Pressure	Pa
Q	Flow rate	m ³ /s
q	Flow rate per unit of width	m ² /s
$R_{air,auto}$	Auto-correlation coefficient of the air-water interfaces	-
$R_{air,auto_min}$	Minimum auto-correlation coefficient of the air-water interfaces	-
$R_{air,cross}$	Longitudinal cross-correlation coefficient of the air-water interfaces	-
$R_{air,cross_max}$	Maximum longitudinal cross-correlation coefficient of the air-water interfaces	-
$R_{air,cross_min}$	Minimum longitudinal cross-correlation coefficient of the air-water interfaces	-
$R_{fs,auto}$	Auto-correlation function of the free-surface elevations	-
$R_{fs,auto_min}$	Minimum auto-correlation coefficient of the free-surface elevations	-

$R_{fs,cross}$	Longitudinal cross-correlation function of the free-surface elevations	-
$R_{fs,cross_max}$	Maximum longitudinal cross-correlation coefficient of the free-surface elevations	-
$R_{fs,cross_min}$	Minimum longitudinal cross-correlation coefficient of the free-surface elevations	-
r	Radius of sphere	m
Re	Reynolds number	-
T	Average travel time of the air-water flow	s
t	time	s
$T_{air,auto}$	Air-water auto-correlation time scale	s
$T_{air,cross}$	Longitudinal air-water cross-correlation time scale	s
t_{ch}	Chord time	s
$t_{ch,mean}$	Time averaged chord time	s
$T_{fs,auto}$	Free-surface auto-correlation time scale	s
$T_{fs,cross}$	Longitudinal free-surface cross-correlation time scale	s
u'	Velocity fluctuation	m/s
V	Time-averaged velocity	m/s
V_{CP}	Interfacial velocity	m/s
V_{max}	Maximum interfacial velocity in the shear region	m/s
V_{recir}	Average interfacial velocity in the recirculation region	m/s
V_1	Inflow velocity upstream of the hydraulic jump	m/s
V_2	Velocity downstream of the hydraulic jump	m/s
W	Width of the channel	m
We	Weber number	-
x	Longitudinal distance relative to the mean jump toe position	m
x_{sg}	Distance from the sluice gate	m
x_{toe}	Instantaneous jump toe position relative to the mean jump location	m
x_{toe_max}	Maximum jump toe oscillation	m
x_{toe_min}	Minimum jump toe oscillation	m
Y_{Cmax}	Characteristic depth where $C = C_{max}$	m
Y_{Cmin}	Characteristic depth where $C = C_{min}$	m
Y_s	Surface of the roller	m
Y_{Vmax}	Characteristic depth where $V_{CP} = V_{max}$	m
Y_{50}	Characteristic depth where $C = 0.5$	m
Y_{90}	Characteristic depth where $C = 0.9$	m
Y_{95}	Characteristic depth where $C = 0.95$	m
Y_{98}	Characteristic depth where $C = 0.98$	m
y	Vertical position above the channel bed	m
$y_{0.5}$	Characteristic depth where $V_{CP} = V_{max}/2$	m
z	Transverse distance relative to the centre line position	m
z_1	Elevation above the datum upstream the hydraulic jump	m
z_2	Elevation above the datum downstream the hydraulic jump	m
δ	Boundary layer thickness	m
ΔH	Rate of energy dissipation	m
ΔP	Amplitude of the pressure fluctuations	Pa
Δx	Longitudinal separation distance between two sampling points measured with the LIDAR	m

Δx_{max}	Maximum longitudinal separation distance between two sampling points	m
Δx_p	Longitudinal separation distance between the conductivity probe tips	m
Δz_p	Transverse separation distance between the conductivity probe tips	m
θ	Slope of the channel	°
λ	Non-dimensional coefficient to correlate velocity fluctuations and pressure fluctuations	-
μ	Dynamic viscosity of water	Ns/m ²
μ_{air}	Dynamic viscosity of air	Ns/m ²
ν	Kinematic viscosity of water	m ² /s
ρ	Density of water	kg/m ³
ρ_{air}	Density of air	kg/m ³
ρ_{air_water}	Density of the air-water mixture	kg/m ³
σ	Surface tension	Nm
τ	Time lag	s
τ_0	Shear stress	N/m ²
\varnothing	Diameter	m
\mathcal{V}	Sphere volume	m ³

LIST OF ABBREVIATIONS

Abbreviations	Description
ADM	Acoustic Displacement Meter
ADV	Acoustic Doppler Velocimeter
ASR	Advective Shear Region
AWCC	Adaptive Window Cross-Correlation
BIV	Bubble Image Velocimetry
CHJ	Classical Hydraulic Jump
CP	Conductivity Probe
FD	Fully Developed inflow Conditions
FFT	Fast Fourier Transformation
IQR	Interquartile Range
LC	Load Cell
LDV	Laser Doppler Velocimeter
LIDAR	LIght Detection and Ranging
NI	National Instruments
PD	Partially Developed inflow conditions
PDF	Probability Distribution Function
PG	Pointer Gauge
PIV	Particle Image Velocimetry
PMF	Probability Mass Function
PST	Phase-Space Thresholding Method
PT	Pitot Tube
TKE	Turbulent Kinetic Energy
UD	Undeveloped flow
UNSW	University of New South Wales
WG	Wire Gauge
WJSR	Wall Jet Shear Region
WRL	Water Research Laboratory

1

INTRODUCTION

The ability to manage and distribute water resources is a crucial factor in the successful development of a society. For example, the success of Greek and Roman civilisations can be associated to the development of hydraulic structures to distribute and manage water supply and water drainage (Wilson 2009). Alyzia dam in Western Greece (Figure 1-1 left) is an example of historical water resource management. Presumably built in the fifth century, it is believed that its role was to provide flood protection to the ancient city of Alyzia (Koutsoyiannis et al. 2008). The stone dam and spillway are still operational today, providing flood protection to nearby communities (Koutsoyiannis et al. 2008). Figure 1-1 (right) shows turbulent flows down the operational spillway with two hydraulic jumps generated due to a tailwater control forcing subcritical flow conditions. While construction techniques, design practises and materials have evolved since the Alyzia dam was built, the dam and the spillway still serve the same purposes today as they did millennia ago providing protection for large floods with effective energy dissipation.

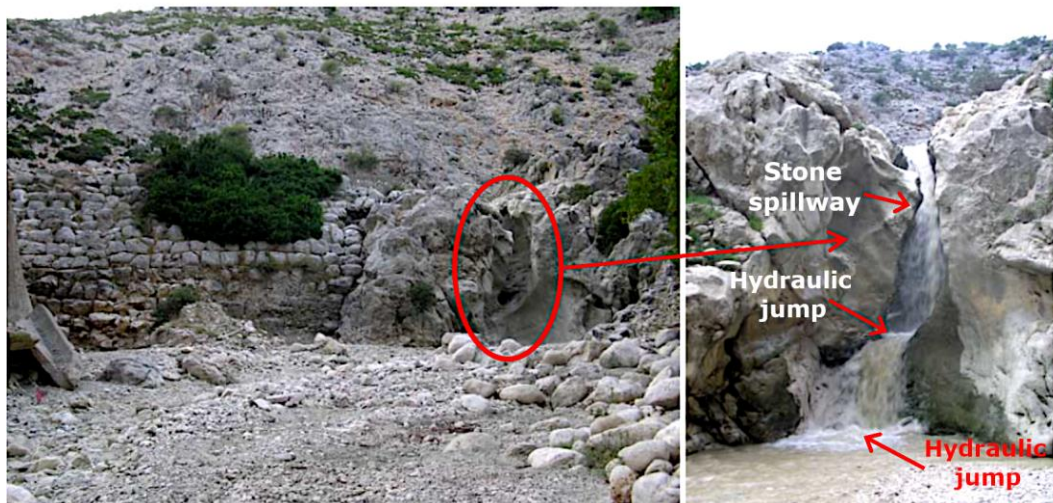


FIGURE 1-1. ALYZIA ANCIENT GREEK DAM. SPILLWAY IN OPERATION AND GENERATION OF HYDRAULIC JUMPS (KOUTSOYIANNIS ET AL. 2008).

Availability of water resources and water management practices are sources of inequality between undeveloped, developing and developed countries. While some undeveloped and developing countries still have deficient sanitation systems which leads to deaths and health problems, appropriate water management and distribution systems are the norm in developed countries (Gleick 1999, 2000). Recently, the adverse impacts of climate change to the global water balance have led to the investigation to improve the water management (Arnell 1999; Lenton and Muller 2009). This international work aims to provide clean water for undeveloped and developing countries while investigating alternatives for the efficient use of water resources worldwide (United Nations 2015). Hydraulic structures, as the physical construction to transport, distribute, and manage the water resources, play a key role in the goal of efficient water management.

Dams are large human-made structures to retain water for water supply, generation of hydroelectric energy, recreational areas and for flood and environmental protection (Altinbilek 2002; Chanson and Carvalho 2015). Worldwide more than 45000 large dams existed at the beginning of the 21st century (Altinbilek 2002). The flood release structures of dams are hydraulic structures designed to convey excess waters in the dam reservoirs. Often these conveyance structures are spillways with an energy dissipation structure at the downstream end which is designed to dissipate the flow energy to prevent river bed erosion further downstream (Chanson and Carvalho 2015). Typical energy dissipation structures are stilling basins which are designed to contain hydraulic jumps at the downstream end of the flow conveyance structure. Hydraulic jump type stilling basins are widely used downstream of spillways due to the simple construction, the high energy dissipation performance and the low risk of cavitation (Hager 1992). Figure 1-2 presents two examples of hydraulic jumps acting as energy dissipaters at a stilling basin downstream of a dam spillway and at a weir structure.



A) MANLY DAM, NEW SOUTH WALES, AUSTRALIA



B) HYDRAULIC JUMP DOWNSTREAM OF THE SCHEMERL-WEIR, NUSSDORF, AUSTRIA (COURTESY OF DR. STEFAN FELDER)

FIGURE 1-2. HYDRAULIC JUMP AS ENERGY DISSIPATER.

A hydraulic jump is an economical and efficient mechanism to dissipate energy as well as to improve water quality conditions. Figure 1-3 presents a typical hydraulic jump with annotation of relevant hydraulic jump features where Q is the flow rate. In addition to the potential to dissipate energy, air-water mass transfer can be enhanced through air entrainment increasing the dissolved oxygen concentration of the flow. In addition, three-dimensional hydraulic jump motions may facilitate mixing processes in industrial applications. Both reaeration and mixing features are also beneficial in applications in wastewater treatment processes. Given the flow characteristics and physical processes which occur within hydraulic jumps, they offer a cost-effective method of dissipating energy, increasing air-water mass transfer and enabling mixing.

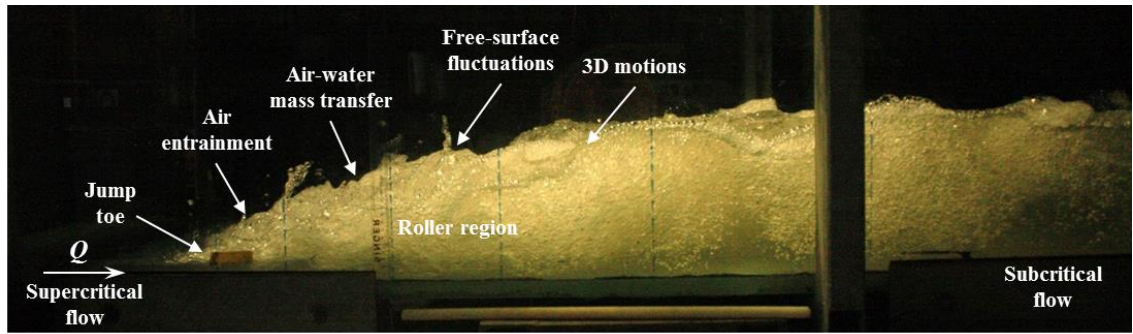
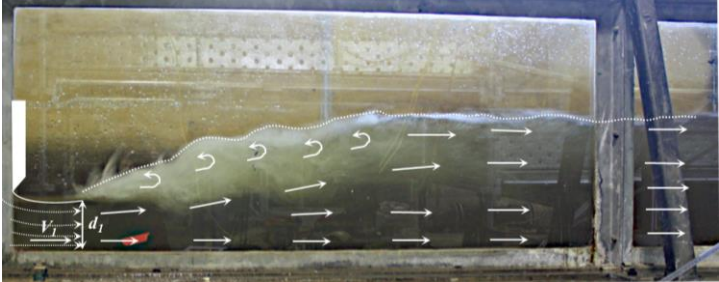
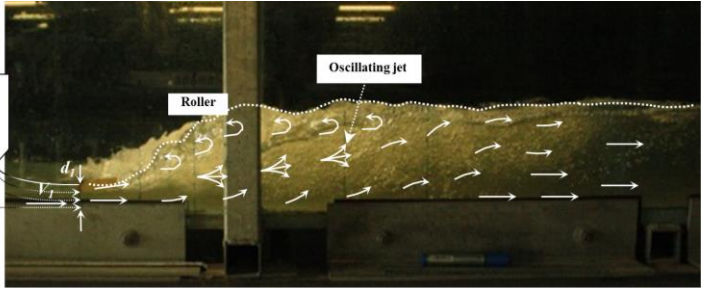
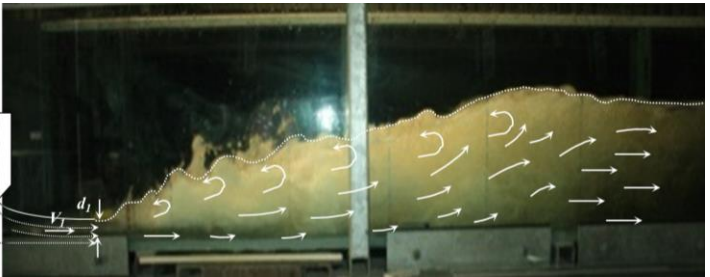
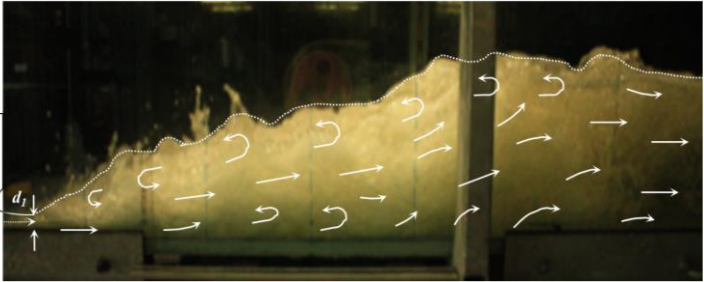


FIGURE 1-3. CHARACTERISTICS OF A TYPICAL HYDRAULIC JUMP ($Fr_1 = 5.1$, $Re = 8.3 \times 10^4$); FLOW FROM LEFT TO RIGHT.

A hydraulic jump is a rapidly varied flow phenomenon at the transition of fast, supercritical flows to slow, subcritical flows. Table 1-1 lists the most common hydraulic jump classification system based on the inflow Froude number ($Fr_1 = V_1/\sqrt{gd_1}$) and energy dissipation percentage $\Delta H/H_1 = (H_1 - H_2)/H_1$ together with photos of hydraulic jumps in the present study where V_1 is the depth-averaged flow velocity upstream of the hydraulic jump, d_1 is the corresponding inflow depth and g is the gravity constant and $H_1 = d_1 + V_1^2/2g + z_1$ and $H_2 = d_2 + V_2^2/2g + z_2$ represent the total head upstream and downstream of the hydraulic jump respectively, z_1 and z_2 and represent the elevation above the datum. The classification of the hydraulic jumps shown in Table 1-1 is limited to hydraulic jumps on horizontal channels and inflow depths larger than 2 cm (Chow 1973; Peterka 1978; Hager 1992).

TABLE 1-1. HYDRAULIC JUMP TYPES IN HORIZONTAL CHANNELS BASED UPON INFLOW FROUDE NUMBER (CHOW 1973; PETERKA 1978; HAGER 1992; CHANSON 2004)

Hydraulic jump type	Fr_1	$\Delta H/H_1$	Characteristics
Undular jump	1 – 1.7	-	 <p>Surface undulations, no air entrainment, negligible energy losses</p>
Pre-jump or weak jump	1.7 – 2.5	<20%	 <p>Smooth water surface, low efficiency</p>

Hydraulic jump type	Fr_1	$\Delta H/H_1$	Characteristics
Transition jump or oscillating jump	2.5 – 4.5	20%-45%	 <p>Wavy free-surface profile, irregular period waves, bank erosion downstream due to the irregular waves travelling far downstream</p>
Stabilised jump or steady jump	4.5 – 9.0	45% - 70%	 <p>Well stabilised jump, large energy dissipation, minimal influence of the tailwater conditions</p>
Choppy jump or strong jump	> 9.0	~85%	 <p>Rough free-surface profile, large amount of spray, large energy dissipation, risk of channel bed erosion</p>

The energy dissipation efficiency and the hydraulic jump stability are strongly influenced by the inflow Froude number which must be carefully selected to avoid undesirable effects (Peterka 1978). For example, undular hydraulic jumps ($1 < Fr_1 < 1.7$) are unstable and can generate damage due to undulations of the free-surface leading to a propagation of energy from the stilling basin into the downstream water body. Choppy jumps or strong jumps ($Fr_1 > 9$) could lead to cavitation effects as a result of high velocities and turbulence (Chow 1973; Peterka 1978; USBR 1987; Hager 1992). Therefore, hydraulic jump stilling basins are typically designed for a specific range of Froude numbers, inflow depths and inflow velocities (Hager 1992). For low Froude numbers ($Fr_1 < 4.5$) and upstream heads less than 10 m, simple hydraulic jump stilling basins are recommended (USBR 1987; Hager 1992; Chanson and Carvalho 2015). For higher Froude numbers ($Fr_1 > 4.5$), stilling basins with chute blocks, baffle blocks and dentated end sills are recommended for velocities lower than 18.3 m/s (USBR 1987). If the

upstream supercritical velocity is higher, baffle blocks should be avoided to prevent cavitation risks (USBR 1987; Chanson and Carvalho 2015). For upstream heads between 30 m and 50 m, only simple stilling basin designs are recommended as these do not produce undesired effects (Hager 1992). For stilling basins with non-conventional designs, extensive physical modelling is required to define the acceptable hydraulic parameters and avoid cavitation. Figure 1-4 presents a non-standard design of a curved stilling basin with baffle blocks downstream of a stepped spillway. The layout, shape, size and form of the concrete guides was supported by detailed physical modelling.



FIGURE 1-4. STILLING BASIN OF HINZE DAM, QUEENSLAND, AUSTRALIA (COURTESY OF DR. STEFAN FELDER).

The complexity of hydraulic jumps has fascinated researchers for more than two centuries leading to a better understanding of external and internal flow features. Past experiments in hydraulic jumps in horizontal and rectangular channels investigated the conjugate depth relationships (e.g. Bélanger 1841; Bakhmeteff 1932; Hager and Bremen 1989), energy dissipation performance (Peterka 1978; Hager 1992); free-surface profiles (e.g. Rajaratnam 1962a; Hager 1993; Mouaze et al. 2005; Murzyn and Chanson 2009a), jump toe oscillations (e.g. Long et al. 1991; Mossa 1999; Zhang et al. 2013), velocity distributions (e.g. Rajaratnam 1965; Hager and Bremen 1989; Wu and Rajaratnam 1995) and air-water flow properties (e.g. Resch and Leutheusser 1974; Chanson and Brattberg 2000). Additional experiments have analysed the internal and external features in non-conventional hydraulic jumps such as hydraulic jumps on sloped channels (e.g. Bakhmeteff and Matzke 1938; Kindsvater 1944;

Hager 1988; Ohtsu and Yasuda 1991; Palermo and Pagliara 2018) and submerged hydraulic jumps (Zare and Baddour 2007; Habibzadeh et al. 2011; 2012). While only a few studies have attempted to investigate the flow features in hydraulic jumps by numerical modelling, there has been an upswing in the quantity and quality of numerical modelling techniques applied to hydraulic jumps during the last decades (e.g. Madsen and Svendsen 1983; McCorquodale and Khalifa 1983; Gonzalez and Bombardelli 2005; Castro-Orgaz and Hager 2009; Richard and Gavriluk 2013; Valero et al. 2018). A comprehensive summary of the advances in numerical modelling in hydraulic jumps is presented in Viti et al. (2019). Although latest numerical modelling analysis have provided good accuracy in terms of time-averaged parameters (Viti et al. 2019), further research is required to validate the accuracy of the numerical simulations (Chanson 2013; Valero et al. 2019) exploring a larger range of air-water flow properties in hydraulic jumps. To date, despite the extensive research conducted to understand the external and internal features in hydraulic jumps, the understanding of the energy dissipation processes associated with complex three-dimensional motions and interactions of entrained air with the flow turbulence are still poorly understood due to limitations in experimental techniques.

Since the lack of the understanding of the internal behaviour in hydraulic jumps has limited the validation of hydraulic jumps in numerical models (Chanson 2013; Valero et al. 2019), this research aims to improve the understanding of the internal and external characteristics and energy dissipation processes in hydraulic jumps through a comprehensive experimental study. The investigation comprises a detailed integral experimental analysis of the air-water flow features, free-surface parameters and internal motions in hydraulic jumps for different inflow conditions and a wide range of Froude and Reynolds numbers through the implementation of novel experimental techniques and instrumentation. The integrated analysis comprised a detailed experimental campaign of:

- Air-water flow properties: For the first time, a detailed analysis of the effects of the inflow conditions upstream of the hydraulic jumps on a range of air-water flow properties in the hydraulic jump was conducted highlighting stronger aeration in fully developed hydraulic jumps.
- Free-surface features: This study quantified the free-surface features and the effect of the jump toe oscillations using a high-resolution LIDAR measurement system. The results provided the most detailed information of the free-surface motions in hydraulic jumps to date.
- Internal motions: The forces acting on a submerged sphere inside the hydraulic jump were measured providing novel characterisations of the large scale three-dimensional internal motions in hydraulic jumps.

The present study integrated the aeration features, free-surface fluctuations and internal motions in order to obtain a clearer picture of the complex mechanisms acting along the hydraulic jump considering time-averaged parameters and instantaneous fluctuations. Regions of larger aeration and stronger external and internal motions were identified as well as the decay of the dissipative motions with increasing distance from the jump toe. These insights are relevant for the understanding of the fundamentals of the internal features in the hydraulic jump as well as the validation of numerical models and future stilling basin designs.

2

LITERATURE REVIEW

Some content of this chapter is taken from the following publication:

Journal Publications

Montano, L., Li, R., and Felder, S. 2018, ‘Continuous measurements of time-varying free-surface profiles in aerated hydraulic jumps with a LIDAR’, *Experimental Thermal and Fluid Science*, vol. 93, pp. 379 – 397.

Montano, L., and Felder, S. 2019 ‘LIDAR observations of free-surface time and length scales in hydraulic jumps’, *Journal of Hydraulic Engineering* (in print, accepted for publication on 14/8/2019)

Conference Proceedings

Montano, L., and Felder, S. 2019, ‘Measuring internal forces in a hydraulic jump with a load cell’, in *Proc., 38th IAHR World Congress*, Panama City, Panama, 10 pages.

Montano, L., and Felder, S. 2018, ‘Effect of inflow conditions on the air-water flow properties in hydraulic jumps’, in *Proc., 21st Australasian in Fluid Mechanics Conference*, Australasian Fluid Mechanics Conference, Adelaide, Australia, 4 pages.

2.1. A BRIEF TIMELINE OF HYDRAULIC JUMP RESEARCH

The first known approach to analyse hydraulic jumps was developed by Leonardo Da Vinci around the 16th century (Hager 1992). Three centuries later, Bidone (1820) undertook the first experimental analysis of hydraulic jumps with low Froude numbers. Bidone (1820) measured the surface depths and the length of the hydraulic jump. In 1828, Bélanger (1928) established the first approach to understand the energy dissipation in hydraulic jumps (Chanson 2009a). He applied the Bernoulli equation to analyse the conjugate flow depths in hydraulic jumps with satisfactory results limited to jumps with low energy dissipation (Hager 1990; Chanson 2009a). In 1841, Bélanger (1941) applied the momentum method to establish the well-known equation of the conjugate depths ratio of hydraulic jumps (Ferriday 1895; Bakhmeteff 1932; Hager 1990; Chanson 2009a). Darcy and Basin (1865) and Merriman (1889) proposed other equations to calculate the upstream and downstream conjugate depths based on experiments with low Froude numbers between $1.48 < Fr_l < 1.82$ and Bidone's (1820) results respectively (Darcy and Basin 1865; Ferriday 1895; Hager 1990). Although the equations did not estimate losses accurately, the data was the input for later analysis (Hager 1990; Hager 1992).

Figure 2-1 presents a chronological summary of the hydraulic jump research between 1820 to 1990. The following paragraphs includes some of the key references and further information is presented in Hager (1992). According to Hager (1992), the historical hydraulic jump research before 1992 can be categorized into four stages (Figure 2-1). The first period before 1929 analysed longitudinal and vertical characteristics of hydraulic jumps based on the application of the momentum equation to calculate the conjugate flow depths and the length of hydraulic jumps. A significant contribution by Safranez (1929) combined his own research and results of previous hydraulic jump experiments by Bidone (1820) and Darcy and Bazin (1865) highlighting the importance of kinematic and gravitational analysis (Froude number) on the hydraulic jump behaviour and energy dissipation. During this stage, hydraulic jumps were emphasized as an alternative to prevent scour in the river embankment downstream of spillways (Kennison 1916a, 1916b; Kozeny 1929). A number of approximations and formulas were proposed to calculate conjugate depths and energy dissipation in hydraulic jumps (Kennison 1916a, 1916b; Kozeny 1929).

The second period was between 1930 and 1949 (Hager 1992). During this stage, the investigation focused on the energy dissipation analysis and its relation to the roller length. According to experimental data, the energy dissipation was associated with turbulence, friction losses and energy flux in the jump roller (Woycicki 1931; Kozeny 1932; Einwachter 1935). The importance of the Froude number representing the ratio of kinematic and gravitational forces in hydraulic jumps increased. For example, Bakhmeteff (1932) used the upstream Froude number

to define the type of hydraulic jump and the energy dissipation rate and Rouse (1934) clarified by dimensional analysis that the Froude number must be considered in the analysis of hydraulic jumps.

The third stage (1955 – 1967) was focused on the internal behaviour of hydraulic jumps (Hager 1992) including the turbulence and velocity fields in hydraulic jumps. Rouse et al. (1959) and Rajaratnam (1962b, 1965, 1967) are some of the most important pioneers in the study of the internal behaviour and turbulence characteristics in hydraulic jumps. Rouse et al. (1959) measured for the first time the turbulence in the roller of the hydraulic jump and the effect of the roller on the energy dissipation. Experimental findings demonstrated that the pressure in the hydraulic jump roller was not hydrostatic and that the wall-jet distribution with a clear maximum velocity at the boundary layer thickness can represent the velocity profile in the non-aerated region of the hydraulic jump (Rajaratnam 1965). A significant number of tests was conducted to measure the energy dissipation and the efficiency of hydraulic jumps downstream of spillways (Peterka 1978).

The last period remarked by Hager (1992) corresponds to 1970 until 1990. Although the first numerical models related to hydraulic jumps appeared during this stage, some experiments re-evaluated the approaches acquired during the first stage. Resch and Leutheusser (1972a, 1972b) and Resch, et al. (1974) evaluated the effect of the inflow conditions on the air entrainment of hydraulic jumps following the analysis conducted by Rouse (1959). Effects of non-prismatic channels on hydraulic jumps as well as potential scale effects in hydraulic jumps were investigated (Hager 1985; Hager and Bremen 1989). McCorquodale and Khalifa (1983) developed a mathematical approach to calculate hydraulic jump characteristics based on the velocity analysis undertaken by Rajaratnam (1965) and Narayanan (1975). The chronological research established by Hager (1992) is regrouped in Figure 2-1:

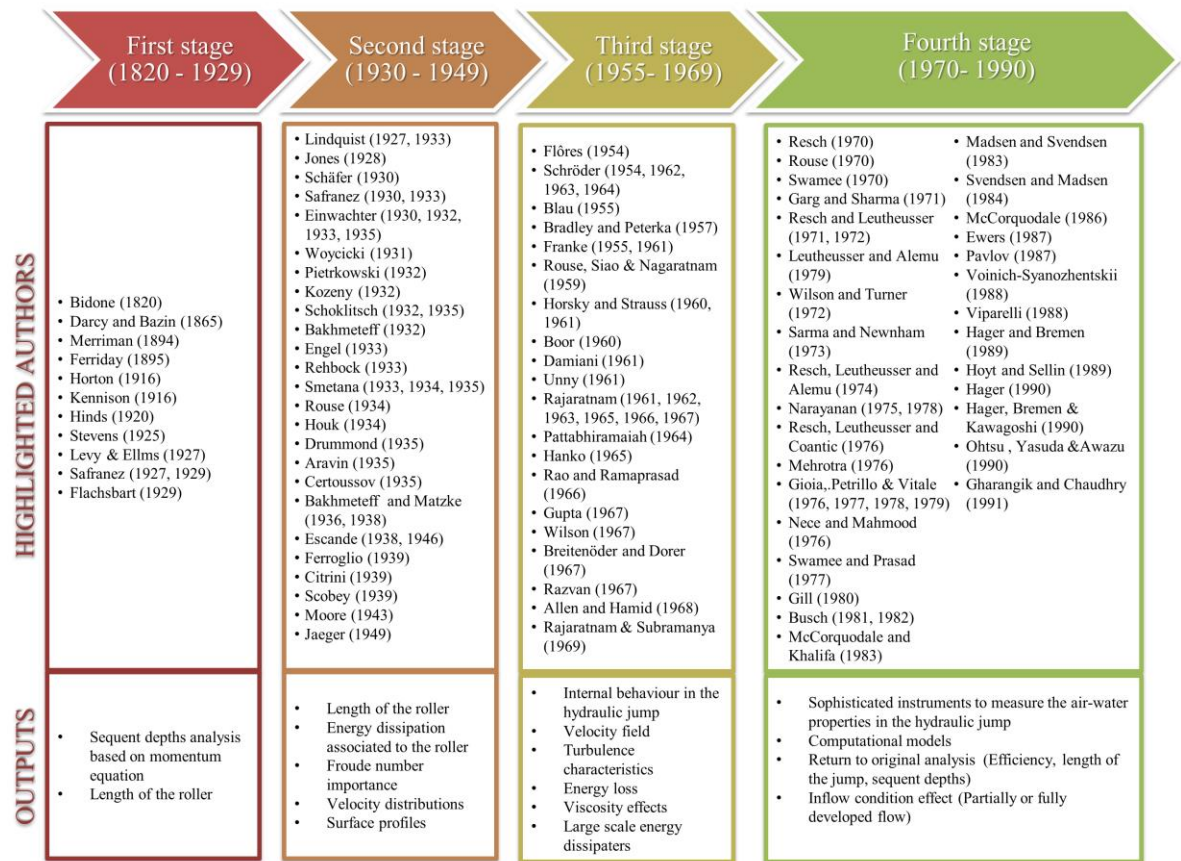


FIGURE 2–1. CHRONOLOGICAL SUMMARY OF HYDRAULIC JUMP RESEARCH ACCORDING TO HAGER (1992)

Since 1990, the “fifth” stage in the analysis of hydraulic jumps has been focused on the air-water flow properties, turbulence and free-surface features of hydraulic jumps through the application of new instrumentation and improved post-processing methods. In monophasic areas of the hydraulic jump (i.e. close to the channel bed and downstream of the jump roller) or in hydraulic jumps with low Froude numbers ($Fr_1 < 3.5$), the velocity and turbulence characteristics have been measured with Pitot tubes (Imai and Nakagawa 1992; Wu and Rajaratnam 1996), Laser Doppler Velocimeter (LDV) (Imai and Nakagawa 1992; Ohtsu, et al. 2001), Particle Image Velocimetry (PIV) (Lennon and Hill 2006; Misra et al. 2006) and Acoustic Doppler Velocimeters (ADV) (Liu et al. 2004a; Mignot and Cienfuegos 2010). In depth analysis of the two-phase flow characteristics of hydraulic jumps has been conducted with single- and double-tip conductivity probes (e.g. Chanson and Brattberg 2000; Chanson 2002; Chanson and Carosi 2007; Wang and Chanson 2016a), single tip optical fibre probes (Murzyn et al. 2005; Zhang et al. 2014) and supported with high-speed camera analysis (Long et al. 1991; Ead and Rajaratnam 2002; Leandro et al. 2012). Recent studies of the free-surface features provided time-averaged profiles, free-surface fluctuations and jump toe oscillations (e.g. Long et al. 1991; Murzyn et al. 2007; Chachereau and Chanson 2011b). Despite the extensive

research engagement in hydraulic jumps since the 19th century, the dissipation mechanism in the hydraulic jump remains unclear.

After this short chronology, the following chapters present a more thorough state-of-the-art review of hydraulic jumps.

2.2. HYDRAULIC JUMP CONCEPTS

The hydraulic jump is a typical example of rapidly varied flow in open channels. It is represented by a rapid transition from supercritical (conjugate depth d_1 and high velocity V_1) to subcritical flow (conjugate depth d_2 and low velocity V_2) (Kennison 1916a; Henderson 1966; Rajaratnam 1967). The transitional region in hydraulic jumps is characterised by surface fluctuations, air entrainment, vortices and air-water flux (Figure 2-2).

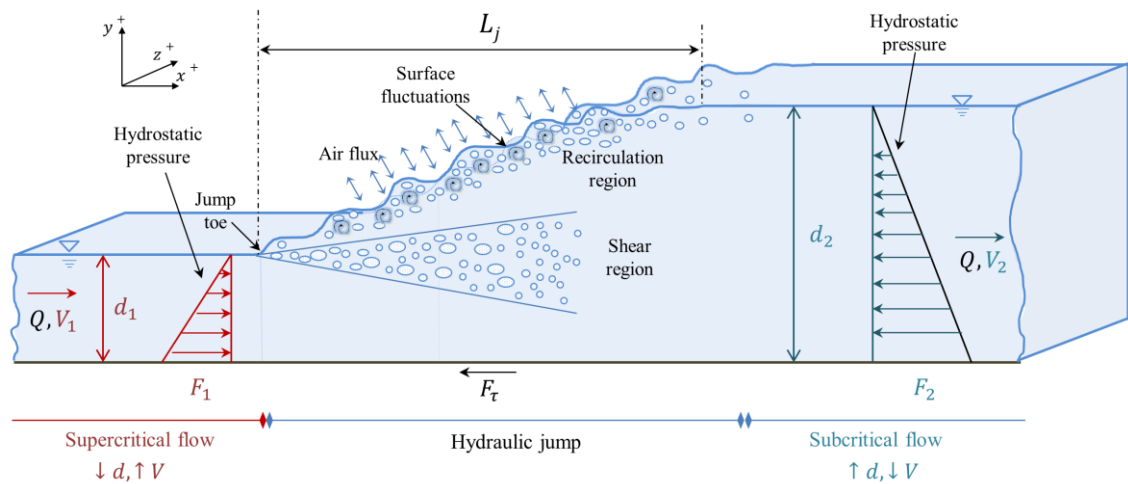


FIGURE 2-2. CLASSICAL HYDRAULIC JUMP SCHEME

Figure 2-2 shows the main features of classical hydraulic jumps defined as hydraulic jumps in horizontal rectangular channels. Figure 2-2 includes the definition of supercritical (red colour) and subcritical (blue colour) flow conditions, hydraulic jump regions, and air-water flow processes. L_j represents the hydraulic jump length defined as the distance from the jump toe to the position where the flow depth becomes levelled (Rajaratnam 1967; Hager and Bremen 1989; Hager et al. 1990; Hager 1992, 1993; Mok 2004). The hydraulic jump is the result of a flow control downstream. The sudden change in flow depth across the hydraulic jump causes turbulence, air entrainment and energy dissipation. The energy losses in hydraulic jumps make it impossible to use the specific energy concept to calculate the conjugate depth ratio. Instead, the continuity and momentum concepts are used:

$$V_1 A_1 = V_2 A_2 \quad (2.1)$$

$$\sum F_x = F_1 - F_2 - F_\tau = \rho Q V_2 - \rho Q V_1 \quad (2.2)$$

where A_1 and A_2 are the cross-sectional areas upstream and downstream of the hydraulic jump, F_1 and F_2 are the upstream and downstream hydrostatic forces, F_τ is the shear force and ρ is the water density.

Due to the high turbulence of hydraulic jumps, the shear stress and potential head losses due to friction at the bed of the channel may be neglected in smooth channels because the friction losses are comparatively small compared to the losses within the jump roller (Harleman 1959; Rajaratnam and Murahari 1971; Chanson and Carvalho 2015). This assumption is only valid in smooth channel beds where the friction losses could be neglected. Research by Harleman (1959) and Rajaratnam (1965) has also highlighted the relevance of the inflow conditions. For partially developed inflows, the boundary layer is not fully developed and is in contact with the bed of the channel increasing the resistance to flow motion leading to a reduction in the downstream conjugate depth (Harleman 1959; Rajaratnam 1965). Neglecting the shear force in the momentum equation may overestimate the downstream flow depth by about 4% for $Fr_1 = 10$ in hydraulic jumps with partially developed inflow conditions (Harleman 1959; Rajaratnam 1965).

Assuming that the hydraulic jump is generated in a smooth frictionless channel, with fully developed inflow conditions, the same flow density upstream and downstream and hydrostatic pressure and uniform velocity distributions upstream and downstream of the hydraulic jump, the combination of Equations 2.1 and 2.2 for rectangular channels results in:

$$\frac{1}{2}\rho g d_1^2 W + \rho V_1^2 W d_1 = \frac{1}{2}\rho g d_2^2 W + \rho V_2^2 W d_2 \quad (2.3a)$$

where W is the width of the channel.

Replacing $V_2 = V_1 \times d_1/d_2$ yields:

$$\frac{V_1^2}{g d_1} = \frac{1}{2} \frac{d_2}{d_1} \left(1 + \frac{d_2}{d_1} \right) \quad (2.3b)$$

For rectangular channels, the upstream Froude number is represented as:

$$Fr_1 = \frac{V_1}{\sqrt{g d_1}} \quad (2.4)$$

Substituting Equation 2.4 into Equation 2.3b results in the well-known conjugate flow depth equation developed by Bélanger (1841) (Ferriday 1895; Bakhmeteff 1932; Hager 1990; Chanson 2009a):

$$\frac{d_2}{d_1} = \frac{1}{2} \left(\sqrt{1 + 8Fr_1^2} - 1 \right) \quad (2.5)$$

Equation 2.5 can be applied to calculate the conjugate flow depth ratio in classical hydraulic jumps.

The efficiency across a classical hydraulic jump is calculated as the difference between the energy upstream and downstream of the hydraulic jump.

$$\frac{H_2}{H_1} = \frac{H_2 - H_1}{H_1} = \frac{(d_2 - d_1)^3}{4d_2d_1} / H_1 \quad (2.6)$$

2.3. ENERGY DISSIPATION PROCESSES IN HYDRAULIC JUMPS

The energy-dissipation capacity in hydraulic jumps is estimated based upon the upstream and downstream flow conditions (Equation 2.6) (Chow 1973). Early experimental studies observed a link between the hydraulic jump roller, inflow Froude number and the energy dissipation (e.g. Safranez 1929; Bakhmeteff 1932; Einwachter 1935). Peterka (1978) conducted a comprehensive series of experiments in large scale models with a wide range of Froude numbers ($2 < Fr_1 < 19$). The results highlighted the influence of Fr_1 in the energy dissipation efficiency in the hydraulic jump with dissipation rates of 7% for $Fr_1 = 2$ and 85% for $Fr_1 = 19$ (Peterka 1978). More recent analysis in the energy dissipation upstream and downstream of the hydraulic jump include the analysis of non-conventional hydraulic jumps including hydraulic jumps on sloped channels and rough channel beds (Beirami and Chamani 2010; Palermo and Pagliara 2018). For non-conventional hydraulic jumps, the energy dissipation rate was also strongly dependent of the inflow Froude number (Beirami and Chamani 2010; Palermo and Pagliara 2018).

The studies presented in the previous paragraph demonstrated the effect of the upstream flow conditions on the efficiency of the hydraulic jump. Since the energy dissipation performance is strongly linked with the fluctuation patterns and turbulent motions inside the hydraulic jump (Madsen and Svendsen 1983; Mignot and Cienfuegos 2010), additional studies have attempted to measure the energetic processes occurring inside the hydraulic jump. Table 2-1 lists relevant previous experimental studies which investigated the turbulence characteristics in hydraulic jumps. Table 2-1 provides details on the inflow conditions where UD represents undeveloped flow, PD partially developed inflow conditions, and FD fully developed inflow conditions, length of the channel L , channel width W , inflow Froude number and Reynolds number $Re = q/v$.

TABLE 2-1. EXPERIMENTAL STUDIES OF INTERNAL ENERGETIC PROCESSES IN HYDRAULIC JUMPS

References	Inflow conditions			<i>L</i> (m)	<i>W</i> (m)	<i>Fr₁</i> (-)	<i>Re</i> (-)	Instrument/ Technique
	UD	PD	FD					
Rouse et al. (1959)	-	-	-	2.7	0.76	2.0 - 6.0	-	Hot film anemometer
Resch and Leuthusser (1972a, b)		x	x	15	0.39	2.85 – 6.00	4.9×10 ⁴ - 1.0×10 ⁵	Hot film anemometer
Liu et al. (2004a)	-	-	-	7.6	0.46	2.00 – 3.32	8.6×10 ⁴ – 1.2×10 ⁵	3D ADV
Lennon and Hill (2006)			x	4.9	0.3	1.37 – 3.00	7.9×10 ⁴ – 9.3×10 ⁵	PIV
Zare and Baddour (2007)		x		4.6	0.23	2.00 – 3.75	3.2×10 ⁴ – 6.1×10 ⁴	3D ADV
Misra et al. (2008)	-	-	-	4.8	0.30	1.19	7.2×10 ⁴	PIV
Murzyn and Chanson (2009a)		x		3.2	0.5	3.1 - 8.5	2.4×10 ⁴ - 6.4×10 ⁴	Conductivity probe
Mignot and Cienfuegos (2010)		x		10	0.95	1.34 – 1.99	6.7×10 ⁴ – 1.7×10 ⁵	3D ADV
Chachereau and Chanson (2011a)		x		3.2	0.5	2 - 5.1	6.6×10 ⁴ - 1.3×10 ⁵	Conductivity probe
Lin et al. (2012)	-	-	-	3.05	0.5	2.4 – 5.35	2×10 ⁴ – 4.5×10 ⁴	PIV/ BIV
Chen and Wang (2013)	-	-	-	5.0	0.5	2.01 – 4.85	7.1×10 ⁴ – 1.2×10 ⁵	3D ADV
Zhang et al. (2014)	x			7.6	0.46	2.0 - 6.7	8.6×10 ⁴ - 1.7×10 ⁵	Optical fiber probe
Kramer and Valero (2019)		x		3.2	0.5	4.25	1.1×10 ⁵	High-speed video camera
Present study		x	x	40	0.6	3.8 - 10	6.4×10 ⁴ - 1.2×10 ⁵	Six-axis load cell

The first approach to measure the turbulence in hydraulic jumps was conducted by Rouse et al. (1959) with a hot-wire anemometer simulating a hydraulic jump in an air duct. While the monophasic experiments could not accurately quantify the turbulent characteristics (Rajaratnam 1965; Liu et al. 2004a), Rouse et al. (1959) discovered larger turbulence in areas of maximum velocity gradients. Resch et al. (1972a and b) quantified the turbulence intensity in fully and partially developed hydraulic jumps discovering larger turbulence for fully developed inflow conditions. Turbulence intensities and Reynolds stresses in hydraulic jumps with low Froude numbers were measured with a Micro ADV by Liu et al. (2004a). Liu et al. (2004a) observed a decay in maximum turbulence intensity and Reynolds stresses with increasing distance from the jump toe and that the longitudinal turbulence intensity was twice as large as the vertical turbulence intensity. Lennon and Hill (2006) and Misra et al (2006, 2008) estimated the turbulent characteristics in hydraulic jumps with PIV. Large turbulent structures were observed in the roller region and near the channel bed. The maximum Turbulent Kinetic Energy (TKE) was downstream of the jump toe while lower TKE was observed in the recirculation region

(Lennon and Hill 2006; Misra et al. 2008). While the results were consistent with the results obtained with ADVs, the PIV measurement were also limited to low Froude numbers. Lin et al. (2012) measured 2D velocity distributions and associated turbulence with PIV technique in conjunction with Bubble Image Velocimetry (BIV) technique in weak and stable hydraulic jumps. The velocity field denoted four flow regions: potential core region characterised by the region affected by the supercritical inflow, boundary layer region associated to the region affected by the boundary layer thickness, mixing layer region established within the positive flow velocity, and the recirculation region characterised by negative velocities (Lin et al. 2012). The horizontal flow velocity was almost twice the vertical velocity (Lin et al. 2012). Larger turbulence were recorded in the lower limit of the mixing layer while low turbulence were observed in the recirculation region (Lin et al. 2012).

Further analysis with ADVs were conducted by Zare and Baddour (2007) in submerged hydraulic jumps showing that the energy losses in submerged jumps are strongly dependant on the inflow Froude number. Mignot and Cienfuegos (2010) measured the turbulence production term and TKE in hydraulic jumps with undeveloped and partially developed inflow conditions using ADVs. Larger turbulence peaks were observed in the upper part of the shear region of the hydraulic jump and an additional turbulence peak was observed close to the channel bed for partially developed inflow conditions (Mignot and Cienfuegos 2010). Murzyn and Chanson (2009b) and Chachereau and Chanson (2011a) estimated the intensity of the air-water interactions in the hydraulic jump based upon cross-correlation functions. The findings showed large intensity with increasing Froude number and with increasing distance from the channel bed (Murzyn and Chanson 2009b; Chachereau and Chanson 2011a). Note that the intensity measure of the air-water interactions was defined as the turbulence intensity in the studies of Murzyn and Chanson (2009b) and Chachereau and Chanson (2011a). Nonetheless, this parameter was defined based upon cross-correlation analysis and only provided an indirect estimation of the velocity fluctuations (Kramer et al 2019b). Micro ADV measurements of the energy dissipation processes in hydraulic jumps and their relationship with the bubble formation and transportation was conducted by Chen and Wang (2013) identifying larger dissipation rates and larger bubble formations with increasing inflow Froude numbers. Zhang et al. (2014) measured the turbulence intensity following the approach of Cartellier (1992). Larger turbulence intensity was recorded close to the jump toe with a maximum in the shear region of the hydraulic jump in agreement with the findings of Liu et al. (2004a) (Zhang et al. 2014). Although the turbulence intensity estimation based on Cartellier (1992) provides an estimation of the velocity fluctuations, this method presents large uncertainty (Kramer et al. 2019b). A recent study by Kramer and Valero (2019) estimated the 2D velocity fluctuations with a high-speed camera. Similar to the results of Liu et al. (2004a), large fluctuations were recorded close

to the jump toe followed by an exponential decay in the streamwise direction (Kramer and Valero 2019).

Previous studies have provided a better understanding of the energy dissipation processes and turbulent characteristics in hydraulic jumps. The analysis of the turbulent fluctuations inside the hydraulic jump was limited to hydraulic jumps with low Froude numbers, 2D analysis or by uncertainties in the instrumentation techniques to estimate the velocity fluctuations. The present study provides a novel characterisation of the three-dimensional internal motions in the hydraulic jump acting on a submerged sphere. This novel technique provides a three-dimensional estimation of the fluctuations and large scale energetic motions along the hydraulic jump.

2.4. AIR-WATER FLOW PROPERTIES IN HYDRAULIC JUMPS

The generation of turbulence in hydraulic jumps is associated with the advective transport of air entrapped at the impingement point of the roller in the shear region and air-water exchanges, water splashes and foam along the free surface of the roller in the recirculation region (Long et al. 1991; Chanson 1996; Chanson and Brattberg 2000; Murzyn et al. 2007; Wang and Chanson 2015). Downstream of the impingement point, the entrapped air breaks up into smaller bubbles due to the shear stresses and flow turbulence, and they are transported as a consequence of the convective and advective processes inside the hydraulic jump (Murzyn et al. 2005). In the upper part of the hydraulic jump, air entrainment and detrainment occur in the recirculation region. This region is characterised by the exchange of air and water and buoyancy effects are more important than the convective processes observed in the shear region (Murzyn et al. 2005; Chanson and Brattberg 2000). The entrained air occurs as air-bubbles, spray or foam (Chanson 1996).

The air-water flow properties are typically measured with phase-detection intrusive probes providing insights into typical air-water flow parameters such as void fraction, bubble count rate and interfacial velocities. The distributions of time-averaged void fraction present two marked regions (Figure 2-3), i.e. a shear region and the recirculation (Chanson 1995; Chanson and Brattberg 2000; Murzyn et al. 2005). In the shear region, the void fraction has a maximum peak C_{max} at Y_{Cmax} corresponding to the maximum advective transport occurring in this zone. A minimum in void fraction C_{min} at Y_{Cmin} occurs at the transition of shear and recirculation regions (Figure 2-3). The void fraction in the recirculation region is characterised by a monotonic increase in C up to the free-surface ($C = 1$) (Chanson 1995, 1996; Chanson and Brattberg 2000; Murzyn et al. 2005).

Figure 2-3 also includes the comparison of a typical void fraction with the theoretical advective diffusion equation for air bubbles in the shear region (Chanson 1995, 1996; Chanson and Brattberg 2000; Murzyn et al. 2005):

$$C = C_{max} \times \exp\left(-\frac{1}{4 \times D^\#} \times \frac{\left(\frac{y - Y_{C_{max}}}{d_1}\right)^2}{\left(\frac{x - x_1}{d_1}\right)}\right) \quad \text{for } 0 < y < Y_{C_{min}} \quad (2.7a)$$

and the analytical diffusion equation of water jets discharging into air in the recirculation region (Brattberg et al. 1998; Murzyn et al. 2005):

$$C = \frac{1}{2} \times \left(1 + \operatorname{erf}\left(\frac{y - Y_{50}}{2 \times \sqrt{\frac{D^* \times (x - x_1)}{V_1}}}\right)\right) \quad \text{for } y > Y_{C_{min}} \quad (2.7b)$$

where y is the vertical position above the channel bed, $D^\# = D_t / (V_1 \times d_1)$, D_t is the diffusivity in the shear region, D^* is the dimensionless diffusivity coefficient in the recirculation region and Y_{50} is the elevation with $C = 0.5$.

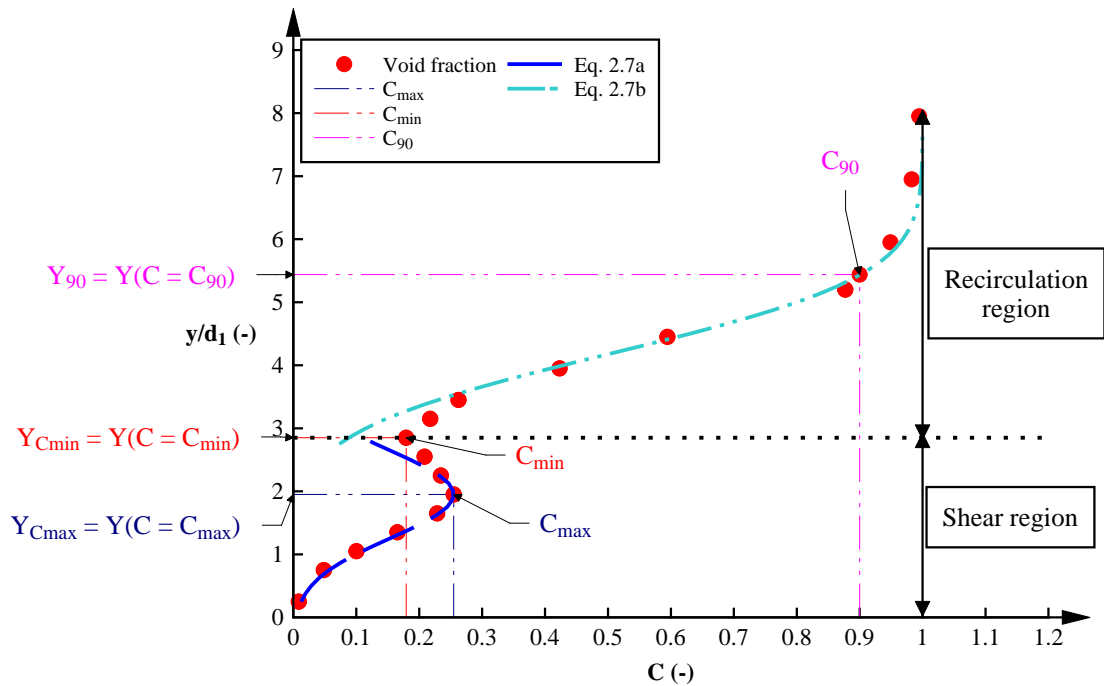


FIGURE 2-3. CONCEPTUAL SKETCH OF VOID FRACTION DISTRIBUTIONS AND VOID FRACTION PARAMETERS IN HYDRAULIC JUMPS ($Fr_1 = 8.5$, $Re = 7.5 \times 10^4$, $x/d_1 = 8$ – PARTIALLY DEVELOPED INFLOW CONDITIONS)

The vertical distributions of the bubble count rate F are characterised by two distinctive peaks in the shear and recirculation regions. The peak in the shear region F_{maxSR} is linked to the break up of bubbles entrapped at the impingement point of the hydraulic jump (Chanson and Brattberg 2000; Chachereau and Chanson 2011a). The maximum within the recirculation region F_{maxRR} representing the air-water packets immersed in the foam structure at this region (Chanson and Brattberg 2000; Murzyn et al. 2005). Figure 2-4 presents a typical dimensionless bubble count rate distribution highlighting the peaks in the shear and recirculation regions. A decrease in the bubble count rate in the transition of shear and recirculation regions can be observed

which is linked to the change in flow patterns between the two flow regions (Chanson and Brattberg 2000).

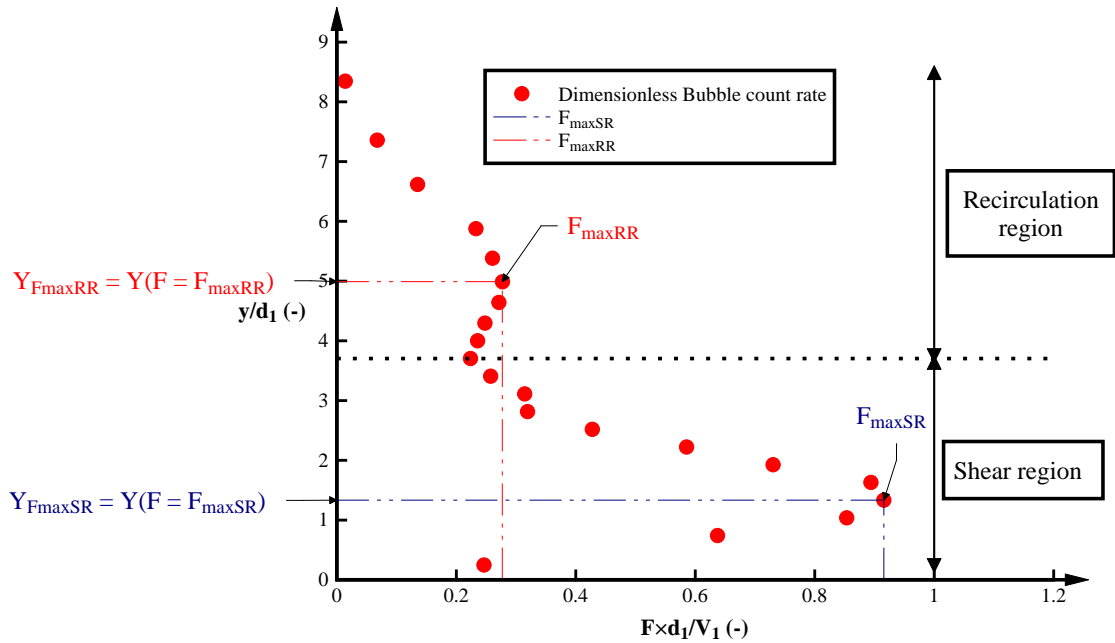


FIGURE 2-4. TYPICAL BUBBLE COUNT RATE DISTRIBUTION AND BUBBLE COUNT RATE PARAMETERS IN HYDRAULIC JUMP ($Fr_1 = 7.0$, $Re = 1.2 \times 10^4$, $x/d_1 = 8$ – PARTIALLY DEVELOPED INFLOW CONDITIONS).

The local time-averaged interfacial velocity (V_{CP}) can be calculated as $V_{CP} = \Delta x_P / T$, where Δx_P is the longitudinal separation distance between the leading and trailing tips of a conductivity probe and T is the average travel time of particles between the two probe tips. In the shear region, the velocity distribution follows closely the wall jet theory (Rajaratnam 1965; Rajaratnam and Murahari 1974; Ohtsu et al. 1990; Chanson and Brattberg 2000) while large data scatter and negative velocities can be observed in the recirculation region (Figure 2-5). These negative velocities are associated with the wake of the probe support and their accuracy is limited (e.g. Chanson and Brattberg, Chanson 2010; Zhang et al. 2014). The velocity profiles in hydraulic jumps can be correlated with a wall jet theory as (Rajaratnam 1965; Chanson and Brattberg 2000; Chanson 2010):

$$\frac{V_{CP}}{V_{max}} = \left(\frac{y}{y_{V_{max}}} \right)^{\frac{1}{N_{CP}}} \quad \text{for } \frac{y}{y_{V_{max}}} < 1 \quad (2.8a)$$

$$\frac{V - V_{recir}}{V_{max} - V_{recir}} = \exp \left\{ -\frac{1}{2} \left[1.765 \left(\frac{y - y_{V_{max}}}{y_{0.5}} \right) \right] \right\} \quad \text{for } 1 < \frac{y}{y_{V_{max}}} < 3 \text{ to } 4 \quad (2.8b)$$

where V_{max} is the maximum velocity in the shear region, $y_{V_{max}}$ is the flow depth where $V_{CP} = V_{max}$, N_{CP} is a power law exponent between 6 and 10, V_{recir} is the average velocity in the recirculation region, and $y_{0.5}$ is the elevation at $V_{CP} = V_{max}/2$.

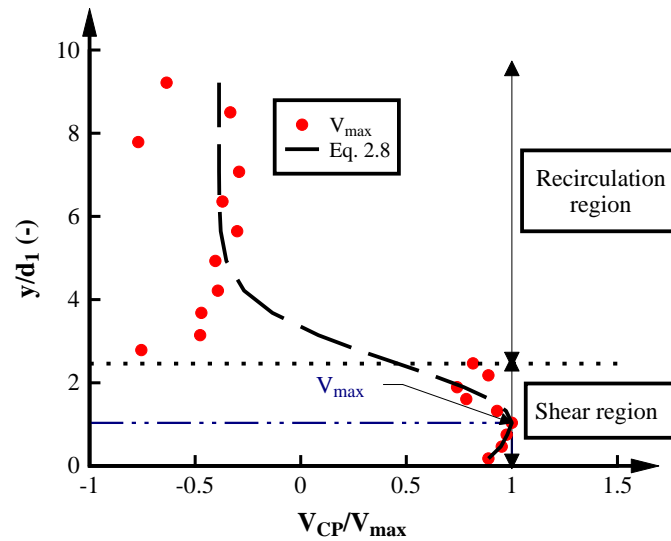


FIGURE 2-5. INTERFACIAL VELOCITY DISTRIBUTIONS AND CHARACTERISTIC PARAMETERS IN HYDRAULIC JUMPS; COMPARISON WALL JET THEORY ($Fr_1 = 8.0$, $Re = 1.2 \times 10^5$, $x/d_1 = 8$ – FULLY DEVELOPED INFLOW CONDITIONS).

Table 2-2 summarises relevant experimental studies of air-water flow properties in smooth channels including important parameters such as inflow conditions, flow rate, length of the channel, channel width, inflow Froude number and Reynolds number. All the experiments presented in Table 2-2 were conducted on smooth channels.

TABLE 2-2. RESEARCH OF AIR-WATER FLOW PROPERTIES IN HYDRAULIC JUMPS ON SMOOTH HORIZONTAL CHANNEL BED

Reference	Inflow conditions			L (m)	W (m)	Fr_1 (-)	Re (-)
	UD	PD	FD				
Rajaratnam (1962b)		x		4.6	0.30	2.4 – 8.7	$3.1 \times 10^4 - 1.1 \times 10^5$
Resch and Leutheusser (1972a)		x	x	11	0.39	2.8 - 6.0	$3.1 \times 10^4 - 7.8 \times 10^4$
Resch and Leutheusser (1972b); Resch et al. (1974)		x	x	15	0.39	2.8 - 6.0	-
Babb and Aus (1981)		x		-	0.46	6	1.2×10^5
Chanson and Qiao (1994)		x		3.2	0.25	4.8 – 8.1	-
Mossa and Tolve (1998)		x		24.4	0.40	6.4 – 7.3	$5.7 \times 10^4 - 5.8 \times 10^4$
Chanson and Brattberg (2000)		x		3.2	0.25	6.3 - 8.5	$3.3 \times 10^4 - 4.4 \times 10^4$
Murzyn et al. (2005)		x		12	0.30	2.0 - 4.8	$4.6 \times 10^4 - 8.8 \times 10^4$
Chanson and Gualtieri (2008)		x		3.2	0.25/0.5	5.1 – 8.6	$2.5 \times 10^4 - 9.8 \times 10^4$
Kucukali and Chanson (2008)		x		3.2	0.5	4.7 - 8.5	$5.5 \times 10^4 - 9.8 \times 10^4$
Murzyn and Chanson (2009b)		x		3.2	0.5	3.1 - 8.5	$2.4 \times 10^4 - 6.4 \times 10^4$
Chanson (2010)		x		3.2	0.5	3.6 - 12.4	$2.9 \times 10^4 - 9.3 \times 10^4$
Chachereau and Chanson (2011a, 2011b)		x		3.2	0.5	2 - 5.1	$6.6 \times 10^4 - 1.3 \times 10^5$
Leandro et al. (2012)		x		3.2	0.5	4.4 – 5.1	$1.1 \times 10^5 - 1.2 \times 10^5$
Wang et al. (2014a)		x		3.2	0.5	3.8 - 7.5	$3.4 \times 10^4 - 1.4 \times 10^5$

Reference	Inflow conditions			<i>L</i> (m)	<i>W</i> (m)	<i>Fr_l</i> (-)	<i>Re</i> (-)
	UD	PD	FD				
Zhang et al. (2014)	x			7.6	0.46	2.0 - 6.7	$8.6 \times 10^4 - 1.7 \times 10^5$
Wang and Chanson (2015)		x		3.2	0.5	3.8 - 8.5	$2.1 \times 10^4 - 1.6 \times 10^5$
Wang and Chanson (2016a, 2016b)		x		3.2	0.5	7.5	$6.8 \times 10^4 - 1.4 \times 10^5$
Takahashi and Ohtsu (2017)		x	x	-	0.4	4.2 - 8.2	6.2×10^4
Present study	x	x		40	0.6	2.1 - 10	$6.2 \times 10^4 - 1.2 \times 10^5$

Table 2-2 shows an extensive range of experimental research of the air-water flow features in classical hydraulic jumps for a wide range of Froude $1.2 < Fr_l < 12.4$ and Reynolds numbers $2.1 \times 10^4 < Re < 1.7 \times 10^5$. The first air-water flow analyses were conducted by Rajaratnam (1962b) using a single tip conductivity probe to estimate the air concentration and the length of the roller. Resch and Leutheusser (1972a) and Resch et al. (1974) investigated the effects of inflow conditions on the air-water flow features and turbulence in hydraulic jumps with a hot-film anemometer. Babb and Aus (1981) also used a hot-film anemometer discovering larger bubble sizes close to the jump toe linked with the breaking up of bubbles due to turbulence, shear and buoyancy. Regardless the significant contribution with the hot-film anemometer into the understanding of the air-water flow properties in aerated hydraulic jumps (Resch and Leutheusser 1971; 1972a; Resch et al. 1974; Babb and Aus 1981), measurements obtained with this instrument were not well processed and could be affected by the susceptibility of the probes to fouling (Naghash 1994; Takahashi and Ohtsu 2017). Chanson and Qiao (1994) measured the air concentration in the hydraulic jump with a single tip conductivity probe confirming three regions in the hydraulic jump: turbulent shear region, boiling flow region and foam region. A maximum void fraction was observed in the shear region with an exponential decrease along the hydraulic jump (Chanson and Qiao 1994). Chanson and Brattberg (2000) investigated air-water flow properties in the shear region of the hydraulic jump with a conductivity probe showing a parabolic relationship between void fraction and bubble count rate and a similarity of the interface velocity distributions with the wall jet analogy by Rajaratnam (1965). Murzyn et al. (2005) measured the air-water flow properties with a fibre-optical probe showing overall good agreement with earlier tests with conductivity probes. Fibre-optical probes were also used by Zhang et al. (2014) providing mean velocities and turbulent fluctuations along the hydraulic jump. In the past decade, detailed information on air-water flow properties in hydraulic jumps has been obtained in a series of experiments at the University of Queensland in the same experimental setup and with partially developed inflow conditions using conductivity probes. These studies focussed upon scale effects (Chanson 2006; Murzyn and Chanson 2008; Chanson and Gualtieri 2008, Chanson 2007a), turbulent time and length

scales (Kucukali and Chanson 2008; Chanson 2007b), bubble distribution and clustering (Chanson 2010; Chachereau and Chanson 2011a), interaction of free-surface fluctuations, roller turbulence and air entrainment (Murzyn and Chanson 2009a; Wang and Chanson 2015), decomposition of velocity components and turbulence characterisation using a triple decomposition technique (Wang et al. 2014a) and an attempt to provide transverse interface velocities (Wang and Chanson 2016a, 2016b). While phase-detection intrusive probes such as conductivity probes and fibre-optical probe are not affected by the formation of vapour bubbles, a problem typically encountered in hot-film anemometers, both instruments are intrusive and can be affected by electrical noise. Moreover, hot-film anemometers, conductivity probes and optical probes are limited to single point measurements and unidirectional flows only.

A non-intrusive technique using a video camera to measure the air concentration was used by Mossa and Tolve (1998). The experiments showed a relationship between vortex break-up and air concentration (Mossa and Tolve 1998). More recent studies compared video observations with the velocity fields measured with the single point measurements obtained with conductivity or optical probes showing good agreement between both methods (Leandro et al. 2012; Kramer and Valero 2019). Nonetheless, high-speed cameras can only measure the air-water flow properties close to the sidewall, a region which may be affected by boundary layer effects.

Takahashi and Ohtsu (2017) revisited the investigations by Resch and Leutheusser (1974) on the effects of inflow conditions on the air-water flow properties in hydraulic jumps. They conducted experiments with a conductivity probe to identify the effects of inflow conditions highlighting a strong effect of the boundary layer development upstream of the hydraulic jump on the void fraction (Takahashi and Ohtsu 2017). While the studies by Resch and Leutheusser (1974) and Takahashi and Ohtsu (2017) highlighted the effects of inflow conditions on flow aeration, there is currently no information on the effect of the inflow condition on the wide range of other air-water flow parameters.

Since the first study conducted by Rajaratnam (1962), different instrumentation has been used to estimate the air-water flow properties in hydraulic jumps. Table 2-3 summarises the instrumentation of previous studies, the measured parameters as well as the instrument limitations.

TABLE 2–3. INSTRUMENTATION TO MEASURE THE AIR-WATER PROPERTIES IN HYDRAULIC JUMPS

Instrument	Parameter	Instrument Limitations							Reference
		Single point measurement	Intrusive	Water quality limitation	Electrical noise	Formation vapour bubbles	Side wall effect	Time-averaged properties	
Hot film anemometer	<ul style="list-style-type: none"> • Void fraction • Bubble size • Turbulence 	x	x	x	x	x	x	x	<ul style="list-style-type: none"> • Resch and Leutheusser (1971, 1972a) • Resch et al. (1974) • Babb and Aus (1981)
Conductivity probe	<ul style="list-style-type: none"> • Void fraction • Bubble count rate • Bubble/ Droplet sizes • Particle clusters • Time/ length scales • Interfacial Velocity 	x	x	x	x		x	x	<ul style="list-style-type: none"> • Rajaratnam (1962b) • Chanson and Brattberg (2000) • Kucukali and Chanson (2008) • Murzyn and Chanson (2009b) • Chanson (2007a, 2007b, 2010) • Chachereau and Chanson (2011a, 2011b) • Wang et al. (2014a) • Wang and Chanson (2015; 2016a, 2016b) • Takahashi and Ohtsu (2017) • Present study
Optical fibre probe	<ul style="list-style-type: none"> • Void fraction • Bubble/ Droplet chord size • Interfacial Velocity • Turbulence intensity 	x	x	x	x		x	x	<ul style="list-style-type: none"> • Murzyn et al. (2005) • Zhang et al. (2014)
High-speed camera	<ul style="list-style-type: none"> • Void fraction • 2D analysis • Velocity • Turbulence 						x		<ul style="list-style-type: none"> • Mossa and Tolve (1998) • Leandro et al. (2012)

The study of the air-water flow properties in hydraulic jumps has engaged significant attention during the last century. The basic air-water features in classical hydraulic jumps have been described with different instrumentation. Nonetheless, the majority of the experiments have been conducted in hydraulic jumps with partially developed inflow conditions (Table 2-2) while experiments by Resch and Leutheusser (1972a), Resch et al. (1974) and Takahashi and Ohtsu (2017) highlighted larger void fraction in fully developed hydraulic jumps. Herein new extensive experiments were conducted to provide a wide range of air-water flow properties for

fully and partially developed inflow conditions highlighting the importance of the boundary layer development upstream of the hydraulic jump on the air-water flow characteristics.

2.5. FREE-SURFACE FLUCTUATIONS AND JUMP TOE OSCILLATIONS

The free-surface fluctuations and jump toe oscillations in hydraulic jumps highlight the dynamic behaviour of the phenomenon. Table 2-4 summarises previous experiments of free-surface fluctuations and jump toe oscillations in hydraulic jumps including d_l , Fr_l , Re and W , as well as the type of experiments, the instrumentation and the investigated free-surface parameter. First attempts to measure the time-averaged free-surface profiles, despite the “violent” jump toe motion, were conducted by Bakhmeteff and Matzke (1936) and Moore (1943) with profilometers at different locations along the hydraulic jump. Experiments were conducted with pointer gauges (e.g. Rouse et al. 1959; Rajaratnam 1962a; Hager 1993), wire gauges (e.g. Mouaze et al. 2005; Murzyn et al. 2007), and Acoustic Displacement Meters (ADMs) (e.g. Murzyn and Chanson 2009a; Chachereau and Chanson 2011b). The time-averaged free-surface profiles can be expressed by empirical equations for $2 < Fr_l < 12$ (Rajaratnam 1962a; Hager 1993). These empirical equations provide the flow depths profile along the centreline of hydraulic jumps using the roller length L_r , the upstream and downstream conjugate depths and the inflow conditions as parameters (Rajaratnam 1962a; Hager 1993). Theoretical predictions of the average free-surface profiles for stationary conditions with good agreement with experimental data have also been provided (McCorquodale and Khalifa 1983; Madsen and Svendsen 1983; Richard and Gavriluk 2013). Currently experimental measurements of the free-surface features have been limited to fixed positions along the hydraulic jump limiting the understanding of the interactions of free-surface motions and jump toe oscillations.

In recent years, the research focussed upon the analysis of free-surface fluctuations (e.g. Mouaze et al. 2005; Murzyn et al. 2007; Murzyn and Chanson 2009a; Chachereau and Chanson 2011b) and their characteristic frequencies (Mok 2004; Murzyn and Chanson 2009a; Chachereau and Chanson 2011b; Wang 2014). Spectral analyses of free-surface fluctuations for hydraulic jumps with $3 < Fr_l < 10$ found dominant free-surface frequencies $1.2 < freq_{fs(dom)} < 4$ Hz. The frequencies increased with increasing Fr_l (Murzyn and Chanson 2009a; Chachereau and Chanson 2011b; Wang 2014). These analyses were based upon single point measurements only.

Simultaneous sampling of free-surface elevations for defined longitudinal distances along the hydraulic jump combined with auto- and cross-correlation techniques can provide the free-surface time and length scales (Mouaze et al. 2005; Murzyn et al. 2007; Chachereau and Chanson 2011b). Previous studies measured the free-surface integral scales with wire gauges (Mouaze et al. 2005; Murzyn et al. 2007), ADMs (Chachereau and Chanson 2011b; Wang and

Murzyn 2017) and high-speed cameras (Mouaze et al. 2005). These experiments showed an increase in length scales with increasing distance from the jump toe (Murzyn et al. 2007; Chachereau and Chanson 2011b). All experiments were conducted for single point measurements only at defined distances between two instruments, and the results were affected by the jump toe oscillation (Mouaze et al. 2005).

Jump toe oscillations have an important effect on the free-surface fluctuations and vortex dynamics in hydraulic jumps (Long et al. 1991; Chanson 2010; Wang and Chanson 2013; Zhang et al. 2013). Long et al. (1991) documented the jump toe oscillations based upon flow visualisations. Subsequent research with a high speed camera and ADMs identified the dominant frequencies of the jump toe $0.5 < freq_{toe} < 2$ Hz (Mossa and Tolve 1998; Chanson and Gualtieri 2008; Murzyn and Chanson 2009a; Chachereau and Chanson 2011b; Wang and Chanson 2015). In experiments with ADMs with sampling durations up to 160 min, an additional jump toe frequency of 0.004 Hz was identified by Wang and Chanson (2015). Recent research of the jump toe perimeters with a video-camera located at the top of the channel showed three-dimensional effects of the jump toe motion (Zhang et al. 2012, 2013; Wang and Chanson 2015; Felder and Chanson 2018).

The use of more advanced instruments such as wire gauges, ADMs and high-speed cameras improved the understanding of the free-surface fluctuations in hydraulic jumps. However, none of these instruments provided continuous and simultaneous time series of the free-surface features along the free-surface of the hydraulic jumps (Table 2-4). The highest spatial resolution of instantaneous free-surface measurements was conducted with ADMs measuring the free-surface fluctuations simultaneously with a distance of about 15 cm between ADMs (Kucukali and Chanson 2008; Murzyn and Chanson 2009a; Chachereau and Chanson 2011b; Wang and Chanson 2015). The distance between each instrument limited a detailed analysis of the spatial and temporal resolution of the time-varying free-surface features of hydraulic jumps.

The strong longitudinal oscillations of hydraulic jumps have limited the recording of the free-surface features near the jump toe. Researchers have therefore assumed a fixed jump toe location and no free-surface fluctuations at the position of the jump toe (Mouaze et al. 2005; Murzyn et al. 2007; Murzyn and Chanson 2009a; Chachereau and Chanson 2011b). Although an influence of the jump toe oscillations on the characteristic free-surface frequencies of hydraulic jumps was detected through simultaneous measurements of free-surface fluctuations and jump toe oscillations with several ADMs located above the free-surface and other ADMs placed horizontally some centimeters above the toe perimeter facing the jump toe (Wang and Chanson 2013; Wang 2014), more detailed measurement of the free-surface features in

hydraulic jumps is needed to incorporate both the jump toe oscillations and free-surface fluctuations simultaneously.

To overcome previous limitations, the present study used LIDAR technology for the recording of the free-surface properties of hydraulic jumps. The LIDAR (Light Detection and Ranging) provided continuous and time-varying free-surface profiles yielding novel information of the dynamic behaviour of the hydraulic jump. The study included the analysis of basic free-surface features such as the mean and free-surface fluctuations and more advanced characterisations including free-surface time and length scales and spectral analyses. The LIDAR allowed the incorporation of jump toe movements into the analysis of the free-surface fluctuations. The experiments were conducted for a wide range of Froude and Reynolds numbers and different inflow conditions providing a clear characterisation of the free-surface features in hydraulic jumps.

TABLE 2–4. EXPERIMENTAL STUDIES OF FREE-SURFACE CHARACTERISTICS IN HYDRAULIC JUMPS

Reference	Inflow conditions			d_1 (m)	Fr_1 (-)	Re (-)	W (m)	Parameter analysed				Instrument (Frequency)	Simultaneous data measured in centreline/ Pixel dimensions for camera
	UD	PD	FD					Free-surface profile	Free-surface fluctuations	Jump toe motions	Free-surface time and length scales		
Bakhmeteff and Matzke (1936)	-	-	-	0.01 – 0.08	2 - 8.6	-	0.15	x				Profilometer	1
Rouse et al. (1959)	-	-	-	-	4	-	0.76	x				Pointer gauge	1
Rajaratnam (1962a)	x			0.024	3.5 – 11.3	-	0.30	x				Pointer gauge	1
Rajaratnam (1965)		x		0.015 – 0.06	2.7 – 9.8	$5.2 \times 10^4 - 1.3 \times 10^5$	0.30	x				-	-
Long et al. (1991)	-	-	-	-	4.0 – 9.0	-	0.47				x	High speed camera	240 x 192 pxs
Hager (1993)	x			0.02 – 0.06	4.3 – 8.9	$2.1 \times 10^5 - 6.9 \times 10^5$	0.50	x				Pointer gauge	1
Mouaze et al. (2005)		x		0.021 – 0.059	2.0 – 4.8	$4.6 \times 10^4 - 8.9 \times 10^4$	0.30	x	x		x	Wire gauge (128 Hz)	1
Murzyn et al. (2007)		x		0.021 – 0.059	1.9 – 4.8	$3.3 \times 10^4 - 8.8 \times 10^4$	0.30		x		x	Wire gauge (128 Hz) High-speed camera (120 Hz)	1 648 x 484 pxs
Kucukali and Chanson (2008)		x		0.024	4.7 – 8.5	$5.0 \times 10^4 - 9.8 \times 10^4$	0.50	x	x			ADM (50 Hz)	1
Chanson and Gualtieri (2008)		x		0.012 – 0.026	5.1 – 8.6	$2.5 \times 10^4 - 9.8 \times 10^4$	0.25 – 0.50				x	High-speed camera	-
Murzyn and Chanson (2009a)		x		0.018	3.1 – 8.5	$2.4 \times 10^4 - 6.4 \times 10^4$	0.50	x	x	x		ADM (50 Hz)	6
Chachereau and Chanson (2011b)		x		0.038 – 0.045	2.4 – 5.1	$6.6 \times 10^4 - 1.3 \times 10^5$	0.50	x	x	x	x	ADM (50 Hz)	7
Zhang et al. (2013)		x		0.025 – 0.027	2.8 – 7.5	$3.8 \times 10^4 - 7.6 \times 10^4$	0.50				x	High-speed camera	-
Wang and Chanson (2015)		x		0.012 – 0.047	3.8 – 8.5	$2.1 \times 10^4 - 1.6 \times 10^5$	0.50	x			x	ADM (50 Hz)	4
Wang and Murzyn (2017)		x		0.025 – 0.027	3.5 - 6.0	$4.8 \times 10^4 - 8.4 \times 10^4$	0.5				x	Video camera (25 Hz)	-
Present study		x	x	0.020 – 0.046	3.6 - 10	$6.2 \times 10^4 - 1.2 \times 10^5$	0.6	x	x	x	x	LIDAR	> 100

2.6. FORCES AND PRESSURE MEASUREMENTS IN HYDRAULIC JUMPS

A full understanding of the internal fluctuations in a hydraulic jump is required because these fluctuations may be responsible for erosion, cavitation and structural destabilisation (Harleman 1955; Schiebe and Bowers 1971; Abdul Khader and Elango 1974; Fiorotto and Rinaldo 1992). The characterisation of the internal fluctuations in hydraulic jumps is commonly conducted through the measurement of the longitudinal and transverse pressure fluctuations at the channel bed (e.g. Abdul Khader and Elango 1974; Fiorotto and Rinaldo 1992). Other researchers have measured vertical pressure distributions in flow direction (Wang et al. 2014b) or measured the drag forces linked with baffle blocks (e.g. Harleman 1955; Rajaratnam 1964a, 1964b; Ohtsu et al. 1991). Table 2-5 summarises previous research on drag forces and pressure fluctuations in hydraulic jumps including the inflow conditions, width and channel length, Froude and Reynolds numbers and the instrumentation as well as the focus of the respective study. The experiments are classified in two experimental approaches comprising drag force and pressure measurements in hydraulic jumps (Table 2-5).

TABLE 2-5. MEASUREMENT OF FORCES AND PRESSURES IN HYDRAULIC JUMPS

References	Inflow conditions			<i>L</i> (m)	<i>W</i> (m)	<i>Fr_I</i> (-)	<i>Re</i> (-)	Parameter analysed		Instrument
	UD	PD	FD					Force Baffle pier	Pressure fluctuations	
Harleman (1955)		x		5.5	0.46	3.0 - 8.0	-	x		Pier force measuring device
Rajaratnam (1964a, 1964b)		x		4.5	0.30	2.9 - 6	-	x		Piezometers
Rajaratnam and Murahari (1971)		x		4.9	0.46	3.1 - 8.5	-	x		Piezometer
Schiebe and Bowers (1971)			x	12	0.5/ 2.74	6.5			x	Pressure transducers
Abdul Khader and Elango (1974)		x		7.7	0.6	4.7 - 6.6	$3.4 \times 10^4 - 1.3 \times 10^5$		x	Pressure cells
Toso and Bowers (1988)	x		x	9.3	0.5	3 - 10	-		x	Pressure transducer/ Piezometers
Ohtsu et al. (1991)			x	4	0.2	3.5-9.5	-	x		Pressure transducer
Fiorotto and Rinaldo (1992)		x		5	0.3	5.0 - 9.5	$4.8 \times 10^4 - 1.2 \times 10^5$		x	Pressure taps
Lopardo (2013)				12	0.65	3.0 - 4.9	1.0×10^5		x	Pressure taps
Wang et al. (2014b)		x		3.2	0.5	3.8 - 8.5	$3.5 \times 10^4 - 8.0 \times 10^4$		x	Pressure probe
Pells (2016)				8.7	0.8	2.0 - 4.0	$1.2 \times 10^5 - 2.5 \times 10^5$	x		Tri-axial load cell

References	Inflow conditions			L (m)	W (m)	Fr_1 (-)	Re (-)	Parameter analysed		Instrument
	UD	PD	FD					Force Baffle pier	Pressure fluctuations	
Present study		x	x	40	0.6	3.8 - 10	$6.2 \times 10^4 -$ 1.2×10^5		Force fluctuations	Six axis load cell

2.6.1. FORCE MEASUREMENTS IN HYDRAULIC JUMPS

The measurement of forces in hydraulic jumps has been focused on the quantification of the drag force on the baffle blocks in hydraulic jumps. Hydraulic jumps with baffle blocks are also known as forced hydraulic jumps. The term pressure drag or drag force is associated with the normal force acting on a body exposed to a fluid (Hoerner 1965). The drag force F_D is represented in the momentum equation across a control volume between the upstream and downstream regions of the hydraulic jump (Figure 2-2) (Harleman 1955; Rajaratnam 1967):

$$\sum F_x = F_1 - F_2 - F_t - F_D = \rho QV_2 - \rho QV_1 \quad (2.9)$$

The drag force on the baffle pier is proportional to the drag coefficient C_d and the frontal area of the block A (Harleman 1955; Hoerner 1965; Rajaratnam 1967):

$$F_D = \frac{C_d \rho V_1^2 A}{2} \quad (2.10)$$

The analysis of the drag forces in baffle piers is important for the safety of hydraulic structures since the location of the baffle pier in the stilling basin may affect significantly the flow behaviour leading to cavitation. For example, baffle piers located near the jump toe will generate violent jumps and higher turbulence (Harleman 1955; Rajaratnam 1964a, 1964b; Rajaratnam and Murahari 1971). The effect of high velocity on baffle piers can generate cavitation leading to a destabilisation of the structure (Harleman 1955). On the contrary, forced hydraulic jumps with baffle piers located far from the jump toe will be similar to classical hydraulic jumps (Rajaratnam 1964a, 1964b; Rajaratnam and Murahari 1971).

A number of previous studies have attempted to measure the drag force on baffle pier structures. Harleman (1955) quantified the forces on a baffle pier with a pier force measuring device able to detect horizontal displacements. The device was mounted above a movable plate in the channel bottom with a maximum force range of 89 N (Harleman 1955). The results suggested that baffle piers are able to stabilise the jump toe oscillations of hydraulic jumps in stilling basins (Harleman 1955). However, the maximum force recorded on the baffle piers was only 20% of the total force recorded at the downstream end of the hydraulic jump (Harleman 1955).

Rajaratnam (1964a, 1964b) estimated the drag coefficients of baffle piers under different arrangements (variation in the baffle pier sizes and Froude numbers) based upon the momentum

equation presented in Equation 2.9. The upstream and downstream flow depths were recorded with pointer gauge and piezometer tappings (Rajaratnam 1964a, 1964b). The drag coefficient was strongly influenced by geometrical characteristics of the baffle piers and its position along the hydraulic jump (Rajaratnam 1964a, 1964b). Drag coefficients between $0.01 < C_d < 0.18$ were observed for baffle piers located far downstream of the jump toe and $0.18 < C_d < 0.46$ were found for baffle piers located close the jump toe (Rajaratnam 1964a, 1964b). Rajaratnam and Murahari (1971) investigated the internal forces in forced hydraulic jumps using piezometers to measure the pressure distributions on the front and rear sides of a baffle pier located at different longitudinal positions along the hydraulic jump. Similar experiments were conducted by Ohtsu et al. (1991). The observations of the dynamic pressures on the front face of the baffle pier located close to the jump toe showed a decrease in pressure with increasing elevation above the channel bed up to a minimum at $y/h_{bp} \cong 0.2 - 0.3$ where h_{bp} is the height of the baffle pier, followed by an increase in the pressure until $y/h_{bp} \cong 0.7 - 0.8$ (Rajaratnam and Murahari 1971; Ohtsu et al. 1991) (Figure 2-6). The shape of the pressure distribution may be related to the formation of an eddy upstream of the baffle pier (Ohtsu et al. 1991). Figure 2-6 presents typical dynamic pressure distributions of Ohtsu et al. (1991) on the upstream face of the baffle block close to the jump toe. If the baffle pier was located at the downstream end of the hydraulic jump, the pressure distribution at the front side of the baffle pier was almost uniform (Rajaratnam and Murahari 1971).

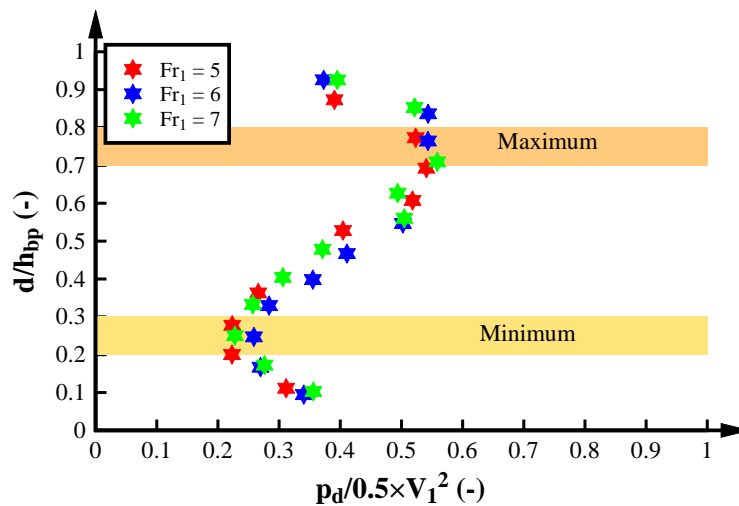


FIGURE 2-6. DYNAMICAL PRESSURE DISTRIBUTION (P_d) ON THE UPSTREAM FACE OF A BAFFLE BLOCK. ADAPTED FROM OHTSU ET AL. (1991).

The pressure at the rear side of the baffle piers was uniform for all longitudinal positions and was smaller compared to the pressures recorded in the upstream face of the block (Rajaratnam and Murahari 1971). Recently, Pells (2016) conducted shear and vertical force measurements at the bed of a steeply sloping channel with a hydraulic jump using a block connected to a triaxial load cell located beneath the bed. While the time-averaged drag force was not affected by the hydraulic jump, the lift force decreased when the hydraulic jump was

above the block which may be associated to a decrease in fluid mixture density due to flow aeration inside the hydraulic jump (Pells 2016). Despite the current understanding of forces acting on baffle piers, and at the channel bed of sloped channels acting as spillways, these previous studies have provided little information on the three-dimensional internal motions in hydraulic jumps.

2.6.2. PRESSURE MEASUREMENTS IN HYDRAULIC JUMPS

Pressure measurements are commonly conducted in the design of stilling basins to avoid erosion and destabilisation inside the basin linked with the formation of a hydraulic jump. Schiebe and Bowers (1971) measured the pressure fluctuations and frequencies in the channel bed beneath a hydraulic jump recording maximum pressure fluctuations beneath the roller corresponding to 5% of the kinetic energy upstream of the hydraulic jump and dominant frequencies of the pressure fluctuations between 0.1 – 1 Hz. Abdul Khader and Elango (1974) measured the pressure fluctuations at the channel bed with five pressure cells for $4.7 < Fr_1 < 6.6$, observing an increase in pressure downstream of the jump toe and maximum pressure fluctuations within the roller region. Further downstream, the pressure decreased (Schiebe and Bowers 1971; Abdul Khader and Elango 1974). Abdul Khader and Elango (1974) observed a larger number of positive pressure fluctuations. A comparison with previous experiments suggested a strong effect of the inflow conditions on the pressure fluctuations at the channel bed (Abdul Khader and Elango 1974). Toso and Bowers (1988) measured the effect of inflow conditions on the pressure fluctuations beneath hydraulic jumps observing larger pressure fluctuations for undeveloped hydraulic jumps which was linked with a faster break-up of turbulence in fully developed hydraulic jumps. Toso and Bowers (1988) recorded maximum pressure fluctuations of about $\Delta P/V_1^2/2g = 0.8$ to 1.0, and the magnitude was similar for undeveloped and fully developed hydraulic jumps.

Fiorotto and Rinaldo (1992) conducted a systematic series of experiments to quantify the horizontal and transverse pressure fluctuations at the channel bed of a hydraulic jump. In agreement with previous studies, a peak in pressure fluctuations was observed beneath the jump roller. The peak decreased with increasing Fr_1 while the location of the peak shifted downstream with increasing Fr_1 within a range of $10 < x/d_1 < 30$ for $5 < Fr_1 < 9.5$ (Fiorotto and Rinaldo 1992). A longitudinal cross-correlation analysis between simultaneous points showed that the correlation increased with increasing distance from the jump toe and increasing inflow Froude number (Fiorotto and Rinaldo 1992). A transverse cross-correlation analysis was conducted showing larger transverse correlation compared with the longitudinal correlation suggesting large transverse eddies inside hydraulic jumps (Fiorotto and Rinaldo 1992).

Lopardo and Romagnoli (2009) and Lopardo (2013) estimated the pressure fluctuations in hydraulic jumps using instantaneous velocities relating the pressure fluctuations to velocity fluctuations (Lopardo 2013):

$$\frac{\overline{u'^2}}{V_1} = \lambda \sqrt{\frac{\sqrt{\overline{p'^2}}}{\rho \times \left(\frac{V_1^2}{2}\right)}} \quad (2.11)$$

where u' is the standard deviation of the velocity, λ a non-dimensional coefficient to correlate velocity fluctuations and pressure fluctuations and p' are the pressure fluctuations. The velocity fluctuations were maximum close to the jump toe, $x/(d_2-d_1) = 3$ for $3 < Fr_1 < 6$ and an increase in fluctuations with increasing Fr_1 (Lopardo and Romagnoli 2009; Lopardo 2013). The maximum velocity fluctuations corresponded to 25% of the inflow velocity (Lopardo and Romagnoli 2009; Lopardo 2013).

Wang et al. (2014b) measured the total pressure distributions at different elevations and cross-sections along the hydraulic jump with a dynamic pressure probe. The experiments suggested that the piezometric pressures can be considered hydrostatic if the void fraction is considered (Wang et al. 2014b). In agreement with previous studies (Schiebe and Bowers 1971; Abdul Khader and Elango 1974), the pressure fluctuations measured with the pressure probe increased with Fr_1 (Wang et al. 2014b). Characteristic pressure frequencies $freq_p$ were identified with maximum frequencies of $8 \text{ Hz} < freq_p < 12 \text{ Hz}$ and low frequencies of $freq_p \cong 2.6 \text{ Hz}$ (Wang et al. 2014b).

Studies over the last fifty years have provided important information on drag force coefficients on baffle piers and longitudinal, transverse pressure fluctuations at the channel bed and the vertical pressure distribution in the hydraulic jumps for a wide range of Froude and Reynolds numbers and different inflow conditions. These studies highlighted the violent fluctuations and strong movements of hydraulic jumps. Although these studies contributed to the understanding of regions of high turbulence, to date, no study has attempted to measure the internal three-dimensional motions in hydraulic jumps. The present study investigated the three-dimensional internal motions inside hydraulic jumps to obtain a clear understanding of the dissipative processes and internal fluctuations in hydraulic jumps.

2.7. SCALE EFFECTS

Hydraulic parameters in laboratory models, unless at full-scale, may be affected by scale effects. In air-water flow studies, the difference in the Reynolds numbers between laboratory experiments ($10^4 < Re < 10^5$) and full-scale structures ($10^6 < Re$) is of at least one order of magnitude highlighting the importance to investigate potential scale effects (Felder and

Chanson 2017). For the scale effect analysis of hydraulic jumps, a systematic dimensional analysis of the representative variables can identify the relevant dimensionless groups. Table 2-6 lists the relevant parameters in the present study.

TABLE 2–6. HYDRAULIC JUMPS PARAMETERS IN RECTANGULAR CHANNELS CONSIDERED IN THE PRESENT STUDY

Category	Selection of parameters in the present study
Measurement location	<ul style="list-style-type: none"> • Longitudinal position (x) • Vertical position (y) • Transverse position (z)
Fluid properties	<ul style="list-style-type: none"> • Density of air (ρ_{air}) • Density of water (ρ) • Dynamic viscosity of air (μ_{air}) • Dynamic viscosity of water (μ) • Surface tension (σ)
Channel geometry	<ul style="list-style-type: none"> • Channel width (W) • Slope (θ) • Bed roughness (k_s) • Length of the channel (L)
Inflow conditions	<ul style="list-style-type: none"> • Inflow depth (d_I) • Inflow velocity (V_I) • Discharge (Q) • Boundary layer thickness (δ) • Gate opening (h_0) • Distance from the sluice gate (x_{sg})
Air-water flow properties	<ul style="list-style-type: none"> • Void fraction (C) • Bubble count rate (F) • Interfacial velocity (V_{CP}) • Chord time (t_{ch}) • Auto-correlation time scales ($T_{air,auto}$) • Longitudinal cross-correlation time scales ($T_{air,cross}$)
Free-surface and jump toe features	<ul style="list-style-type: none"> • Flow depth (d) • Free-surface fluctuations (d') • Jump toe oscillations (x_{toe}) • Jump toe frequency ($freq_{toe}$) • Dominant free-surface frequency ($freq_{fs(dom)}$) • Auto-correlation time scales ($T_{fs,auto}$) • Longitudinal cross-correlation time scales ($T_{fs,cross}$) • Integral length scale (L_{fs})
Internal forces	<ul style="list-style-type: none"> • Time-averaged streamwise force (F_x) • Time-averaged transverse force (F_z) • Time-averaged vertical force (F_y) • Streamwise force fluctuations (F_x') • Transverse force fluctuations (F_z') • Vertical force fluctuations (F_y')

A dimensional analysis for the variables in Table 2-6, provides (Chanson 2006; Chanson 2007a; Murzyn and Chanson 2008; Chanson and Gualtieri 2008):

$$C, F, V_{CP}, u', t_{ch}, d, d', x_{toe}, F_x, F_x' \dots = f(x, y, z, d_1, V_1, u_1', x_1, \delta, W, \rho_{air}, \rho, \mu_{air}, \mu, \sigma, g, \dots) \quad (2.12)$$

Equation 2.12 can be rewritten as (Chanson 2006; Chanson 2007a; Murzyn and Chanson 2008; Chanson and Gualtieri 2008):

$$C, \frac{F \times d_1}{V_1}, \frac{V_{CP}}{\sqrt{gd_1}}, \frac{u'}{V_1}, \frac{t_{ch}}{d_1}, \frac{d}{d_1}, \frac{d'}{d_1}, \frac{x_{toe}}{d_1}, \frac{F_x}{F_{u/s}}, \frac{F'_x}{F_{u/s}} \dots = f\left(\frac{x}{d_1}, \frac{y}{d_1}, \frac{z}{d_1}, Fr_1, \frac{u'_1}{V_1}, \frac{x_1}{d_1}, \frac{\delta}{d_1}, \frac{W}{d_1}, Re, We \dots\right) \quad (2.13)$$

where $F_{u/s}$ is the total incoming force upstream of the hydraulic jump ($F_{u/s} = F_I + \rho d_1 V_I$). Equation 2.13 shows the dependency of the air-water flow properties on the Froude number (ratio of inertia to gravity effects, $Fr_1 = V_I/\sqrt{gd_1}$), Reynolds number (ratio of inertia to viscous effects, $Re = V_I \times d_1/\nu$) and Weber number (ratio of inertia to surface tension effects, $We = \rho \times V_I^2 \times d_1/\sigma$) (Henderson 1966; Chanson 2004). Using geometric similarity, simultaneous scaling of Froude, Reynolds and Weber is impossible resulting in unavoidable scale effects. For scenarios with same fluids in model and prototype, a rearrangement of Froude, Reynolds and Weber numbers results in the Morton number ($Mo = We^3/Fr_1^2 Re^4$). The Morton number is a dimensionless parameter representing only the fluid properties and the gravity and can replace the Weber number. In flow cases with the same fluid, i.e. air and water in the present study, the similitude of the Morton number is accomplished accounting for negligible effects of the surface tension (Chanson 2006; Murzyn and Chanson 2008; Chanson and Chachereau 2013).

Table 2-7 presents previous studies on scale effects in hydraulic jumps including the inflow conditions, length and width of the channel, Froude and Reynolds numbers and the investigated parameters.

TABLE 2-7. INVESTIGATION OF SCALE EFFECTS IN HYDRAULIC JUMPS

References	Inflow conditions		L (m)	W (m)	Fr ₁ (-)	Re (-)	Parameters analysed				
	PD	FD					Air-water flow properties	Free-surface and jump toe features	Internal forces	Parameters	
Chanson (2006, 2007a)	x		3.2	0.25 - 0.5	5.1 - 8.6	2.5×10 ⁴ - 9.8×10 ⁴	x				C F t _{ch} t _{ch,cluster} T _{air,cross}
Murzyn and Chanson (2008)	x		3.2	0.5	5.1 - 8.3	3.8×10 ⁴ - 6.2×10 ⁴	x				C F t _{ch}
Chanson and Gualtieri (2008)	x		3.2	0.25 - 0.5	5.1 - 8.6	2.5×10 ⁴ - 9.8×10 ⁴	x				C F
Chanson and Chachereau (2013)	x		3.2	0.5	5.1	2.5×10 ⁴ - 1.3×10 ⁵	x				C F V

References	Inflow conditions		<i>L</i> (m)	<i>W</i> (m)	<i>Fr₁</i> (-)	<i>Re</i> (-)	Parameters analysed			
	PD	FD					Air-water flow properties	Free-surface and jump toe features	Internal forces	Parameters
										<i>T_{air,auto}</i>
										<i>t_{ch,cluster}</i>
										<i>x_{toe}'</i>
								x		<i>freq_{toe}</i>
										<i>d_{max}'</i>
										<i>freq_{fs}</i>
Wang (2014)	x		3.2	0.5	3.8 - 7.5	$3.4 \times 10^4 - 1.4 \times 10^5$				<i>C</i>
										<i>F</i>
										<i>V</i>
							x			<i>t_{ch}</i>
										<i>t_{ch,cluster}</i>
										<i>L_{fs}</i>
Felder and Chanson (2016a, 2018)		x	3.2	0.5	3.8 - 4.6	$9.0 \times 10^4 - 2.1 \times 10^5$			x	<i>C</i>
										<i>F</i>
										<i>V</i>
										<i>T_{air,auto}</i>
										<i>T_{air,cross}</i>
										<i>C</i>
										<i>F</i>
										<i>V_{CP}</i>
							x			<i>t_{ch,mean}</i>
										<i>T_{air,auto}</i>
										<i>T_{air,cross}</i>
										<i>d</i>
										<i>d_{max}'</i>
										<i>x_{toe,min} - x_{toe,max}}}</i>
										<i>x_{toe}'</i>
										<i>freq_{toe}</i>
Present study	x	x	40	0.6	3.6 - 10	$6.2 \times 10^4 - 1.2 \times 10^5$			x	<i>freq_{fs(dom)}}</i>
										<i>freq_{fs(sec)}}</i>
										<i>T_{fs,auto}</i>
										<i>L_{fs}</i>
										<i>F_x</i>
										<i>F_z</i>
										<i>F_y</i>
										<i>F_x'</i>
										<i>F_z'</i>
										<i>F_y'</i>
										<i>freq_{Fx,dom}}</i>
										<i>freq_{Fz,dom}}</i>
										<i>freq_{Fy,dom}}</i>

Several studies identified scale effects in the air-water flow properties and free-surface features in hydraulic jumps (Table 2-8). The majority of these studies were analysed in partially developed inflow conditions apart from the study conducted by Felder and Chanson (2016a, 2018) in hydraulic jumps on a rough channel bed (Table 2-7). The analysis of scale effects in

terms of air-water flow properties showed no scale effects in void fractions for $6 \times 10^4 < Re < 2.1 \times 10^5$ (Chanson 2006, 2007a; Murzyn and Chanson 2008; Chanson and Gualtieri 2008; Chanson and Chachereau 2013; Wang 2014; Felder and Chanson 2016a, 2018). The bubble count rate, chord time distribution, cluster properties and turbulence levels are affected by scale effects unless the experiment is at full scale (Chanson 2006, 2007a; Murzyn and Chanson 2008; Chanson and Chachereau 2013; Wang 2014; Felder and Chanson 2016a, 2018). The interfacial velocity presented no scale effects for $Re > 3 \times 10^4$ (Chanson and Chachereau 2013; Wang 2014) and the turbulent scales showed small scale effects for $Re < 6 \times 10^4$ in smooth channels (Wang 2014; Felder and Chanson 2016a, 2018). Small scale effects were observed in terms of void fraction, bubble count rate and chord time distributions for channel widths between $0.25 \leq W \leq 0.5$ and $8 \leq W/d_I \leq 22$ (Chanson 2006, 2007a).

Few studies have analysed the scale effects on the free-surface features of hydraulic jumps. The jump toe oscillations and the maximum fluctuations of the free-surface had no scale effects. The characteristic frequency of the jump toe movement and the free-surface fluctuations showed scale effects for $Re < 1 \times 10^5$ (Chanson 2006; Wang 2014) (Table 2-8).

TABLE 2-8. SUMMARY OF SCALE EFFECTS IN TERMS OF FROUDE SIMILITUDE IN HYDRAULIC JUMPS BASED ON PREVIOUS LITERATURE (CHANSON 2006; 2007a, MURZYN AND CHANSON 2008; CHANSON AND GUALTIERI 2008; CHANSON AND CHACHEREAU 2013; WANG 2014; FELDER AND CHANSON 2016a, 2018)

No scale effects	Minimum value required to minimise scale effects		Unavoidable scale effects in experimental models
	Variable	Variables	
x_{toe} d_{max}	C	$Re > 6 \times 10^4$	F
	V	$Re > 3 \times 10^4$	t_{ch} $t_{ch,cluster}$
	$T_{air,auto}$	$Re > 6 \times 10^4$	
	$T_{air,cross}$	$Re > 6 \times 10^4$	
	L_{fs}	$Re > 6 \times 10^4$	
	$freq_{toe}$	$Re > 1 \times 10^5$	
	$freq_{fs}$	$Re > 1 \times 10^5$	

Overall, several studies have investigated scale effects in the air-water flow properties in the hydraulic jump. However, no information is known for scale effects under fully developed inflow conditions for hydraulic jumps in smooth channel beds. The scale effects on the free-surface features in hydraulic jumps are limited to point measurements and no information is known on potential scale effects in terms of the free-surface time and length scales in hydraulic jumps. The present study quantified the scale effects on fully developed hydraulic jumps including the analysis of the air-water flow properties and free-surface features. An additional systematic analysis of potential scale effects in terms of internal motions was also conducted to identify any similitude in the dissipative fluctuations of a hydraulic jump.

2.8. THESIS OVERVIEW AND OBJECTIVES

A hydraulic jump is a fascinating complex phenomenon engaging the attention of many researchers for almost two centuries. The complex dynamic structures associated with the rapid transition from supercritical to subcritical flow is relevant for many applications since hydraulic jumps are characterised by strong turbulent motion associated with flow aeration, dissipative processes, enhancement of air-water mass transfer, free-surface fluctuations, internal motions responsible for erosion, cavitation and structural destabilisation, amongst others. Initial approaches to understand hydraulic jumps used the momentum approach providing the conjugate flow depth ratio. Experimental evidence provided the roller length, basic free-surface features, internal velocities and turbulence estimates, while most recent studies focused on the in-depth understanding of the air-water flow properties, turbulent scales, free-surface dynamics and pressure fluctuations. Despite significant advances in the understanding of the dynamic flow processes in hydraulic jumps, the understanding of the three-dimensional dissipative processes and internal movements in hydraulic jumps remains limited.

Herein the present study aims to provide a better understanding of the energy dissipation processes in hydraulic jumps combining novel experimental results of a) air-water flow properties, b) free-surface fluctuations and jump toe oscillations and c) internal three-dimensional forces on a submerged sphere inside hydraulic jumps.

In terms of time-averaged air-water flow properties, the advective and recirculation processes in hydraulic jumps are well understood for a wide range of Froude and Reynolds numbers. However, the majority of previous studies of the air-water flow properties have been limited to partially developed inflow conditions. Herein new experiments were conducted to investigate the air-water flow properties in hydraulic jumps under partially and fully developed inflow conditions allowing a direct assessment of the effect of inflow conditions upon a range of air-water flow properties. Scale effects were tested for both fully and partially developed hydraulic jumps. A comparison of the air-water flow features between classical hydraulic jumps and hydraulic jumps on a mild slope was also conducted providing a more complete characterisation on the air-water flow properties in hydraulic jumps as well as highlighting potential advantages of sloped channels for design applications.

Previous research of the free-surface fluctuations in hydraulic jumps has been conducted at fixed measurement locations along the hydraulic jump limiting information of the free-surface profiles, free-surface fluctuations, and free-surface scales. A description of the time-variation and the free-surface fluctuations based upon a limited number of measurement positions does not provide a full picture of the dynamic behaviour nor does it account for the longitudinal hydraulic jump movements. Herein, the present study measured the time-varying free-surface features in hydraulic jumps with a LIDAR continuously providing the most

detailed information of the free-surface properties to date. The study provided detailed information of free-surface profiles, free-surface fluctuations, characteristic frequencies, and free-surface turbulent time and length scales as well as the jump toe oscillations and frequencies. The experiments were conducted for partially and fully developed inflow conditions and a wide range of Froude and Reynolds numbers to identify any effect of inflow conditions and potential scale effects in terms of free-surface characteristics.

The hydraulic jump is a violent phenomenon able to generate erosion and destabilisation due to the strong three-dimensional forces acting beneath the jump roller. Previous studies of the internal forces have mostly focused on the quantification of the forces on baffle blocks and the pressure fluctuations at the apron of stilling basins. The three-dimensional behaviour associated with the dissipative processes in hydraulic jumps remains however widely unclear. Herein the present research measured the internal three-dimensional forces acting on a submerged sphere inside hydraulic jumps at different vertical and longitudinal positions and in channel centreline. The forces were measured with a six-axis load cell providing a simultaneous three-dimensional force profile acting on the sphere inside of the hydraulic jump. The experiments were conducted for a wide range of Froude and Reynolds numbers and for partially and fully developed inflow conditions. The observations of the internal forces on the submerged sphere provided new insights into the three-dimensional motions inside hydraulic jumps including their fluctuations and frequencies as well as indirect measurements of the dissipative processes in hydraulic jumps.

The better understanding of the air-water flow properties, free-surface fluctuations, jump toe oscillations and internal motions were combined to obtain the most distinct understanding of the flow processes in hydraulic jumps to date. The present study identified regions of larger aeration, free-surface fluctuations and internal motions providing a clear picture of the dissipative features along the hydraulic jump. The closer understanding of the three-dimensional flow behaviour and dissipative mechanisms may be of significant relevance for future validation of numerical models and associated improvements in stilling basin designs. Table 2-9 shows the thesis outline and a brief description of the content of each chapter:

TABLE 2-9. THESIS OUTLINE

Chapter	Description
Chapter1. Introduction	Description of hydraulic jumps and relevance in the hydraulic structures
Chapter2. Literature review	Bibliographic summary and objectives of the thesis.
Chapter 3. Experimental modelling and methodology	Description of the experimental facilities, instrumentation and data processing methods.

Chapter	Description
Chapter 4. Air-water flow properties	Presentation and comparative analysis of air-water flow properties in hydraulic jumps with partially and fully developed inflow conditions highlighting a strong effect of the inflow condition upon the air-water flow properties.
Chapter 5. Free-surface fluctuations and jump toe oscillations	Presentation of LIDAR measurements of time-varying free-surface features and jump toe movements with high spatial and temporal resolution. Results include basic and advanced free-surface properties providing the most detailed description of free-surface features of partially and fully developed hydraulic jumps to date.
Chapter 6. Internal motions in Hydraulic Jumps	Presentation of unique three-dimensional internal motions in hydraulic jumps based upon force measurements on a submerged sphere inside hydraulic jumps with partially and fully developed inflow conditions.
Chapter 7. Discussion	This chapter brings together the key findings of previous chapters combining the air-water flow properties, free-surface fluctuations and internal forces to provide a clear identification of the hydraulic jump features and qualitative understanding of the energy dissipation processes.
Chapter 8. Conclusions and future research	Summary of the outputs of this thesis and future research suggestions.

3

EXPERIMENTAL CONFIGURATION AND METHODOLOGY

Some content of this chapter is taken from the following publications:

Journal Publications

Montano, L., Li, R., and Felder, S. 2018. ‘Continuous measurements of time-varying free-surface profiles in aerated hydraulic jumps with a LIDAR’, *Experimental Thermal and Fluid Science*, vol. 93, pp. 379 – 397.

Montano, L., and Felder, S. 2019 ‘LIDAR observations of free-surface time and length scales in hydraulic jumps’, *Journal of Hydraulic Engineering* (in print, accepted for publication on 14/8/2019)

Conference Proceedings

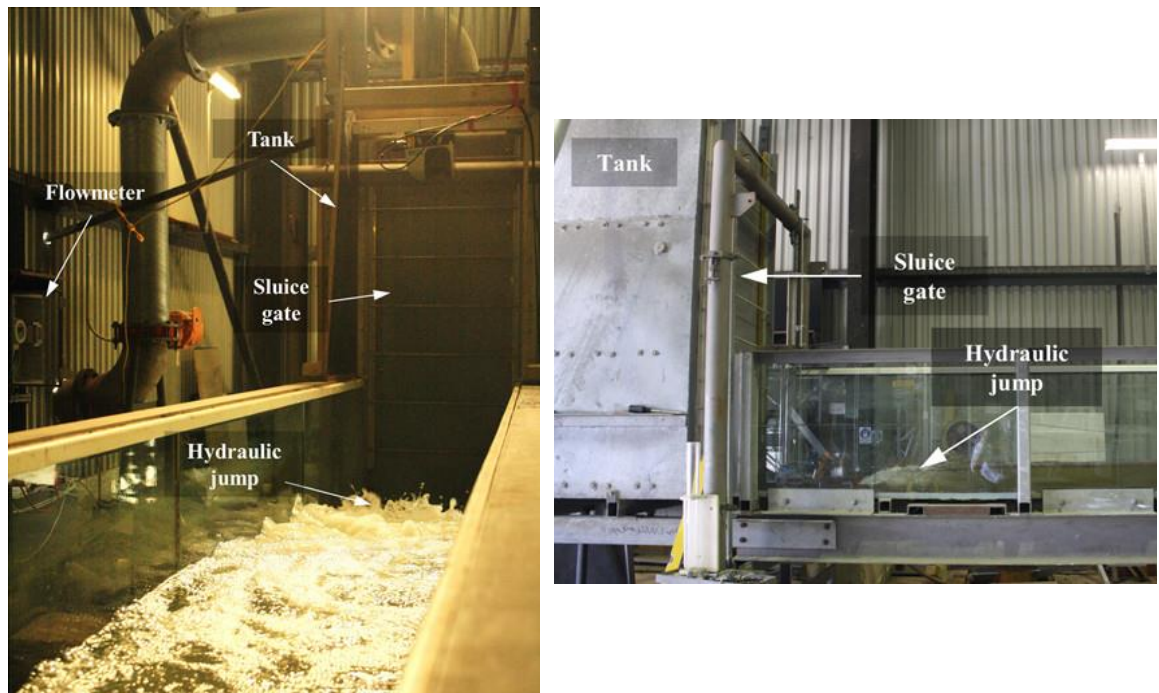
Montano, L., and Felder, S. 2019, ‘Measuring internal forces in a hydraulic jump with a load cell’, in *Proc., 38th IAHR World Congress*, Panama City, Panama, 10 pages.

Montano, L., and Felder, S. 2018, ‘LIDAR measurements of free-surface profiles and turbulent scales in a hydraulic jump’, in *Proc., 7th IAHR International Symposium on Hydraulic Structures*, Aachen, Germany, 10 pages.

Montano, L., and Felder, S. 2018, ‘Effect of inflow conditions on the air-water flow properties in hydraulic jumps’, in *Proc., 21st Australasian in Fluid Mechanics Conference*, Australasian Fluid Mechanics Conference, Adelaide, Australia, 4 pages.

3.1. EXPERIMENTAL FACILITY

All experiments were undertaken at the UNSW Water Research Laboratory. The experiments were conducted in a horizontal rectangular channel with glass sidewalls which was 40 m long, 0.6 m wide and 0.6 m high. The supercritical inflow conditions were generated downstream of a sluice gate with a rounded upstream corner ($\varnothing = 5$ cm) providing uniform inflow conditions (Figure 3-1). Constant flow rates were supplied from Manly Dam feeding a header tank of 2 m height. The longitudinal position of the hydraulic jump was controlled with a tail gate located at the downstream end of the channel. Figure 3-2 shows the experimental setup for hydraulic jumps downstream of the sluice gate including hydraulic jumps with partially and fully developed inflow conditions as well as the instrumentation. The sluice gate acted as a flow control and identical Froude and Reynolds numbers were achieved for different inflow conditions by adjustment of the gate opening (h_0).



A) UPSTREAM VIEW ($Fr_1 = 7.0$, $Re = 1.1 \times 10^5$).

B) SIDE VIEW ($Fr_1 = 3.2$, $Re = 4.8 \times 10^4$). FLOW FROM LEFT TO RIGHT.

FIGURE 3-1. PHOTO OF THE EXPERIMENTAL SETUP OF HYDRAULIC JUMPS DOWNSTREAM OF A SLUICE GATE.

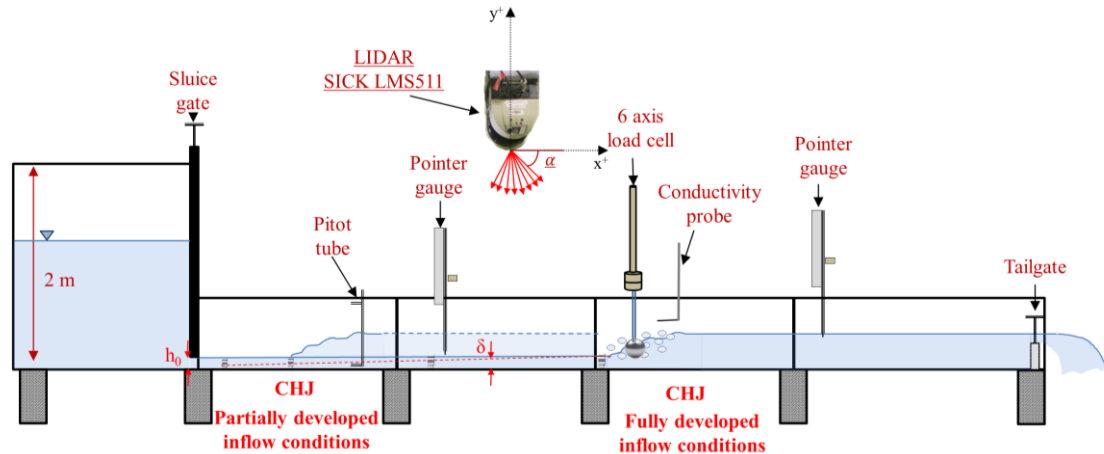


FIGURE 3-2. EXPERIMENTAL SETUP OF HYDRAULIC JUMPS DOWNSTREAM OF A SLUICE GATE (NOT TO SCALE).

3.2. INSTRUMENTATION

3.2.1. AIR-WATER FLOW PROPERTIES

All air-water flow properties were measured with a conductivity probe, which has been tested as a reliable instrument to estimate the air entrainment in air-water flows (Chanson and Toombes 2002; Felder and Pfister 2017). The conductivity probe is an intrusive instrument which records instantaneous changes in the electrical resistance of two electrodes, one electrode is a fully insulated platinum wire with an uninsulated tip facing the flow and the second electrode is a grounded metal needle surrounding the wire (Nassos and Bankoff 1967; Herringe and Davis 1974, 1976, 1978; Nagash 1994; Chanson 2002). Since the air resistance is 1000 times larger than the resistance of water, the needle-tip probe can identify changes in the resistance of the surrounding phase making the probe an accurate instrument to detect the local air-water interfaces at a fixed position (Herringe and Davis 1974, 1976, 1978; Chanson 2002). The conductivity probe used in the present study have been developed at WRL and successfully benchmarked recently against established phase-detection intrusive probe systems (Felder and Chanson 2016a; Felder and Pfister 2017, Felder et al. 2019). The data acquisition consisted of an electronic box self-developed at WRL that excited the probe tips and sent the raw signal information to a portable National Instruments USB-9162 card which was the communication interface between the electronic box and a PC. The raw data were acquired with a LabVIEW software developed at WRL (Figure 3-3).

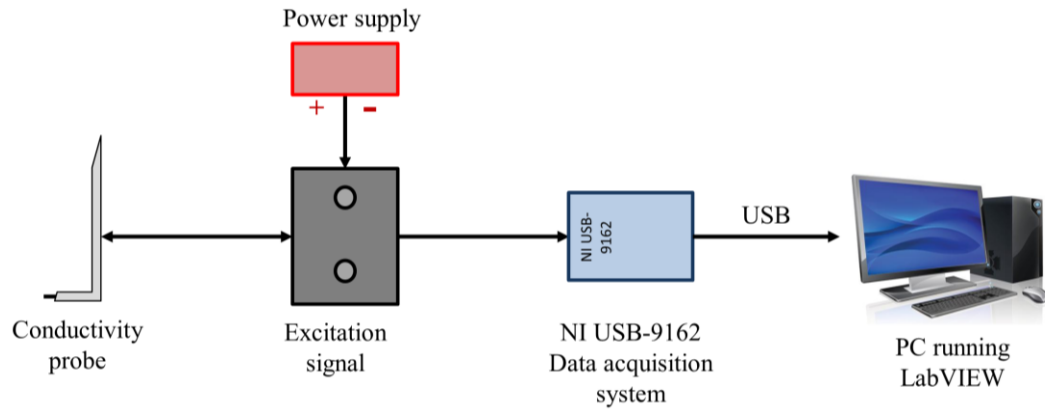
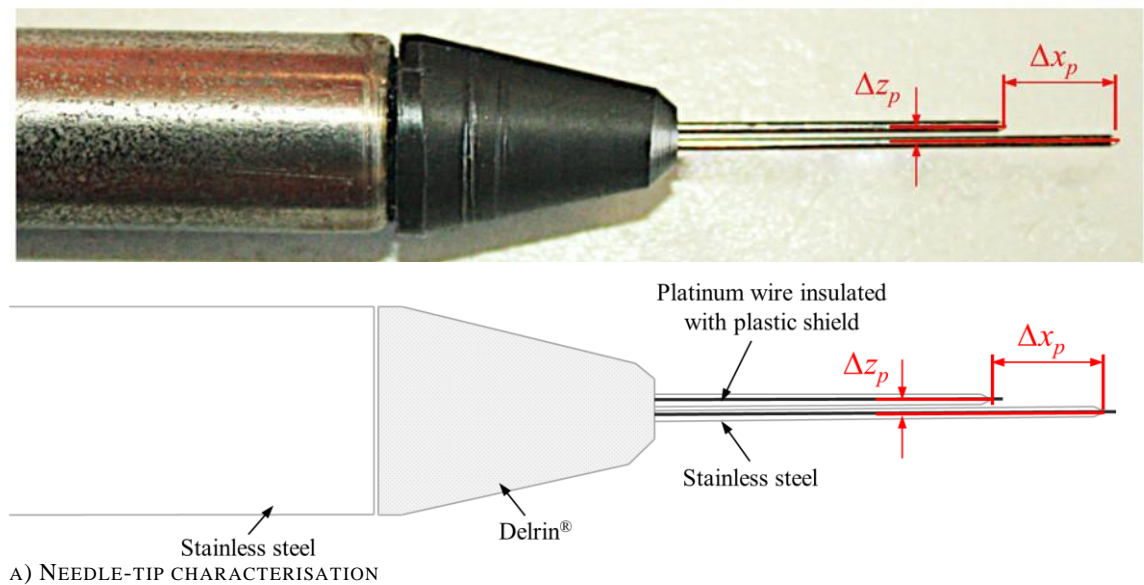
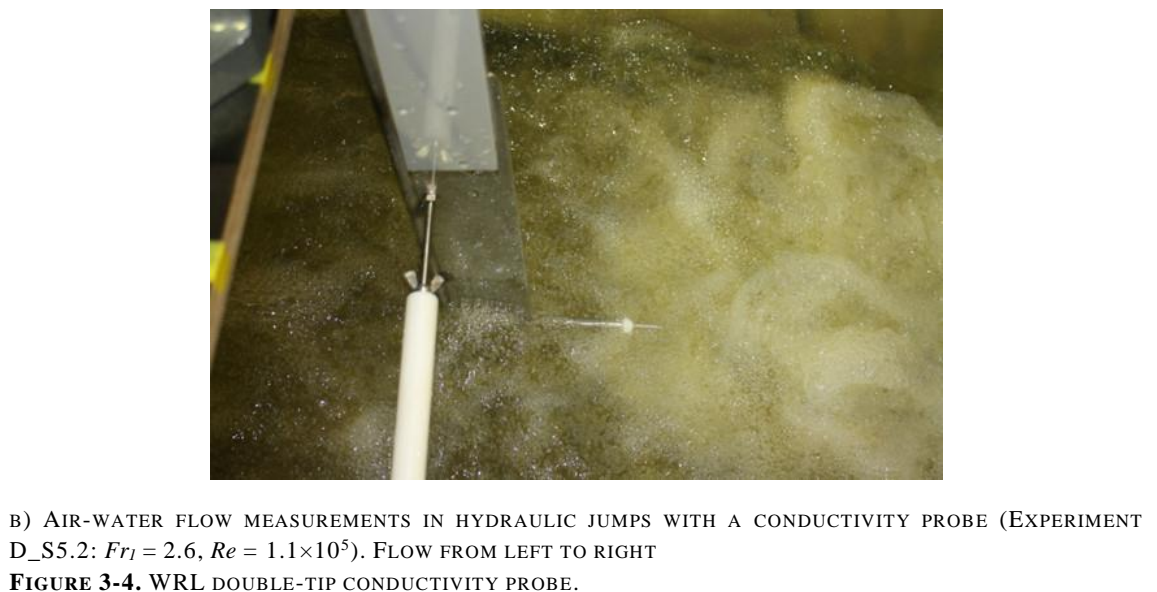


FIGURE 3-3. DATA ACQUISITION DIAGRAM OF THE CONDUCTIVITY PROBE.

The WRL conductivity probe had two identical platinum tips insulated with an epoxy with an inner electrode diameter of $\varnothing = 0.125$ mm and surrounded by a stainless steel hypodermic needle with an outer diameter of $\varnothing = 0.5$ mm (Figure 3-4).



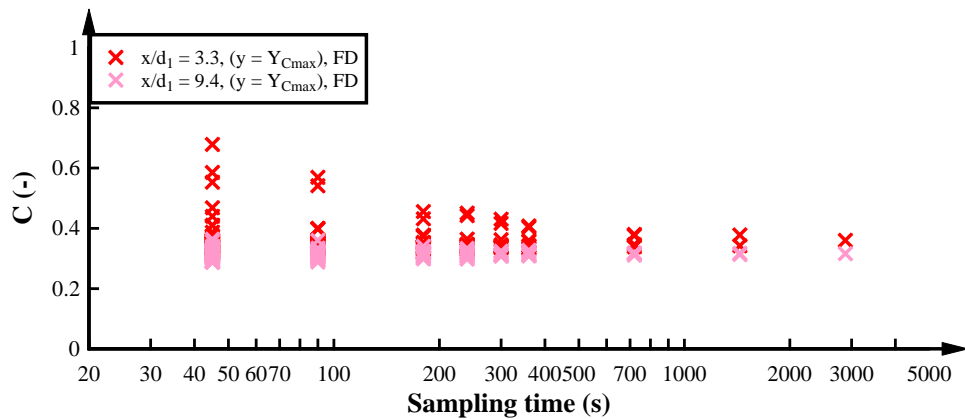
A) NEEDLE-TIP CHARACTERISATION



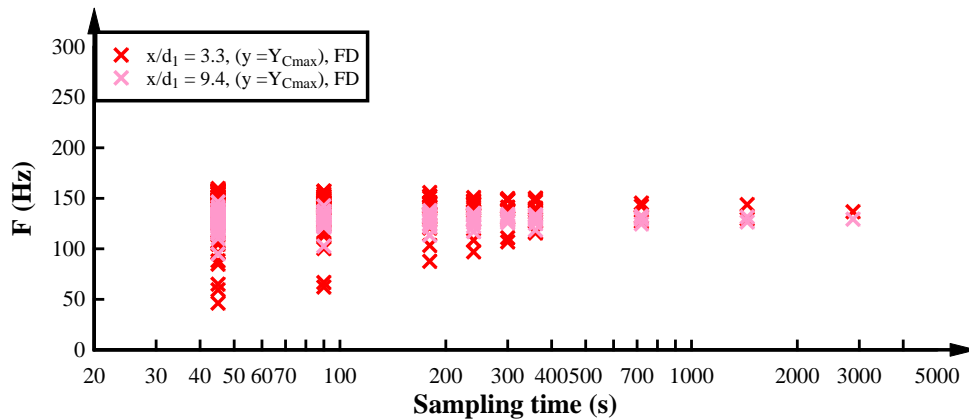
B) AIR-WATER FLOW MEASUREMENTS IN HYDRAULIC JUMPS WITH A CONDUCTIVITY PROBE (EXPERIMENT D_S5.2: $Fr_l = 2.6$, $Re = 1.1 \times 10^5$). FLOW FROM LEFT TO RIGHT

FIGURE 3-4. WRL DOUBLE-TIP CONDUCTIVITY PROBE.

The probe was positioned in channel centre line at different cross-sections along the hydraulic jump. The longitudinal and transversal separation distances between the probe's leading and trailing tips were $\Delta X_p = 7.9$ mm and $\Delta Z_p = 1$ mm respectively. A detailed sensitivity analysis of the effect of sampling time on the void fraction and bubble count rates was conducted for a sampling rate of 20 kHz (Appendix B.2). The sensitivity analysis results indicated a re-evaluation of the minimum sampling duration of previous studies suggesting minimum sampling durations of 5 to 6 minutes close to the jump toe $x/d_1 \leq 8$, and 4 minutes further downstream $x/d_1 > 8$ where x is the distance from the jump toe position relative to mean jump toe position (Figure 3-5). A longer sampling duration is required to avoid large deviations and data scatter in the air-water flow properties as observed in previous studies with shorter sampling times (e.g. Chanson and Brattberg 2000; Wang 2014; Takahashi and Ohtsu 2017). All air-water flow measurements downstream the sluice gate were therefore conducted for 5 and 4 minutes respectively. Figure 3-5 presents the results of the sensitivity analysis of the sampling duration for the void fraction and the bubble count rate with $Fr_1 = 9$ and $Re = 8.8 \times 10^4$. Further results of the sensitivity analysis are provided in Appendix B.2.



A) VOID FRACTION SENSITIVITY ANALYSIS AT THE MAXIMUM VOID FRACTION LOCATION



B) BUBBLE COUNT RATE SENSITIVITY ANALYSIS AT THE MAXIMUM VOID FRACTION LOCATION

FIGURE 3-5. EFFECT OF SAMPLING DURATION ON THE VOID FRACTION AND BUBBLE COUNT RATE MEASUREMENTS FOR HYDRAULIC JUMPS DOWNSTREAM OF THE SLUICE GATE WITH $Fr_1 = 8.8$ AND $Re = 8.8 \times 10^4$. FD: FULLY DEVELOPED INFLOW CONDITIONS, PD: PARTIALLY DEVELOPED INFLOW CONDITIONS.

3.2.2. FREE SURFACE FLUCTUATIONS AND JUMP TOE OSCILLATIONS

The free-surface fluctuations and jump toe oscillations in the hydraulic jumps were recorded with a LIDAR. A LIDAR (LIght Detection and Ranging Instrument) is a non-intrusive instrument which operates based upon the Time-Of-Flight principle (Gokturk et al. 2004; Allis et al. 2011; Blenkinsopp et al. 2012). This principle estimates the distance between the LIDAR and a target based upon the travel time by the pulse of light (laser) transmitted from the LIDAR and the target surface (Gokturk et al. 2004; Bufton et al. 1991; Blenkinsopp et al. 2012). The LIDAR provides basic spatial and temporal data which enable the LIDAR use in a range of different research fields (Allis et al. 2011). Airborne LIDAR has been widely used in large scale topographic and geomorphological applications (Bufton et al. 1991; Irish and Lillycrop 1999; Allis et al. 2011; Blenkinsopp et al. 2012). In coastal engineering applications, LIDAR has been first used to measure ocean waves (Ross and Cardone 1970), while more recent studies used LIDARs for more detailed recordings of the wave characteristics (Irish and Lillycrop 1999; Irish et al. 2006; Belmont et al. 2007; Vousdoukas 2014). Research at prototype and laboratory scale validated the LIDAR as a reliable instrument to measure the free-surface profiles in highly aerated waves or waves with high turbidity levels (Blenkinsopp et al. 2010; Allis et al. 2011; Blenkinsopp et al. 2012).

In the present study, the free-surface features, jump toe oscillations, characteristic frequencies and free-surface time and length scales were recorded non-intrusively with a SICK LIDAR LMS511 located upstream of the jump toe (Figure 3-6 and Figure 3-7). The LIDAR was carefully positioned in channel centreline about 0.5 m upstream of the jump toe and at an elevation of about 1.5 m above the flume for both hydraulic jumps downstream of a sloped channel and downstream of the sluice gate. Figure 3-6 shows a sketch of the experimental setup of the LIDAR for hydraulic jumps located downstream of sloped channels including the LIDAR location, the laser beam direction and typical laser beam transformations such as reflection, refraction and absorption. Figure 3-7 presents a photo of the experimental setup of the LIDAR for hydraulic jumps downstream of the sluice gate. The LIDAR measured the free-surface profiles in polar coordinates providing the position of the free-surface in terms of the angle and the distance per time step (SICK 2015). The angular resolution of the LIDAR was 0.25 degrees with a field of maximum view of 190 degrees (SICK 2015). For the experimental setup herein, the LIDAR scanned at 35 Hz for a sampling duration of at least 30 minutes. A sensitivity analysis was conducted to identify the minimum sampling duration (Appendix B.3).

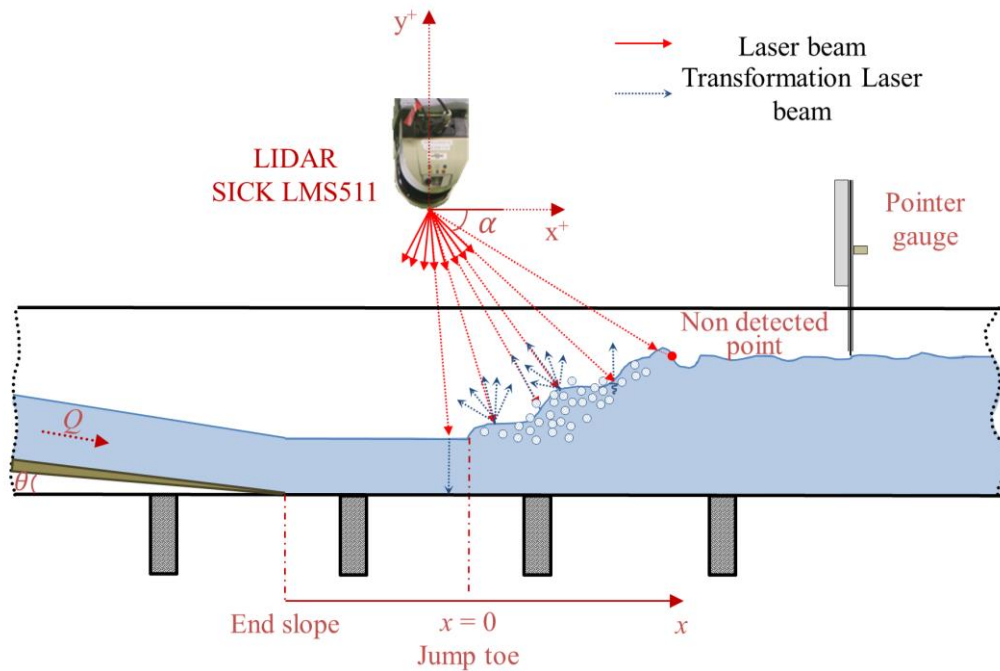
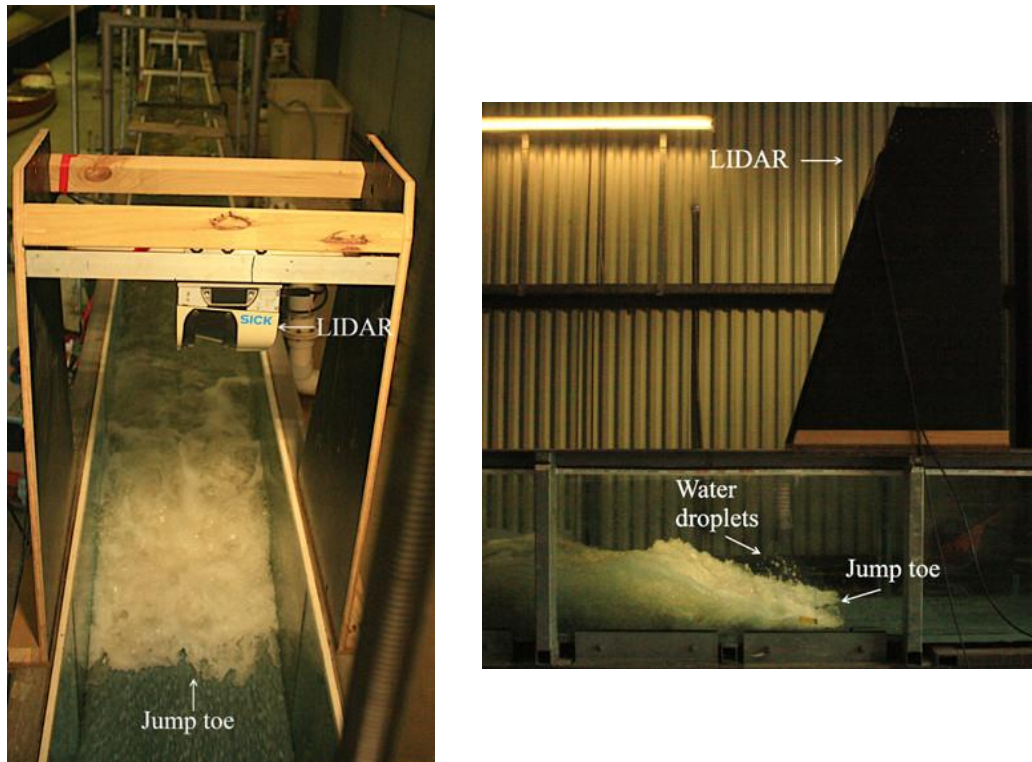


FIGURE 3-6. LABORATORY SETUP OF LIDAR EXPERIMENTS IN HYDRAULIC JUMPS DOWNSTREAM OF A SLOPED CHANNEL. RED ARROWS: LASER BEAMS; BLUE ARROWS: TRANSFORMATION OF LASER BEAMS INCLUDING REFLECTION, REFRACTION OR ABSORPTION.



A) VIEW IN FLOW DIRECTION HIGHLIGHTING THE JUMP TOE B) SIDE VIEW (FLOW FROM RIGHT TO LEFT)

FIGURE 3-7. PHOTOS OF THE EXPERIMENTAL SETUP INCLUDING LIDAR POSITIONING WITH TYPICAL HYDRAULIC JUMP DOWNSTREAM OF THE SLUICE GATE (EXPERIMENT E_FD: $Fr_1 = 8.5$, $Re = 7.5 \times 10^4$).

The Lidar LMS511 was connected to a power supply source and to a programmable logic controller which communicated the raw data to a PC. The data was acquired with the software SOPAS Engineering Tool provided by SICK (Figure 3-8).

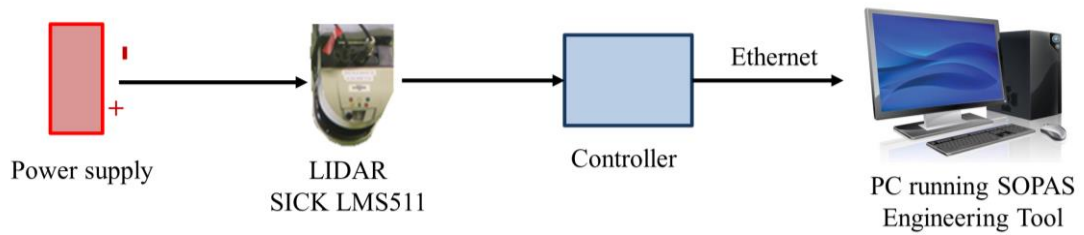


FIGURE 3-8. DATA ACQUISITION DIAGRAM OF THE LIDAR.

3.2.3. FORCES ON SUBMERGED SPHERE INSIDE HYDRAULIC JUMP

Load cells have been widely used in the analysis of flow-induced forces including drag and lift forces in sediment transport (Dwivedi et al. 2011), vibration analysis (Assi et al. 2009), waves (Schutten et al. 2004), flood analysis (Jiang et al. 2014; Smith et al. 2017), aquaculture (Biehle et al. 1998; Schutten et al. 2004; Lader et al. 2014; Strand et al. 2016), among others. In the present study, the forces acting upon a sphere submerged inside hydraulic jumps were measured with a six-axis load cell M3813B manufactured by Sunrise Instruments®. The load cell is composed by 6 channels connected to strain gauge bridges that convert any change in the resistance of the circuit into Voltage. The force sensor was able to measure the longitudinal F_x , vertical F_y and transverse F_z forces of up to 70 N as well as the longitudinal M_x , vertical M_y and transverse M_z torques of up to 3 Nm. Figure 3-9 presents the dimensions and definitions of the axes of the load cell.

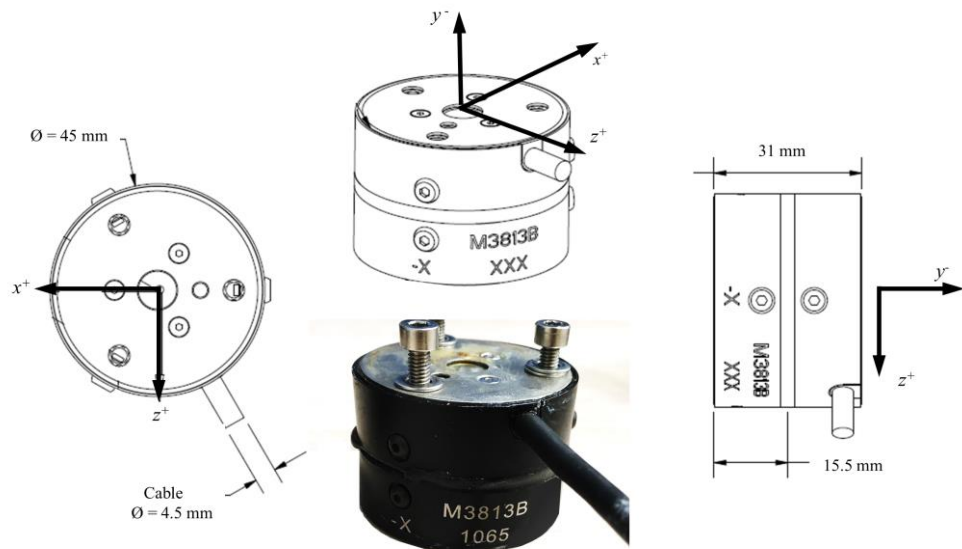


FIGURE 3-9. SIX-AXIS LOAD CELL M3813B. ADAPTED FROM DATA SHEET INFORMATION FROM SUNRISE INSTRUMENTS® (2018).

The six channels of the load cell were excited with an Interface Box M8128 which translated any small changes in resistance of the strain gauges of the load cell into a Voltage. The interface box communicated directly with a PC using the Sunrise Instruments acquisition software iDAS R&D (Figure 3-10).

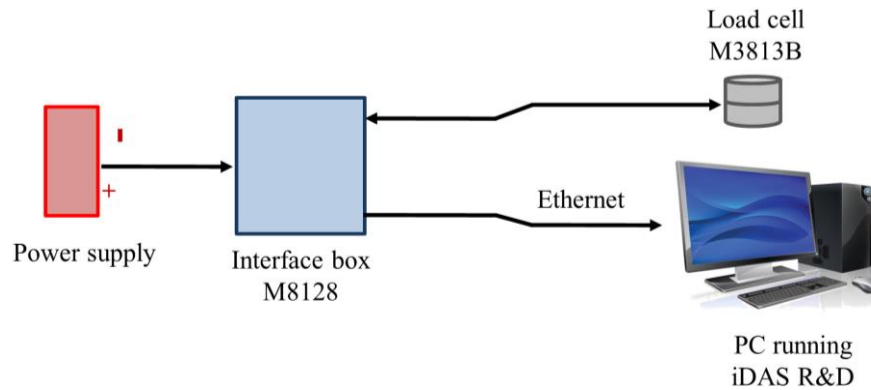
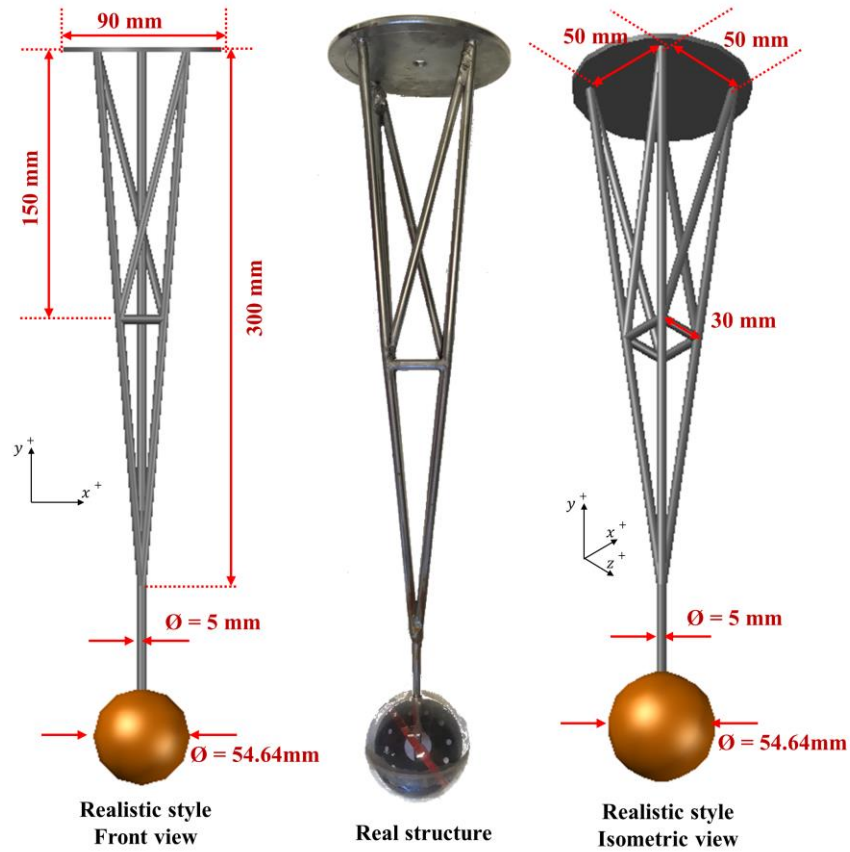
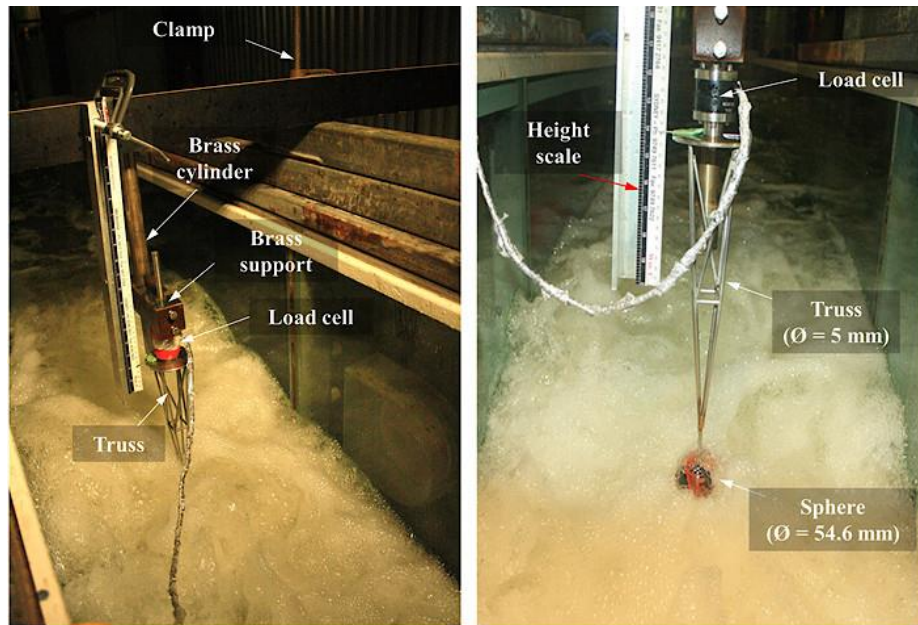


FIGURE 3-10. DATA ACQUISITION DIAGRAM OF THE LOAD CELL.

Figure 3-11 shows the experimental setup for the force measurements on a submerged sphere inside the hydraulic jumps with a load cell. The load cell was supported by a thick bar of 5 cm connected to a rigid circular cylinder made of brass attached to a 4 cm thick solid brass bar which was clamped on both sides of the flume (Figure 3-11). The load cell was attached to a stainless-steel truss ($\varnothing = 5$ mm) connected to a water filled plastic sphere with diameter $\varnothing = 54.64$ mm (Figure 3-11A). Note that the sphere and truss diameters were selected as the combination generating the most accurate results in known flow conditions (Appendix H). The pressure sensors used in the measurement of the pressure fluctuations at the channel bed in hydraulic jumps was susceptible to self-excitation due to the internal frequencies in the hydraulic jump (Abdul Khader and Elango 1974; Fiorotto and Rinaldo 1992). Therefore, the design of the system and the support frame were carefully selected through an iterative process removing the effect of the natural frequency of the system in conjunction with the internal frequencies of the hydraulic jump. The final design reduced the self-excitation of the force measurement system (Figure 3-11A and B). Details of the iterative process to identify the final support structure design are presented in Appendix H



A) SKETCH OF THE STAINLESS-STEEL TRUSS STRUCTURE AND THE WATER FILLED PLASTIC SPHERE



B) EXPERIMENTAL SETUP OF FORCE MEASUREMENTS WITH THE LOAD CELL (EXPERIMENT G: $Fr_1 = 10$, $Re = 8.8 \times 10^4$).

FIGURE 3-11. MEASUREMENT OF THREE-DIMENSIONAL INTERNAL FORCES IN HYDRAULIC JUMPS WITH A LOAD CELL.

For all flow conditions, the forces on the submerged sphere were measured with a sampling frequency of 1 kHz. The sampling duration was 450 s close to the jump toe and 300 s further downstream. The sampling duration was defined based on sensitivity analysis (Appendix

B.4). The internal forces were measured at the centreline of the channel positioning the sphere at different elevations above the channel bed and at five different cross-sections along the hydraulic jump. The elevation was measured with an accuracy of ± 0.5 mm. The minimum elevation of the underside of the sphere was 1 mm above the channel bed while the maximum elevation was defined as the position where half of the sphere was non-submerged on average. Meaningless forces were recorded for elevations where the sphere was mostly out of the water.

3.2.4. INFLOW DEPTHS

In hydraulic jumps, the inflow depth plays an important role in the determination of the inflow Froude number and subsequently, the hydraulic jump efficiency. The characterisation of the clear water depth in turbulent supercritical flows, such as flows below and downstream of a sluice gate is difficult due to the flow's turbulence, air entrapment and free-surface fluctuations (Ohtsu and Yasuda 1994). In the present study, the free-surface profiles downstream of the sluice gate were measured with a pointer gauge in the channel centre line within an accuracy of ± 0.5 mm (Figure 3-12) and validated with indirect measurements of the equivalent clear water flow depth using a conductivity probe at different locations downstream of the sluice gate. Overall, the conductivity probe data were in agreement with the average data recorded with the pointer gauge for $Re < 9 \times 10^4$. For $Re > 9 \times 10^4$, the inflow depth recorded with the conductivity probe corresponded to the maximum flow depth measured with the pointer gauge. The comparison of the flow depths measured with the conductivity probe and the pointer gauge is presented in Chapter 4.



A) SIDE VIEW



B) VIEW AGAINST FLOW DIRECTION

FIGURE 3-12. POINTER GAUGE MEASUREMENTS DOWNSTREAM OF THE SLUICE GATE ($Q = 0.048$ m³/s, $h_0 = 0.027$ m).

3.2.5. INFLOW CONDITIONS

The inflow conditions upstream of the hydraulic were further quantified with a pitot tube ($\varnothing = 3$ mm). The Pitot tube consisted of a total head tapping and a ring of static pressure taps located 3 cm downstream. The pitot tube's total head tapping was aligned with the flow direction. The pitot tube was located in channel centreline and shifted in vertical direction with a digital height gauge within an accuracy of ± 0.1 mm. The velocity distributions were measured at different

elevations and different cross-sections upstream of the hydraulic jump. Figure 3-13 shows a photo of the pitot tube in the channel. The velocity distributions combined with the flow depths measurements were used to characterise the inflow conditions including the upstream flow depth and Froude number as well as the boundary layer development downstream of the sluice gate. The velocity distributions upstream the hydraulic jump are presented in Chapter 4.



FIGURE 3-13. PITOT TUBE MEASUREMENTS IN FULLY DEVELOPED FLOWS DOWNSTREAM OF THE SLUICE GATE; NOTE THE FREE-SURFACE ROUGHNESS IN THE HIGH-VELOCITY FLOWS ($Q = 0.059 \text{ m}^3/\text{s}$, $h_0 = 0.03 \text{ m}$).

3.3. POST-PROCESSING OF RAW DATA

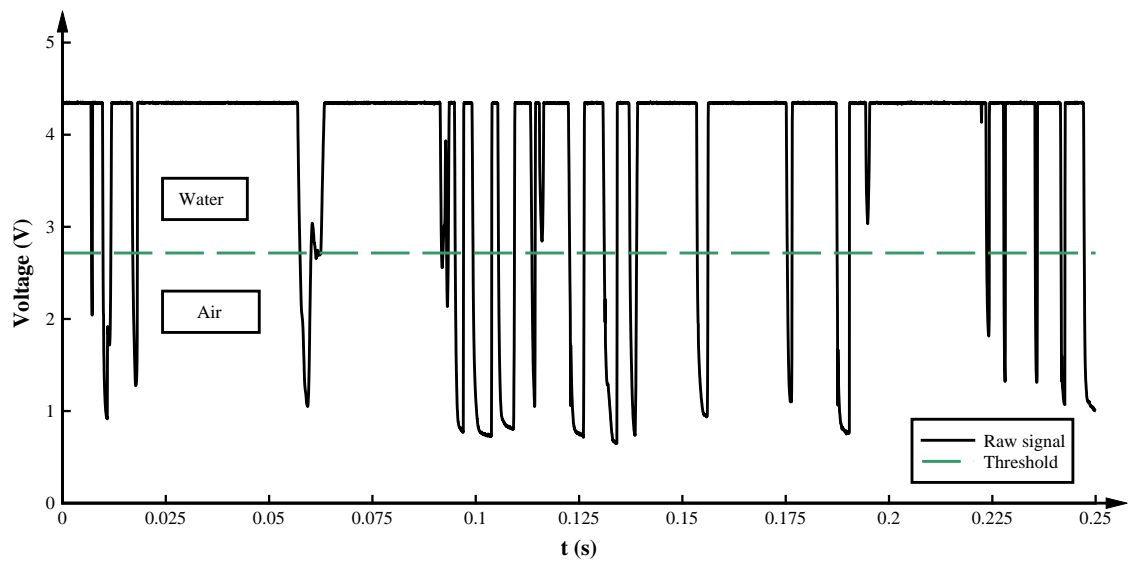
3.3.1. AIR-WATER FLOW PROPERTIES

The air-water flow properties were measured with a double-tip conductivity probe. The recorded raw data were analysed providing a wide range of air-water flow properties including the void fraction C , bubble count rate F , interfacial velocities V_{CP} , auto-correlation time scales $T_{air,auto}$, the longitudinal cross-correlation time scales $T_{air,cross}$ and chord times t_{ch} .

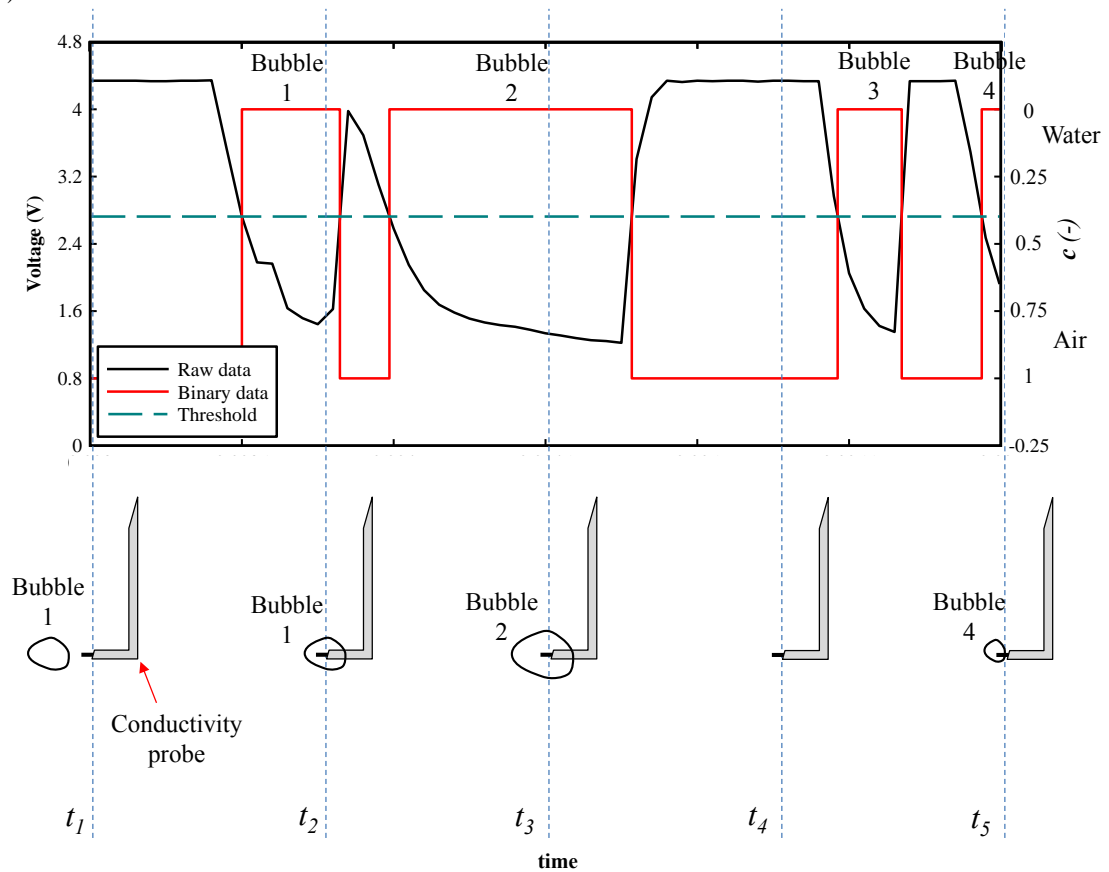
A typical raw data signal of the leading tip of the conductivity probe is shown in Figures 3-14A and B. Figure 3-14A presents a time series of raw Voltage signals. The raw signal drops when the tip of the probe is in contact with air and increases suddenly when the tip is surrounded by water since the resistivity of the air is 1000 times larger compared to water (Figure 3-14A). Note that the change in Voltage between air and water phases is not instantaneous due to the wetting and drying time of the tip. The air-water flow data processing was automated by a Fortran code developed by Felder (2013, 2018). The analysis of the air-water flow properties in the hydraulic jump followed two different data processing techniques: i.e. a single threshold technique and the statistical analysis of the raw signals (Felder 2013, 2018).

3.3.1.1. SINGLE-THRESHOLD TECHNIQUE

The single threshold technique is valid in air-water flows where the voltage signal presents bimodal distributions (Cartellier and Achard 1991; Toombes 2002; Felder 2013). The single threshold used for the present study was selected as the 50% of the difference between the peaks of the bimodal probability function of the raw voltage signals for each probe tip and measurement location (Felder 2013; Felder and Chanson 2015). Figure 3-14A presents the raw data signal and the 50% threshold. The single threshold technique converted the raw signal data into binary instantaneous void fractions c where any value larger than the threshold was identified as water ($c = 0$) while values lower than the threshold were identified as air ($c = 1$) (Felder 2013). Figure 3-14B presents the phase change between air and water when an air bubble pierces the probe tip as well as a binary time series of instantaneous void fractions c .



A) TYPICAL CONDUCTIVITY PROBE SIGNAL



B) SKETCH OF THE AIR-WATER PHASE CHANGE AND CONVERSION FROM RAW DATA TO BINARY DATA

FIGURE 3-14. TYPICAL CONDUCTIVITY PROBE RAW DATA SIGNAL OBTAINED WITH ONE TIP AND CORRESPONDING INSTANTENEOUS VOID FRACTION C .

The average of the instantaneous void fractions over the measurement time provided the time-averaged void fraction C at any location in the hydraulic jump:

$$C = \frac{1}{N} \sum_{i=1}^N c_i \quad (3.1)$$

where N is the total number of samples estimated as the sampling frequency times the sampling time. The void fraction of the leading tip was used in this study, while the trailing tip data were used for quality check of the leading tip data.

The bubble count rate F estimates the number of bubbles or droplets per second impacting the probe tip, i.e. the number of interface changes from water to air and air to water per second.

In air-water flows, air bubbles are defined as entities of air surrounded by water for $C < 0.3$ (bubbly flow region) while water droplets are known as entities of water surrounded by air for $C > 0.7$ (spray region) (Toombes 2002; Gonzalez et al. 2005; Felder and Chanson 2016b). The intermediate region $0.3 < C < 0.7$ presents a complex mixture of air bubbles and water droplets (Toombes 2002; Gonzalez et al. 2005; Felder and Chanson 2016b). The air bubble chord times t_{ch} , are defined as the time between interface changes within the bubbly flow region. While they do not represent the sizes of the air bubbles, the chord times are proportional to the bubble sizes.

The time-averaged chord time $t_{ch,mean}$ was defined as an average size of the air-water phase defined as:

$$t_{ch,mean} = \frac{C}{F} \quad (3.2)$$

The chord times were calculated for the leading tip only.

3.3.1.2. STATISTICAL ANALYSIS OF THE RAW SIGNAL

Statistical analysis of the raw signals considered the raw data of the simultaneously sampled leading and trailing tips providing the local time averaged interfacial velocity V_{CP} and the auto- and cross-correlation time scales $T_{air,auto}$ and $T_{air,cross}$.

The interfacial velocity represents the average mixture velocity and is estimated as:

$$V_{CP} = \frac{\Delta x_p}{T} \quad (3.3)$$

To avoid correlation signal biasing for the large data set, the correlation analysis was conducted for 15 non-overlapping segments (Hayes 1996; Chanson and Carosi 2007; Felder and Chanson 2015).

The auto-correlation time scales $T_{air,auto}$ represent a characteristic longitudinal advective time in air-water flows. $T_{air,auto}$ was calculated based upon the raw signal at a given location (Chanson and Carosi 2007):

$$T_{air,auto} = \int_{\tau=0}^{\tau=\tau(R_{air,auto}=0 || R_{air,auto}=R_{air,auto-min})} R_{air,auto}(\tau) d\tau \quad (3.4)$$

where τ is the time lag, $R_{air,auto}$ is the auto-correlation function of the raw signal at a given position and $R_{air,auto,min}$ is the minimum auto-correlation coefficient. $T_{air,auto}$ was calculated for the leading tip signal.

The longitudinal cross-correlation time scale $T_{air,cross}$ provides a characteristic longitudinal time scale of the bubbly-flow structures in the hydraulic jump. $T_{air,cross}$ was estimated based on the cross-correlation analysis of the raw signals of the leading and trailing tips of the conductivity probe (Chanson and Carosi 2007):

$$T_{air,cross} = \int_{\tau=\tau(R_{air,cross}=R_{air,cross,max})}^{\tau=\tau(R_{air,cross}=0||R_{air,cross}=R_{air,cross,min})} R_{xz}(\tau) d\tau \quad (3.5)$$

where $R_{air,cross}$ is the cross-correlation function and $R_{air,cross,min}$ and $R_{air,cross,max}$ are the minimum and maximum longitudinal cross-correlation coefficients respectively. Both auto- and cross-correlation time scales were calculated based upon an integration of the correlation function from the maximum correlation coefficient to the first crossing with the x-axis. In cases where the cross-correlation function did not cross the x-axis, the maximum integration limit of Equation 3.5 was selected as the minimum cross-correlation coefficient.

3.3.2. FREE SURFACE FLUCTUATIONS AND JUMP TOE OSCILLATIONS

3.3.2.1. POST-PROCESSING OF RAW LIDAR SIGNALS

The LIDAR recorded continuous and time-varying free-surface profiles along the hydraulic jump providing raw signals in terms of the angle and distance between LIDAR and free-surface (Figure 3-6). Post-processing tools were self-developed in MATLAB including raw data pre-processing, data filtering and basic and advanced analyses of the free-surface characteristics and jump toe movements. Figure 3-15 presents the post-processing flow chart of the MATLAB code.

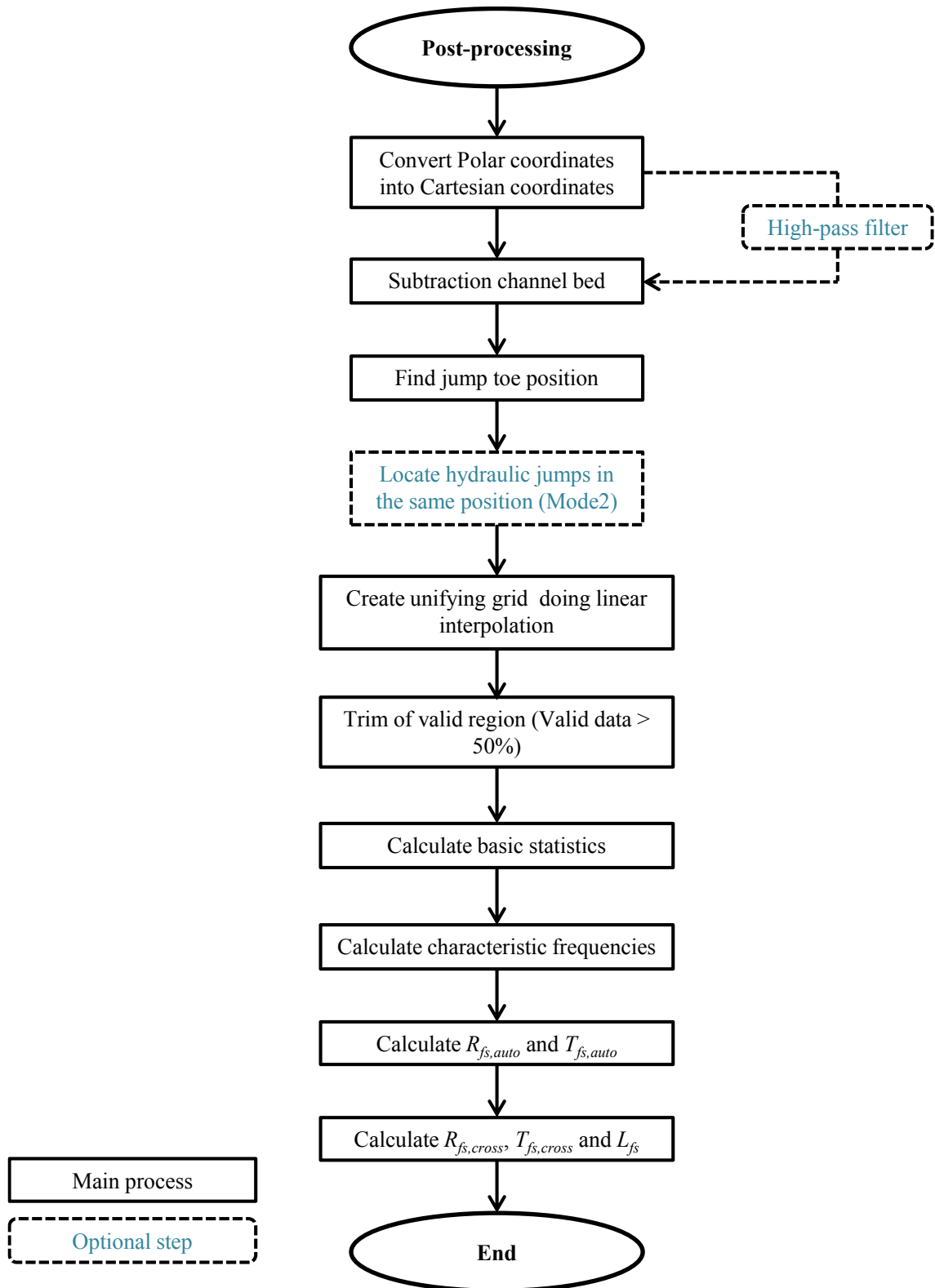
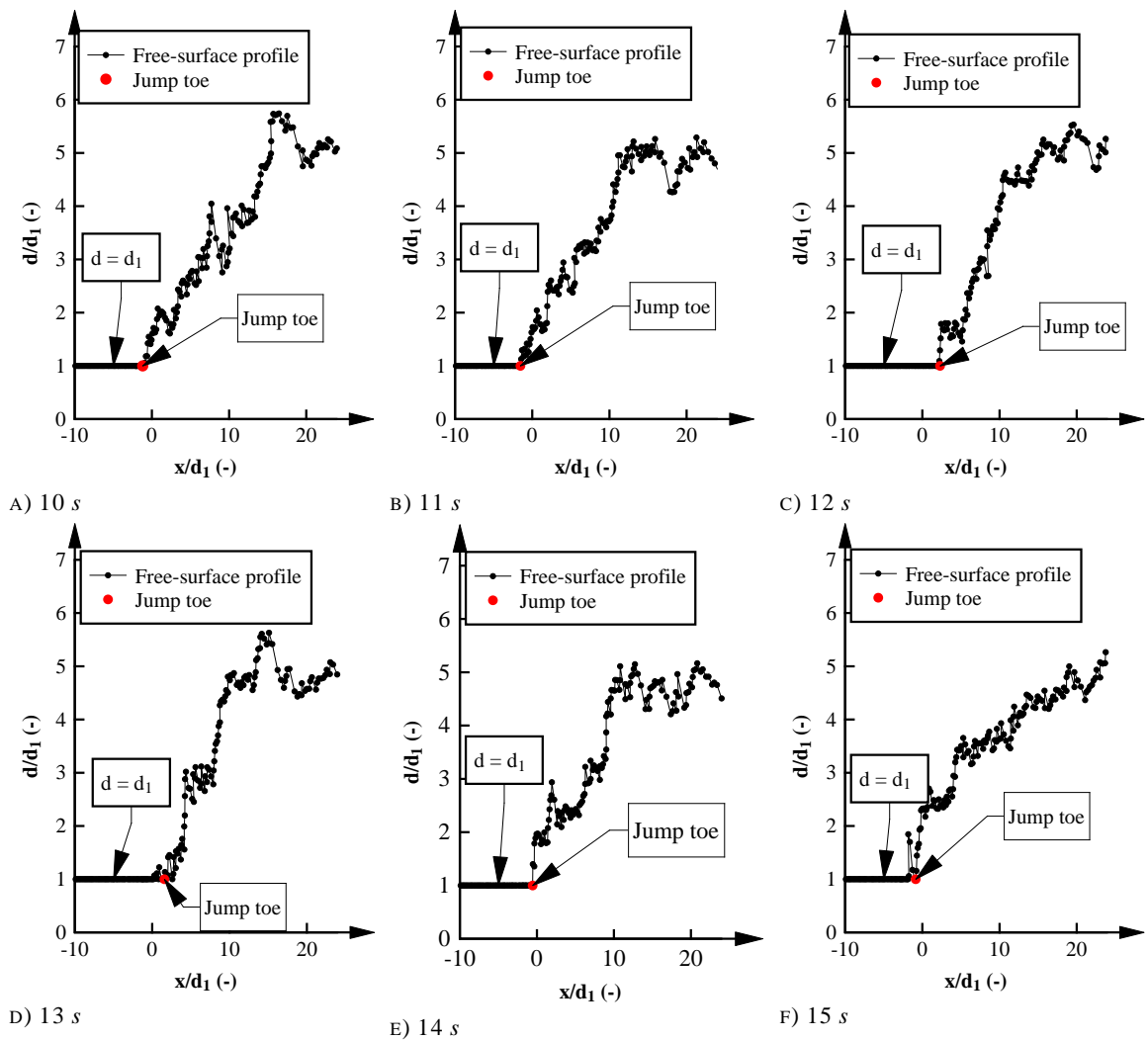


FIGURE 3-15. FLOW CHART OF THE POST-PROCESSING OF THE LIDAR DATA

The first stage comprised the generation of Cartesian coordinates obtaining a 2-dimensional data grid of free-surface elevations along the hydraulic jump. To obtain the free-surface profiles, the water elevation was obtained by the subtraction of the profile of the dry channel in respect to the instantaneous free-surface profiles of the hydraulic jump. The jump toe

position was then selected for every time step. Figure 3-16 shows an example of the selection of the jump toe position. The jump toe was defined as the initial position of increasing free-surface upstream of the hydraulic jump (Figures 3-16A, B, C, E, G and H). In some cases, water splashes and inflow turbulence generated increases in the flow depth upstream of the jump toe (Figures 3-16D, F, I). In these cases, the jump toe position was selected as the maximum longitudinal position where the flow depth was equal to the inflow flow depth and the free-surface profile presented a consistent increase in the flow depth. Once selected the jump toe, all upstream flow depths were defined as $d = d_1$.



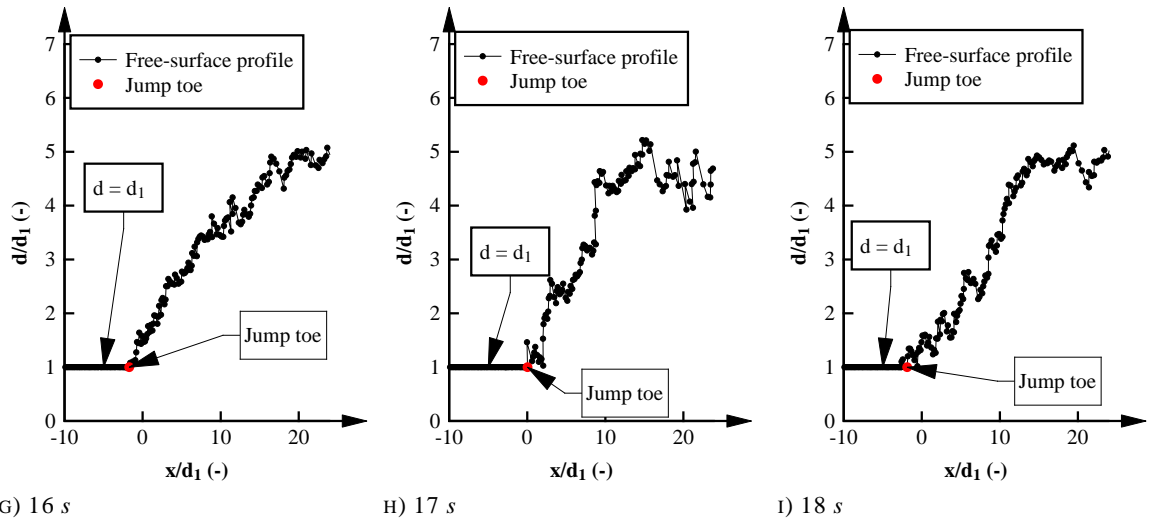


FIGURE 3-16. EXAMPLE OF RAW FREE-SURFACE DATA AND JUMP TOE SELECTION AT NINE DIFFERENT TIME STEPS. TIME STEPS BETWEEN GRAPHS: 35 Hz (EXPERIMENT I_FD: $Fr_1 = 3.8$, $Re = 9.5 \times 10^4$).

In a next step the free-surface profiles for each time step were shifted to the mean jump toe position (Mode 2). This step was optional and further clarification of this step and Mode 2 is presented in Section 3.3.2.2.

All data were interpolated linearly to generate a unifying grid for all instantaneous hydraulic jump profiles. For each hydraulic jump, the interpolation provided more than 56,000 different free-surface profiles over the sampling duration with a separation in x-direction of 1 to 2 centimetres between data points. These free-surface profiles were used for the analysis of the free-surface characteristics and jump toe oscillations. An example of the instantaneous free-surface profiles recorded with the LIDAR is shown in Figure 3-16 and a time series of 10 s is provided in the Digital Appendix as “Movie 3_1”.

In a next step the raw data were filtered. Data in the non-aerated flow regions upstream of the jump toe and in the low aerated flow regions towards the downstream end of the hydraulic jump roller were removed. In areas with low aeration, the data quality was reduced significantly due to poor signal reflection and large numbers of non-detected data. Any non-detected data obtained by the LIDAR were replaced by the linear interpolated value of the two adjacent known values. At any position where the signal detection was lower than 50% of the entire data sample the data at that location and at all locations further downstream, were not considered. Following the removal of invalid data, a basic statistical analysis of the free-surface profiles was conducted yielding the mean, median and the percentiles as well as the standard deviations of the free-surface elevations. Characteristic frequencies were identified with Fast Fourier Transform (FFT) analyses along the hydraulic jump. Advanced auto- and cross-correlation analyses provided the longitudinal free-surface integral time and length scales $T_{fs,auto}$ and $T_{fs,cross}$. $T_{fs,auto}$ represented a characteristic longitudinal advective time scale at every measurement location and was calculated based upon the raw free-surface signal at a given location:

$$T_{fs,auto} = \int_{\tau=0}^{\tau=\tau(R_{fs,auto}=0 || R_{fs,auto}=R_{fs,auto_min})} R_{fs,auto}(\tau) d\tau \quad (3.6)$$

where $R_{fs,auto}$ is the auto-correlation function of the free-surface elevation, and $R_{fs,auto_min}$ is the minimum auto-correlation coefficient. The corresponding cross-correlation time scales $T_{fs,cross}$ in the longitudinal direction were calculated between two simultaneously sampled measurement points with known longitudinal separation distance Δx (Chachereau and Chanson 2011b):

$$T_{fs,cross} = \int_{\tau=\tau(R_{fs,cross}=R_{fs,cross_max})}^{\tau=\tau(R_{fs,cross}=0 || R_{xx'}=R_{fs,cross_min})} R_{fs,cross}(\tau) d\tau \quad (3.7)$$

where $R_{fs,cross}$ is the longitudinal cross-correlation function and $R_{fs,cross_min}$ and $R_{fs,cross_max}$ are the minimum and maximum longitudinal cross-correlation coefficients respectively. Both auto- and cross-correlation time scales were calculated based upon an integration of the correlation function from the maximum correlation coefficient to the first crossing of the x-axis. When the correlation function did not cross the x-axis, $R_{fs,auto_min}$ and $R_{fs,cross_min}$ respectively were selected as the integration limits.

The free-surface integral length scales L_{fs} provide an estimate of the large free-surface motions interacting in the streamwise direction along the hydraulic jump. The length scales are calculated based upon the maximum cross-correlation coefficient $R_{fs,cross_max}$ between two sampling points with distance Δx . The integration of $R_{fs,cross_max}$ up to a distance where $R_{fs,cross_max} = 0$ (Murzyn et al. 2007) or up to the maximum sensor separation distance Δx_{max} (Chachereau and Chanson 2011b) provides L_{fs} as:

$$L_{fs} = \int_{\Delta x=0}^{\Delta x=\Delta x_{max}} R_{fs,cross_max}(x) dx \quad (3.8)$$

To identify any inherent correlation of the LIDAR signals, the raw signals of the LIDAR of the channel bed without water was used. Figures 3-17A and B present the auto-correlation and cross-correlation functions of the LIDAR signal on the dry channel bed highlighting that there was no inherent self-correlation of the LIDAR signals for $R_{fs,auto}$ and $R_{fs,cross}$. The analysis was repeated for different positions and for different data sets recorded at different times confirming that no inherent self-correlation in the present study.

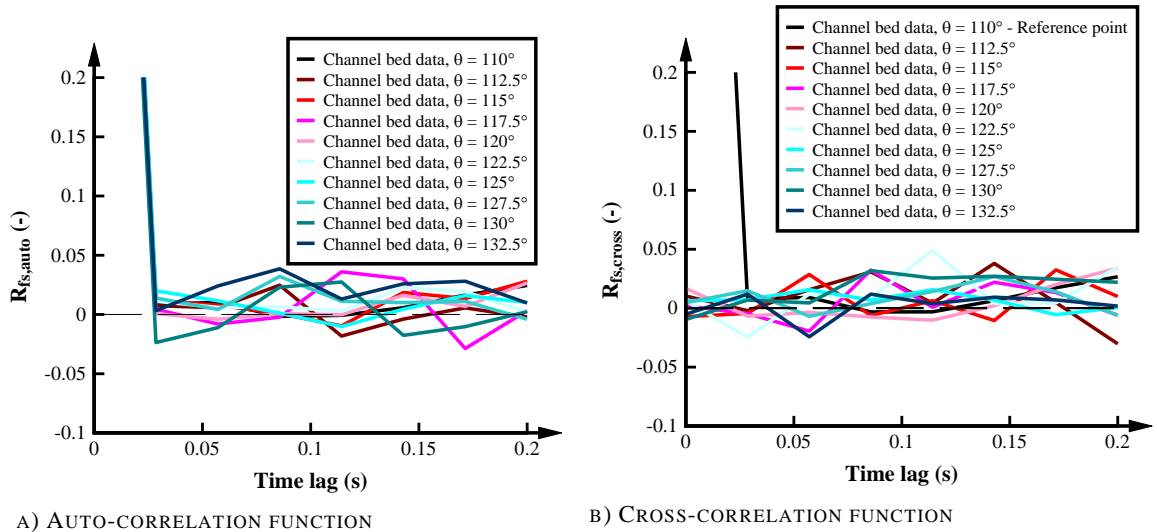


FIGURE 3-17. CORRELATION FUNCTIONS OF THE RAW LIDAR SIGNAL OF A DRY CHANNEL BED.

An additional and optional analysis was conducted to evaluate the free-surface features when the slow motions of the jump toe were removed (Figure 3-15). The analysis was conducted by applying a high-pass filter of 0.1 Hz in agreement with previous studies (Chachereau and Chanson 2010). The results of the application of the high-pass filter are discussed in Chapter 5.

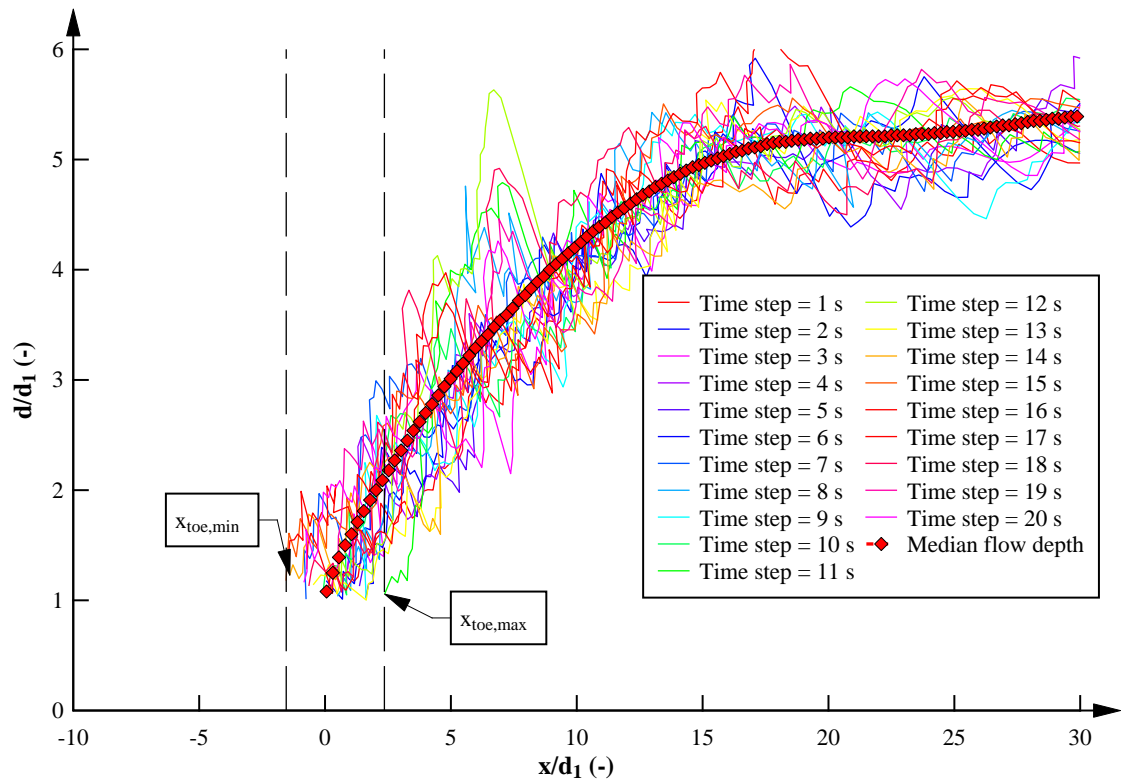
3.3.2.2. POST-PROCESSING MODES: FREE JUMP TOE MOVEMENT AND FIXED JUMP TOE

In the present study, two analysis modes were used to analyse the effect of the jump toe oscillation into the free-surface features since previous studies were limited by single point measurements (Sub-chapter 2.5). The first analysis mode (Mode 1) considered a free-movement of the jump toe (Figure 3-18A) while the second analysis mode (Mode 2) adjusted each instantaneous hydraulic jump profile at a fixed jump toe position, i.e. the mean jump location $x = 0$ (Figure 3-18B).

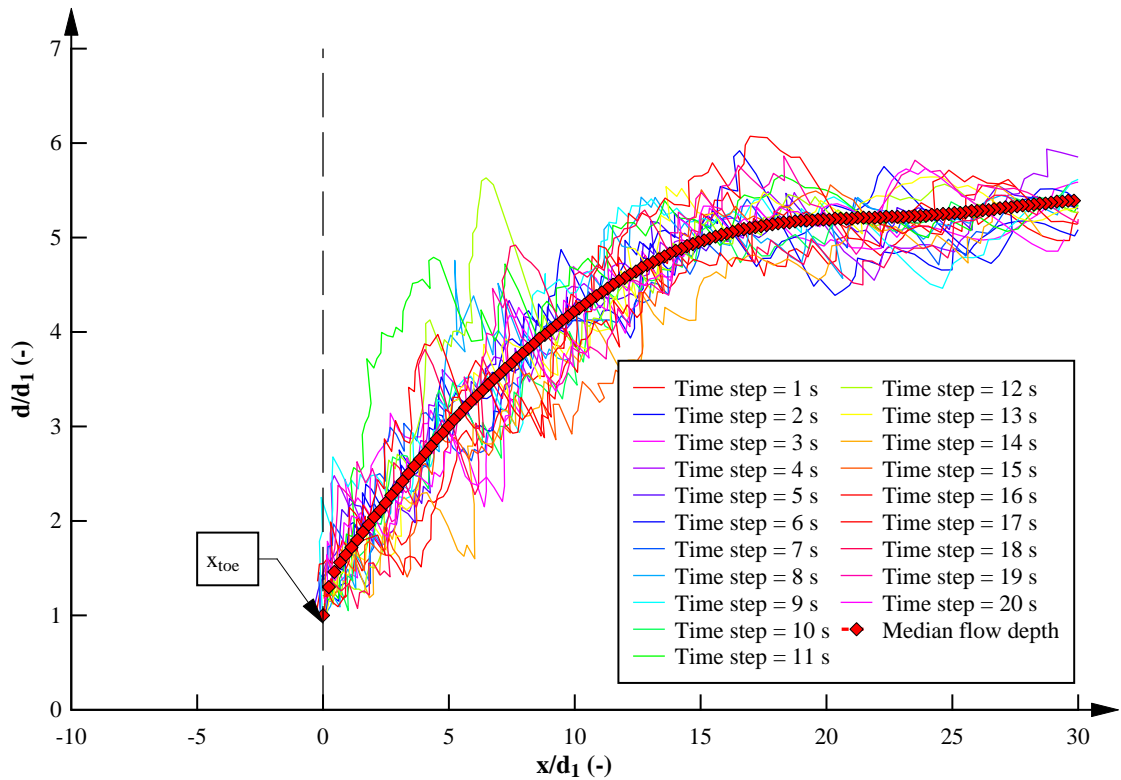
Figure 3-18 shows an example of the two analysis modes for 20 dimensionless free surface profiles d/d_1 as a function of x/d_1 with a time step of 1 second between profiles as well as the corresponding median flow depth profile. Figure 3-18A shows an example of the analysis conducted under free jump toe movement (Mode 1). In this condition, the instantaneous jump toe location differed for each time step highlighting the strong jump toe oscillations and their effect on the time-averaged free-surface profiles (Figure 3-18A). For example, the dimensionless amplitude of the jump toe oscillation for the 20 sample profiles, was about $(x_{toe,max} - x_{toe,min})/d_1 = 4$ (Figure 3-18A), where $x_{toe,max}$ is the maximum oscillation of the jump toe in positive direction and $x_{toe,min}$ the maximum oscillation in negative x-direction. Figure 3-18B shows the same time steps presented in Figure 3-18A under the consideration of fixed jump toe position (Mode 2), i.e. the jump toe position of each time step was fixed at the same mean value $x/d_1 = 0$. Note that the median free-surface profiles differed between Modes 1 and 2 due to the

jump toe oscillations. For example in Figure 3-18B, near the jump toe ($x/d_1 = 0.2$), the maximum difference was about 15%. Little differences in the median profiles for Modes 1 and 2 were observed for $x/d_1 > 2$.

The combination of these two analysis modes provided new insights into the free-surface characteristics in fully aerated hydraulic jumps including the effects of jump toe oscillations on the free-surface fluctuations and the range of characteristic frequencies along hydraulic jumps.



A) FREE JUMP TOE MOVEMENT (MODE 1)



B) FIXED JUMP TOE POSITION (MODE 2)

FIGURE 3-18. TEMPORAL VARIATION OF 20 FREE-SURFACE PROFILES WITH 1 S TIME STEPS; COMPARISON OF MODES 1 AND 2. MEDIAN PROFILES IN RED ($Fr_1 = 4.6$, $Re = 1 \times 10^5$).

3.3.3. FORCES

The three-dimensional forces on the submerged sphere of 54.64 mm diameter were measured for all flow conditions (Figure 3-11). When the sphere together with parts of the truss structure were submerged within the hydraulic jump (Figure 3-11), the measured forces represented a combined force of sphere and truss sections. To quantify the forces only on the sphere, two experiments were conducted at each measurement position: (1) measurements with the sphere and the truss and (2) measurements only with the truss. The subtraction of the forces of the truss structure from the combined system provided the forces on the sphere. Note that for the upper part of the jump roller, the sphere was partially submerged, while it was permanently fully submerged within the air-water flows closer to the channel bed. Since load cells are susceptible to electronic drift (Pells 2016), the load cell was zeroed prior to each measurement. The zero condition represented an initial recording of the truss structure and the water filled sphere without any load, i.e. the force was recorded when the sphere was outside of the hydraulic jump in air.

Figure 3-19 presents a diagram of the data post-processing of the load cell raw data. The diagram presents a bifurcation between the forces recorded with the truss alone (*truss*) and the combined truss and sphere (*truss+sphere*). For both conditions, the raw Voltage data comprised the forces on the submerged structure within the hydraulic jump (Raw data *HJ*) and the zero

condition prior to the measurements (Raw data *zero condition*). All Voltage data were converted to Newtons using a calibration matrix provided by the manufacturer of the load cell Sunrise instruments®. A low-pass filter of 20 Hz was applied to the load cell data to eliminate the natural frequency of the system (Detailed information on the natural frequency of the system is provided in Appendix B.3). After filtering, the mean values of the *zero condition* forces (F_{x_zero} , F_{y_zero} , F_{z_zero}) were subtracted from the instantaneous forces (f_{x_HJ} , f_{y_HJ} , f_{z_HJ}) recorded inside the hydraulic jump. Afterwards, the mean forces of the truss alone (F_{x_truss} , F_{y_truss} , F_{z_truss}) and the combined truss and the sphere ($F_{x_truss+sphere}$, $F_{y_truss+sphere}$, $F_{z_truss+sphere}$) were quantified. The mean forces (F_x , F_y , F_z) on the sphere were calculated as the subtraction of the mean values of the combined truss and the sphere minus the mean values of the truss.

To reduce the number of outliers influencing the force measurements, the phase-space thresholding method proposed by Goring and Nikora (2002) and modified by Wahl (2003) was used for all force raw data with a data replacement of less than 0.5% (Further details on the phase-space thresholding method are provided in Appendix B.3). The force fluctuations (F_x' , F_y' , F_z'), FFT and auto-correlation functions of the forces in the three directions (T_{Fx} , T_{Fz} , T_{Fy}) were estimated based upon the combined truss and the sphere data.

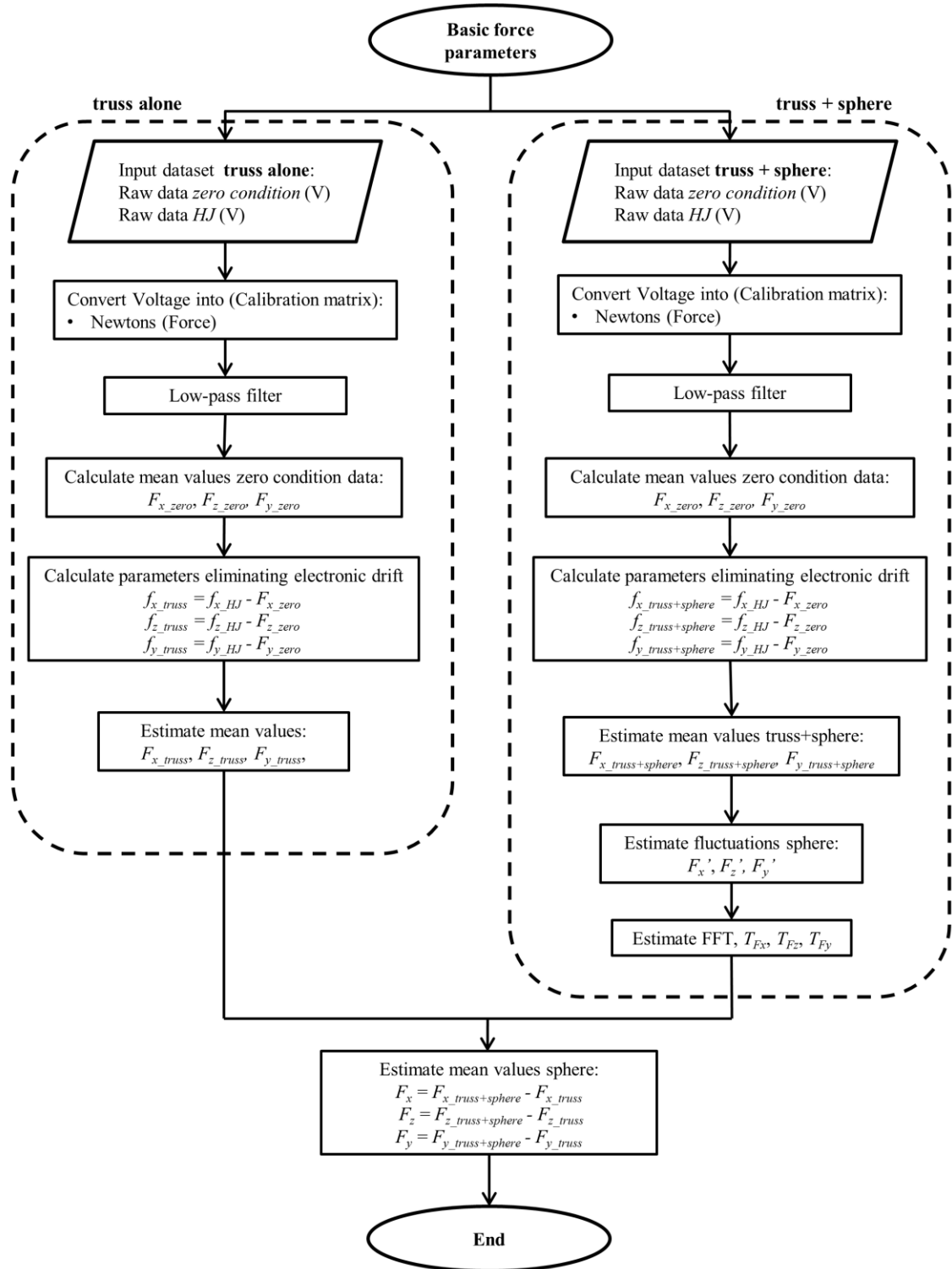


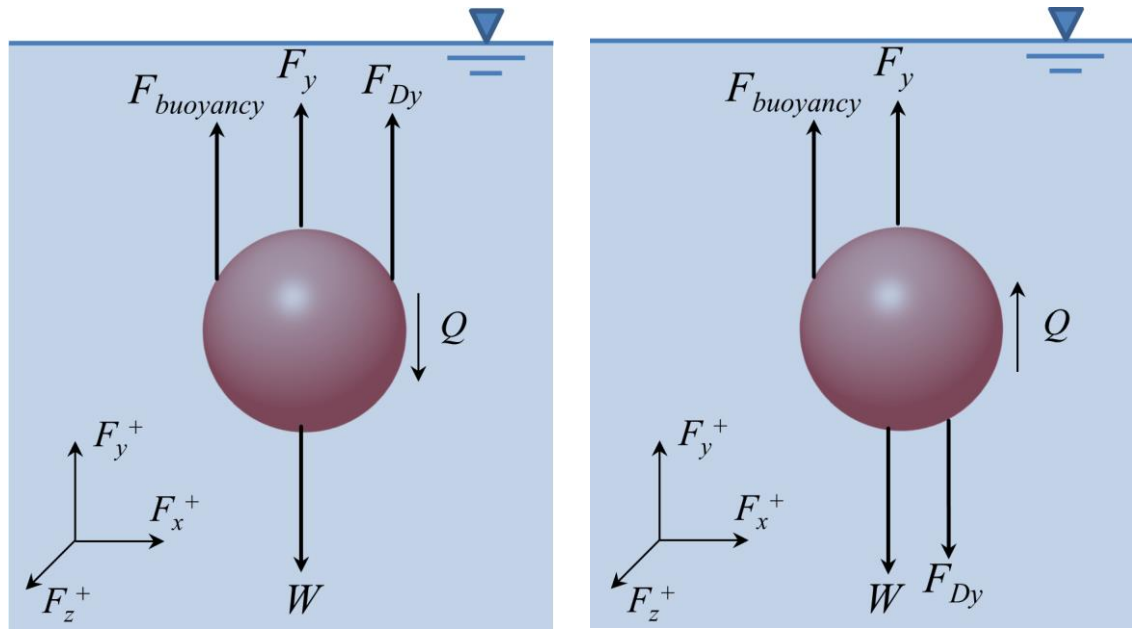
FIGURE 3-19. LOAD CELL POST-PROCESSING FLOW CHART OF BASIC FORCE PARAMETERS.

Note that the vertical force F_y represents the sum of the buoyancy forces $F_{buoyancy}$, the dynamic drag force F_{Dy} and the weight W of the sphere (Figure 3-20). While $F_{buoyancy}$ estimates the upward force due to the volume displaced by the sphere in the two-phase fluid, F_{Dy} characterises the dynamic vertical motions in the hydraulic jump and their flow direction, i.e. a positive drag force F_{Dy} means a negative downward flow direction (Figure 3-20A) and negative

drag force represents a positive upwards flow motion (Figure 3-20B). The weight of the sphere was not considered in the force balance since the load cell was zeroed with the sphere in the air. The total vertical force F_y measured with the load cell was therefore represented by:

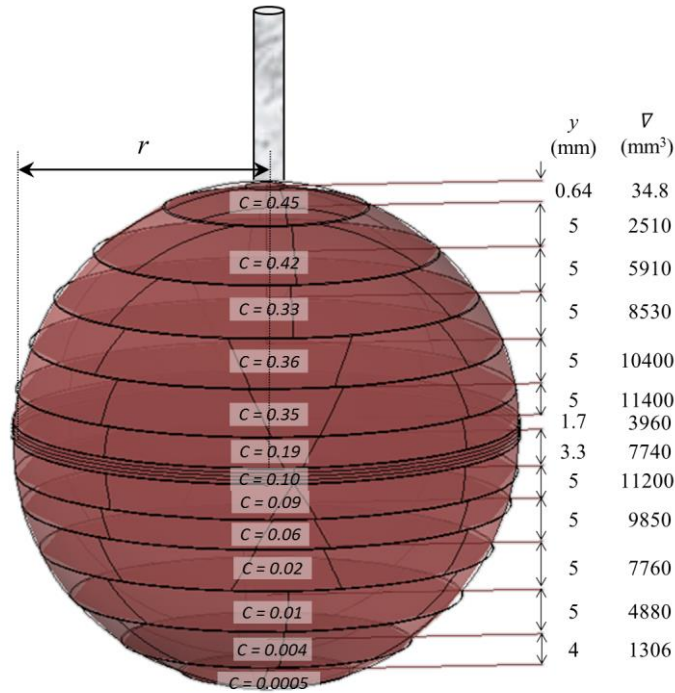
$$F_y = F_{buoyancy} + F_{Dy} = \rho_{air_water} g \nabla + F_{Dy} \quad (3.9)$$

where ρ_{air_water} is the density of the air-water mixture surrounding the sphere and ∇ is the volume of the sphere. $F_{buoyancy}$ was calculated based upon ρ_{air_water} which was estimated using the local time-averaged void fractions measured with the conductivity probe (Figure 3-21), i.e. $\rho_{air_water} = \rho \times (1 - C_{avg})$ (Wang et al. 2014b; Takahashi and Ohtsu 2017). F_{Dy} was estimated as the difference between the vertical force directly measured with the load cell and the buoyancy force, i.e. $F_{Dy} = F_y - F_{buoyancy}$.



A) POSITIVE F_{Dy} INDICATING DOWNWARDS FLUID MOTION B) NEGATIVE F_{Dy} INDICATING UPWARDS FLUID MOTION

FIGURE 3–20. VERTICAL FORCE DIAGRAM AND DEFINITION OF RELEVANT FORCES



$$V_i = \frac{\pi}{3} [y_{i+1}^2(3r - y_{i+1}) - y_i^2(3r - y_i)]$$

$$C_{avg} = \frac{\sum(C_i \times V_i)}{\sum V_i} = 0.1203$$

$$\rho_{air_water} = \rho \times (1 - C_{avg}) = 880 \text{ kg/m}^3$$

FIGURE 3–21. ESTIMATION OF THE LOCAL TIME-AVERAGED VOID FRACTION; EXAMPLE OF VOID FRACTION DATA FOR EXPERIMENT H: $Fr_1 = 3.8$, $Re = 6.2 \times 10^4$, $x/d_1 = 3$ - FULLY DEVELOPED INFLOW CONDITIONS.

3.4. DATA VALIDATION, LIMITATIONS AND UNCERTAINTIES

The hydraulic jump is a complex dynamic phenomenon characterised by large turbulence and continuous fluctuations. Any measurements comprise uncertainties related to the intense motions of hydraulic jumps as well as the limitations of the instrumentation. In the present study, the average jump toe position was selected as the reference point to locate the initial positioning of the hydraulic jump. The unstable and dynamic behaviour of the hydraulic jump added uncertainty to the selection of this initial location. The position of the hydraulic jump toe was therefore identified with a visual indicator at the channel side and the experiments did not start until the jump toe position of the hydraulic jump was oscillating around this indicator. Figure 3-22 shows an example of four hydraulic jumps located at the visual indicator position (yellow tape). The hydraulic jump was oscillating along the yellow tape resulting in positioning uncertainties. This uncertainty was estimated based on the absolute difference of the maximum and minimum jump toe oscillations recorded with the LIDAR giving an average uncertainty of ± 0.009 m for all experiments.

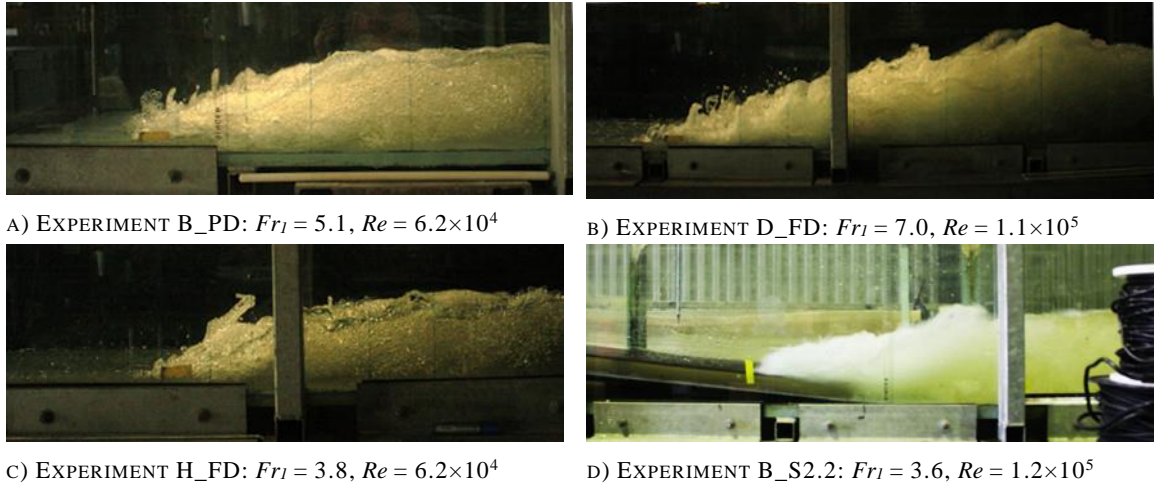


FIGURE 3-22. LOCATION OF THE MEAN JUMP TOE POSITION IN SELECTED HYDRAULIC JUMPS

3.4.1. FLOW DISCHARGE

The flow discharge was measured with an ABB WaterMaster FET100 electromagnetic flowmeter with $\pm 0.4\%$ accuracy based on the flowmeter datasheet. Figure 3-23 presents a recorded time series for an average flow rate of $Q = 67$ l/s for a duration of 600 s. The variation of the flow rate in Figure 3-23 indicated an uncertainty of 0.34% which is in agreement with the flow meter specifications.

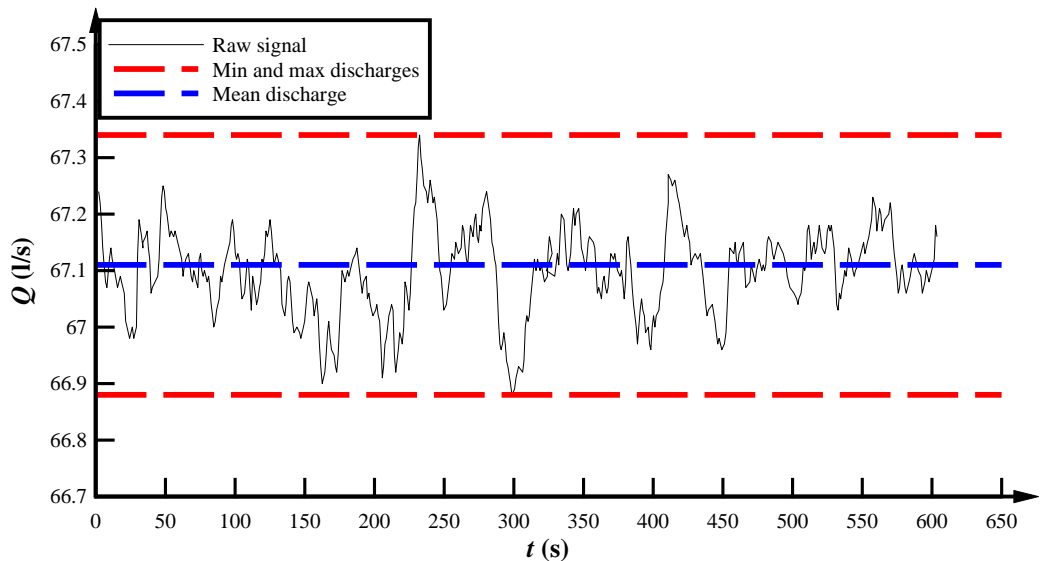


FIGURE 3-23. DISCHARGE FLUCTUATIONS DURING ACCURACY TEST OF FLOW RATES

3.4.2. AIR-WATER FLOW PROPERTIES

The conductivity probe was shifted in y-direction with a digital height gauge within an accuracy of ± 0.5 mm. The probe was located in channel centreline within ± 0.5 mm accuracy. The conductivity probe measurements can be strongly affected by contaminants on the probe tips, electrical noise and short- and long-term signal decay (Toombes 2002). To avoid erroneous measurements, before any conductivity probe recording, the raw signal was verified to confirm accurate Voltage levels and clear differences between air and water interfaces. The WRL

conductivity probes in the present study did not experience any short- and long-term signal decay and had very low noise levels.

The variation of the air-water flow properties was affected by the position along the hydraulic jump, the vertical elevation above the channel bed y . Table 3-1 presents the range of variation in void fraction and the bubble count rate for selected experiments including the sampling time, Fr_1 , Re , the longitudinal position, and the range of variations in C and F at $y = Y_{Cmax}$ and $y = Y_{Cmin}$. For hydraulic jumps downstream of the sluice gate and a sampling duration of at least 300 s, the maximum variation of C occurred close to the jump toe. Smaller deviations were observed in hydraulic jumps with partially developed inflow conditions. Overall, the measurement of the air-water flow properties in hydraulic jumps presented large data scatter associated to the unstable behaviour of hydraulic jumps. An increase in sampling durations resulted in a lesser variation in C and F values providing more reliable information of the air-water flow properties. Further details in the sensitivity analysis of the sampling duration are provided in Appendix B.2. Based upon the sensitivity analysis, the core air-water flow measurements of the present thesis, i.e. the hydraulic jumps downstream of the sluice gate were measured with sampling durations of 5 and 4 minutes respectively to provide the most accurate possible results. Note that these sampling durations are significantly larger compared to previous air-water flow studies of hydraulic jumps.

TABLE 3-1. RANGE OF VARIATION OF BASIC AIR-WATER FLOW PROPERTIES IN HYDRAULIC JUMPS MEASURED WITH A CONDUCTIVITY PROBE.

Similar Exp.	Sampling time (s)	Fr_1	Re	x/d_1	($\%$) ΔC		($\%$) F	
					(Y_{Cmax})	(Y_{Cmin})	(Y_{Cmax})	(Y_{Cmin})
A_FD	360			3.3	3	3	10	5
	300	5.1	8.3×10^4	5.8	6	5	8	18
	300			9.4	0.5	12	7	30
A_PD	300	5.1	8.3×10^4	5.8	3	-	7	-
G_FD	360			3.3	7	5	25	5
	300	10	8.8×10^4	5.8	3.6	8.5	15	7
	300			9.4	1.6	5	6	7
G_PD	300	10	8.8×10^4	5.8	1.3	-	2.5	-

3.4.3. FREE-SURFACE FLUCTUATIONS AND JUMP TOE OSCILLATIONS

The free-surface fluctuations and jump toe oscillations were measured with the LIDAR (SICK LMS511). According to the instrument specifications, for distances between 1 to 10 m, the LIDAR had a resolution of ± 24 mm, a systematic error of ± 25 mm and a statistical error of ± 6 mm (SICK 2015). The diameter of the laser beam of the Lidar increased with increasing distance from the Lidar position (SICK 2015) with a maximum laser beam diameter of about 2 cm at the downstream end of strong hydraulic jumps ($x = 4$ m) as per the manufacturer information. Laboratory experiments of breaking waves with the same LMS511 LIDAR

suggested an accuracy of about 6 mm in a comparative analysis with a wave resistance probe (Blenkinsopp et al. 2012; Streicher et al. 2013; Damiani and Valentini 2014). The present experimental setup was of similar scale and therefore experimental accuracy may be of similar order of magnitude due to the similarity between breaking waves and hydraulic jumps.

To validate the signal characteristics of the LIDAR, a sensitivity analysis of the probability mass function (PMF) of the fluctuations of the raw signal without the mean was conducted for the dry channel bed, following the approach of Kramer et al. (2019a) and Zhang et al. (2018). Figure 3-24 shows an example of the sensitivity analysis. Figure 3-24A presents the time series of the raw signal fluctuations (removing the mean) in comparison with the time series of the raw signal fluctuations with an initial high-pass filter of 0.1 Hz showing negligible differences between the filtered and raw signals. The PMF of the fluctuations with eliminated mean is shown in Figure 3-24B. The PMF showed similar Gaussian distributions for the raw and filtered data suggesting negligible intrinsic noise of the LIDAR. The high-pass filter reduced the peak of the Gaussian distribution resulting in lesser free-surface fluctuations. Figure 3-24C shows the Fast Fourier Transformation (FFT) for the raw and filtered data. The FFT for the raw signal showed no clear peak for the lower frequencies suggesting that it may not be necessary to apply any high-pass filtering to the raw signal. Further details on the effects of high-pass filtering on the free-surface signal of the hydraulic jump are discussed in Chapter 5.

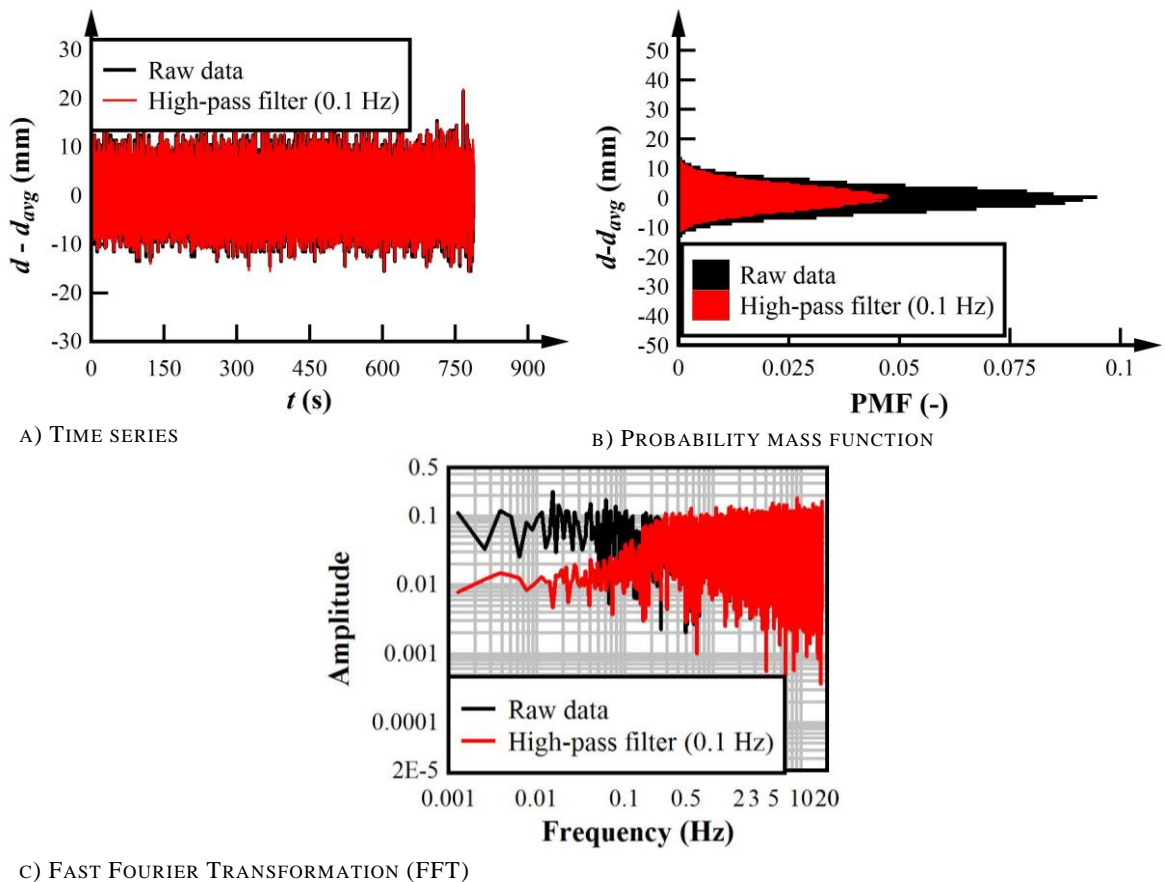


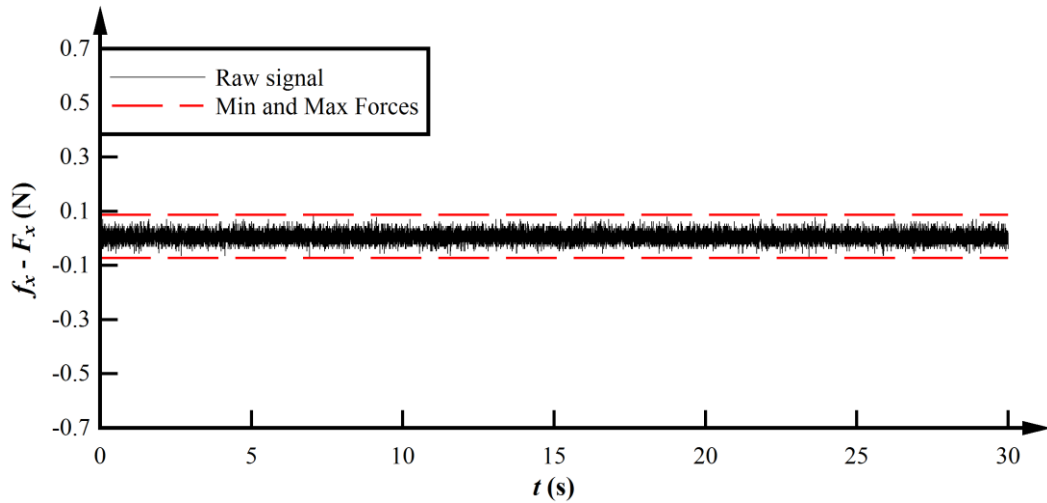
FIGURE 3-24. SENSITIVITY ANALYSIS OF THE PROBABILITY MASS FUNCTION OF THE RAW AND HIGH-PASS FILTERED SIGNAL OF THE LIDAR MEASUREMENTS OF THE CHANNEL BED

Laser light instruments are susceptible to optical issues related to the LIDAR location (incidence angle) and the transformation of the laser beam reaching the target object including transmission, absorption or refraction (Irish et al. 2006; Allis et al. 2011; Blenkinsopp et al. 2012; SICK 2015). The transformation of the laser beam depends on the reflectivity of the target object which means that a poor reflective medium, such as clear water, would not provide reliable data (Allis et al. 2011; Blenkinsopp et al. 2010; SICK 2015). For white bubbly flows such as in fully-aerated hydraulic jumps, the laser beam hitting the air-water surface experiences a diffuse reflection transforming the laser beam in multiple reflected rays increasing the probability of LIDAR detection (Harry et al. 2010). To reduce transmission, refraction and absorption effects, the experiments were limited to fully aerated hydraulic jumps and locations with at least 50% valid data. The positioning of the LIDAR upstream of the hydraulic jump provided a close-to-perpendicular angle between LIDAR beam and free-surface of the hydraulic jumps.

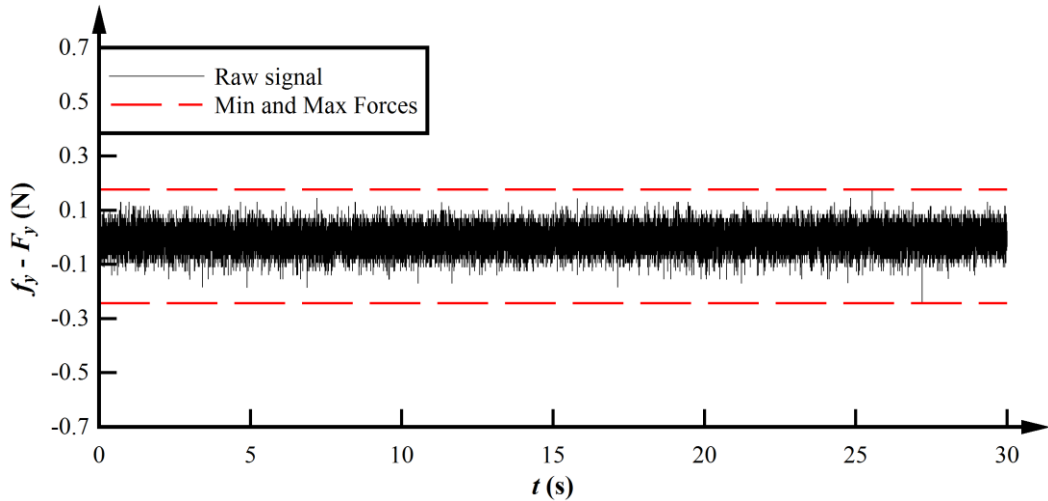
In addition to optical issues, the strong free-surface deformations in hydraulic jumps resulted in splashes of water droplets and air-water blobs and fingers above the surface which could interfere with the LIDAR recordings. A sensitivity analysis suggested that any filtering of outliers at the free-surface may result in elimination of valid information of the free-surface features including ejected droplets and “finger-like” splashes (Appendix C.2). Hence, the free-surface analysis was conducted without any outlier filtering. Areas located immediately downstream of strong free-surface formations may not be detected by the laser beam being identified as non-detected points (Figure 3-6). Any non-detected data obtained by the LIDAR were replaced by the linear interpolated value of the two adjacent known values.

3.4.4. FORCES

The forces on the submerged sphere in the hydraulic jump were measured with a six axial load cell. To avoid electrical noise, the external cable of the load cell was shielded with an aluminium layer (Figure 3-11B). Figure 3-25 presents typical instantaneous raw signals of the horizontal and transverse forces f_x and f_y for a 200 s duration at rest, i.e. without any external load. Note that the mean force values were subtracted in Figure 3-25 (F_x and F_y for longitudinal and vertical forces respectively) The variation in f_x was about ± 0.1 N while f_y had larger fluctuations of about ± 0.25 N. f_z had similar fluctuations to f_x .



A) INSTANTANEOUS RAW SIGNAL OF THE LONGITUDINAL FORCES f_x REMOVING THE MEAN F_x



B) INSTANTANEOUS RAW SIGNAL OF THE VERTICAL FORCES f_y REMOVING THE MEAN F_y

FIGURE 3-25. EXAMPLES OF RAW FORCE SIGNALS FOR DRY CONDITION

The load cell recordings were validated adding known loads to the three axes of the load cell in dry conditions. Figure 3-26 presents the force measurements in x , y and z directions in dry conditions for forces between 0 and 30 N. The load cell was able to measure accurately the forces in dry conditions with differences between real and measured force of about 1% for all directions.

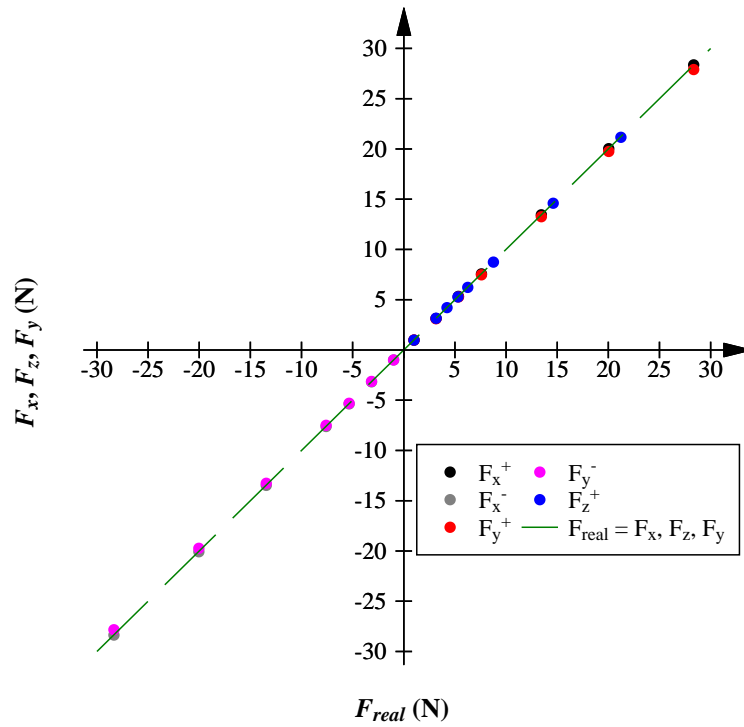


FIGURE 3-26. VALIDATION OF THE SIX-AXIS LOAD CELL PERFORMANCE IN DRY CONDITIONS.

An additional test was conducted to select the sphere size. This analysis was conducted with submerged spheres of diameters between $0.035 \leq \phi_{sphere} \leq 0.082$ m attached to rods of $5 < \phi_{rod} < 11$ mm thickness in uniform flow conditions. The spheres were positioned at different elevations from the channel bed in a horizontal smooth open channel flow. Figure 3-27 presents the drag force measurements $F_{Dx,measured}$ with the different sphere sizes. The experiments were compared to the theoretical drag force $F_{Dx,theory}$ estimated with Equation 2.10 as the sum of the drag force on the sphere and the stainless steel rod. The experiments with a rod diameter of $\phi_{rod} = 6$ mm presented differences up to 0.15 N indicating large influence of the rod and the wake of the sphere on the drag force measurements. While the experiments with the sphere of $\phi_{sphere} = 0.035$ m diameter agreed better with $F_{Dx,theory}$, the combination of a sphere of $\phi_{sphere} = 0.054$ m diameter and rod thickness of $\phi_{rod} = 5$ mm fitted best the theoretical drag force for $Re \geq 6.8 \times 10^4$. Large differences were observed for a sphere of $\phi_{sphere} = 0.082$ m and a rod of $\phi_{rod} = 11$ mm which disturbed the flow significantly (Not shown). A further validation was conducted with the sphere of $\phi_{sphere} = 0.054$ m attached to the truss structure presented in Figure 3-11A. The theoretical drag force was estimated as the difference in the drag force of the sphere and the truss and the drag force of the truss alone. The results showed good agreement with $F_{Dx,theory}$ suggesting that the combination of the sphere size and the truss structure proposed in Figure 3-11 was the best available system to measure the forces on the sphere inside hydraulic jumps. Additional sensitivity analysis of the truss structure is presented in Appendix H.

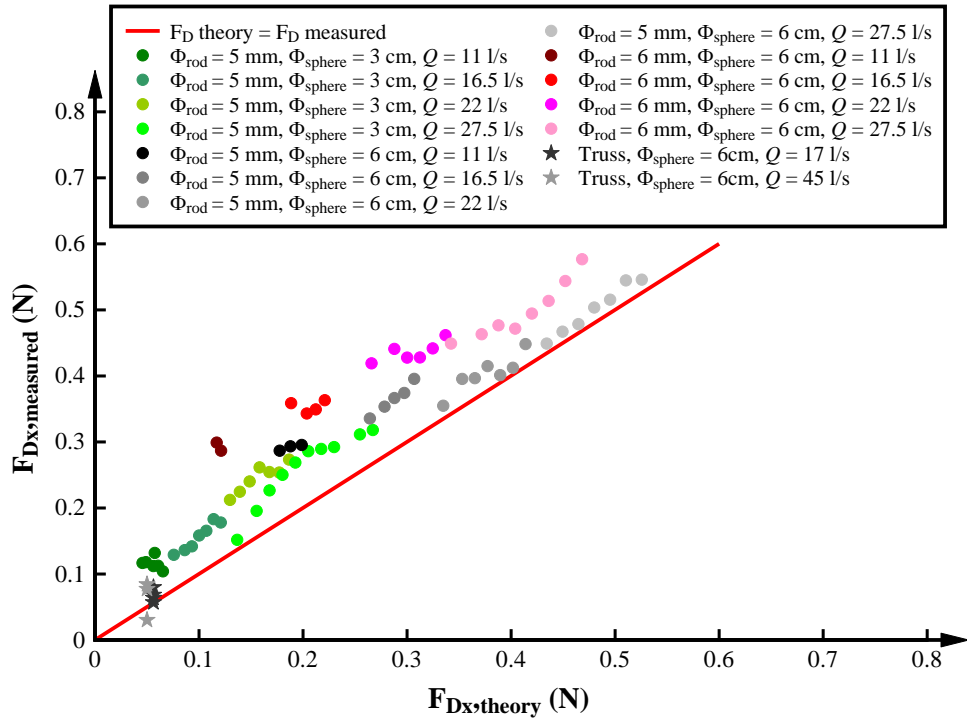


FIGURE 3-27. VALIDATION OF FORCE MEASUREMENTS WITH THE SIX-AXIS LOAD CELL IN UNIFORM FLOW CONDITIONS

Note that the recording of the internal forces with a submerged sphere in the hydraulic jump are strongly dependant of the sphere size. While a microscopic sphere would be able to capture microscopic turbulent scale motions, larger sphere diameters would integrate the small- and large-scale eddies simultaneously influencing the force recording. Nonetheless, as discussed previously, spheres with smaller diameter were more vulnerable to the influence of the rod wake (Figure 3-27). In the present study, the selection of the sphere diameter of $\phi_{sphere} = 0.054$ m and rod thickness of $\phi_{rod} = 5$ mm minimised the wake effect of the rod although it was limited to large-scale eddies. Further research is recommended to analyse the internal forces of the hydraulic jump with smaller sphere diameters and rod structures. Since the system would be less robust, special designs should be considered to increase the resonant frequency of the system and avoid self-excitation.

3.5. FLOW CONDITIONS

The present study analysed hydraulic jumps with different boundary layer development upstream of the hydraulic jump for a wide range of Froude and Reynolds numbers. 17 hydraulic jumps were tested experimentally comprising partially and fully developed inflow conditions. Table 3-2 summarizes the experimental flow conditions including d_1 , Fr_1 , Re , the ratio of the boundary layer depth at the jump toe position (δ), the inflow gate height h_0 , the distance from the sluice gate to the jump toe x_{sg} , and the instrumentation where PG is the Pointer Gauge, PT is

the Pitot Tube, CP is the Conductivity probe and LC is referred to the six-axis Load Cell (See section 3.2).

TABLE 3-2. EXPERIMENTAL FLOW CONDITION IN THE PRESENT STUDY.

Test	d_I (m)	Q (m ³ s ⁻¹)	Fr_I	Re	h_0 (m)	x_{sg} (m)	δ/d_I	Instrumentation			
								PG	CP	LIDAR	LC
A_PD	0.03	0.05	5.1	8.33×10^4	0.027	0.50	0.4	x	x	x	x
A_FD	0.03	0.05	5.1	8.33×10^4	0.025	2.44	1.4	x	x	x	x
B_PD	0.0248	0.037	5.1	6.17×10^4	0.022	0.58	0.5	x	x	x	x
B_FD	0.0248	0.037	5.1	6.17×10^4	0.018	1.87	1.5	x	x	x	x
C_PD	0.02	0.037	7.0	6.17×10^4	0.0175	0.46	0.5	x	x	x	x
C_FD	0.02	0.037	7.0	6.17×10^4	0.014	1.45	1.5	x	x	x	x
D_PD	0.03	0.068	7.0	1.13×10^5	0.027	0.71	0.5	x	x	x	x
D_FD	0.03	0.068	7.0	1.13×10^5	0.019	1.97	1.5	x	x	x	x
E_PD	0.02	0.045	8.5	7.50×10^4	0.019	0.50	0.5	x	x	x	x
E_FD	0.02	0.045	8.5	7.50×10^4	0.016	1.66	1.5	x	x	x	x
F_PD	0.027	0.07	8.4	1.17×10^5	0.024	0.63	0.5	x	x	x	x
F_FD	0.028	0.07	8.0	1.17×10^5	0.020	2.07	1.5	x	x	x	x
G_PD	0.02	0.053	10.0	8.83×10^4	0.017	0.45	0.5	x	x	x	x
G_FD	0.02	0.053	10.0	8.83×10^4	0.014	1.45	1.5	x	x	x	x
H_PD	0.03	0.037	3.8	6.17×10^4	0.026	0.68	0.5	x	x	x	x
H_FD	0.03	0.037	3.8	6.17×10^4	0.022	2.28	1.5	x	x	x	x
I_FD	0.04	0.057	3.8	9.50×10^4	0.0275	2.85	1.5	x	x	x	x

The following chapters present the experimental results of the measurements of the air-water flow properties, the free-surface features and the internal three-dimensional motions of a submerged sphere in the hydraulic jump.

4

AIR-WATER FLOW PROPERTIES

Some content of this chapter is taken from the following publication:

Conference Proceedings

Montano, L, and Felder, S. 2018, 'Effect of inflow conditions on the air-water flow properties in hydraulic jumps', in *Proc., 21st Australasian Fluid Mechanics Conference*, Adelaide, Australia, 4 pages.

4.1. INTRODUCTION

Air-water flow properties in hydraulic jumps have been extensively investigated during the last 50 years providing a clear understanding of the aeration features along classical hydraulic jumps with partially developed inflow conditions. A detailed description of the current knowledge was presented in Chapter 2.4. Only a few studies have investigated the effect of the boundary layer development upstream of the hydraulic jump on the air-water flow properties (Resch and Leutheusser 1972a; Resch et al. 1974; Takahashi and Ohtsu 2017) highlighting that hydraulic jumps with fully developed inflow conditions had larger void fractions and bubble sizes. This effect was linked to larger turbulence levels in fully developed inflows upstream of the hydraulic jump. While these studies provided some first insights into the importance of the inflow conditions, new experiments were conducted in the present study to test the effect of the inflow conditions for a wider range of air-water flow properties including void fraction, bubble count rate, interfacial velocity, chord times and auto- and cross-correlation time scales.

The present study also recorded air-water flow properties on sloped channels. The analysis was conducted in Type B and Type D jumps for three channel slopes $\theta = 1.25^\circ$, 2.5° and 5° providing novel information about void fractions, bubble count rate, interfacial velocity and bubble chord sizes. The comparison of air-water flow properties of hydraulic jumps on sloped channels with comparable hydraulic jumps on a horizontal bed is provided in Appendix F. Note that all experiments were conducted in smooth channels, and no flow pre-aeration was observed upstream of any of the hydraulic jumps. Table 4–1 summarises the flow conditions for the air-water flow experiments including the inflow conditions, the dimensionless boundary layer thickness δ/h_0 , the distance from the sluice gate to the mean jump toe x_{sg} , the flow rate per unit of width q , the inflow flow depth d_1 and the Froude Fr_1 and Reynolds Re numbers.

TABLE 4–1. EXPERIMENTAL FLOW CONDITIONS FOR MEASUREMENT OF AIR-WATER FLOW PROPERTIES

Experiment	Inflow condition	δ/d_1 (-)	x_{sg} (m)	q (m ² /s)	d_1 (m)	Fr_1 (-)	Re (-)
A	PD	0.4	0.5	0.083	0.030	5.1	8.3×10^4
	FD	1.4	2.44	0.083	0.030	5.1	8.3×10^4
B	PD	0.5	0.58	0.062	0.025	5.1	6.2×10^4
	FD	1.5	1.87	0.062	0.025	5.1	6.2×10^4
C	PD	0.5	0.46	0.062	0.020	7.0	6.2×10^4
	FD	1.5	1.45	0.062	0.020	7.0	6.2×10^4
D	PD	0.5	0.71	0.113	0.030	7.0	1.1×10^5
	FD	1.5	1.97	0.113	0.030	7.0	1.1×10^5
E	PD	0.5	0.50	0.075	0.020	8.5	7.5×10^4
	FD	1.5	1.66	0.075	0.020	8.5	7.5×10^4
F	PD	0.5	0.63	0.117	0.027	8.4	1.2×10^5
	FD	1.5	2.07	0.117	0.028	8.0	1.2×10^5

Experiment	Inflow condition	δ/d_1 (-)	x_{sg} (m)	q (m ² /s)	d_1 (m)	Fr_1 (-)	Re (-)
G	PD	0.5	0.45	0.088	0.020	10	8.8×10^4
	FD	1.5	1.45	0.088	0.020	10	8.8×10^4
H	PD	0.5	0.68	0.062	0.030	3.8	6.2×10^4
	FD	1.5	2.28	0.062	0.030	3.8	6.2×10^4
I	FD	1.5	2.85	0.095	0.040	3.8	9.5×10^4

4.2. VISUAL OBSERVATIONS OF AIR-WATER FLOW PATTERNS

The transition from supercritical to subcritical flows in hydraulic jumps was characterised by a sudden increase in flow depth, large air entrainment in the roller region (represented by the white colour) and large instabilities along the jump roller (Figure 4-1). All hydraulic jumps presented periodic longitudinal oscillations linked with the vortex formation and pairing in the roller region of the hydraulic jumps (e.g. Long et al. 1991; Mossa and Tolve 1998; Mok 2004). At the jump toe position (Figure 4-1), the flow depth increased suddenly and air was entrapped at the impingement point of the hydraulic jump. The entrapped air-bubbles were advected and broken up in smaller bubbles by the shear stress and the large vortical structures in the roller region of the hydraulic jump. Some of these smaller air bubbles were transported into regions of lesser shear stress resulting in bubble coalescence accompanied by an upwards direction towards the recirculation region. Beneath the roller region, a clear water core was consistently observed close to the channel bed independent of the hydraulic jump conditions. In the upper part of the hydraulic jump, the flow had large free-surface fluctuations, water splashes and foam formed by air-water entities. At the downstream end of the hydraulic jump, the flow was less aerated comprising comparatively larger bubbles with an upwards direction due to dominating buoyancy effects. A wavy free-surface profile was typically observed in the downstream part of the hydraulic jump.

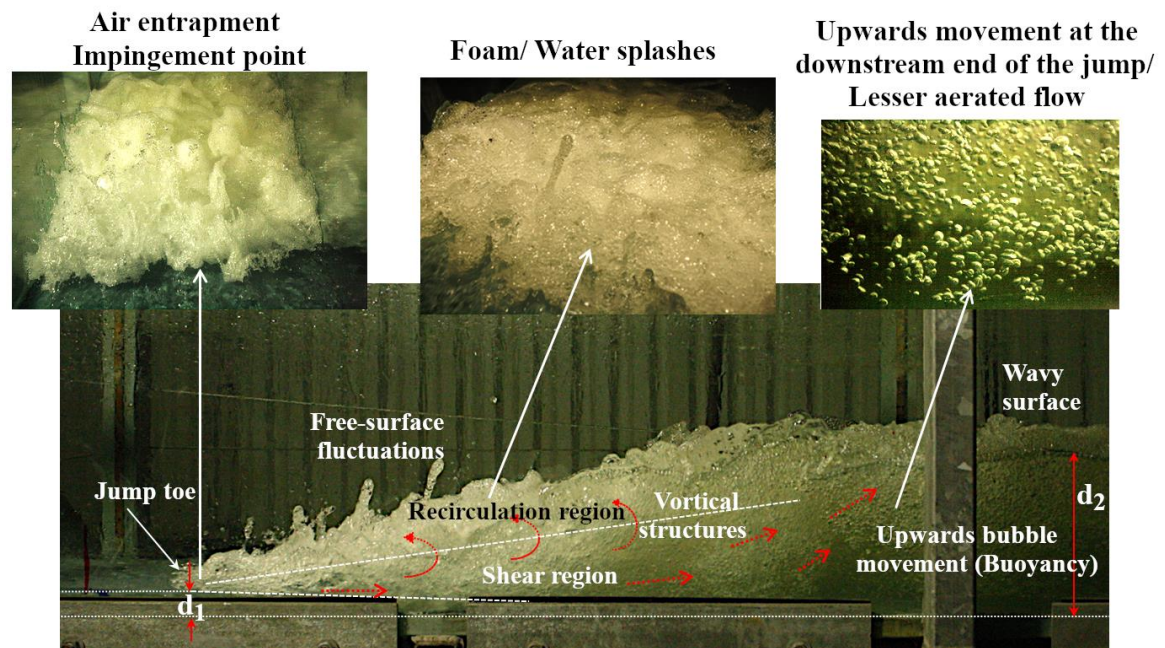
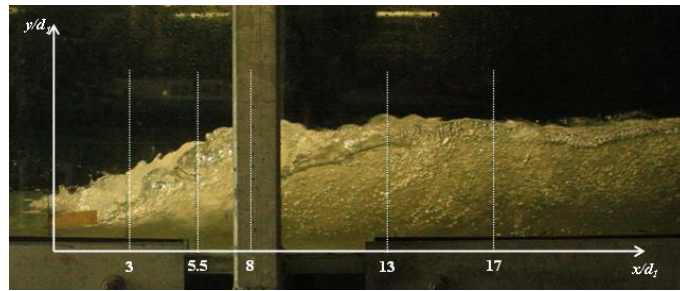
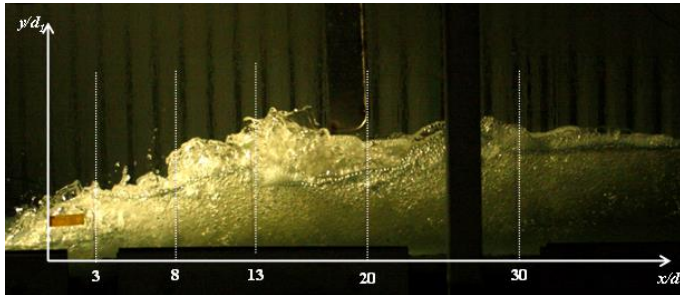


FIGURE 4-1. AERATION FEATURES IN THE HYDRAULIC JUMP

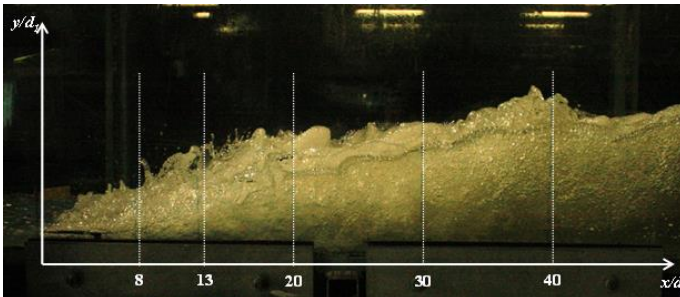
Figure 4-2 presents typical hydraulic jumps with similar Reynolds number and different Froude numbers. The cross-sections for the conductivity probe measurements are added as reference lines. Visual observations showed an increase in aeration, free-surface instabilities and water splashes with increasing Froude numbers. Hydraulic jumps with $3.8 \leq Fr_1 < 4.5$ had large surface instabilities, steeply increased in flow depth along the roller region and lower aeration compared to hydraulic jumps with larger Froude numbers (Figure 4-2A). The pulsating behaviour and instabilities of the present jumps were typical of transition jumps $2.5 \leq Fr_1 \leq 4.5$ as indicated in Table 1-1 (Chow 1973; Peterka 1978; Hager 1992). Hydraulic jumps with $5.1 \leq Fr_1 < 8.5$ were stronger aerated, and the increase in flow depth along the roller region was more gradual compared to transition jumps (Figure 4-2B - D). The appearance of these hydraulic jumps resembled stabilised jumps which occur for $4.5 \leq Fr_1 \leq 9$ (Chow 1973; Peterka 1978; Hager 1992) (Table 1-1). Large aeration and instabilities as well as large spray and water splashes were observed for hydraulic jumps with $Fr_1 = 10$ (Figure 4-2E). This type of hydraulic jump is known as Choppo jump and occurs for $Fr_1 > 9$ (Chow 1973; Peterka 1978; Hager 1992) (Table 1-1). Stronger aeration was consistently observed in hydraulic jumps with larger Reynolds numbers highlighting the effect of larger inflow turbulence levels on the flow aeration in hydraulic jumps.



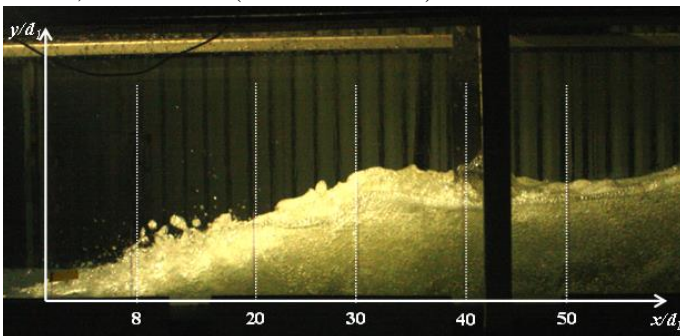
A) EXPERIMENT H: $Fr_1 = 3.8$, $Re = 6.2 \times 10^4$ (TRANSITION JUMP)



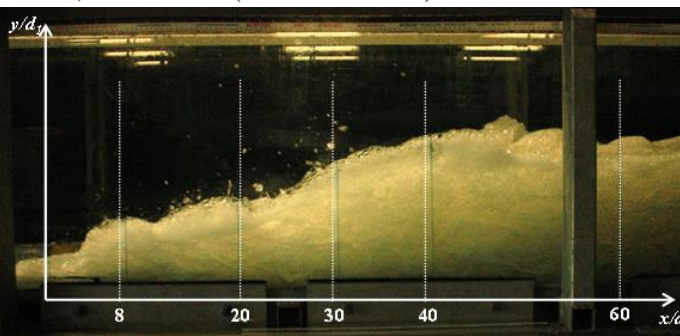
B) EXPERIMENT B: $Fr_1 = 5.1$, $Re = 6.2 \times 10^4$ (STABILISED JUMP)



C) EXPERIMENT C: $Fr_1 = 7.0$, $Re = 6.2 \times 10^4$ (STABILISED JUMP)



D) EXPERIMENT E: $Fr_1 = 8.5$, $Re = 7.5 \times 10^4$ (STABILISED JUMP)



E) EXPERIMENT G: $Fr_1 = 10$, $Re = 8.8 \times 10^4$ (CHOPPY JUMP)

FIGURE 4-2. FLOW PATTERNS IN HYDRAULIC JUMPS IN THE PRESENT STUDY

4.3. EFFECT OF INFLOW CONDITIONS ON AIR-WATER FLOW PROPERTY DISTRIBUTIONS IN HYDRAULIC JUMPS

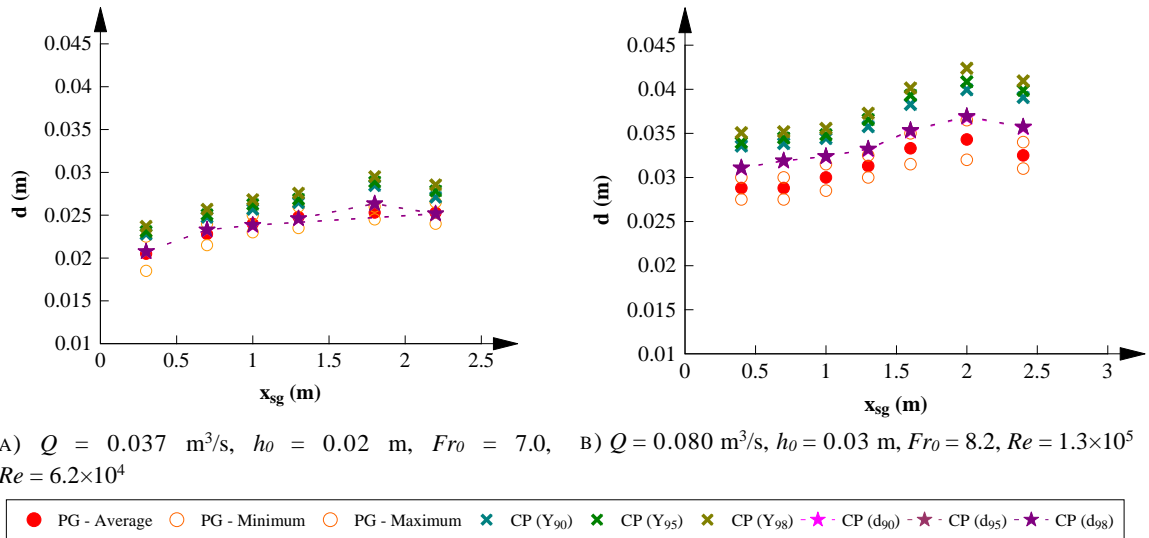
4.3.1. FLOW PROPERTIES UPSTREAM OF HYDRAULIC JUMPS

The flow depths in the supercritical region downstream of the sluice gate were measured with a pointer gauge at different cross-sections and validated with measurements of the free-surface roughness using a conductivity probe. The analysis was conducted for flow rates $0.037 < Q < 0.080$ m³/s, gate openings $0.02 < h_0 < 0.04$ m and Froude numbers at the gate $3.2 < Fr_0 < 12.3$.

Figure 4-3 shows examples of the flow depths measured with the pointer gauge (PG) and the conductivity probe (CP) as function of x_{sg} . The pointer gauge measurements comprise the average, minimum and maximum flow depths. The conductivity probe measurements include the characteristic flow depths Y_{90} , Y_{95} and Y_{98} which represent flow depths where $C = 90\%$, 95% and 98% respectively as well as the equivalent clear-water flow depths calculated for the respective percentiles d_{90} , d_{95} and d_{98} :

$$d_{\#\#} = \int_{y=0}^{y=Y_{\#\#}} (1 - C) \times dy \quad (4.1)$$

For all flow conditions, the flow depths increased with increasing distance from the sluice gate linked with flow deceleration due to shear stress at the channel bed (Figure 4-3). Some data scatter was observed especially for hydraulic jumps with large Re . Maximum differences of about 2 mm were identified between Y_{90} and Y_{98} and the maximum differences between d_{90} and d_{98} were about 0.2 mm. The deviations increased slightly with increasing Fr_0 and x_{sg} . The small differences between Y_{90} and Y_{98} and d_{90} and d_{98} suggested a rapid increase in the void fractions within the upper part of the high-velocity flows. For $Re < 9 \times 10^4$, the average free-surface depths measured with the pointer gauge agreed well with d_{90} , d_{95} and d_{98} with average differences of 2% (Figure 4-3A). For $Re \geq 9 \times 10^4$, the flow was more turbulent and the free-surface had larger fluctuations, resulting in a closer agreement of the equivalent clear-water flow depths with the maximum pointer gauge recording differing 4% on average (Figure 4-3B). Therefore, the flow depths were assessed as the average recording of the pointer gauge for $Re < 9 \times 10^4$ and as the maximum pointer gauge reading for $Re > 9 \times 10^4$.



A) $Q = 0.037 \text{ m}^3/\text{s}$, $h_0 = 0.02 \text{ m}$, $Fr_0 = 7.0$, $Re = 6.2 \times 10^4$ B) $Q = 0.080 \text{ m}^3/\text{s}$, $h_0 = 0.03 \text{ m}$, $Fr_0 = 8.2$, $Re = 1.3 \times 10^5$

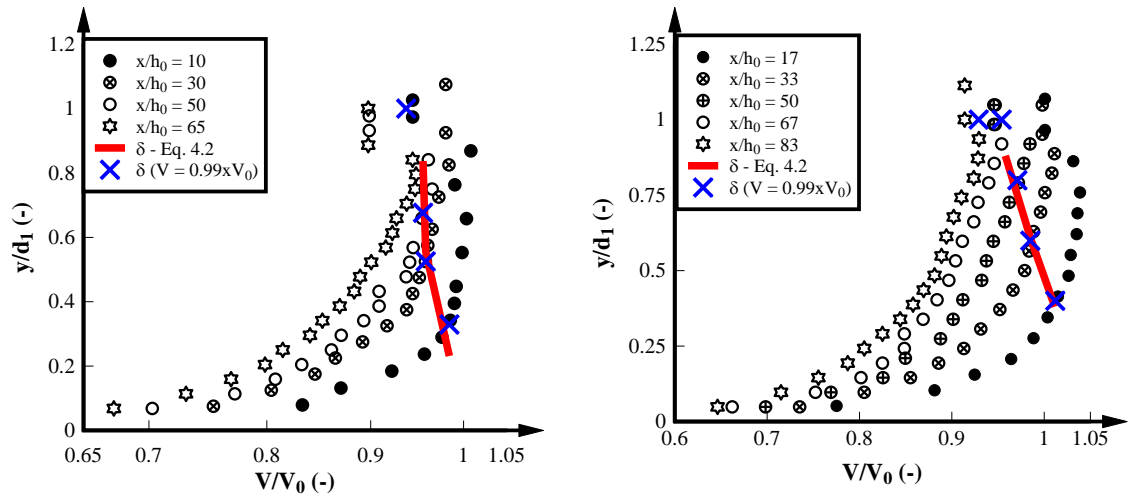
FIGURE 4-3. FREE-SURFACE PROFILES IN THE SUPERCRITICAL REGION DOWNSTREAM OF A SLUICE GATE. COMPARISON OF FLOW DEPTH MEASUREMENTS WITH POINTER GAUGE (PG) AND CONDUCTIVITY PROBE (CP).

At several cross-sections downstream of the sluice gate, the time-averaged velocities V were measured with the Pitot tube. Figure 4-4 shows typical dimensionless velocity distributions V/V_0 as a function of y/d_1 at different positions x_{sg}/h_0 for two configurations, where V_0 is the free-stream velocity. The measured velocities close to the channel bed were small increasing with distance from the channel bed. For the same flow rate and gate opening, the magnitude of the velocities decreased with increasing distance downstream of the sluice gate as a result of the increase in the shear stress, boundary layer development and inflow depth in downstream direction. The estimation of the shear stress in the supercritical region is included in Appendix A.1. Similar velocity distributions were observed for all discharges and gate openings. At all cross-sections, the boundary layer thickness δ was determined as the elevation where the local velocity was 99% of the free-stream velocity.

The growth rate of the turbulent boundary layer was in close agreement with the empirical equation by Wang (2014):

$$\frac{\delta}{d_1} = 0.0366 \times \left(\frac{x}{h_0}\right)^{4/5} \quad (4.2)$$

Note that the empirical equation provided by Wang (2014) considered δ/h_0 instead of δ/d_1 . The values of δ are highlighted in Figure 4-4 showing the close agreement between the present data and Equation 4.2. The boundary layer development was used to assess the upstream inflow conditions. If $d < \delta$, the flow was considered as partially developed while the flow was fully developed for $d \geq \delta$.

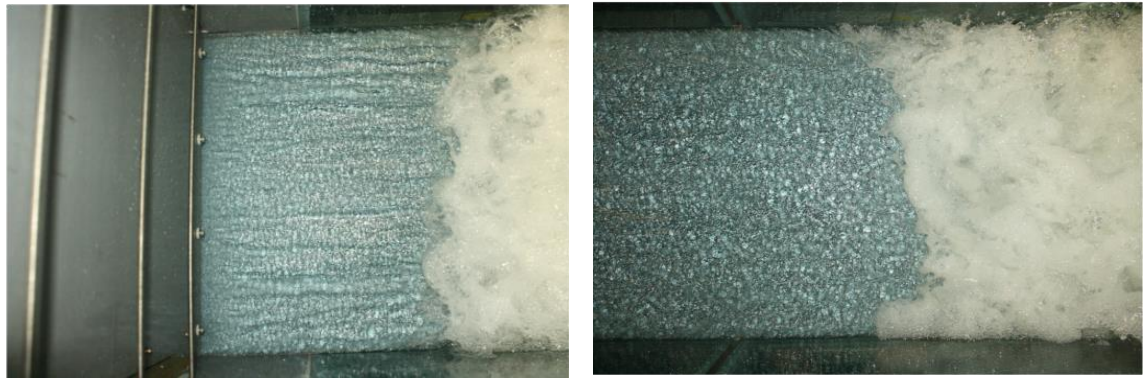


A) $Q = 0.053 \text{ m}^3/\text{s}$, $h_0 = 0.02 \text{ m}$, $Fr_0 = 4.4$

B) $Q = 0.058 \text{ m}^3/\text{s}$, $h_0 = 0.03 \text{ m}$, $Fr_0 = 3.2$

FIGURE 4-4. VELOCITY DISTRIBUTIONS AT SEVERAL CROSS-SECTIONS DOWNSTREAM OF THE SLUICE GATE. COMPARISON OF ESTIMATED BOUNDARY LAYER THICKNESS AND EQUATION 4.2

Figure 4-5 shows the free-surface roughness upstream of a hydraulic jump with partially and fully developed inflow conditions respectively. Flows with partially developed inflow conditions had small amplitude free-surface waves and an almost smooth profile (Fig. 4-5A), while the free-surface in fully developed inflows showed free-surface roughness (Fig. 4-5B). The observations of the fully developed inflows are of similar appearance compared to flow conditions upstream of hydraulic jumps of Ohtsu and Yasuda (1994) and Takahashi and Ohtsu (2017). Further details of the flow conditions and the air-water flow properties in the supercritical flows upstream of the hydraulic jumps are presented in Appendix A.1.



A) PARTIALLY DEVELOPED INFLOW CONDITIONS
($\delta/d_1 = 0.5$)

B) FULLY DEVELOPED INFLOW CONDITIONS
($\delta/d_1 = 1.2$)

FIGURE 4-5. INFLOW CONDITIONS UPSTREAM OF HYDRAULIC JUMPS. EXPERIMENT E: $Fr_1 = 8.5$, $Re = 7.5 \times 10^4$.

4.3.2. FLOW PATTERNS

The visual observations showed similar aeration, turbulence and free-surface features for hydraulic with partially and fully developed inflow conditions. In the roller region, no differences were observed between the two hydraulic jump types. Both hydraulic jumps had large air entrainment at the impingement point as well as strong free-surface fluctuations, water

splashes and foam in the upper part of the hydraulic jump. At the downstream end, larger whitish colour was observed in hydraulic jumps with partially developed inflow conditions (Figure 4-6B) while hydraulic jumps with fully developed inflow conditions showed a larger clear water layer close to the channel bed suggesting a stronger upwards directed jump roller compared to partially developed inflow conditions (Figure 4-6A). A comparative video of hydraulic jumps with similar Froude and Reynolds numbers and different inflow conditions is provided as Movie 4_1 in a Digital Appendix.



A) EXPERIMENT E: $Fr_1 = 8.5$, $Re = 7.5 \times 10^4$, $x_{sg} = 1.66$ m, $\delta = 0.03$ m - FULLY DEVELOPED INFLOW CONDITIONS



B) EXPERIMENT E: $Fr_1 = 8.5$, $Re = 7.5 \times 10^4$, $x_{sg} = 0.5$ m, $\delta = 0.01$ m - PARTIALLY DEVELOPED INFLOW CONDITIONS

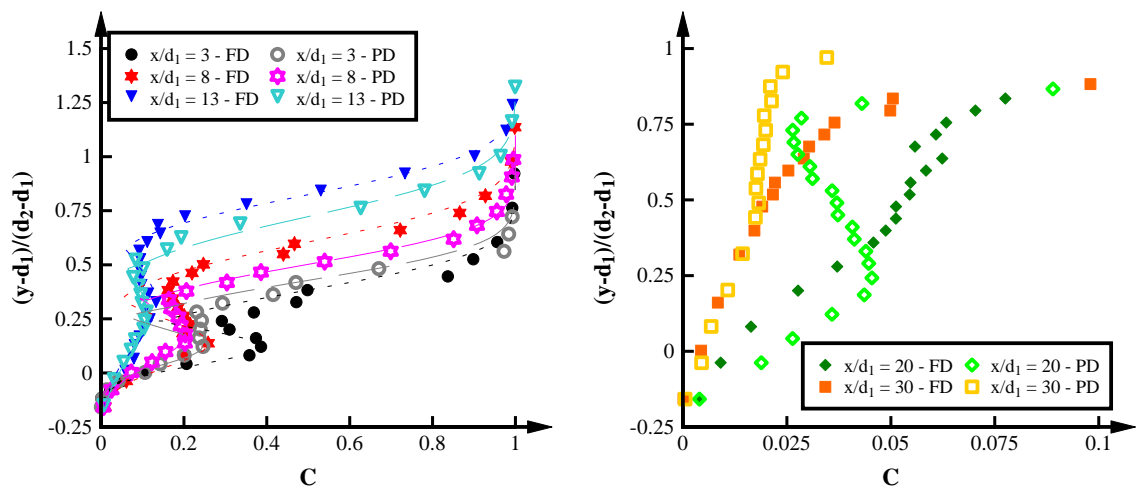
FIGURE 4-6. COMPARISON IN THE FLOW PATTERNS BETWEEN HYDRAULIC JUMPS WITH FULLY AND PARTIALLY DEVELOPED INFLOW CONDITIONS

4.3.3. VOID FRACTION

Figure 4-7 presents a comparison of the void fraction distributions for fully and partially developed inflow conditions as a function of the dimensionless elevation above the channel bed $(y-d_1)/(d_2-d_1)$. For all cross-sections, the void fraction distributions followed a typical shape with a clear peak in the shear region characterised by the air entrapped at the impingement point followed by a decrease until C_{min} . In the recirculation region, the void fraction presented a monotonic increase with increasing the elevation until reaching the free-surface. The void fraction distributions were also in agreement with previous studies conducted on hydraulic jumps with partially and fully developed inflow condition (e.g. Chanson 2009b; Wang 2014; Takahashi and Ohtsu 2017).

The comparison of C for fully and partially developed inflow conditions was conducted at the same dimensionless distance and for identical Froude and Reynolds numbers. The hydraulic jump with fully developed inflow conditions showed larger void fractions in the shear region at all cross-sections due to more unstable free-surface at the jump toe position as indicated by Takahashi and Ohtsu (2017) (Figure 4-7A). In the recirculation region, although the void fraction showed similar distributions between hydraulic jumps with fully and partially developed inflow conditions, the flow depth was higher in fully developed hydraulic jumps which may be related to the reduction in the shear stress in fully developed hydraulic jumps. Further details about the increase in the flow depth in fully developed hydraulic jumps are introduced in Chapter 5. At the downstream end of the hydraulic jump (Figure 4-7B), the void fraction distribution in fully developed hydraulic jumps presented an almost monotonic increase in the void fraction while partially developed hydraulic jumps still presented a clear advective peak in the shear region. This result suggested that the air-bubbles in the hydraulic jump with fully developed inflow conditions were more affected by buoyancy effects at the downstream end of the hydraulic jump.

All void fraction distributions presented good agreement with the theoretical advective diffusion equations in the shear region and analytical diffusion equation in the recirculation region (Equations 2.7a and b respectively) independent of the inflow conditions. The results indicated that for fully and partially developed inflow conditions, the void fractions followed the advective transport of bubbles in the shear region and a water jet profile in the recirculation region.



A) VOID FRACTION DISTRIBUTION CLOSE TO THE JUMP TOE

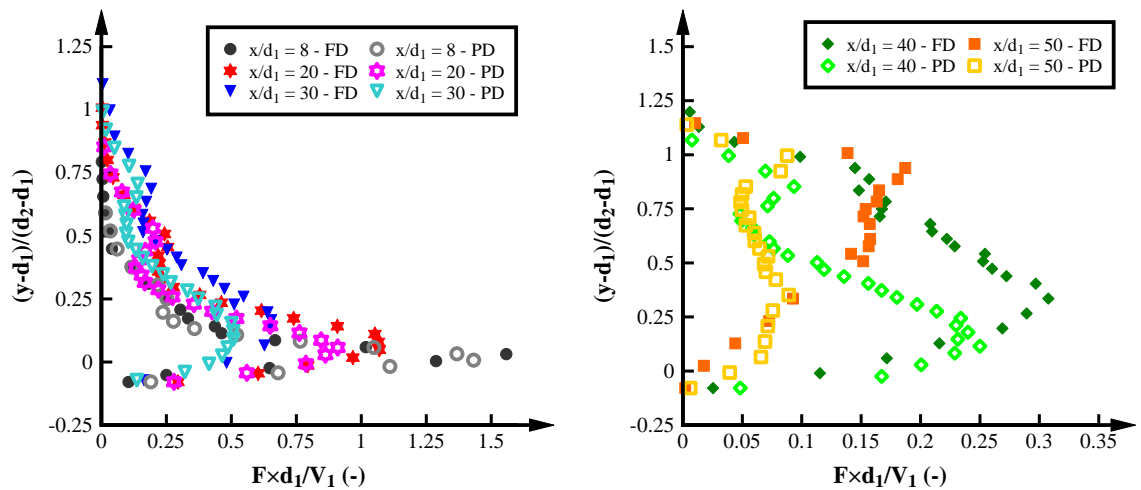
B) VOID FRACTION DISTRIBUTION AT THE DOWNSTREAM END OF THE HYDRAULIC JUMP

FIGURE 4-7. COMPARISON OF VOID FRACTION DISTRIBUTIONS FOR FULLY (FD) AND PARTIALLY (PD) DEVELOPED INFLOW CONDITIONS AT SEVERAL CROSS SECTIONS ALONG THE HYDRAULIC JUMP: EXPERIMENT B: $Fr_1 = 5.1$, $Re = 6.2 \times 10^4$. COMPARISON WITH THE ADVECTIVE DIFFUSION EQUATION FOR AIR BUBBLES IN HYDRAULIC JUMPS (EQUATIONS 2.7a AND 2.7b: DOTTED LINE = FULLY DEVELOPED INFLOW CONDITIONS; DASHED LINES = PARTIALLY DEVELOPED INFLOW CONDITIONS).

4.3.4. BUBBLE COUNT RATE

Figure 4-8 presents typical bubble count rate distributions for hydraulic jumps with partially and fully developed inflow conditions at different cross-sections along the hydraulic jump. For all cross-sections and independent of the inflow conditions, the bubble count rate distributions showed typical shapes with one peak in the shear region F_{maxSR} representing the break-up of bubbles entrapped at the impingement point at the jump toe and a second peak in the recirculation region F_{maxRR} referring to the air-water mixture of bubbles of small and large sizes in the upper part of the hydraulic jump. The shape of the bubble count rate distributions was in agreement with previous experiments conducted with partially developed inflow conditions (e.g. Chanson 2009b; Chachereau and Chanson 2010; Wang 2014).

For both inflow conditions, the bubble count rate decreased with increasing distance from the jump toe while the elevation of F_{maxSR} and F_{maxRR} increased. Large differences were consistently observed in bubble count rate distributions along the hydraulic jump with fully and partially developed inflow conditions in both the shear and recirculation regions with larger bubble count rates for fully developed hydraulic jumps. The differences were more significant in the shear region highlighting lesser break-up of bubbles linked with less entrapped air for partially developed hydraulic jumps. At the downstream end, the fully developed hydraulic jumps showed a more drastic increase in the bubble count rate suggesting significant larger number of bubbles in the recirculation region.



A) BUBBLE COUNT RATE DISTRIBUTION CLOSE TO THE JUMP TOE

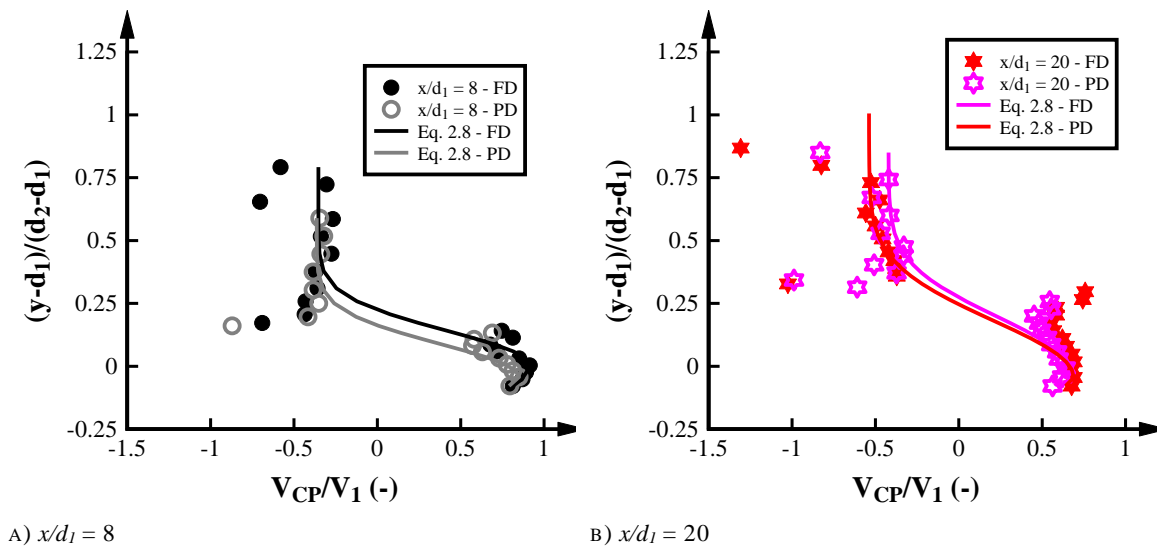
B) BUBBLE COUNT RATE DISTRIBUTION AT THE DOWNSTREAM END OF THE HYDRAULIC JUMP

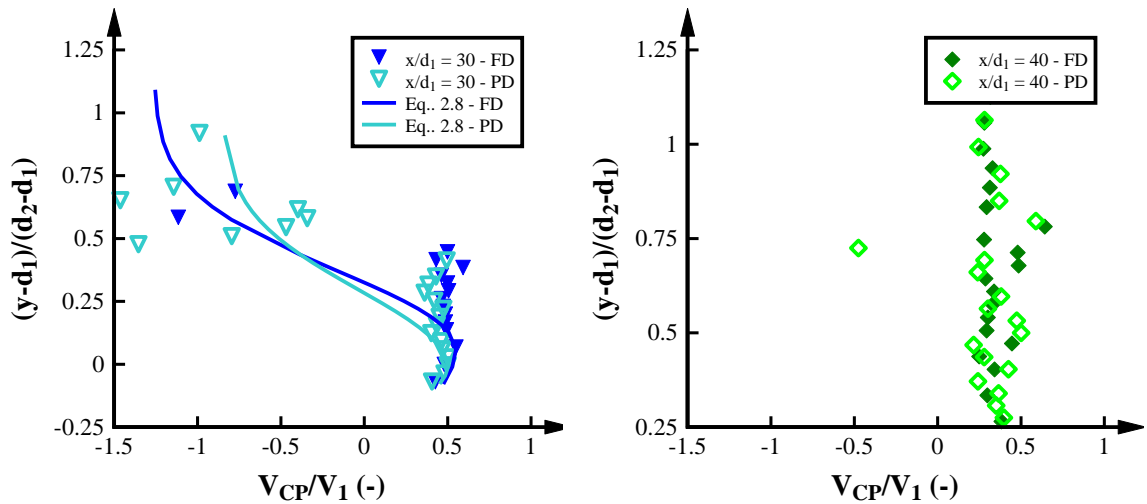
FIGURE 4-8. COMPARISON OF BUBBLE COUNT RATE DISTRIBUTIONS FOR A HYDRAULIC JUMP WITH FULLY (FD) AND PARTIALLY (PD) DEVELOPED INFLOW CONDITIONS: EXPERIMENT F: $Fr_1 = 8.4$, $Re = 1.2 \times 10^5$.

4.3.5. INTERFACIAL VELOCITY

Figure 4-9 shows typical dimensionless interfacial velocity distributions as a function of $(y-d_1)/(d_2-d_1)$ at different cross-sections along the hydraulic jump. The velocity distributions resembled a wall jet in the shear region and had negative velocities in the recirculation region. Figure 4-9 includes a comparison with the wall jet theoretical equation in hydraulic jumps (Equation 2.8) (Rajaratnam 1965; Chanson and Brattberg 2000; Chanson 2010).

All hydraulic jumps compared well with the wall jet theory in the lower part of the hydraulic jump exhibiting a maximum velocity V_{max} in the shear region despite some data scatter. Negative velocities were consistently observed in the recirculation region of the hydraulic jumps (Figure 4-9). Close to the jump toe $x/d_1 \leq 20$, the hydraulic jumps with partially developed inflow conditions had slightly lower interfacial velocities in the shear region while the velocities in the recirculation region were similar (Figures 4-9A and B). The larger interfacial velocity close to the jump toe for fully developed inflow conditions may be linked with larger free-stream flow velocities and turbulence near the free-surface. Further downstream, $x/d_1 > 20$, the interfacial velocities were consistently similar for both inflow conditions (Figure 4-9C and D). No differences were observed in the recirculation region between hydraulic jumps with fully and partially developed inflow conditions (Figure 4-9). To refine the velocity distributions in the recirculation region, further analysis could be conducted with the Adaptive window cross-correlation (AWCC) proposed by Kramer et al. (2019b) and Kramer and Valero (2019).





c) $x/d_1 = 30$

d) $x/d_1 = 40$

FIGURE 4-9. COMPARISON OF THE INTERFACIAL VELOCITY DISTRIBUTIONS FOR FULLY (FD) AND PARTIALLY (PD) DEVELOPED INFLOW CONDITIONS AT DIFFERENT CROSS-SECTIONS ALONG THE HYDRAULIC JUMP: EXPERIMENT F: $Fr_1 = 8.0$, $Re = 1.2 \times 10^5$.

4.3.6. AIR BUBBLE CHORD TIMES

Figure 4-10 presents typical distributions of the dimensionless time-averaged bubble chord time $t_{ch,mean} \times V_1/d_1$ in the shear region for hydraulic jumps with fully and partially developed inflow conditions. The bubble count rate distributions for both inflow conditions were added as reference. For all cross-sections and independent of the Froude and Reynolds numbers, $t_{ch,mean} \times V_1/d_1$ increased with increasing elevation from the channel bed (Wang 2014). The increase was gradual until $y/d_1 = Y_{FmaxSR}$ followed by a faster increase in the upper part of the shear region. Close to the channel bed, $t_{ch,mean} \times V_1/d_1$ increased with increasing distance from the jump toe, suggesting larger mean bubble chord sizes far downstream of the jump toe (Wang 2014).

While the trends and distributions were similar for hydraulic jumps with fully and partially developed inflow conditions, smaller bubble sizes were observed in the shear region close to the jump toe for hydraulic jumps with partially developed inflow conditions. This result confirmed larger air pockets entrapped at the impingement point of the hydraulic jump for fully developed inflow conditions. Further downstream, the size of the bubbles became larger in partially developed hydraulic jumps which may be linked with lesser air entrapped and lesser interfacial velocities resulting in lesser shear stress and lesser break-up of bubbles.

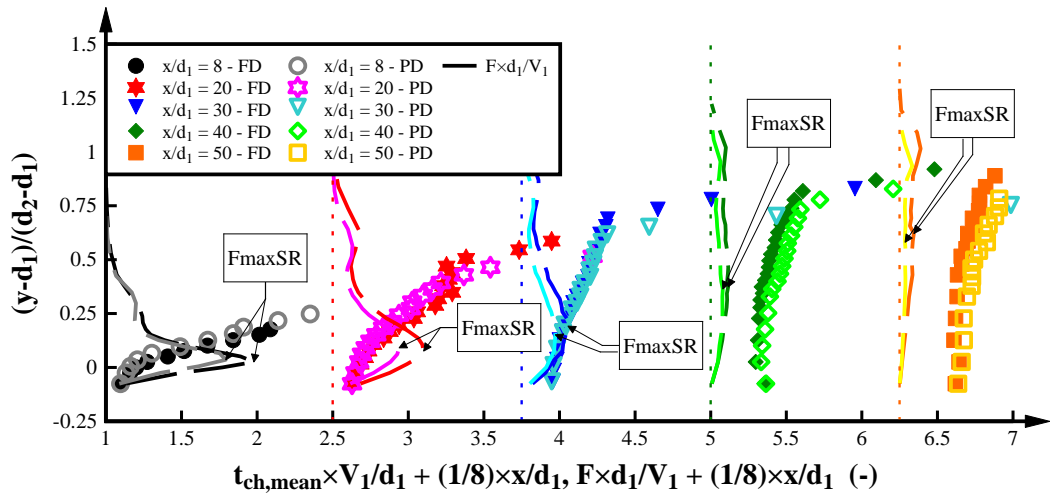


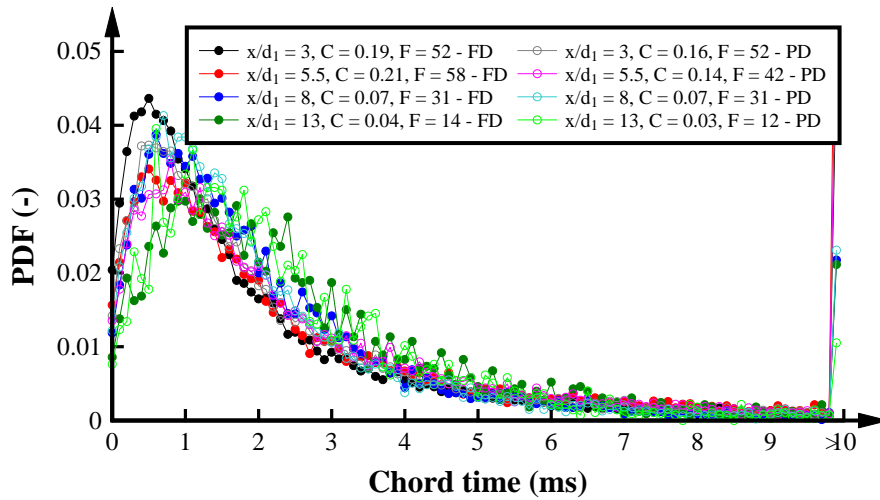
FIGURE 4-10. DISTRIBUTION OF TIME-AVERAGED BUBBLE CHORD TIMES FOR HYDRAULIC JUMPS WITH FULLY (FD) AND PARTIALLY (PD) DEVELOPED INFLOW CONDITIONS: EXPERIMENT E: $Fr_1 = 8.5$, $Re = 7.5 \times 10^4$. DOTTED LINES REPRESENT THE CROSS-SECTION POSITION AND DASHED LINES INDICATE THE BUBBLE COUNT RATE DISTRIBUTIONS.

Figure 4-11 presents the probability distribution functions (PDF) of the air bubble chord times at $y = Y_{FmaxSR}$ for selected hydraulic jumps with fully and partially developed inflow conditions. The PDF considered a chord time interval of 0.1s. Note that air bubble chord times larger than 10 ms were considered in the interval >10 ms.

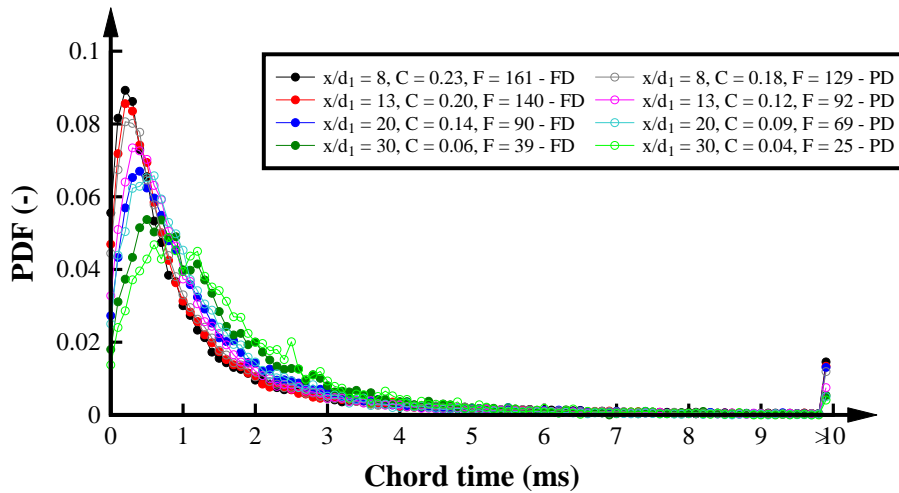
The PDF of the air bubble chord time showed a large percentage of small bubbles for all hydraulic jumps independent of the inflow conditions. A sharper peak was observed with increasing Froude and Reynolds numbers associated with larger shear stress levels resulting in comparatively smaller bubble sizes (Figure 4-11). The characteristic peak in the PDF of the bubble chord times decreased with increasing distance from the jump toe suggesting a more even distribution of bubble sizes towards the downstream end of the hydraulic jump. The flatter distribution was linked with flow deceleration, as mentioned by Wang (2014). The decay in the characteristic peak in the bubble chord time with increasing distance from the jump toe was lower for hydraulic jumps with $Fr_1 < 3.8$ (Figure 4-11A) with a percentage of 4.4% close to the jump toe ($x/d_1 = 3$) and 3% at the downstream end of the hydraulic jump ($x/d_1 = 13$). In contrast, hydraulic jumps with large Froude and Reynolds numbers (Figure 4-11C) showed a drastic drop in the percentage of small bubble sizes from 15% close to the jump toe ($x/d_1 = 8$) to 6% at the end of the hydraulic jump ($x/d_1 = 40$). These results suggested lesser bubble size variations for weak hydraulic jumps while stronger shear stresses lead to stronger bubble size variations in stronger hydraulic jumps.

Close to the jump toe and at $y = Y_{FmaxSR}$, fully developed hydraulic jumps showed a larger percentage of small bubbles compared to partially developed hydraulic jumps in consistency with the larger C and F_{maxSR} in fully developed hydraulic jumps. Note that the difference in the characteristic chord time peak between fully and partially developed inflow conditions

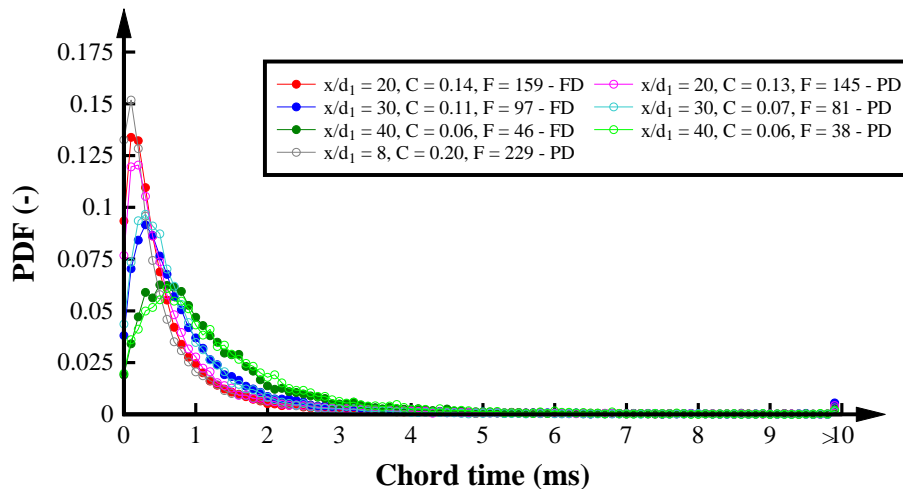
decreased with increasing distance from the jump toe suggesting closer similarities in the chord time distributions at the downstream end of the hydraulic jump and for $y = Y_{FmaxSR}$.



A) EXPERIMENT H: $Fr_1 = 3.8$, $Re = 6.2 \times 10^4$



B) EXPERIMENT C: $Fr_1 = 7.0$, $Re = 6.2 \times 10^4$



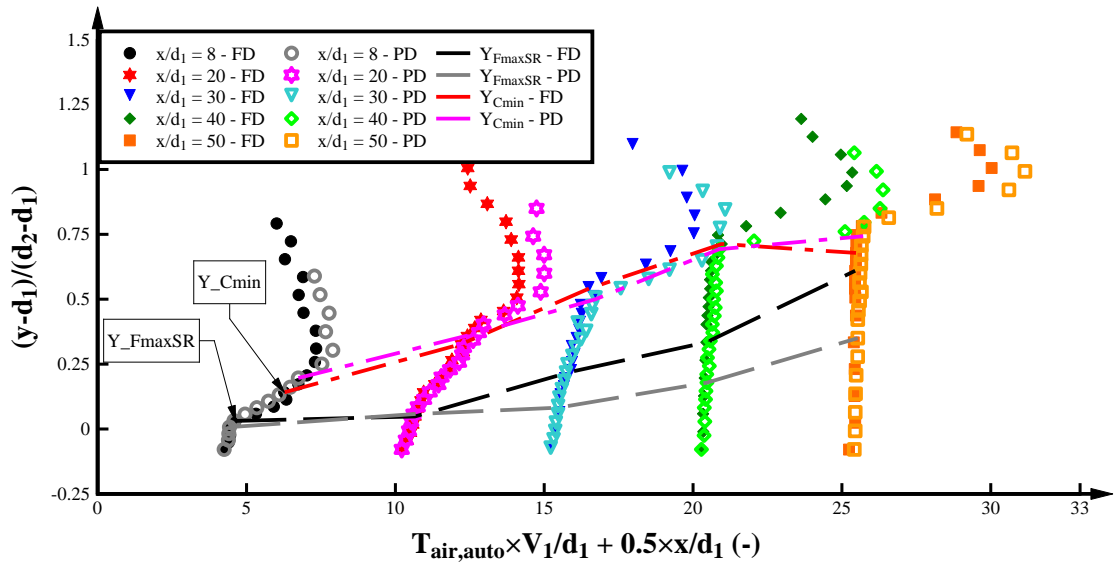
C) EXPERIMENT F: $Fr_1 = 8.0$, $Re = 1.2 \times 10^5$

FIGURE 4-11. PDF OF THE AIR BUBBLE CHORD TIMES FOR $y = Y_{Fmax,SR}$ AT DIFFERENT CROSS-SECTIONS ALONG THE HYDRAULIC JUMP FOR FULLY (FD) AND PARTIALLY (PD) DEVELOPED INFLOW CONDITIONS

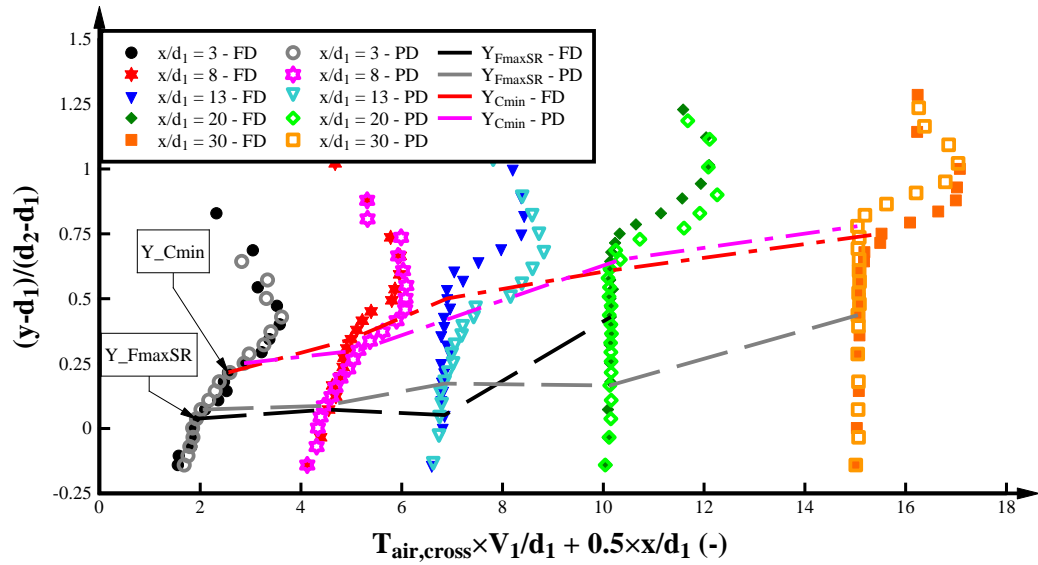
4.3.7. AUTO-AND CROSS-CORRELATION TIME SCALES

Figure 4-12 presents typical distributions of the dimensionless auto- and cross-correlation time scales along hydraulic jumps. The elevation of the maximum bubble count rate in the shear region (Y_{FmaxSR}) and the elevation at the boundary between the shear and recirculation regions (Y_{Cmin}) are added as reference. For each cross-section, $T_{air,auto} \times V_1/d_1$ and $T_{air,cross} \times V_1/d_1$ increased with increasing elevation from the channel bed. A faster increase was observed at $y = Y_{FmaxSR}$ indicating larger signal correlations in the upper part of the shear region. In the recirculation region, $T_{air,auto} \times V_1/d_1$ and $T_{air,cross} \times V_1/d_1$ increased suddenly followed by a gradual decrease towards the free-surface. The increase in the correlation in the recirculation region may be linked with large coherence of the free-surface region of the hydraulic jump (Wang 2014).

The comparison of hydraulic jumps with fully and partially developed inflow conditions showed minor differences in auto- and cross-correlation time scales. The lifetime of the bubbly flow structures was similar in the shear region independent of the inflow conditions. Larger correlation time scales were observed in the recirculation region for hydraulic jumps with partially developed inflow conditions. This observation suggested that the air-water flow data were more correlated in partially developed hydraulic jumps. Overall slightly larger differences between fully and partially developed hydraulic jumps were observed in terms of $T_{air,auto}$.



A) AUTO-CORRELATION TIME SCALES (EXPERIMENT F: $Fr_1 = 8.0$, $Re = 1.2 \times 10^5$)



B) CROSS-CORRELATION TIME SCALES (EXPERIMENT B: $Fr_1 = 5.1$, $Re = 6.2 \times 10^4$)

FIGURE 4-12. DISTRIBUTIONS OF AIR-WATER AUTO- AND CROSS-CORRELATION TIME SCALES FOR HYDRAULIC JUMPS WITH FULLY (FD) AND PARTIALLY (PD) DEVELOPED INFLOW CONDITIONS. DASHED LINES = Y_{FmaxSR} , AND DOTTED-DASHED LINES = Y_{Cmin} .

4.4. EFFECT OF INFLOW CONDITIONS ON THE DECAY IN CHARACTERISTIC AIR-WATER FLOW PARAMETERS

The distributions of air-water flow properties in hydraulic jumps (Chapter 4.3) showed strong aerated regions close to the jump toe while a much reduced aeration was observed at the downstream end of the hydraulic jump linked with buoyancy effects. This chapter provides further details on the decay of the main characteristic air-water flow parameters along the hydraulic jumps with fully and partially developed inflow conditions. A comparison of the present decays and previous studies is presented in Appendix D.

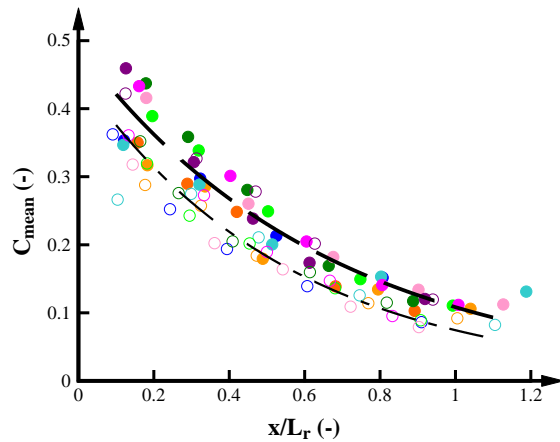
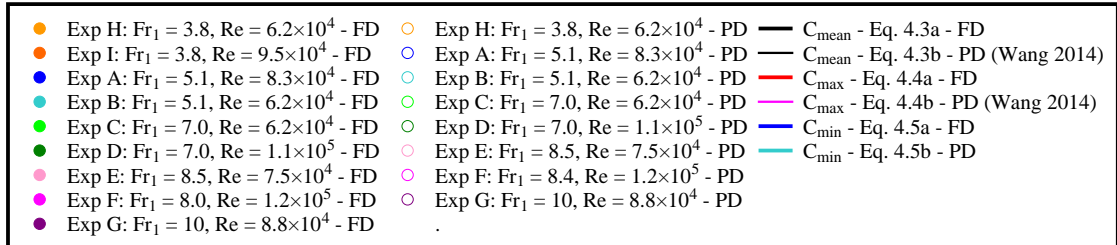
4.4.1. DECAY IN THE VOID FRACTION

Figure 4-13 presents the decay in characteristic void fraction parameters C_{mean} , C_{max} and C_{min} as function of x/L_r where L_r represents the roller length defined as the distance between the jump toe and the end of the roller (see Chapter 5.3). C_{mean} , C_{max} and C_{min} decreased with increasing x/L_r for all hydraulic jumps. Apart from experiment H ($Fr_1 = 3.8$, $Re = 6.2 \times 10^4$) with very low aeration, the decay in void fractions was similar for all experiments indicating similar de-aeration rates independent of the Froude and Reynolds numbers. Larger void fractions were consistently observed for hydraulic jumps with fully developed inflow conditions due to larger air entrapment at the impingement region of the hydraulic jump linked with larger inflow turbulence (Takahashi and Ohtsu 2017). Void fraction parameters for partially and fully developed inflow conditions showed differences of up to 10% close to the jump toe. A faster decay in C_{max} and C_{min} was observed in hydraulic jumps with fully developed inflow conditions suggesting a faster bubble diffusion and flow dispersion. At the downstream end of the

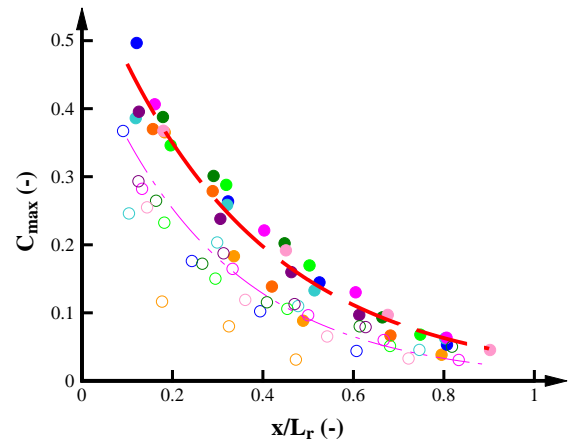
hydraulic jump, lesser differences were observed between fully and partially developed inflow conditions with negligible differences for $x/L_r > 0.8$. The decay in C_{mean} and C_{max} for all experiments with partially developed inflow conditions followed the empirical equation of Wang (2014) while new empirical equations were found for C_{mean} and C_{max} in hydraulic jumps with fully developed inflow conditions and for C_{min} for both inflow conditions (Table 4-2). Table 4-2 summarises these equations. Note that the advective peak observed in the shear region was only identified for $x/L_r < 1$ and therefore, the decay of C_{max} only included this region.

TABLE 4-2. EMPIRICAL EQUATIONS OF THE DECAY IN CHARACTERISTIC VOID FRACTION PARAMETERS

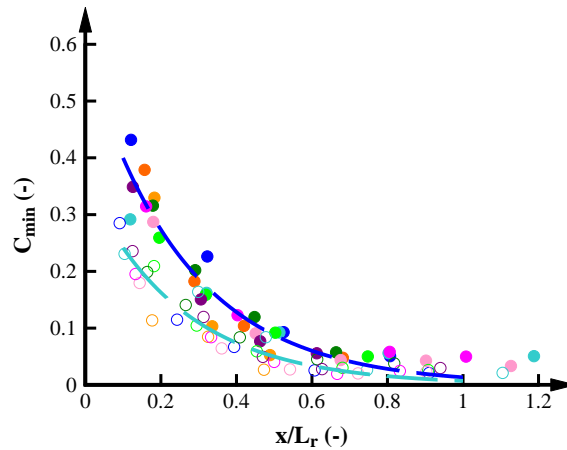
Parameter	Fully developed inflow conditions	Partially developed inflow conditions
C_{mean}	$C_{max} = 0.49 \times \exp\left(-1.51 \times \frac{x}{L_r}\right)$ for $3.8 \leq Fr_1 \leq 10$ $R^2 = 0.92$ Eq. 4.3a	$C_{mean} = 0.45 \times \exp\left(-1.8 \times \frac{x}{L_r}\right)$ for $3.8 \leq Fr_1 \leq 10$ Eq. 4.3b (Wang 2014)
C_{max}	$C_{max} = 0.62 \times \exp\left(-2.86 \times \frac{x}{L_r}\right)$ for $5.1 \leq Fr_1 \leq 10$ $R^2 = 0.95$ Eq. 4.4a	$C_{max} = 0.5 \times \exp\left(-3.4 \times \frac{x}{L_r}\right)$ for $3.8 \leq Fr_1 \leq 10$ Eq. 4.4b (Wang 2014)
C_{min}	$C_{min} = 0.584 \times \exp\left(-3.79 \times \frac{x}{L_r}\right)$ for $3.8 \leq Fr_1 \leq 10$ $R^2 = 0.93$ Eq. 4.5a	$C_{min} = 0.358 \times \exp\left(-3.94 \times \frac{x}{L_r}\right)$ for $3.8 \leq Fr_1 \leq 10$ $R^2 = 0.92$ Eq. 4.5b



A) MEAN VOID FRACTION



B) MAXIMUM VOID FRACTION



C) MINIMUM VOID FRACTION

FIGURE 4-13. COMPARISON ON THE DECAY OF CHARACTERISTIC VOID FRACTION PARAMETERS FOR HYDRAULIC JUMPS WITH FULLY (FD) AND PARTIALLY (PD) DEVELOPED INFLOW CONDITIONS.

Figure 4-14 presents a comparison of characteristic void fraction parameters for hydraulic jumps with fully and partially developed inflow conditions. C_{mean} was almost similar for both inflow conditions with slightly larger C_{mean} in hydraulic jumps with fully developed inflow conditions. Larger C_{min} and C_{max} were consistently observed for fully developed inflow conditions with stronger differences for larger values. In general, hydraulic jumps with fully developed inflow conditions were characterised by larger aeration.

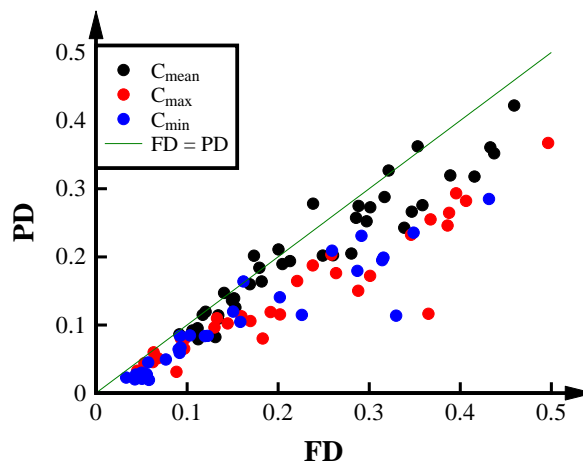
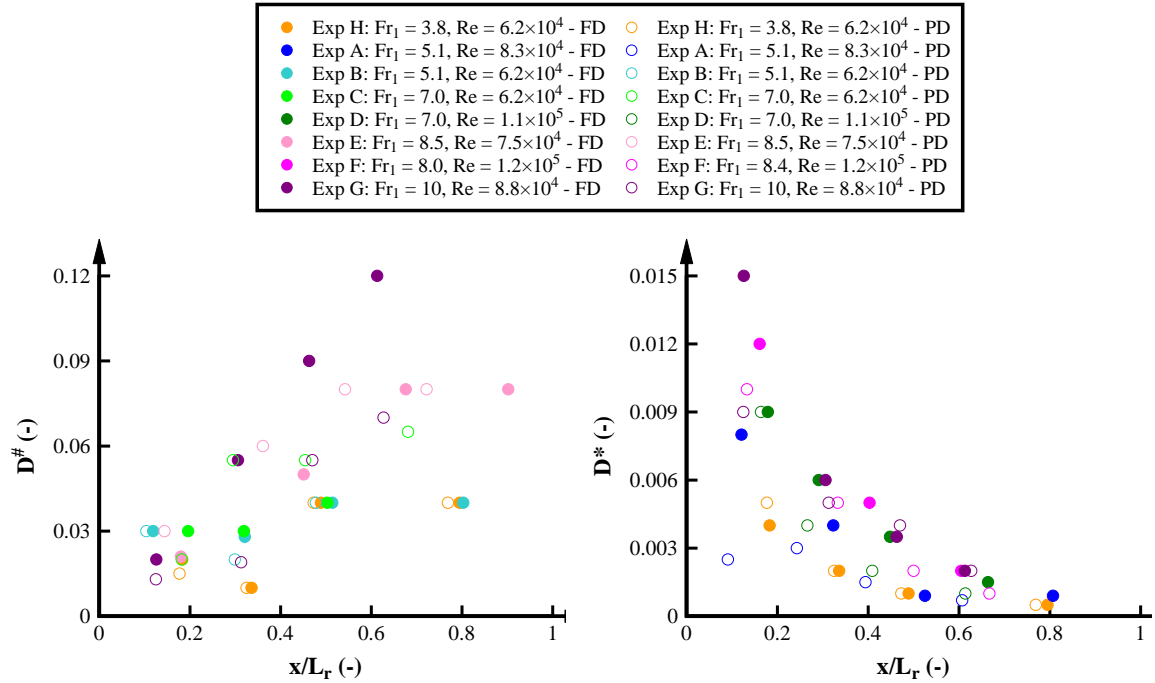


FIGURE 4-14. COMPARISON IN CHARACTERISTIC VOID FRACTION PARAMETERS IN HYDRAULICS JUMPS WITH FULLY (FD) AND PARTIALLY (PD) DEVELOPED INFLOW CONDITIONS

Figure 4-15 presents the distributions of dimensionless diffusivity in the shear region $D^\#$ and in the recirculation region D^* (Figures 4-15A and B respectively) as a function of x/L_r . $D^\#$ and D^* were selected fitting void fraction data to Equations 2.7a and b respectively. In agreement with previous studies (Chanson 2010; Wang 2014; Felder and Chanson 2016a), $D^\#$ increase with increasing distance from the jump toe for all experiments while $D^\#$ decreased with increasing distance from the jump toe. $D^\#$ had large data scatter and no clear differences were identified between hydraulic jumps with fully and partially developed inflow conditions. For

regions close to the jump toe, larger values of D^* were observed for hydraulic jumps with fully developed inflow conditions while the differences decreased towards the downstream end of the hydraulic jumps.



A) DIFFUSIVITY COEFFICIENT SHEAR REGION

B) DIFFUSIVITY COEFFICIENT RECIRCULATION REGION

FIGURE 4-15. COMPARISON OF THE DECAY IN DIMENSIONLESS DIFFUSIVITY FOR HYDRAULIC JUMPS WITH FULLY AND PARTIALLY DEVELOPED INFLOW CONDITIONS

4.4.2. DECAY IN THE BUBBLE COUNT RATE

Figure 4-16A presents the decay in the dimensionless maximum bubble count rate in the shear region $F_{maxSR} \times d_1/V_1$ as a function of x/L_r . The maximum bubble count rate in the shear region for the fully developed case was in most of the cases, more than 20% larger compared to the hydraulic jump with partially developed inflow conditions. For most of the experiments, F_{maxSR} decreased faster for hydraulic jumps with fully developed inflow conditions.

Figure 4-16B illustrates the decay in the dimensionless maximum bubble count rate $F_{maxRR} \times d_1/V_1$ in the recirculation region. Larger $F_{maxRR} \times d_1/V_1$ was observed with increasing Re while lower $F_{maxRR} \times d_1/V_1$ was identified for larger Froude numbers. Larger $F_{maxRR} \times d_1/V_1$ were observed for fully developed hydraulic jumps with more significant differences at the downstream end of the hydraulic jump suggesting larger number of bubbles merged and affected by buoyancy forces in fully developed hydraulic jumps.

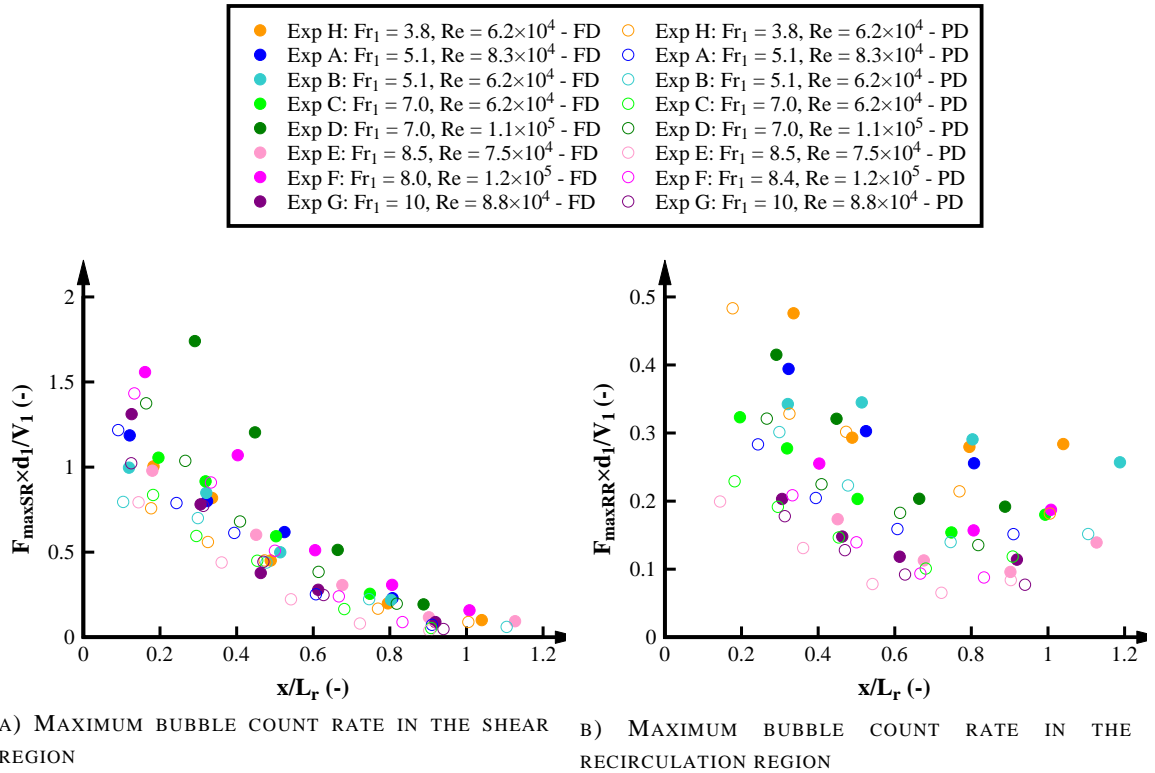


FIGURE 4-16. COMPARISON OF THE DECAY IN CHARACTERISTIC BUBBLE COUNT RATE PARAMETERS FOR HYDRAULIC JUMPS WITH FULLY (FD) AND PARTIALLY (PD) DEVELOPED INFLOW CONDITIONS

4.4.3. CHARACTERISTIC ELEVATIONS

Figure 4-17 compares the characteristic elevations for hydraulic jumps with fully and partially developed inflow conditions. Close to the jump toe, the elevations corresponding to the maximum void fraction Y_{Cmax} was similar to d_j highlighting that the largest advective motions were observed at the same elevation of the impingement point of the hydraulic jump (Figure 4-17A). Further downstream, Y_{Cmax} increased linearly. No differences in Y_{Cmax} were found in terms of inflow conditions. Figure 4-17B presents the longitudinal distributions of Y_{90} showing an increase until $x = L_r$ followed by an almost constant flow depth. The increase in Y_{90} is consistent with the free-surface profile in hydraulic jumps (see Chapter 5.2). Y_{90} was similar for hydraulic jumps with fully and partially developed inflow conditions.

The elevation corresponding to the maximum bubble count rate in the shear region Y_{FmaxSR} is presented in Figure 4-17C. In the first half of the jump roller, no significant differences in the elevations were observed associated with the strong advective motion close to the jump toe. Further downstream, Y_{FmaxSR} increased gradually linked with buoyancy effects. No clear differences were observed between hydraulic jumps with fully and partially developed inflow conditions. The elevation of the maximum bubble count rate in the recirculation region Y_{FmaxRR} was similar in shape to the mean free-surface profile (see Chapter 5.2) (Figure 4-17D). Similar elevations were for hydraulic jumps with fully and partially developed inflow conditions.

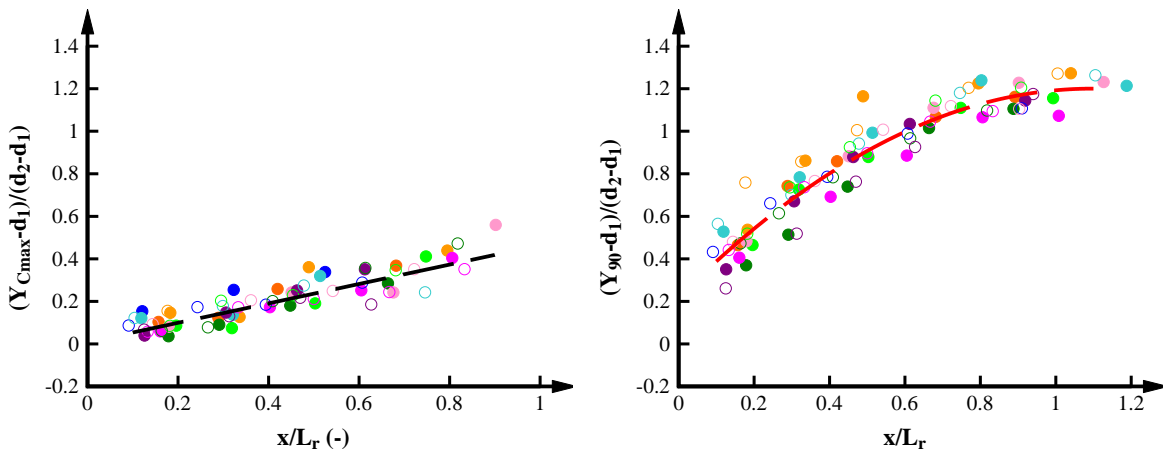
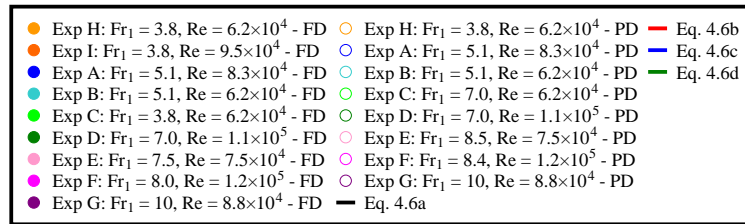
Overall, the characteristic elevations of the air-water flow properties were not affected by the inflow conditions and were well correlated by:

$$\frac{Y_{C_{max}}-d_1}{d_2-d_1} = 0.008 + 0.456 \left(\frac{x}{L_r} \right) \quad \text{for } 3.8 \leq Fr_I \leq 10 \quad \text{Eq. 4.6a}$$

$$\frac{Y_{90}-d_1}{d_2-d_1} = -13 + 14.2 \times \cos \left(0.341 \left(\frac{x}{L_r} \right) - 0.374 \right) \quad \text{for } 3.8 \leq Fr_I \leq 10 \quad \text{Eq. 4.6b}$$

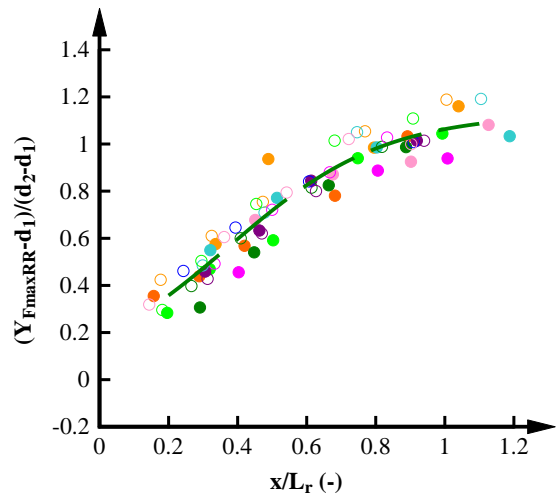
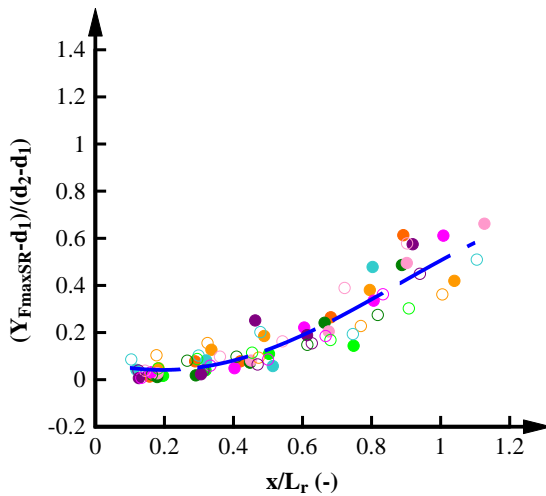
$$\frac{Y_{F_{maxSR}}-d_1}{d_2-d_1} = 0.4 + 0.36 \times \cos \left(2.32 \left(\frac{x}{L_r} \right) - 2.69 \right) \quad \text{for } 3.8 \leq Fr_I \leq 10 \quad \text{Eq. 4.6c}$$

$$\frac{Y_{F_{maxRR}}-d_1}{d_2-d_1} = \frac{1.13}{\left\{ 1 + 5.24 \times \exp \left[-4.42 \left(\frac{x}{L_r} \right) \right] \right\}} \quad \text{for } 3.8 \leq Fr_I \leq 10 \quad \text{Eq. 4.6d}$$



A) ELEVATION WHERE $C = C_{max}$

B) ELEVATION WHERE $C = 0.9$



C) ELEVATION WHERE $F = F_{maxSR}$

D) ELEVATION WHERE $F = F_{maxRR}$

FIGURE 4-17. COMPARISON OF CHARACTERISTIC ELEVATIONS FOR HYDRAULIC JUMPS WITH FULLY (FD) AND PARTIALLY (PD) DEVELOPED INFLOW CONDITIONS

4.4.4. DECAY IN THE INTERFACIAL VELOCITY

Figure 4-18A illustrates the decay in V_{max} along the hydraulic jumps showing a similar decay for all experiments and independent of Froude and Reynolds numbers. While slightly larger values of V_{max} were observed for fully developed inflow conditions, the decay for both inflow conditions was well fitted by the exponential function of Wang (2014) for partially developed inflow conditions: $V_{max}/V_I = 1.1 \times \exp(-1.2 \times x/L_r)$.

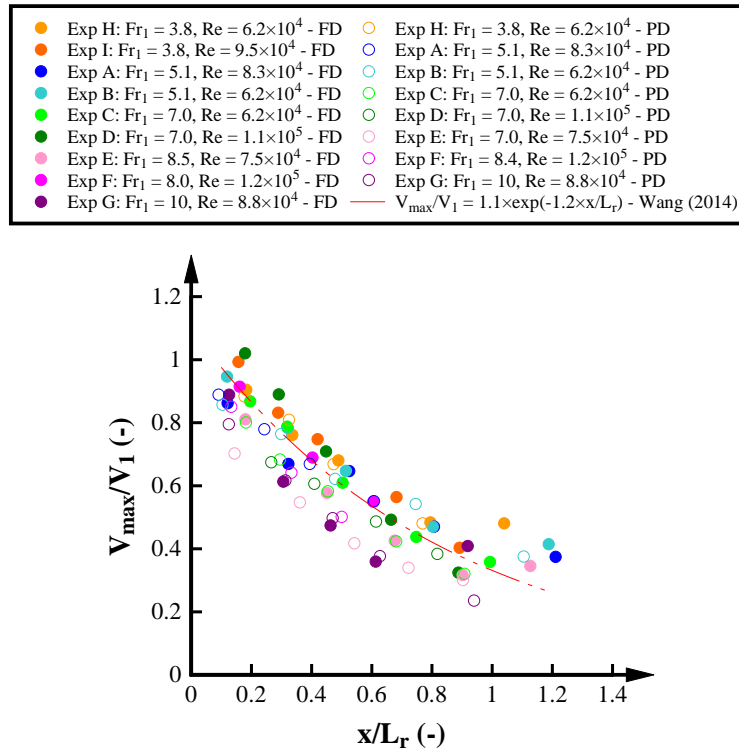


FIGURE 4-18. MAXIMUM INTERFACIAL VELOCITY DECAY FOR HYDRAULIC JUMPS WITH FULLY (FD) AND PARTIALLY (PD) DEVELOPED INFLOW CONDITIONS

4.4.5. DECAY IN THE CHORD TIME

The chord time with the highest probability is defined as the mode of the chord times $t_{ch,mode}$. Figure 4-19 presents the longitudinal distribution of $t_{ch,mode} \times V_I/d_I$ at $y = Y_{FmaxSR}$ as function of x/L_r . For $x/L_r \leq 0.5$, $t_{ch,mode} \times V_I/d_I \approx 30$ for all experiments indicating that the shear stress level and flow deceleration was almost constant close to the jump toe. Further downstream $x/L_r > 0.5$, $t_{ch,mode} \times V_I/d_I$ increased with increasing distance from the jump toe, suggesting larger chord times at the downstream end of the jump in agreement with Figure 4-10. Within this region, slightly larger values of $t_{ch,mode} \times V_I/d_I$ were observed for hydraulic jumps with partially developed inflows. The increase in $t_{ch,mode}$ for $x/L_r > 0.5$ may be linked with flow deceleration due to a reduction in flow velocities and lesser shear stress in the second half of the hydraulic jump leading into bubble coalescence (Chanson 2006; Wang 2014).

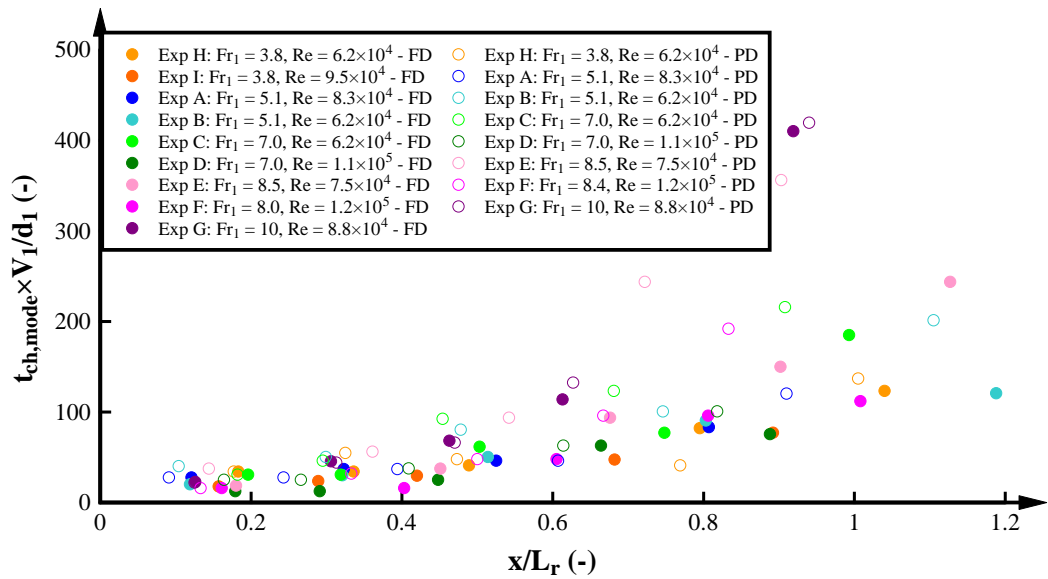


FIGURE 4-19 MODE OF THE CHORD TIME DISTRIBUTION FOR $y = Y_{Fmax,SR}$ FOR HYDRAULIC JUMPS WITH FULLY (FD) AND PARTIALLY (PD) DEVELOPED INFLOW CONDITIONS

4.5. SCALE EFFECTS

The present chapter includes the key findings in the analysis of scale effects in terms of air-water flow properties in hydraulic jumps with fully developed inflow conditions. The analysis was based upon a Froude similitude. A large range of properties were compared and all data including partially developed inflow conditions are presented in Appendix E.

Figure 4-20 presents the comparative analysis in the air-water flow properties for hydraulic jumps with similar Froude number including distributions of void fraction (Figure 4-20A), bubble count rate (Figure 4-20B), interfacial velocity (Figure 4-20C), time-averaged chord time (Figure 4-20D), auto-correlation time scales (Figure 4-20E) and cross-correlation time scales (Figure 4-20F).

The void fraction distributions showed no scale effects in terms of Froude similitude for Reynolds numbers $6.2 \times 10^4 < Re < 1.2 \times 10^5$ for hydraulic jumps with fully developed inflow conditions. In contrast the bubble count rate distributions were consistently larger for larger Reynolds numbers indicating scale effects. The interfacial velocity distributions close to the jump toe showed slightly larger interfacial velocities for hydraulic jumps with larger Reynolds numbers. Further downstream, and in the recirculation region, the interfacial velocity distributions were very close indicating no scale effects for the range of Reynolds numbers in the present study. For identical Froude numbers, larger mean chord times were observed for lower Reynolds numbers. The results were consistently observed for all the experiments. With increasing the Reynolds numbers and under similar Froude numbers, the auto-correlation time scale in the recirculation region decreased (Figure 4-20E). Similar results were observed in terms of the cross-correlation time scales (Figure 4-20F) suggesting scale effects in the auto-

and cross-correlation time scales. This finding is in agreement with previous studies in partially developed hydraulic jumps (Chanson and Chachereau 2013; Wang 2014). (Murzyn and Chanson 2008; Chanson and Chachereau 2013; Wang 2014; Wang and Chanson 2016c; Felder and Chanson 2016a).

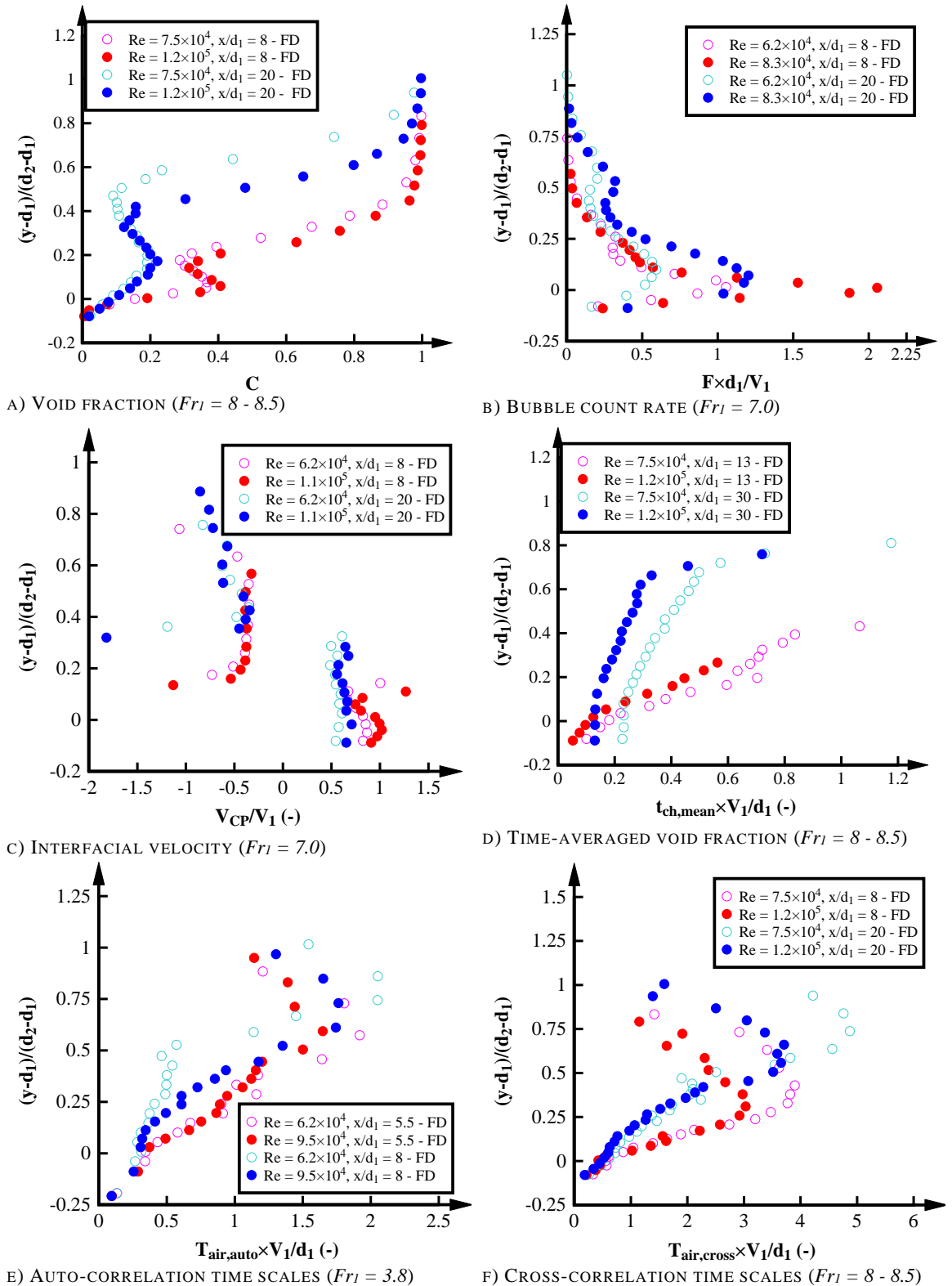


FIGURE 4-20. COMPARATIVE ANALYSIS OF SCALE EFFECTS IN THE AIR-WATER FLOW PROPERTIES FOR HYDRAULIC JUMPS WITH FULLY DEVELOPED INFLOW CONDITIONS (FD) USING A FROUDE SIMILITUDE.

4.6. SUMMARY

This chapter presented the results of an extensive investigation of air-water flow properties in hydraulic jumps with partially and fully developed inflow conditions and for $3.8 \leq Fr_l \leq 10$ and $6.2 \times 10^4 \leq Re \leq 1.2 \times 10^5$. Figure 4-21 presents a summary graph including the air-water flow parameters at different cross-sections along a hydraulic jump with fully developed inflow conditions as well as the time-averaged free-surface profile measured with the LIDAR (Chapter 5.2). Note that the void fraction distribution only includes the shear region in order to highlight the advective motions. The void fraction presented a clear maximum peak in agreement with the advective diffusion equation for $x/L_r \leq 0.7$ (Chanson and Brattberg 2000; Chanson 2006; Chanson 2007b). Large bubble count rate peaks were observed in the shear region highlighting the larger shear stress and break-up of bubbles within this region (Chanson and Brattberg 2000; Chanson 2006; Kucukali and Chanson 2007). The interfacial velocity showed an increase with increasing the elevation until reaching a maximum peak in the shear region in agreement with the wall jet velocity distribution (Rajaratnam 1965; Chanson and Brattberg 2000). Independent of the cross-section, the time-averaged chord time presented an increase with increasing the elevation indicating bubble coalescence and an increase in the bubble sizes towards the recirculation region (Wang 2014). All air-water flow parameters decayed with distance from the jump toe leading to an almost uniform and non-aerated region at the downstream end of the hydraulic jump ($x/L_r > 0.7$) with larger time-averaged chord times due to flow deceleration (Wang 2014). The shape of the air-water flow distributions in fully developed inflow conditions were in close agreement with typical trends observed in partially developed hydraulic jumps (e.g. Chanson and Brattberg 2000; Chanson 2006; Wang 2014). The increase in the time-averaged free-surface profile measured with the LIDAR was in agreement with the characteristics elevations measured with the conductivity probe Y_{50} and Y_{90} . While Y_{90} was located well above the mean free-surface profile recorded with the LIDAR, Y_{50} was continuously overlapping the time-averaged profile.

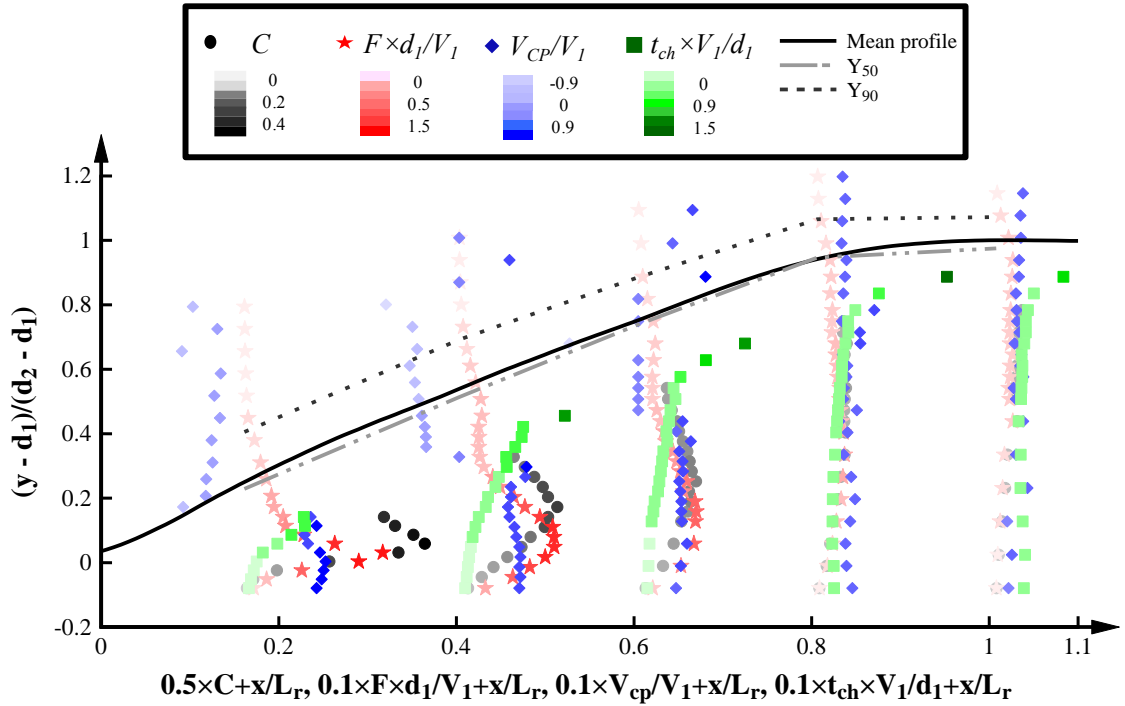


FIGURE 4-21. COMPILATION OF THE AIR-WATER FLOW PARAMETERS IN HYDRAULIC JUMPS WITH FULLY DEVELOPED INFLOW CONDITIONS.

Overall, the fully developed hydraulic jump showed larger aeration, larger number of bubbles, and larger interfacial velocities confirming a strong effect of the inflow conditions on the air-water flow properties in hydraulic jumps with differences up to 20% close to the jump toe. A conceptual sketch of the effect of the inflow conditions in the air-water flow properties is included in Chapter 7.6. Table 4-3 presents a summary of the effect of the inflow conditions and scale effects in terms of Froude similitude in the air-water flow properties in hydraulic jumps.

TABLE 4-3. SUMMARY TABLE OF THE EFFECT OF THE INFLOW CONDITIONS AND SCALE EFFECTS IN THE AERATION FEATURES IN HYDRAULIC JUMPS

Parameter	Comparison PD vs FD	Scale effects $6.2 \times 10^4 < Re < 1.2 \times 10^5$
Void fraction (C)	Lower void fraction in PD	No scale effects
Mean void fraction (C_{mean})	Lower C_{mean} in PD	No scale effects
Maximum void fraction (C_{max})	Lower C_{max} in PD	No scale effects
Bubble count rate (F)	Lower F in PD	Scale effects: Larger F for larger Re
Maximum bubble count rate in the shear region (F_{maxSR})	Lower F_{maxSR} in PD	Scale effects: Larger F_{maxSR} for larger Re
Maximum bubble count rate in the recirculation region (F_{maxRR})	Lower F_{maxRR} in PD	Scale effects: Larger F_{maxRR} for larger Re
Interfacial velocity (V_{CP})	Lower V_{CP} in PD close to the jump toe	No scale effects
Maximum interfacial velocity (V_{max})	Slight lower V_{max} in PD close to the jump toe	No scale effects
Average velocity in the recirculation region (V_{recir})	No differences	No scale effects

Parameter	Comparison PD vs FD	Scale effects $6.2 \times 10^4 < Re < 1.2 \times 10^5$
Time-averaged bubble chord time $t_{ch,mean}$	<ul style="list-style-type: none"> • Smaller $t_{ch,mean}$ in PD close to the jump toe • Larger $t_{ch,mean}$ in PD at the downstream end of the hydraulic jump 	Scale effects: Lower $t_{ch,mean}$ for larger Re
Auto-correlation time scale of the air-water flow properties ($T_{air,auto}$)	<ul style="list-style-type: none"> • Similar $T_{air,auto}$ in the shear region • Larger $T_{air,auto}$ in PD in the recirculation region 	Scale effects: Lower $T_{air,auto}$ for larger Re
Cross-correlation time scale of the air-water flow properties ($T_{air,cross}$)	<ul style="list-style-type: none"> • Similar $T_{air,cross}$ in the shear region • Larger $T_{air,cross}$ in PD in the recirculation region 	Scale effects: Lower $T_{air,cross}$ for larger Re

5

FREE-SURFACE CHARACTERISTICS AND JUMP TOE OSCILLATIONS

Some content of this chapter is taken from the following publication:

Journal Publications

Montano, L., Li, R., and Felder, S. 2018, ‘Continuous measurements of time-varying free-surface profiles in aerated hydraulic jumps with a LIDAR’, *Experimental Thermal and Fluid Science*, vol. 93, pp. 379 – 397.

Montano, L., and Felder, S. 2019. ‘An experimental study of air-water flows in hydraulic jumps on flat slopes’, *Journal of Hydraulic Research* (in print, accepted for publication on 14/6/2019)

Montano, L., and Felder, S. 2019 ‘LIDAR observations of free-surface time and length scales in hydraulic jumps’, *Journal of Hydraulic Engineering* (in print, accepted for publication on 14/8/2019)

Conference Proceedings

Montano, L., and Felder, S. 2018, ‘LIDAR measurements of free-surface profiles and turbulent scales in a hydraulic jump’, in *Proc., 7th IAHR International Symposium on Hydraulic Structures*, Aachen, Germany, 10 pages.

5.1. INTRODUCTION

The free-surface profiles of hydraulic jumps are characterised by strong fluctuations, water splashes and foam resulting in a complex mix of dynamic free-surface structures. Figure 5-1 shows hydraulic jump photos with time steps of 0.1s revealing significant variations in the free-surface profiles. While the hydraulic jump at time 0s shows an almost smooth free-surface profile with some water splashes above the hydraulic jump, at time 0.1s, the hydraulic jump shows the formation of a large water projection looking like “fingers”. The structure is clearly observed at time 0.2s while it almost disappeared at time 0.3 s. The fast changes of the free-surface structures in hydraulic jump highlight the dynamic and violent behaviour of this phenomenon. The majority of these free-surface structures were observed in the roller region of the hydraulic jump close to the jump toe while the downstream end of the hydraulic jumps was characterised by a smoother profile with smaller free-surface fluctuations.

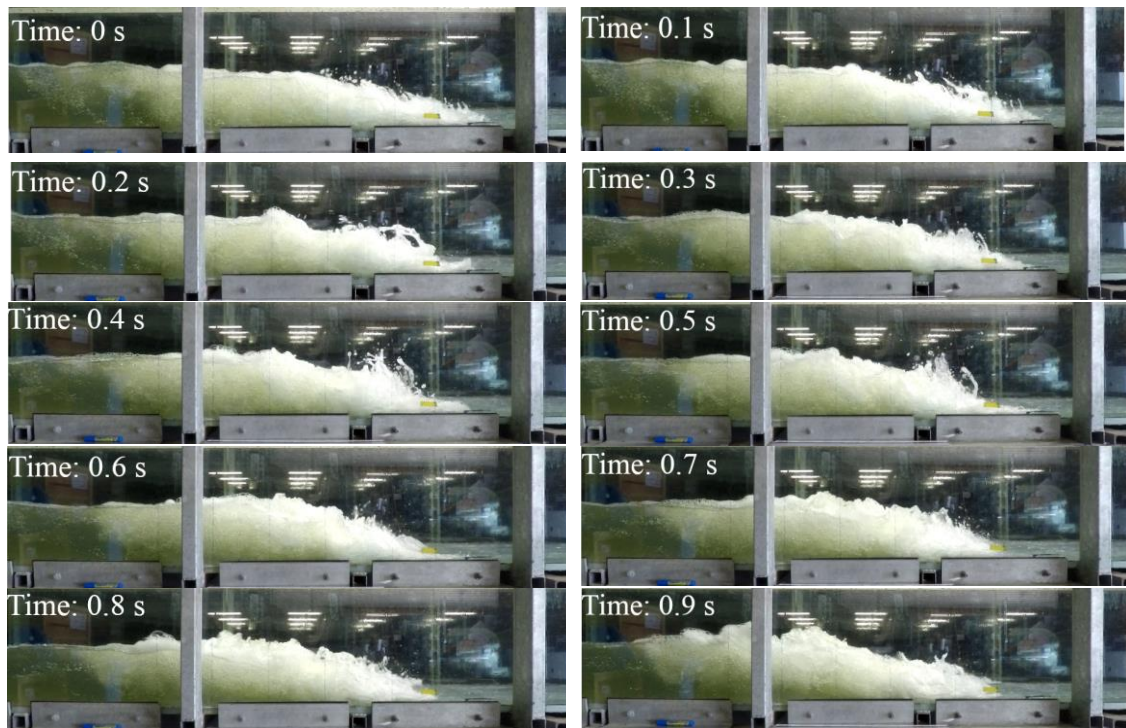


FIGURE 5–1. PHOTOS OF FREE-SURFACE PROFILES IN A HYDRAULIC JUMP WITH TIME STEPS OF 0.1 s, EXPERIMENT E: $Fr_1 = 8.5$, $Re = 7.5 \times 10^4$, FULLY DEVELOPED INFLOW CONDITIONS. FLOW FROM RIGHT TO LEFT.

Previous studies measured the free-surface profiles at fixed locations limiting the understanding of temporal and spatial fluctuations in hydraulic jumps including the interactions between jump toe oscillations and free-surface fluctuations as indicated in Chapter 2. A more detailed analysis of the free-surface features in hydraulic jumps is needed. Herein, the present study used a LIDAR for continuous and instantaneous measurements of the free-surface profile and jump toe oscillations along the channel centreline for fully aerated hydraulic jumps. The

experiments were conducted in two different configurations: a) downstream of a sluice gate and b) downstream of a sloped section. Table 5–1 shows the experimental flow conditions for the LIDAR measurements including the inflow conditions, the position of the LIDAR upstream the jump toe, the inflow depth and the Froude and Reynolds numbers. The LIDAR was always located 0.5 m upstream of the jump toe for fully developed inflow conditions. However, for partially developed inflow conditions, the position of the LIDAR changed between experiments due to the sluice gate at the upstream end.

TABLE 5–1. EXPERIMENTAL FLOW CONDITIONS FOR LIDAR MEASUREMENTS OF THE FREE-SURFACE

Experiment	Sluice gate	Sloped channel	Inflow condition	x_{sg} (m)	LIDAR position upstream of the HJ (m)	d_1 (m)	Fr_1 (-)	Re (-)
A	x		PD	0.5	0.24	0.03	5.1	8.3×10^4
	x		FD	2.44	0.50	0.03	5.1	8.3×10^4
B	x		PD	0.58	0.32	0.025	5.1	6.2×10^4
	x		FD	1.87	0.50	0.025	5.1	6.2×10^4
C	x		PD	0.46	0.20	0.02	7.0	6.2×10^4
	x		FD	1.45	0.50	0.02	7.0	6.2×10^4
D	x		PD	0.71	0.45	0.03	7.0	1.1×10^5
	x		FD	1.97	0.50	0.03	7.0	1.1×10^5
E	x		PD	0.50	0.24	0.02	8.5	7.5×10^4
	x		FD	1.66	0.50	0.0205	8.2	7.5×10^4
F	x		PD	0.63	0.37	0.027	8.4	1.2×10^5
	x		FD	2.07	0.50	0.028	8.0	1.2×10^5
G	x		PD	0.45	0.19	0.02	10	8.8×10^4
	x		FD	1.45	0.50	0.02	10	8.8×10^4
H	x		PD	0.68	0.42	0.03	3.8	6.2×10^4
	x		FD	2.28	0.50	0.03	3.8	6.2×10^4
I	x		FD	2.85	0.50	0.04	3.8	9.5×10^4
CHJ_S5.1		$\theta = 5^\circ$	FD		1.00	0.040	4.6	1×10^5
CHJ_S5.2		$\theta = 5^\circ$	FD		1.00	0.032	4.7	8.4×10^4

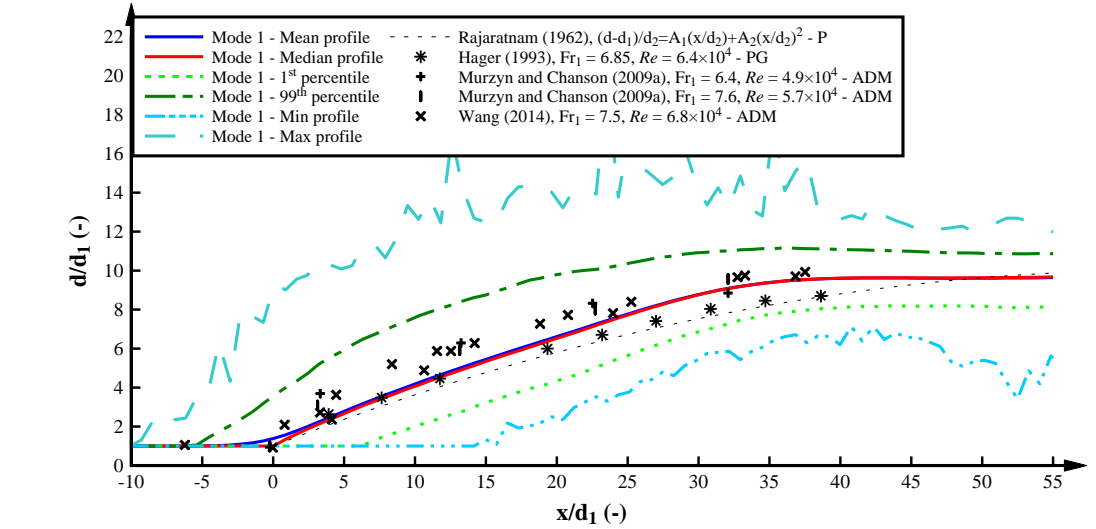
5.2. TIME-AVERAGED FREE-SURFACE PROFILES

The time-averaged free-surface profiles were recorded for all experiments (Table 5-1). Figure 5-2 shows a typical time-averaged free-surface profile for a free-jump toe movement condition (Mode 1) and fixing the free-surface profiles to the mean jump toe position (Mode 2) including the mean, median, minimum, maximum and 10th and 90th percentiles of the flow depth d/d_1 as function of x/d_1 . Despite the strong fluctuations in the free-surface (Figure 5-1), the mean free-

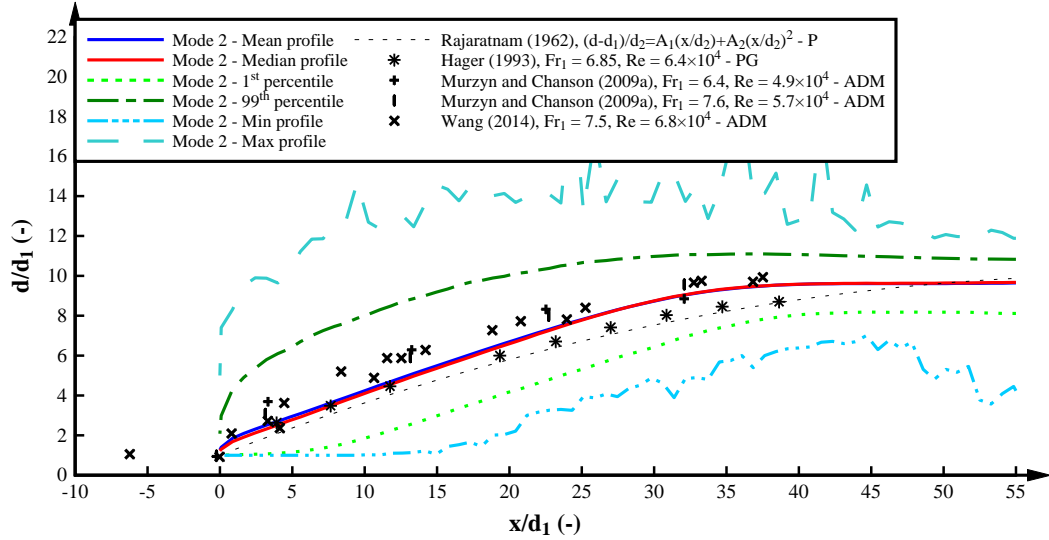
surface profile in Figure 5-2 was smooth and monotonic, and similar to past observations by Bakhmeteff and Matzke (1936) and Hager (1993).

For Mode 1 (Free jump toe movement), some differences between mean and median flow depths were found close to the jump toe for $-4 < x/d_1 < 15$, with a maximum difference of 27% for $x/d_1 \approx 0$ (Figure 5-2A). These differences were associated with the jump toe oscillations. For $x/d_1 > 15$, the mean and median profiles were almost identical showing a monotonic increase approaching the downstream conjugate depth. The flow depth percentiles showed a higher data deviation near the jump toe with a maximum difference of about 222% between 10th and 90th flow depth percentile for $x/d_1 = 3.22$. The differences in 10th and 90th percentiles decreased in downstream direction approaching a difference of 20% for $x/d_1 = 20$. The large difference close to the jump toe was associated with higher turbulence and stronger fluctuations in this region (Mouaze *et al.* 2005; Murzyn and Chanson 2009a; Chachereau and Chanson 2011b). The minimum and maximum flow depths provided the smallest and largest flow depths during the sampling duration. Herein the intersection of the 1st and 99th percentile profiles with the upstream inflow depth d_1 provided the minimum and maximum amplitude of the jump toe oscillations (Figure 5-2A). For example in Figure 5-2A, the amplitude of the jump toe oscillation was 232 mm highlighting the significant variation of the longitudinal jump toe positions. Further characterisation of the jump toe oscillations are described in Section 5.4.

Figure 5-2B presents the time-averaged profiles for Mode 2 (Fixed jump toe position). While there was close agreement between the two processing modes in terms of mean depth and percentiles, close to the jump toe some differences were observed. For Mode 2 at $x/d_1 = 0$, $d = d_1$ increasing monotonically in downstream direction (Figure 5-2B). In contrast, The LIDAR measurements of the flow depths in the hydraulic jump with free-moving jump toe (Mode 1) resulted in flow depths $d > d_1$ for $x/d_1 < 0$ (Figure 5-2A). Downstream the jump toe, Mode 2 presented slightly larger mean depths (e.g. a difference between Modes 1 and 2 of 18% at $x/d_1 = 1.66$). For $x/d_1 > 7$, the mean profiles were almost identical highlighting a rapid monotonic increase in the flow depth along the hydraulic jump roller until $x/d_1 = 40$. The present data of hydraulic jumps with free-moving jump toe confirmed a close link between jump toe oscillations and free-surface features for $x/d_1 < 7$. Further downstream $x/d_1 > 7$, good agreement was found between Modes 1 and 2 suggesting that the influence of the jump toe oscillations on the mean flow depth is limited to the region closest to the jump toe. Close to the jump toe, the free-surface data recorded in previous studies showed better agreement with the analysis of fixed jump toe position (Mode 2) suggesting that previous analysis did not consider the free jump toe movement in the measurement of the free-surface features in hydraulic jumps.



A) FREE JUMP TOE MOVEMENT (MODE 1)



B) FIXED JUMP TOE POSITION (MODE 2)

FIGURE 5–2. TYPICAL BASIC FREE-SURFACE CHARACTERISTICS IN A HYDRAULIC JUMP MEASURED WITH A LIDAR AND COMPARISON WITH PREVIOUS LITERATURE. EXPERIMENT C: $Fr_1 = 7.0$, $Re = 6.2 \times 10^4$, FULLY DEVELOPED INFLOW CONDITIONS. P: PIEZOMETER, PG: POINTER GAUGE, ADM: ACOUSTIC DISPLACEMENT METER.

Figure 5-3 shows a summary of the mean flow depths d/d_1 in the present study for Mode 1 with fully and partially developed inflow conditions as a function of x/d_1 . Overall, with increasing inflow Froude numbers, the dimensionless flow depths increased which was consistent with the experimental data of previous studies (e.g. Mouaze et al. 2005; Murzyn and Chanson 2009a; Chachereau and Chanson 2011b). Larger flow depths and steeper profiles were recorded in the roller region for hydraulic jumps with fully developed inflow conditions. The present data were compared with the free-surface measurements of hydraulic jumps with undeveloped and partially developed inflow conditions conducted with pointer gauges (PG), wire gauges (WG) and ADMs. Hydraulic jumps with similar Froude numbers are shown in the same colour scheme. For each

group of Froude numbers, close similarities were observed between previous studies and the LIDAR data.

The largest differences between previous studies and LIDAR recording were observed in the roller region of the hydraulic jump associated with the strong free-surface fluctuations and jump toe oscillations. For all experiments, pointer gauge measurements were in close agreement with LIDAR, the wire gauges showed lower free-surface profiles and the ADM measured higher profiles, i.e. the LIDAR measured an intermediate area between wire gauges and ADMs. The deviations between the LIDAR data and the wire gauge may be associated with the discontinuous contact of the wire gauge with the aerated free-surface (Murzyn and Chanson 2009a) while the differences with the ADM were associated to differences in the instrument footprints leading to different penetration depths (Zhang et al. 2018; Kramer et al. 2019a). Despite the differences, the shape of the free-surface profile was similar for all instruments suggesting that the LIDAR is a suitable instrument for the recording of free-surface features.

The LIDAR has an advantage in being able to measure the free-surface profiles almost instantaneously with a high spatial resolution. While previous instruments can only measure the free-surface elevation at a fixed location, the LIDAR provided a detailed free-surface profile with multiple simultaneous measurement points along the jump roller. Further detailed experiments are needed to directly compare the LIDAR performance with other types of instrumentation in simultaneous experiments including with wire gauges and ADMs.

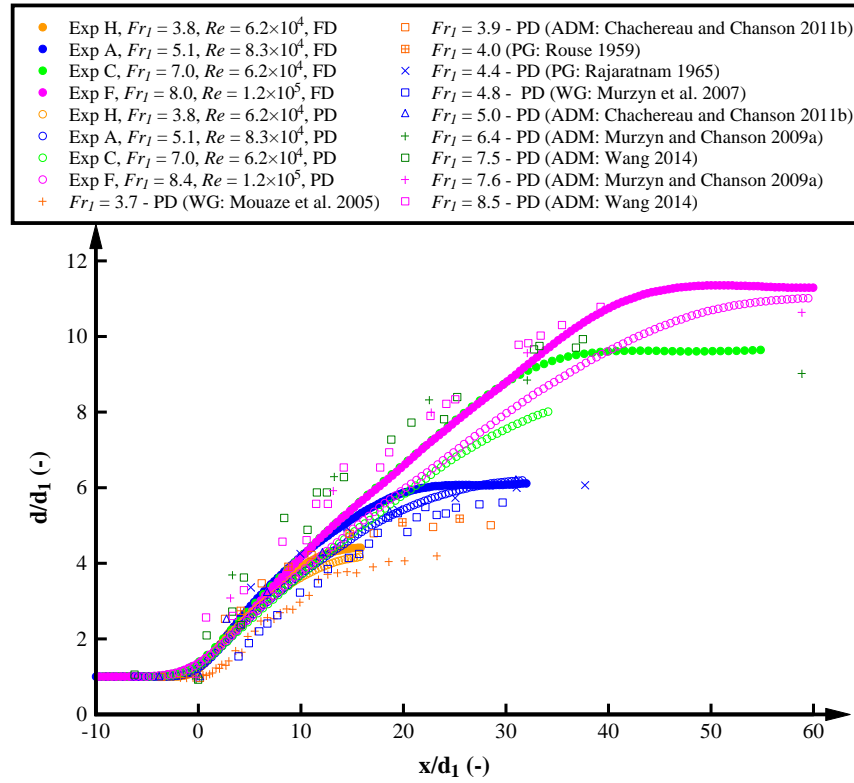
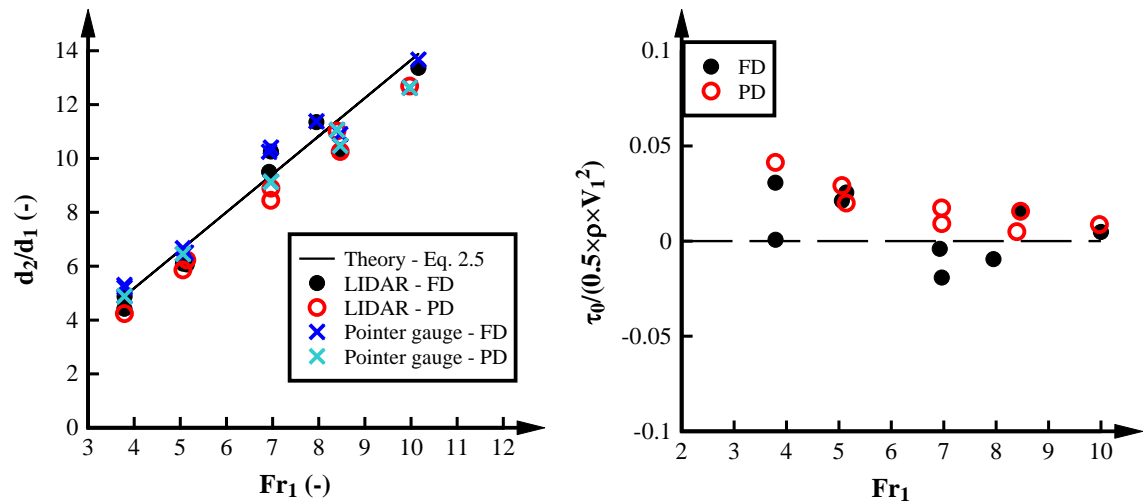


FIGURE 5–3. TIME-AVERAGED FREE-SURFACE PROFILES OF HYDRAULIC JUMPS IN THE PRESENT STUDY WITH FREE-JUMP TOE MOVEMENT (MODE 1) AND FULLY (FD) AND PARTIALLY (PD) DEVELOPED INFLOW CONDITIONS AND COMPARISON WITH PREVIOUS LITERATURE WITH PARTIALLY DEVELOPED INFLOW CONDITIONS (WG: WIRE GAUGE, PG: POINTER GAUGE, ADM: ACOUSTIC DISPLACEMENT METER).

Figure 5-4A presents the conjugate flow depth ratio d_2/d_1 measured with the LIDAR in fully and partially developed inflow conditions as function of the inflow Froude number. The conjugate depth measured with the LIDAR represents the flow depth at $x = L_r$ where L_r represents the roller length. The results were compared with pointer gauge measurements and the Bélanger equation (Equation 2.5). Overall, the conjugate depth ratio measured with the LIDAR showed close agreement with Bélanger equation and pointer gauge measurements with small deviations potentially linked with channel bed roughness and measurement accuracy (Chapter 3.4.3.). This result confirms the LIDAR as a valid instrument to remotely identify the roller length and the corresponding conjugate depth. Further description of the roller length in the hydraulic jump is presented in Chapter 5.2. Figure 5-5B presents the dimensionless shear stress $\tau_0/0.5\rho V_1^2$ in the channel bed beneath the hydraulic jump estimated based upon the LIDAR information and the momentum equation presented in Equation 2.2. Despite the deviations, the dimensionless shear stress is close to zero for fully and partially developed inflow conditions suggesting minor shear stress beneath the hydraulic jumps. The negligible shear stress was mostly observed in hydraulic jumps with large Froude numbers characterised by stronger energetic processes and lesser influence of the losses close to the channel bed. For low Froude numbers, the hydraulic jumps

were less violent and were slightly affected by shear stress. Therefore, slight larger shear stress was observed in partially developed hydraulic jumps since the flow resistance was more significant when the flow was not fully developed (Rajaratnam 1965).



A) CONJUGATE FLOW DEPTH; COMPARISON WITH BÉLANGER EQUATION AND PG DATA.

B) BED SHEAR STRESS

FIGURE 5-4. CONJUGATE DEPTH RATIO AND SHEAR STRESS AS FUNCTION OF THE FROUDE NUMBER IN HYDRAULIC JUMPS WITH FULLY (FD) AND PARTIALLY (PD) DEVELOPED INFLOW CONDITIONS.

5.3. HYDRAULIC JUMP LENGTH

Per definition, L_j is defined as the distance where the flow depth becomes levelled (Rajaratnam 1967; Hager and Bremen 1989; Hager et al. 1990; Hager 1992; 1993; Mok 2004) while L_r represents the length between the jump toe and the end of the backward flow (Rajaratnam 1967; Hager and Bremen 1989; Hager et al. 1990; Hager 1992; Mok 2004). The present study considered L_r as the longitudinal position recorded by the LIDAR where the gradient of the median profile became negative representing the distance of maximum roller upwelling. The estimated L_r measured with the LIDAR was compared with previous experiments and the semi-empirical equation proposed by Hager et al. (1990) and Wang (2014) (Figure 5-5). Data from Woycicki (1934) was taken from Bradley and Peterka (1957). LIDAR data is shown in solid symbols, pink colour represents previous measurements of L_j and grey colour represents previous measurements of L_r . Large differences were identified between the present data and the experiments of Woycicki (1934), Bakhmeteff and Matzke (1936) for $Fr_1 < 4$, and Rajaratnam (1967) since they measured the hydraulic jump length suggesting that $L_j > L_r$ for the range of Froude numbers analysed. L_r measured with the LIDAR agreed well with the measurements of L_r by Safranez (1929), Rajaratnam (1967) and the semi-empirical equation proposed by Hager et al. (1990). This result indicated that the location of the maximum upwelling point is in close agreement with the stagnation flow region in the hydraulic jump. The deviations in data of

Bakhmeteff and Matzke (1936) for $Fr_1 > 4$ were related to scale effects (Bradley and Peterka 1957). Note that L_j measured by Murzyn et al. (2007) and Wang (2014) showed large deviations from the measurements of L_j from previous authors (Woycicki 1934; Rajaratnam 1967) suggesting some limitations in the measurement of jump lengths in channel with relatively short lengths.

The LIDAR data showed good agreement with the roller length measurements. Despite some data scatter, hydraulic jumps with partially developed inflow conditions showed slight larger roller lengths which may be related to the less steep profile. The increase in the roller length measured with the LIDAR as function of Fr_1 fitted well with the semi-empirical equation proposed by Hager et al. (1990):

$$\frac{L_r}{d_1} = -12 + 160 \tanh\left(\frac{Fr_1}{20}\right) \quad \text{for } 3.6 < Fr_1 < 10 \quad (5.1)$$

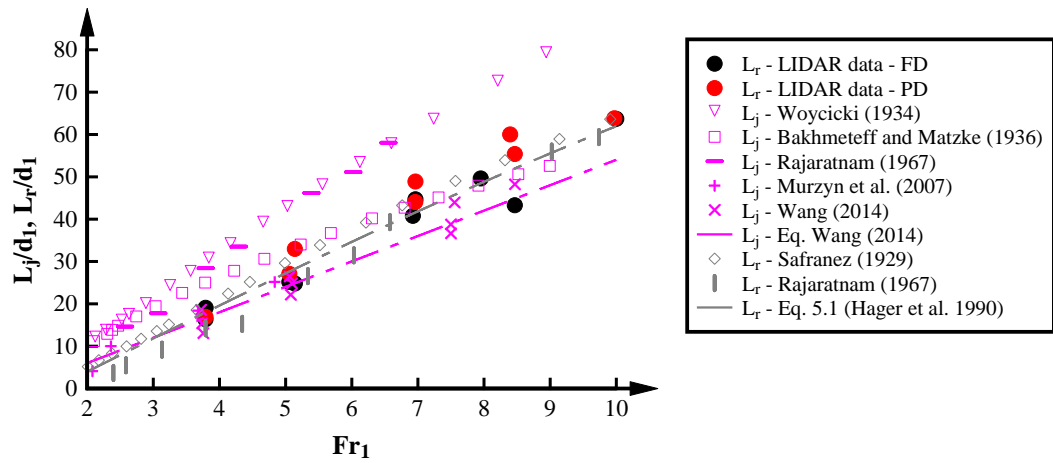


FIGURE 5–5 COMPARISON OF ROLLER LENGTH IN THE PRESENT STUDY WITH PREVIOUS OBSERVATIONS OF JUMP AND ROLLER LENGTHS AND WITH THE SEMI-EMPIRICAL EQUATION OF HAGER ET AL. (1990).

Figure 5-6 shows the dimensionless free-surface profiles $(d-d_1)/(d_2-d_1)$ for Mode 1 and fully and partially developed inflow conditions as function of x/L_r . For different Froude and Reynolds numbers, the time-averaged free-surface profiles of Mode 1 and for fully and partially developed inflow conditions showed self-similarity in the free-surface profiles in the roller region in agreement with previous studies (Hager 1993; Murzyn et al. 2007; Wang 2014). The present free-surface profiles for fully and partially developed inflow conditions measured with the LIDAR fitted well with a polynomial equation with $R^2 = 0.99$:

$$\frac{d-d_1}{d_2-d_1} = 0.0147 + 1.74 \left(\frac{x}{L_r}\right) - 0.75 \left(\frac{x}{L_r}\right)^2 \quad \text{for } 3.6 < Fr_1 < 10 \quad (5.2)$$

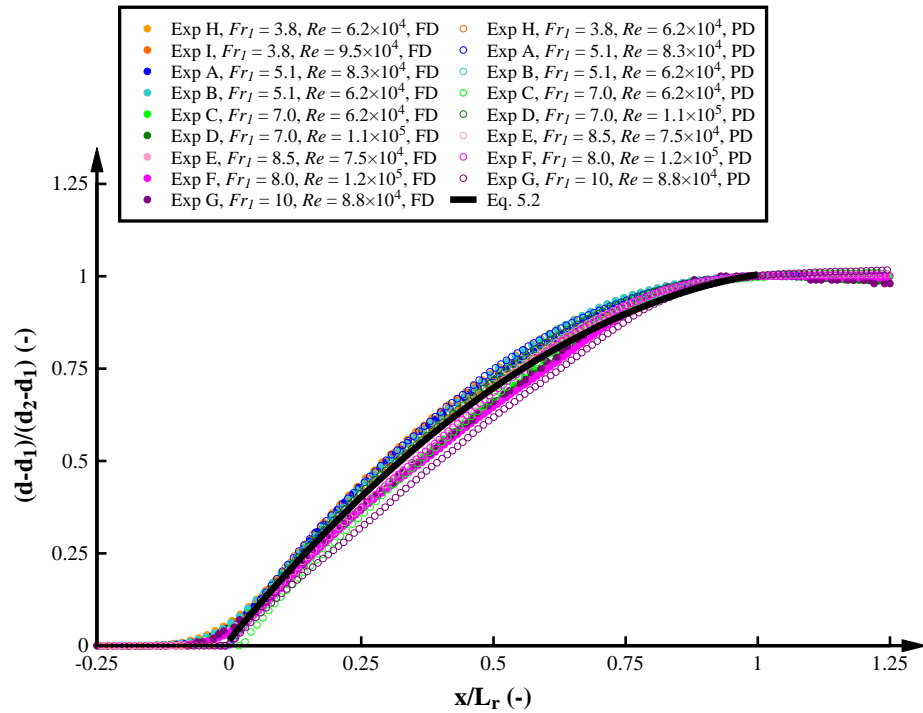


FIGURE 5-6. TIME-AVERAGED FREE-SURFACE PROFILES MEASURED WITH THE LIDAR IN HYDRAULIC JUMPS WITH FULLY (FD) AND PARTIALLY (PD) DEVELOPED INFLOW CONDITIONS.

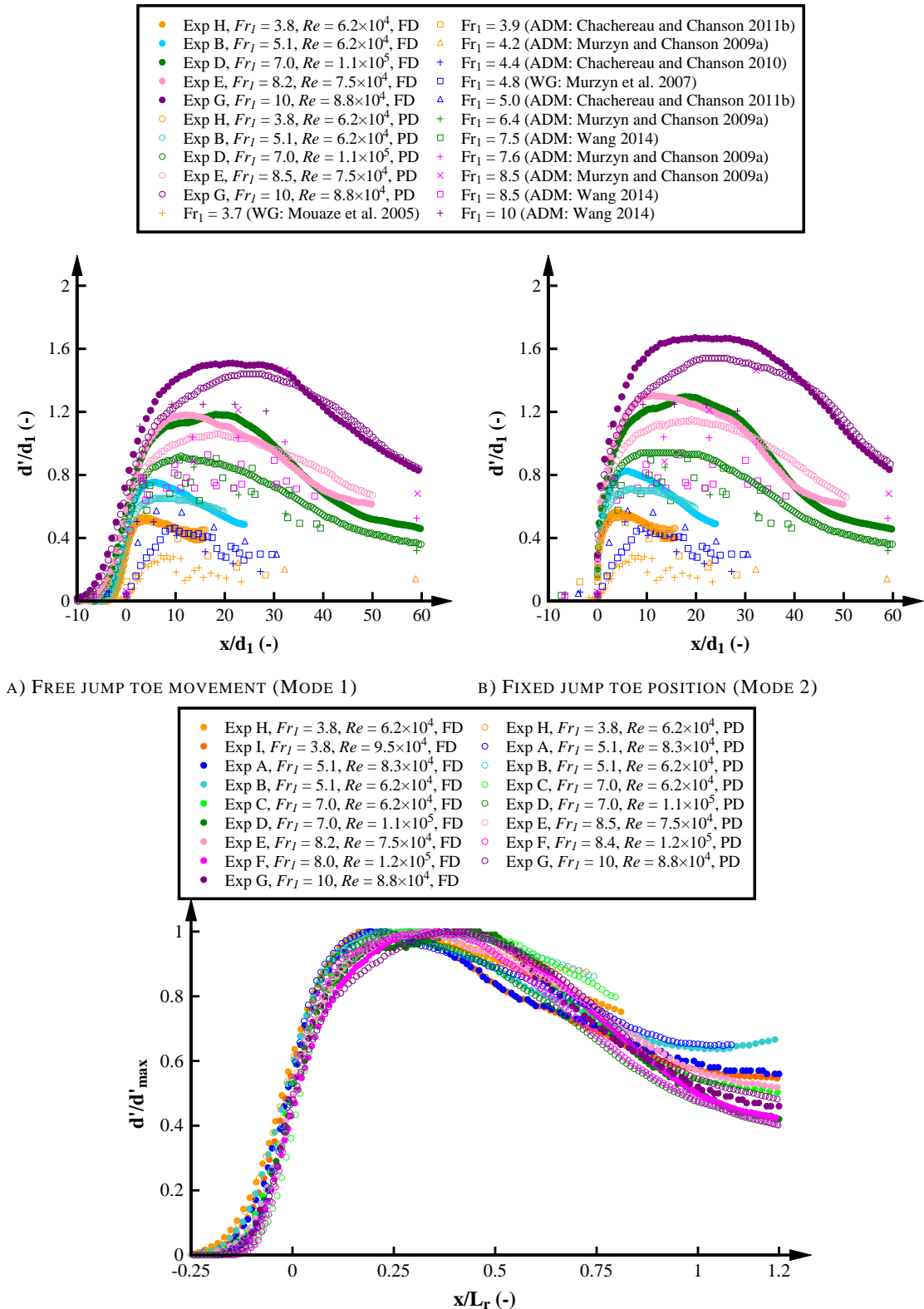
5.4. FREE-SURFACE FLUCTUATIONS

Figures 5-7 present the longitudinal distribution of the standard deviation of the free-surface elevations. Figure 5-7a and b present d'/d_l for Modes 1 and 2 as a function of x/d_l and Figure 5-7c shows d'/d'_{max} for all experiments in the present study as function of x/L_r where d'_{max} is the maximum free-surface fluctuation. Data from previous studies with similar Froude numbers are added for comparison. The hydraulic jump presented larger free-surface fluctuations close to the jump toe with a maximum peak in the roller region followed by a gradual decrease approaching the area of the conjugate flow depth region. The results indicated that the largest free-surface fluctuations linked with turbulence and strong vertical motions were observed in the roller region. For hydraulic jumps with $Fr_l < 7.0$, the maximum free-surface fluctuation showed a sharper peak at $x/L_r = 0.2$ while for larger Froude numbers, the maximum free-surface fluctuation comprised a longer region along the hydraulic jump between $0.2 < x/L_r < 0.5$. Figure 5-7c confirmed self-similarity in the free-surface fluctuations for all experiments conducted in the present study with different inflow conditions and different Froude and Reynolds numbers. The longitudinal distribution of the free-surface fluctuations were in agreement with previous measurements of the free-surface with wire gauges and ADMs (Murzyn et al. 2007; Murzyn and Chanson 2009a; Chachereau and Chanson 2011; Wang 2014) and pressure fluctuations at the channel bed (Schiebe and Bowers 1971; Abdul Khader and Elango 1974; Fiorotto and Rinaldo 1992). Note that

previous observations of free-surface fluctuations suggested no or negligible standard deviation at the mean jump toe position since no jump toe oscillations were taken into consideration (Mouaze et al. 2005; Murzyn et al. 2007; Murzyn and Chanson 2009a; Chachereau and Chanson 2011b). The present results using a fixed jump toe analysis (Mode 2) showed therefore a better agreement with previous studies (Figure 5-7B). In contrast, the standard deviation in free-surface elevations for the free-moving jump toe (Mode 1) showed distinct differences in the region closest to the jump toe with free-surface fluctuations as far upstream as $x/d_1 = -13$ for experiment G (Figure 5-7A). These observations highlighted the effect of the jump toe oscillations.

For all experiments, the free-surface fluctuations of the hydraulic jumps increased with increasing inflow Froude numbers which is in agreement with previous studies (e.g. Kucukali and Chanson 2008; Murzyn and Chanson 2009a). The results showed larger free-surface fluctuations for hydraulic jumps with fully developed inflow conditions suggesting that turbulence reaching the free-surface upstream of the hydraulic jump led to stronger free-surface fluctuations. The difference increased with increasing inflow Froude number indicating that the free-surface motions in fully developed hydraulic jumps were more sensitive to the increase in the inertia upstream.

For all experiments conducted downstream of the sluice gate, d'/d_1 was slightly larger for Mode 2 in the roller region suggesting a larger variation in flow depths for the fixed jump condition. The result was consistent with a larger 90th percentile of the flow depths for Mode 2 (Figure 5-2). The maximum standard deviations for Mode 2 were about 10% higher for all experiments compared to Mode 1. Towards the downstream end of the hydraulic jump, the standard deviations in free-surface elevations for Modes 1 and 2 became similar highlighting lesser effects of the jump toe oscillations on the free-surface fluctuations in the latter part of the jump roller.



C) FREE-SURFACE FLUCTUATIONS DISTRIBUTION FOR FULLY (FD) AND PARTIALLY (PD) DEVELOPED INFLOW CONDITIONS, FREE-JUMP TOE MOVEMENT (MODE 1).
FIGURE 5-7. FREE-SURFACE FLUCTUATIONS OF HYDRAULIC JUMPS WITH FULLY (FD) AND PARTIALLY (PD) DEVELOPED INFLOW CONDITIONS AND COMPARISON WITH PREVIOUS LITERATURE (WG: WIRE GAUGE, ADM: ACOUSTIC DISPLACEMENT METER).

Figure 5-8 presents the results of all experiments in dimensionless terms d'_{max}/d_1 for fully and partially developed inflow conditions as function of the inflow Froude number and a comparison with previous literature. For all experiments, the free-surface fluctuations increased with increasing Fr_1 and minor differences were observed between Mode 1 and Mode 2. The maximum free-surface fluctuations were larger in fully developed hydraulic jumps with increasing differences with increasing Fr_1 (Figure 5-8). Apart from the experiments conducted by Murzyn et al. (2007) and Wang (2014), good agreement was observed between the experiments conducted under partially developed inflow conditions and previous studies (Kucukali and Chanson 2008; Murzyn and Chanson 2009a; Chachereau and Chanson 2011b) (Figure 5-8). The results suggested that the maximum free-surface fluctuation detected by the LIDAR agreed with the observations recorded with the ADM. An explanation for the larger values of d'_{max}/d_1 in the present study compared to the experiments by Murzyn et al. (2007) and Wang (2014) may be linked with the higher spatial resolution of the free-surface data with the LIDAR which allowed a more robust determination of the largest value of d'_{max} along the hydraulic jump, while the fixed instrumentation of previous studies limited the observations of d'_{max} to selected positions along the hydraulic jump only. The present data in fully and partially developed inflow conditions were best correlated by a linear equation with $R^2 = 0.94$ and 0.96 respectively:

Fully developed inflow conditions:

$$\frac{d'_{max}}{d_1} = 0.173 \times (Fr_1 - 0.613) \quad \text{for } 3.6 < Fr_1 < 10 \quad (5.3a)$$

Partially developed inflow conditions:

$$\frac{d'_{max}}{d_1} = 0.153 \times (Fr_1 - 0.652) \quad \text{for } 3.6 < Fr_1 < 10 \quad (5.3b)$$

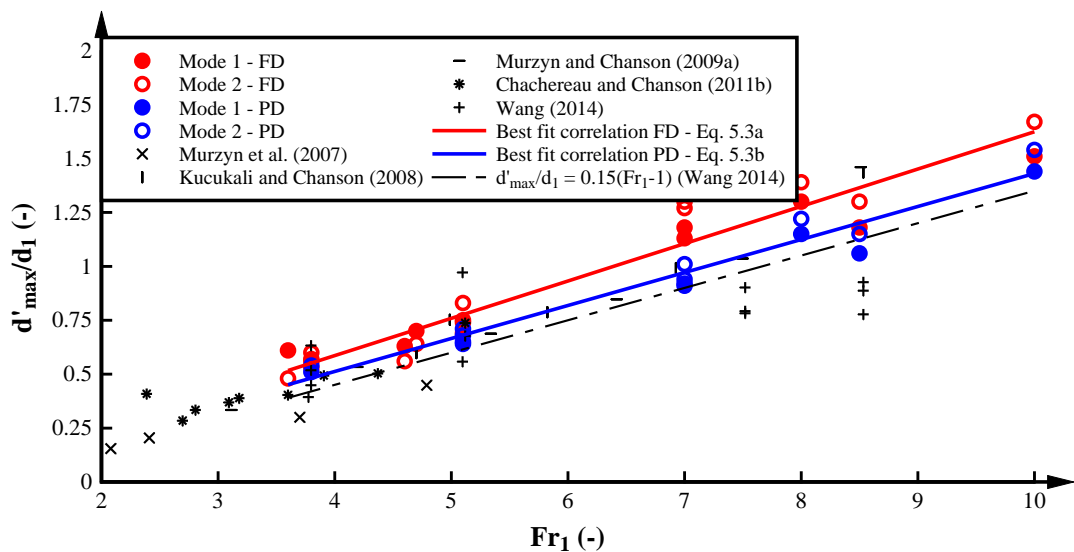
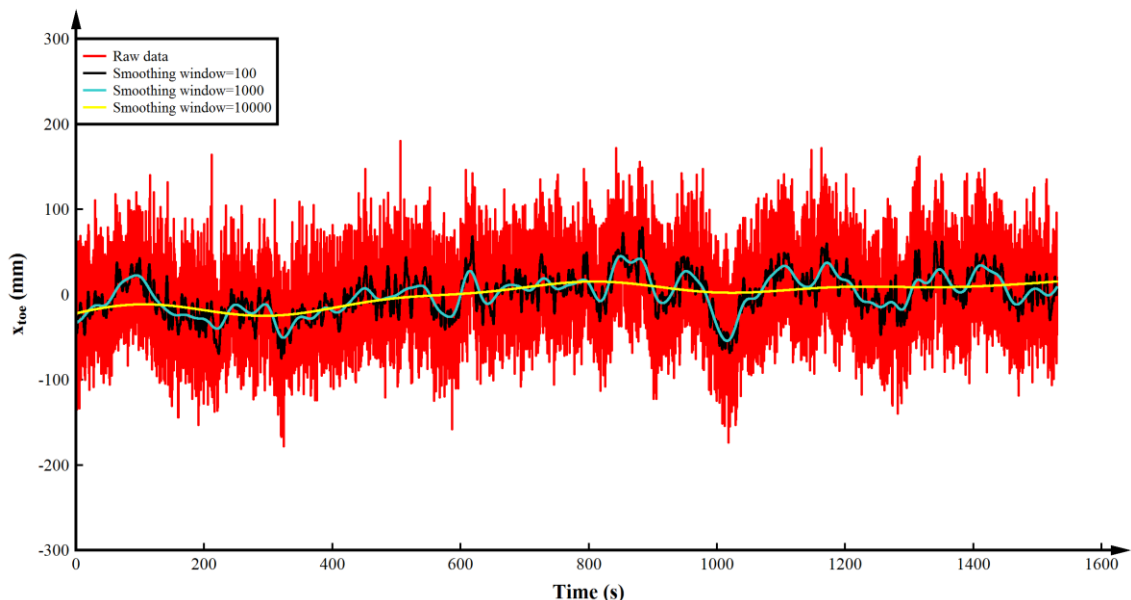


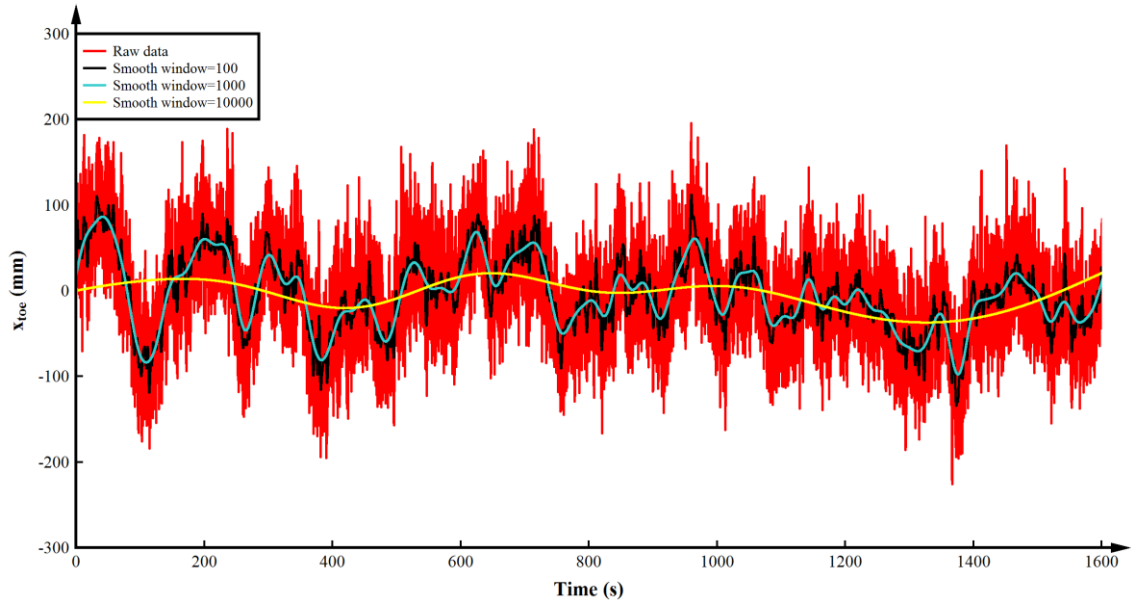
FIGURE 5–8. MAXIMUM FREE-SURFACE FLUCTUATIONS FOR DIFFERENT INFLOW FROUDE NUMBERS; COMPARISON OF PRESENT DATA FOR MODES 1 AND 2 AND FULLY (FD) AND PARTIALLY (PD) DEVELOPED INFLOW CONDITIONS WITH PREVIOUS DATA AND EQUATION 5.2.

5.5. JUMP TOE OSCILLATIONS

Jump toe oscillations play an important role in the free-surface fluctuations and vortex dynamics in hydraulic jumps (Long et al. 1991; Chanson 2010; Wang and Chanson 2013). Jump toe amplitude and oscillations were measured with the LIDAR for the free-moving jump case (Mode 1). Figure 5-9 shows typical raw signals of the dimensional jump toe oscillations for two experiments with identical Froude number. One of the experiments was conducted downstream of the sluice gate (Figure 5-9A) while the second one corresponded to a hydraulic jump downstream of the sloped channel (Figure 5-9B). The raw jump toe data of Experiment A (Figure 5-9A) illustrated an oscillation of the jump toe within a range of -178 mm to 180 mm with a standard deviation of 44.12 mm. Experiment CHJ_S5.1 presented a jump toe range between -225 mm to 221 mm with a standard deviation of 56 mm. To obtain a better understanding of the frequencies of the jump toe oscillations, simple smoothing of the raw data was conducted and the smoothed signals with 100 data points (black colour), 1000 data points (blue colour) and 10000 data points (yellow colour) are added in Figure 5-9. The smoothing pronounced periodic oscillations of the jump toe providing an estimation of the characteristic frequencies. Frequencies of about 0.2 Hz, 0.01 Hz and 0.002 Hz were observed for both jumps (smoothing window of 100, 1000 and 10000 data points respectively). Despite the similarity in the oscillation frequencies, hydraulic jumps downstream of a sluice gate (Experiment CHJ_S5.1 – Figure 5-9B) showed larger toe instabilities with more marked oscillation patterns suggesting an effect of the slope on the jump toe oscillations. The overall jump toe oscillation pattern was similar for all experiments.



A) EXPERIMENT A: $Fr_1 = 5.1$, $Re = 8.3 \times 10^4$, FULLY DEVELOPED INFLOW CONDITIONS



B) EXPERIMENT CHJ_S5.1: $Fr_1 = 4.6$, $Re = 1.0 \times 10^5$, FULLY DEVELOPED INFLOW CONDITIONS
FIGURE 5–9. RAW DATA OF JUMP TOE OSCILLATIONS MEASURED WITH THE LIDAR.

Figure 5-10 shows a box and whisker plot of the jump toe oscillations for all hydraulic jumps with fully developed inflow conditions including the median, skewness and kurtosis values. The box and whisker plot shows a visual comparison of distributions of the same variable for different conditions (Devore et al. 2013). Lower and higher whiskers indicated the 1st and 99th percentiles respectively, the box represented the interquartile range (IQR) defined as the difference between the 75th and 25th percentiles and the centred line represented the median or 50th percentile (Figure 5-10). For all hydraulic jumps, the probability distribution functions of the jump toe positions showed mean and median values close to zero suggesting unimodal jump toe distributions. The jump toe oscillations increased with increasing Froude numbers with a variation of $-4 < x/d_1 < 4$ for $Fr_1 = 3.8$ to $-7 < x/d_1 < 8$ for $Fr_1 = 10$.

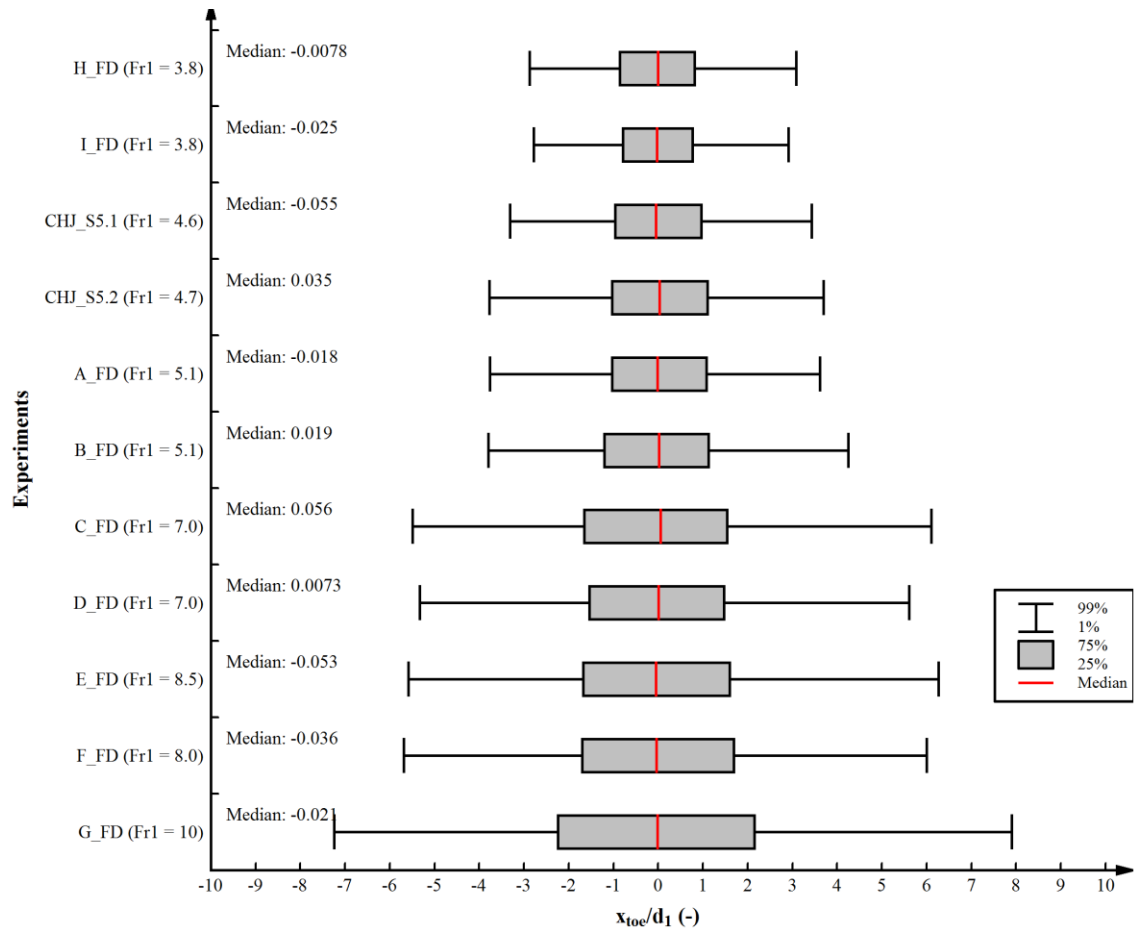


FIGURE 5–10. BOX AND WHISKER PLOT OF JUMP TOE OSCILLATIONS. LOWER AND HIGHER WHISKERS PRESENT MINIMUM AND MAXIMUM OSCILLATIONS, LOWER AND HIGHER EXTERNAL LINES PRESENT THE 25TH AND 75TH PERCENTILES; RED MIDDLE LINE REPRESENTS THE MEDIAN.

Table 5-2 lists the results of dimensionless minimum and maximum jump toe locations $x_{toe,min}/d_1$ and $x_{toe,max}/d_1$ respectively as well as the jump toe oscillations x_{toe}'/d_1 (Note that these parameters represent the 1st and 99th percentiles) and the characteristic frequencies of the jump toe oscillations $freq_{toe}$. The results showed an increase in jump toe amplitude $(x_{toe,max} - x_{toe,min})/d_1$ with increasing Froude number independent of the Reynolds number. Overall, hydraulic jumps downstream of the sloped channel had slightly larger amplitudes for similar Froude numbers. The standard deviation of the jump toe oscillations x_{toe}'/d_1 was also affected by the inflow Froude number. The experiments with larger Froude numbers had higher dimensionless standard deviations for both partially and fully developed inflow conditions (Table 5-2). This observation was in agreement with previous studies (Long et al. 1991; Wang 2014). The characteristic frequencies of the jump toe oscillations $freq_{toe}$ were also recorded with typical frequencies of $0.2 < freq_{toe} < 1.6$ Hz (Table 5-2). These frequencies agreed with previous observations (Mossa and Tolve 1998; Chanson and Gualtieri 2008, Murzyn and Chanson 2009a).

TABLE 5–2. JUMP TOE OSCILLATIONS IN FULLY AND PARTIALLY DEVELOPED HYDRAULIC JUMPS MEASURED WITH THE LIDAR

Experiment	Fr_1 (-)	Re (-)	$x_{toe,min}/d_1$ (-)	$x_{toe,max}/d_1$ (-)	$(x_{toe,min} - x_{toe,max})/d_1$ (-)	x_{toe}'/d_1 (-)	$freq_{toe}$ (Hz)
A_PD	5.1	8.3×10^4	-3.28	3.86	7.14	1.42	0.2 – 1
A_FD	5.1	8.3×10^4	-3.76	3.61	7.37	1.48	0.4 – 1.3
B_PD	5.1	6.2×10^4	-3.53	4.22	7.76	1.50	0.25-1.0
B_FD	5.1	6.2×10^4	-3.13	3.05	6.63	1.33	0.5 – 1.2
C_PD	7.0	6.2×10^4	-4.95	5.99	10.94	2.05	0.24-1.0
C_FD	7.0	6.2×10^4	-5.5	6.1	11.6	2.27	0.4 – 1.2
D_PD	7.0	1.1×10^5	-4.44	4.85	9.29	1.86	0.37 – 1.1
D_FD	7.0	1.1×10^5	-5.33	5.61	10.94	2.14	0.5 – 1.5
E_PD	8.5	7.5×10^4	-5.23	5.97	11.79	2.17	0.2 – 0.9
E_FD	8.5	7.5×10^4	-5.58	6.26	11.84	2.35	0.4 – 1.0
F_PD	8.4	1.2×10^5	-4.86	5.76	10.62	2.07	0.2 – 1.2
F_FD	8.0	1.2×10^5	-5.68	6.00	11.68	2.39	0.6 – 1.5
G_PD	10	8.8×10^4	-6.97	7.91	14.88	2.91	0.5 – 1.0
G_FD	10	8.8×10^4	-7.24	7.90	15.14	3.05	0.5 – 1.2
H_PD	3.8	6.2×10^4	-2.85	3.35	6.201	1.21	0.4 – 1.0
H_FD	3.8	6.2×10^4	-2.88	3.08	5.96	1.18	0.3 – 1.0
I_FD	3.8	9.5×10^4	-2.78	2.91	5.69	1.14	0.5 – 1.0
CHJ_S5.1_FD	4.6	1×10^5	-3.30	3.43	6.73	1.37	0.3 – 1.3
CHJ_S5.2_FD	4.7	8.4×10^4	-3.77	3.69	7.46	1.51	0.3 – 1.3

Figure 5-11 presents dimensionless jump toe oscillations x_{toe}'/d_1 for hydraulic jumps with partially and fully developed inflow conditions as function of the inflow Froude number. For both conditions, the jump toe oscillations and amplitude increased with the increase in Fr_1 . Larger jump toe oscillations were observed for hydraulic jumps with fully developed inflow conditions (Figure 5-11) with differences of about 10%. The present for fully and partially fully developed flow data were well correlated with a linear function ($R^2 = 0.97$ and 0.94 respectively):

Fully developed inflow conditions:

$$\frac{x_{toe}'}{d_1} = 0.298 \times (Fr_1 + 0.016) \quad \text{for } 3.6 < Fr_1 < 10 \quad (5.4a)$$

Partially developed inflow conditions

$$\frac{x_{toe}'}{d_1} = 0.254 \times (Fr_1 + 0.653) \quad \text{for } 3.6 < Fr_1 < 10 \quad (5.4b)$$

The present observations were also compared with video data by Long et al. (1991) and ADM data by Wang (2014) (Figure 5-11). The jump toe oscillations in the partially developed

hydraulic jump presented similarities with the oscillations recorded by Long et al. (1991). In contrast, the LIDAR identified larger jump toe oscillations compared with the ADM values of Wang (2014). The difference may be linked with the positioning of the ADM above the inflows leading to a recording of the jump toe at a higher elevation compared to the LIDAR. A further reason may be linked with thresholding techniques applied to the ADM data. A simultaneous comparison of LIDAR and other instrumentation is needed to provide clarity.

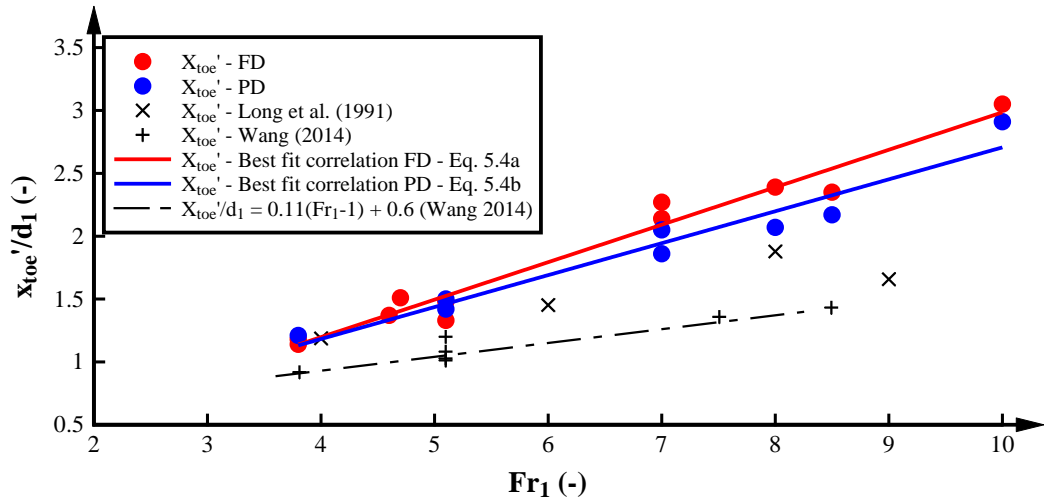


FIGURE 5–11. JUMP TOE OSCILLATIONS AS FUNCTION OF INFLOW FROUDE NUMBER FOR HYDRAULIC JUMPS WITH FULLY (FD) AND PARTIALLY (PD) DEVELOPED INFLOW CONDITIONS; COMPARISON OF PRESENT RESULTS WITH PREVIOUS OBSERVATIONS AND EQUATION 5.3.

The range of the characteristic frequencies of the jump toe $freq_{toe}$ can be presented in terms of a Strouhal number $freq_{toe} \times d_1 / V_1$. The characteristic frequency range was selected as a range of frequencies with the largest energy density in the frequency spectrum. Figure 5-12 presents the effect of the inflow conditions on the Strouhal number range as function of Fr_1 and the comparison with previous studies with hydraulic jumps formed immediately downstream the sluice gate (Undeveloped conditions - UD) and partially developed (PD) inflow conditions. Slightly larger Strouhal numbers were observed for fully developed inflow conditions suggesting more frequent jump toe motions. The Strouhal number range was in agreement with previous studies.

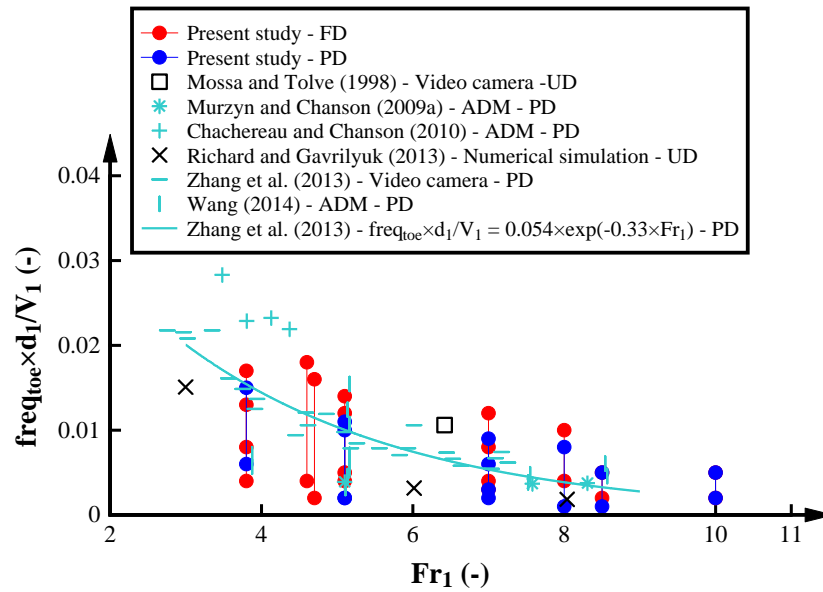


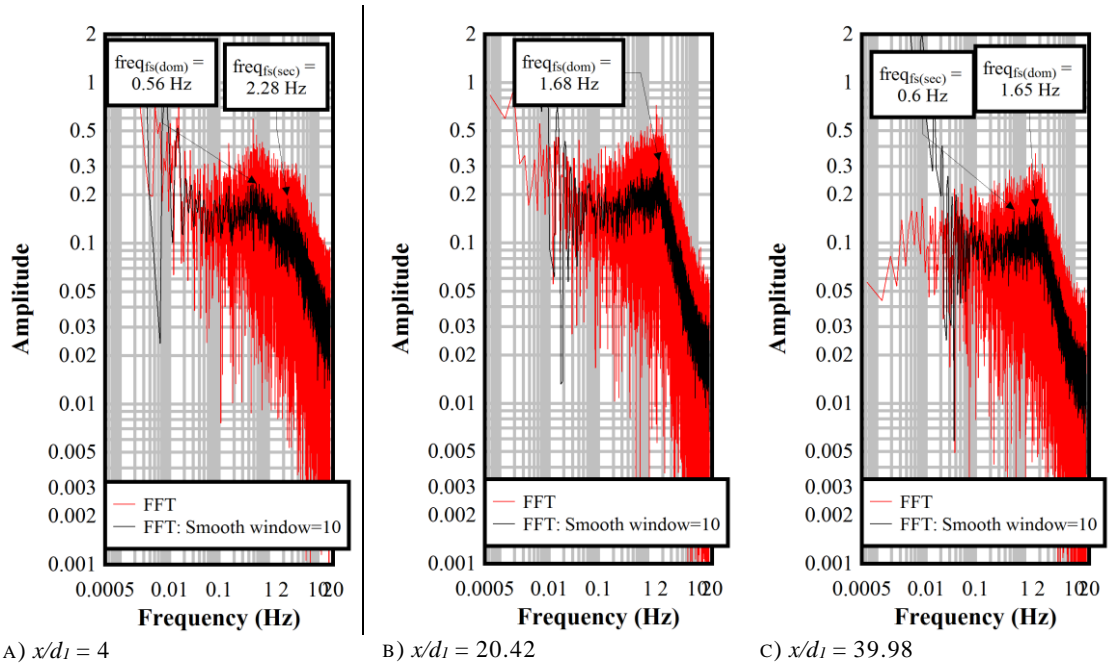
FIGURE 5–12. COMPARISON OF THE JUMP TOE CHARACTERISTIC FREQUENCIES BETWEEN HYDRAULIC JUMPS WITH FULLY (FD) AND PARTIALLY (PD) DEVELOPED INFLOW CONDITIONS.

5.6. CHARACTERISTIC FREQUENCIES OF THE FREE-SURFACE

A FFT analysis of the free-surface fluctuations was conducted. The analysis identified a range of characteristic frequencies of the free-surface fluctuations $freq_{fs}$ along the centreline of the hydraulic jumps. The analysis was conducted for both analysis modes, i.e. Modes 1 and 2.

5.6.1. MODE 1

A typical spectral analysis for Mode 1 is shown in Figure 5-13 for three different locations along a hydraulic jump and fully developed inflow conditions. For $x/d_1 = 4$ (Figure 5-13A), two characteristic frequencies of about 0.6 Hz and of about 2.3 Hz were identified. The first frequency was dominant $freq_{fs(dom)}$ and coincided with the dominant frequency of the jump toe oscillations, i.e. $freq_{fs(dom)} = freq_{toe}$ (Chapter 5.5) indicating a close link between the jump toe oscillations and the free-surface fluctuations close to the jump toe (Wang and Chanson 2013). A secondary frequency $freq_{fs(sec)}$ of 2.3 Hz agreed with typical free-surface frequencies reported previously (Murzyn and Chanson 2009a; Chachereau and Chanson 2011b). Further downstream for $x/d_1 = 30$, a dominant frequency of 1.7 Hz was identified (Figure 5-13B). For $x/d_1 = 40$, close to the conjugate depth region of the hydraulic jump, two characteristic frequencies of about 0.6 Hz and 1.65 Hz were observed (Figure 5-13C). While the former frequency was similar to the jump toe oscillations, the latter frequency was consistent with the reported values of free-surface fluctuations. The frequency patterns shown in Figure 5-13 were consistently observed for all hydraulic jumps including partially and fully developed inflow conditions.



A) $x/d_1 = 4$ B) $x/d_1 = 20.42$ C) $x/d_1 = 39.98$
FIGURE 5–13. FFT ANALYSIS AND CHARACTERISTIC FREQUENCIES FOR A HYDRAULIC JUMP WITH FREE MOVING JUMP TOE (MODE 1), EXPERIMENT C: $Fr_1 = 7.0$, $Re = 6.2 \times 10^4$, FULLY DEVELOPED INFLOW CONDITIONS.

Previous studies of free-surface fluctuations in hydraulic jumps identified characteristic frequencies in the range of $1 \leq freq_{fs} \leq 4$ Hz at selected positions along the jump roller (Murzyn and Chanson 2009a; Chachereau and Chanson 2011b; Wang 2014). The present experiments provided for the first time a continuous signal along the hydraulic jump and a continuous FFT analysis was conducted along the jump roller. An example of the variation of the free-surface frequencies with the distance from the jump toe for Mode 1 is provided in a Digital Appendix as Movie 5_1. Figure 5-14 shows characteristic frequencies for two experiments with fully and partially developed inflow conditions for Mode 1. A frequency classification between dominant and secondary frequencies was conducted manually and Figure 5-14 shows the $freq_{fs(dom)}$ and $freq_{fs(sec)}$ for fully and partially developed inflow conditions. In cases where two frequencies were equally dominant, green symbols were used. Some data scatter suggested a range of frequencies rather than a single dominant frequency confirming the features of hydraulic jumps as turbulent, unsteady and complex.

All experiments had similar frequency patterns along the hydraulic jump (Figure 5-14). At the jump toe, dominant frequencies were in the range of $0.2 \leq freq_{fs(dom)} \leq 1.5$ Hz and secondary frequencies between $1.5 \leq freq_{fs(sec)} \leq 4$ Hz, within the jump roller dominant frequencies were between $1.5 \leq freq_{fs(dom)} \leq 4$ Hz and at the end of the jump, frequencies were within $0.1 \leq freq_{fs(dom)} \leq 3$ Hz. For low Froude numbers, dominant frequencies between $0.1 \leq freq_{fs(dom)} \leq 0.5$ Hz were observed at the downstream end of the jump. Data scatter increased with increasing Froude

number associated with larger free-surface fluctuations and instability. Two dominant frequencies (green symbols in Figure 5-14) were observed in regions of transitions between dominant frequencies (Figure 5-14). Overall $freq_{fs(dom)}$ were similar between fully and partially developed inflow conditions while some differences were found in terms of the $freq_{fs(sec)}$, i.e. secondary frequencies between $0.5 \leq freq_{fs(sec)} \leq 1.5$ Hz were not observed for partially developed inflows in the roller region for most of the experiments. This result may be linked with the lesser free-surface fluctuations in partially developed hydraulic jumps.

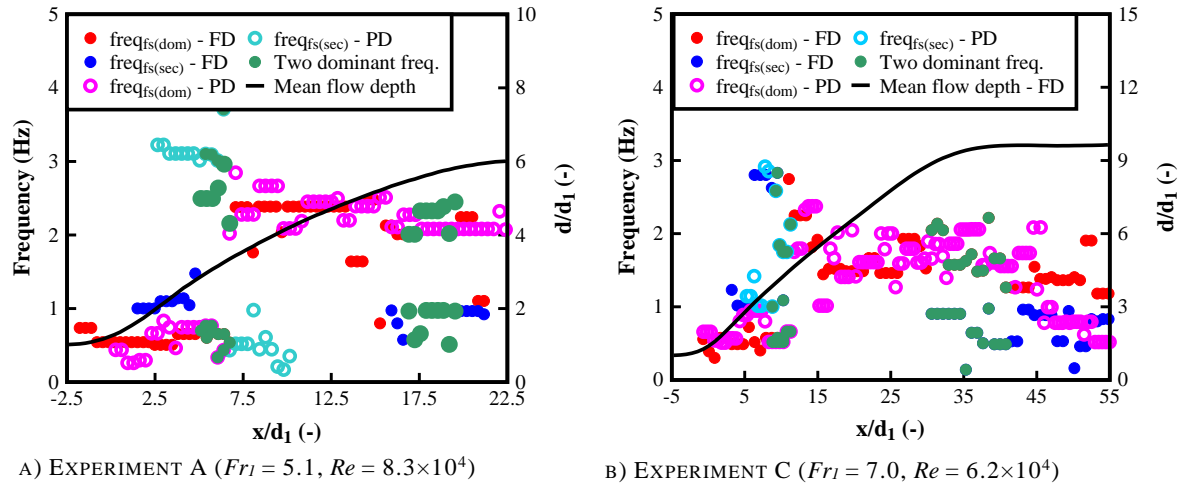


FIGURE 5–14. CHARACTERISTIC FREQUENCIES IN HYDRAULIC JUMPS WITH FREE-MOVING JUMP TOE (MODE 1) AND FULLY (FD) AND PARTIALLY (PD) DEVELOPED INFLOW CONDITIONS. RED SYMBOLS: DOMINANT FREQUENCY; BLUE SYMBOLS: SECONDARY FREQUENCY; GREEN SYMBOLS: TWO DOMINANT FREQUENCIES. BLACK LINE: MEAN FLOW DEPTH d/d_1 .

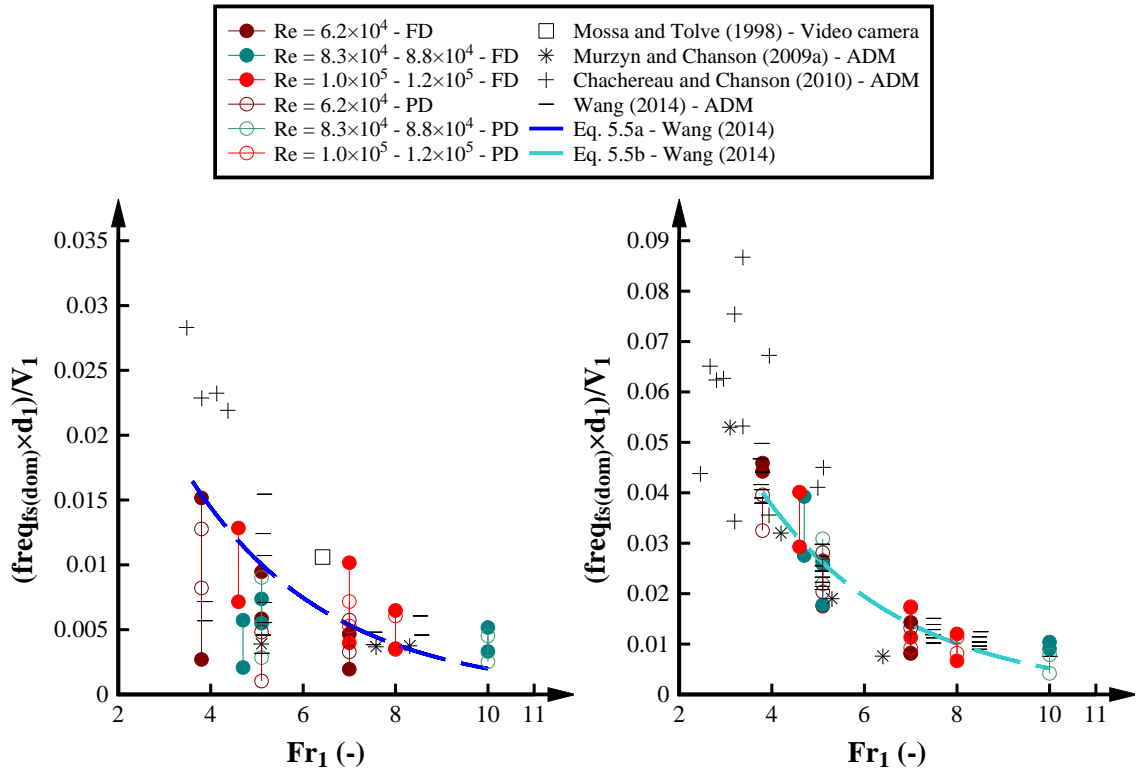
Figure 5-15 presents the decay in the dominant frequencies in the jump toe region (Figure 5-15A) and in the roller region (Figure 5-15B) as function of the Froude number. All frequencies are presented in terms of a Strouhal number ($freq_{fs} \times d_1 / V_1$). Both frequencies showed a decrease in the Strouhal number with increasing Froude number. A faster decay was observed in the dominant frequencies recorded in the roller region. The dominant frequencies in the jump toe region agreed well with the jump toe oscillations. The frequency range in the roller region agreed well with the free-surface frequency analysis recorded with ADMs (Murzyn and Chanson 2009a, Chachereau and Chanson 2010; Wang 2014). The frequency decay was similar between hydraulic jumps with fully and partially developed inflow conditions. Both frequency decays agreed well with the empirical equations proposed by Wang (2014):

Jump toe frequency:

$$\frac{freq_{toe} \times d_1}{V_1} = 0.054 * \exp(-0.33 \times Fr_1) \quad (5.5a) \text{ (Wang 2014)}$$

Dominant frequency free-surface fluctuation:

$$\frac{freq_{fs(dom)} \times d_1}{V_1} = 0.140 * \exp(-0.329 \times Fr_1) \quad (5.5b) \text{ (Wang 2014)}$$



A) DOMINANT FREQUENCY JUMP TOE REGION. B) DOMINANT FREQUENCY ROLLER REGION.
 COMPARISON WITH PREVIOUS STUDIES AND COMPARISON WITH PREVIOUS STUDIES AND
 EQUATION 5.5a (WANG 2014). EQUATION 5.5b (WANG 2014).

FIGURE 5–15. CHARACTERISTIC FREQUENCIES FOR HYDRAULIC JUMPS WITH FULLY (FD) AND PARTIALLY (PD) DEVELOPED INFLOW CONDITIONS AS FUNCTION OF THE FROUDE NUMBER.

5.6.2. MODE 2

A spectral analysis of the free-surface fluctuations was also conducted for Mode 2. Note that the analysis with a fixed jump toe (Mode 2) represented an indirect filtering of the jump toe oscillations and therefore, provided the free-surface frequency spectrum without the influence of the jump toe oscillation in the regions close to the jump toe. Figure 5-16 presents typical FFT results for Mode 2 at three different dimensionless positions along the jump roller. Two frequency peaks of about 0.6 Hz and 1.5 to 2.5 Hz were identified at all locations (Figure 5-16). In comparison to Mode 1, the fixed jump toe analysis (Mode 2) reduced the jump toe oscillation frequency close to the jump toe. Overall the analysis for Mode 2 confirmed characteristic free-surface fluctuations in hydraulic jumps. The characteristic free-surface frequencies between 1.5 and 3 Hz were independent of the jump toe oscillations since they were confirmed for both jump toe analysis modes.

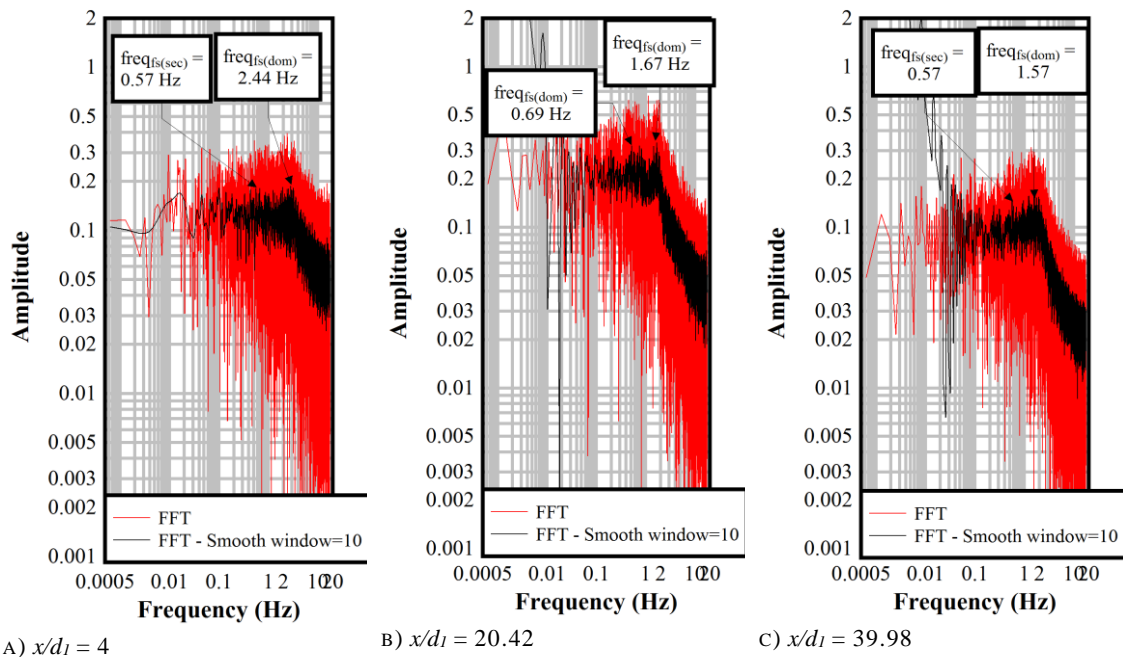


FIGURE 5-16. FFT ANALYSIS AND CHARACTERISTIC FREQUENCIES FOR A HYDRAULIC JUMP WITH FIXED JUMP TOE (MODE 2): EXPERIMENT C: $Fr_1 = 7.0$, $Re = 6.2 \times 10^4$, FULLY DEVELOPED INFLOW CONDITIONS.

Characteristic frequencies for selected experiments with Mode 2 are shown in Figure 5-17 including dominant, secondary and cases with two dominant frequencies. An example of the variation of the free-surface frequencies with the distance from the jump toe for Mode 2 is included in the Digital Appendix as Movie 5_2. Despite scatter in the frequency values, frequency regions were identified near the jump toe, within the jump roller and towards the downstream end of the roller. Near the jump toe, the dominant frequencies were $1 < freq_{fs(dom)} < 3$ Hz. In the jump roller, the frequency range showed two dominant frequencies with frequencies between $0.5 \leq freq_{fs} \leq 3$ Hz with the majority of dominant frequencies within the range of $0.5 \leq freq_{fs(dom)} \leq 1$ Hz. Towards the downstream end of the roller, a dominant frequency of about $0.1 \leq freq_{fs(dom)} \leq 1.5$ Hz was observed for the majority of cases and secondary frequencies of $1.5 \leq freq_{fs(sec)} \leq 3$ Hz. Mode 2 showed frequencies between 0.5 – 1.5 Hz which were not observed for Mode 1 and dominant frequencies in the jump toe region corresponding to the free-surface frequency range of $1 \leq freq_{fs(dom)} \leq 3$ Hz. These findings suggested that Mode 2 acted as a frequency filter of Mode 1.

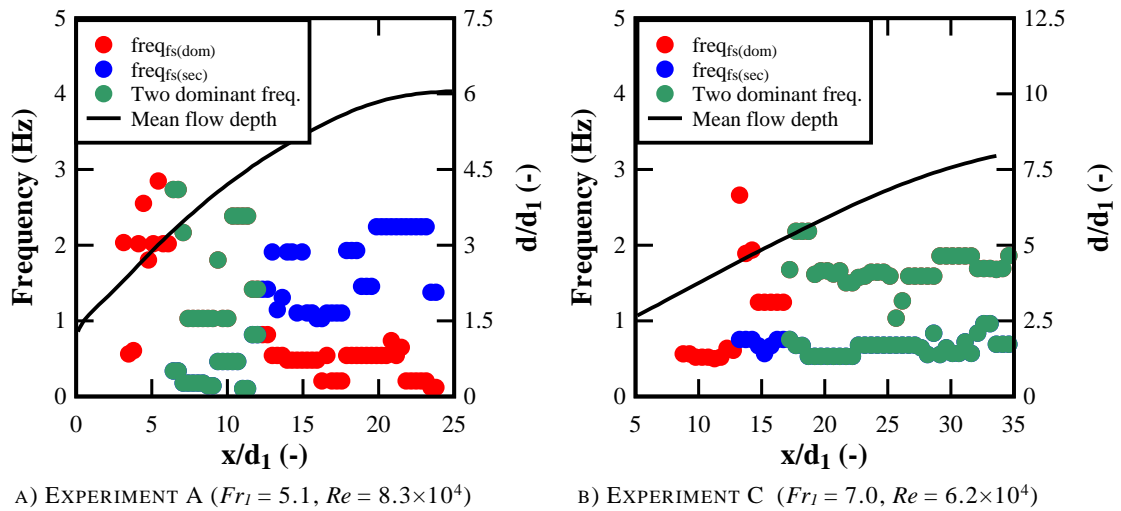
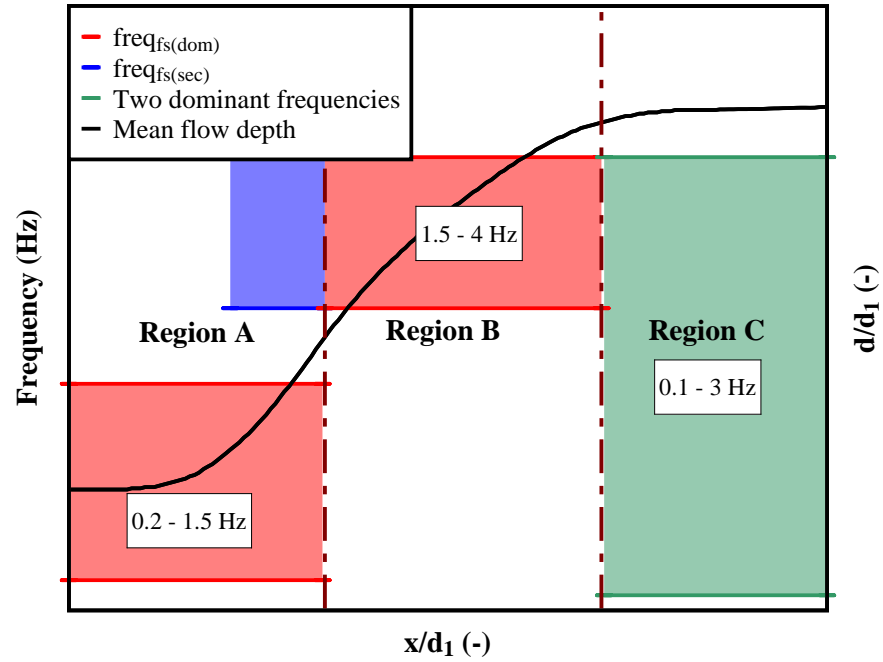


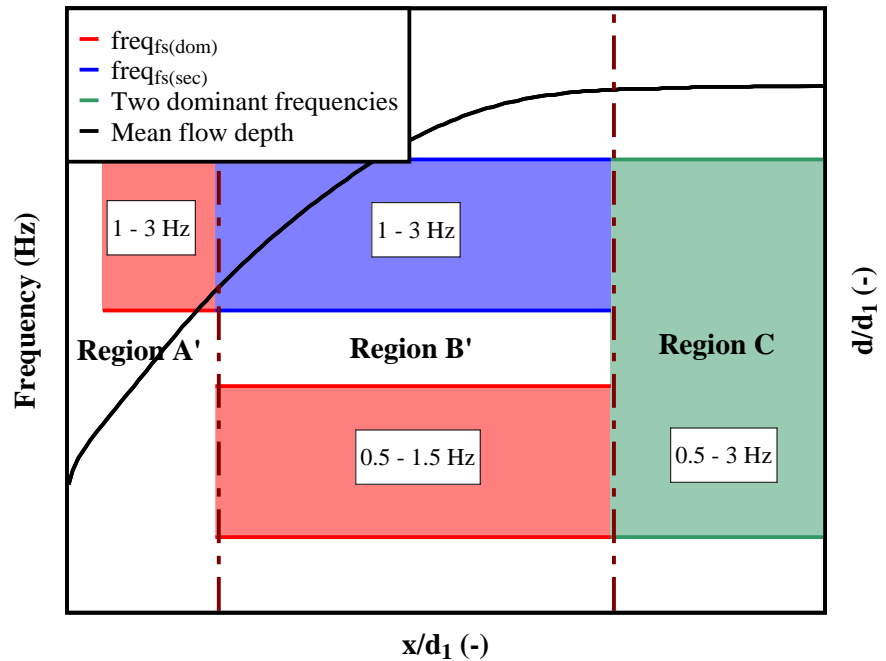
FIGURE 5-17. CHARACTERISTIC FREQUENCIES FOR HYDRAULIC JUMPS WITH FULLY DEVELOPED INFLOW CONDITIONS WITH FIXED JUMP TOE (MODE 2). RED SYMBOLS: DOMINANT FREQUENCY; BLUE SYMBOLS: SECONDARY FREQUENCY; GREEN SYMBOLS: TWO DOMINANT FREQUENCIES. BLACK LINE: MEAN FLOW DEPTH d/d_1 .

5.6.3. FREE-SURFACE FREQUENCY REGIONS

Based on the analysis of characteristic free-surface fluctuations for both analysis modes, distinctive frequency patterns were identified matching characteristic flow regions within hydraulic jumps. Based upon the observed dominant and secondary frequencies for the hydraulic jumps with Mode 1, a characteristic frequency pattern of dominant and secondary frequencies was identified (Figure 5-18A). Three characteristic free-surface frequency regions within hydraulic jumps were identified comprising the area near the mean jump toe “Jump toe region” (Region A), the “Jump roller region” (Region B) with predominantly one defined frequency peak, and the “Conjugate flow depth region” (Region C) towards the downstream end of the roller (Figure 5-18A). The conjugate depth region corresponded to the region with no negative velocities as presented in Chapter 7. The characteristic free-surface regions in Mode 2 (Figure 5-18B) mostly confirmed the findings for Mode 1. Three characteristic regions were identified comprising Region A’ just downstream of the jump toe which is purely affected by the free-surface fluctuations, Region B’ which is characterized by two characteristics peaks, and the conjugate depth Region C which was consistent with Mode 1.



A) MODE 1



B) MODE 2

FIGURE 5-18. CHARACTERISTIC FREE-SURFACE FREQUENCY REGIONS IN HYDRAULIC JUMPS.

5.7. AUTO-CORRELATION TIME SCALES

The free-surface auto-correlation time scale $T_{fs,auto}$ represents a characteristic advective time of the turbulent free-surface features along the hydraulic jump surface. Auto-correlation time scales inside the air-water flows in hydraulic jumps have been studied previously (e.g. Chanson 2007a; Chanson and Chachereau 2013; Wang et al. 2014) and the present study calculated the auto-correlation time scales for the first time. Figure 5-19 shows typical dimensionless results

$T_{fs,auto} \times (g/d_1)^{0.5}$ for two selected hydraulic jumps with fully and partially developed inflow conditions as function of x/d_1 . The time scales are shown for Mode 1, for Mode 2 and for Mode 1 using both a 0.1 and 0.5 Hz high-pass filter (Figure 5-16). The mean free-surface profile and the minimum and maximum jump toe locations are included as reference.

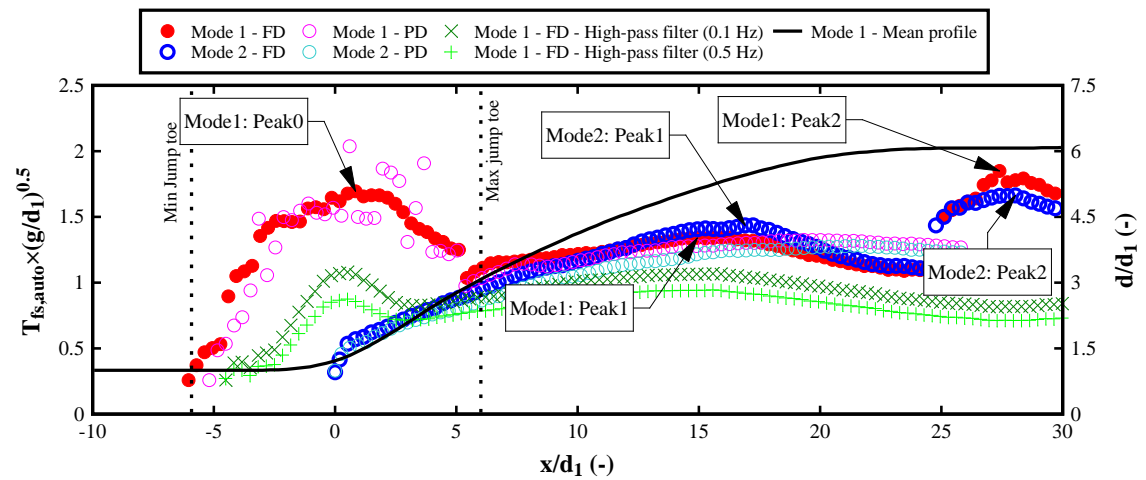
For Mode 1 and fully developed inflow conditions, $T_{fs,auto} \times (g/d_1)^{0.5}$ varied strongly along the hydraulic jump (Figure 5-19). Large auto-correlation times scales were observed close to the jump toe with a marked peak of up to $T_{fs,auto} \times (g/d_1)^{0.5} = 2.5$ for Experiment G (Mode1: Peak0). This peak was linked with the influence of the inflow depth, which reoccurred in the time series of free-surface data affected by the longitudinal jump toe movements, increasing the auto-correlation function and the resulting time scales. (Appendix G). Downstream of this peak, the time scale declined linked with the decreasing influence of the jump toe movements. Downstream of the maximum jump toe oscillation, the auto-correlation time scales increased up to a second peak (Mode1: Peak1), which is consistent with an increase in large vortical structures along hydraulic jumps which are also reflected at the free-surface. A small third peak was also identified in the conjugate flow depth regions (Mode1: Peak2). This third peak was more obvious in experiments with low Froude numbers and large Reynolds numbers and could be linked with low aeration in the conjugate depth region for the weakest hydraulic jumps.

For Mode 2, $T_{fs,auto} \times (g/d_1)^{0.5}$ was minimum at $x/d_1 = 0$, followed by a monotonic increase until a maximum peak in the roller region (Mode2: Peak1) (Figure 5-19). Mode2: Peak1 was consistent with Mode1: Peak1. For small Froude and Reynolds numbers, there were little differences in $T_{fs,auto} \times (g/d_1)^{0.5}$ between the two processing modes, albeit larger time scales for Mode 2. This observation was consistent with elevated auto-correlation functions for Mode 2 which appear to be directly linked with the shifting of the jump locations to the mean jump toe position and not related to the LIDAR signals. For large Froude and Reynolds numbers ($Fr_1 \geq 7$; $Re \geq 1.1 \times 10^5$), the auto-correlation functions for Mode 2 were mostly positive increasing the upper integration limit of Equation 3.7 and resulting in elevated $T_{fs,auto}$ values for Mode2:Peak1 (Figure 5-19B).

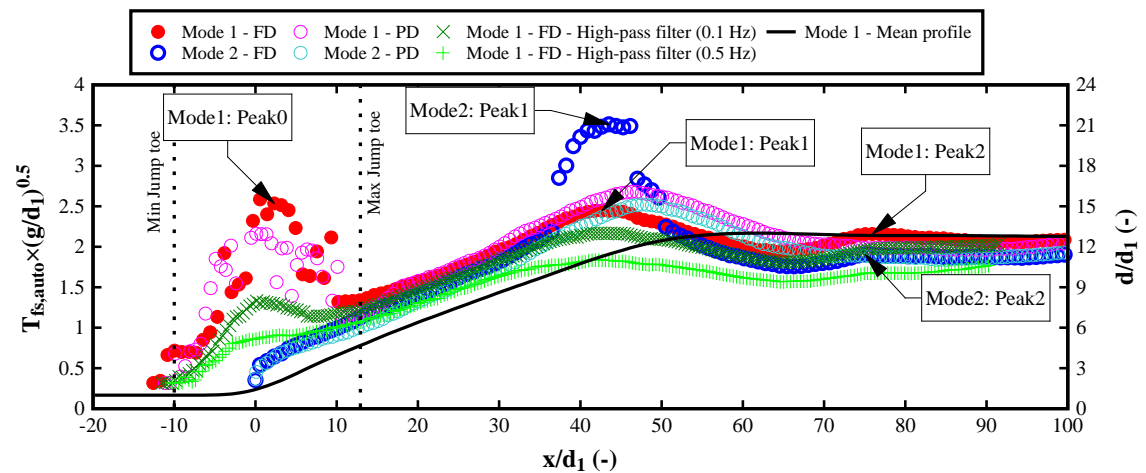
Different high-pass filters were also tested on the raw data to artificially remove the slow longitudinal movements of the hydraulic jump (Figure 5-19). Following the approach of Chachereau and Chanson (2010), a high-pass filter of 0.1 Hz was used leading to a reduction in magnitudes in $T_{fs,auto} \times (g/d_1)^{0.5}$ while the locations of the peaks were consistent with the unfiltered Mode 1 data. It appeared that the high-pass filtering did not only remove the slow jump toe oscillations, but instead reduced consistently the auto-correlation functions and the resulting auto-

correlation time scales. A sensitivity analysis with a high-pass filter of 0.5 Hz was also conducted confirming a strong effect of raw signal filtering upon the free-surface time and length scales.

Potential effects of inflow conditions on the free-surface auto-correlation time scales were also investigated (Figure 5-19). The $T_{fs,auto}$ distribution for hydraulic jumps with partially developed inflow conditions presented a large peak close to the jump toe followed by a second peak in the roller region, in agreement with the distribution in fully developed inflow conditions. Albeit minor deviations in the maximum peaks, the trend of the auto-correlation curves between partially and fully developed inflow conditions was similar along the hydraulic jump. For Mode 2, larger $T_{fs,auto}$ were observed in the roller region for fully developed hydraulic jumps linked potentially with larger free-surface fluctuations leading to larger coherent structures.



A) EXPERIMENT A: $Fr_1 = 5.1$, $Re = 8.3 \times 10^4$



B) EXPERIMENT G: $Fr_1 = 10$, $Re = 8.8 \times 10^4$

FIGURE 5-19. FREE-SURFACE AUTO-CORRELATION TIME SCALES ALONG HYDRAULIC JUMPS WITH FULLY (FD) AND PARTIALLY (PD) DEVELOPED INFLOW CONDITIONS.

Figure 5-20 presents the free-surface auto-correlation time scales for all hydraulic jumps for Mode 1 as function of x/L_r . All $T_{fs,auto}$ curves had similar shapes independent of the Froude

and Reynolds numbers. For most of the experiments, the largest peak in the auto-correlation time scales was observed near the mean jump toe location ($x/L_r < 0.2$) suggesting that the turbulent scales in the jump are dominated by the jump toe oscillations when considering a free-jump toe movement (Mode 1). Large data scatter at the jump toe location was observed for the hydraulic jumps located downstream of the sloped channel which may be related to the stronger jump toe instabilities of these jumps (e.g. Figure 5-9). The second peak (Mode1: Peak1) was located in the roller region of the hydraulic jump for all experiments ($0.2 < x/L_r < 1$). For Mode1: Peak1, the peak increased with increasing Froude numbers independent of the Reynolds numbers and the inflow conditions. For hydraulic jumps with large aeration, Mode1:Peak2 was located in the conjugate depth region ($x/L_r > 1$) and the auto-correlation time scale increased with increasing Fr_1 . Apart from experiment G ($Fr_1 = 10, Re = 8.8 \times 10^4$) corresponding to the experiment with the largest Froude number, larger $T_{fs,auto}$ was continuously observed in fully developed hydraulic jumps linked with the larger free-surface fluctuations and instabilities.

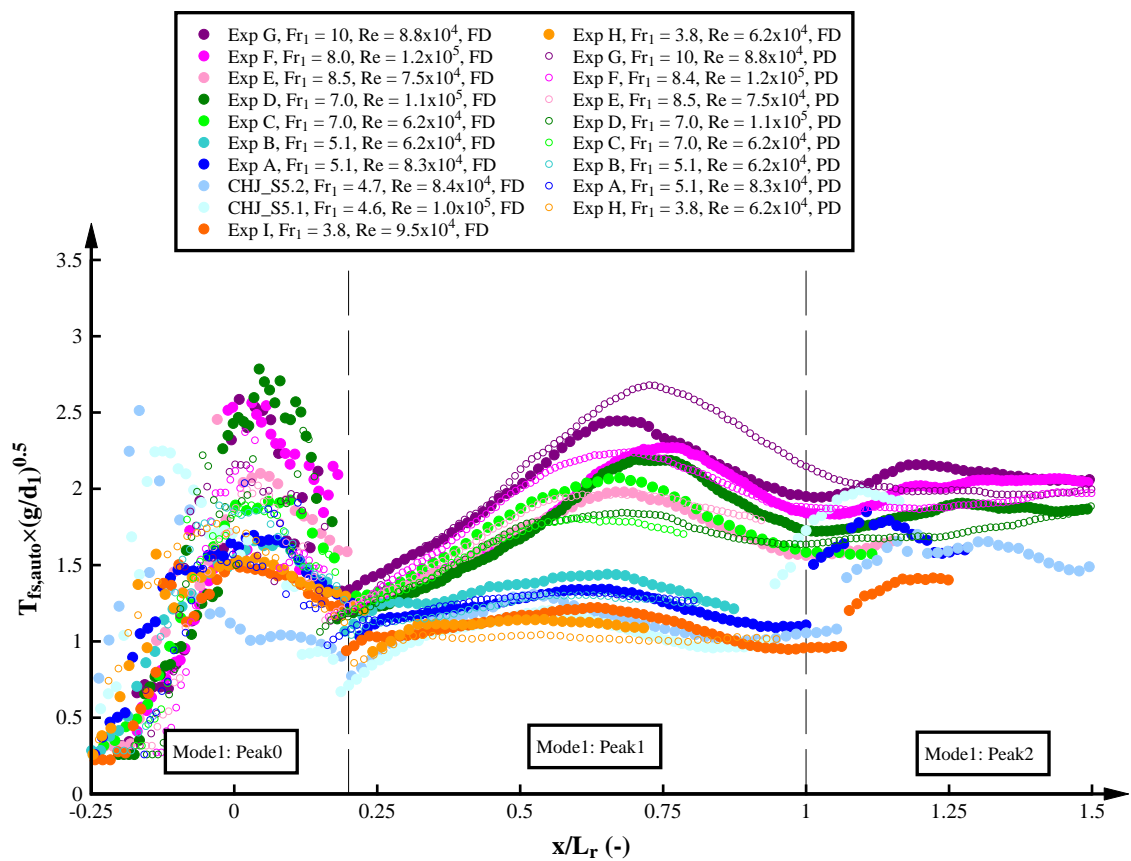


FIGURE 5–20. FREE-SURFACE AUTO-CORRELATION TIME SCALES ALONG HYDRAULIC JUMPS WITH FULLY (FD) AND PARTIALLY (PD) DEVELOPED INFLOW CONDITIONS FOR MODE 1.

Figure 5-21 presents all present free-surface auto-correlation time scales for Mode 2 as function of $x/x_{Mode2:Peak1}$ where $x_{Mode2:Peak1}$ represents the distance at the position of the first peak in $T_{fs,auto}$ (Mode2: Peak1). Independent of the Froude and Reynolds numbers and inflow

conditions, $T_{fs,auto}$ in Mode 2 had similar shapes for all experiments. An increase in $T_{fs,auto}$ was observed with increasing Fr_1 . The sudden increase in $T_{fs,auto}$ in the roller region was only observed for the stronger and more aerated hydraulic jumps ($Fr_1 \geq 7$ and $Re \geq 8.8$). Despite hydraulic jumps with partially developed inflow conditions presented the same distribution in the auto-correlation time scale in Mode 2, smaller peaks in the roller region were identified which may be linked with lesser aeration and lesser fluctuations in these hydraulic jumps.

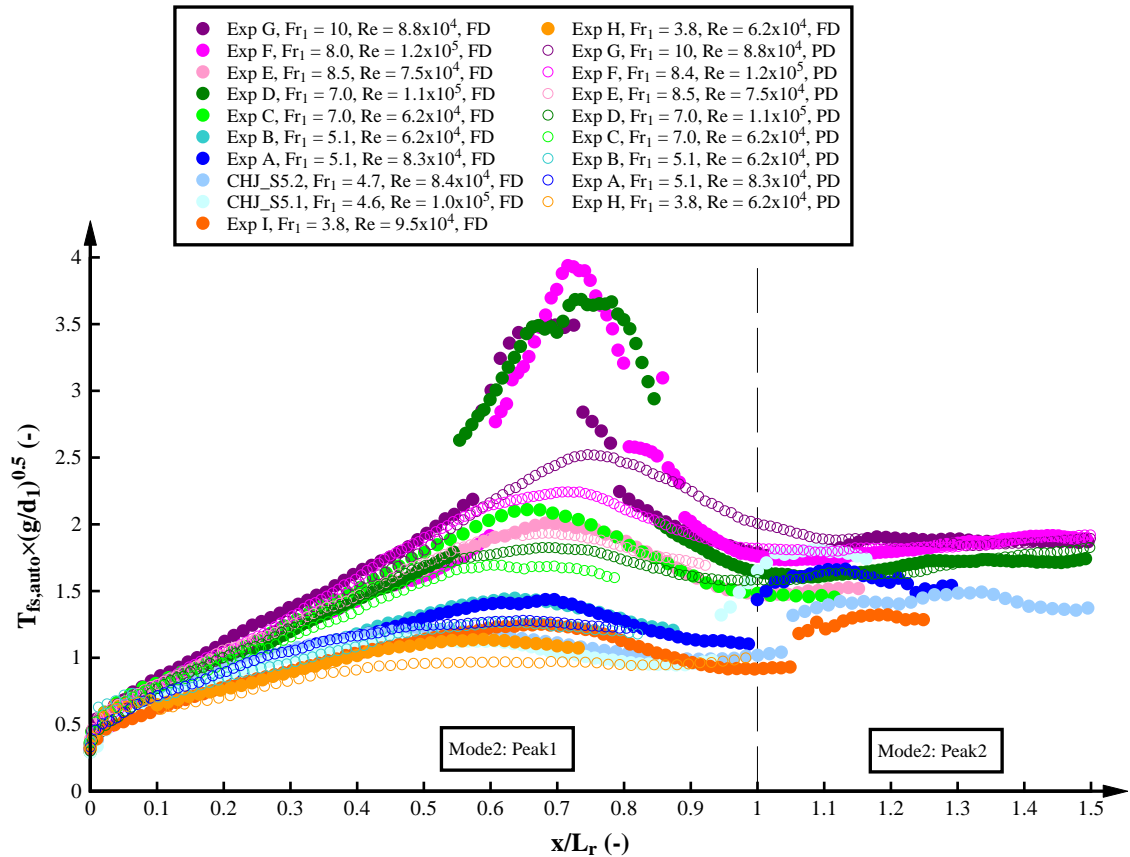


FIGURE 5–21. FREE-SURFACE AUTO-CORRELATION TIME SCALES ALONG HYDRAULIC JUMPS WITH FULLY (FD) AND PARTIALLY (PD) DEVELOPED INFLOW CONDITIONS FOR MODE 2.

The maximum peaks in the auto-correlation time scales $T_{fs,auto_max} \times (g/d_1)^{0.5}$ were identified in three different regions of the hydraulic jumps comprising the jump toe region (Mode1: Peak0), the roller region (Mode1: Peak1; Mode2: Peak1) and the conjugate depth region (Mode1: Peak2; Mode2: Peak2). The peak values for all hydraulic jumps are shown in Figure 5-22 as function of Fr_1 . Figure 5-22A shows the maximum auto-correlation time scales for Mode1: Peak0. The maximum auto-correlation time scales showed large data scatter linked with the effect of the d_1 in the raw signal. Apart from the data scatter, $T_{fs,auto_max} \times (g/d_1)^{0.5}$ increased with increasing Froude number and slight larger $T_{fs,auto_max} \times (g/d_1)^{0.5}$ were observed for partially developed hydraulic jumps. For $Fr_1 \geq 7$, the auto-correlation time scales at the jump toe region were almost constant suggesting similar advective motions in the strongest hydraulic jumps.

Figure 5-22B shows the maximum auto-correlation time scales for Mode1: Peak1 in the roller region. $T_{fs,auto_max} \times (g/d_1)^{0.5}$ increased with increasing Fr_1 for both fully and partially developed inflow conditions. While $T_{fs,auto_max} \times (g/d_1)^{0.5}$ for fully developed conditions was slightly larger for $Fr_1 \leq 7.0$, $T_{fs,auto_max} \times (g/d_1)^{0.5}$ was similar for $Fr_1 > 7$. Similar results were observed for the maximum peaks in Mode 2 (Mode2:Peak1) (Figure 5-22C). Larger auto-correlation time scales were observed for fully developed inflow conditions for $Fr_1 \leq 7.0$. These results indicated that for $Fr_1 \leq 7.0$, the advective structures are larger for hydraulic jumps with fully developed inflow conditions. Note that for $Fr_1 > 7$, larger $T_{fs,auto_max} \times (g/d_1)^{0.5}$ were observed in Mode 2 in fully developed inflow conditions linked with a mostly positive correlations for large Reynolds numbers. An increase in the auto-correlation time scales with increasing Reynolds number was observed for Mode1:Peak0. Otherwise, no clear trend was observed between $T_{fs,auto_max} \times (g/d_1)^{0.5}$ and the Reynolds number.

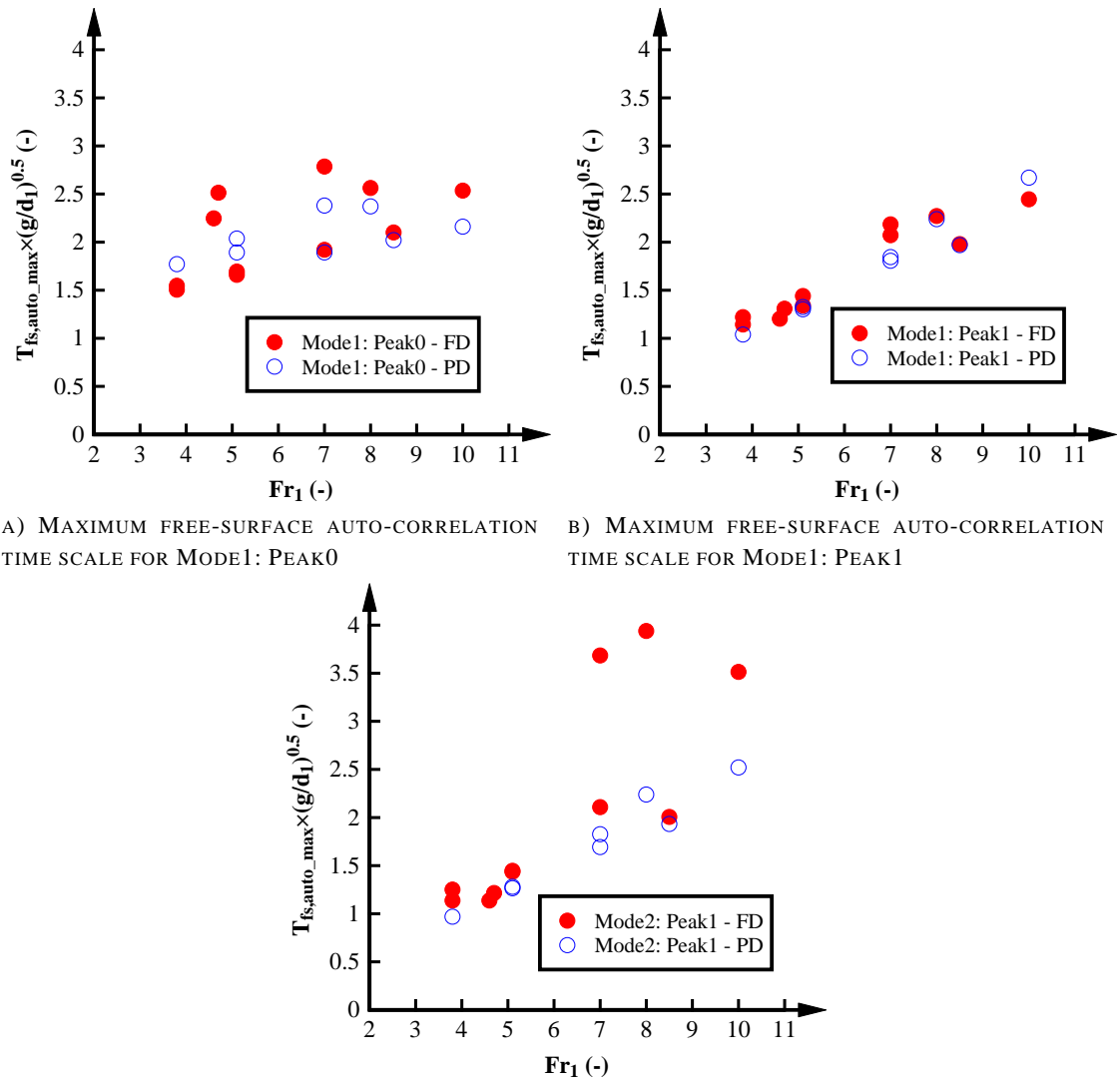


FIGURE 5-22. FREE-SURFACE AUTO-CORRELATION TIME SCALES FOR HYDRAULIC JUMPS WITH FULLY (FD) AND PARTIALLY (PD) DEVELOPED INFLOW CONDITIONS

5.8. CROSS-CORRELATION TIME SCALES

The longitudinal cross-correlation time scale $T_{fs,cross}$ provided a measure of the longitudinal coherent free-surface structures of hydraulic jumps based on the distance between two points of known distance (Chachereau and Chanson 2010; Wang 2014). While the auto-correlation time scales were calculated for a single point location, the cross-correlation time scales were calculated for a range of separation distances Δx . Figure 5-23 shows typical dimensionless longitudinal cross-correlation time scales $T_{fs,cross} \times (g/d_1)^{0.5}$ for Mode 1 and fully and partially developed inflow conditions as a function of $\Delta x/d_1$ between a fixed point of analysis $(x/d_1)_0$ and the cross-correlated points measured within a distance $\Delta x/d_1$. The LIDAR delay between two adjacent points of analysis ($\Delta x \approx 1$ cm) with an angular resolution of 0.25° and frequency of 35 Hz was smaller than 4×10^{-5} s and was considered negligible. However, further research with higher sampling rates and angular resolution is suggested to test potential effects of the recording delay of two adjacent points on the cross-correlation time scales.

Independent of the starting points of the cross-correlation analyses, $T_{fs,cross} \times (g/d_1)^{0.5}$ declined with increasing distance between correlated data points $\Delta x/d_1$. This pattern was consistent for different regions along the hydraulic jump. The correlation time scale for $\Delta x/d_1 = 0$ corresponded to the auto-correlation time scale. Likewise, the curve of $T_{fs,cross} \times (g/d_1)^{0.5}$ at different $(x/d_1)_0$ was strongly influenced by the initial time scale value, i.e. $T_{fs,auto} = T_{fs,cross}$. In Figure 5-23, four distinct regions are shown reflecting different patterns of $T_{fs,cross} \times (g/d_1)^{0.5}$. While only selected points per region are shown, the behavior of all curves in each region was similar. In the region upstream of the mean jump toe, $-2.25 < (x/d_1)_0 < 0.09$, $T_{fs,cross} \times (g/d_1)^{0.5}$ increased with an increase in $(x/d_1)_0$ (Figure 5-23A) which was consistent with the increase in the auto-correlation functions and time scales. A sudden decline at $\Delta x/d_1 = 7.85$ suggested a strong drop in the structure coherence until this point. For a region close to the mean jump toe (Figure 5-23B), $0.87 < (x/d_1)_0 < 3.22$, the longitudinal cross-correlation time scales showed similar patterns and similar values for different locations $(x/d_1)_0$. Further downstream, for $4.00 < (x/d_1)_0 < 15.73$, (Figure 5-23C), $T_{fs,cross} \times (g/d_1)^{0.5}$ showed again an increase with an increase in $(x/d_1)_0$ representing the area of the roller region of the hydraulic jump. For $16.51 < (x/d_1)_0 < 40$, large cross-correlation time scales were observed reflecting the region of the maximum auto-correlation time scale at the roller region suggesting large coherence of the longitudinal turbulent free-surface structures of the hydraulic jump in the roller region. For all locations, $T_{fs,cross} \times (g/d_1)^{0.5}$ decreased with increasing $\Delta x/d_1$.

The cross-correlation shape was similar for hydraulic jumps with fully and partially developed inflow conditions with a decrease in $T_{fs,cross} \times (g/d_1)^{0.5}$ with increasing $\Delta x/d_1$. For $Fr_1 \leq 7$

(Figure 5-23), the advective coherent structures in the hydraulic jump were influenced by the inflow conditions and larger correlation was continuously observed for fully developed inflow conditions. Nonetheless, for $Fr_1 > 7$, the correlation was almost similar between fully and partially developed inflow conditions. The similarity in the cross-correlation time scale for larger Froude numbers suggested that the incoming turbulence upstream of the hydraulic jump may be negligible in the scenarios of large Froude numbers.

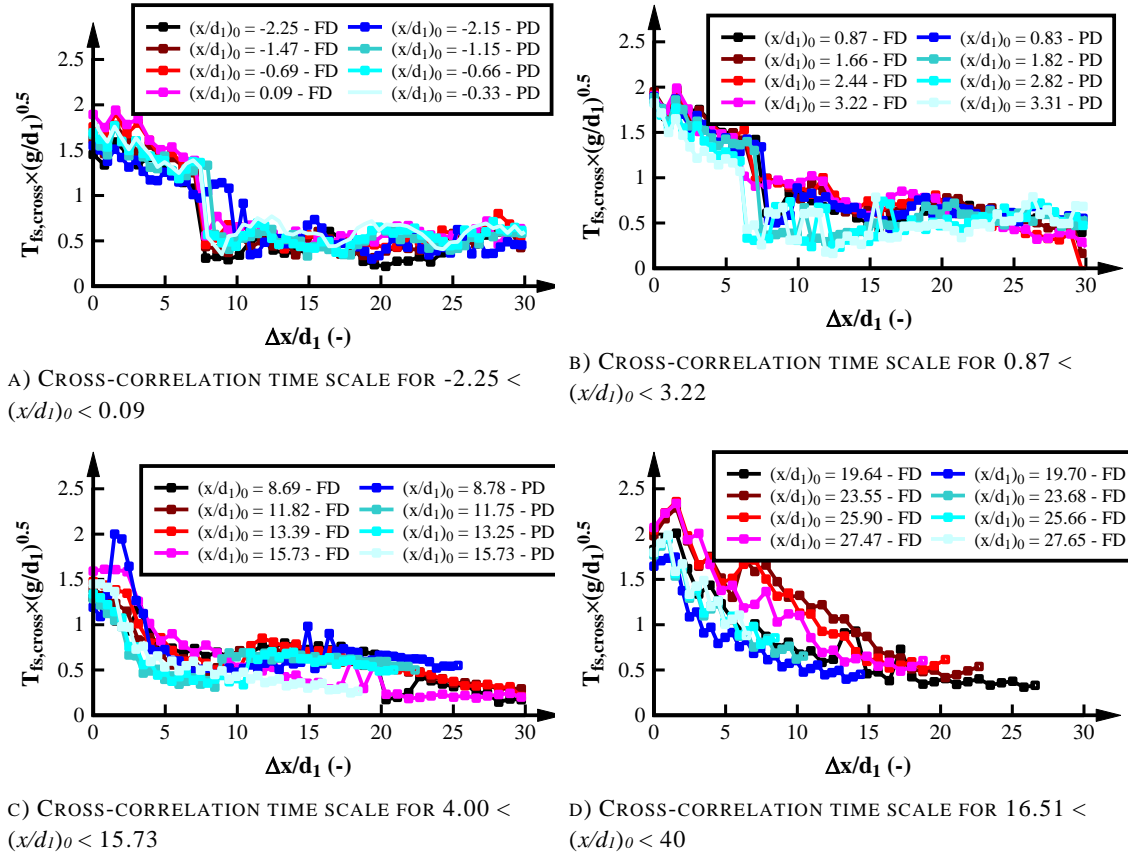


FIGURE 5–23. DIMENSIONLESS CROSS-CORRELATION INTEGRAL FREE-SURFACE TIME SCALES IN HYDRAULIC JUMPS WITH FULLY (FD) AND PARTIALLY (PD) DEVELOPED INFLOW CONDITIONS FOR MODE 1. EXPERIMENT C ($Fr_1 = 7.0$, $Re = 6.2 \times 10^4$).

5.9. INTEGRAL LENGTH SCALES

The free-surface integral length scales L_{fs} provide an estimation of the large streamwise turbulent structures of the free-surface motions along the hydraulic jump. They were calculated based upon the high-spatial resolution data for both data processing modes and Equation 3.8. The upper integration limit in the calculation of L_{fs} (Equation 3.8), Δx_{max} , is defined as the maximum separation distance between two free-surface locations where the correlation coefficients should be close to 0 (Murzyn et al. 2007). Figure 5-24 shows typical distributions of $R_{fs,cross_max}$ for different longitudinal hydraulic jump positions $(x/d_1)_0$. For all data shown in Figure 5-24, $R_{fs,cross_max}$ crossed the x-axis for $(x/d_1)_0 < 21$. For $(x/d_1)_0 > 21$, $R_{fs,cross_max}$ was always positive with

increasing minimum $R_{fs,cross_max}$ values with increasing $(x/d_1)_0$. For correlation functions with positive values of $R_{fs,cross_max}$, the selection of the minimum $R_{fs,cross_max}$ value was adopted as being the most meaningful upper integration limit for the calculation of the integral length scales.

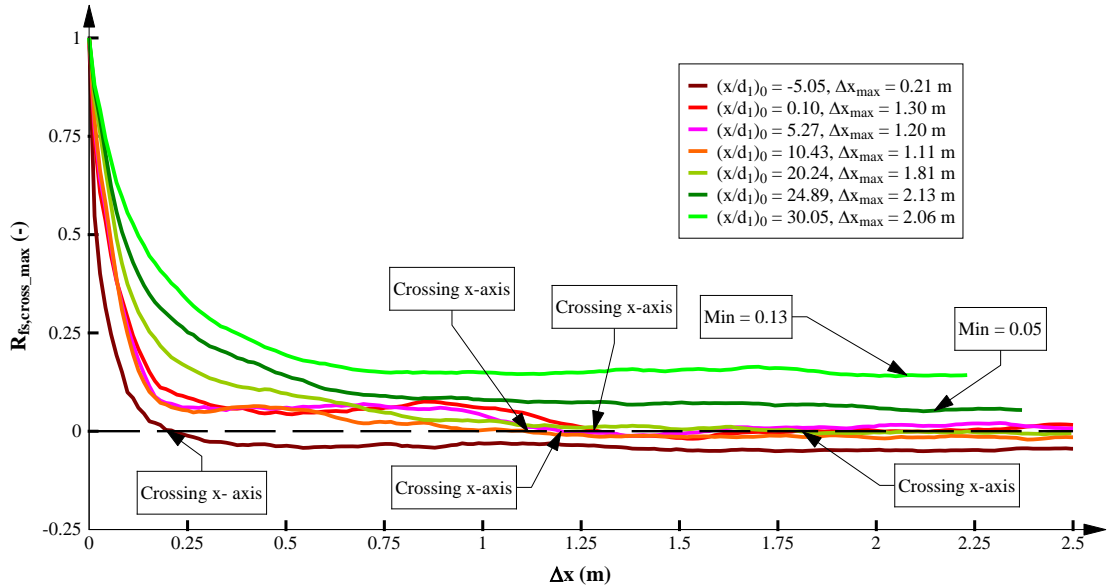


FIGURE 5–24. MAXIMUM CROSS-CORRELATION COEFFICIENTS ALONG A HYDRAULIC JUMP.

The maximum cross-correlation coefficient provided the longitudinal correlation between two points of analysis. Figure 5-25 shows typical values of $R_{fs,cross_max}$ as function of the normalized dimensionless separation distance $(\Delta x/d_1)/(\Delta x/d_1)_{30}$, where $(\Delta x/d_1)_{30}$ corresponded to $R_{fs,cross_max} = 0.3$ following the approach by Chachereau and Chanson (2011b). Figure 5-25 includes the present LIDAR data for fully and partially developed inflow conditions, ADM data from Chachereau and Chanson (2011b) and the empirical equation of Chachereau and Chanson (2011b) ($R_{fs,cross_max} = \exp[-1.24 \times (\Delta x/d_1)/(\Delta x/d_1)_{30}]$) for experiments conducted with similar Froude and Reynolds numbers. The present maximum cross-correlation coefficients showed good agreement with previous experimental data and fitted well with a logistic equation with $R^2 = 0.98$:

$$R_{fs,cross_max} = - \frac{0.077}{(1 - 1.075 \times e^{0.156[(\Delta x/d_1)/(\Delta x/d_1)_{30}]})} \quad (5.6)$$

A good agreement of LIDAR data and the empirical equation of Chachereau and Chanson (2011b) was in particular observed for $(\Delta x/d_1)/(\Delta x/d_1)_{30} < 1$. Further downstream for $(\Delta x/d_1)/(\Delta x/d_1)_{30} > 1$, the exponential decay was followed by a slight increase in the maximum correlation coefficients associated with large data scatter and an increase of non-detected data points towards the downstream end of the roller. Despite the data scatter, Equation 5.6 predicted the decay in maximum correlation coefficients well (Figure 5-25).

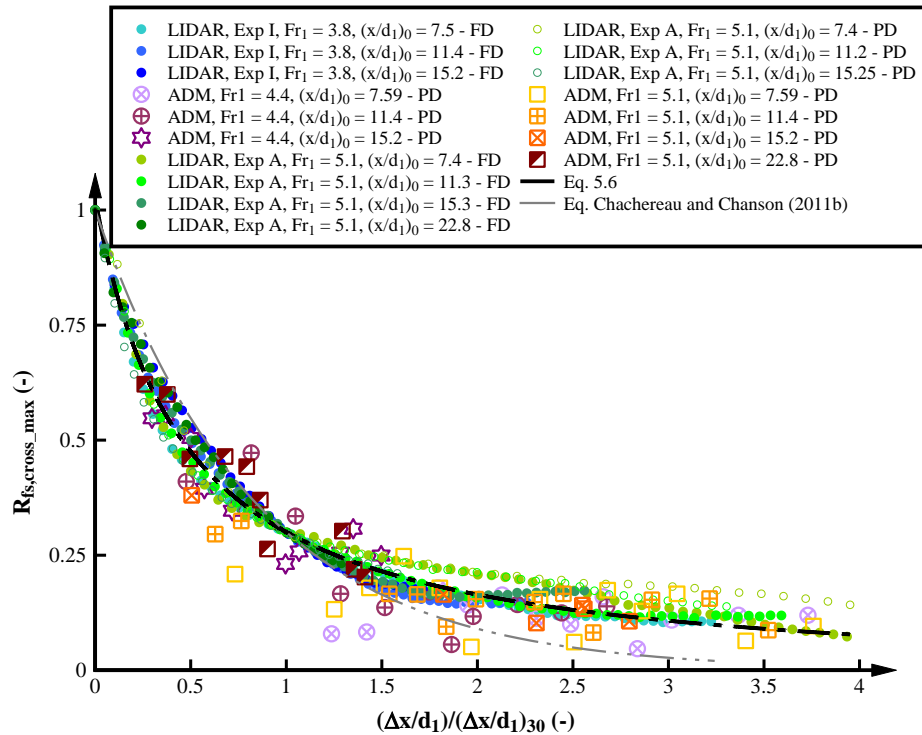


FIGURE 5–25. MAXIMUM CROSS-CORRELATION COEFFICIENTS IN HYDRAULIC JUMPS WITH FULLY (FD) AND PARTIALLY (PD) DEVELOPED INFLOW CONDITIONS AS FUNCTION OF THE NORMALIZED DIMENSIONLESS SEPARATION DISTANCE; COMPARISON WITH EQUATION 5.5 AND ADM DATA AND EMPIRICAL EQUATION OF CHACHEREAU AND CHANSON (2011B).

Figure 5-26 shows the integral free-surface length scales as function of x/d_1 for two example cases and for both processing modes and fully and partially developed inflow conditions. For Mode 1, L_{fs} started upstream of the mean jump toe location increasing to a maximum length scale L_{fs_max} close to the mean jump toe position. This peak may be related to the jump toe oscillations leading to a frequent recording of $d = d_1$ and an increase in cross-correlation values. Further downstream, a small second peak was observed in the roller region which was most pronounced for hydraulic jumps with strongest aeration (Figure 5-26B). A small third peak in the conjugate depth region was only observed in hydraulic jumps with large Froude and Reynolds numbers. The length scales for Mode 2 increased sharply from $x/d_1 = 0$ until $L_{xy,max}$ at the beginning of the roller region. It appeared that the positioning of the free-surface profiles at the mean jump toe position increased the similarity of the free-surface profiles leading to an increase in cross-correlation coefficients and resulting length scales. The similarities in free-surface features appeared to increase with Fr_1 . Two further peaks for Mode 2 were consistent with Mode 1 for large Froude and Reynolds numbers (Figure 5-26). Note that the estimation of the length scales was limited to the roller region due to an increasing number of meaningless data in the conjugate depth region linked with low flow aeration. The calculation of the length scales was stopped when less than 50% of data points were valid. The length scales in the later part of the

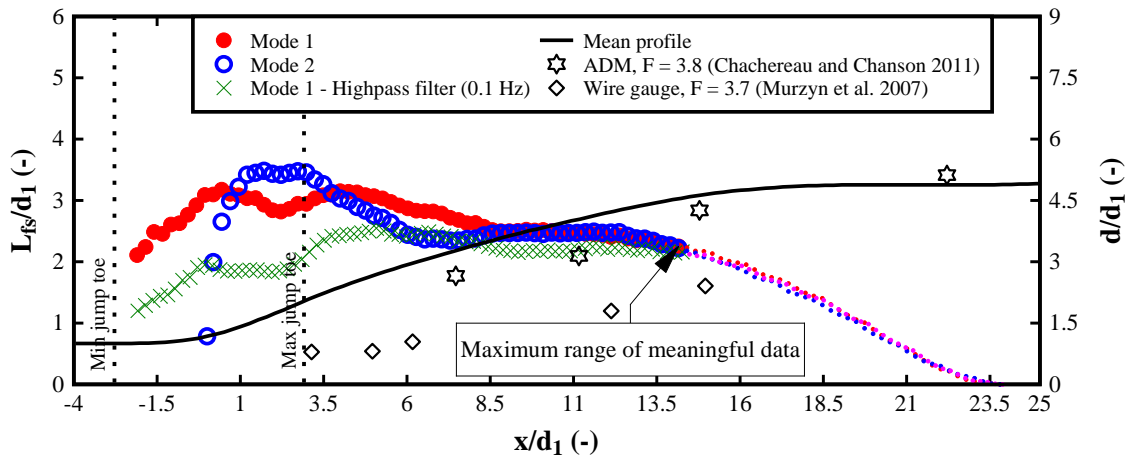
hydraulic jump are therefore shown with reduced symbol sizes providing only limited information on the length scales in the low aerated part of the hydraulic jumps.

The length scales resulting from a high-pass filtering of 0.1 Hz are also shown in Figure 5-26. While the high-pass filter removed the slow motions of the hydraulic jump leading to a reduction in free-surface scales close to the jump toe, further downstream the free-surface scales were also affected despite little influence of the jump toe movements. The cross-correlation function was strongly affected by the high-pass filtering, resulting in a drop of the length scales close to the jump toe. In contrast, the post-processing with Mode 2, i.e. the “perfect” jump motion filter, provided contrary results indicating an increase in the cross-correlation function and associated length scales. This result suggested that the high-pass filtering may not remove the jump toe oscillations, but reduce the magnitude of the free-surface scales more generally. Mode 2 was effective in the removal of the jump toe movements on the free-surface scales without affecting the raw free-surface data (Figures 5-26). Herein the free-surface scales in the latter part of the hydraulic jump were similar for Mode 1 and Mode 2 suggesting that the effect of the jump toe movements was spatially limited. .

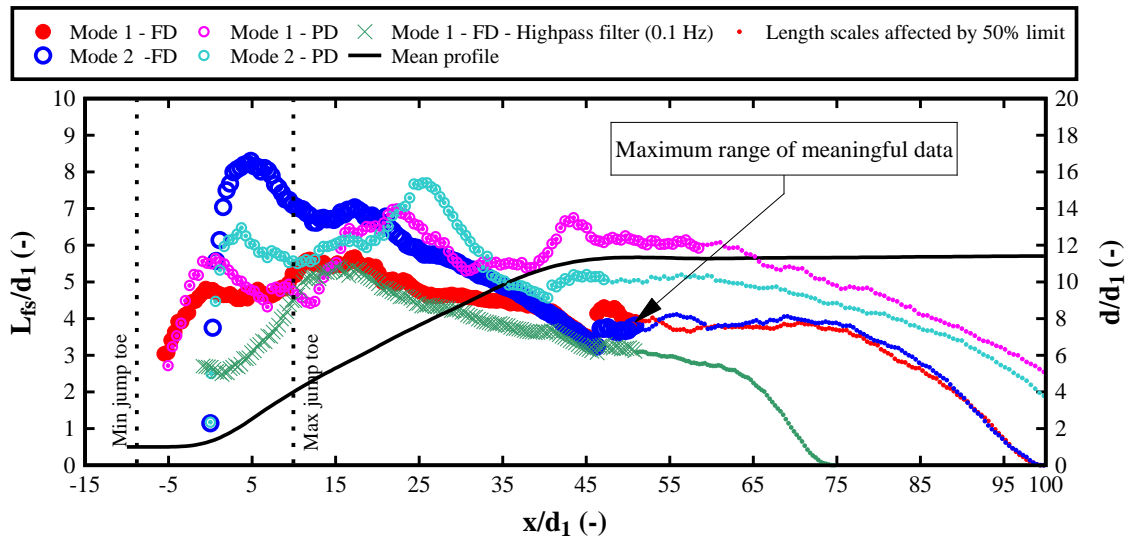
Figure 5-26A also shows a comparison of the present data with length scales observed with ADMs with $\Delta x_{max} = 0.23$ m (Chachereau and Chanson 2011b) and wire gauges with $\Delta x_{max} = 0.10$ m (Murzyn et al. 2007) for comparable Froude numbers. Note that the estimation of the free-surface scales in previous studies was limited by the fixed positioning of the instrumentation. For both previous studies, the length scales were overall lower and increased with increasing distance from the jump toe. While the order of magnitude of the length scales was similar, the observations highlighted some distinct differences which could not be fully explained. The differences may be associated with the different instrumentation, more detailed spatial information obtained with the LIDAR resulting in a better identification of ΔX_{max} , and the fixed upper integration limits used by Chachereau and Chanson (2011b). Other reasons could be linked with different experimental facilities, inflow conditions as well as potential differences in the footprint and the resulting penetration depth of the LIDAR beam and the ADMs. Simultaneous measurements using LIDAR, ADMs and wire gauges is strongly recommended to allow a direct comparison of the free-surface time and length scales obtained with different instrumentation. Such a comparative analysis should also include all other free-surface properties.

The shape of the length scale was similar for hydraulic jumps with fully and partially developed inflow conditions. For the condition of free jump toe movement, the length scale along the hydraulic jump was larger in fully developed hydraulic jumps with $Fr_1 < 7$ and smaller for $Fr_1 > 7$. This result suggested that for large Froude number, hydraulic jumps with fully developed

inflow conditions and at regions located close to the jump toe presented smaller flow structures maybe linked with stronger fluctuations and instabilities. Note that the estimation of L_{fs} in hydraulic jumps with $Fr_1 < 7$ was strongly affected by the range of valid data and the larger L_{fs} in fully developed flows may be related by longer valid data region in these hydraulic jumps. For a fixed jump toe movement (Mode 2), hydraulic jumps with fully developed inflow conditions showed larger L_{fs} close to the jump toe and smaller L_{fs} at the roller region in agreement with the results of Mode 1.



A) EXPERIMENT I: $Fr_1 = 3.8$, $Re = 9.5 \times 10^4$; COMPARISON WITH PREVIOUS DATA OF CHACHEREAU AND CHANSON (2011B) WITH $\Delta x_{max} = 0.23 \text{ m}$ AND MURZYN ET AL. (2007) WITH $\Delta x_{max} = 0.10 \text{ m}$



B) EXPERIMENT F: $Fr_1 = 8.0$, $Re = 1.2 \times 10^5$

FIGURE 5-26. INTEGRAL FREE-SURFACE LENGTH SCALES ALONG HYDRAULIC JUMPS WITH FULLY (FD) AND PARTIALLY (PD) DEVELOPED INFLOW CONDITIONS.

Figure 5-27 presents the dimensionless integral free-surface length scales for all experiments as function of x/L_r for Mode 2. Independent of the Froude number, the distributions of L_{fs} had similar shapes for all experiments. The length scales increased with increasing Fr_1 . Two

length scale peaks were observed. One peak was located close to the jump toe and the second peak was located at the jump roller. For most experiments, the largest peak was located close to the jump toe region. Additionally, for large Reynolds numbers ($Re > 8 \times 10^4$), a large drop in the length scale was observed at the roller region of the jump related to the transition between the roller region and the conjugate flow depth region.

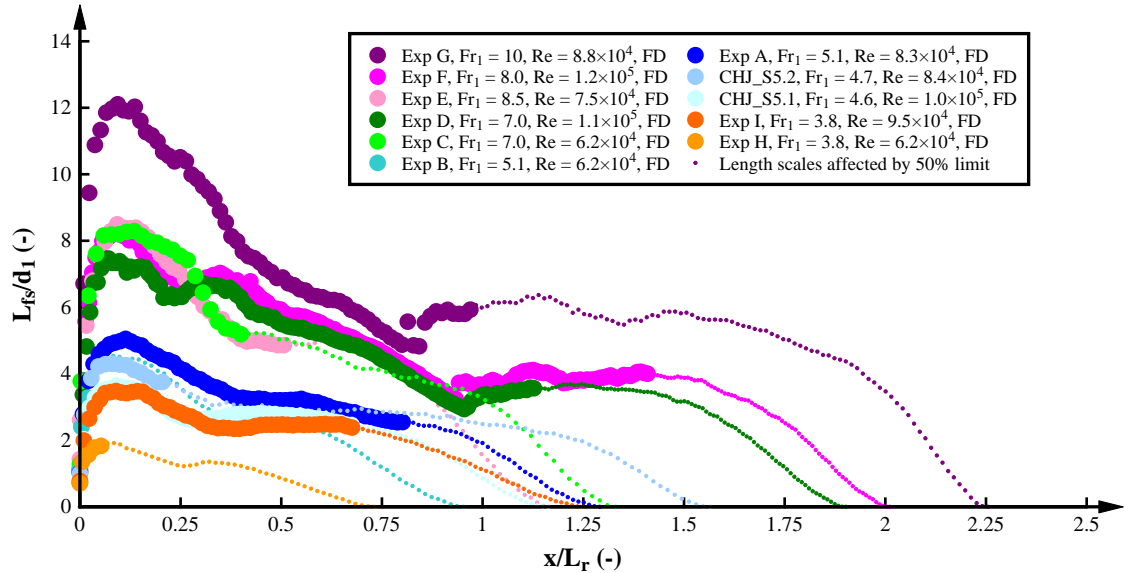


FIGURE 5-27. INTEGRAL FREE-SURFACE LENGTH SCALES ALONG HYDRAULIC JUMPS WITH FULLY DEVELOPED INFLOW CONDITIONS (FD) FOR MODE 2.

Figure 5-28 presents the dimensionless maximum length scales L_{fs_max}/d_1 as function of Fr_1 for both processing modes and fully and partially developed inflow conditions. For Mode 1 and fully developed inflow conditions, L_{fs_max}/d_1 was almost constant despite some data scatter with an average of $L_{fs_max}/d_1 = 4.9$ suggesting similar dimensionless scales in the jump toe region independent of the Froude number. In contrast, L_{fs_max}/d_1 for Mode 2 increased linearly with increasing Froude number ($R^2 = 0.98$):

$$\frac{L_{fs_max}}{d_1} = 1.452(Fr_1 - 1.952) \quad (5.7)$$

The range of dimensional maximum length scales for Mode 1 was $6 < L_{fs_max} < 26$ cm with most data of $6 < L_{fs_max} < 14$ cm and for Mode 2 $6 < L_{fs_max} < 24$ cm. For Mode 1 and partially developed inflow conditions, lower length scale peaks were observed for partially developed inflow conditions and $Fr_1 \leq 5.1$ (Figure 5-28). The lower values may be related to the lower aeration in partially developed inflow conditions as indicated in Chapter 4 resulting in a smaller integration area in Equation 3.8. For $Fr_1 > 7.0$, the length scales were similar to the length scales identified in fully developed inflow conditions. Lower free-surface integral length scales close to the jump toe were observed for partially developed inflow conditions in Mode 2 with average

reduction of about 30% (Figure 5-28). The results suggested larger streamwise structures for fully developed hydraulic jumps for Mode 2.

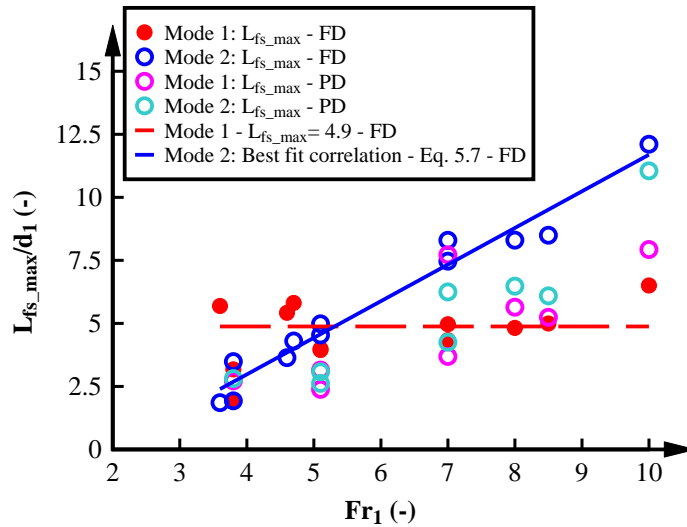


FIGURE 5-28. MAXIMUM INTEGRAL FREE-SURFACE LENGTH SCALES AS FUNCTION OF THE INFLOW FROUDE NUMBER IN HYDRAULIC JUMPS WITH FULLY (FD) AND PARTIALLY (PD) DEVELOPED INFLOW CONDITIONS; COMPARISON WITH EQUATION 5.6 FOR MODE 2.

5.10. SCALE EFFECTS

The present chapter presents an analysis of the scale effects in free-surface features in hydraulic jumps for a wide range of Reynolds numbers ($6.2 \times 10^4 < Re < 1.2 \times 10^5$) and in terms of Froude similitude. Hydraulic jumps with larger Reynolds numbers are represented with solid darker symbols.

The scale effect analysis of d'_{max} , x_{toe} , $freq_{toe}$ and $freq_{fs}$ are included in Figure 5-29. The maximum free-surface fluctuations and the jump toe oscillations were similar for the range of Reynolds numbers analysed suggesting no scale effects (Figure 5-29A and B). The scale effects in the jump toe frequencies were analysed in terms of the Strouhal number $freq_{toe} \times d_1 / V_1$ (Figure 5-29C). Despite data scatter, the ranges of Strouhal numbers showed a slight increase with increasing Reynolds number suggesting minor scale effects. The effects of Froude similitude on the characteristic free-surface frequencies were investigated for Mode 1. The analysis was conducted for both dominant $freq_{fs(dom)}$ and secondary frequencies $freq_{fs(sec)}$ in the jump toe region (Figure 5-29D and E) and in the roller region (Figure 5-29F). All frequencies are presented in terms of a Strouhal number. Overall, no scale effects were identified in the characteristic frequencies of the free-surface (Figure 5-29D - F). Nonetheless, some deviations were observed for hydraulic jumps located downstream of the sloped channel linked with differences in the frequency patterns and flow conditions as indicated in Chapter 5.5. The results disagreed with the findings of Wang (2014). This difference may be linked with the analysis of a range of

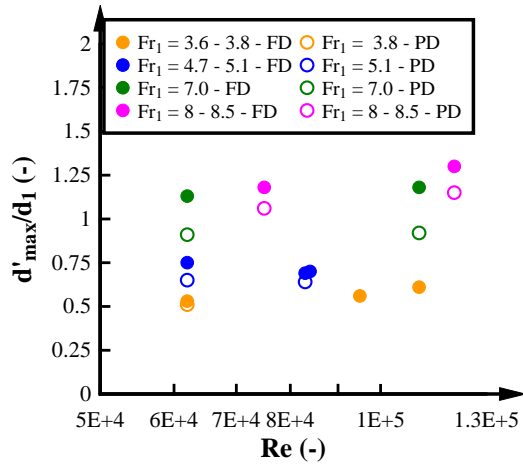
characteristic frequencies in the present study compared to a single value in the study of Wang (2014). Nonetheless, the frequency magnitude is similar between both studies. Overall, the results on the basic free-surface features were consistent between hydraulic jumps with fully and partially developed inflow conditions and were in agreement with the findings of Wang (2014), Wang and Chanson (2016c) in hydraulic jumps with partially developed inflow conditions.

The free-surface turbulent scales are presented in Figure 5-30. Figure 5-30A shows the maximum auto-correlation time scale in the jump toe region (Mode1: Peak0) as function of the Reynolds number. For the same inflow Froude number, the maximum peak in the auto-correlation time scale showed an increase with increasing Reynolds number. Some data scatter was observed which may be linked to the sensibility of the auto-correlation time scale estimation to changes in the maximum integration limit of the auto-correlation time scale equation (Equation 3.6). Figure 5-30B shows the scale effects analysis for the maximum auto-correlation time scale at the roller region of Mode 1 (Mode1: Peak1). Despite some data scatter, the maximum peak was similar for the same Froude number and different range of Reynolds numbers indicating no scale effects in terms of Froude similitude. Without considering the large peaks in fully developed inflow conditions for the large Reynolds numbers, the maximum peak in the auto-correlation function for Mode2: Peak 1 remained almost constant with the same Froude number suggesting no scale effects in terms of Froude similitude (Figure 5-30C).

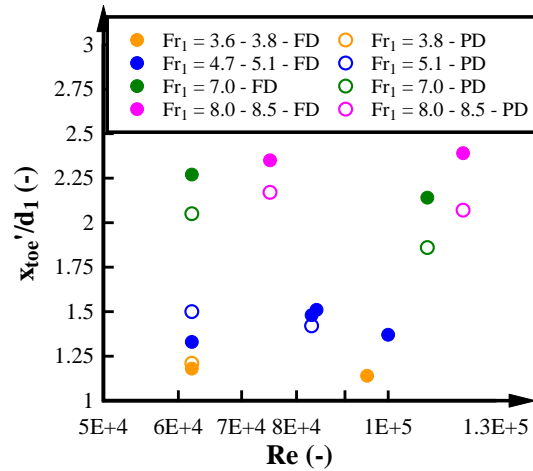
Figures 5-30D present the maximum integral length scale for Mode 1 in terms of a Froude similitude. Large data scatter was observed and no clear trend was observed in terms of Froude similitude. The scatter was linked with the strong dependence of the length scale and the valid aerated region. Figure 5-30E shows the scale effects for the maximum length scale for Mode 2. Despite some data scatter, similar length scales were observed for different Reynolds numbers suggesting no scale effects. The overall results were consistent for fully and partially developed inflow conditions.

Free-surface dynamics and internal motions in fully aerated hydraulic jumps

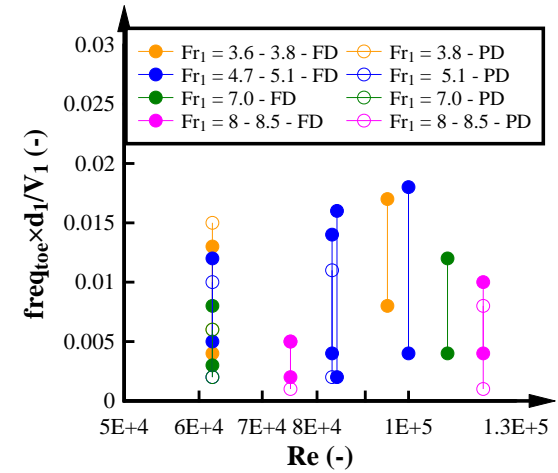
Chapter 5. Free-surface characteristics and jump toe oscillations



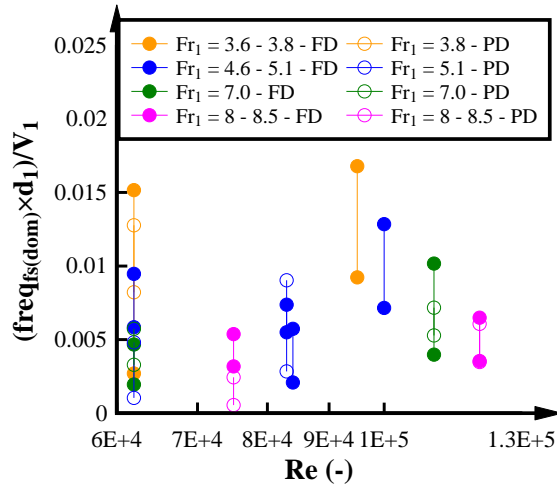
A) FREE-SURFACE FLUCTUATIONS



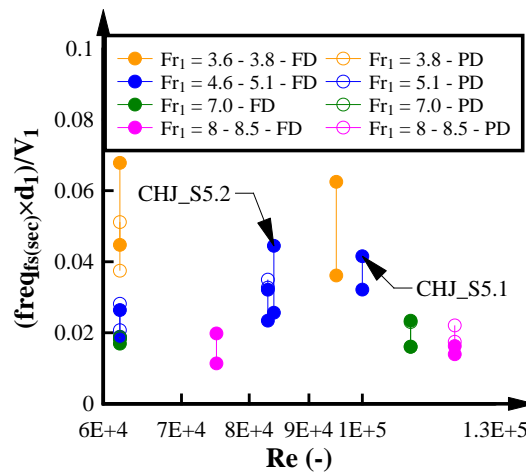
B) JUMP TOE OSCILLATIONS



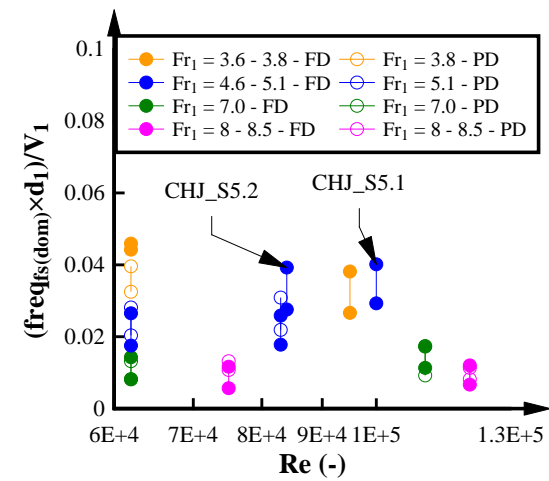
C) JUMP TOE DOMINANT FREQUENCY



D) DOMINANT FREQUENCY FREE-SURFACE FLUCTUATIONS (JUMP TOE REGION)



E) SECONDARY FREQUENCY FREE-SURFACE FLUCTUATIONS (JUMP TOE REGION)



F) DOMINANT FREQUENCY FREE-SURFACE FLUCTUATIONS (ROLLER REGION)

FIGURE 5-29. SCALE EFFECTS IN FREE-SURFACE FEATURES IN HYDRAULIC JUMPS WITH FULLY (FD) AND PARTIALLY (PD) DEVELOPED INFLOW CONDITIONS.

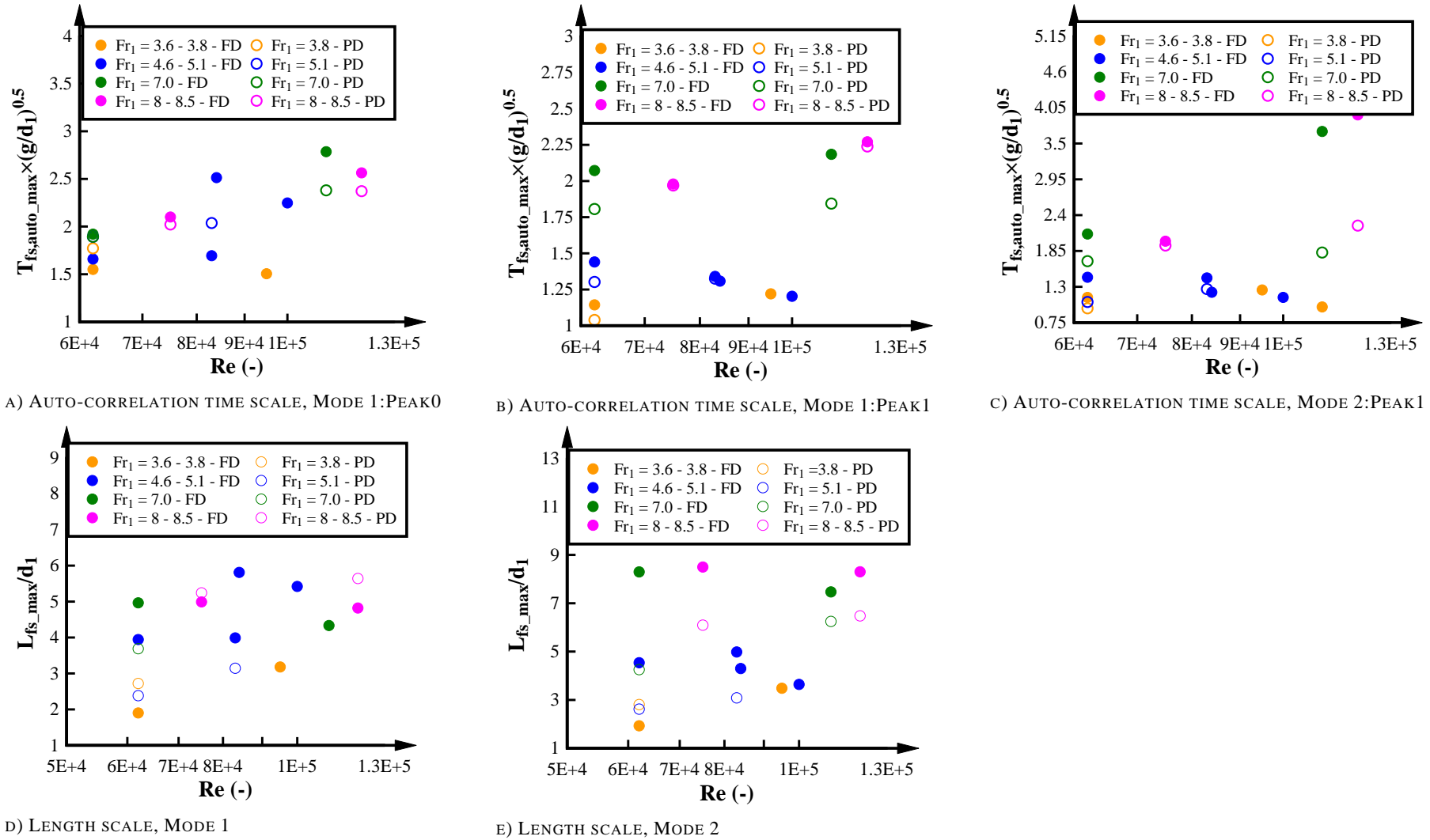


FIGURE 5–30. SCALE EFFECTS IN FREE-SURFACE TURBULENT SCALES IN HYDRAULIC JUMPS WITH FULLY (FD) AND PARTIALLY (PD) DEVELOPED INFLOW CONDITIONS.

5.11. SUMMARY

The free-surface features in aerated hydraulic jumps with fully and partially developed inflow conditions were investigated for a wide range of Froude and Reynolds numbers with a LIDAR. The LIDAR was able to measure the time-varying free-surface profiles and jump toe positions within the aerated flow regions non-intrusively and continuously. The raw LIDAR signals with high-spatial and temporal resolution were analysed using two approaches comprising a freely moving jump (Mode 1) and a fixed jump toe position (Mode 2). The present study investigated the use of a LIDAR in hydraulic jumps for the first time. The close agreement with previous data validated the use of a LIDAR as a non-intrusive instrumentation in hydraulic jumps. Herein the LIDAR provided the spatially most detailed observations of the time-varying free-surface profiles to date.

The mean free-surface profiles and the 10th and 90th percentiles presented close similarities between both analysis modes with some deviations close to the jump toe position. Large free-surface fluctuations were observed close to the jump toe for Mode 1 and Mode 2 with slightly larger free-surface fluctuations for Mode 2. Jump toe amplitude and oscillations were also measured with the LIDAR indicating larger jump toe amplitudes and oscillations with increasing Froude numbers. An FFT of the jump toe oscillations showed characteristic frequencies in a range of $0.2 < F_{toe} < 1.6$ Hz. A continuous spectral analysis of the free-surface fluctuations was conducted identifying three characteristic free-surface regions within hydraulic jumps comprising the jump toe region, the roller region and the conjugate depth region. Within these flow regions, the characteristic dominant frequencies were $0.2 \leq freq_{fs(dom)} \leq 1.5$ Hz, $1.5 \leq freq_{fs(dom)} \leq 4$ Hz and $0.1 \leq freq_{fs(dom)} \leq 3$ Hz respectively.

Advanced signal processing based upon auto- and cross-correlation analyses provided continuous estimates of the free-surface time and length scales. Characteristic maxima in auto-correlation time scales were observed close to the jump toe for Mode 1 as well as in the roller region and conjugate flow depth regions. The maximum auto-correlation time scales in the roller and conjugate flow depth regions increased with increasing Froude number while a more constant value was observed close to the jump toe.

The free-surface cross-correlation time scales were also calculated as a measure of the longitudinal free-surface structures in the hydraulic jump between two points of analysis. The maximum cross-correlation time scale values were closely linked to the auto-correlation time scales for both processing modes showing larger cross-correlation values for Mode 1 close to the jump toe. The cross-correlation analysis was used for the calculation of the free-surface length

scales which was strongly affected by the jump toe movement and the hydraulic jump roller. For both analysis modes, maxima in free-surface length scales were observed close to the jump toe. For Mode 2, the maximum length scales increased with increasing Froude number, while they were almost constant for Mode 1. It appeared that Mode 2 was an effective approach to separate the jump toe oscillations from the free-surface fluctuations providing a robust estimation of the free-surface time and length scales within fully aerated hydraulic jumps.

Overall, the analysis of the free-surface features along the hydraulic jump highlighted different regions (Figure 5-31): The jump toe region characterised by large jump toe oscillations, increase in the free-surface fluctuations, lower frequencies and larger turbulent scales; the roller region characterised by the maximum free-surface fluctuation peak followed by a decrease in the free-surface fluctuations and turbulent scales and an increase in the free-surface frequencies; and the conjugate depth region characterised as an stable region with lower fluctuations, turbulent scales and free-surface frequencies. While the free-surface parameters behaved different in each region, a strong interaction and influence of the jump toe movements was continuously observed along the hydraulic jump.

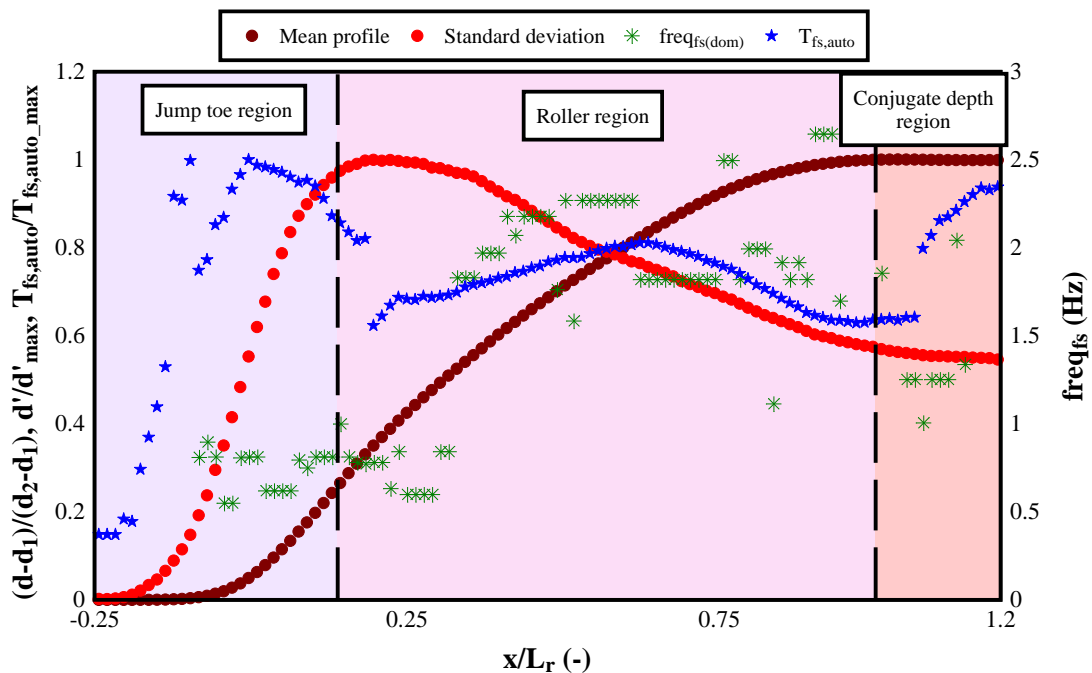


FIGURE 5-31. COMPILATION OF THE FREE-SURFACE PARAMETERS IN THE HYDRAULIC JUMP – MODE 1 (EXPERIMENT I: $Fr_1 = 3.8$, $Re = 9.5 \times 10^5$ FULLY DEVELOPED INFLOW CONDITIONS).

The inflow conditions upstream the hydraulic jump showed an effect in the free-surface features of the hydraulic jump. Larger conjugate depths, a steeper free-surface profile, stronger jump toe oscillations, and larger auto-correlation time scales and length scales were observed in fully developed hydraulic jumps. This result highlights stronger instabilities and oscillations in

fully developed hydraulic jumps linked with the upstream turbulence. Further research in the free-surface features analysis in hydraulic jumps should therefore consider the inflow conditions. Table 5-3 presents a summary of the effect of the inflow conditions and the scale effects in the free-surface parameters of hydraulic jumps.

TABLE 5-3. SUMMARY TABLE OF THE EFFECT OF THE INFLOW CONDITIONS AND SCALE EFFECTS ON THE FREE-SURFACE PARAMETERS OF HYDRAULIC JUMPS

Parameter	Comparison PD vs FD	Scale effects
		Froude similitude $6.2 \times 10^4 < Re < 1.2 \times 10^5$
Time-averaged free-surface profile d	Flatter free-surface profile in PD Lower d_2/d_1 in PD	
Maximum free-surface fluctuations d'_{max}/d_1	Lower maximum free-surface fluctuations in PD	No scale effects
Jump toe oscillations x_{toe}/d_1	Lower jump toe oscillations in PD	No scale effects
Jump toe dominant frequency $(F_{toe} \times d_1)/V_1$	Slight lower dominant frequency range in PD	Minor Scale effects (average Strouhal number): Slight increase in $(F_{toe} \times d_1)/V_1$ with increasing Re
Free-surface dominant frequency in the jump toe region $(F_{fs(dom)} \times d_1)/V_1$	No clear differences	No scale effects
Free-surface secondary frequency in the jump toe region $(F_{fs(sec)} \times d_1)/V_1$	No clear differences	No scale effects
Free-surface dominant frequency in the roller region $(F_{fs(dom)} \times d_1)/V_1$	No clear differences	No scale effects
Maximum free-surface auto-correlation time scale at the jump toe region for Mode 1 $(T_{fs,auto_max} \times (g/d_1)^{0.5} - \text{Mode1:Peak0})$	No clear differences	Scale effects: Increase in $(T_{fs,auto_max} \times (g/d_1)^{0.5})$ with increasing Re
Maximum free-surface auto-correlation time scale at the roller region for Mode 1 $(T_{fs,auto_max} \times (g/d_1)^{0.5} - \text{Mode1:Peak1})$	Lower $T_{fs,auto_max} \times (g/d_1)^{0.5}$ for $Fr_1 \leq 7$ in PD. Similar $T_{fs,auto_max} \times (g/d_1)^{0.5}$ for $Fr_1 > 7$.	No scale effects
Maximum free-surface auto-correlation time scale at the roller region for Mode 2 $(T_{fs,auto_max} \times (g/d_1)^{0.5} - \text{Mode2:Peak1})$	Lower $T_{fs,auto_max} \times (g/d_1)^{0.5}$ for $Fr_1 \leq 7$ in PD.	No scale effects
Maximum free-surface integral length scale close to the jump toe for Mode 1 L_{fs_max}	No clear differences	No clear trend
Maximum free-surface integral length scale close to the jump toe for Mode 2 L_{fs_max}	Lower L_{fs_max}/d_1 in PD.	No scale effects

6

INTERNAL FORCES IN HYDRAULIC JUMPS

Some content of this chapter is taken from the following publication:

Conference Proceedings

Montano, L, and Felder, S 2019, 'Measuring internal forces in a hydraulic jump with a load cell', in *Proc., 38th IAHR World Congress*, Panama City, Panama, 10 pages.

6.1. INTRODUCTION

The dissipative processes in hydraulic jumps are strongly related to the internal vortices and movements acting inside the jumps. The present study indirectly measured internal three dimensional motions for the first time. Figure 6-1 presents typical instantaneous 3D forces on a submerged sphere inside the hydraulic jump. The force signal corresponded to the forces exerted on the sphere representing the instantaneous trajectory of the sphere inside the hydraulic jump. The trajectory of the forces showed three-dimensional, oscillatory and unstable motions inside the hydraulic jump. The red point indicates the time-averaged position. An example high-resolution movie corresponding to the data in Figure 6-1 can be found in the Digital Appendix as Movie 6_1. Figure 6-1 highlights the need to consider the three-dimensionality of motions inside hydraulic jumps to fully understand the complexity of the interactions of flow aeration, free-surface fluctuations and large scale turbulence.

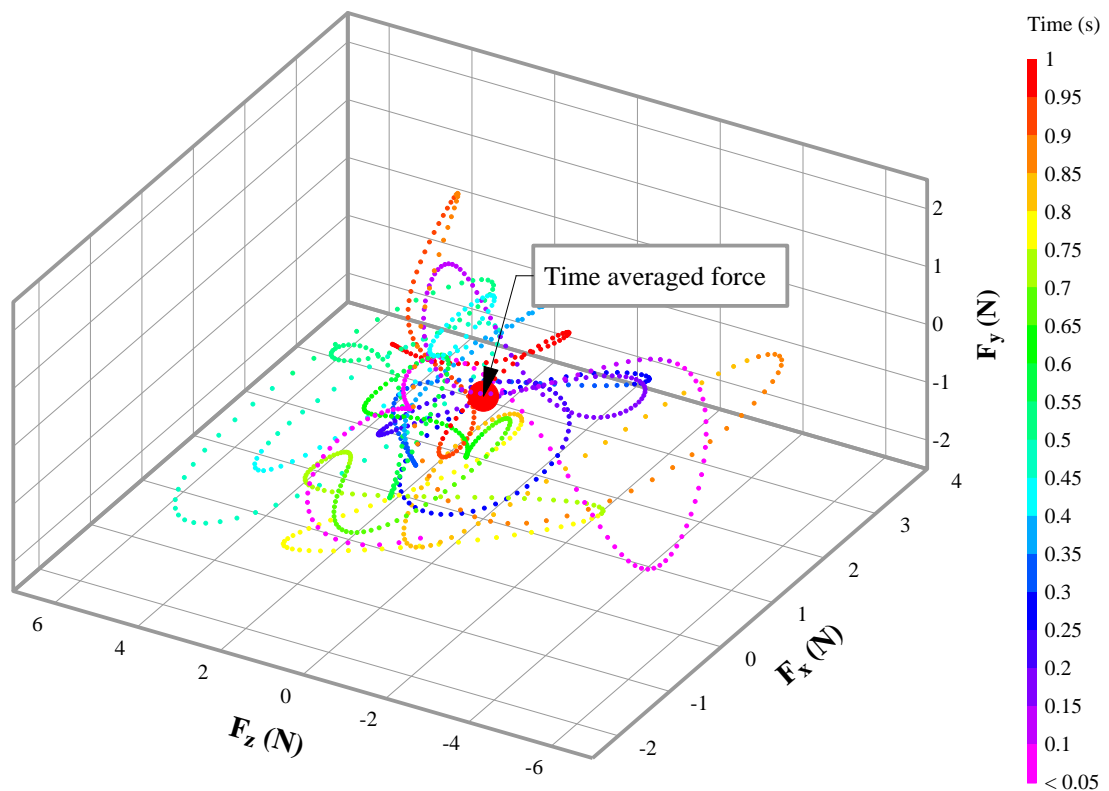


FIGURE 6–1. TRAJECTORY OF THE INSTANTANEOUS FORCES ON A SUBMERGED SPHERE INSIDE A HYDRAULIC JUMP (EXPERIMENT F: $Fr_l = 8.0$, $Re = 1.2 \times 10^5$, $x/d_l = 20$, $y/d_l = 2.1$, FULLY DEVELOPED INFLOW CONDITIONS).

Previous studies have provided some information about the internal motions in hydraulic jumps by the quantification of the drag forces generated on baffle piers (e.g. Harleman 1955; Rajaratnam and Murahari 1971; Ohtsu et al. 1991), the measurement of the longitudinal and transverse pressure fluctuations at the channel bed (e.g. Abdul Khader and Elango 1974;

Fiorotto and Rinaldo 1992) and the measurement of streamwise pressure fluctuations at different elevations (Wang et al. 2014b). These studies have provided a good understanding the analysis of the internal motions in hydraulic jumps in one dimension. Additional studies have measured the turbulent characteristics and 2D velocity distributions in weak hydraulic jumps (e.g. Liu et al. 2004a; Lennon and Hill 2006; Lin et al. 2012). Nonetheless, these studies were limited to low aerated hydraulic jumps. To date, there is no information on the distribution of the transverse motions and the associated 3D behaviour in hydraulic jumps. Herein, the present study measured the three-dimensional forces on a submerged sphere providing new insights into the three-dimensional motions in hydraulic jumps. More information on the instrumentation, the experimental setup and the post-processing of the raw data was provided in Chapter 3. The experiments were conducted for hydraulic jumps downstream of a sluice gate for fully and partially developed inflow conditions and for a wide range of Froude and Reynolds numbers. The force measurements were conducted at different elevations and different cross-sections along the hydraulic jumps as shown in Figure 6-2. The number of vertical positions at the five measured cross-sections was linked with the respective flow depth at each cross-section. The minimum elevation corresponded to the lower side of the sphere being 1 mm above the channel bed while the maximum elevation was defined as the position where half of the sphere was submerged on average. In most cases the sphere was fully submerged while the latter case defined a condition with partially submerged sphere. The first section was located close to the jump toe, the second and third sections along the jump roller, the fourth section close to the end of the roller and the last cross-section was located at the downstream end of the jump in the conjugate flow depth region (Figure 6-2).

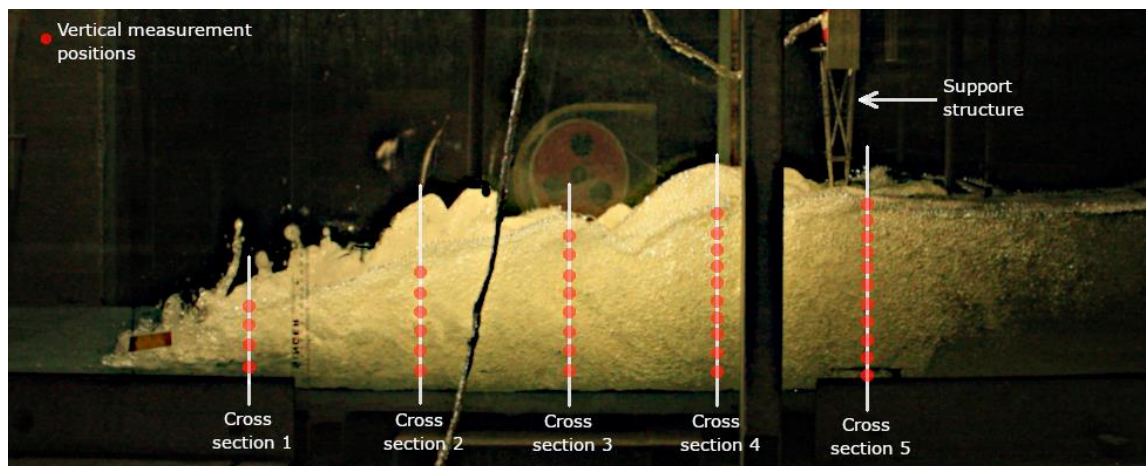


FIGURE 6–2. VERTICAL MEASUREMENT POSITIONS AT FIVE DIFFERENT CROSS-SECTIONS ALONG THE HYDRAULIC JUMP. EXPERIMENT E: $Fr_1 = 8.5$, $Re = 7.5 \times 10^4$, PARTIALLY DEVELOPED INFLOW CONDITIONS.

Table 6-1 summarises the experimental flow conditions for the experiments with submerged sphere including the inflow conditions PD and FD, d_1 , Fr_1 and Re .

TABLE 6–1. EXPERIMENTAL FLOW CONDITIONS FOR MEASUREMENTS OF INTERNAL MOTIONS IN HYDRAULIC JUMPS USING A SUBMERGED SPHERE

Experiment	Inflow condition		d_1 (m)	Fr_1 (-)	Re (-)
	PD	FD			
A	x		0.03	5.1	8.3×10^4
		x	0.03	5.1	8.3×10^4
B	x		0.025	5.1	6.2×10^4
		x	0.025	5.1	6.2×10^4
C	x		0.02	7.0	6.2×10^4
		x	0.02	7.0	6.2×10^4
D	x		0.03	7.0	1.1×10^5
		x	0.03	7.0	1.1×10^5
E	x		0.02	8.5	7.5×10^4
		x	0.0205	8.2	7.5×10^4
F	x		0.027	8.4	1.2×10^5
		x	0.028	8.0	1.2×10^5
G	x		0.02	10	8.8×10^4
		x	0.02	10	8.8×10^4
H	x		0.03	3.8	6.2×10^4
		x	0.03	3.8	6.2×10^4
I		x	0.04	3.8	9.5×10^4

6.2. TIME-AVERAGED FORCES

The time-averaged forces on the sphere were recorded for a period of 450 s close to the jump toe and 300 s further downstream. Figure 6-3 shows the vertical distribution of the dimensionless time-averaged streamwise force in x-direction $F_x/F_{u/s}$ (Figure 6-3A), transverse force in z-direction $F_z/F_{u/s}$ (Figure 6-3B), buoyancy force in y-direction $F_{buoyancy}/F_{u/s}$ (Figure 6-3C) and vertical drag force in y-direction $F_{Dy}/F_{u/s}$ (Figure 6-3D) as a function of y/d_1 , where $F_{u/s}$ is the incoming total force on a width equal to the sphere diameter comprising the hydrostatic component F_1 and the dynamic component ρQV_1 just upstream the hydraulic jump over the full inflow depth d_1 .

Distinctive features were observed in the force distributions. F_x decreased in downstream direction x/d_1 having the largest streamwise forces close to the channel bed at $y/d_1 \approx 1$. This may be related to the maxima in the wall jet-like velocities close to the channel bed of hydraulic jumps (Rajaratnam 1965; Ohtsu et al. 1990a; Chanson and Brattberg 2000) (Figure 6-3A). For regions close to the jump toe, at $x/d_1 \leq 30$, $F_x/F_{u/s}$ decreased with increasing elevation resembling velocity distributions in hydraulic jumps with larger flow velocities close to the channel bed and negative velocities in the recirculation region in the upper part of the hydraulic jump. Further downstream, $x/d_1 > 30$, the forces became more uniform across the flow column linked with a more uniform velocity distribution (Chapter 4.3.5). For $x/d_1 \geq 40$, irrespective of

the elevation most of the streamwise forces on the sphere agreed well with an estimated streamwise drag force $F_{Dx_{d/s}}$ at the downstream end of the hydraulic jump ($F_{Dx_{d/s}} = 0.5 \times C_d \times \rho \times A_s \times V_2^2$ where $C_d \approx 0.44$ based on the observed Reynolds number, ρ is the water density, A_s is the sphere area and V_2 is the average velocity at the downstream end of the hydraulic jump). The overall shape of the streamwise force distributions was in agreement with the vertical profiles of mean total pressure distributions for comparable Froude numbers by Wang et al. (2014b).

The mean transverse force were overall close to zero in channel centreline for all experiments (Figure 6-3B). This result highlighted the symmetry of the present experiments. Small deviations of about 0.1 N were observed for data near the channel bed and close to the jump toe which may be linked with strong fluctuations in this region, inaccuracy in instrument alignment and potential non-symmetric inflow conditions. Note that the force deviation in the transverse force was within the range of the raw signal fluctuations without any load (Chapter 3.4.4).

The vertical force F_y measured with the load cell represented the sum of the buoyancy force $F_{buoyancy}$ and the vertical drag force F_{Dy} as described in Chapter 3.3.3. $F_{buoyancy}$ estimates the upward force due to the volume displaced by the sphere in the two-phase fluid and is strongly dependent on the local void fraction. F_{Dy} characterises the dynamic vertical motions and provides the overall vertical direction of the flow motions inside the hydraulic jump. Typical distributions of $F_{buoyancy}$ and F_{Dy} are presented in Figures 6-3C and 6-3D respectively. Note that the analysis was conducted only for cases with fully submerged sphere to minimise uncertainties when the sphere was exposed to the air. The buoyancy force was always positive representing the upward force exerted by the fluid on the sphere. A minimum $F_{buoyancy}$ was observed at each cross-section linked with maxima in void fractions. Slightly lower buoyancy forces were recorded close to the jump toe due to larger aeration ($F_{buoyancy}/F_{us} \approx 0.2$). At the downstream end of the hydraulic jump ($x/d_l > 30$), the buoyancy force was larger and almost constant linked with low void fractions in this region. In contrast to $F_{buoyancy}$, F_{Dy} was negative for most of the locations (Figure 6-3D). Since the drag force acts opposite to the flow direction, negative F_{Dy} represents upward flow motions. For $x/d_l \leq 20$, F_{Dy} had a distinct minimum in the shear region suggesting a maximum positive force at $y/d_l \approx 2.2$ followed by a reduction in the upwards motion in the recirculation region. This result highlighted strong positive motions in the shear region close to the jump toe linked with the roller formation. At the downstream end of the hydraulic jump $x/d_l > 20$, the drag force was close to zero suggesting minor vertical flow motions. More detailed information about the raw force data and the time-averaged forces is presented in Appendix I.

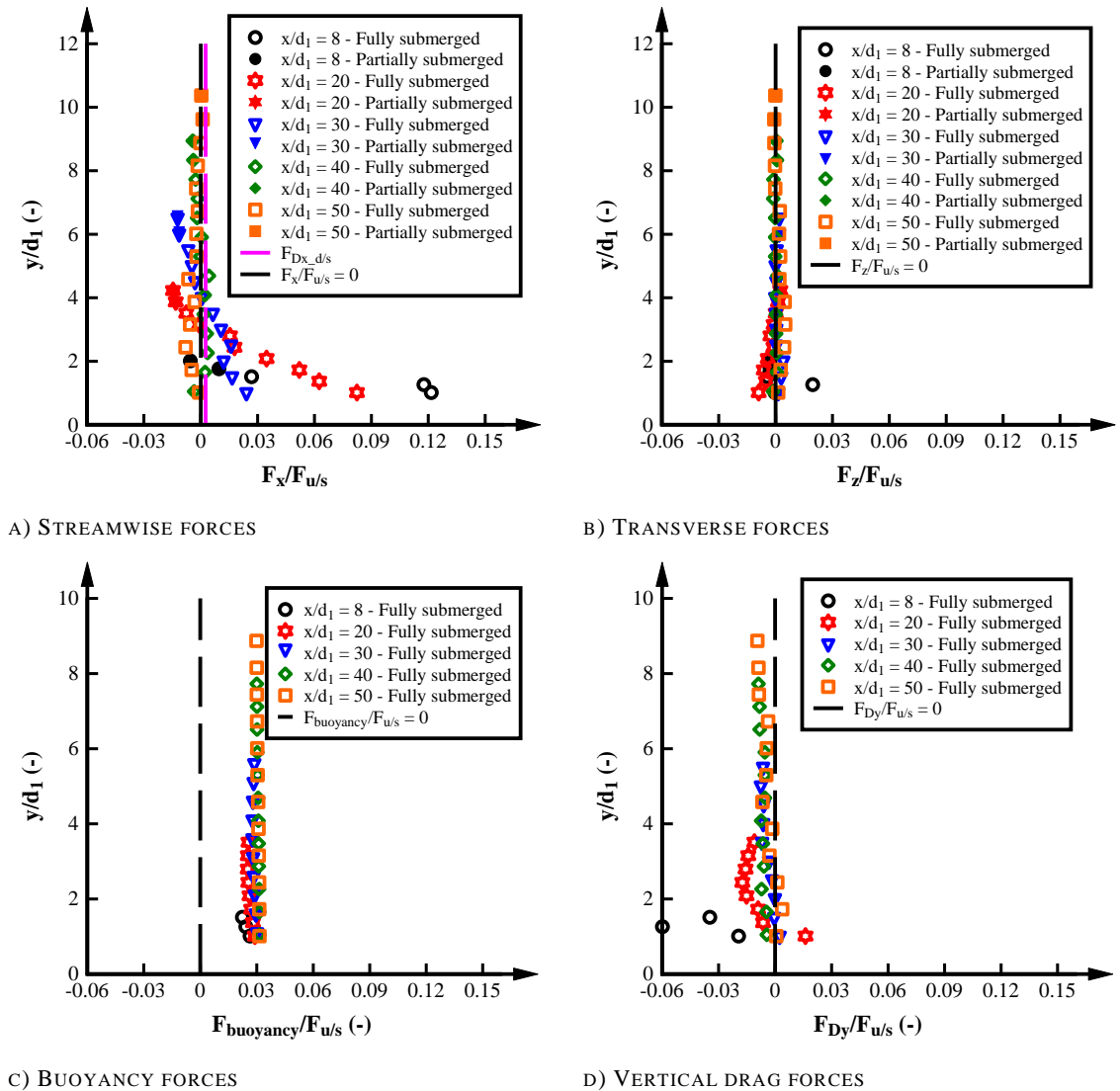
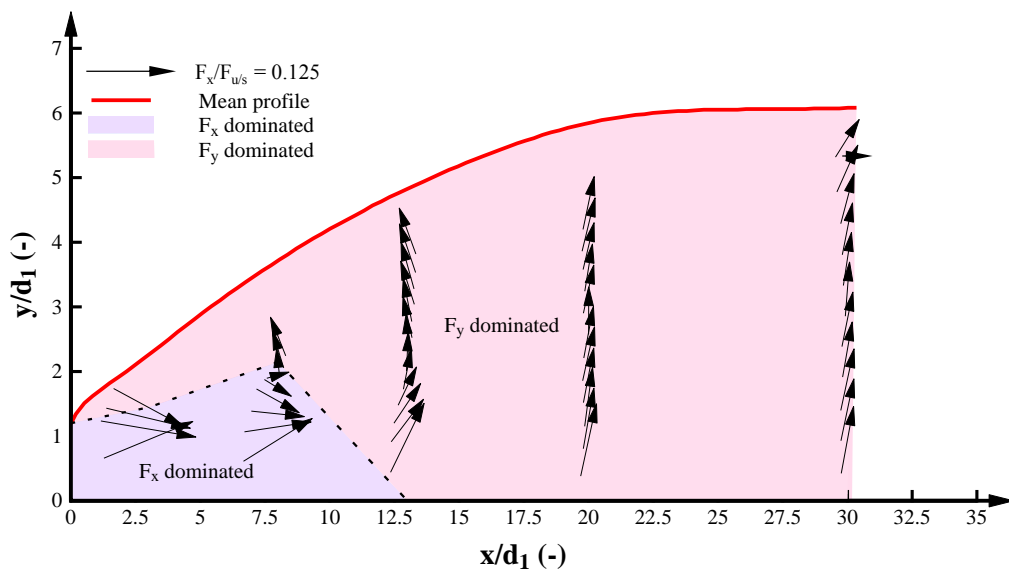


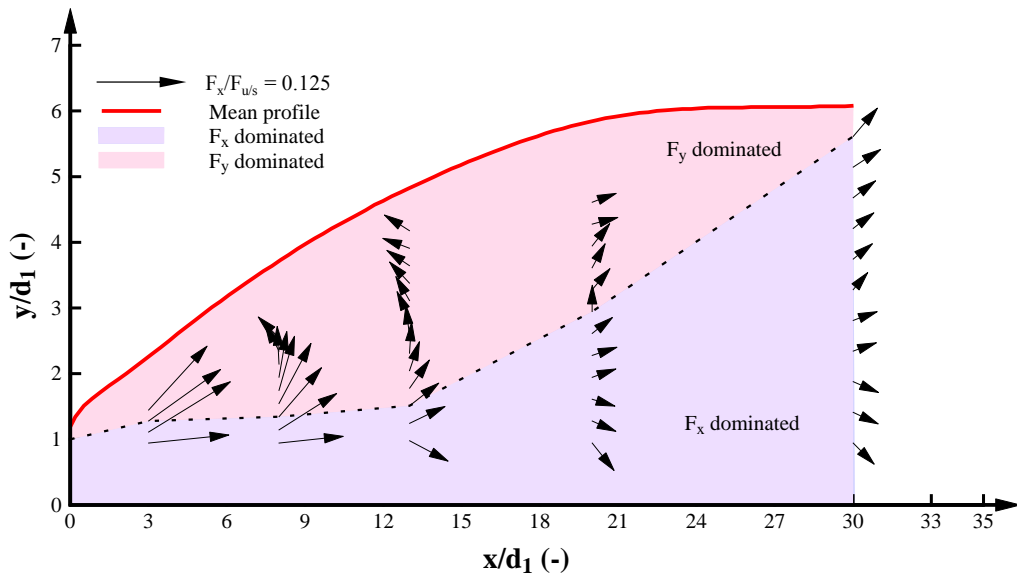
FIGURE 6-3. DISTRIBUTION OF THE TIME-AVERAGED FORCES AT DIFFERENT CROSS-SECTIONS ALONG A HYDRAULIC JUMP (EXPERIMENT F: $Fr_1 = 8.0$, $Re = 1.2 \times 10^5$, FULLY DEVELOPED INFLOW CONDITIONS).

Figure 6-4 presents typical time-averaged two-dimensional force distributions of streamwise and vertical forces. The time-averaged transverse forces are not included since they are close to zero in channel centreline. Figure 6-4A illustrates the total vertical force $F_y = F_{buoyancy} + F_{Dy}$ and Figure 6-4B the negative drag force $-F_{Dy}$ in order to consider the flow direction opposite to the drag force. The vector field for F_y highlighted that the largest forces were located close to the jump toe while the forces decreased in x- and y-directions with increasing distance from the jump toe (Figure 6-4A). Close to the jump toe, the dominant force was the streamwise force linked to the large streamwise velocities in this region. The overall flow direction was upwards linked with the roller formation. Figure 6-4A also shows the negative streamwise forces in the recirculation region linked with the flow reversal in this part of the hydraulic jump. At the downstream end, the hydraulic jump was mostly dominated by the vertical forces indicating lesser streamwise motions and stronger influence of the buoyancy.

When considering $-F_{Dy}$ (Figure 6-4B), the lower part of the hydraulic jump was dominated by the streamwise forces while the upper part was dominated by the vertical flow motions. Overall, the force field in Figure 6-4B agreed well with time-averaged two-dimensional velocity distributions in weak hydraulic jumps recorded with MicroADVs and PIVs (Liu et al. 2004a; Lin et al. 2012). The force distributions indicated a wall jet velocity distribution in the lower part of the hydraulic jump and a recirculation region in the upper part of the jump roller and more uniform force distributions further downstream. Similar results were observed for all hydraulic jumps. Close to the channel bed, the force field showed some downward forces. It is believed that these forces were recorded as the result of the strong advective flow hitting the sphere pushing the sphere downwards and further research with smaller sphere diameters is required to validate the vertical forces close to the channel bed. Overall, for the understanding of the internal motions in the hydraulic jump, Figure 6-4B is more relevant since it provides an estimation of the time-averaged flow direction in the hydraulic jump removing the effect of the buoyancy forces presented in Figure 6-4A.



A) CONSIDERING TOTAL VERTICAL FORCE ($F_{buoyancy} + F_{Dy}$)



B) CONSIDERING OPPOSITE DRAG FORCE ($-F_{Dy}$)

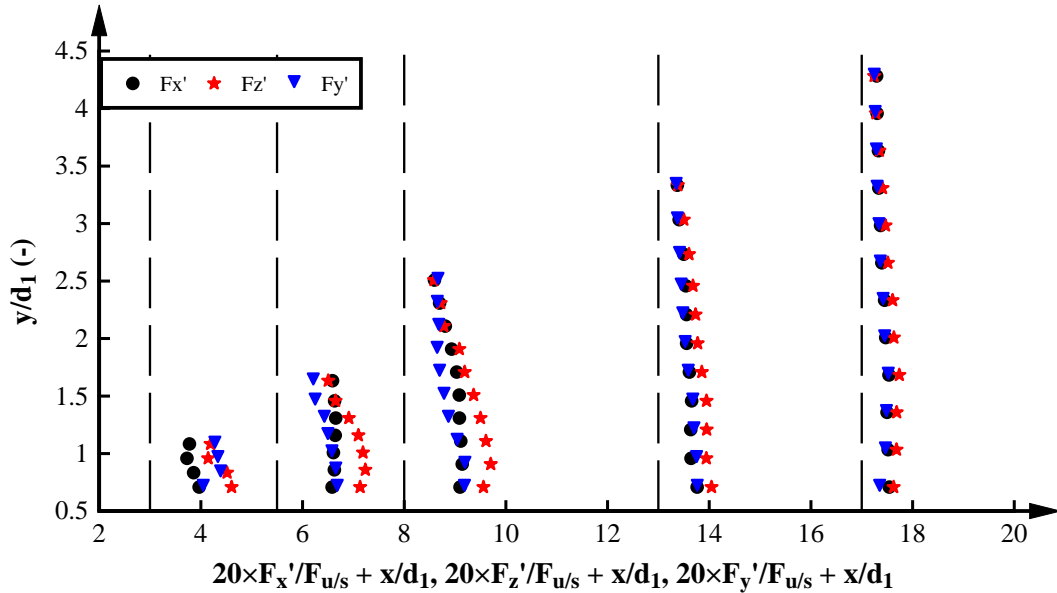
FIGURE 6-4. TWO-DIMENSIONAL DISTRIBUTION OF THE TIME-AVERAGED FORCES IN HYDRAULIC JUMPS IN THE CHANNEL CENTRELINE: EXPERIMENT A: $Fr_1 = 5.1$, $Re = 8.3 \times 10^4$ – FULLY DEVELOPED INFLOW CONDITIONS.

6.3. FORCE FLUCTUATIONS

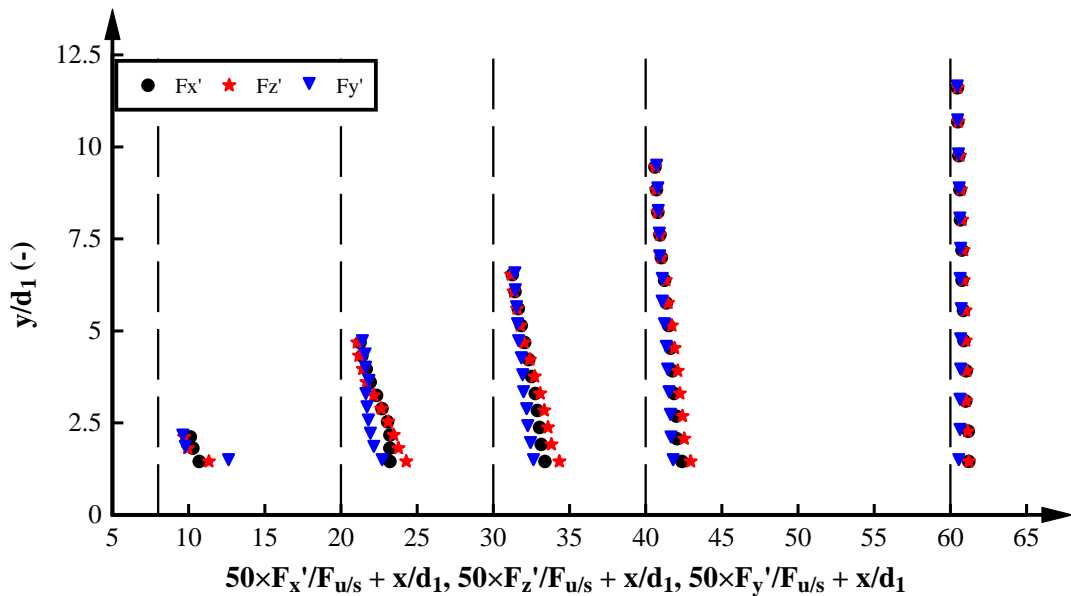
The force fluctuations are represented by the standard deviations of the raw forces on the submerged sphere. Figure 6-5 presents typical distributions of the streamwise F_x' , transverse F_z' and vertical F_y' force fluctuations at five cross-sections along the hydraulic jump. Note that F_y' comprised the fluctuations of the raw vertical forces comprising the buoyancy and the vertical drag forces. For all force fluctuation components, maxima were observed in the shear region downstream of the the jump toe, and the fluctuations decreased with increasing distance from the jump toe. The results agreed with pressure fluctuations measured in the channel bed below hydraulic jumps (Schiebe and Bowers 1971; Abdul Kadher and Elango 1974; Toso and Bowers 1988; Fiorotto and Rinaldo 1992) and profiles of pressure fluctuations in streamwise direction (Wang et al. 2014).

In the recirculation region, similar fluctuations were observed for the three force components. In the shear region, some differences were observed. For experiments with $Fr_1 < 7$ (Figure 6-5A), larger fluctuations in transverse direction were consistently observed along the hydraulic jump while similar force fluctuations were observed for streamwise and vertical forces ($F_z' > F_x' \approx F_y'$) (Figure 6-5A). For $Fr_1 \geq 7$ (Figure 6-5B), the streamwise force fluctuations were larger than the vertical force fluctuations and the transverse force fluctuations were consistently larger ($F_z' > F_x' > F_y'$) (Figure 6-5B). The transverse and streamwise force fluctuations were similar at the downstream end of the hydraulic jumps ($F_z' \approx F_x'$). The ratio in maxima of streamwise and transverse force fluctuations was about 72% while the ratio in maxima for the vertical and transverse force fluctuations was about 72% for

$Fr_1 < 7$ and 61% for $Fr_1 \geq 7$. This observation suggested the dominance of the transverse force fluctuations and the importance to consider motions in all flow directions for dissipative processes inside hydraulic jumps. Further details on the force fluctuations can be found in Appendix I.



A) EXPERIMENT I: $Fr_1 = 3.8$, $Re = 9.5 \times 10^4$ – FULLY DEVELOPED

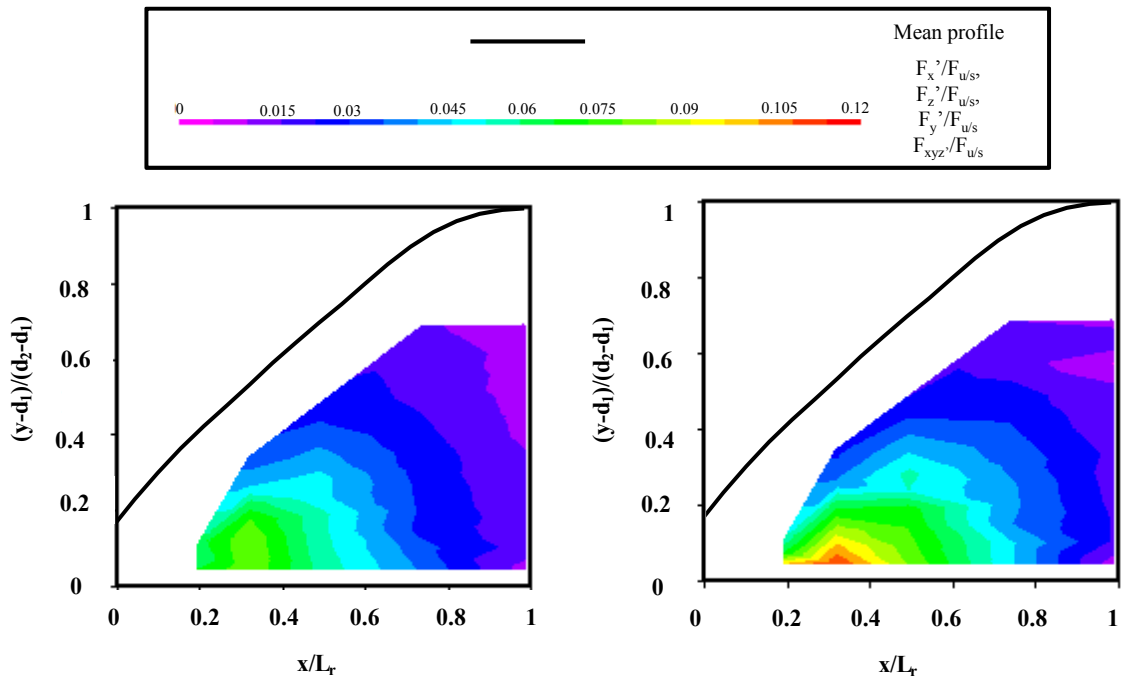


B) EXPERIMENT G: $Fr_1 = 10$, $Re = 8.8 \times 10^4$ – FULLY DEVELOPED

FIGURE 6-5. COMPARISON OF DISTRIBUTIONS OF FORCE FLUCTUATIONS IN X, Y AND Z-DIRECTIONS ALONG SELECTED HYDRAULIC JUMPS

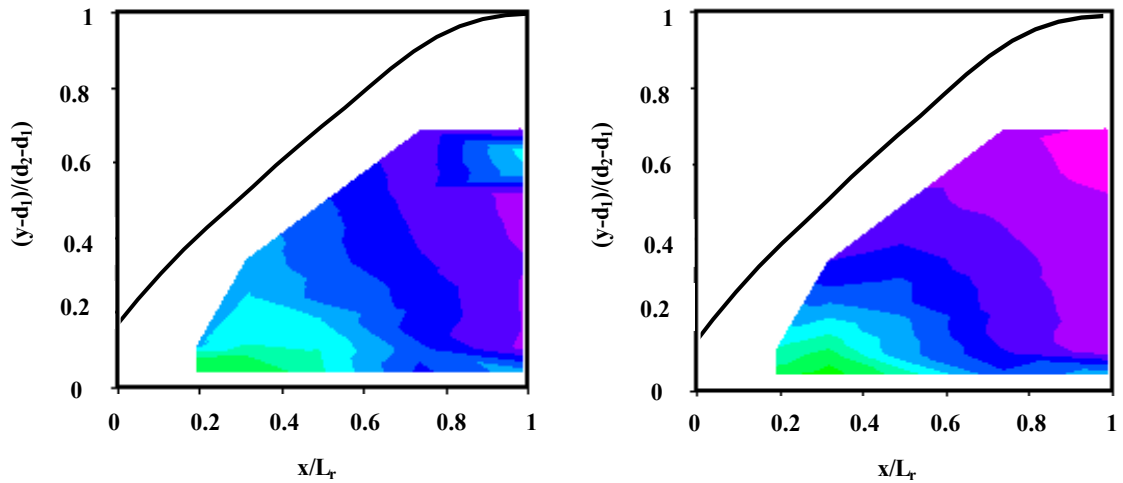
Figure 6-6 presents typical contour plots of the streamwise, transverse and vertical force fluctuations in a hydraulic jump (Figure 6-6A-C) as well as the resultant force fluctuations F_{xyz}' (Figure 6-6D). All force fluctuations decreased with increasing distance from the jump toe and with increasing elevation. The largest streamwise force fluctuations were observed in the shear region between $0.3 < x/L_r < 0.4$ and $0.05 < (y-d_1)/(d_2-d_1) < 0.2$. The largest transverse force

fluctuations comprised a longer longitudinal area in the hydraulic jump compared to F_x' with between $0.3 < x/L_r < 0.6$. The area of larger force fluctuations in F_y' was limited to a small region close to the channel bed. Overall, the vertical force fluctuations presented the lesser variation along the hydraulic jump. The resultant force fluctuations F_{xyz}' had the largest fluctuations in the shear region close to the jump toe. The fluctuation showed a rapid decrease with increasing elevation indicating weaker force fluctuations in the recirculation region. At the downstream end of the hydraulic jump, the fluctuations remained almost constant independent of the elevation. The results indicated the strongest intensity in motions close to the jump toe and in the lower part of the hydraulic jump. The decay in fluctuations agreed well with previous measurements of turbulence intensity in weak hydraulic jumps highlighting a rapid decay in the turbulence intensity with increasing distance from the jump toe (Liu et al. 2004a; Lennon and Hill 2006; Misra et al. 2006, 2008; Mignot and Cienfuegos 2010). This result suggests that the force fluctuations inside fully aerated hydraulic jumps may provide some information on large scale turbulent motions inside strong hydraulic jumps.



A) STREAMWISE FORCE FLUCTUATIONS

B) TRANSVERSE FORCE FLUCTUATIONS



C) VERTICAL FORCE FLUCTUATIONS

D) RESULTANT FORCE FLUCTUATIONS

FIGURE 6–6. CONTOUR PLOTS OF THE FORCE FLUCTUATIONS IN A HYDRAULIC JUMP. EXPERIMENT F: $Fr_1 = 8.0$, $Re = 1.2 \times 10^5$ – FULLY DEVELOPED INFLOW CONDITIONS

6.4. CHARACTERISTIC FREQUENCIES

A spectral analysis of the streamwise, transverse and vertical raw force signals was conducted for all experiments providing distinctive frequencies along the hydraulic jump. Figure 6-7 presents the distribution of the dominant frequencies in x-, z- and y-directions, $freq_{F_x,dom}$, $freq_{F_z,dom}$, $freq_{F_y,dom}$ for the same hydraulic jump. The dominant streamwise frequencies were typically $0.5 < freq_{F_x,dom} < 1.5$ similar to the frequencies of the jump toe oscillations (Figure 6-7a) indicating an effect of the jump toe movements on the streamwise force frequencies. Note that the estimation of the dominant frequency in the x-direction may have been affected by the high-pass filter of 20 Hz to remove the resonant frequency of the system. Large frequencies were in particular recorded in regions close to the jump toe ($freq_{F_x,dom} > 4$ Hz) suggesting that some faster movements in the x-direction were characteristic close to the jump toe.

The transverse forces had frequencies similar to the jump toe movements $0.5 < freq_{F_z,dom} < 1.5$ for cross-sections immediately downstream of the jump toe (Figure 6-7B). Further downstream $2.5 < freq_{F_z,dom} < 7.5$ with decreasing frequencies with increasing distance from the jump toe reaching $0.5 < freq_{F_z,dom} < 2$ at the downstream end. Note that the decay in the transverse frequencies was similar to the decay in the standard deviations. The vertical forces had dominant frequencies $0.5 < freq_{F_y,dom} < 1.5$ close to the jump toe (Figure 6-7C). Further downstream, $1.5 < freq_{F_y,dom} < 4$.

Overall, close to the jump toe the frequencies in all three directions was similar to the jump toe frequencies. Further downstream, $freq_{F_z,dom} > freq_{F_y,dom} > freq_{F_x,dom}$ indicating that the transverse forces on the sphere were varying fastest while the streamwise forces represented the slowest motions. The results suggested that the transverse motions are important for the characterisation of hydraulic jump motions and future research should aim to further investigate

this. Further details of the frequency analysis in x-, z- and y-directions is presented in Appendix I.

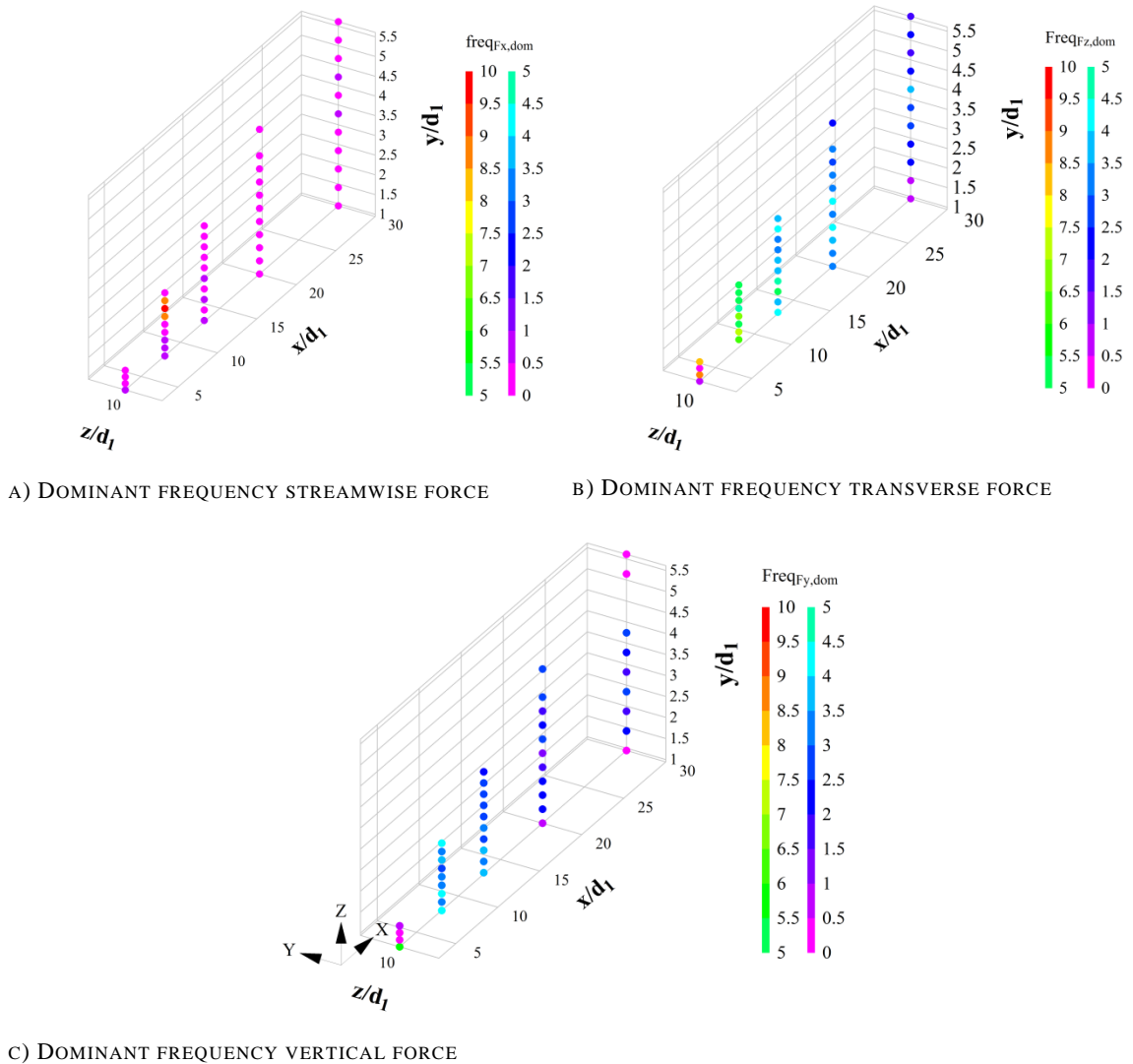


FIGURE 6-7. DISTRIBUTIONS OF THE CHARACTERISTIC FREQUENCIES OF THE MOTIONS OF THE SUBMERGED SPHERE INSIDE THE HYDRAULIC JUMP. EXPERIMENT A: $Fr_1 = 5.1$, $Re = 8.3 \times 10^5$ – FULLY DEVELOPED

Figure 6-8 presents the Strouhal numbers of the cross-sectional averaged dominant frequencies as a function of Fr_1 . The Strouhal number of $freq_{Fx,dom,avg}$ decreased with increasing Froude numbers (Figure 6-8A) in agreement with the decrease in frequencies of the jump toe oscillation (see Chapter 5.5). The cross-sectional streamwise dominant frequencies were within the range of $0.001 < freq_{Fx,dom,avg} \times d_1 / V_1 < 0.0125$. Note that the dominant streamwise frequencies were only meaningful for $Fr_1 \leq 8.5$ due to stronger scatter in frequencies for $Fr_1 = 10$. The cross-sectional transverse frequencies $freq_{Fz,dom,avg}$ were characterised by large data scatter suggesting a large variation in the frequencies along the hydraulic jump. Larger $freq_{Fz,dom,avg}$ were observed for the lower Froude numbers and for larger Reynolds numbers (darker colours) (Figure 6-8B). The Strouhal number range for the transverse frequencies was $0.001 < freq_{Fz,dom,avg} \times d_1 / V_1 < 0.11$. Similar to $freq_{Fz,dom,avg}$, the Strouhal number of the vertical

frequencies $freq_{Fy,dom,avg} \times d_1/V_1$ showed large variations with an overall decrease with increasing Fr_1 (Figure 6-8C). The Strouhal number for the vertical frequency was $0.004 < freq_{Fy,dom,avg} \times d_1/V_1 < 0.06$.

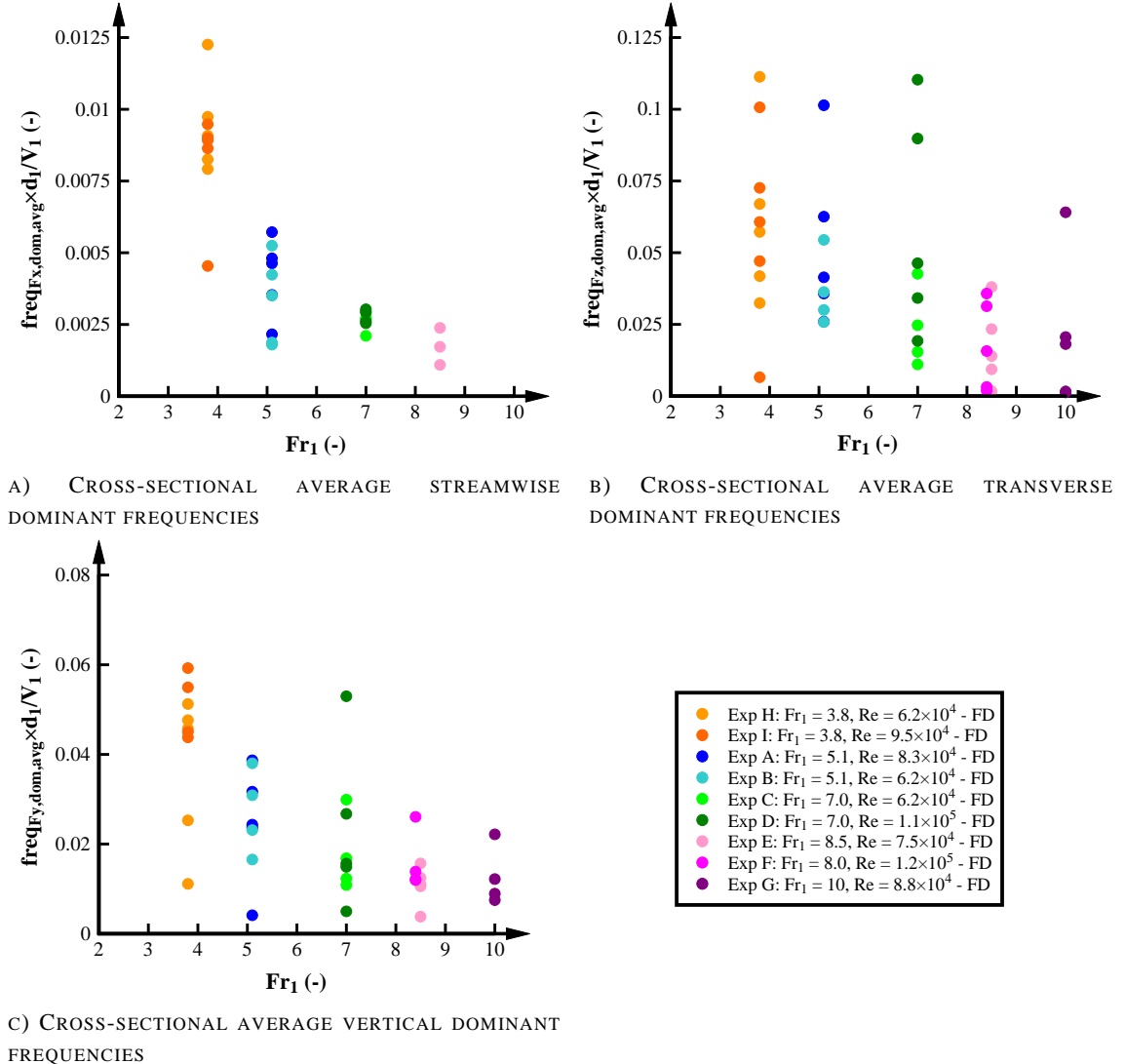


FIGURE 6-8. STROUHAL NUMBER OF THE CROSS-SECTIONAL AVERAGED DOMINANT FREQUENCIES AS A FUNCTION OF Fr_1 IN HYDRAULIC JUMPS WITH FULLY DEVELOPED INFLOW CONDITIONS (FD).

Figure 6-9 presents the distribution of the Strouhal number of the streamwise forces for hydraulic jumps with similar Reynolds numbers. The Strouhal number was estimated based upon the sphere diameter (Φ_{sphere}) and the local time-averaged streamwise interfacial velocity measured with the conductivity probe ($V_{CP,avg}$). Note that the estimation of $V_{CP,avg}$ considered the volume of the sphere and followed the same methodology for the selection of the local time-averaged void fraction as presented in Figure 3-21. The distribution of the Strouhal number showed large data scatter linked with the scatter observed in the interfacial velocities and the streamwise dominant frequencies (Figure 6-9). Apart from the data scatter, larger Strouhal numbers were observed close to the channel bed followed by a sudden decrease between $0.05 < (y-d_1)/(d_2-d_1) < 0.25$ and a further increase in the upper part. The increase in the Strouhal

number in the upper part of the hydraulic jump may be linked with the effect of the recirculation region and negative velocities. This information should be further investigated considering the AWCC proposed by Kramer et al. (2019b) and Kramer and Valero (2019) as indicated in Chapter 4.3.5. Larger Strouhal numbers could be identified for the experiments conducted with the lower Froude number associated with the lower interfacial velocities and less unsteady flow. The experiments conducted with the larger Froude number showed the smallest Strouhal number indicating faster flow velocities and turbulent motions. Note that the Strouhal number of the vortex-shedding of a sphere in uniform flow conditions is equal to 0.2 for $Re > 1 \times 10^4$ (Sakamoto and Haniu 1990). The lower Strouhal numbers observed in the present study showed that the sphere oscillation in hydraulic jumps is less frequent compared to the vortex shedding under uniform flow conditions which may be linked with the large-scale vortices. Further research is suggested with spheres of smaller size to identify the effects of smaller turbulent scales in the Strouhal number.

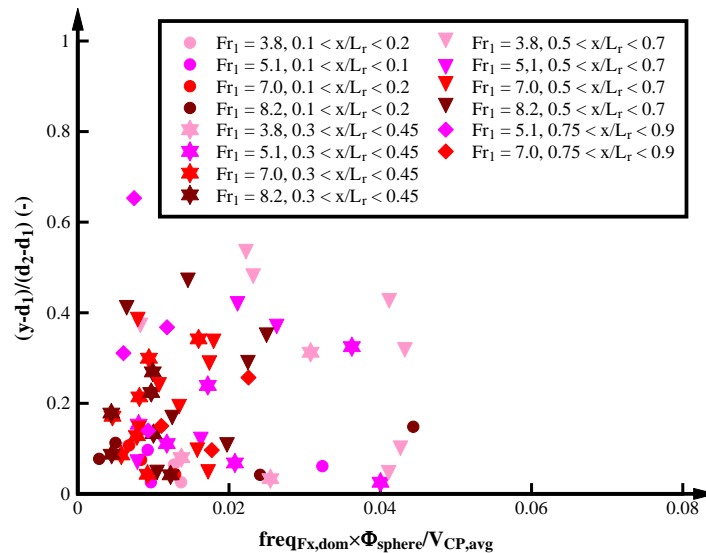
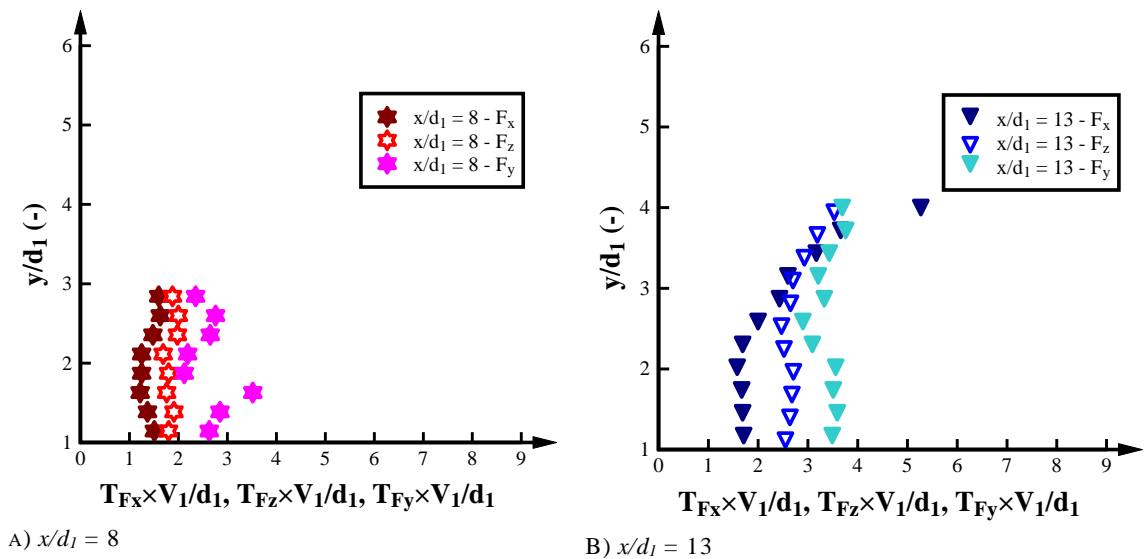


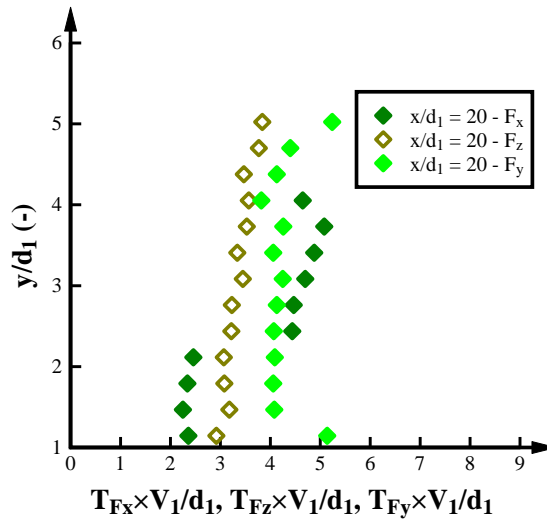
FIGURE 6–9. DISTRIBUTION OF THE STROUHAL NUMBER OF THE STREAMWISE DOMINANT FREQUENCIES ESTIMATED BASED UPON THE SPHERE DIAMETER AND THE INTERFACIAL VELOCITY.

Overall, the Strouhal number estimated based upon the sphere diameter and the interfacial velocities (Figure 6-9) were slightly larger compared with the Strouhal number estimated with d_I and V_I (Figure 6-8a). This result is linked with the lower time-averaged interfacial velocities along the hydraulic jumps compared to the inflow velocity. This statement suggests that the Strouhal number estimated based upon the interfacial velocity provided a better identification of the variation of the oscillation patterns along hydraulic jumps. The analysis of the Strouhal number based upon the internal velocities and the sphere diameter should be further explored in the vertical and transversal directions which is still limited due to lack of experimental information in the vertical and transversal flow velocities.

6.5. AUTO-CORRELATION TIME SCALES

The auto-correlation time scales were also calculated. Independent of the force direction, an increase in the auto-correlation time scales was continuously observed with increasing distance from the jump toe indicating larger turbulent structures furthest downstream from the jump toe. A detailed description of the auto-correlation time scales in x-, z- and y- directions is provided in Appendix I. Figure 6-10 presents the comparison of typical time scales in streamwise T_{F_x} , transverse T_{F_z} and vertical T_{F_y} directions at cross-sections along the hydraulic jump. Due to large data scatter, the cross-section located immediately downstream the jump toe and at the downstream end of the hydraulic jump were not meaningful. Overall $T_{F_y} > T_{F_z} > T_{F_x}$ indicated larger vortical structures in the vertical direction and smaller structures in the streamwise direction. The results confirmed the three-dimensionality of hydraulic jumps indicating different sizes of large vortical structures in different flow directions. The larger correlation of the transverse forces on the sphere compared to the streamwise forces was consistent with the finding of Fiorotto and Rinaldo (1992) for pressure fluctuations at the channel bed. Larger streamwise auto-correlation time scales at $x/d_1 = 20$ were consistently observed which was linked with the reduction in flow velocity at this location leading to larger time scales at the downstream end of the hydraulic jump (Figure 6-10C).





A) $x/d_1 = 20$

FIGURE 6–10. COMPARISON OF THE STREAMWISE, TRANSVERSE AND VERTICAL AUTO-CORRELATION TIME SCALES OF THE FORCES ON A SUBMERGED SPHERE IN A HYDRAULIC JUMP. EXPERIMENT B: $Fr_1 = 5.1$, $Re = 6.2 \times 10^4$ – FULLY DEVELOPED

6.6. DECAY IN THE INTERNAL FORCE PARAMETERS

The strongest motions and largest fluctuations of the forces on the sphere are in the shear region just downstream of the jump toe. The motions decreased with increasing distance from the jump toe indicating a decay in the energetic processes along the hydraulic jump. Figure 6-11 presents the decay of the maximum force parameters in streamwise, transverse and vertical directions along the hydraulic jump.

Figure 6-11A presents the decay in the dimensionless peaks in streamwise forces $F_{x,max}F_{u/s}$ as a function of x/L_r . $F_{x,max}F_{u/s}$ showed the largest forces close to the jump toe and a decrease with increasing distance from the jump toe suggesting lesser streamwise motions at the downstream end of the hydraulic jump. Note that the estimation of the maximum streamwise forces was limited by the sphere size and the force may be underestimated in cases where the maximum force occurs extremely close to the channel bed. The decay in the maximum streamwise forces was well correlated by ($R^2 = 0.84$):

$$\frac{F_{x,max}}{F_{u/s}} = 0.208 \times \exp \left[2.55 \times \left(\frac{x}{L_r} \right) \right] \quad \text{for } 3.8 < Fr_1 < 10 \quad (6.1)$$

For regions located close to the jump toe, the vertical drag forces had a minimum $F_{Dy,min}$ in regions of largest upward movements. Figure 6-11B presents the decay of $F_{Dy,min}/F_{buoyancy,water}$ as a function of x/L_r where $F_{buoyancy,water}$ represents the buoyant force estimated with the density of water. $F_{Dy,min}/F_{buoyancy,water}$ increased with increasing distance from the jump toe indicating a decrease in the upwards motions along the hydraulic jumps. The decay rate was similar for all hydraulic jumps best fitted by an exponential decay ($R^2 = 0.82$):

$$\frac{F_{Dy,max}}{F_{buoyancy,water}} = -2.41 \times \exp \left[-3.11 \times \left(\frac{x}{L_r} \right) \right] \quad \text{for } 3.8 < Fr_1 < 10 \quad (6.2)$$

Figures 6-11C, D and E present the decay of the maximum streamwise, transverse and vertical force fluctuations respectively. Large data scatter was observed for maximum force fluctuations close to the jump toe which may be associated with the strong jump toe motions or the low flow depth affecting the overall force measurements. Further downstream, the maximum force fluctuations decreased linearly with increasing distance from the jump toe for all experiments. The peaks in streamwise, transverse and vertical force fluctuations were well correlated by linear equations with $R^2 = 0.91$, 0.91 and 0.81 respectively:

$$\frac{F'_{x,max}}{F_{u/s}} = 0.083 - 0.06 \times \left(\frac{x}{L_r} \right) \quad \text{for } 3.8 < Fr_1 < 10 \quad (6.3)$$

$$\frac{F'_{z,max}}{F_{u/s}} = 0.118 - 0.09 \times \left(\frac{x}{L_r} \right) \quad \text{for } 3.8 < Fr_1 < 10 \quad (6.4)$$

$$\frac{F'_{y,max}}{F_{u/s}} = 0.0785 - 0.06 \times \left(\frac{x}{L_r} \right) \quad \text{for } 3.8 < Fr_1 < 10 \quad (6.5)$$

A faster decay was observed in the transverse force fluctuations whereas the linear decay in the streamwise and vertical force fluctuations was similar. This result confirms the importance of the transverse forces in hydraulic jumps.

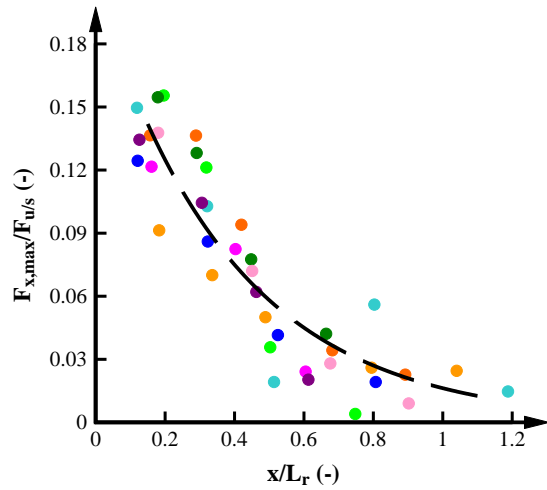
Figure 6-12 presents the decay in the cross-sectional average frequencies along the hydraulic jump. $freq_{Fx,dom,avg}$ remained almost constant independent of the distances from the jump toe indicating consistent internal motions along the hydraulic jump (Figure 6-12A). Some decrease in the dominant frequency was observed at the downstream end for $Fr_1 < 7$ which may be linked to inconclusive frequency peaks due to small streamwise force fluctuations in this region. Close similarities were observed in the frequency decay between transverse and vertical forces. Figures 6-12B and C present the decay of $freq_{Fz,dom,avg} \times d_1/V_1$ and $freq_{Fy,dom,avg} \times d_1/V_1$ along the hydraulic jumps. Note that cross-sections with strong differences in frequencies across the vertical profile were not considered in the analysis. Apart from $x/L_r < 0.2$, where the dominant frequencies were below 0.02 due to the uncertainties linked with low flow depths and jump toe oscillations, for $x/L_r \geq 0.2$, the Strouhal number decreased with increasing distance from the jump toe suggesting faster movements at the beginning of the roller region. The Strouhal numbers decreased with increasing inflow Froude numbers. At cross-sections close to the jump toe, a range of dimensionless frequencies was observed $0.003 < freq_{Fy,dom,avg} \times d_1/V_1 < 0.01$. These frequencies corresponded to the jump toe frequencies and were considerably lower compared with the dominant frequencies observed further downstream. For the transverse forces and the same Froude numbers, an increase in Reynolds numbers corresponded to larger Strouhal numbers indicating a dependency of internal motions with Re in transverse direction. Overall,

the dominant transverse and vertical frequencies were a function of the distance from the jump toe, Froude and Reynolds numbers. The cross-sectional average transverse and vertical frequencies agreed well with power laws with $R^2 = 0.90$ and 0.91 respectively:

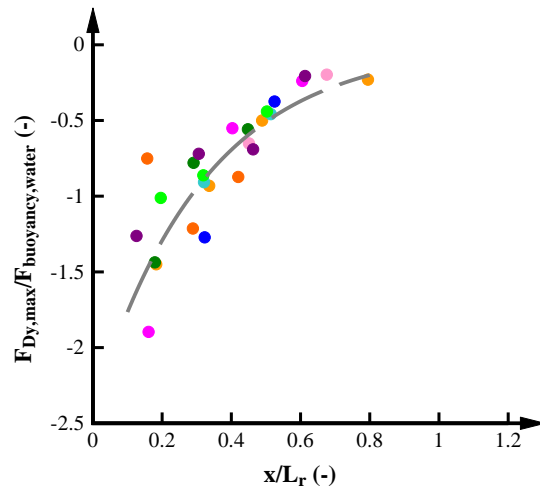
$$\frac{F_z'_{dom,avg}}{F_{u/s}} = 10^{-3.983} \left(\frac{x}{L_r}\right)^{-0.831} Fr_1^{-1.098} Re^{0.6464} \quad \text{for } 3.8 < Fr_1 < 10 \quad (6.6)$$

$$\frac{F_y'_{dom,avg}}{F_{u/s}} = 0.97 \left(\frac{x}{L_r}\right)^{0.37-0.19 \times Fr_1} Fr_1^{-2.34} \quad \text{for } 3.8 < Fr_1 < 10 \quad (6.7)$$

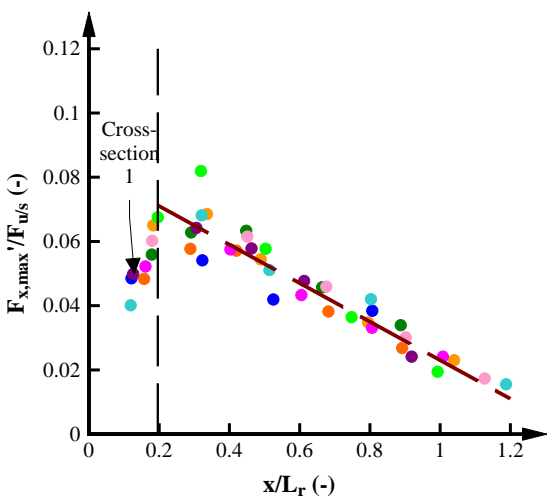
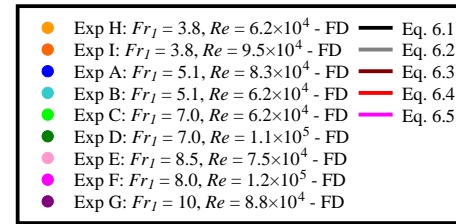
Overall, the decay in the time-averaged streamwise and vertical forces was rapid in the first half of the hydraulic jumps followed by a less steep decrease in the second half. This result suggested a rapid variation in the forces close to the jump toe and more similar forces at the downstream end of the hydraulic jumps. In contrast, the decay in the force fluctuations in all directions showed a constant decay along the hydraulic jump suggesting a continuous reduction in the force fluctuations. There was no decay in the dimensionless cross-sectional frequencies in streamwise direction while a fast decay in the transverse and vertical frequencies was observed in the first half of the hydraulic jumps followed by a flatter decay in the second half.



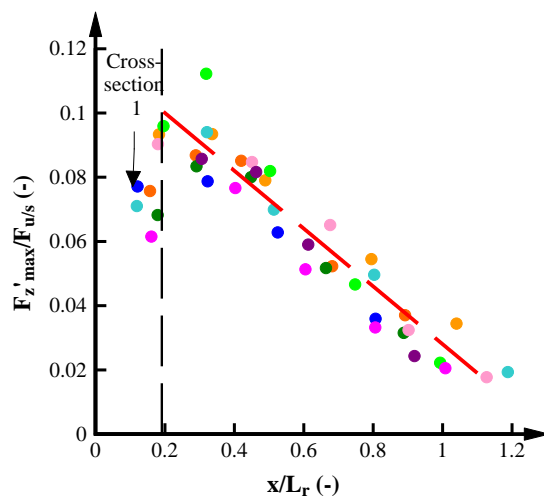
A) $F_{x,max}$. COMPARISON WITH EQ. 6.1.



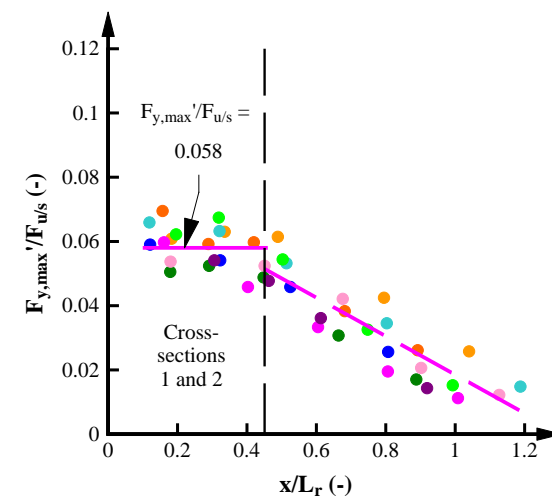
B) $F_{Dy,max}$. COMPARISON WITH EQ. 6.2.



C) $F'_{x,max}$. COMPARISON WITH EQ. 6.3.



D) $F'_{z,max}$. COMPARISON WITH EQ. 6.4.



E) $F'_{y,max}$. COMPARISON WITH EQ. 6.5.

FIGURE 6-11. DECAY OF FORCE PARAMETERS ALONG HYDRAULIC JUMPS WITH FULLY DEVELOPED INFLOW CONDITIONS (FD).

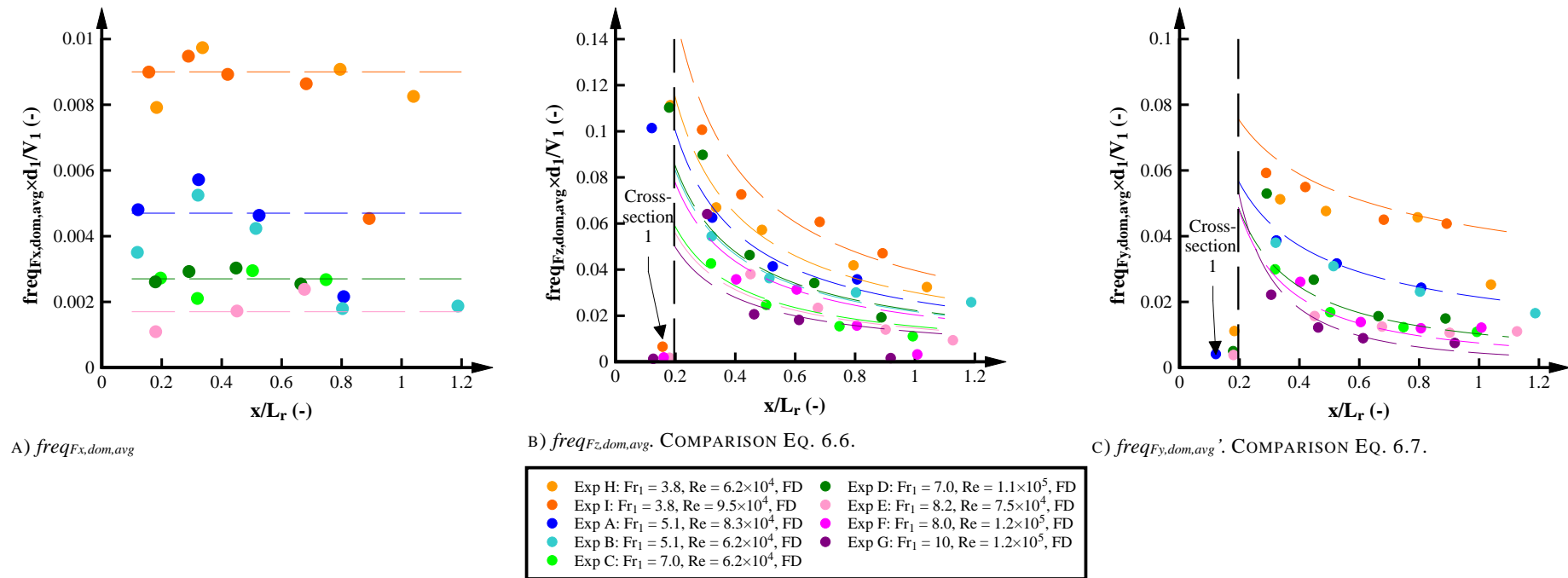
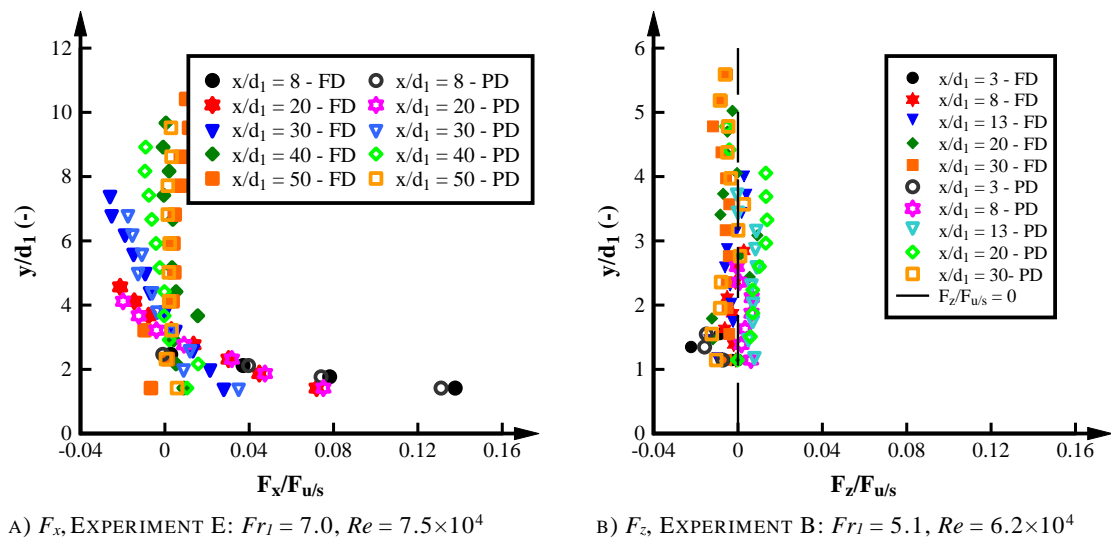
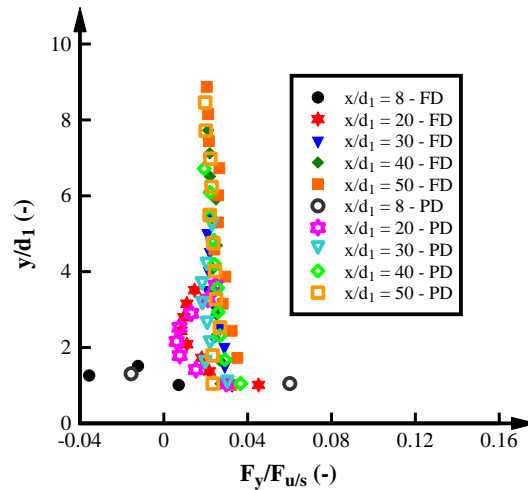


FIGURE 6–12. DECAY OF FREQUENCY PARAMETERS ALONG HYDRAULIC JUMPS WITH FULLY DEVELOPED INFLOW CONDITIONS (FD). DASHED LINES = COMPARISON WITH EQUATIONS 6.6 AND 6.7.

6.7. EFFECT OF INFLOW CONDITIONS

The inflow conditions may affect the forces on the submerged sphere inside the hydraulic jump. Figures 6-13A-C present the comparison in the time-averaged forces for typical hydraulic jumps with fully and partially developed inflow conditions. Apart from some data scatter, the distributions of the time-averaged forces were similar for hydraulic jumps with fully and partially developed inflow conditions. The streamwise time-averaged forces in partially developed inflow conditions decreased with increasing distance from the jump toe and with increasing elevation from the channel bed (Figure 6-13A). The gradient of the decay was in agreement with observations in hydraulic jumps with fully developed inflow conditions for identical Froude and Reynolds numbers. The time-averaged transverse forces were close to zero for hydraulic jumps with fully and partially developed inflow conditions (Figure 6-13B). Similar time-averaged total vertical forces were recorded for hydraulic jumps with fully and partially developed inflow conditions (Figure 6-13C). For most of the hydraulic jumps, the vertical location of the minimum vertical force was higher in fully developed hydraulic jumps linked with higher free-surface profile in these hydraulic jumps (Chapter 5.2). Overall, the analysis in the time-averaged forces showed that the internal motions in the hydraulic jump were not influenced by the inflow conditions.





C) F_y , EXPERIMENT F: $Fr_1 = 8.0$, $Re = 1.2 \times 10^5$

FIGURE 6–13. COMPARISON OF THE TIME-AVERAGED FORCES BETWEEN HYDRAULIC JUMPS WITH FULLY (FD) AND PARTIALLY (PD) DEVELOPED INFLOW CONDITIONS

Figures 6-14A-C present the effect of the inflow conditions on the maximum dimensionless force fluctuations in hydraulic jumps. For x-, z- and y-directions and independent of the Froude or Reynolds numbers, the force fluctuations in hydraulic jumps with partially developed inflow conditions showed lower fluctuations for the same dimensionless distance. This difference is linked with longer roller lengths observed in partially developed hydraulic jumps as presented in Chapter 5.3. Otherwise, the decay rate of the maximum force fluctuation was similar between hydraulic jumps with partially and fully developed inflow conditions.

Figures 6-15A-C present the comparison of the cross-sectional average dominant frequencies for hydraulic jumps with fully and partially developed inflow conditions. $freq_{F_x, dom, avg}$ remained almost constant independent of the distances from the jump for both fully and partially developed inflow conditions (Figure 6-15A). Apart from experiment H ($Fr_1 = 3.8$, $Re = 6.2 \times 10^4$), the dimensionless dominant frequencies in the streamwise direction were similar for hydraulic jumps with fully and partially developed inflow conditions. The difference in experiment H may be related to the low force fluctuations in hydraulic jumps with low Froude numbers resulting in some uncertainties in the frequency analysis. Minor differences in the dominant transverse frequencies were observed for hydraulic jumps with fully and partially developed inflow conditions (Figure 6-15B). The results suggested that the characteristic frequencies of the transverse forces were independent of the inflow conditions. The dominant vertical frequencies were also similar for hydraulic jumps with fully and partially developed inflow conditions apart from Experiment H (Figure 6-15C).

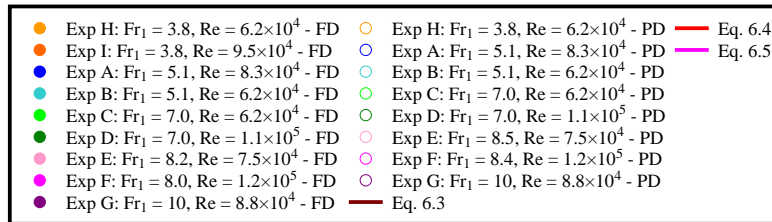
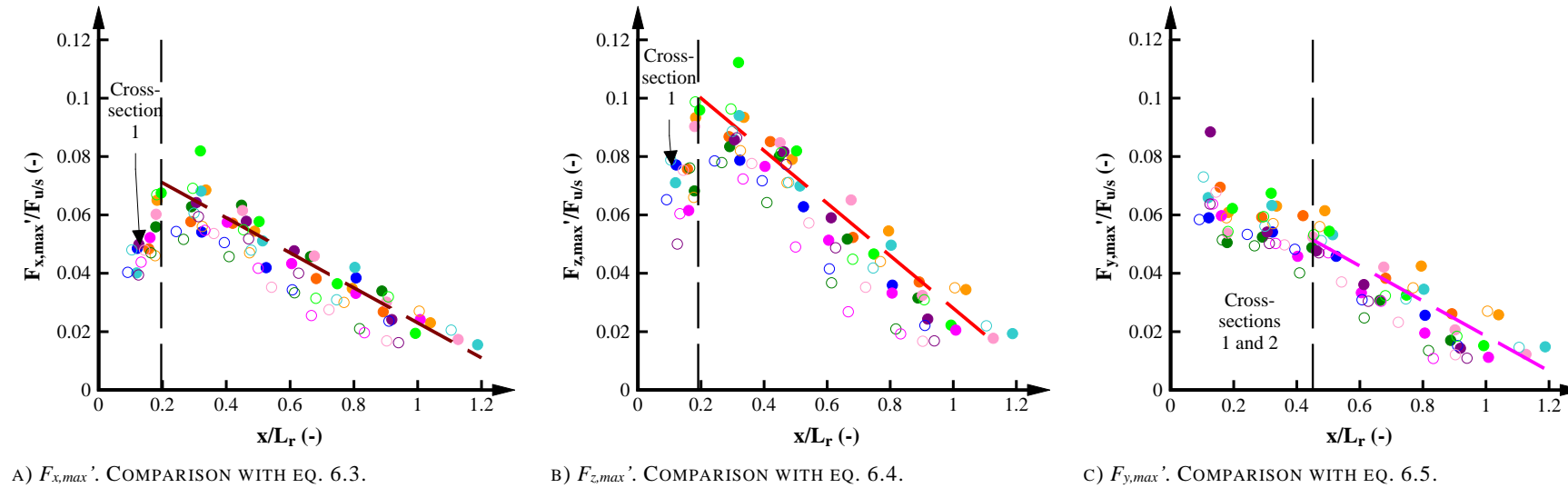
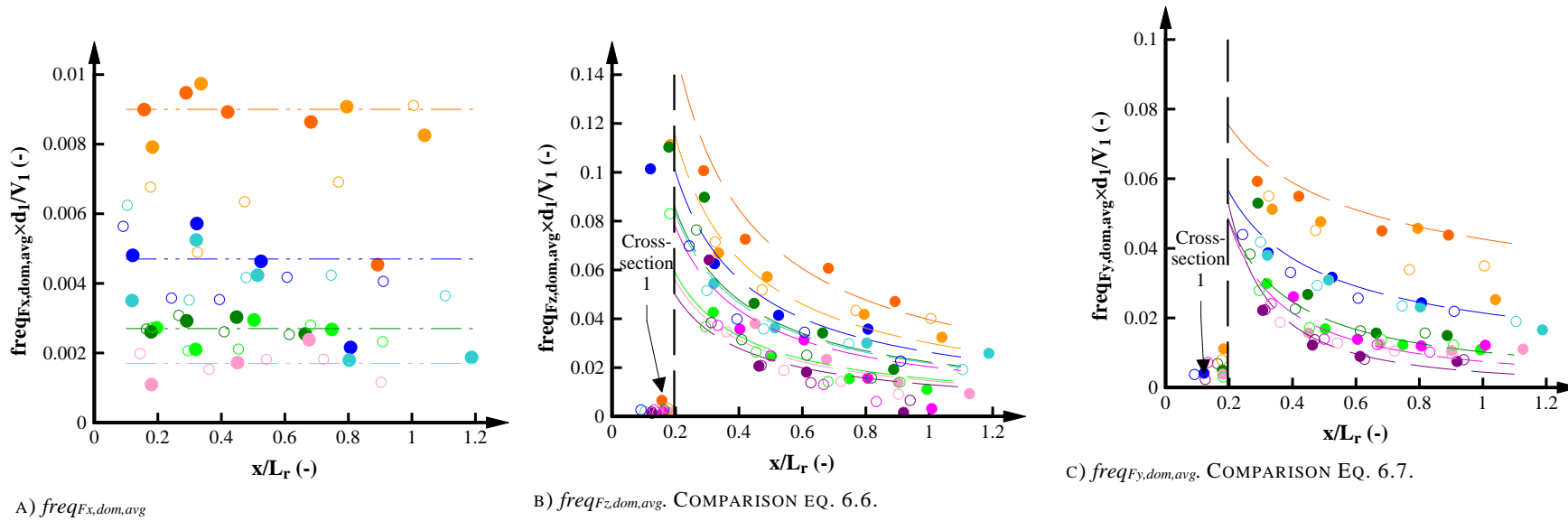


FIGURE 6-14. COMPARISON OF THE MAXIMUM FORCE FLUCTUATIONS FOR HYDRAULIC JUMPS WITH FULLY (FD) AND PARTIALLY (PD) DEVELOPED INFLOW CONDITIONS



● Exp H: $Fr_1 = 3.8$, $Re = 6.2 \times 10^4$, FD	○ Exp H: $Fr_1 = 3.8$, $Re = 6.2 \times 10^4$, PD
● Exp I: $Fr_1 = 3.8$, $Re = 9.5 \times 10^4$, FD	○ Exp A: $Fr_1 = 5.1$, $Re = 8.3 \times 10^4$, PD
● Exp A: $Fr_1 = 5.1$, $Re = 8.3 \times 10^4$, FD	○ Exp B: $Fr_1 = 5.1$, $Re = 6.2 \times 10^4$, PD
● Exp B: $Fr_1 = 5.1$, $Re = 6.2 \times 10^4$, FD	○ Exp C: $Fr_1 = 7.0$, $Re = 6.2 \times 10^4$, PD
● Exp C: $Fr_1 = 7.0$, $Re = 6.2 \times 10^4$, FD	○ Exp D: $Fr_1 = 7.0$, $Re = 1.1 \times 10^5$, PD
● Exp D: $Fr_1 = 7.0$, $Re = 1.1 \times 10^5$, FD	○ Exp E: $Fr_1 = 8.5$, $Re = 7.5 \times 10^4$, PD
● Exp E: $Fr_1 = 8.2$, $Re = 7.5 \times 10^4$, FD	○ Exp F: $Fr_1 = 8.4$, $Re = 1.2 \times 10^5$, PD
● Exp F: $Fr_1 = 8.0$, $Re = 1.2 \times 10^5$, FD	○ Exp G: $Fr_1 = 10$, $Re = 1.2 \times 10^5$, PD
● Exp G: $Fr_1 = 10$, $Re = 1.2 \times 10^5$, FD	

FIGURE 6-15. COMPARISON OF THE DIMENSIONLESS DOMINANT FREQUENCY FOR HYDRAULIC JUMPS WITH FULLY (FD) AND PARTIALLY (PD) DEVELOPED INFLOW CONDITIONS

6.8. SCALE EFFECTS

This chapter presents an analysis of the scale effects in terms of the forces on the submerged sphere inside the hydraulic jumps with fully developed inflow conditions. Hydraulic jumps with larger Reynolds numbers are represented with solid darker symbols. Figure 6-16A presents the vertical distributions of the streamwise forces for hydraulic jumps with similar Froude numbers and different Reynolds numbers. Apart from some data scatter, the vertical distributions of the streamwise forces showed minor differences with increasing Reynolds numbers suggesting no scale effects. These similarities were consistently observed at different cross-sections along the hydraulic jump indicating similar forces independent of the Reynolds numbers. The time-averaged transverse forces were also similar independent of the Reynolds numbers with force values close to zero suggesting symmetry in the measurements and no scale effects (Figure 6-16B). Figure 6-16C presents the vertical drag forces showing more negative drag forces for hydraulic jumps with lower Reynolds numbers in regions close to the jump toe indicating stronger upwards movements for less turbulent inflows. Further downstream, similar vertical drag forces were observed for different Reynolds numbers. The buoyancy forces showed similar upwards movements independent of the Reynolds numbers (Not shown in the present chapter) which was consistent with the void fraction distributions which did not show scale effects (Chapter 4.5).

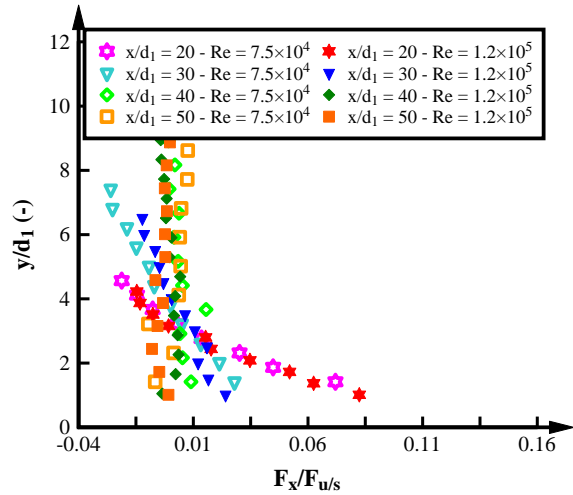
Figures 6-16D-F present the comparison of the vertical distributions of the streamwise, transverse and vertical force fluctuations respectively for identical Froude numbers. Independent of the Reynolds numbers, the shape of the vertical distributions of the force fluctuations in the streamwise, transverse and vertical directions was similar. Close to the jump toe, larger dimensionless fluctuations were observed for experiments with lower Reynolds numbers indicating scale effects. For regions located at the downstream end of the hydraulic jump, the dimensionless force fluctuations were similar for different Reynolds numbers indicating no scale effects. This result suggested that the force fluctuations in the roller region of the hydraulic jump are affected by scale effects while the conjugate depth region was not.

Figures 6-16G-I summarise the scale effect analyses of the dominant frequencies in the streamwise, transverse and vertical forces in hydraulic jumps in terms of a Froude similitude. The comparison was conducted for experiments with identical Froude numbers at similar locations x/L_r . Figure 6-16G presents the cross-sectional average dominant frequency in streamwise direction as function of the Reynolds numbers. For most of the analyses, no significant scale effects were observed indicating that the dimensionless dominant streamwise frequencies are independent of the Reynolds number. Figure 6-16H shows the dimensionless average dominant frequency of the transverse forces as a function of Reynolds numbers. A

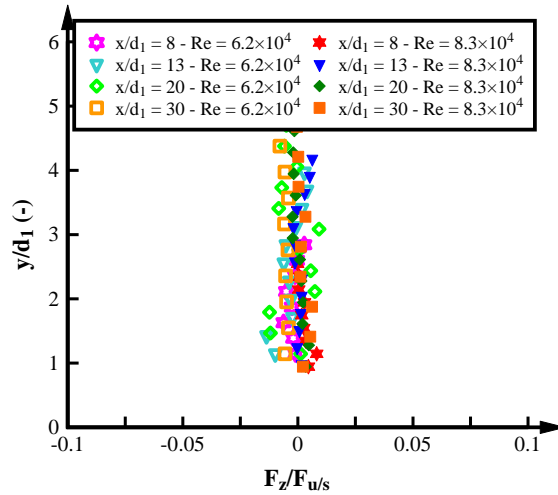
slight increase in the dominant transverse frequencies was observed with increasing Reynolds number. The increase was less prominent for experiments with $Fr_1 = 8.0$. Overall, the dimensionless dominant transverse frequency was a function of both Froude and Reynolds number as suggested in Eq. 6.6. The scale effects analysis of the dimensionless dominant vertical frequencies showed a minor increase in the dominant vertical frequency with increasing Reynolds number for $x/L_r < 0.5$ (Figure 6-16I). No scale effects were identified for regions located at the downstream end of the hydraulic jumps.

Free-surface dynamics and internal motions in fully aerated hydraulic jumps

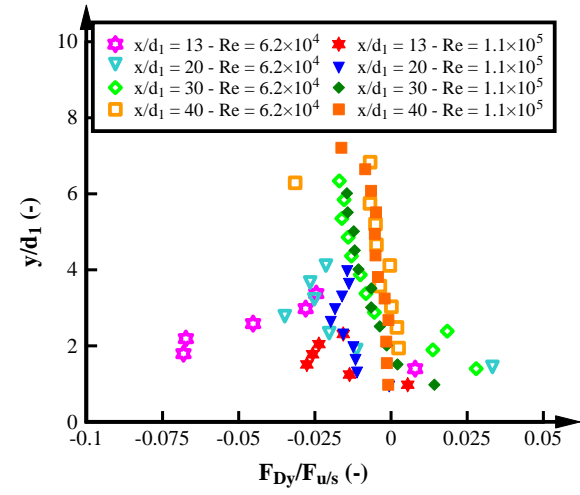
Chapter 6. Internal forces in Hydraulic Jumps



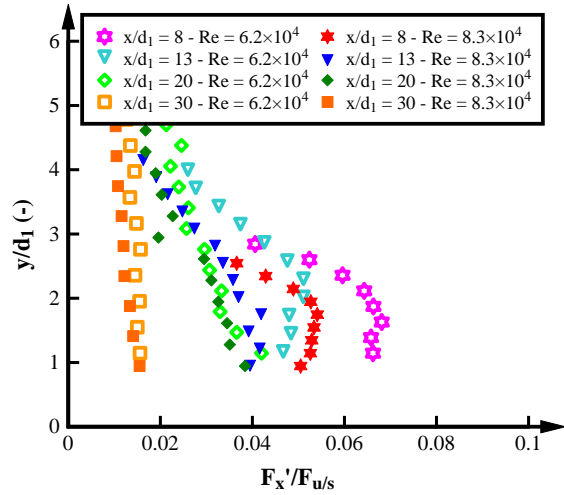
A) TIME-AVERAGED STREAMWISE FORCE. $Fr_l = 8.0 - 8.2$



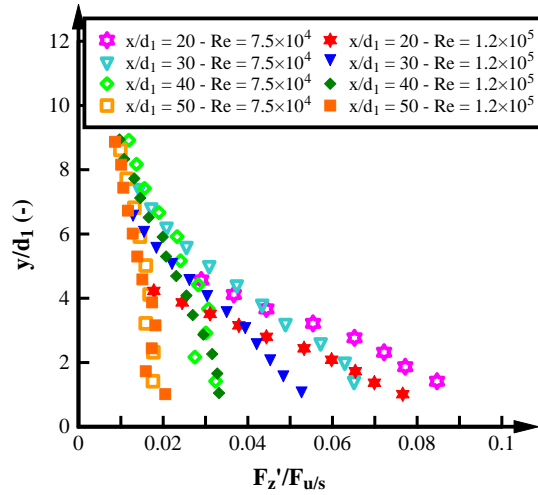
B) TIME-AVERAGED TRANSVERSE FORCE. $Fr_l = 5.1$



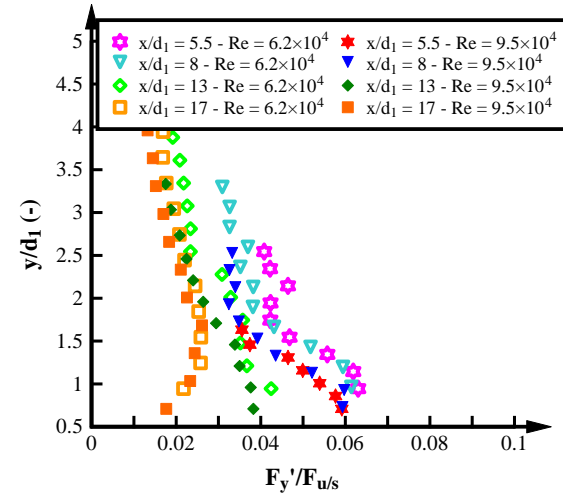
C) TIME-AVERAGED VERTICAL DRAG FORCE. $Fr_l = 7.0$



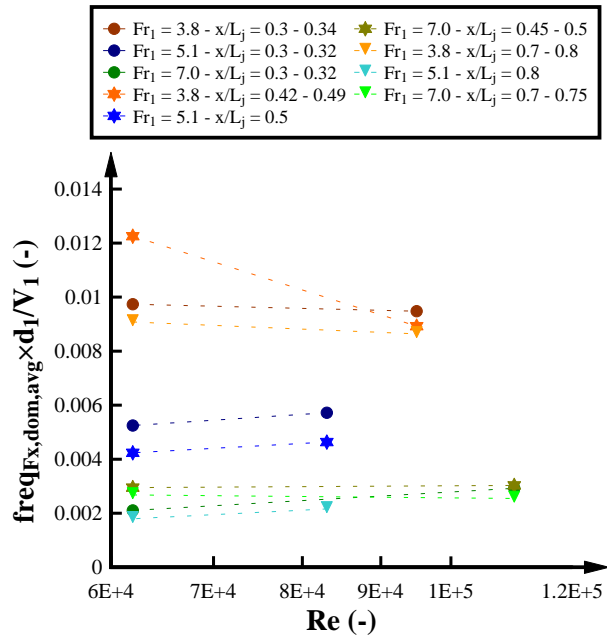
D) STREAMWISE FORCE FLUCTUATIONS. $Fr_l = 5.1$



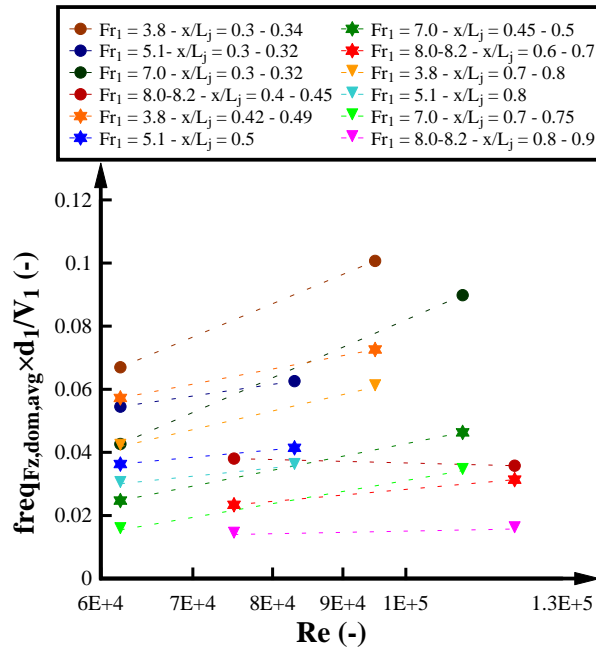
E) TRANSVERSE FORCE FLUCTUATIONS. $Fr_l = 8.0 - 8.2$



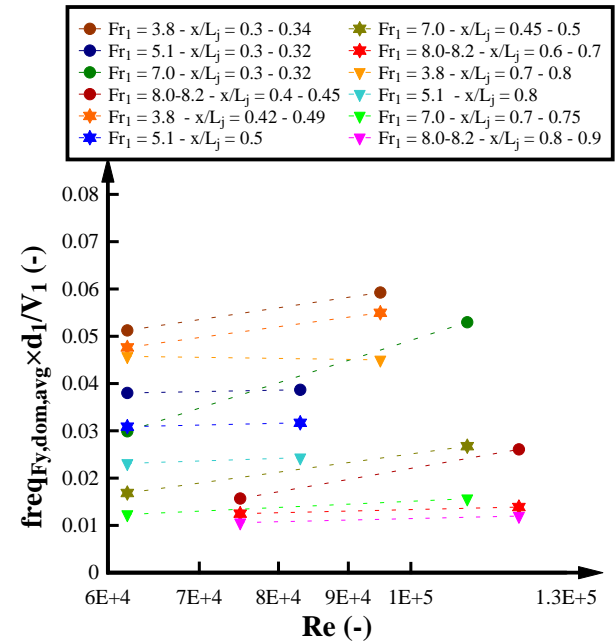
F) VERTICAL FORCE FLUCTUATIONS. $Fr_l = 3.8$



G) DOMINANT STREAMWISE FREQUENCIES



H) DOMINANT TRANSVERSE FREQUENCIES



I) DOMINANT VERTICAL FREQUENCIES

FIGURE 6-16. SCALE EFFECTS IN THE FORCE PARAMETERS IN HYDRAULIC JUMPS WITH FULLY DEVELOPED INFLOW CONDITIONS

6.9. SUMMARY

This chapter introduced a novel technique to quantify three-dimensional internal forces on a submerged sphere inside hydraulic jumps. The internal forces on the sphere were measured with a six-axis load cell mounted above the flume. The new system was employed to measure the forces, force fluctuations and characteristic frequencies in fully and partially developed hydraulic jumps with $3.8 < Fr_1 < 10$ and $6.2 \times 10^4 < Re < 1.2 \times 10^5$. The present study showed the suitability of the novel force measurement system for the direct measurement of internal flow motions in hydraulic jumps. The present results highlighted the strong three dimensionality of the internal flow motions and the need to include all flow directions into the internal analysis of the flow processes in hydraulic jumps.

Larger streamwise and vertical mean forces were recorded close to the jump toe while the transverse mean forces were almost zero. The largest forces close to the jump toe were in agreement with the higher velocities and vortex formation in this region. The vertical force was predominantly influenced by the void fraction surrounding the sphere showing lower forces in more aerated regions. The time-averaged force field showed dominant streamwise forces close to the channel bed near the jump toe while the buoyancy force dominated the upper part of the hydraulic jumps and regions far downstream of the jump toe.

Large force fluctuations were measured close to the jump toe in all directions reflecting the presence of large-scale motions within the flows. The peak in the streamwise force fluctuations occurred close to the location of the maximum bubble count rate and the strongest fluctuations were recorded in the transverse force component. The ratio between the maximum streamwise and transverse force fluctuations was approximately 72% while the ratio between the maximum vertical and transverse force fluctuations was about 72% for $Fr_1 < 7$ and 61% for experiments with $Fr_1 \geq 7$.

The frequency analysis identified dominant frequency ranges inside the hydraulic jump of about 0.3 Hz to 1.5 Hz, 1.5 Hz to 4 Hz and 4 Hz to 10 Hz. The first two frequency ranges were consistent with the dominant frequencies associated with the jump toe movements and free-surface fluctuations while the latter one appeared to correspond to the internal characteristic frequencies inside hydraulic jumps. Overall, $freq_{Fz,dom} > freq_{Fy,dom} > freq_{Fx,dom}$ indicating that the transverse forces had the fastest motions while the streamwise forces had the slowest motions.

An increase in the auto-correlation time scales in the streamwise, transverse and vertical direction was observed with increasing distance from the jump toe indicating an increase in large vortical structures along the hydraulic jump. For all cross-sections, $T_{Fy} > T_{Fz} > T_{Fx}$

indicating largest vortical structures in the vertical direction and smaller structures in the streamwise direction.

Figure 6-17 presents a summary of the internal forces on a sphere inside a hydraulic jump. The larger time-averaged forces and force fluctuations were consistently observed close to the jump toe in the shear region of the hydraulic jump. The magnitude of the forces and force fluctuations became weaker with increasing distance from the jump toe and in the upper region of the hydraulic jump. The observations of the forces on the submerged sphere provided novel observations of the internal three-dimensional motions in hydraulic jumps as well as a deeper understanding of the physical and dissipative processes along hydraulic jumps.

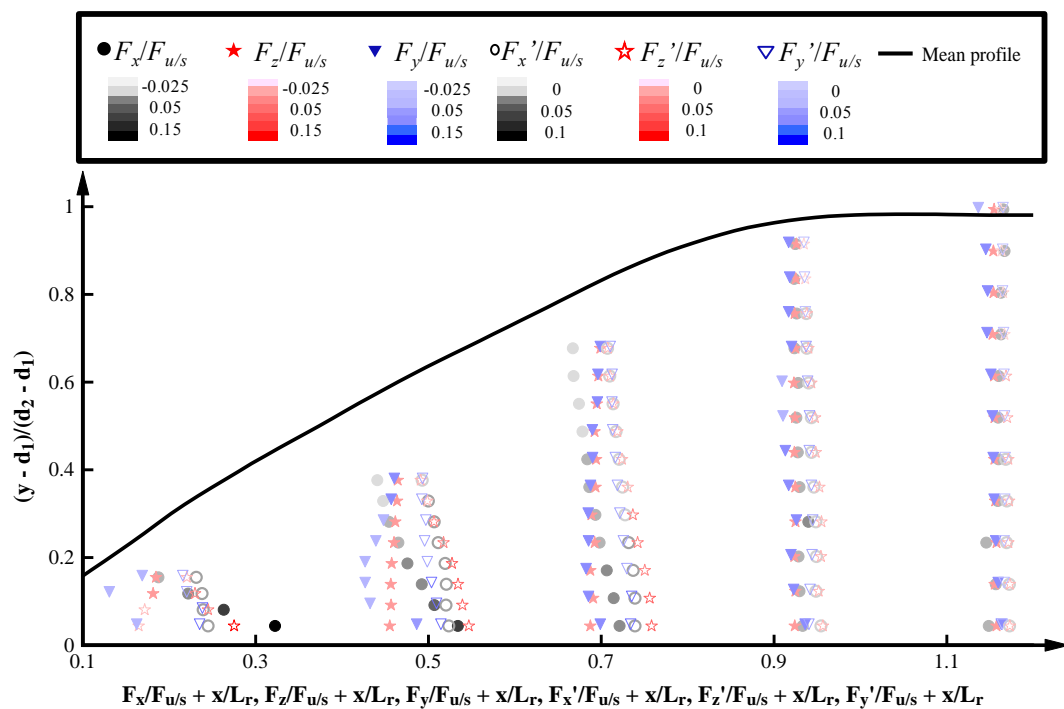


FIGURE 6–17. COMPILATION OF THE INTERNAL FORCES MEASURED OVER A SPHERE IN A HYDRAULIC JUMP WITH FULLY DEVELOPED INFLOW CONDITIONS (EXPERIMENT E: $Fr_l = 8.2$, $Re = 7.5 \times 10^4$, FULLY DEVELOPED INFLOW CONDITIONS).

The present study investigated any potential effect of the boundary layer development upstream the hydraulic jump into the internal motions of the hydraulic jump. The results showed some effects in terms of the time-averaged forces and free-surface fluctuations. An additional analysis of the scale effects in terms of Froude similitude was also conducted highlighting some parameters affected by scale effects. Table 6-2 presents a summary of the effects of the inflow conditions and the scale effects in the internal forces of hydraulic jumps.

TABLE 6–2. SUMMARY TABLE OF THE EFFECT OF THE INFLOW CONDITIONS AND SCALE EFFECTS IN THE INTERNAL MOTIONS IN THE HYDRAULIC JUMP

Parameter	Comparison PD vs FD	Scale effects $6.2 \times 10^4 < Re < 1.2 \times 10^5$
Time-averaged streamwise force (F_x)	No differences	No scale effects

Parameter	Comparison PD vs FD	Scale effects $6.2 \times 10^4 < Re < 1.2 \times 10^5$
Time-averaged transverse force (F_z)	Slight larger deviations from zero in PD	No scale effects
Time-averaged vertical force (F_y)	$F_{Dy,max}$ occurred in a lower vertical position in PD	<ul style="list-style-type: none"> • Scale effects: More negative F_{Dy} for lower Re close to the jump toe. • No scale effects in F_{Dy} at the downstream end of the hydraulic jump • No scale effects in $F_{buoyancy}$
Streamwise force fluctuations (F_x')	Lower fluctuations for the same x/L_r in PD. Similar decay.	<ul style="list-style-type: none"> • Roller region: Scale effects: Lower $F_x'/F_{u/s}$ with increase in Re • Conjugate depth region: No scale effects
Transverse force fluctuations (F_z')	Lower fluctuations for the same x/L_r in PD. Similar decay.	<ul style="list-style-type: none"> • Roller region: Scale effects: Lower $F_z'/F_{u/s}$ with increase in Re • Conjugate depth region: No scale effects
Vertical force fluctuations (F_y')	Lower fluctuations for the same x/L_r in PD. Similar decay.	<ul style="list-style-type: none"> • Roller region: Scale effects: Lower $F_y'/F_{u/s}$ with increase in Re • Conjugate depth region: No scale effects
Averaged dominant streamwise frequency ($freq_{F_x,dom,avg}$)	No differences	No scale effects
Averaged dominant transverse frequency ($freq_{F_z,dom,avg}$)	No differences	Scale effects: Larger $freq_{F_z,dom,avg}$ with increase in Re
Averaged dominant vertical frequency ($freq_{F_y,dom,avg}$)	No differences	<ul style="list-style-type: none"> • Close to the jump toe: Minor scale effects: Larger $freq_{F_y,dom,avg}$ with increase in Re • Downstream end of the jump: No scale effects

7

DISCUSSION

7.1. INTRODUCTION

The hydraulic jump is one of the most complex hydraulic phenomena. The strong turbulence combined with large aeration and free-surface fluctuations have resulted in experimental and numerical limitations and a better understanding of the hydraulic jump dynamics is needed. This research utilised novel experimental techniques to expand the current understanding of hydraulic jumps providing a) the most detailed analysis of the time-varying free-surface features using a LIDAR, b) a unique quantification of the three-dimensional motions inside hydraulic jumps via force measurements on a submerged sphere and c) the estimation of the effects of the inflow conditions on the air-water flow properties, the free-surface features and internal motions. This chapter combines the results of previous chapters, i.e. air-water flow properties (Chapter 4), free-surface features (Chapter 5) and internal motions (Chapter 6) to obtain a better definition of the dynamic behaviour along hydraulic jumps.

Hydraulic jumps are characterised by air-water interactions, free-surface fluctuations and strong three-dimensional motions. Two distinctive air-water flow regions are commonly distinguished in hydraulic jumps, a) the shear region (SR) which occurs in the lower part of the hydraulic jump, which is characterised by air entrapment, large advective motions and bubble break-up (Chanson 1996; Chanson and Brattberg 2000; Murzyn et al. 2005), and b) the recirculation region (RR), which occurs in the upper part of the hydraulic jump and is characterised by flow recirculation, water splashes and foam (Chanson 1996; Murzyn et al. 2005; Chanson and Brattberg 2000).

Figure 7-1 presents an overview of the shear and recirculation regions combining characteristic parameters of the present experiments for fully developed inflow conditions including the time-averaged free-surface profiles, the locations of characteristic air-water flow parameters and the characteristic force fluctuations. All data for fully developed inflow conditions are illustrated along a non-dimensional hydraulic jump showing close similarity for all parameters. The time-averaged free-surface profiles increased along the transition from supercritical shallow fast flows to subcritical deep slow flows at the downstream end. The elevations of the maximum and minimum void fractions C_{max} and C_{min} increased with increasing distance reflecting the increasing relevance of the buoyancy on the entrained air bubbles in downstream direction. The elevation corresponding to C_{min} represented the boundary between the shear and recirculation regions and all parameters located above C_{min} were in the recirculation region. Despite some data scatter, the boundary between the shear and recirculation regions could be represented by a linear equation ($R^2 = 0.91$):

$$\frac{y-d_1}{d_2-d_1} = -0.004 + 1.036 \times (x/L_r) \quad (7.1)$$

The location of the maximum bubble count rate in the shear region F_{maxSR} was slightly below C_{max} suggesting that the higher levels of shear stress occurred below the impingement region as consequence of a dissymmetry in the diffusion process between the air entrainment and the vorticity affecting the bubbles (Chanson and Brattberg 2000; Chanson 2006). The elevations corresponding to the maximum bubble count rates in the recirculation region F_{maxRR} and the elevations Y_{50} corresponding to $C = 0.5$, were similar to the time-averaged free-surface profiles recorded with the LIDAR (Figure 7-1). The maximum interfacial velocities V_{max} were recorded close to the channel bed in agreement with the wall jet shape of the velocity distributions (Rajaratnam 1965; Chanson and Brattberg 2000). Similarly, the maximum force fluctuations $F_x'_{max}, F_z'_{max}, F_y'_{max}$ were observed close to the channel bed indicating faster interfacial velocities, stronger fluctuating motions and instabilities in this region.

The shear region comprised characteristic maxima in flow advection (C_{max}, F_{maxSR}), interfacial velocities (V_{max}) and force fluctuations ($F_x'_{max}, F_z'_{max}, F_y'_{max}$). The maximum flow aeration consistently occurred in the upper part of the shear region and the maximum velocities and force fluctuations close to the channel bed. A subdivision of the shear region is therefore proposed: a) the advective shear region (ASR) and b) the wall jet shear region (WJSR) (Figure 7-1). ASR is characterised by maximum aeration and advective transport, while WJSR comprises the largest velocities and flow instabilities. Similar regions were defined previously based upon the 2D velocity fields in steady hydraulic jumps with $4.5 < Fr_l < 5.35$ (Lin et al. 2012). Note that F_{maxSR} was located in the WJSR close to the jump toe ($x/L_r < 0.5$) and within the ASR further downstream ($x/L_r > 0.5$) highlighting the effect of the buoyancy in the second half of the hydraulic jump. The limit between ASR and WJSR can be estimated by an exponential equation (Figure 7-1):

$$\frac{y-d_1}{d_2-d_1} = 0.054 \times e^{2.023\left(\frac{x}{L_r}\right)} \quad (7.2)$$

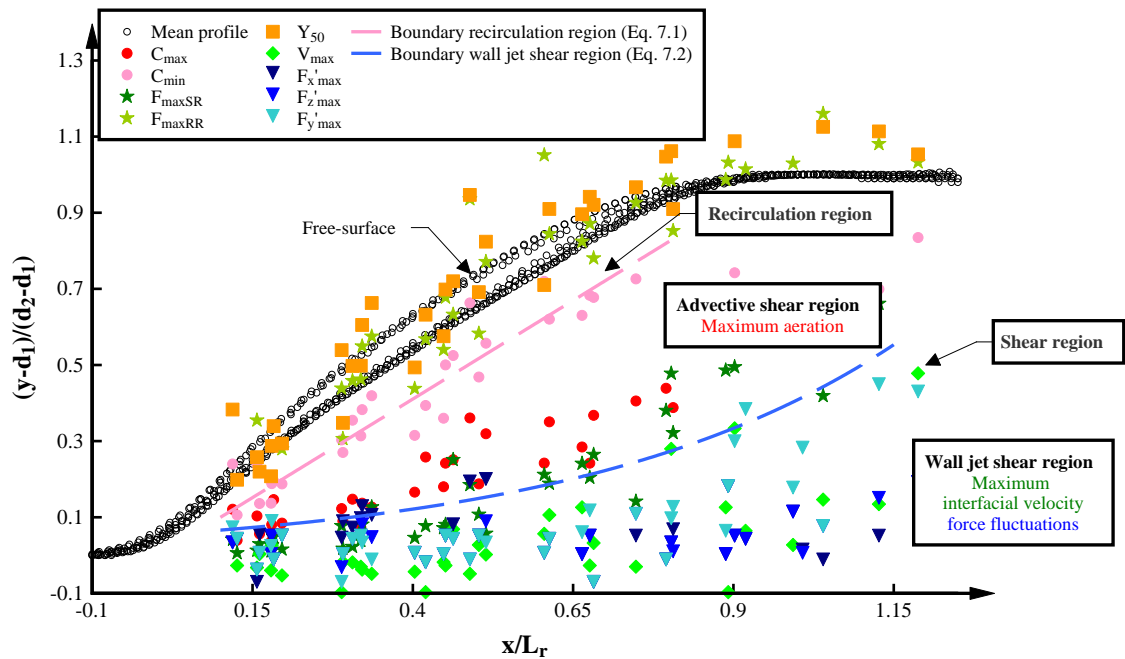


FIGURE 7-1. SUMMARY OF CHARACTERISTIC AIR-WATER FLOW AND FORCE PARAMETERS FOR ALL HYDRAULIC JUMPS WITH FULLY DEVELOPED INFLOW CONDITIONS; DEFINITION OF HYDRAULIC JUMP REGIONS.

7.2. TIME-AVERAGED PROPERTIES IN HYDRAULIC JUMPS

The time-averaged analysis of hydraulic jumps provides a “static” picture of the dynamic patterns of hydraulic jumps. Although the time-averaged properties do not provide an understanding of the time-varying processes, they provide important insights into typical hydraulic jump features. Figure 7-2 presents dimensionless contour plots of the most relevant time-averaged air-water flow properties (Figures 7-2A-D) and mean force properties (Figures 7-2E and F) for the present hydraulic jumps with fully developed inflow conditions. In Figure 7-2, the mean free-surface profile, and the boundaries of the wall jet shear and recirculation regions are shown as reference. Each contour plot includes all present data of hydraulic jumps with fully developed inflow conditions highlighting similar patterns and self-similarity in time-averaged flow properties independent of the Froude and Reynolds numbers (Figure 7-2).

Figure 7-2A presents the contour plot of all void fraction distributions. Low void fractions were observed in the wall jet shear region while C_{max} consistently occurred in the advective shear region. The void fractions decayed continuously along the shear region with a tendency of upwards motions towards the free-surface due to the buoyancy effects and the overall trajectory in the transition from supercritical to subcritical flows (Chanson 2006; Chanson 2007b). This upwards motion resulted in continuous air detrainment as observed in the similarity in void fraction levels in the recirculation region along the hydraulic jump (Figure 7-2A). Note that the time-averaged free-surface profiles were close to $C = 0.5$ (Y_{50}).

The contour plot of the normalised bubble count rates F/F_{maxSR_HJ} are shown in Figure 7-2B. The maximum bubble count rates were observed in the wall jet shear region suggesting the largest shear stress and break-up of air within this region. The WJSR is also characterised by the largest interfacial velocities (Chanson and Brattberg 2000; Chanson 2006; Kucukali and Chanson 2007) and strongest streamwise forces (Figure 7-2D and F respectively). The bubble count rate decreased gradually with increasing distance from the jump toe and elevation from the channel bed (Chanson and Brattberg 2000; Murzyn et al. 2005; Kucukali and Chanson 2007). Note that in the second half of the hydraulic jump ($x/L_r > 0.5$), the bubble count rate was less than 25% of the maximum bubble count rate suggesting a significant drop in the number of bubbles in this region. In the recirculation region, the bubble count rate represented the quantification of an air-water mixture rather than a quantification of a passage of bubbles (Murzyn et al. 2005). These structures presented similar bubble count rates along the hydraulic jump representing 15% of the maximum bubble count rate.

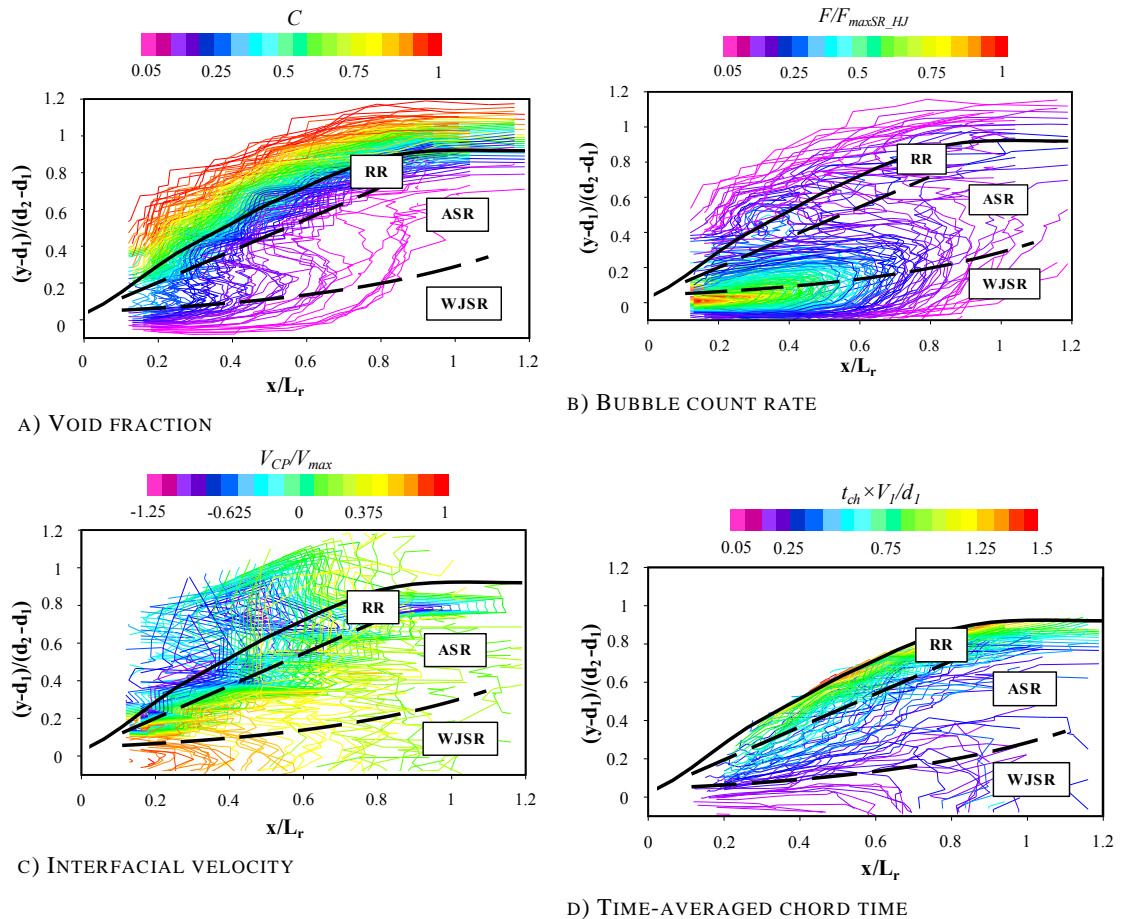
Figure 7-2C presents the contour plots of the interfacial velocities. The maximum velocity was recorded close to the jump toe in the wall jet shear region; V_{max} decreased gradually with increasing distance from the jump toe (Rajaratnam 1965; Ohtsu and Yasuda 1990a; Chanson and Brattberg 2000; Murzyn and Chanson 2007; Wang 2014) with velocities of $0.2 \times V_{max}$ at the downstream end of the hydraulic jump. In the advective shear region, the velocity distributions were almost constant, i.e. $0.4 \times V_{max}$. Large data scatter and negative velocities were recorded in the recirculation region (Hager 1992; Chanson and Brattberg 2000; Zhang et al. 2014; Kramer and Valero 2019).

The time-averaged chord times are presented in Figure 7-2D. The chord times increased with increasing elevation highlighting larger chord times in the recirculation region with $t_{ch,mean} \times V_l/d_l > 1$ at the mean free-surface profile indicating bubble collapse towards the upper part of the hydraulic jump. The large bubble sizes are linked with large void fractions and low bubble count rates in the recirculation region. In the wall jet shear region, an increase in the time-averaged chord times with increasing distance from the jump toe suggested a horizontal bubble merging due to flow deceleration associated with a decrease in the interfacial velocity (Wang 2014). This region was also characterised by a decrease in aeration and bubble count rate region, indicating lesser number of bubbles of larger size. In the advective shear region, the time-averaged chord times were almost constant t of about $t_{ch,mean} \times V_l/d_l = 0.4$ in agreement with an almost constant interfacial velocity.

The contour lines of the normalised time averaged streamwise forces $F_{x,max}/F_{x,max_HJ}$ are shown in Figure 7-2E. The largest forces were consistently observed in the wall jet shear region close to the jump toe in agreement with the largest interfacial velocities (Figure 7-2C). The forces

decreased along the hydraulic jump resulting in $F_{x,max}/F_{x,max_HJ} < 0.5$ for $x/L_r > 0.4$. This result highlighted that the strongest forces were enclosed within the first half of the hydraulic jump. In the advective shear region, the streamwise forces were close to zero while negative forces were recorded in the recirculation region. Overall the time-averaged streamwise forces showed good agreement with the velocity distributions (Figure 7-2C).

Figure 7-2F presents the contour plots of the normalised vertical drag force $F_{Dy}/F_{Dy,max_HJ}$. Some data scatter was identified in the wall jet shear region linked with the limitations of vertical force recordings close to the channel bed. Despite the data scatter, the maximum vertical drag forces were consistently observed close to the jump toe linked with stronger vortex shedding resulting in larger upwards motions at this region. The forces decreased longitudinally with values close to zero at the downstream end of the hydraulic jump in the conjugate depth region.



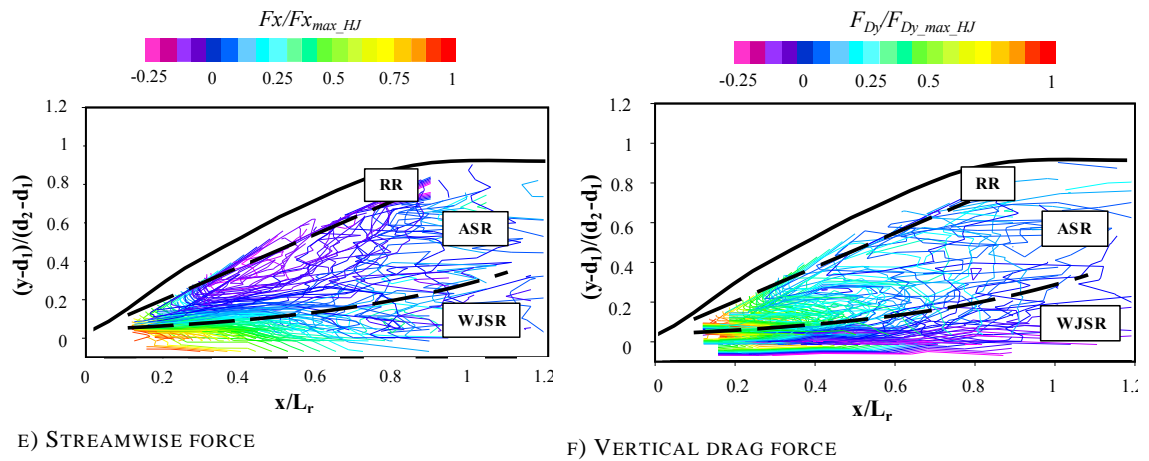


FIGURE 7-2. CONTOUR PLOTS OF TIME-AVERAGED AIR-WATER FLOW PROPERTIES AND FORCE PARAMETERS IN HYDRAULIC JUMPS WITH FULLY DEVELOPED INFLOW CONDITIONS. WJSR: WALL JET SHEAR REGION; ASR: ADVECTIVE SHEAR REGION; RR: RECIRCULATION REGION.

All time-averaged properties varied along the hydraulic jumps associated with the rapid transition from super- to subcritical flows. Figure 7-3 presents a sketch summarising typical properties along a hydraulic jump. Note that the void fraction distributions are only shown in the shear region (Figure 7-3). Clear advective peaks in the void fractions together with distinct peaks in bubble count rate and interfacial velocities respectively were identified in the jump toe and roller regions ($x/L_r < 0.7$). In contrast, minimal aeration and more uniform velocity distributions were observed towards the downstream end of the roller region and in the conjugate depth region. Negative motions were observed in the interfacial velocities and the forces in the recirculation region for $x/L_r < 0.7$ while no flow recirculation was observed at the downstream end of the roller region.

In the jump toe region, the hydraulic jump was characterised by larger aeration ($C > 0.4$ and $F \times d_1/V_1 = 1$), largest velocities ($V_{CP}/V_{max} > 0.6$) and strongest streamwise and vertical forces ($F_{xy}/F_{u/s} > 0.1$). Further downstream, in the roller region, the violent and instable motions were weakened with increasing distance from the jump toe representing a qualitative quantification of the energy dissipation along the hydraulic jump. Despite the large flow instabilities, and free-surface fluctuations, minor forces were recorded in the recirculation region along the hydraulic jump suggesting low effects of the recirculation region on the dissipative processes. At the downstream end, the flow was more stable, with minor aeration and weak forces indicating that most of the dissipative processes occurred further upstream in the shear region of the hydraulic jump together with the largest advective motions and break-up of bubbles.

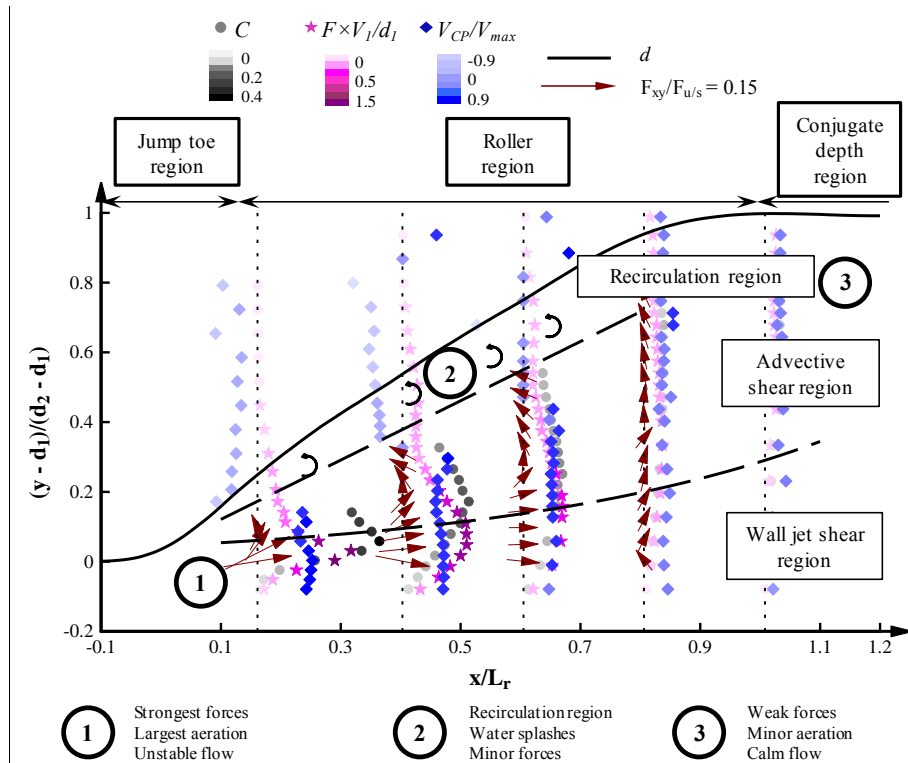


FIGURE 7-3. SUMMARY OF THE TIME-AVERAGED PROPERTIES IN A HYDRAULIC JUMP WITH FULLY DEVELOPED INFLOW CONDITIONS (EXPERIMENT F: $Fr_1 = 8.0$, $Re = 1.2 \times 10^5$).

7.3. FLUCTUATIONS IN HYDRAULIC JUMPS

The hydraulic jump is a dynamic phenomenon characterised by flow instabilities and internal and external fluctuations, i.e. instantaneous variations in free-surface profiles, flow aeration and internal motions. The fluctuations are linked with energy dissipation processes (Madsen and Svendsen 1983; Mignot and Cienfuegos 2010). Figure 7-4 presents a summary of the jump toe oscillations, free-surface and force fluctuations in all present hydraulic jumps with fully developed inflow conditions. All data collapsed relatively well irrespective of Froude and Reynolds numbers highlighting self-similarity in the fluctuations of the free-surface, jump toe and internal motions. The standard deviation of the jump toe motions was within $-0.06 < x/L_r < 0.06$. Large fluctuations of the free-surface were observed along the hydraulic jumps with maximum fluctuations in the first half of the hydraulic jump for $0.2 < x/L_r < 0.5$. This observation was consistent with previous studies (Murzyn et al. 2007; Murzyn and Chanson 2009a; Chachereau and Chanson 2011; Wang 2014). This region was characterised by the strongest free-surface instabilities and water splashes. The maximum force fluctuations on the sphere occurred in the wall jet shear region within the first half of the hydraulic jump $x/L_r < 0.5$ linked with the faster flow velocities and associated turbulence due to the supercritical flow impingement at the jump toe (Lin et al. 2012). The force fluctuations decreased along the hydraulic jump and with increasing elevation from the channel bed representing the energy dissipation rate along the hydraulic jumps. While the strongest force fluctuations occurred in the wall jet region for $0.2 <$

$x/L_r < 0.5$, significant force fluctuations were continuously observed along the hydraulic jump in the shear region with $F_x'/F_{x' \max}$, $F_z'/F_{z' \max}$, $F_y'/F_{y' \max} = 0.5$ for $x/L_r = 0.8$. This observation provided an estimate of the remaining energy at the downstream end of the roller region.

The analysis of the hydraulic jump fluctuations highlighted the wall jet shear region downstream of the jump toe as the area of strongest motions and largest dissipative processes in hydraulic jumps. This region is characterised by the largest bubble break-up linked with the largest shear stress (Chanson and Brattberg 2000; Chanson 2006), largest interfacial velocities (Chanson and Brattberg 2000; Murzyn and Chanson 2007; Wang 2014) and strongest time-averaged streamwise and vertical forces (Chapter 7.2). The strongest time-averaged motions within the wall jet shear region and close to the jump toe led to more significant flow disturbances, largest oscillations and flow instabilities especially in the transverse flow direction. Further downstream, the three-dimensional force fluctuations decreased linearly with increasing distance from the jump toe suggesting a constant decay in the large-scale turbulent motions along the hydraulic jump (Chapter 6.6). The decay was faster in the transverse direction highlighting the importance of the transverse motions on the dissipative processes inside hydraulic jumps. Overall, Figure 7-4 presents a clear picture of the external and internal fluctuations along the hydraulic jumps providing new insights into the dissipative processes in hydraulic jumps. Such information may provide useful guidance for stilling basin designs.

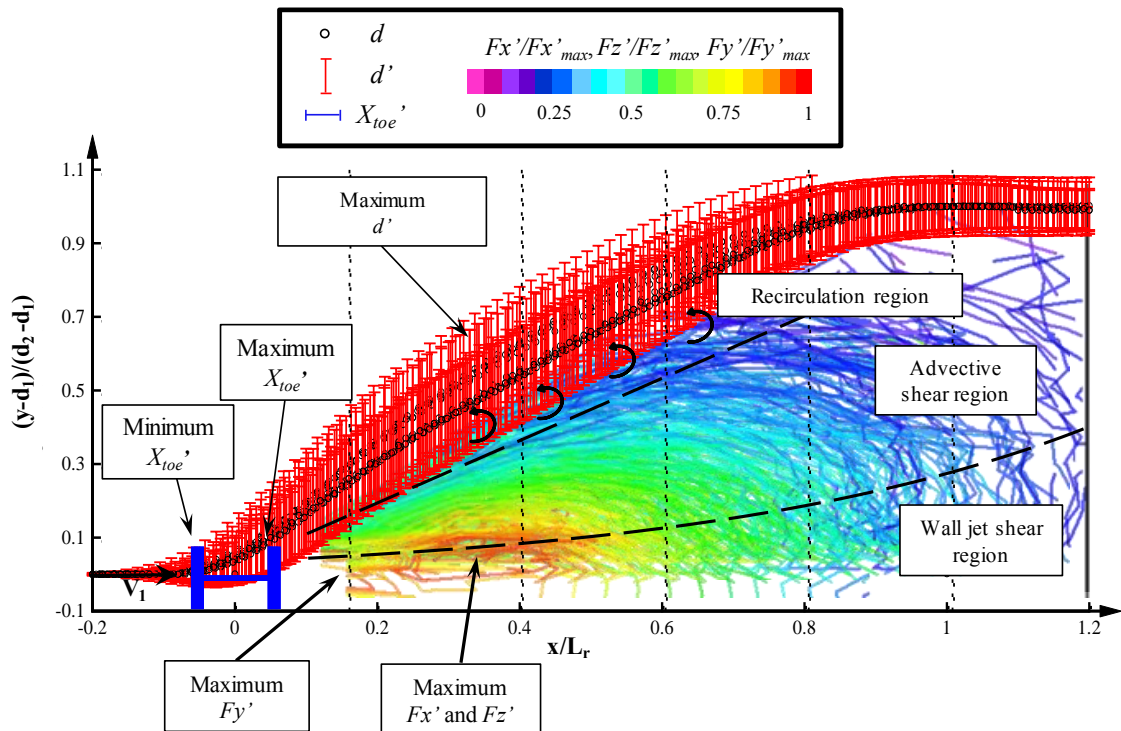


FIGURE 7-4. SIMILARITY IN FLUCTUATIONS ALONG HYDRAULIC JUMPS WITH FULLY DEVELOPED INFLOW CONDITIONS.

7.4. CHARACTERISTIC FREQUENCIES IN HYDRAULIC JUMPS

Frequency analyses were conducted for all present hydraulic jumps to identify the distribution of the characteristic frequencies of the jump toe oscillations, free-surface fluctuations and the internal three-dimensional motions of the submerged sphere. Figure 7-5 presents a contour plot of the dominant frequencies along a hydraulic jump with fully developed inflow conditions. In the upper part of the hydraulic jump, the characteristic frequencies of the free-surface and the frequencies of the submerged sphere were similar with $1.5 < freq_{fs} < 4$ Hz and in agreement with reported free-surface frequencies (Murzyn and Chanson 2009a; Chachereau and Chanson 2011b). These frequencies represent the fluctuations of the free-surface features comprising vertical flow instabilities and water splashes. Note that the free-surface frequencies remained almost constant along the hydraulic jump in contrast with the longitudinal variations of the free-surface fluctuations (Figure 7-4). This result suggested that the oscillation patterns were similar along the hydraulic jump albeit the amplitude of the fluctuations weakened with the distance. Close to the jump toe ($x/L_r < 0.2$), the characteristic frequencies were dominated by the jump toe oscillations with free-surface and internal force frequencies between 0.5 and 1.5 Hz. This result highlighted the influence of the jump toe oscillations on the internal and external motions of hydraulic jumps. For $0.2 < x/L_r < 0.5$, the internal force frequencies in the streamwise and transverse directions were $0.5 \text{ Hz} < freq_{F_x} < 9 \text{ Hz}$ and $2.5 \text{ Hz} < freq_{F_z} < 10 \text{ Hz}$ respectively indicating that the most intense motions occurred just downstream of the jump toe. These frequencies were similar to streamwise frequencies recorded with a pressure sensor by Wang et al. (2014b). Note that the largest frequencies were observed in the advective shear region while the largest fluctuations occurred in the wall jet shear region (Chapter 7.3). This result suggested that the internal characteristic frequencies in the hydraulic jump may be more related to the influence of the vortical structures and reverse flow motions and lesser with the regions of strongest force fluctuations. Further downstream, the internal motions in the hydraulic jump became weaker with characteristic frequencies between $0.5 \leq freq_{F_x}, freq_{F_z} \leq 4$ Hz in streamwise and transverse directions. At the downstream end of the hydraulic jumps, slower motions were recorded with frequencies predominantly between 0.5 and 3 Hz. The frequencies of the vertical forces on the sphere were consistently $1.5 < freq_{F_y} < 4$ in agreement with the frequencies of the free-surface motions. In agreement with the time-averaged properties (Chapter 7.2) and the fluctuation features (Chapter 7.3), the internal characteristic frequencies along the hydraulic jump were faster at the beginning of the roller region and decreased with increasing distance from the jump toe. This result confirmed that the largest dynamic behaviour in the hydraulic jump occurred within the first half of the hydraulic jump followed by a decay in the energetic motions with increasing distance from the jump toe (Chapter 6.6).

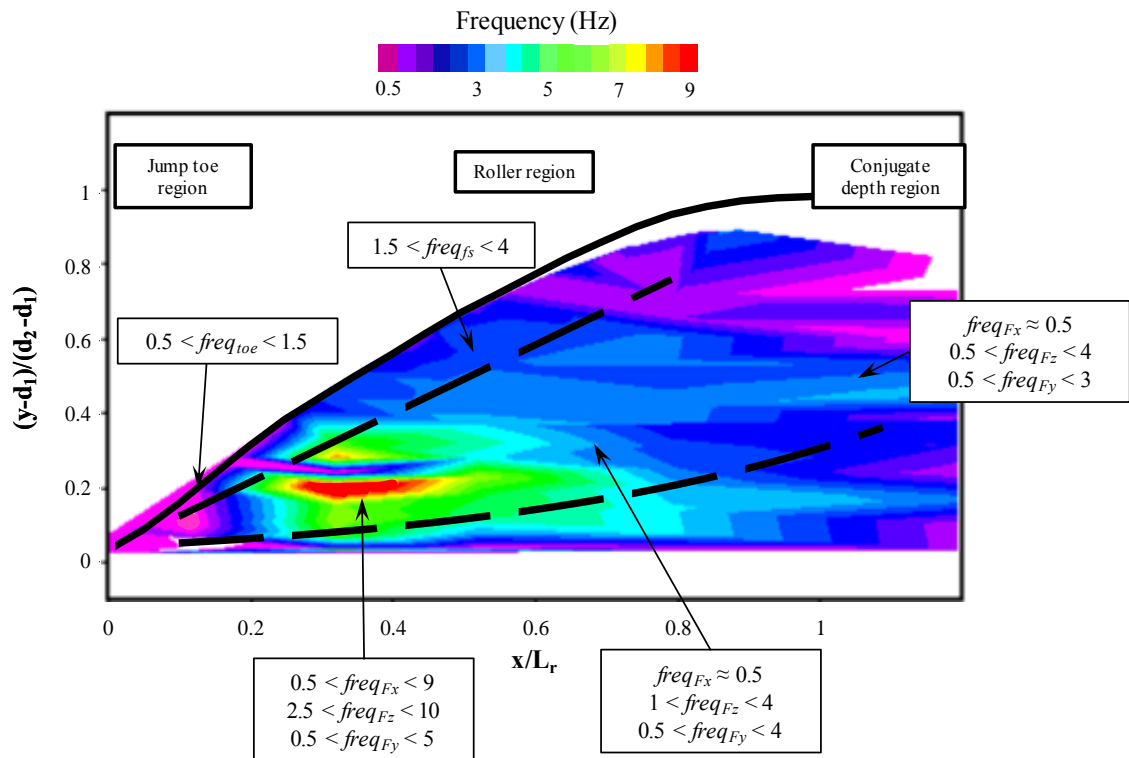


FIGURE 7-5. CHARACTERISTIC FREQUENCIES OF THE MOTIONS IN HYDRAULIC JUMPS WITH FULLY DEVELOPED INFLOW CONDITIONS (EXPERIMENT B: $Fr_1 = 5.1$, $Re = 6.2 \times 10^4$).

7.5. AUTO-CORRELATION TIME SCALES ALONG HYDRAULIC JUMPS

The auto-correlation time scales represent an estimation of the lifetime of the advective vortical structures in the hydraulic jump. Figure 7-6 presents typical auto-correlation time scale distributions of the air-water flow properties ($T_{air,auto}$) (Chapter 4.3.7), of the free-surface motions ($T_{fs,auto}$) (Chapter 5.7) and of the streamwise forces on the sphere ($T_{Fx,auto}$) (Chapter 6.5) in a hydraulic jump with fully developed inflow conditions. The mean free-surface profile as well as the boundaries of the wall jet shear and recirculation regions are included for reference. The internal auto-correlation time scales ($T_{air,auto}$ and $T_{Fx,auto}$) were measured at five different cross sections while the ($T_{fs,auto}$) were measured continuously along the hydraulic jump's surface. Note that the free-surface time scales are only illustrated at the five cross-sections for better comparison (Figure 7-6).

The auto-correlation time scales of the bubbly flow structures represent the advective coherence of the bubbly flow structures given by the conductivity probe raw signal (Chanson and Carosi 2007). $T_{air,auto}$ increased with increasing elevation up to a maximum in the recirculation region. This result suggested larger coherence in the bubbly flow structures in the upper part of the hydraulic jumps linked with larger air-water flow structures near the free-surface (Wang 2014; Wang and Murzyn 2017). The auto-correlation time scales of the streamwise forces on the submerged sphere measured the lifetime of the large scale vortical structures in the hydraulic

jump. Smaller $T_{Fx,auto}$ were observed in the shear region while an increase in the vortical structures was observed towards the recirculation region. While $T_{Fx,auto}$ and $T_{air,auto}$ measured different parts of the flow motions (large scale forces versus air-water flow structures), the distributions of $T_{air,auto}$ and $T_{Fx,auto}$ showed overall similar trends indicating a relationship between the bubbly flow structures and the large vortices in hydraulic jumps. An increase in $T_{Fx,auto}$ was recorded at the downstream end of the hydraulic jump potentially linked with the slow periodic oscillations in the subcritical region of the hydraulic jump resulting in large signal correlation. Figure 7-6 also presents the free-surface auto-correlation time scales at the five cross-sections. $T_{fs,auto}$ represents a characteristic advective time of the turbulent free-surface motions along the surface of the hydraulic jump. Larger $T_{fs,auto}$ were observed close to the jump toe linked with the influence of the inflow depth at this region which increased the auto-correlation function and the resulting time scale. Further downstream, the free-surface auto-correlation time scales were considerably larger compared to the auto-correlation time scales of the bubbly flow structures and the streamwise forces. The difference may be linked with the different flow structures. $T_{air,auto}$ represented the small scale air-water flow structures (Chanson and Carosi 2007), $T_{Fx,auto}$ measured the large vortical structures captured by the submerged sphere ($\varnothing_{sphere} = 0.054$ m) and $T_{fs,auto}$ represented the coherent structures along the free-surface of the roller. Apart from some deviations in the magnitude of the auto-correlation time scales, the trends of all auto-correlation scales showed shorter lifetime of turbulent structures in the lower part of the hydraulic jump and large turbulent structures in the upper region.

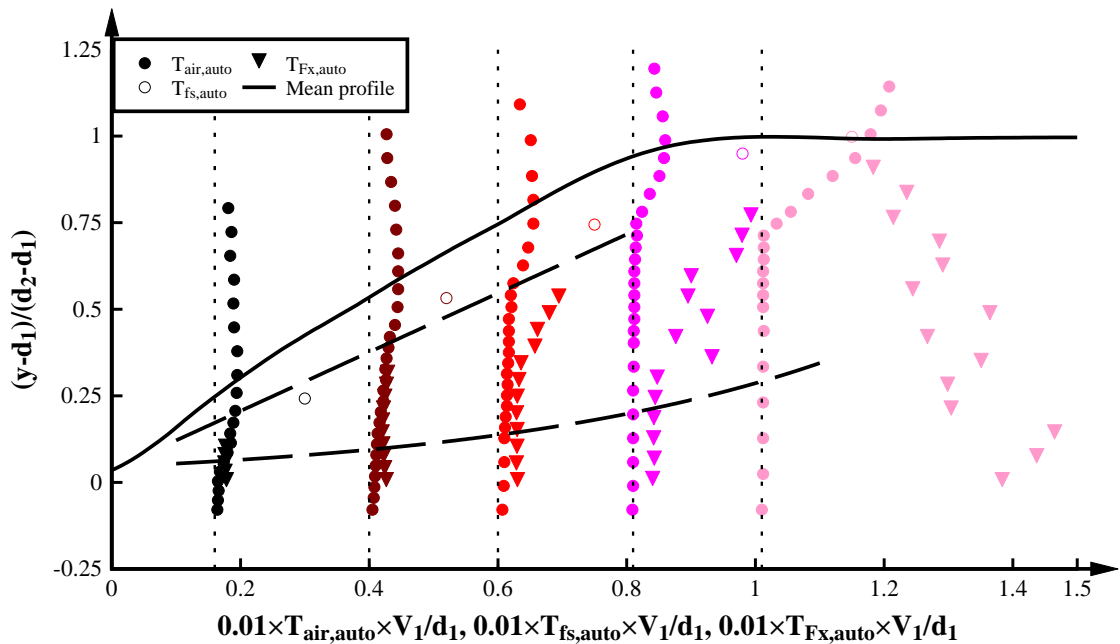


FIGURE 7-6. AUTO-CORRELATION TIME SCALES IN A HYDRAULIC JUMP WITH FULLY DEVELOPED INFLOW CONDITIONS (EXPERIMENT F: $Fr_1 = 8.0$, $Re = 1.2 \times 10^5$).

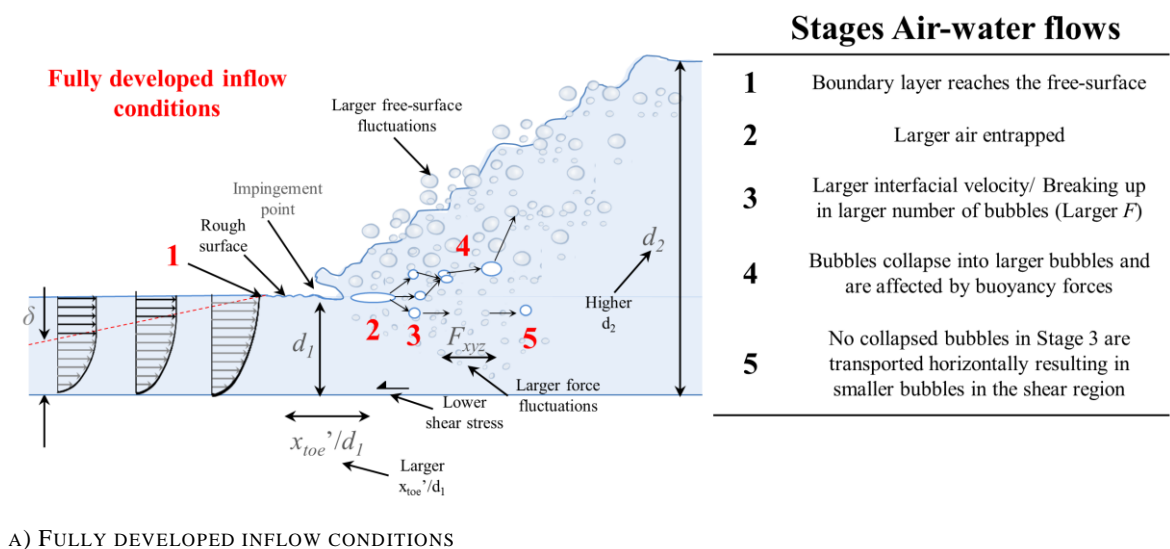
7.6. EFFECT OF INFLOW CONDITIONS

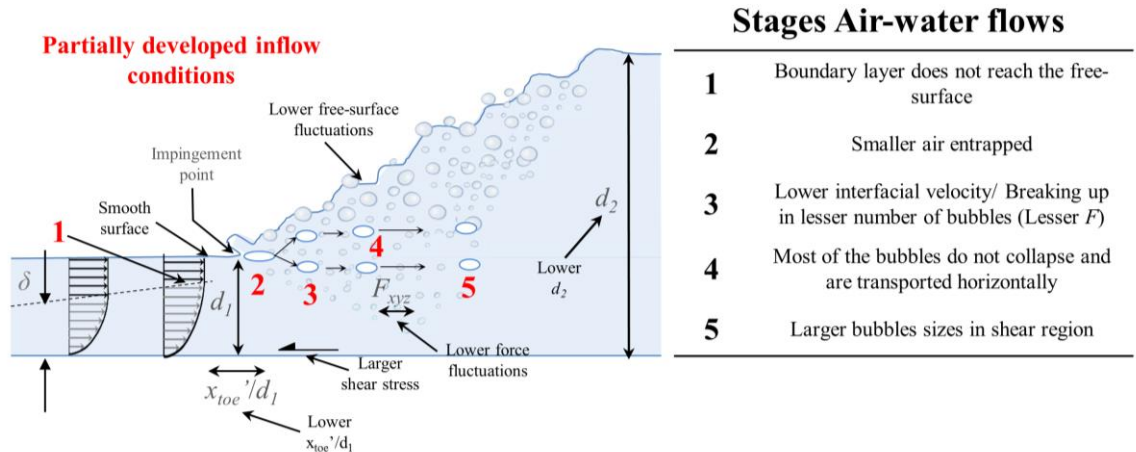
A comparative analysis of hydraulic jumps with fully and partially developed inflow conditions was performed for the full range of air-water flow properties, free-surface features and internal motions (Chapters 4, 5 and 6 respectively). Hydraulic jumps with fully developed inflow conditions had larger void fractions, which were previously observed by Takahashi and Ohtsu (2017). Novel findings showed that fully developed hydraulic jumps had larger number of bubbles, larger interfacial velocities and larger time-averaged chord times in the first half of the jump and smaller chord times at the downstream end confirming a significant effect of the inflow conditions on the air-water flow properties. The free-surface features were also affected by the inflow conditions. Larger conjugate depths, a steeper free-surface profile, stronger jump toe oscillations, and larger auto-correlation time scales and free-surface integral length scales were observed in fully developed hydraulic jumps. While the time-averaged internal forces on the sphere were similar independent of the inflow conditions, larger three-dimensional force fluctuations were consistently observed for fully developed hydraulic jumps. Overall, fully developed inflow conditions resulted in stronger aeration, instabilities and oscillations linked with larger turbulence upstream of the hydraulic jump. The inflow conditions play an important role in the characterisation of hydraulic jumps and should be taken into consideration.

Figure 7-7 presents a conceptual sketch of the effect of the inflow conditions on the aeration, free-surface features and internal motions in hydraulic jumps together with stages of the air-water flow dispersion along the hydraulic jump. In fully developed hydraulic jumps (Figure 7-7A), the boundary layer reached the free-surface upstream of the hydraulic jump (Stage 1) resulting in a rough free-surface and subsequent larger air entrapped at the impingement point of the hydraulic jump (Stage 2) (Takahashi and Ohtsu 2017). The larger amount of entrapped air combined with the larger interfacial velocities and shear stresses in the bubbly flow region resulted in larger break-up of bubbles, larger bubble count rates and smaller bubble sizes (Stage 3). A proportion of these bubbles merged into bubbles of larger sizes in the second half of the hydraulic jump linked with slower velocities and increasing relevance of the buoyancy compared to the advective motions. The dominance of the buoyancy forces led to upwards bubble motions (Stage 4) (Chanson 2006; Chanson 2007b). It seems that the larger number of bubbles in the upper region of the hydraulic jumps may contribute to larger free-surface fluctuations and instabilities. The larger interfacial velocities also increased the internal force fluctuations in the hydraulic jump. The non-collapsed bubbles observed in Stage 3 are transported horizontally due to the lower buoyant forces acting over the air-bubbles as the bubble size is smaller (Stage 5). This last stage resulted in small bubble sizes at the downstream end of fully developed hydraulic jumps as observed in the measurement of small bubble chord times at this region. Since the shear stress is

lower in fully developed hydraulic jumps, less flow resistance may be observed in the momentum balance (Rajaratnam 1965; 1967) and the depth of the hydraulic jumps may be larger compared to partially developed hydraulic jumps.

Figure 7-7B presents the conceptual sketch of the internal and external features in hydraulic jumps with partially developed inflow conditions. The partially developed hydraulic jump had a smoother free-surface upstream of the jump toe (Stage 1) leading to lower air entrapment at the impingement point (Stage 2) (Takahashi and Ohtsu 2017). Since the interfacial velocity was slower due to smaller free-stream flow velocities and larger flow resistance (Rajaratnam 1965; 1967), the bubble break-up was less intense compared to fully developed hydraulic jumps resulting in a smaller bubble count rates (Stage 3). Most of these bubbles did not collapse into larger bubbles and were transported horizontally to the downstream end of the hydraulic jump since the advective motions in small bubble sizes were dominant over the buoyancy forces (Stage 4). This statement was confirmed by remaining advective peak in the shear region at the downstream end of partially developed hydraulic jumps (Figure 4-7), the lower number of bubbles in the recirculation region reflecting lesser buoyancy effects, and larger mean bubble chord times in the shear region at the downstream end of partially developed hydraulic jumps (Stage 5). The lower interfacial velocities in partially developed hydraulic jumps resulted in lower force fluctuations. Likewise, larger shear stress at the channel bed led to larger flow resistance in partially developed hydraulic jumps (Rajaratnam 1965; 1967) resulting in lower conjugate flow depths. The deviations in the internal and external features of hydraulic jumps with different inflow conditions highlighted the importance of considering the inflow conditions in the analysis of hydraulic jumps.





B) PARTIALLY DEVELOPED INFLOW CONDITIONS

FIGURE 7-7. CONCEPTUAL SKETCH OF THE EFFECTS OF THE INFLOW CONDITIONS ON THE FLOW FEATURES OF HYDRAULIC JUMPS WITH PARTIALLY AND FULLY DEVELOPED INFLOW CONDITIONS; FIGURES ADAPTED AND EXTENDED FROM TAKAHASHI AND OHTSU (2017).

7.7. SCALE EFFECTS

Scale effects were investigated for all parameters in the present study based upon a Froude similitude comprising the air-water flow properties (Chapter 4.5), the free-surface features (Chapter 5.10) and the internal hydraulic jump forces on the sphere (Chapter 6.8). Scale effects were tested for a range of Reynolds numbers $6.2 \times 10^4 < Re < 1.2 \times 10^5$. While some parameters were affected by scale effects highlighting the limitations of the analysis of hydraulic jumps at laboratory scale, most of the parameters showed no scale effects for the range of Re in the present study. Table 7-1 summarises the investigated parameters providing an overview of the parameters affected by scale effects.

TABLE 7-1. SCALE EFFECTS IN FULLY DEVELOPED HYDRAULIC JUMPS.

	SCALE EFFECTS	NO SCALE EFFECTS
Air-water flow properties	F	C
	$t_{ch,mean}$	V_{CP}
	$T_{air,auto}$	V_{recir}
	$T_{air,cross}$	
Free-surface features		d
		d'_{max}
	F_{toe}	$x_{toe,min} - x_{toe,max}$
	$T_{fs,auto,max} - \text{Mode1:Peak0}$	x_{toe}'
	$L_{fs} - \text{Mode 2}$	$F_{fs(dom)}$
		$F_{fs(sec)}$
		$T_{fs,auto,max} - \text{Mode1:Peak1}$
		$T_{fs,auto,max} - \text{Mode2:Peak1}$
Internal forces on the sphere	F_{Dy} close to jump toe	F_x
	F_x' (Roller region)	F_z
	F_z' (Roller region)	F_{Dy} downstream end hydraulic jump
	F_y' (Roller region)	$F_{buoyancy}$
	$freq F_{z,dom,avg}$	F_x' (Conjugate depth region)

SCALE EFFECTS	NO SCALE EFFECTS
	F_z' (Conjugate depth region)
	F_y' (Conjugate depth region)
	$freq_{F_x, dom, avg}$
	$freq_{F_y, dom, avg}$

The present study showed that a larger number of air-water flows, free-surface and internal force parameters was not affected by scale effects for Reynolds numbers between $6.2 \times 10^4 < Re < 1.2 \times 10^5$. Nonetheless, further experiments should be conducted to validate scale effects in prototype scale, i.e. $Re > 1 \times 10^6$. Note that the self-similarity of the force parameters was significantly linked with the sphere size and large-scale turbulent eddies. Different scale effect results may be obtained when considering microscopic-scale motions.

7.8. DESIGN CONSIDERATIONS

This study expanded the knowledge of hydraulic jumps in terms of the air-water flow properties, free-surface features and three-dimensional internal motions. The improved understanding of the external and internal characteristics of hydraulic jumps can be used for better validation of numerical models or for improvement of the design considerations of stilling basin energy dissipators including:

1. Future stilling basin designs must consider the inflow conditions. Any design neglecting the inflow conditions may result in under- or over-estimation of the aeration features, free-surface fluctuations or internal motions. For all the experiments, hydraulic jumps with fully developed inflow conditions presented stronger flow disturbances including larger aeration and stronger free-surface and internal fluctuations. This outcome is significant since most of real-life hydraulic jumps may occur in fully developed inflow conditions with pre-aerated flow and the majority of the experimental results of previous studies were limited to partially developed flows. Although the present study did not present pre-entrainment of air, the differences between fully and partially developed inflow conditions highlighted the requirement of extending future research in fully developed hydraulic jumps.
2. The present study captured the most detailed information of the free-surface motions and jump toe oscillations non-intrusively with a LIDAR. The LIDAR technology obtained for the first time continuous information of the free-surface features along the hydraulic jumps with more than 100 points simultaneously together with the jump toe movements. This information is relevant for the design of stilling basins where the jump toe stability analysis together with the free-surface profile and fluctuations are fundamental (Hager 1992; Bradley and Peterka 1957; Hager and Damei 1992; Pagliara

and Palermo 2015; Chanson and Carvalho 2015). In addition, the simultaneous recording of the jump toe oscillations together with the free-surface fluctuations confirmed strong interactions between them as observed in previous visual observations (Long et al. 1991; Mossa and Tolve 1998). Future designs may consider a more detailed quantification of the interaction between jump toe oscillations and free-surface fluctuations with the LIDAR to validate and enhance dissipation efficiency as well as geometry and structural requirements. Overall, the present study validated the LIDAR as a promising technology in the analysis of the free-surface features in fully aerated hydraulic jumps with the capability of expanding the use of the LIDAR in prototype and real-scale stilling basins.

3. The present study expanded the understanding of the three-dimensional motions together with the aeration features along classical hydraulic jumps. The analysis of the time-averaged properties and the external and internal fluctuations in the hydraulic jump highlighted regions of stronger flow aeration and stronger three-dimensional flow motions. These results showed self-similarity in all experiments providing a descriptive picture which may be used as a basis for future designs considering aeration, jump instabilities and energetic dissipative processes along the hydraulic jump. A summary table combining the key findings in the present study is presented in Table 7-2. This table presents the level of aeration, forces and fluctuations for the wall jet shear region, advective shear region or recirculation region and the corresponding jump toe region, roller region or conjugate depth region. This information provides a description of the hydraulic jump features and may be used as a guidance for future designs. For example, based upon Table 7-2, the most robust stilling basin design should be located between the jump toe and roller regions corresponding to the areas of largest flow velocities and largest force fluctuations. Additionally, since the largest dissipation processes were identified within the wall jet shear region between $0.2 < x/L_r < 0.5$, future research aiming to enhance the efficiency of hydraulic jumps should evaluate techniques to increase the dissipative motions outside of this region, i.e. at $x/L_r > 0.5$. The LIDAR recordings also identified that the region of the largest free-surface fluctuations occurred in the roller region between $0.2 < x/L_r < 0.5$ providing a guidance for the dimension and design of the stilling basin walls. Overall, the present study provided a comprehensive information for design considerations and further research is recommended to validate the time-averaged and fluctuation features in a broader spectrum of stilling basin arrangements.

TABLE 7-2. LEVEL OF AERATION, FORCES AND FLUCTUATIONS BASED UPON THE LOCATION OF INTEREST IN THE HYDRAULIC JUMP.

	Jump toe region	Roller region	Conjugate depth region
Wall jet shear region	<ul style="list-style-type: none"> • Jump toe oscillation effects • Large bubble break-up • Large velocities • Large streamwise forces • Maximum force fluctuations 	<ul style="list-style-type: none"> • Moderate bubble break-up • Moderate velocities • Moderate streamwise forces • Large force fluctuations until $x/L_r < 0.5$. 	<ul style="list-style-type: none"> • No bubble break-up • Slow velocities • Minor streamwise forces • Minor force fluctuations
Advective shear region	<ul style="list-style-type: none"> • Jump toe oscillation effects • Maximum flow aeration • Moderate bubble break-up • Moderate velocities • Moderate streamwise forces • Moderate force fluctuations 	<ul style="list-style-type: none"> • Moderate flow aeration • Moderate bubble break-up • Bubble coalescence in the second half of the roller • Moderate velocities • Minor streamwise forces (Reaching stagnation point) • Moderate force fluctuations 	<ul style="list-style-type: none"> • Minor to null flow aeration • Null bubble break-up • Minor velocities • Minor streamwise forces • Minor force fluctuations
Recirculation region	<ul style="list-style-type: none"> • Jump toe oscillation effects • Foam formed by air-water entities • Negative velocities • Negative streamwise forces • Large free-surface fluctuations 	<ul style="list-style-type: none"> • Foam formed by air-water entities • Negative velocities • Negative streamwise forces • Largest free-surface fluctuations 	<ul style="list-style-type: none"> • Minor to null flow aeration • Null bubble break-up • Minor velocities • Minor streamwise forces • Minor free-surface fluctuations

8

CONCLUSIONS AND FUTURE RESEARCH

The present study expanded the current understanding of hydraulic jumps through an extensive experimental study of air-water flow properties, free-surface features and internal motions in hydraulic jumps for a range of Froude numbers $3.6 < Fr_l < 10$ and Reynolds numbers $6.2 \times 10^4 < Re < 1.2 \times 10^5$. The experiments applied novel experimental techniques to obtain the most detailed picture of the external and internal features of hydraulic jumps as well as a closer approach of the dissipative flow processes inside hydraulic jumps.

The air-water flow properties were measured with state-of-the-art double-tip conductivity probes in hydraulic jumps with fully and partially developed inflow conditions. Hydraulic jumps with fully developed inflow conditions had larger air entrapment at the impingement point of the hydraulic jump leading to larger void fractions and bubble count rates along the hydraulic jump. Close to the jump toe, fully developed hydraulic jumps showed differences of up to 10% in the void fraction and 20% in the bubble count rate. Slightly larger interfacial velocities and larger bubble chord times were identified close to the jump toe in fully developed hydraulic jumps linked with larger free-stream velocities and lesser flow resistance. Further downstream, larger time-averaged bubble chord times were identified in hydraulic jumps with partially developed inflow conditions indicating lesser break-up of bubbles close to the impingement point due to lesser interfacial velocities. Overall, the air-water flow properties in hydraulic jumps are strongly affected by the boundary layer development upstream of hydraulic jumps.

The free-surface features were measured with a LIDAR providing the most detailed information of the time-varying free-surface features and jump toe oscillations in hydraulic jumps to date. Two analysis modes were defined comprising a freely moving jump toe and a fixed jump toe position in order to identify the effect of the jump toe oscillations on the free-surface features. The time-averaged free-surface profiles increased with increasing distance from the jump toe while the free-surface fluctuations peaked in the first half of the roller ($0.2 \leq x/L_r \leq 0.5$). Larger jump toe oscillations were recorded with increasing Froude number. Frequency analysis of the jump toe movements showed characteristic frequencies of $0.2 < freq_{toe} < 1.6$ Hz in agreement with previous studies. The continuous observations of the characteristic frequencies of the free-surface highlighted three characteristic free-surface regions along hydraulic jumps comprising the jump toe region, the roller region and the conjugate depth region. The free-surface characteristic dominant frequencies for the characteristic free-surface regions were $0.2 \leq freq_{fs(dom)} \leq 1.5$ Hz, $1.5 \leq freq_{fs(dom)} \leq 4$ Hz and $0.1 \leq freq_{fs(dom)} \leq 3$ Hz respectively. Auto-correlation time scales were largest close to the jump toe for the free jump toe movement linked with the jump toe oscillations. Large auto-correlation time scales were also observed in the roller region of the hydraulic jumps for fixed and freely moving hydraulic jumps suggesting a larger lifetime of the free-surface features within this region. Larger length

scales were observed close to the jump toe for both analysis modes. The analysis of the fixed jump toe movement provided a better quantification of the turbulent scales without the influence of the jump toe oscillations. The LIDAR appears to be a promising instrument for other types of air-water flows and for the use of air-water flow measurements at larger scale. Further detailed experiments are needed to compare the LIDAR performance with other types of instrumentation such as acoustic displacement meters and wire gauges in simultaneous experiments. The comparison of these non-intrusive methods to measure the flow depths should also be compared with typical air-water measurement techniques such as phase-detection intrusive probes.

The present study introduced a new technique to measure the internal three-dimensional motions in hydraulic jumps. The internal forces were measured in channel centreline with a three-dimensional load cell attached to a submerged sphere. The 3D forces on the sphere were measured at different locations along the hydraulic jump in order to obtain a picture of the three-dimensional motions in hydraulic jumps. Large streamwise (x) and vertical (y) forces were recorded close to the jump toe in the shear region of the hydraulic jump. The time-averaged transverse (z) forces were close to zero highlighting the symmetry of the experiments. The largest force fluctuations in x -, y -, and z -directions occurred close to the jump toe and close to the channel bed. The strongest fluctuations were recorded in the transverse direction highlighting the importance to consider motions in all flow directions for dissipative processes inside hydraulic jumps. A frequency analysis of the internal forces showed characteristic frequencies of the jump toe oscillations close to the jump toe region ($0.5 < freq_{F_x, dom}, freq_{F_z, dom}, freq_{F_y, dom} < 1.5$) and characteristic frequencies of the free-surface motions in the upper region along the hydraulic jump ($1.5 < freq_{F_x, dom}, freq_{F_z, dom}, freq_{F_y, dom} < 4$). In the roller region of the hydraulic jump, large streamwise and transverse frequencies were recorded related to the strong motions within this region ($0.5 \text{ Hz} < freq_{F_x, dom} < 9 \text{ Hz}$ and $2.5 \text{ Hz} < freq_{F_z, dom} < 10 \text{ Hz}$). Overall, the analysis of the forces on the submerged sphere provided novel information on the three-dimensional motions in hydraulic jumps. The results showed larger three-dimensional motions close to the jump toe and in the shear region. The internal fluctuations in the hydraulic jump decreased linearly with increasing distance from the jump toe indicating a constant decay in the large dissipative motions along the hydraulic jump. Although the present study provided a closer understanding of the large scale dissipative motions inside hydraulic jumps, further research is required to better understand the small-scale energy dissipation processes along hydraulic jumps. Likewise, additional experiments should aim to estimate the internal forces close to the channel bed since the present study was limited by the sphere size. The natural frequency of the measurement system should also be increased above 50 Hz to avoid possible resonance in the streamwise forces.

The composition of the air-water flow properties, free-surface features and internal motions suggested three vertical flow regions in hydraulic jumps: Wall jet shear region, advective shear region and recirculation region.

- The wall jet shear region is located close to the channel bed. This region is characterised by the largest interfacial velocities, larger time-averaged forces and higher force fluctuations.
- The advective shear region represents the region of largest aeration in hydraulic jumps. The air entrained at the impingement point of the hydraulic jump is predominantly transported along the advective shear region.
- The recirculation region is located in the upper part of the hydraulic jump and is characterised by reversed flow motions and high free-surface fluctuations.

These regions were consistently observed in all experiments suggesting that the region of stronger dissipative processes is located close to the jump toe and close to the channel bed.

The present study expanded the knowledge of hydraulic jumps with fully and partially developed inflow conditions and for a wide range of Froude and Reynolds numbers. The experimental results showed that the inflow conditions must be considered in any future research in order to avoid under- or overestimation of the aeration features, free-surface fluctuations or internal motions. The LIDAR technique provided the most detailed free-surface information of the free-surface features and the jump toe movements of the hydraulic jump. This information is relevant for future stilling basin designs where the jump toe stability and the amplitude of free-surface fluctuations are fundamental. Moreover, the present study highlighted the importance of considering jump toe oscillations and free-surface fluctuations simultaneously since both mechanisms are strongly related. The quantification of the three-dimensional internal motions in the hydraulic jump provided a closer understanding of the large scale dissipative motions inside hydraulic jumps. This information provided the most detailed picture of the dynamic behaviour along the hydraulic jump together with the dissipation decay of the internal motions. The better understanding of the large dissipative motions in hydraulic jumps may be considered as guidance for improving future stilling basin designs as well as future validation of numerical models. In general, all experiments showed self-similarity indicating that despite the dynamic and chaotic behaviour of hydraulic jumps, the internal and external features of hydraulic jumps are governed by similar time-averaged and fluctuation patterns.

Although this research deepened the current understanding of the internal and external features in hydraulic jumps, the full understanding of the dissipative processes occurring along the hydraulic jump remains limited. Future research must consider the analysis of hydraulic jumps under real-life conditions, i.e. fully developed hydraulic jumps and pre-aerated

conditions. The LIDAR technique was validated as a promising technology for the analysis of the free-surface in fully aerated hydraulic jumps. Future research should consider expanding the use of the LIDAR to a wider range of fully-aerated flows as well as prototype models providing a potential new mechanism for real-life monitoring of fully-aerated flow conditions. The three-dimensional analysis of the internal motions along the hydraulic jump showed the relevance of the transverse motions in the dissipative processes. Nonetheless, there is limited information of the transverse characteristics along the hydraulic jumps. Future research should expand the analysis of the internal features in the transverse direction to obtain a closer understanding of the energy dissipation mechanisms in the hydraulic jump. Overall, the hydraulic jump is still considered as one of the most complex hydraulic phenomena and the full understanding of its internal behaviour and energy dissipation processes still require passionate scientists willing to understand the hydraulic jump and its dissipative and chaotic mechanisms.

9

REFERENCES

Abdul Khader, MH., and Elango, K. 1974, 'Turbulent pressure field beneath a hydraulic jump', *Journal of Hydraulic Research*, vol. 12, no. 4, pp. 469–489.

Allis, MJ., Peirson, WL, and Banner, ML. 2011, 'Application of LiDAR as a measurement tool for waves', In *The Twenty-first International Offshore and Polar Engineering Conference*. International Society of Offshore and Polar Engineers.

Altinbilek, D. 2002, 'The Role of Dams in Development', *International Journal of Water Resources Development*, vol. 18, no. 1, pp. 9–24.

Arnell, NW. 1999, 'Climate Change and global water resources', *Global Environmental Change*, vol.9, pp. S31-S49.

Assi, GRS., Bearman, PW., and Kitney, N. 2009, 'Low drag solutions for suppressing vortex-induced vibration of circular cylinders', *Journal of Fluids and Structures*, vol. 25, pp. 666-675.

Babb, AF., and Aus, HC. 1981, 'Measurements of Air in Flowing Water', *Journal of Hydraulic Division*, vol. 107, HY12, pp. 1615–1630.

Bakhmeteff, BA. 1932, 'The Hydraulic Jump and Related Phenomena'. *Transactions of the American Society of Mechanical Engineers*, vol. 54, Paper APM 54-1, pp. 1-12.

Bakhmeteff, BA., and Matzke, AE. 1936, 'The hydraulic jump in terms of dynamic similarity'. In *Proceedings of the American Society of Civil Engineers*, vol. 61, no. 2, pp. 145-162.

Bakhmeteff, B.A., and Matzke, A.E. 1938, ‘The hydraulic jump in sloped channels’, *Transactions ASME*, vol. 60, HYD-60-1, pp. 111-118.

Beirami, M.K., and Chamani, M.R. 2010, ‘Hydraulic Jumps on Sloping Channels: Roller length and energy loss’, *Canadian Journal of Civil Engineering*, vol. 37, no. 4, pp. 535–543.

Bélanger, JB. 1828, *Essai sur la solution numérique de quelques problèmes relatifs au mouvement permanent des eaux courantes (Essay on the numerical solution of some problems relative to steady flow of water)*, Chez Carilian-Goeury, Libraire, Des Corps Royaux des Ponts et Chaussées et des Mines, No. 41, Paris, France.

Bélanger, JB. 1841, *Notes sur l’Hydraulique (Notes on Hydraulic Engineering)*, Ecole Royale des Ponts et Chaussées, Paris, France, session 1841-1842, 223 pages. (In French)

Belmont, MR., Horwood, JMK., Thurley, RWF., and Baker, J. 2007, ‘Shallow angle wave profiling lidar’, *Journal of Atmospheric and Oceanic Technology*, vol. 24, no. 6, pp. 1150-1156.

Bidone, G. 1820, *Expériences sur le remou et sur la propagation des ondes (Experiences about the eddies and waves propagation)*, Turin: De L’Imprimerie Royale. (In French)

Biehle, G., Speck, T., and Spatz, H.-Ch. 1998, ‘Hydrodynamics and Biomechanics of the Submerged Water Moss *Fontinalis antipyretica* – a Comparison of Specimens from Habitats with Different Flow Velocities’, *Botanica Acta*, vol. 111, pp. 42-50.

Blenkinsopp, CE., Mole, MA., Turner, IL., and Peirson, WL. 2010. ‘Measurements of the time-varying free-surface profile across the swash zone obtained using an industrial LIDAR’, *Coastal Engineering*, vol. 57, no. 11, pp. 1059-1065.

Blenkinsopp, CE., Turner, IL., Allis, MJ., Peirson, WL., and Garden, LE. 2012, ‘Application of LiDAR technology for measurement of time-varying free-surface profiles in a laboratory wave flume’, *Coastal Engineering*, vol. 68, pp. 1-5.

Bradley, JN., and Peterka, AJ. 1957. ‘Hydraulic design of stilling basins: stilling basin with sloping apron (Basin V)’, *Journal of the Hydraulics Division*, vol. 83, no. HY5, Paper 1405, pp. 1–32.

Brattberg, T., Chanson, H., and Toombes, L. 1998, 'Experimental Investigations of Free-Surface Aeration in the Developing Flow of Two-Dimensional Water Jets', *Transactions of the ASME*, vol. 120, pp. 738-744.

Buften, JL., Garvin, JB., Cavanaugh, JF., Ramos-Izquierdo, LA., Clem, TD., and Krabill, WB. 1991. 'Airborne lidar for profiling of surface topography', *Optical Engineering*, vol. 30, no. 1, pp. 72-78.

Cartellier, A. 1992, 'Simultaneous void fraction measurement, bubble velocity, and size estimate using a single optical probe in gas-liquid two-phase flows', *Review of Scientific Instruments*, vol. 63, no. 11, pp. 5442-5453.

Cartellier, A., and Achard, JL. 1991, 'Local phase detection probes in fluid/fluid two-phase flows', *Review of Scientific Instruments*, vol. 62, no. 2, pp. 279-303.

Castro-Orgaz, O., and Hager, WH. 2009, 'Classical hydraulic jump: Basic flow features', *Journal of Hydraulic Research*, vol. 47, pp. 744-754.

Çengel, YA., and Cimbala, JM. 2014, *Fluid Mechanics. Fundamentals and applications*, Third edition, McGraw-Hill, United States of America.

Chachereau, Y., and Chanson, H. 2010. 'Free-surface turbulent fluctuations and air-water flow measurements in hydraulic jumps with small inflow Froude numbers', *Hydraulic Model Report No. CH78/10*, School of Civil Engineering, The University of Queensland, Brisbane, Australia, 133 pages.

Chachereau, Y., and Chanson, H. 2011a, 'Bubbly flow measurements in hydraulic jumps with small inflow Froude numbers', *International Journal of Multiphase Flow*, vol. 37, pp. 555-564.

Chachereau, Y., and Chanson, H. 2011b, 'Free-surface fluctuations and turbulence in hydraulic jumps', *Experimental Thermal and Fluid Science*, vol. 35, no. 6, pp. 896-909.

Chanson, H. 1995, 'Air entrainment in two-dimensional turbulent shear flows with partially developed inflow conditions', *International Journal of Multiphase Flow*, vol. 21, no. 6, pp. 1107-1121.

Chanson, H. 1996, 'Air entrainment in hydraulic jumps', in *Air-bubble entrainment in Free-Surface Turbulent Shear Flows*, Academic Press Inc, San Diego, California, USA, pp 73 - 92.

Chanson, H. 2002, 'Air-Water Flow Measurements with Intrusive, Phase-Detection Probes: Can We Improve Their Interpretation?', *Journal of Hydraulic Engineering*, vol. 128, no. 3, pp. 252–255.

Chanson, H. 2004, *The hydraulics of Open Channel Flow: An introduction*, 2nd edition, Elsevier Butterworth-Heinemann, Oxford, UK,.

Chanson, H. 2006, 'Air bubble entrainment in hydraulic jumps. Similitude and scale effects', *Report No. CH57/05*, Dept. of Civil Engineering, The University of Queensland, Australia, 68 pages.

Chanson, H. 2007a, 'Dynamic similarity and scale effects affecting air bubble entrainment in hydraulic jumps', in *6th International Conference on Multiphase Flow ICMF 2007*, Leipzig, Germany.

Chanson, H. 2007b, 'Bubbly flow structure in hydraulic jump', *European Journal of Mechanics B/Fluids*, vol. 26, pp. 367–384.

Chanson, H. 2009a, 'Development of the Bélanger Equation and Backwater', *Journal of Hydraulic Engineering*, vol. 135, no. 3, pp. 159–163.

Chanson, H. 2009b, 'Advective diffusion of air bubbles in hydraulic jumps with large Froude numbers: An experimental study', *Report No. CH75/09*, School of Civil Engineering, The University of Queensland, Brisbane, Australia, 91 pages.

Chanson, H. 2009c, *Applied Hydrodynamics: An Introduction to Ideal and Real Fluid Flows*, CRC Press, Taylor and Francis Group, Leiden, The Netherlands.

Chanson, H. 2010, 'Convective transport of air bubbles in strong hydraulic jumps', *International Journal of Multiphase Flow*, vol. 36, pp. 798–814.

Chanson, H. 2013, 'Hydraulics of aerated flows: qui pro quo?', *Journal of Hydraulic Research*, vol. 51, no. 3, pp. 223–243.

Chanson, H., and Brattberg, T. 2000, 'Experimental study of the air-water shear flow in a hydraulic jump', *International Journal of Multiphase Flow*, vol. 26, no. 4, pp. 583–607.

Chanson, H., and Carosi, G. 2007, 'Advanced post-processing and correlation analyses in high-velocity air-water flows', *Environmental Fluid Mechanics*, vol. 7, no. 6, pp. 495–508.

Chanson, H., and Carvalho, R. 2015, 'Hydraulic Jumps and Stilling Basins' in *Energy dissipation in Hydraulic Structures*, IAHR Monograph, CRC Press, Taylor & Francis Group, Leiden, The Netherlands, pp. 65 - 104.

Chanson, H., and Chachereau, Y. 2013, 'Scale effects affecting two-phase flow properties in hydraulic jumps with small inflow Froude number', *Experimental Thermal and Fluid Science*, vol. 45, pp. 234 - 242.

Chanson, H., and Gualtieri, C. 2008, 'Similitude and scale effects of air entrainment in hydraulic jumps', *Journal of Hydraulic Research*, vol. 46, no. 1, pp. 35–44.

Chanson, H., and Toombes, L. 2002, 'Air-water flows down stepped chutes: turbulence and flow structure observations', *International Journal of Multiphase Flow*, vol. 28, pp. 1737–1761.

Chanson, H., and Qiao, GL. 1994, 'Air Bubble Entrainment and Gas Transfer at Hydraulic Jumps', *Research Report No. CE149*, Dept. of Civil Engineering, The University of Queensland, Australia, 71 pages.

Chen, S., and Wang, J. 2013, 'On energy dissipation of hydraulic jumps at low Froude numbers considering bubbles formation and transportation process', *Hydraulic Engineering – Xie (Ed.)*, pp. 91-96.

Chow, VT 1973, *Open Channel Hydraulics*, McGraw-Hill Book Company, United States of America, 681 pages.

Damiani, L., and Valentini, N. 2014, 'Terrestrial Laser Scanner as a measurement instrument for laboratory water waves', In *SCORE@ POLIBA*, Cangemi Editore spa., vol. 1, pp. 63-67.

Darcy, H., and Bazin, H. 1865, *Recherches Hydrauliques: Expériences sur le mouvement varié (Hydraulic research: Experiences about varied flow)*, Imprimerie Impériale, Paris, France. (In French).

Devore, J., Farnum, N., & Doi, J. 2013, ‘*Applied statistics for engineers and scientists*, United States of America. Brooks/Cole, Cengage Learning.

Dwivedi, A, Melville, BW, Shamseldin, AY, and Tushar, KG 2011, ‘Analysis of hydrodynamic lift on a bed sediment particle’. *Journal of Geophysical Research*, vol. 116, F02015, pp. 1-19.

Ead, SA., and Rajaratnam, N. 2002, ‘Hydraulic jumps on corrugated beds’, *Journal of Hydraulic Engineering*, vol. 128, no. 7, pp. 656–663.

Einwachter, J. 1935, ‘Wassersprung – und Deckwalzenlänge (Hydraulic jump and length of the roller)’. *Wasserkraft und wasserwirtschaft*, vol. 30, no. 8, pp. 85-88 (In German).

Felder, S. 2013, ‘Air-Water Flow Properties on Stepped Spillways for Embankment Dams: Aeration, Energy Dissipation and Turbulence on Uniform, Non-Uniform and Pooled Stepped Chutes’, *Ph.D. Thesis*, School of Civil Engineering, The University of Queensland, Australia, 506 pages.

Felder, S. 2018, “StefanFelder/Air-water-flow-data-analysis-software-for-double- tip-phase-detection-intrusive-probes (Version v1.0). Zenodo. <http://doi.org/10.5281/zenodo.2448251>.

Felder, S., and Chanson, H. 2015, ‘Phase-detection probe measurements in high-velocity free-surface flows including a discussion of key sampling parameters’. *Experimental Thermal and Fluid Science*, vol. 61, pp. 66-78.

Felder, S., and Chanson, H. 2016a, ‘An experimental Study of Air-water Flows in Hydraulic Jumps with Channel Bed Roughness’, *WRL Research Report WRL 259*, Water Research Laboratory, School of Civil and Environmental Engineering, University of New South Wales, Sydney, 166 pages.

Felder, S., and Chanson, H. 2016b, ‘Air-water flow characteristics in high-velocity free-surface flows with 50% void fraction’, *International Journal of Multiphase Flow*, vol. 85, pp. 186-195.

Felder, S., and Chanson, H. 2017, ‘Scale effects in microscopic air-water flow properties in high-velocity free-surface flows’, *Experimental Thermal and Fluid Science*, vol. 83, pp. 19-36.

Felder, S., and Chanson, H. 2018, 'Air-water Flow Patterns of Hydraulic Jumps on Uniform Beds Macroroughness', *Journal of Hydraulic Engineering*, vol. 144, no. 3, 04017068.

Felder, S., and Pfister, M. 2017, 'Comparative analyses of phase-detective intrusive probes in high-velocity air-water flows', *International Journal of Multiphase Flow*, vol. 90, pp. 88-101.

Felder, S. and Severi, A. 2016, 'Entrapped Air in High-velocity Free-surface Flows on a Flat-sloped Spillway', in *Proc. of 20th Australasian Fluid Mechanics Conference*, Perth, WA, Australia, 05 - 08 December.

Felder, S., Hohermuth, B., and Boes, R.M. 2019, 'High-velocity air-water flows downstream of sluice gates including selection of optimum phase-detection probe', *International Journal of Multiphase Flow*, vol. 116, pp. 203-220.

Ferriday, R. 1895, 'The hydraulic jump', *Engineering News*, vol. 34, no.2, pp. 28.

Fiorotto, V., and Rinaldo, A. (1992). 'Turbulent pressure fluctuations under hydraulic jumps', *Journal of Hydraulic Research*, vol. 30, no. 4, pp. 499–520.

Gleick, PH. 1999, 'The Human Right to Water', *Water Policy*, vol.1, no. 5, pp. 487-503.

Gleick, PH. 2000, 'A look at Twenty-first Century Water Resources Development', *Water International*, vol. 25, no. 1, pp. 127–138.

Gokturk, SB., Yalcin, H., and Bamji, C. 2004, 'A time-of-flight depth sensor-system description, issues and solutions', In *Computer Vision and Pattern Recognition Workshop, 2004. CVPRW'04. Conference on*, IEEE, pp. 35-45.

Gonzalez, A., and Bombardelli, F. 2005, 'Two-phase flow theoretical and numerical models for hydraulic jumps, including air entrainment', in *Proc. of 31st IAHR World Congress*, Beijing, China, 16 - 21 September.

Gonzalez, CA., Takahashi, M., and Chanson, H. 2005, 'Effects of step roughness in skimming flows: An experimental study', *Research Report CE160*, Dept. of Civil Engineering, The University of Queensland, Australia, 154 pages.

Goring, DG., and Nikora, VI. 2002, 'Despiking Acoustic Doppler Velocimeter Data', *Journal of Hydraulic Engineering*, vol. 128, no. 1, pp. 117-126.

Gunal, M., and Narayanan, R. 1996, 'Hydraulic jump in Sloping Channels', *Journal of Hydraulic Engineering*, vol. 122, no. 8, pp. 436–442.

Habibzadeh, A., Wu, S., Ade, F., Rajaratnam, N., and Loewen, MR. 2011, 'Exploratory Study of Submerged Hydraulic Jumps with Blocks', *Journal of Hydraulic Engineering*, vol. 137, no. 6, pp. 706–710.

Habibzadeh, A., Loewen, MR., and Rajaratnam, N. 2012, 'Performance of Baffle Blocks in Submerged Hydraulic Jumps', *Journal of Hydraulic Engineering*, vol. 138, no. 10, pp. 902–908.

Hager, WH. 1985, 'Hydraulic Jump in non-prismatic rectangular channels'. *Journal of Hydraulic Research*, vol. 23, no. 1, pp. 21-35.

Hager, WH. 1988, 'B-jump in Sloping Channel', *Journal of Hydraulic Research*, vol. 26, no. 5, pp. 539–558.

Hager, WH. 1990, 'Geschichte des Wassersprungs (History of Hydraulic Jumps)', *Schweizer Ingenieur und Architekt*, vol. 108, no. 25, pp. 728–735. (In German)

Hager, WH. 1992, *Energy dissipators and Hydraulic Jump*, Netherlands: Kluwer Academic Publishers.

Hager, WH. 1993, 'Classical hydraulic jump: free surface profile', *Canadian Journal of Civil Engineering*, vol. 20, no. 3, pp. 536–539.

Hager, WH., and Bremen, R. 1989, 'Classical Hydraulic Jump: Sequent Depths', *Journal of Hydraulic Research*, vol. 27, no. 5, pp. 565-585.

Hager, W.H., and Damei, L. 1992, 'Sill-controlled energy dissipator', *Journal of Hydraulic Research*, vol. 30, no. 2, pp. 165–181.

Hager, WH., Bremen, R., and Kawagoshi, N. 1990, 'Classical hydraulic jump: length of the roller', *Journal of Hydraulic Research*, vol. 28, no. 5, pp. 591–608.

Harleman, DRF. 1955, 'Effect of baffle piers on stilling basin performance', *Journal of the Boston Society of Civil Engineers*, vol. 42, no. 2, pp. 84–99.

Harleman, DRF. 1959, Discussion of 'Turbulence characteristics of the hydraulic jump' by Rouse, H, Siao, TT, and Nagaratnam, S, *Transactions of the ASCE*, vol. 124, pp. 959-962.

Harry, M., Zhang, H., Lemckert, C., and Colleter, G. 2010, '3D spatial definition of a water surface', In *The Ninth ISOPE Pacific/Asia Offshore Mechanics Symposium*. International Society of Offshore and Polar Engineers.

Hayes, MH. 1996, *Statistical Digital Signal Processing and Modeling*, John Wiley, New York, USA

Henderson, FM. 1966, *Open Channel Flow*, MacMillan Publishing Co., INC, New York.

Herringe, RA., and Davis, MR. 1974, 'Detection of instantaneous phase changes in gas-liquid mixtures', *Journal of Physics E: Scientific Instruments*, vol. 7, pp. 807–812.

Herringe, RA., and Davis, MR. 1976, 'Structural development of gas-liquid mixture flows', *Journal of Fluid Mechanics*, vol. 73, no. 1, pp. 97–123.

Herringe, RA., and Davis, MR. 1978, 'Flow structure and distribution effects in gas-liquid mixture flows', *International Journal of Multiphase Flow*, vol. 4, pp. 461–486.

Hoerner, S. F. (1965). *Fluid-Dynamic Drag: Practical Information on Aerodynamic Drag and Hydrodynamic Resistance*, Hoerner Fluid Dynamics, United States of America.

Imai, S., and Nakagawa, T. 1992, 'On velocity measurements in hydraulic jumps using LDV, small propeller and pitot tube'. In *11th Australasian Fluid Mechanics Conference*. University of Tasmania, Hobart, Australia, 14 – 18 December.

Irish, JL., and Lillycrop, WJ. 1999, 'Scanning laser mapping of the coastal zone: The SHOALS system', *ISPRS Journal of Photogrammetry and Remote Sensing*, vol. 54, no. 2, pp. 123-129.

Irish, JL., Wozencraft, JM., Grant Cunningham, A., and Giroud, C. 2006, 'Nonintrusive Measurement of Ocean Waves: Lidar Wave Gauge', *Journal of Atmospheric and Oceanic Technology*, vol 23, no. 11, pp. 1559–1572.

Jiang, LJ., Shao, WY., Zhu, DZ., Sun, ZL. 2014, 'Forces on surface-piercing vertical cylinder groups on flooding staircase', *Journal of Fluids and Structures*, vol 46, pp. 17–28.

Kawagoshi, N., and Hager, W.H. 1990, 'B Jump in sloping channel, II', *Journal of Hydraulic Research*, vol. 28, no. 4, pp. 461–480.

Kennison, KR. 1916a, 'The Hydraulic Jump in Open Channel Flow at High Velocity', *Transactions American Society of Civil Engineers*, vol. 80, no. 1, pp. 338-353.

Kennison, KR. 1916b, 'Computing the Hydraulic Jumps', *Engineering News*, vol. 76, no. 23, pp. 1096.

Kindsvater, CE. 1944, 'The hydraulic jump in sloping channels', *Transactions ASCE*, vol. 108, no. 109, pp. 1107–1154.

Koutsoyiannis, D., Zarkadoulas, N., Angelakis, AN., Tchobanoglous, G. 2008, 'Urban Water Management in Ancient Greece: Legacies and Lessons', *Journal of Water Resources Planning and Management*, vol. 134, no. 1, pp. 45-54.

Kozeny, J. 1929, 'Der Wassersprung (The Hydraulic Jump)', *Die Wasserwirtschaft*, vol. 22, pp. 537-540 (In German).

Kozeny, J. 1932, 'Sind Wasserwalzen Energievernichter? (Energy dissipation in Hydraulic jumps?)', *Die Wasserwirtschaft*, vol. 25, no. 11, pp. 143-144 (In German).

Kramer, M., and Valero, D. 2019, 'Turbulence and self-similarity in highly-aerated shear flows: the stable hydraulic jump', *International Journal of Multiphase Flow, Preprint*

Kramer, M., Chanson, H., and Felder S. 2019a, 'Can we improve the non-intrusive characterisation of high-velocity air-water flows? Application of LIDAR technology to stepped spillways', *Journal of Hydraulic Research*, DOI: 10.1080/00221686.2019.1581670.

Kramer, M., Valero, D., Chanson, H., and Bung, DB. 2019b, 'Towards reliable turbulence estimations with phase-detection probes: an adaptive window cross-correlation technique', *Experiments in Fluids*, vol. 60, no. 2.

Kucukali, S., and Chanson, H. 2007, 'Turbulence in hydraulic jumps: Experimental measurements', *Report No. CH62/07*, Division of Civil Engineering, The University of Queensland, Australia, 98 pages.

Kucukali, S., and Chanson, H. 2008, 'Turbulence measurements in the bubbly flow region of hydraulic jumps', *Experimental Thermal and Fluid Science*, vol. 33, no. 1, pp. 41–53.

Lader, P., Enerhaug, B., Fredheim, A., Klebert, P., and Pettersen, B. 2014, 'Forces on a cruciform/ sphere structure in uniform current', *Ocean Engineering*, vol. 82, pp. 180-190.

Leandro, J., Carvahlo, R., Chachareau, Y., and Chanson, H. 2012, 'Estimating void fraction in a hydraulic jump by measurements of pixel intensity', *Experiments in Fluids*, vol. 52, no. 5, pp. 1307–1318.

Lennon, JM., and Hill, DF. 2006, 'Particle Image Velocity Measurements of Undular and Hydraulic Jumps', *Journal of Hydraulic Engineering*, vol. 132, no. 12, pp. 1283–1294.

Lenton, R., and Muller, M. 2009, *Integrated Water Resources Management in Practice. Better water management for development*, Earthscan, London, pp. 1-14.

Lin, C., Hsieh, SC., Lin, IJ., Chang, KA., & Raikar, RV. 2012, 'Flow property and self-similarity in steady hydraulic jumps', *Experiments in Fluids*, vol. 53, no. 5, pp. 1591-1616.

Liu, M., Rajaratnam, N., and Zhu, DZ. 2004a, 'Turbulence Structure of Hydraulic Jumps of Low Froude Numbers', *Journal of Hydraulic Engineering*, vol. 130, no. 6, pp. 511–520.

Liu, H., Shah, S., and Jiang, W. 2004b, 'On-line outlier detection and data cleaning', *Computers & chemical engineering*, vol. 28, no. 9, pp. 1635-1647.

Long, D., Rajaratnam, N., Steffler, PM., and Smy, PR. 1991, 'Structure of flow in hydraulic jumps', *Journal of Hydraulic Research*, vol. 29, no. 2, pp. 207–218.

Lopardo, RA. 2013, 'Extreme Velocity Fluctuations below Free Hydraulic Jumps', *Journal of Engineering, Hindawi Publishing Corporation*, Article ID 678064.

Lopardo, RA., and Rimagnoli, M. 2009, 'Pressure and velocity fluctuations in stilling basins', in *Advances in Water Resources and Hydraulic Engineering*, Springer, Berlin, Heidelberg.

Madsen, PA., Svendsen, IA. 1983, 'Turbulent bores and hydraulic Jumps', *Journal of Fluid Mechanics*, vol. 129, pp. 1–25.

McCorquodale, JA. and Khalifa, A. 1983, 'Internal Flow in Hydraulic Jumps', *Journal of Hydraulic Engineering*, vol. 109, no. 5, pp. 684–701.

Merriman, M. 1889, *A Treatise on Hydraulics*, John Wiley and Sons: New York.

Mignot, E., and Cienfuegos, R. 2010, 'Energy Dissipation and Turbulent Production in Weak Hydraulic Jumps', *Journal of Hydraulic Engineering*, vol. 136, no. 2, pp. 116–121.

Misra, SK., Thomas, M., Kambhamettu, M., Kirby, JT., Veron, F., and Brocchini, M. 2006, 'Estimation of complex air-water interfaces from particle image velocimetry images', *Experiments in Fluids*, vol. 40, pp. 764–775.

Misra, SK., Kirby, JT., Brocchini, M., Veron, F., Thomas, M., and Kambhamettu, C. 2008, 'The mean and turbulent flow structure of a weak hydraulic jump', *Physics of Fluids*, vol. 20, 035106.

Mok, KM. 2004, 'Relation of surface roller eddy formation and surface fluctuation in hydraulic jumps', *Journal of Hydraulic Research*, vol. 42, no. 2, pp. 207–212.

Moore, WL. 1943, 'Energy loss at the base of a free overfall', *Transactions of the American Society of Civil Engineers*, vol. 108, no. 1, pp. 1343–1360.

Mossa, M. 1999, 'On the oscillating characteristics of hydraulic jumps', *Journal of Hydraulic Research*, vol. 37, no. 4, pp. 541-558.

Mossa, M., and Tolve, U. 1998, 'Flow Visualization in Bubbly Two-Phase Hydraulic Jump', *Journal of Fluids Engineering*, vol. 120, pp. 160-165.

Mouaze, D., Murzyn, F., Chaplin, JR. 2005, 'Free-surface length scale estimation in hydraulic jumps', *Journal of Fluids Engineering*, vol. 127, pp. 1191-1193.

Murzyn, F., and Chanson, H. 2007, 'Free-surface, bubbly flow and turbulence measurements in hydraulic jumps', *Report No. CH63/07*, Division of Civil Engineering, The University of Queensland, Australia, 118 pages.

Murzyn, F., and Chanson, H. 2008, 'Experimental assessment of scale effects affecting two-phase flow properties in hydraulic jumps', *Experiments in Fluids*, vol. 45, no. 3, pp. 513–521.

Murzyn, F., and Chanson, H. 2009a, 'Free-surface fluctuations in hydraulic jumps: Experimental observations', *Experimental Thermal and Fluid Science*, vol. 33, no. 7, pp. 1055-1064.

Murzyn, F., and Chanson, H. 2009b, 'Experimental investigation of bubbly flow and turbulence in hydraulic jumps', *Environmental Fluid Mechanics*, vol. 9, pp. 143-159.

Murzyn, F., Mouaze, D., and Chaplin, JR. 2005, 'Optical fibre probe measurements of bubbly flow in hydraulic jumps', *International Journal of Multiphase Flow*, vol. 31, pp. 141–154.

Murzyn, F., Mouaze, D., and Chaplin, JR. 2007, 'Air-water interface dynamics and free surface features in hydraulic jumps', *Journal of Hydraulic Research*, vol. 45, no. 5, pp. 679–685.

Naghash, M. 1994, Void fraction measurement techniques for gas-liquid bubbly flows in closed conduits: A literature review. In C. A. Pugh (Ed.), *Fundamentals and Advancements in Hydraulic Measurements and Experimentation*, New York: American Society of Civil Engineers, pp. 278 – 288.

Narayanan, R. 1975, 'Wall Jet Analogy to Hydraulic Jump', *Journal of the Hydraulic Division*, HY3, pp. 347–359.

Nassos, GP., and Bankoff, SG. 1967, 'Local Resistivity Probe for Study of Point Properties of Gas-Liquid Flows', *The Canadian Journal of Chemical Engineering*, vol. 45, pp. 271–274.

Ohtsu, I., and Yasuda, Y. 1990, 'Discussion of 'B-Jump in Sloping Channel' by Hager WH, *Journal of Hydraulic Research*, vol. 28, no. 1, pp. 105-119.

Ohtsu, I. and Yasuda, Y. 1991, 'Hydraulic Jump in Sloping Channels', *Journal of Hydraulic Engineering*, vol. 117, no. 7, pp. 905-921.

Ohtsu, I., and Yasuda, Y. 1994, 'Characteristics of Supercritical Flow below Sluice Gate', *Journal of Hydraulic Engineering*, vol. 120, no. 3, pp. 332-346.

Ohtsu, I., Yasuda, Y., and Awazu, S. 1990, 'Free and submerged hydraulic jumps in rectangular channels', *Report of Research Institute of Science and Technology*, No. 35, Nihon University, Japan, pp. 32-46.

Ohtsu, I., Yasuda, Y., and Yamanaka, Y. 1991, 'Drag on vertical sill of forced jump', *Journal of Hydraulic Research*, vol. 29, no. 1, pp. 29-47.

Ohtsu, I., Yasuda, Y., and Gotoh, H. 2001, 'Hydraulic condition for undular-jump formations', *Journal of Hydraulic Research*, vol. 39, no. 2, pp. 203-209.

Pagliara, S. and Palermo, M. 2015, 'Hydraulic jumps on rough and smooth beds:

aggregate approach for horizontal and adverse-sloped beds’, *Journal of Hydraulic Research*, vol. 53, no. 2, 243-252.

Palermo, M., and Pagliara, S. 2018, ‘Semi-theoretical approach for energy dissipation estimation at hydraulic jumps on rough sloped channels’, *Journal of Hydraulic Research*, pp. 1-10.

Pearson, R. K. 2002, ‘Outliers in process modeling and identification’, *IEEE Transactions on control systems technology*, vol. 10, no. 1, pp. 55-63.

Pells, S. 2016, ‘Erosion of rocks in spillways’, *Ph.D. Thesis*, School of Civil and Environmental Engineering, Faculty of Engineering, University of New South Wales, 1982 pages.

Peterka, AJ. 1978, *Hydraulic Design of Stilling Basins and Energy Dissipators*. United States Department of the Interior, Bureau of Reclamation, Engineering Monograph No. 25, Denver, Colorado, USA, 240 pages.

Rajaratnam, N. 1962a, ‘Profile equation for the hydraulic jump’, *Water Power*, vol. 14, pp. 324–327.

Rajaratnam, N. 1962b, ‘An experimental study of the air entrainment characteristics of Hydraulic Jump’, *Journal The Institution of Engineers (India)*, vol. 42, no. 7, pp. 247–273.

Rajaratnam, N. 1964a, ‘The forced hydraulic jump’, *Water Power*, vol. 16, no. 1, pp. 14–19.

Rajaratnam, N. 1964b, ‘The forced hydraulic jump (Continuation)’. *Water Power*, vol. 16, no. 2, pp. 61–65.

Rajaratnam, N. 1965, ‘The hydraulic jump as a wall jet’, *Journal of Hydraulic Division*, vol. 91, no. 5, pp. 107–132.

Rajaratnam, N. 1966. ‘The Hydraulic Jump in Sloping Channels’, *Irrigation and power*, vol. 23, no. 2, pp. 137-149.

Rajaratnam, N. 1967, ‘Hydraulic Jumps’, *Advances in Hydrosience*, vol. 4, pp. 197-280.

Rajaratnam, N., and Murahari, V. 1971, ‘A Contribution to Forced Hydraulic Jumps’, *Journal of Hydraulic Research*, vol. 9, no. 2, pp. 217–240.

Rajaratnam, N., and Murahari, V. 1974, 'Flow characteristics of sloping channel jumps', *Journal of the Hydraulics Division*, HY6, pp. 731–740.

Resch, FJ., and Leutheusser, HJ. 1971, 'Mesures de turbulence dans le ressaut hydraulique (Measurements of turbulence in the hydraulic jump)', *La Houille Blanche*, vol. 1, pp. 17–31 (In French).

Resch, FJ., and Leutheusser, HJ. 1972a, 'Le ressaut hydraulique : mesures de turbulence dans la région diphasique (The hydraulic jump: Turbulence measurements in the diphasic region)', *La Houille Blanche*, vol. 4, pp. 279–293 (In French).

Resch, FJ., and Leutheusser, HJ. 1972b, 'Reynolds stress measurements in hydraulic jumps', *Journal of Hydraulic Research*, vol. 10, no. 4, pp. 409-430.

Resch, FJ., Leutheusser, HJ., and Alemu, S. 1974, 'Bubbly two phase flow in Hydraulic Jumps', *Journal of Hydraulic Division*, vol. 100, no. 1, pp. 137–149.

Richard, GL., Gavriluk, SL. 2013, 'The classical hydraulic jump in a model of shear shallow-water flows', *Journal of Fluid Mechanics*, vol. 725, pp. 492-521.

Ross, DB., Cardone, VJ., and Conaway, JW. 1970, 'Laser and microwave observations of sea-surface condition for fetch-limited 17-to 25-m/s winds', *IEEE Transactions on Geoscience Electronics*, vol. 8, no. 4, pp. 326-336.

Rouse, H. 1934, 'On the Use of Dimensionless Numbers', *Civil Engineering*, vol. 4, no. 2, pp. 563-568.

Rouse, H., Siao, TT., and Nagaratnam, S. 1959, 'Turbulence characteristics of the hydraulic jump', *Transactions of the ASCE*, vol. 124, pp. 926–966.

Safranez, K. 1929, 'Untersuchungen Über den Wechselsprung (Studies about the Hydraulic Jump)', *Bauingenieur*, vol. 10, no. 38, pp. 668 - 677 (In German).

Sakamoto, H., and Haniu, H. 1990, 'A Study on Vortex Shedding From Spheres in a Uniform Flow'. *Transactions of the ASME*, vol. 112, pp. 386 - 392

Schiebe, FR., and Bowers, CE. 1971, 'Boundary Pressure Fluctuations Due to Macroturbulence in Hydraulic Jumps'. *Symposia on Turbulence in Liquid*, vol. 84, pp. 133 - 139

Schutten, J., Dainty, J., and Davy, AJ. 2004, 'Wave-induced Hydraulic Forces on Submerged Aquatic Plants in Shallow Lakes', *Annals of Botany*, vol. 93, pp. 333-341.

Severi, A. 2018, 'Aeration performance and Flow resistance in High-Velocity Flows over Moderately Sloped Spillways with micro-rough bed', *Ph.D. Thesis*, School of Civil and Environmental Engineering, UNSW Sydney, Australia, 226 pages.

Severi, A., and Felder, S 2017, 'Flow properties and shear stress on a flat-sloped spillway', in *E-Proc., 37th IAHR World Congress*, Kuala Lumpur, Malaysia, 10 pages.

SICK. AG. 2015, *LMS5xx Laser Measurement Sensors: Operating Instructions*, SICK AG, Waldkirch, Germany.

Smith, G., Modra, B., Felder, S. 2017, 'Experimental Testing of Flood Hazard Curves for a Partially Submerged Vehicle', *Proc., 13th Hydraulics in Water Engineering Conference (HIWE2017)*, Engineers Australia, Sydney, Australia, pp. 107-115.

Strand, IM., Sørensen, AJ., Volent, Z., Lader, P. 2016, 'Experimental study of current forces and deformations on a half ellipsoidal closed flexible fish cage', *Journal of Fluids and Structures*, vol. 65, pp. 108-120.

Streicher, M., Hofland, B., and Lindenbergh, RC. 2013, 'Laser ranging for monitoring water waves in the new Deltares Delta Flume', *ISPRS*.

Sunrise Instruments 2018, *Six axis circular load cell D45mm F70N*, accessed 06 February 2019, < <http://www.srisensor.com/case/common/upload/2018/01/19/61637HP.pdf>>.

Takahashi, M., and Ohtsu, I. 2017, 'Effects of inflows on air entrainment in hydraulic jumps below a gate', *Journal of Hydraulic Research*, vol. 55, no. 2, pp. 259–268.

Toombes, L. 2002, 'Experimental study of Air-Water Flow Properties on Low-Gradient Stepped Cascades', *Ph.D. Thesis*, Dept. of Civil Engineering, The University of Queensland, Australia, 304 pages.

Toombes, L., and Chanson, H. 2007, 'Surface waves and roughness in self-aerated supercritical flow', *Environmental Fluid Mechanics*, vol. 7, pp. 259–270.

Toso, JW., and Bowers, CE. 1988, 'Extreme Pressures in Hydraulic-Jump Stilling Basins', *Journal of Hydraulic Engineering*, vol. 114, no. 8, pp. 829 - 843.

United Nations 2015, *Transforming our world: The 2030 agenda for sustainable development*, United Nations General Assembly on 25 September 2015, New York, United Nations.

USBR 1987, 'Spillways'. In *Design of Small Dams*, Third Ed., Water Resources Technical Publication, pp. 339 – 434.

Valero, D. 2018, 'On the Fluid Mechanics of Self-Aeration in Open Channel Flows', *Ph.D. Thesis*, Hydraulics in Environmental and Civil Engineering, Faculty of Applied Sciences, Université de Liège. Faculty of Civil Engineering, Aachen University of Applied Sciences, 334 pages.

Valero, D., Bung, DB., and Crookston, BM. 2018, 'Energy dissipation of a Type III basin under design and adverse conditions for stepped and smooth spillways', *Journal of Hydraulic Engineering*, vol. 144, 04018036.

Valero, D., Viti, N., and Gualtieri, C. 2019, 'Numerical Simulation of Hydraulic Jumps. Part 1: Experimental Data for Modelling Performance Assessment', *Water*, vol. 11, no. 36, pp. 1-16.

Viti, N., Valero, D., and Gualtieri, C. 2019, 'Numerical Simulation of Hydraulic Jumps. Part 2: Recent Results and Future Outlook', *Water*, vol. 11, no. 28, pp. 1-18.

Vousdoukas, MI., Kirupakaramoorthy, T., Oumeraci, H., De La Torre, M., Wübbold, F., Wagner, B. and Schimmels, S. 2014, 'The role of combined laser scanning and video techniques in monitoring wave-by-wave swash zone processes', *Coastal Engineering*, vol. 83, pp. 150-165.

Wahl, T.L. 2003, 'Discussion of 'Despiking Acoustic Doppler Velocimeter Data' by Derek G. Goring and Vladimir I. Nikora', *Journal of Hydraulic Engineering*, vol. 129, pp. 484-487.

Wang, H. 2014, 'Turbulence and air entrainment in hydraulic jumps', *Ph.D. Thesis*, School of Civil Engineering, The University of Queensland, Australia, 341 pages.

Wang, H., and Chanson, H. 2013, 'Free-surface deformation and two-phase flow measurements in hydraulic jumps', *Research Report No. CH91/13*, School of Civil Engineering, The University of Queensland, Australia, 108 pages.

Wang, H., and Chanson, H. 2015, 'Experimental Study of Turbulent Fluctuations in Hydraulic Jumps', *Journal of Hydraulic Engineering*, vol. 141, no. 7, 04015010.

Wang, H., and Chanson, H. 2016a, 'Application of an array of four phase-detection probe sensors to hydraulic jumps at large Reynolds numbers', In A. Soldati (Ed.), *9th International Conference on Multiphase Flow*, Firenze, Italy: ICMF, pp. 5–10.

Wang, H., and Chanson, H. 2016b, 'Velocity field in hydraulic jumps at large Reynolds numbers: Development of an array of two dual-tip phase-detection probes', *Research Report No. CH100/15*, School of Civil Engineering, The University of Queensland, Australia, 72 pages.

Wang, H., and Chanson, H. 2016c, 'Self similarity and scale effects in physical modelling of hydraulic jump roller dynamics, air entrainment and turbulent scales', *Environmental Fluid Mechanics*, vol. 16, 1087-1110.

Wang, H., and Murzyn, F. 2017, 'Experimental assessment of characteristic turbulent scales in two-phase flow of hydraulic jump: from bottom to free surface', *Environmental Fluid Mechanics*, vol. 17, no. 1, 7-25.

Wang, H., Felder, S., and Chanson, H. 2014a, 'An experimental study of turbulent two-phase flow in hydraulic jumps and application of a triple decomposition technique', *Experiments in Fluids*, vol. 55, no. 7, pp. 1-18.

Wang, H., Murzyn, F., and Chanson, H. 2014b, 'Total pressure fluctuations and two-phase flow turbulence in hydraulic jumps', *Experiments in Fluids*, vol. 55, no. 11, pp. 1-16.

Wilson, AI. 2009, 'Hydraulic Engineering and Water Supply' in J.P. Oleson (ed.), *The Oxford Handbook of Engineering and Technology in the Classical World*, Oxford University Press, United States of America.

Woycicki, K. 1931, *Wassersprung, Deckwalze and Ausfluss unter einer Schütze*, Dissertation presented at the Institute of Technology Zurich, ETH, vol. 639, Verlag der Polnischen Akademie der Technischen Wissenschaft, Warschau (In German).

Wu, S., and Rajaratnam, N. 1995, 'Free jumps, submerged jumps and wall jets', *Journal of Hydraulic Research*, vol. 33, no. 2, pp. 197-212.

Wu, S., and Rajaratnam, N. 1996, 'Transition from Hydraulic Jump to Open Channel Flow', *Journal of Hydraulic Engineering*, vol. 122, no. 9, pp. 526–528.

Zare, HK., and Baddour, RE. 2007, 'Three-dimensional study of spatial submerged hydraulic jump', *Canadian Journal of Civil Engineering*, vol. 34, pp. 1140–1148.

Zhang, G., Wang, H., Chanson, H. 2012, 'Air entrainment and turbulence in hydraulic jump: Free-surface fluctuations and integral turbulent scales', in *4th IAHR International Symposium on Hydraulic Structures*, Porto, Portugal.

Zhang, G., Wang, H., Chanson, H. 2013, 'Turbulence and aeration in hydraulic jumps: free-surface fluctuation and integral turbulent scale measurements', *Environmental Fluid Mechanics*, vol. 13, pp. 189–204.

Zhang, W., Liu, M., Zhu, DZ., and Rajaratnam, N. 2014, 'Mean and Turbulent Bubble Velocities in Free Jumps for Small to Intermediate Froude Numbers', *Hydraulic Engineering*, vol. 140, no. 11, pp. 1–9.

Zhang, G., Valero, D., Bung, DB., and Chanson, H. 2018, 'On the estimation of free-surface turbulence using ultrasonic sensors', *Flow Measurement and Instrumentation*, vol. 60, pp. 171–184.

APPENDICES

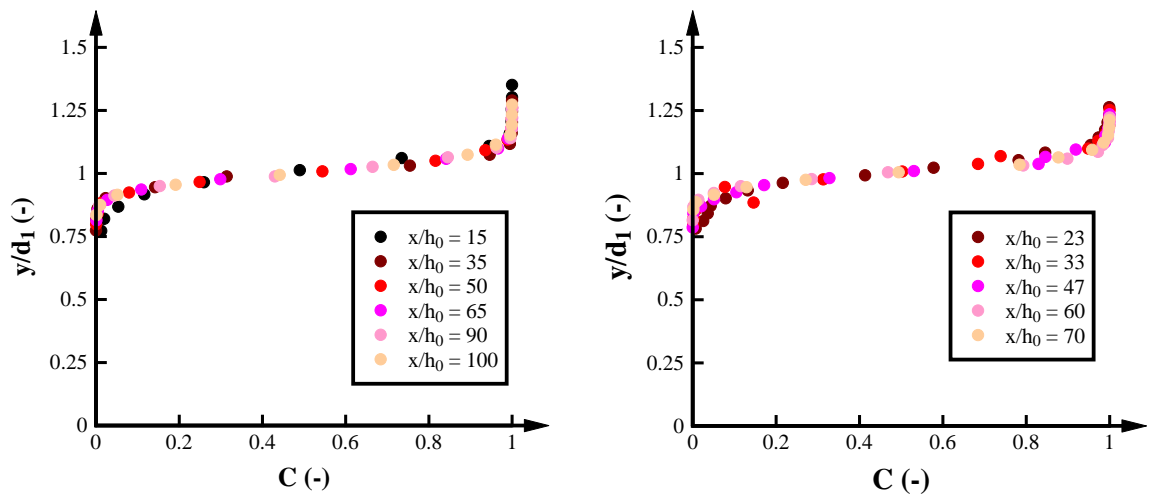
A. INFLOW CONDITIONS

A.1. AIR-WATER FLOW PROPERTIES

In the supercritical region downstream the sluice gate, no flow pre-aeration in the form of air bubbles was observed since the channel bed was smooth. Nonetheless, the free-surface became rougher with increasing distance from the sluice gate suggesting air-entrapment. A series of experiments were conducted to identify the air-water flow properties in the supercritical region of the hydraulic jump. The analysis was conducted for flow rates $0.037 < Q < 0.080 \text{ m}^3/\text{s}$, gate openings $0.02 \text{ m} < h_0 < 0.04 \text{ m}$ and Froude numbers at the gate $3.2 < Fr_0 < 12.3$.

A.1.1. VOID FRACTION

The void fraction distribution C in the supercritical region showed an S-profile which is characteristic of supercritical self-aerated flows (Toombes and Chanson 2007; Severi 2018). The profile indicated no flow aeration below $y/d_1 < 0.75$ and air entrapment between $0.75 < y/d_1 < 1.1$. The void fractions distributions were similar for the different cross-sections analysed.

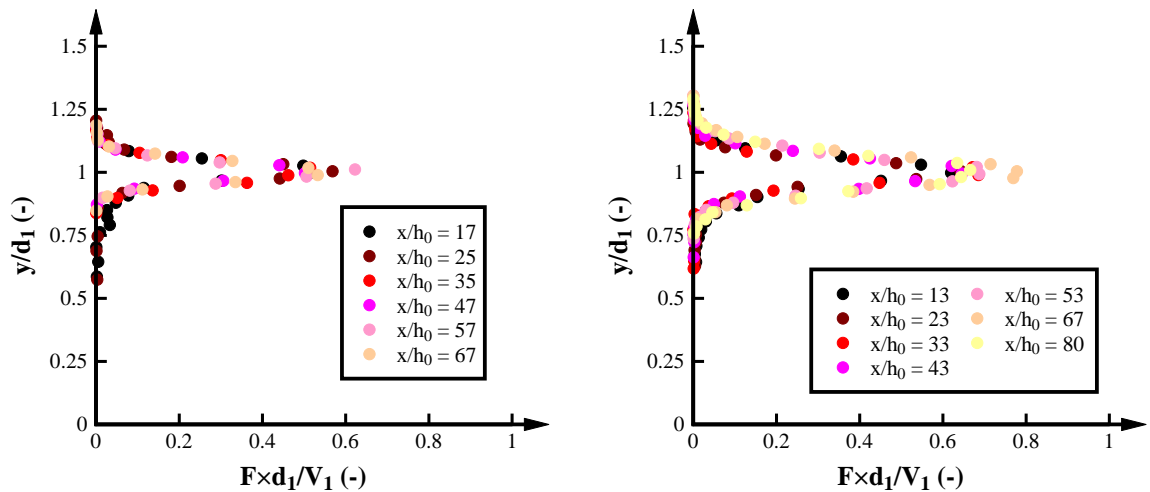


A) $Q = 0.037 \text{ m}^3/\text{s}$, $h_0 = 0.02 \text{ m}$, $Fr_0 = 7.0$, $Re = 6.2 \times 10^4$ B) $Q = 0.059 \text{ m}^3/\text{s}$, $h_0 = 0.03 \text{ m}$, $Fr_0 = 6.0$, $Re = 9.8 \times 10^4$

FIGURE A-1. VOID FRACTION DISTRIBUTION SUPERCRITICAL REGION DOWNSTREAM THE SLUICE GATE

A.1.2. BUBBLE COUNT RATE

The bubble count rate F in the shear region presented a large peak between $0.75 < F \times d_1 / V_1 < 1.2$ highlighting the entrapment of air in the upper part of the supercritical region. No bubble count rate was identified for $y/d_1 < 0.75$ and $y/d_1 > 1.2$ confirming no air entrainment within the flow. The bubble count rate increased with increasing the flow rate.

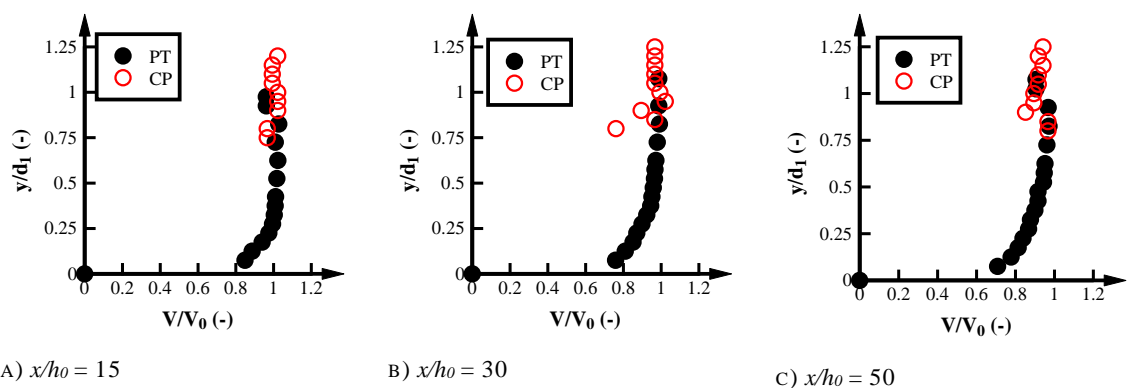


A) $Q = 0.037 \text{ m}^3/\text{s}$, $h_0 = 0.03 \text{ m}$, $Fr_0 = 3.8$, $Re = 6.2 \times 10^4$ B) $Q = 0.080 \text{ m}^3/\text{s}$, $h_0 = 0.03 \text{ m}$, $Fr_0 = 6.0$, $Re = 1.3 \times 10^5$

FIGURE A-2. BUBBLE COUNT RATE DISTRIBUTION SUPERCRITICAL REGION DOWNSTREAM THE SLUICE GATE

A.1.3. INTERFACIAL VELOCITY

Figure A-3 shows typical dimensionless velocity distributions V/V_0 as a function of y/d_1 at different positions downstream the sluice gate x_{sg}/h_0 . The measured velocities close to the channel bed were small increasing with distance from the channel bed following the non-slip condition. The interfacial velocity distribution measured with the conductivity probe (CP) in the upper part of the supercritical flow was compared to the mono-phase velocity distribution recorded with the pitot tube (PT) presenting good agreement. This result confirmed that the two-phase flow velocity is accurately representing the velocity of the clear-water flow. For the same flow rate and gate opening, the magnitude of the velocities decreased with increasing distance downstream of the sluice gate as a result of the boundary layer development and increase in flow depth in downstream direction.



A) $x/h_0 = 15$

B) $x/h_0 = 30$

C) $x/h_0 = 50$

FIGURE A-3. VELOCITY DISTRIBUTION SUPERCRITICAL REGION DOWNSTREAM THE SLUICE GATE. PT: PITOT TUBE; CP: CONDUCTIVITY PROBE.

The increase in the flow depth was associated with the shear stress at the channel bed. Since the mass is conserved throughout the channel, the mass deficit close to the channel bed due to the shear stress is replaced in the upper part of the free-stream flow resulting in larger

flow depths (Çengel and Cimbala 2014). The shear stress, defined as $\tau_0 = \rho V_*^2$ could be estimated based on the log law approach:

$$\frac{V}{V_*} = \frac{1}{\kappa} \ln \frac{y \times V_*}{\nu} + B \quad (\text{A.1})$$

Where V_* is the shear velocity, κ is 0.4 and B is 5.0 based on data's best fit and ν is the kinematic viscosity. Note that Equation A.1 is only valid for the inner flow region i.e. $y/\delta < 0.1$ to 0.15 (Chanson 2009c; Severi and Felder 2017). Figure A-4 presents the estimation of the boundary layer distribution on the channel bed based on the experimental results and the comparison with the log law and the one-seventh-power law represented by $V/V_0 = (y/\delta)^{1/7}$. The velocity distribution of all experiments presented good agreement with the log-law while large deviations were identified with the one-seventh law. Therefore, the shear stress was estimated based on the shear velocity estimated based upon the log-law.

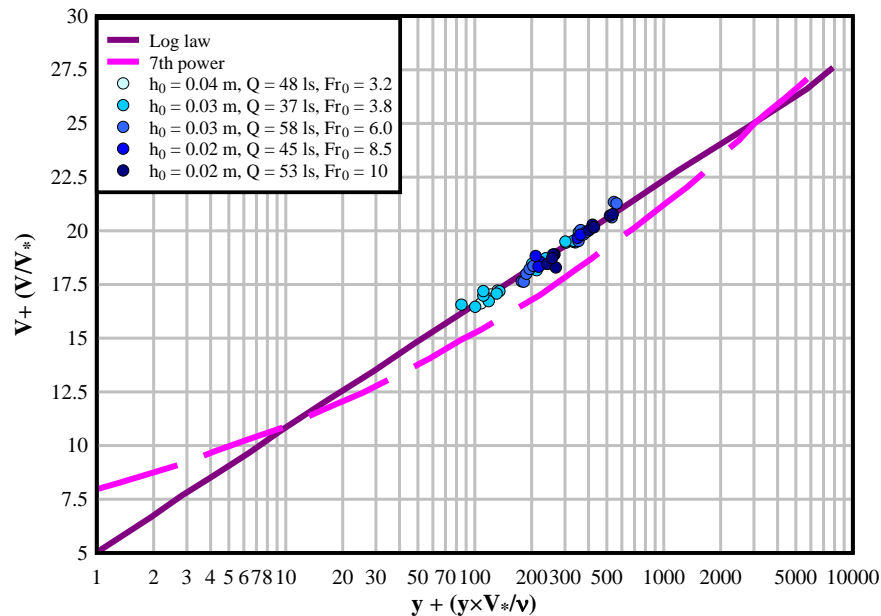


FIGURE A-4. COMPARISON OF THE BOUNDARY LAYER DISTRIBUTION ON THE CHANNEL BED WITH LOG-LAW AND ONE-SEVENTH-POWER LAW APPROACHES.

The shear stress represents the resistance of the flow motions close to the channel bed and is represented in terms of the dynamic viscosity μ and the change of the velocity respect to the flow depth, i.e. $\tau_0 = \mu \times (\partial V / \partial y)$. Note that $(\partial V / \partial y)$ close to the channel bed decreases with increasing distance from the sluice gate due to the boundary layer development (Chanson 2009c; Çengel and Cimbala 2014). Figure A-5 presents the dimensionless shear stress $\tau_0 / \rho g d_1$ as function of x_{sg} for different flow conditions. Larger $\tau_0 / \rho g d_1$ were identified for larger Fr_0 . The shear stress also decreased with increasing distance from the sluice gate in agreement with the decrease in $(\partial V / \partial y)$. The decrease in $\tau_0 / \rho g d_1$ was more significant for larger Fr_0 indicating larger losses for larger Froude numbers. Overall, the analysis of the shear stress downstream the sluice gate confirmed larger shear stresses close to the sluice gate and a reduction with increasing

distance from the jump toe. Therefore, hydraulic jumps with partially developed inflow conditions will present larger shear stress compared to fully developed hydraulic jumps.

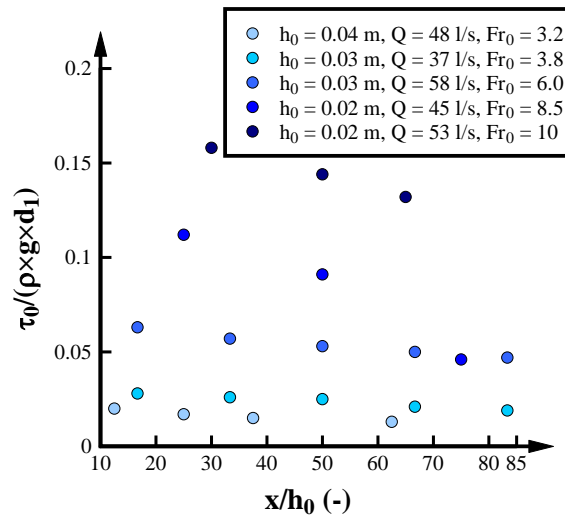


FIGURE A-5. SHEAR STRESS AS FUNCTION OF THE DISTANCE FROM THE SLUICE GATE

B. SENSITIVITY ANALYSIS OF THE SAMPLING TIME

B.1. INTRODUCTION

The hydraulic jump is a complex and unstable phenomenon characterised by the sudden transition from fast to slow flows. In the transition region, the hydraulic jump is characterised by large flow disturbances, air entrainment, free-surface fluctuations and three-dimensional motions. Extensive experiments have been conducted to better understand the complexity of this phenomenon including analysis of the air-water flow properties (.g. Resch and Leutheusser 1972b; Chanson and Brattberg 2000; Murzyn et al. 2005; Wang et al. 2014), free-surface fluctuations (Chachereau and Chanson 2011b; Wang and Chanson 2015) and pressure fluctuations (e.g. Abdul Khader and Elango 1974; Fiorotto and Rinaldo 1992; Wang et al. 2014b). Due to the large turbulence and flow instabilities in hydraulic jumps, the sampling time plays an important role in the estimation of reliable experimental parameters. Table B-1 presents a summary of the sampling time for different experimental analysis in hydraulic jumps.

TABLE B-1. SAMPLING TIME OF EXPERIMENTAL ANALYSIS IN HYDRAULIC JUMPS

Reference	Experimental emphasis			Instrument	Maximum sampling time (s)
	Air-water flow properties	Free-surface fluctuations	Force baffle piers/ Pressure fluctuations		
Resch et al. (1974)	x			Hot-film anemometer	102.4
Babb and Aus (1981)	x			Hot-film anemometer	10
Chanson and Brattberg (2000)	x			Conductivity probe	10
Murzyn et al. (2005)	x			Optical fibre probe	120
Chanson and Gualtieri (2008)	x			Conductivity probe	45
Kucukali and Chanson (2008)	x			Conductivity probe	48
Murzyn and Chanson (2009b)	x			Conductivity probe	45
Chachereau and Chanson (2011a, 2011b)	x			Conductivity probe	45
Zhang et al. (2014)	x			Optical fibre probe	120
Takahashi and Ohtsu (2017)	x			Conductivity probe	45
Mouaze et al. (2005)		x		Wire gauges	5
Murzyn et al. (2007)		x		Wire gauge	5
Kucukali and Chanson (2008)		x		ADM	1200

Reference	Experimental emphasis			Instrument	Maximum sampling time (s)
	Air-water flow properties	Free-surface fluctuations	Force bafflers/ Pressure fluctuations		
Murzyn and Chanson (2009a)		x		ADM (50 Hz)	600
Chachereau and Chanson (2011)		x		ADM (50 Hz)	600
Wang and Chanson (2015)		x		ADM (50 Hz)	540
Abdul Khader and Elango (1974)			x	Pressure cells	900
Toso and Bowers (1988)			x	Pressure transducer/ Piezometers	600
Fiorotto and Rinaldo (1992)			x	Pressure taps	900
Wang et al. (2014b)			x	Pressure probe	180
	x			Conductivity probe	2880
Present study		x		LIDAR	3600
			x	Six-axis load cell	900

The present study conducted a comprehensive sensitivity analysis of the sampling time for the recording of the air-water flow properties, free-surface fluctuations and three-dimensional internal forces in hydraulic jumps. The aim of the analysis was to identify the minimum time length required to obtain valid information.

B.2. AIR-WATER FLOW PROPERTIES

The air-water flow parameters detection is significantly affected by the sampling duration. Previous studies recorded the air-water flow properties during 45 s to 120 s among which most of the experiments performed with conductivity probes have been conducted during 45 s. The selection of 45 s in hydraulic jumps was initially defined by Chanson (2007a) and Chanson and Gualtieri (2008) by a sensitivity analysis with sampling times between 0.7 s and 300 s. The sensitivity analysis followed the procedure proposed by Toombes on a stepped spillway (2002). Since the selection of a minimum sampling time in the analysis of the air-water flow properties in hydraulic jumps considered a maximum sampling time duration of 300 s, the present study re-evaluated the minimum sampling on the void fraction, bubble count rate and interfacial velocity considering a longer sampling time in the analysis, i.e. sensitivity analysis with sampling times between 45s to 2880 s.

The sensitivity analysis was conducted in hydraulic jumps downstream the sluice gate comprising hydraulic jumps with fully and partially developed inflow conditions. The analysis considered two different discharges, three cross-sections and two vertical positions: $Y_{C_{max}}$ and $Y_{C_{min}}$ representing the elevation of the maximum void fraction C_{max} and minimum void fraction

C_{min} respectively. The sample durations were tested between 45 to 2880 s with a sampling frequency of 20 kHz. Table B-2 presents the experimental conditions comprising the discharge Q , the sluice gate opening h_0 , the Froude number at the gate Fr_0 , inflow condition where FD represents fully developed hydraulic jumps and PD represents partially developed inflow conditions, the cross-section position relative to the jump toe x/d_1 and the elevation y .

TABLE B-2. SENSITIVITY ANALYSIS OF SAMPLING DURATION FOR HYDRAULIC JUMPS DOWNSTREAM THE SLUICE GATE.

Experiment	Q (l/s)	h_0 (m)	Fr_0 (-)	Inflow condition	x/d_1 (-)	y	
						Y_{Cmax}	Y_{Cmin}
Hydraulic jumps d/s a sluice gate $Q = 53$ l/s	53	0.02	10	FD	3.3	x	x
				FD	5.8	x	x
				PD	5.8	x	
				FD	9.4	x	x
Hydraulic jumps d/s a sluice gate $Q = 59$ l/s	59	0.03	6.0	FD	3.3	x	x
				FD	5.8	x	x
				PD	5.8	x	
				FD	9.4	x	x

B.2.1. VOID FRACTION

Figures B-1 and B-2 present the variation in the void fraction for $Q = 53$ l/s and $Q = 59$ l/s respectively. The void fraction scatter decreased with increasing distance from the jump toe. While for the sampling time of 45 s and fully developed inflow conditions C_{max} varied between $0.3 < C < 0.7$ for $x/d_1 = 3.3$, the range decreased to $0.29 < C < 0.36$ at $x/d_1 = 9.4$. A significant decrease in the effect of the sampling time in the void fraction was observed for partially developed inflow conditions. Larger variation in the void fraction was observed for the experiment with the largest Froude number ($Q = 53$ l/s, $h_0 = 0.02$ m). Note that the large data scatter observed in Figure B-2B was linked with the measurement of the void fraction in the recirculation region. Based upon the void fraction sensitivity analysis, the minimum sampling time close to the jump toe should be 300 s, and 240 for cross-sections located further downstream.

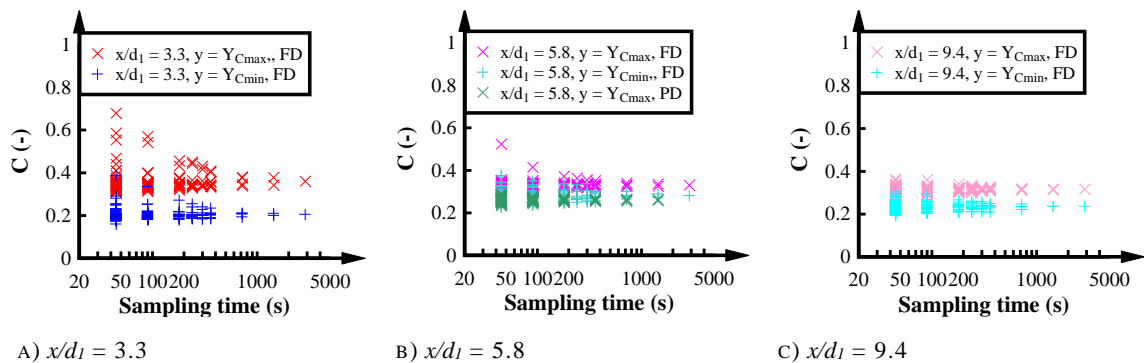
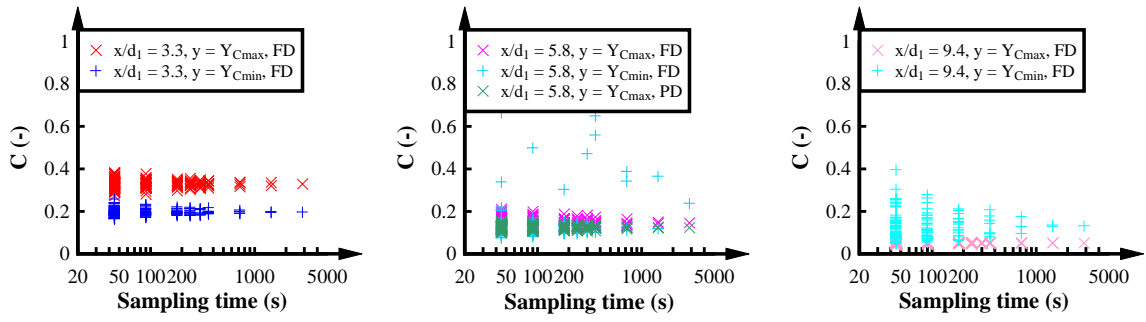


FIGURE B-1. EFFECT OF SAMPLING DURATION IN THE VOID FRACTION MEASUREMENTS FOR HYDRAULIC JUMPS DOWNSTREAM OF THE SLUICE GATE WITH $Q = 53$ l/s.



A) $x/d_1 = 3.3$

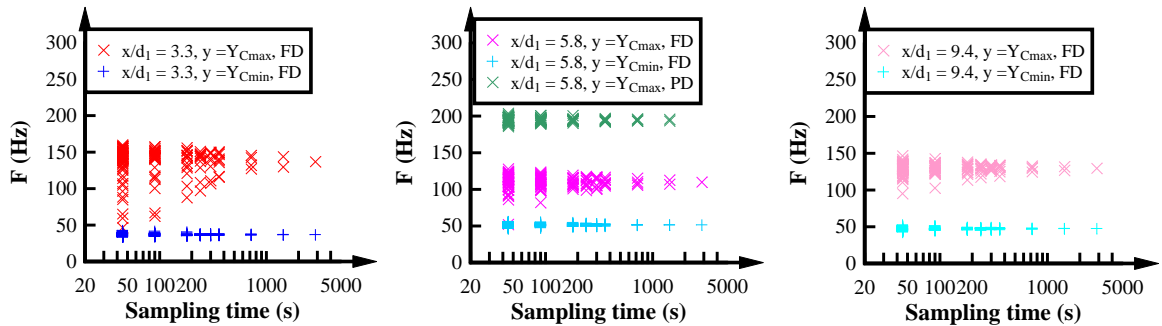
B) $x/d_1 = 5.8$

C) $x/d_1 = 9.4$

FIGURE B-2. EFFECT OF SAMPLING DURATION IN THE VOID FRACTION MEASUREMENTS FOR HYDRAULIC JUMPS DOWNSTREAM OF THE SLUICE GATE WITH $Q = 59$ l/s AND FULLY (FD) AND PARTIALLY (PD) DEVELOPED INFLOW CONDITIONS.

B.2.2. BUBBLE COUNT RATE

Figure B-3 and B-4 shows the effect of the sampling duration in the bubble count rate values for $Q = 53$ l/s and $Q = 59$ l/s respectively. Close to the jump toe, large differences in the bubble count rate were observed for the sampling time of 45 s for both experiments. Lower variations were observed for the hydraulic jumps with partially developed inflow conditions. Based upon the analysis of the effect of the sampling time in the bubble count rate, the minimum sampling time should be 300 s close to the jump toe and 200 s further downstream.

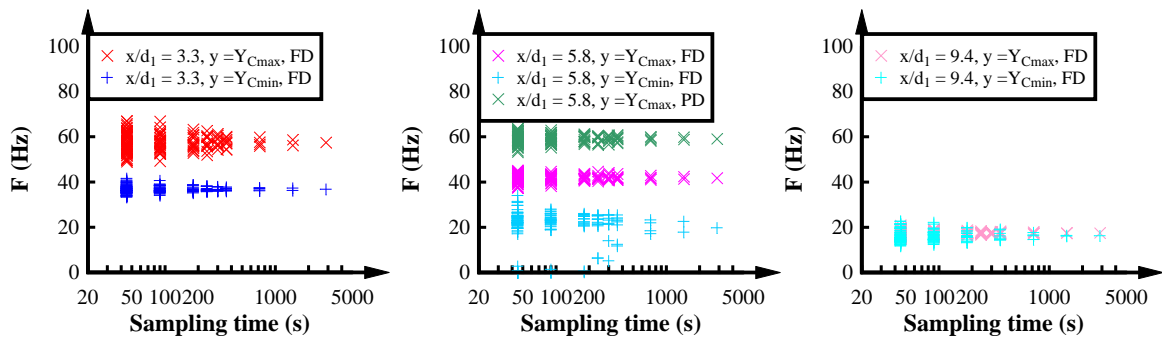


A) $x/d_1 = 3.3$

B) $x/d_1 = 5.8$

C) $x/d_1 = 9.4$

FIGURE B-3. EFFECT OF SAMPLING DURATION IN THE BUBBLE COUNT RATE MEASUREMENTS FOR HYDRAULIC JUMPS DOWNSTREAM OF THE SLUICE GATE WITH $Q = 53$ l/s.



A) $x/d_1 = 3.3$

B) $x/d_1 = 5.8$

C) $x/d_1 = 9.4$

FIGURE B-4. EFFECT OF SAMPLING DURATION IN THE BUBBLE COUNT RATE MEASUREMENTS FOR HYDRAULIC JUMPS DOWNSTREAM OF THE SLUICE GATE WITH $Q = 59$ l/s AND FULLY (FD) AND PARTIALLY (PD) DEVELOPED INFLOW CONDITIONS.

B.2.3. INTERFACIAL VELOCITY

Figure B-5 and B-6 presents the variation of the time-averaged interfacial velocity with the sampling time at different positions along the hydraulic jump. The sensitivity analysis of the interfacial velocity was limited to the shear region in the hydraulic jump because large data scatter was observed in the recirculation region due to the negative velocities. Overall, the variation of the interfacial velocities along the hydraulic jump for both conditions remained similar. Large variation in the interfacial velocity was observed for a sampling time of 45 s. Negligible differences were observed for sampling times above 180 s for all the conditions.

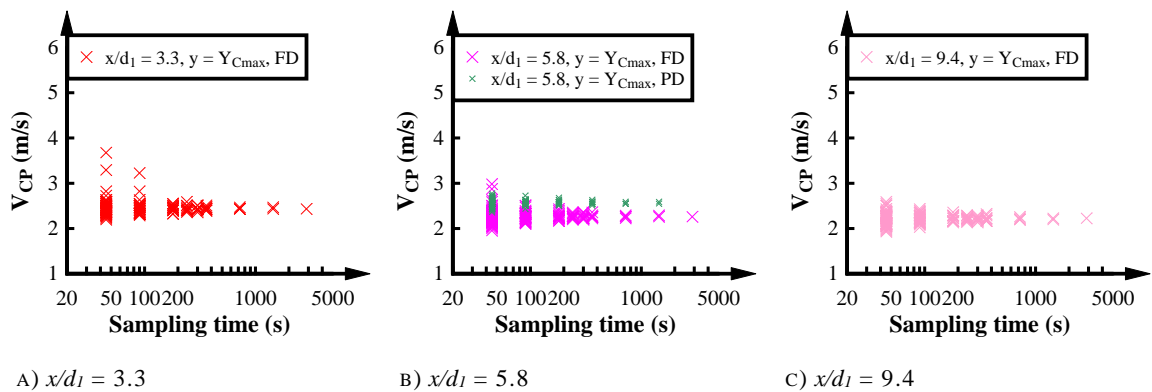


FIGURE B-5. EFFECT OF SAMPLING DURATION IN THE INTERFACIAL VELOCITY MEASUREMENTS FOR HYDRAULIC JUMPS DOWNSTREAM OF THE SLUICE GATE WITH $Q = 53$ l/s AND FULLY (FD) AND PARTIALLY (PD) DEVELOPED INFLOW CONDITIONS.

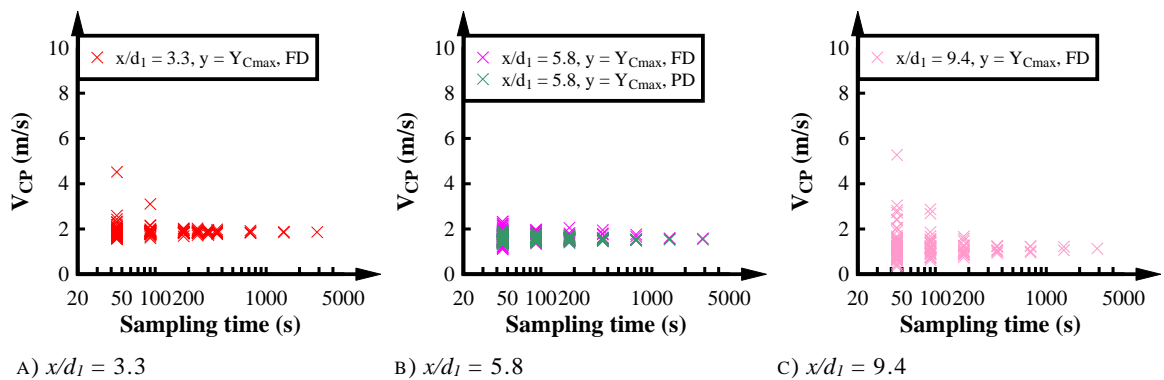


FIGURE B-6. EFFECT OF SAMPLING DURATION IN THE INTERFACIAL VELOCITY MEASUREMENTS FOR HYDRAULIC JUMPS DOWNSTREAM OF THE SLUICE GATE WITH $Q = 59$ l/s AND FULLY (FD) AND PARTIALLY (PD) DEVELOPED INFLOW CONDITIONS.

B.2.4. MINIMUM SAMPLING TIME AIR-WATER FLOW PARAMETERS

The longer sensitivity analysis of the sampling time showed a re-evaluation of the minimum sampling duration required to obtain more reliable air-water flow information. At all cross-sections, all the parameters presented large data variation for a sampling time of 45 s suggesting that the sampling time used in the previous studies is not sufficient to acquire optimum air-water flow measurements. Figure B-7 presents a comparison in the air-water flow parameters for a sampling time of 45s (previous studies) and 300 s (present study). Despite the distribution of the void fraction and the bubble count rate remained similar, a longer sampling time provided lesser data scatter and a clear definition of the advective peak in the hydraulic jump. Larger data

scatter was observed close to the jump toe while lesser variations were identified further downstream. From all air-water flow parameters analysed, the void fraction represented the parameter with larger deviation. Therefore, for the present study, the minimum sampling time for the measurement of the air-water flows close to the jump toe were 300 s while measurements of at least 240 s conducted further downstream.

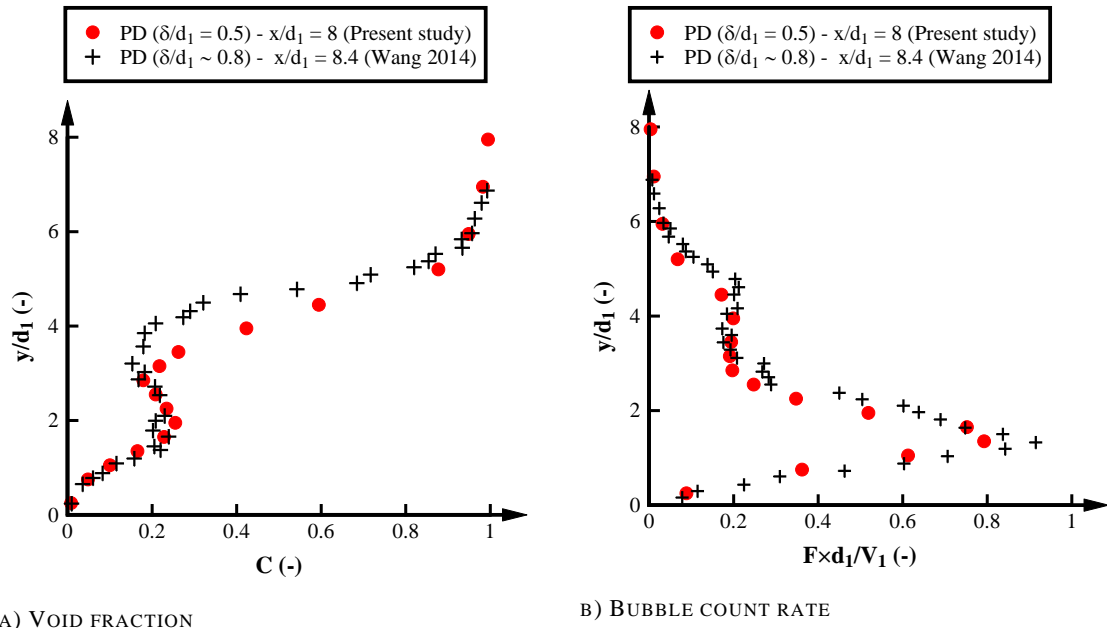


FIGURE B-7. COMPARISON OF DIFFERENT SAMPLING TIMES IN THE AIR-WATER FLOW PROPERTIES IN A HYDRAULIC JUMP WITH PARTIALLY DEVELOPED INFLOW CONDITIONS (PD).

B.3. FREE-SURFACE FEATURES

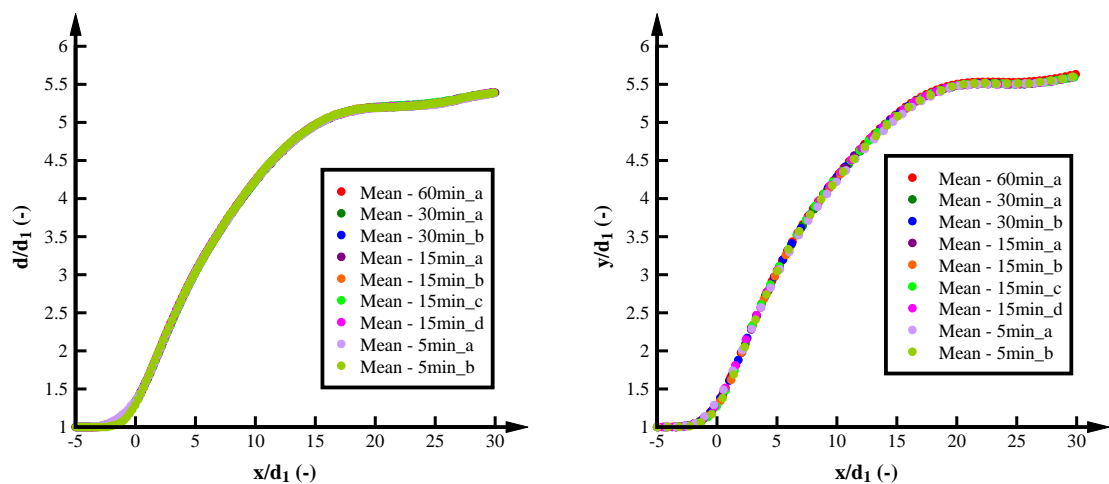
Early studies of the free-surface fluctuations in hydraulic jumps with wire gauges were conducted for 5 seconds sampling time (Mouaze et al. 2005; Murzyn et al. 2007) (Table B-1). Subsequent experiments performed with ADMs expanded the recording of the free-surface profiles for sampling times between 540 s to 1200 s. The present study validated the minimum sampling time for the analysis of the free-surface profile in hydraulic jumps with a LIDAR for key free-surface parameters including the time-averaged free-surface profile, free-surface fluctuations, dominant frequencies of the free-surface fluctuations and jump toe oscillations features. The sensitivity analysis comprised the recording of hydraulic jumps located downstream sloped channels and downstream of the sluice gate with an inflow Froude numbers of 4.6 and 4.4 respectively. The sampling duration was analysed within a range of 5 minutes to 1 hour.

TABLE B-3. SENSITIVITY ANALYSIS OF SAMPLING DURATION OF THE FREE-SURFACE FEATURES IN HYDRAULIC JUMPS.

Experiment	Q (l/s)	d_1 (m)	Fr_0 (-)	Sampling time test	
				Sampling time (min)	Test
Hydraulic jumps d/s of the slope	68	0.04	4.6	60	60min_a
				30	30min_a
				30	30min_b
				15	15min_a
				15	15min_b
				15	15min_c
				15	15min_d
				5	5min_a
Hydraulic jumps d/s a sluice gate	43	0.03	4.4	60	60min_a
				30	30min_a
				30	30min_b
				15	15min_a
				15	15min_b
				15	15min_c
				15	15min_d
				5	5min_a
				5	5min_b

B.3.1. TIME-AVERAGED FREE-SURFACE PROFILE

Figures B-8A and B-8B present the time-averaged mean profiles for different sampling times for the hydraulic jumps downstream the sloped channel and downstream the sluice gate respectively. The time-averaged free-surface profile was similar between all the analysis with some differences near the jump toe position. The relative difference respect the sampling time of 60 min showed differences of 1% for sampling times of 30 mins and 4% for 5 minutes sampling duration. Overall, the sampling duration of 30 minutes presented a more similar time-averaged profile compared with the analysis of one hour.



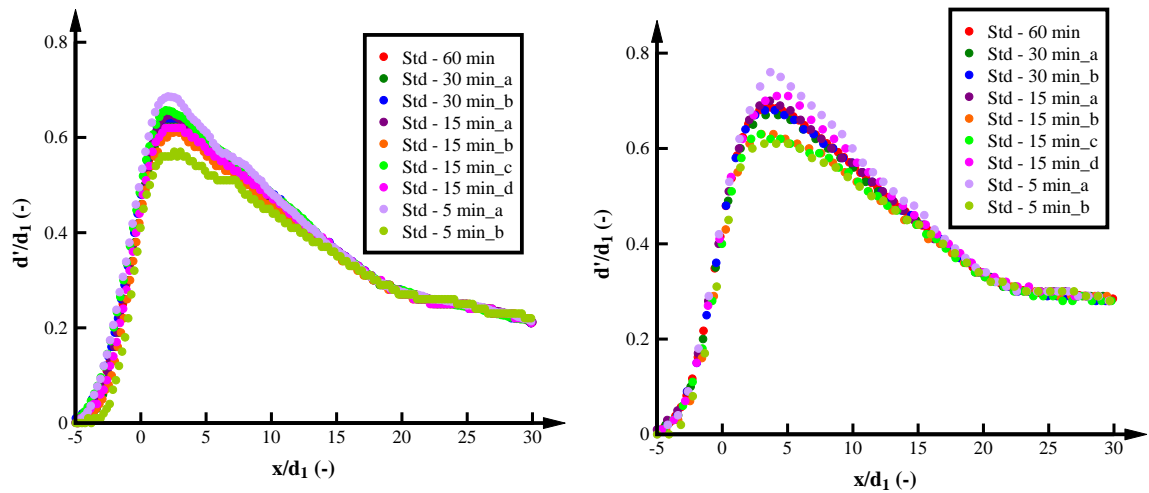
A) HYDRAULIC JUMP D/S SLOPED CHANNEL

B) HYDRAULIC JUMP D/S THE SLUICE GATE

FIGURE B-8. EFFECT OF SAMPLING DURATION IN THE TIME-AVERAGED FREE-SURFACE PROFILE.

B.3.2. FREE-SURFACE FLUCTUATIONS

The sensitivity analysis of the sampling time of the free-surface fluctuations is presented in Figures B-9. The free-surface fluctuations were significantly affected by the sampling duration presenting deviations of 10% for the sampling durations of 5 minutes and 15 minutes compared to the one hour sampling duration. The 30 minutes sampling duration showed differences of 2 % suggesting an optimum sampling time for the free-surface fluctuations in the hydraulic jump.



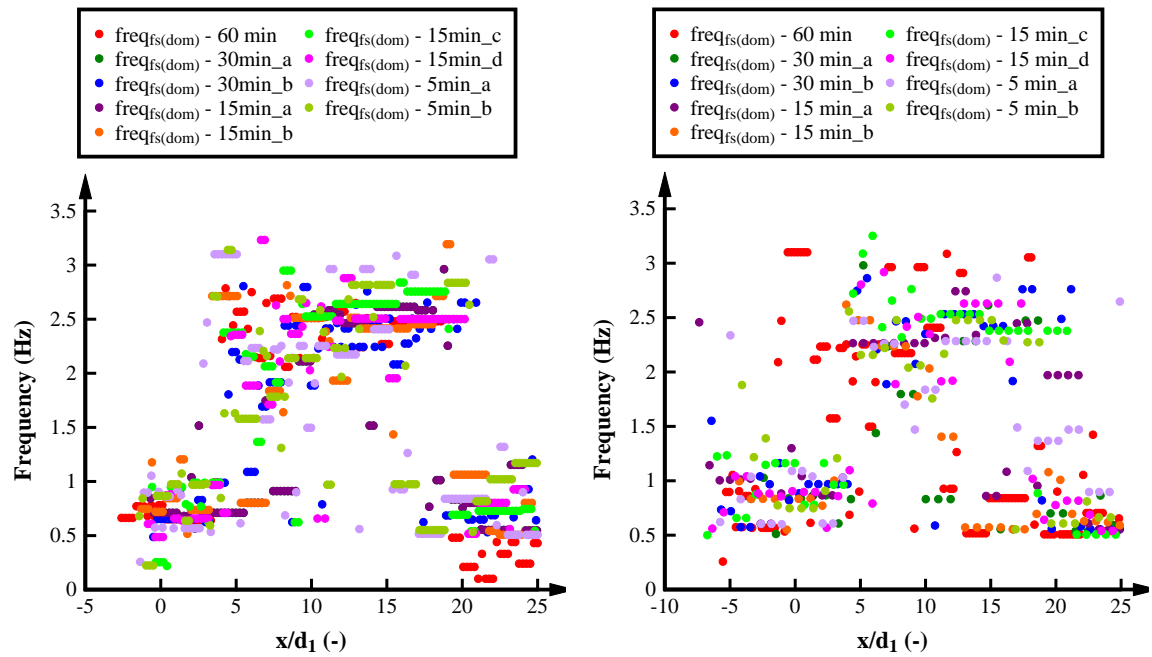
A) HYDRAULIC JUMP D/S SLOPED CHANNEL

B) HYDRAULIC JUMP D/S THE SLUICE GATE

FIGURE B-9. EFFECT OF SAMPLING DURATION IN THE FREE-SURFACE FLUCTUATIONS.

B.3.3. DOMINANT FREQUENCIES FREE-SURFACE

The dominant frequency in the free-surface fluctuations was defined as the frequency with the highest energy amplitude in the frequency spectrum. Figure B-10 presents the sensitivity analysis conducted in the characteristic frequencies of the free-surface fluctuations. Overall, independent of the sampling time, all the experiments showed a similar trend, with a range of dominant frequencies between 0.2 – 1 Hz in the jump toe region, 1.5 – 3.5 in the free-surface region and 0.2-1.5 in the conjugate depth region.



A) HYDRAULIC JUMP D/S SLOPED CHANNEL

B) HYDRAULIC JUMP D/S THE SLUICE GATE

FIGURE B-10. EFFECT OF SAMPLING DURATION IN THE CHARACTERISTIC FREQUENCIES OF THE FREE-SURFACE FLUCTUATIONS.

B.3.4. JUMP TOE OSCILLATIONS

Tables B-4 and B-5 presents the sensitivity analysis on the sampling time duration for the jump toe oscillations in the hydraulic jump. The jump toe oscillation for sampling times of 30 minutes was consistent with the jump toe oscillation observed during 1 hour with differences of 3% in the jump toe oscillations x_{toe}/d_1 and 5% in the jump toe amplitude $(x_{toe,max}-x_{toe,min})/d_1$. The dominant frequencies presented slight deviations although the frequency value was still in the expected range of jump toe frequencies. The jump toe parameters for sampling times of 15 and 5 mins presented significant deviations compared with 1 hour sampling time. The jump toe oscillations differed 5% and 15% for sampling times of 15 and 5 minutes respectively while the jump toe amplitude presented differences of 16% for the sampling period of 15 minutes and 20% for the 5 minutes sampling duration.

TABLE B-4. SENSITIVITY ANALYSIS OF SAMPLING DURATION OF THE FREE-SURFACE FEATURES IN HYDRAULIC JUMPS.

Test	$(x_{toe,max} - x_{toe,min})/d_1$	x_{toe}/d_1	$freq_{toe}$	Skewness	Kurtosis
60 min	12.3	1.47	0.9	-0.07	0.03
30 min_a	11.67	1.42	0.58	0.08	-0.08
30 min_b	12.3	1.51	0.64	-0.19	0.09
15 min_a	10.3	1.51	0.65	-0.019	-0.26
15 min_b	11.68	1.39	0.74	0.16	0.17
15 min_c	11.39	1.56	0.99	-0.27	-0.017
15 min_d	11.73	1.44	0.63	-0.03	0.057
5 min_a	9.83	1.64	0.53	-0.24	-0.37
5 min_b	9.82	1.25	0.5/0.95	0.26	0.16

TABLE B-5. SENSITIVITY ANALYSIS OF SAMPLING DURATION OF THE FREE-SURFACE FEATURES IN HYDRAULIC JUMPS.

Test	$(x_{toe,max} - x_{toe,min})/d_1$	x_{toe}'/d_1	$freq_{toe}$	Skewness	Kurtosis
60 min	16.06	1.70	0.83	0.29	0.44
30 min_a	14.57	1.65	0.79	0.23	0.28
30 min_b	15.88	1.69	0.96	0.26	0.47
15 min_a	14.57	1.72	0.83	0.20	0.24
15 min_b	12.29	1.49	0.85	0.07	0.02
15 min_c	13.74	1.51	1	0.03	0.080
15 min_d	15.59	1.79	0.83	0.57	0.96
5 min_a	12.45	1.89	0.80	0.45	0.082
5 min_a	9.51	1.42	0.83	0.009	-0.14

B.3.5. MINIMUM SAMPLING TIME FREE-SURFACE FLUCTUATIONS

The free-surface features in the hydraulic jumps measured with the LIDAR were strongly affected by the sampling time duration. Overall, measurements of the free-surface features during 5 and 15 minutes presented large deviations in free-surface fluctuations and jump toe oscillations compared to the measurements conducted for 1 hour. For all the free-surface parameters, a sampling time of 30 minutes was selected as the minimum time required to obtain reliable information with the LIDAR.

B.4. INTERNAL FORCES

The analysis of internal motions in hydraulic jumps have been performed by the recording of transverse and vertical pressure fluctuations in the channel bottom (e.g. Abdul Khader and Elango 1974; Fiorotto and Rinaldo 1992) and in the vertical pressure distribution (Wang et al. 2014b). The pressure fluctuations in the channel bottom have been conducted for sampling times between 600 s to 900 s while the analysis of the vertical pressure distribution was conducted for 180 s. A sensitivity analysis was conducted to validate the minimum sampling time required to measure the internal three-dimensional forces over a sphere in the hydraulic jump with a load cell. The analysis was conducted for four hydraulic jumps with different inflow Froude numbers at different cross-sections and at $y = Y_{Cmax}$ and $y = Y_{Cmin}$ for sampling durations between 28 s to 900 s. Table B-6 presents the experiments conducted for the analysis of minimum sampling time of internal force measurements in hydraulic jumps with a load cell.

TABLE B-6. SENSITIVITY ANALYSIS OF SAMPLING DURATION OF THE FREE-SURFACE FEATURES IN HYDRAULIC JUMPS.

Experiment	Fr_1	Re	Inflow condition	x/d_1 (-)	y	
					Y_{Cmax}	Y_{Cmin}
Experiment A	5.1	8.3×10^4	PD	8	x	x
				20	x	x
Experiment C	7.0	6.2×10^4	PD	8	x	x
				20	x	x
Experiment E	8.5	7.5×10^4	FD	8	x	x

Experiment	Fr_1	Re	Inflow condition	x/d_1 (-)	y	
					Y_{Cmax}	Y_{Cmin}
					20	x

B.4.1. TIME-AVERAGED FORCES

The time-averaged streamwise forces were recorded at different cross-sections along the hydraulic jump and different elevations. Figure B-11 presents the effect of the sampling time in the time-averaged streamwise forces for $y = Y_{Cmax}$ and $y = Y_{Cmin}$ at regions close and far from the jump toe. Larger data deviations were observed in the streamwise forces for regions close to the jump toe and Y_{Cmax} suggesting a minimum sampling time of 300 s. For Y_{Cmin} and at the downstream end of the hydraulic jump, the streamwise forces did not present a significant variation with the increase in the sampling time suggesting sampling time durations of 200 s.

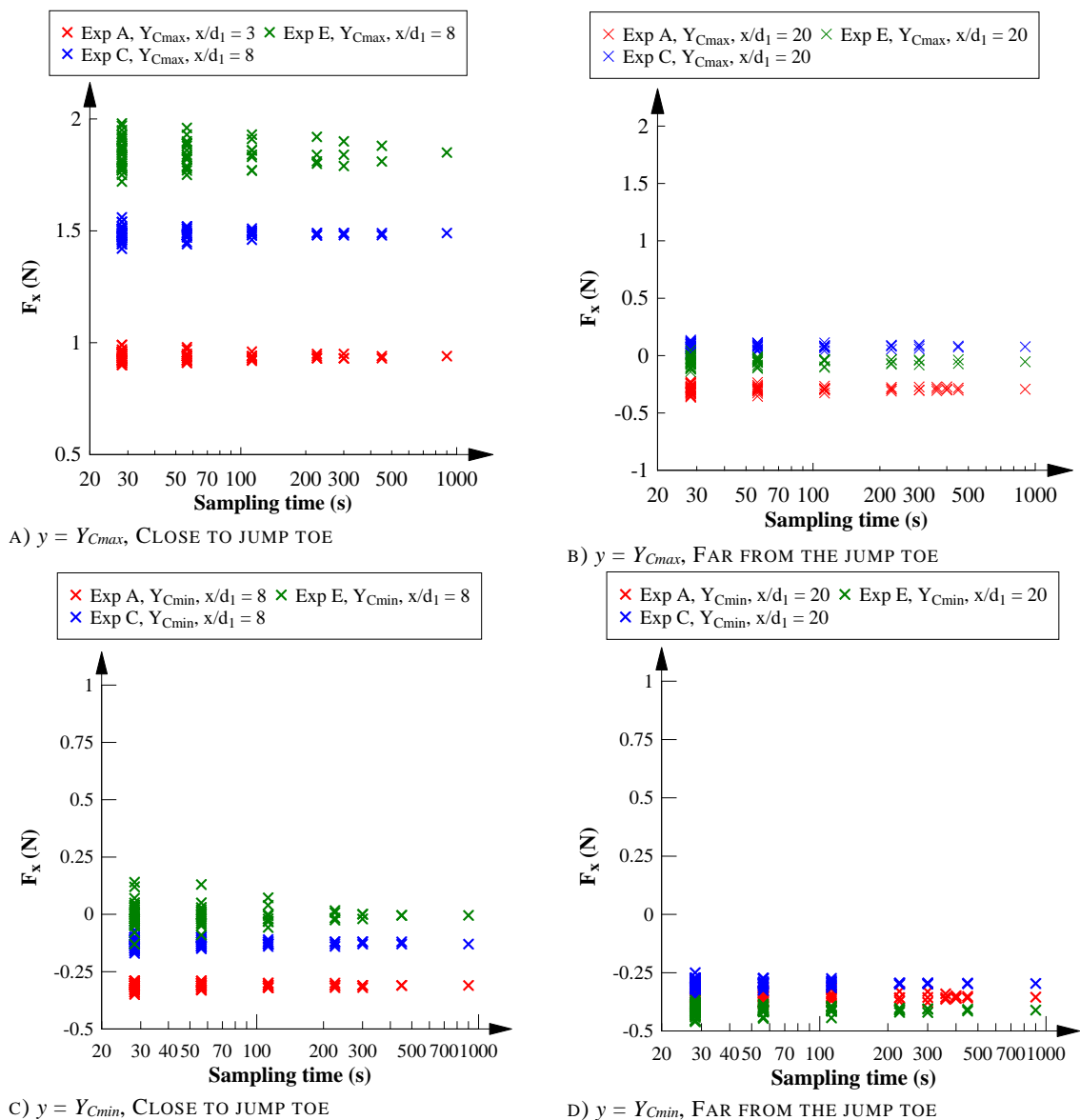


FIGURE B-11. EFFECT OF SAMPLING DURATION IN THE TIME-AVERAGED STREAMWISE FORCE.

The sensitivity analysis of the required sampling time for the analysis of the time-averaged transverse forces is presented in Figure B-12. Independent of the sampling time, the

time-averaged transverse forces were always close to zero and minor differences were observed with increasing the sampling duration. For the analysis of the transverse forces, sampling durations of 100 s seemed accurate and reliable.

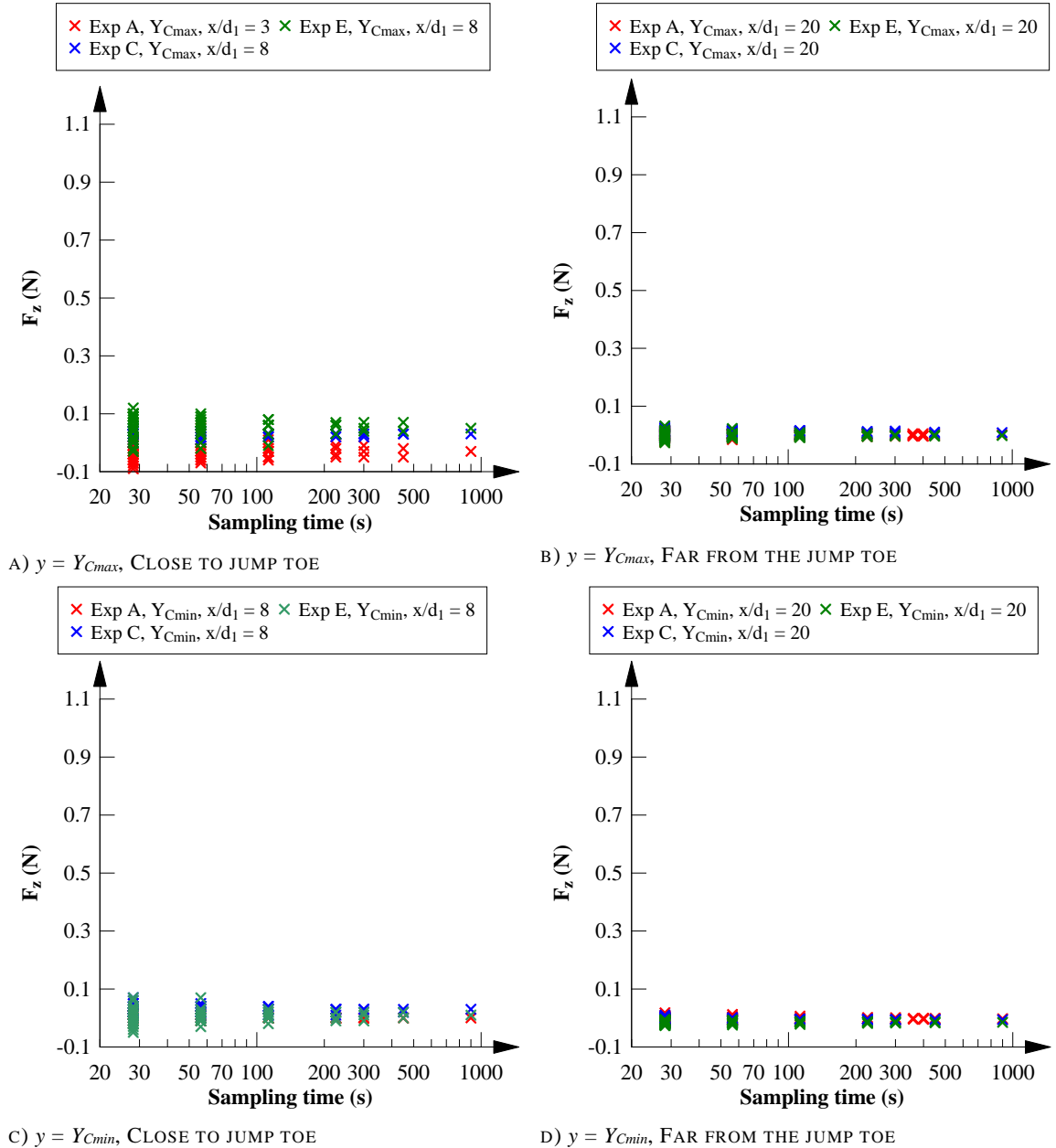


FIGURE B-12. EFFECT OF SAMPLING DURATION IN THE TIME-AVERAGED TRANSVERSE FORCES.

Figure B-13 presents the sensitivity analysis of the sampling time duration in the measurement of the time-averaged vertical forces measured over a sphere in a hydraulic jump. Larger deviation was observed in Y_{Cmax} close to the jump toe indicating a minimum sampling time of 300 s for an accurate estimation of the vertical forces. Lesser influence of the sampling time was observed in Y_{Cmin} and at the downstream end of the hydraulic jump with reliable sampling time durations of 100 s.

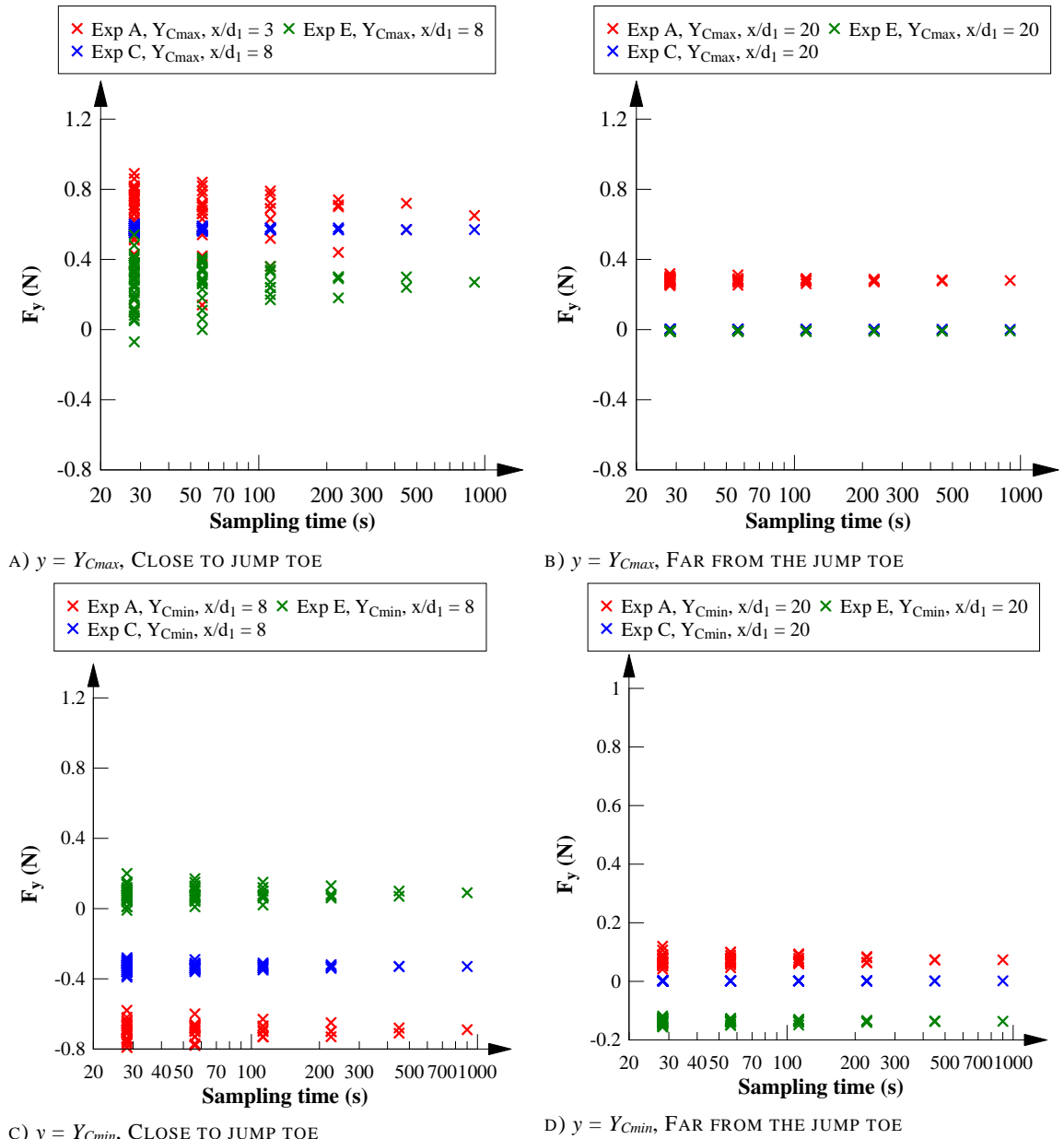


FIGURE B-13. EFFECT OF SAMPLING DURATION IN THE TIME-AVERAGED VERTICAL FORCES.

B.4.2. FORCE FLUCTUATIONS

The sensitivity analysis of the streamwise force fluctuations is included in Figure B-14 for Y_{Cmax} and Y_{Cmin} . The force fluctuations were strongly influenced by the sampling time with large variation for sampling times lower than 100 s for all the positions analysed throughout the hydraulic jump. For most of the experiments, the data scatter decreased with increasing distance from the jump toe suggesting minimum sampling times of 450 s for regions located close to the jump toe and larger than 300 s further downstream.

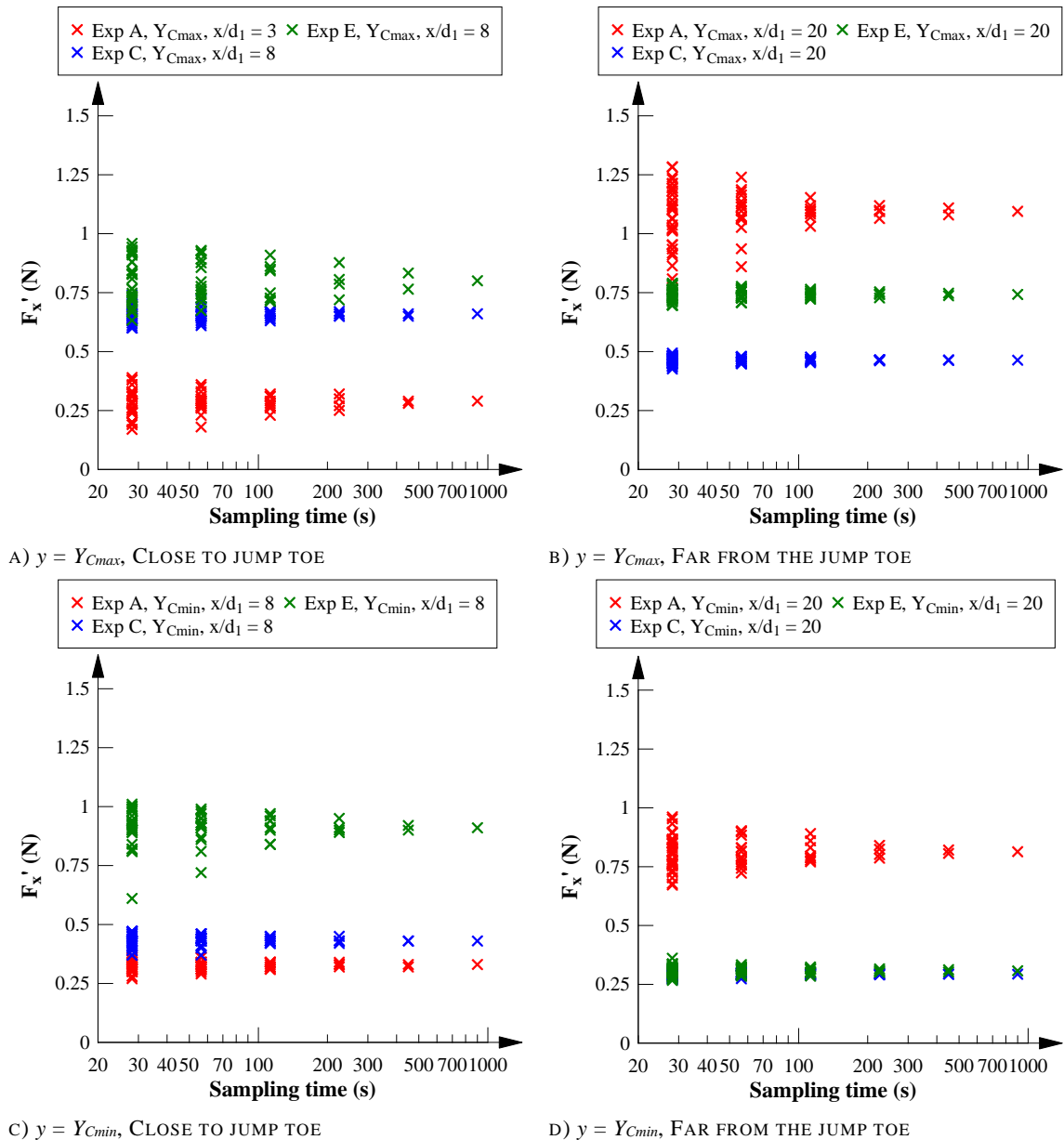


FIGURE B-14. EFFECT OF SAMPLING DURATION IN THE TIME-AVERAGED VERTICAL FORCES.

The fluctuations of the transverse forces were also significantly affected by the sampling time with variations of almost 0.5 N for sampling times of 30 s at regions located close to the jump toe (Figure B-15). Lesser data scatter were observed for Y_{Cmin} indicating lesser transverse fluctuations in the upper part of the hydraulic jump. For regions located close to the jump toe, a minimum sampling time of 300 s was suggested while minimum sampling times of 200 s were identified for regions located further downstream.

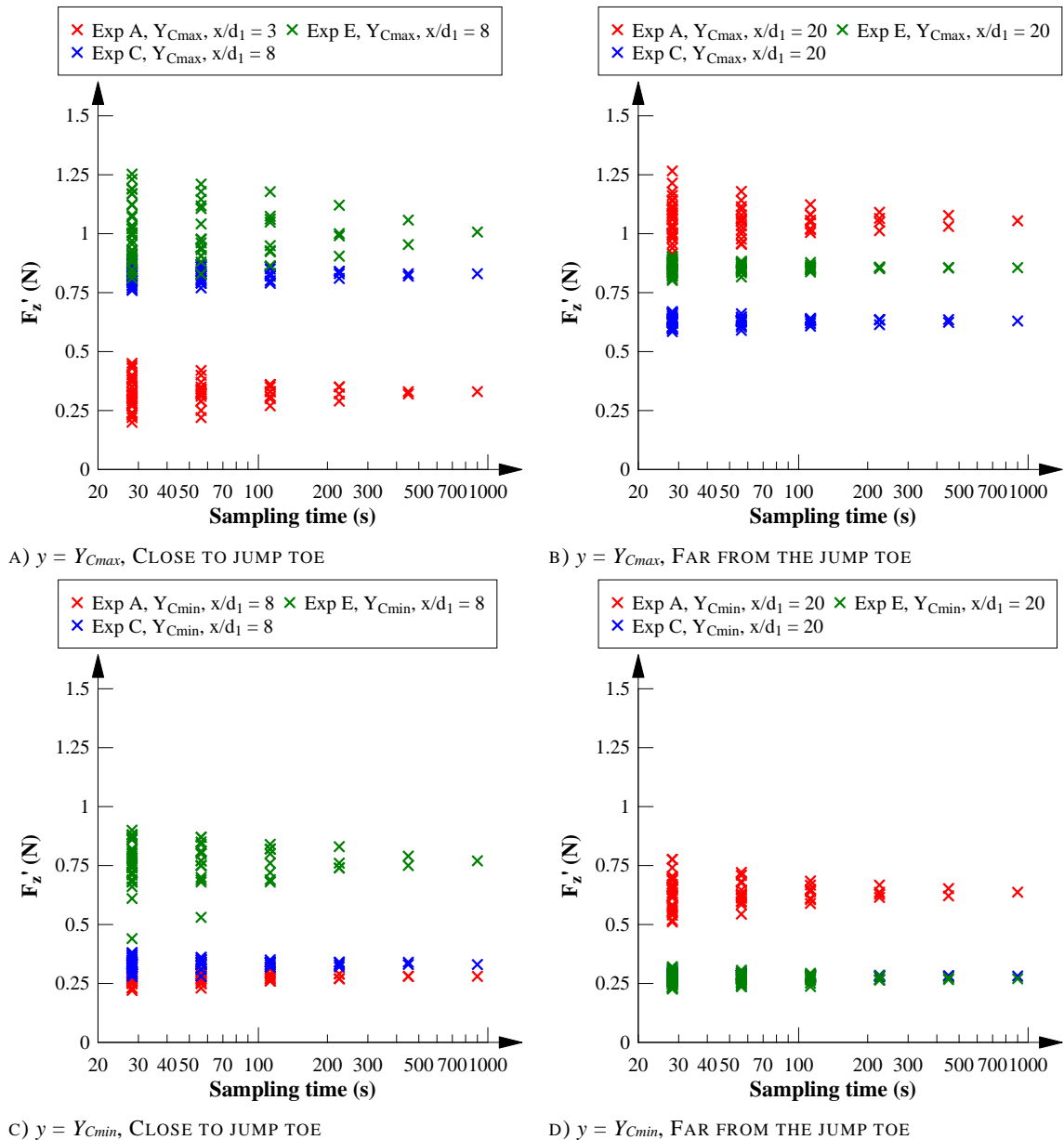


FIGURE B-15. EFFECT OF SAMPLING DURATION IN THE TIME-AVERAGED VERTICAL FORCES.

The vertical force fluctuations presented lesser scatter compared to the longitudinal and transverse force fluctuations. Large data variation was observed for the measurement of the forces at Y_{Cmax} close to the jump toe suggesting minimum sampling durations of 200 s. For regions located at the downstream end of the hydraulic jump and at Y_{Cmin} , minimal influence of the sampling time was observed indicating that a sampling time of 100 s may be optimum for obtaining reliable information.

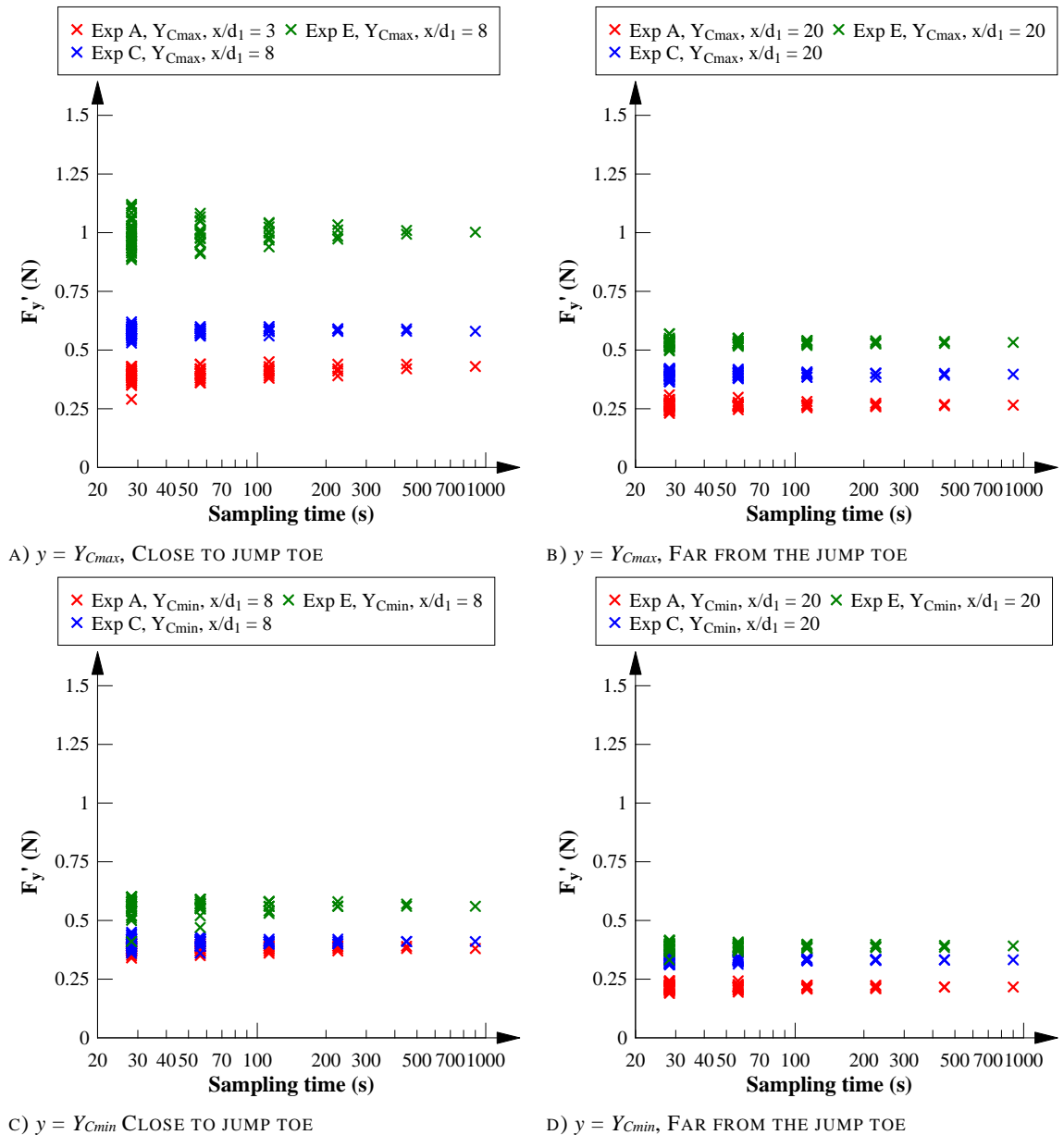


FIGURE B-16. EFFECT OF SAMPLING DURATION IN THE TIME-AVERAGED VERTICAL FORCES.

B.3.5. MINIMUM SAMPLING TIME INTERNAL FORCES

The estimation of the internal forces over a sphere measured with a load cell in a hydraulic jump presented large deviations for regions located close to the jump toe for short sampling times. The sensitivity analysis conducted for a maximum recording of 900 s suggested minimum sampling times of 300 s close to the jump toe and 200 s further downstream. The present study selected a sampling duration of 450 for regions located close to the jump toe and 300 s in the roller and conjugate depth regions.

C. FILTERING TECHNIQUES

C.1. INTRODUCTION

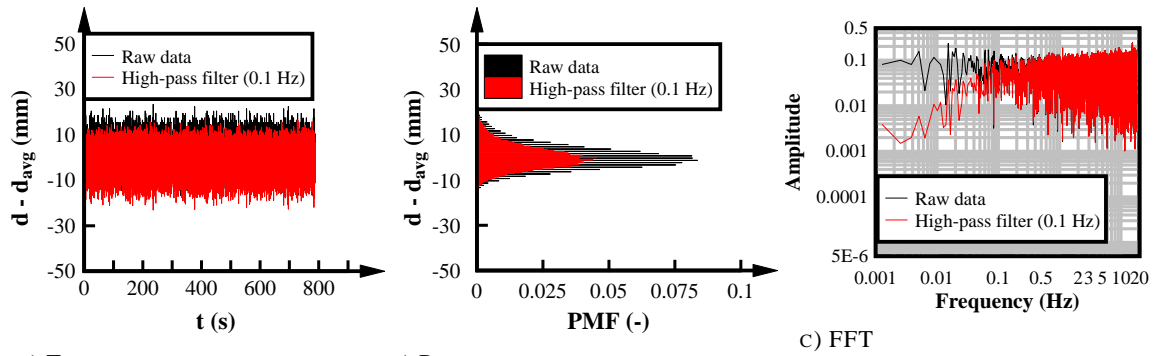
The hydraulic jump is a complex dynamic phenomenon characterised by large turbulence and continuous fluctuations. Any measurements in hydraulic jumps comprise uncertainties related to the large oscillating motion of the hydraulic jump as well as the instrumentation. To minimise the instrument uncertainty, the raw data measured in the hydraulic jump was analysed and a filter analysis was applied if required. The present chapter presents a summary of the filtering techniques analysed in the present study.

C.2. LIDAR

The LIDAR (LIght Detection and Ranging Instrument) is a non-intrusive instrument which operates based upon the Time-Of-Flight principle (Gokturk et al. 2004; Allis et al. 2011; Blenkinsopp et al. 2012). This principle estimates the distance between the LIDAR and a target based upon the travel time by the pulse of light (laser) transmitted from the LIDAR and the target surface (Gokturk et al. 2004; Bufton et al. 1991; Blenkisopp et al. 2012). Laser light instruments are susceptible to optical issues related to the LIDAR location (incidence angle) and the transformation of the laser beam reaching the target object including transmission, absorption or refraction (Irish et al. 2006; Allis et al. 2011; Blenkinsopp et al. 2012; SICK 2015). In addition to the optical issues, the strong free-surface deformations in hydraulic jumps resulted in splashes of water droplets above the surface which could interfere with the LIDAR recordings. A sensitivity analysis of LIDAR performance was conducted in the present study through the application of different filtering techniques:

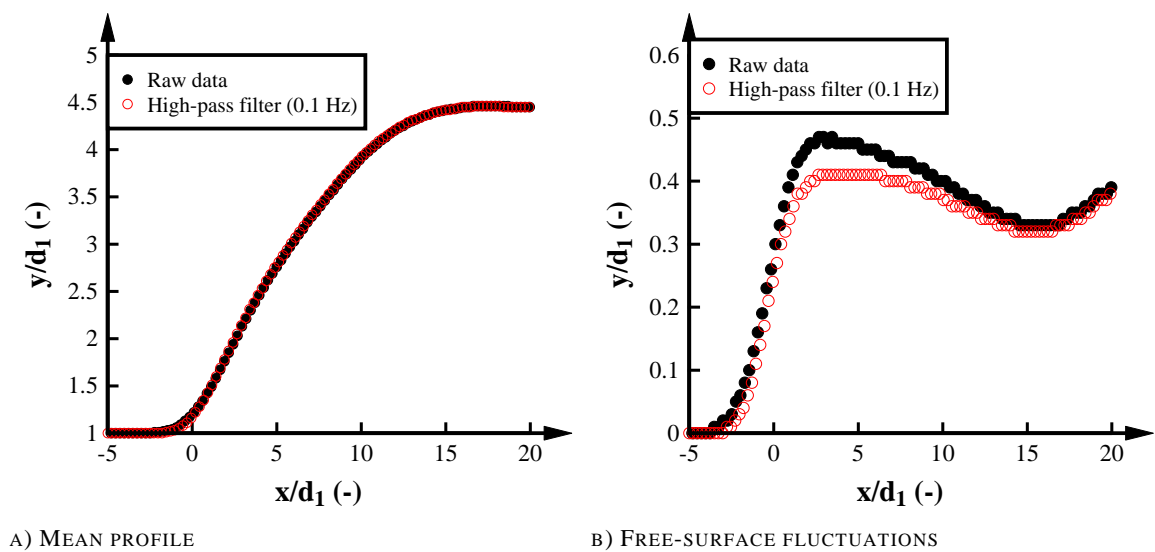
C.2.1. HIGH-PASS FILTER

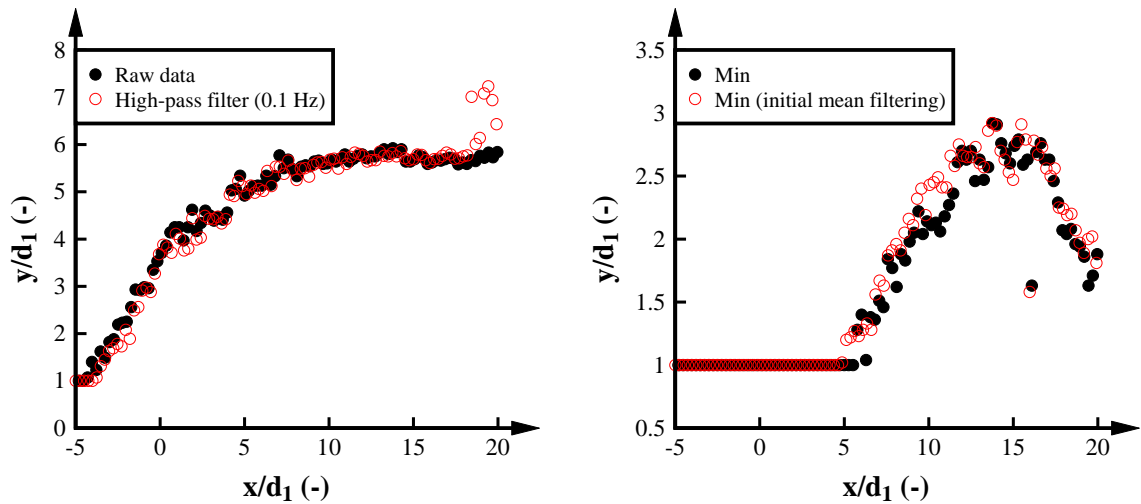
Some instruments are susceptible to intrinsic noise, specially at low frequencies. To validate the signal characteristics of the LIDAR, a sensitivity analysis of the probability mass function (PMF) of the fluctuations of the raw signal (eliminating the mean) was conducted in the dry channel bed following the approach of Kramer et al. (2019a) and Zhang et al. (2018). Figure C-1 presents the effect of the high-pass filter of 0.1 Hz in the dry channel. Overall, the raw signal resembled a typical Gaussian distribution for dry and wet conditions suggesting negligible intrinsic noise of the LIDAR. The filtered data presented also a Gaussian distribution but with a significant decrease in the PMF peak suggesting that a high-pass filter of 0.1 Hz was eliminating valid free-surface data.



A) TIME SERIES B) PROBABILITY MASS FUNCTION C) FFT
FIGURE C-1. SENSITIVITY ANALYSIS OF THE PROBABILITY MASS DISTRIBUTION OF THE RAW SIGNAL IN THE HYDRAULIC JUMP.

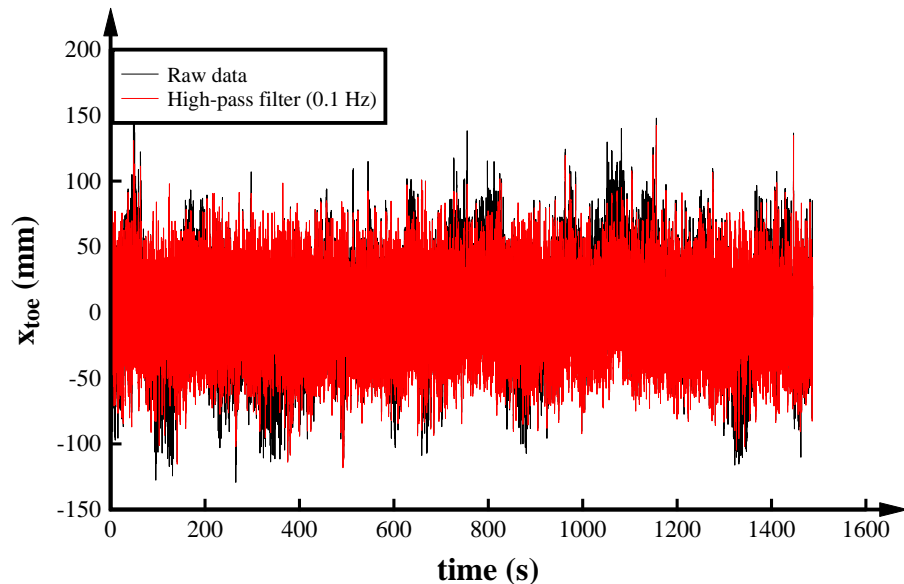
Figure C-2 presents a further validation of the effect of the high-pass filter of 0.1 Hz in the basic free-surface features in the hydraulic jump. Minor differences were identified in the time-averaged free-surface profile with deviations up to 3% close to the mean jump toe position (Figure C-2A). Larger deviations were observed in the free-surface fluctuations with more than 10% reduction in the free-surface fluctuations close to the jump toe region suggesting a significant effect of the high-pass filter (Figure C-2B). Some deviations were also observed in the maximum and minimum free-surface profiles with differences of about 30% compared to the raw data (Figures C-2C and D). Note that the high-pass filtered reduced slightly the maximum free-surface profile whereas the minimum free-surface profile increased (Figures C-2C and D). The jump toe oscillations were also affected by the high-pass filter with a reduction in the jump toe amplitude from 282 mm for raw data conditions to 260 mm with the high-pass filter condition. Lower jump toe oscillations were also observed in the high-pass filter analysis with a reduction of 20% compared to the raw data condition.





C) MAXIMUM PROFILE

D) MINIMUM PROFILE



E) JUMP TOE OSCILLATIONS

FIGURE C-2. SENSITIVITY ANALYSIS OF THE HIGH-PASS FILTERING IN THE BASIC FREE-SURFACE PARAMETERS IN THE HYDRAULIC JUMP.

C.2.2. HAMPEL FILTER

The free-surface profile in strong hydraulic jumps is characterised by large flow disturbances and water splashes which may be identified as outliers. These outliers were identified using a Hampel filter known as one of the most accurate identifiers of deviations (Pearson 2002; Liu et al. 2004b). The Hampel identifier calculated the median and the standard deviation of N surrounding data points, and any data points with a median of more than M times the standard deviation were identified as an outlier and replaced by the median (Pearson 2002; Liu et al. 2004b). Figure C-3 presents examples of the Hampel filter in the free-surface profile at random time steps. Although the modification of the Hampel identifier in the free-surface profile was minor (less than 8% of the data was replaced by the median of the surrounding points), the replaced data observed in Figure C-3 did not represent an outlier and it should not be removed from the raw data.

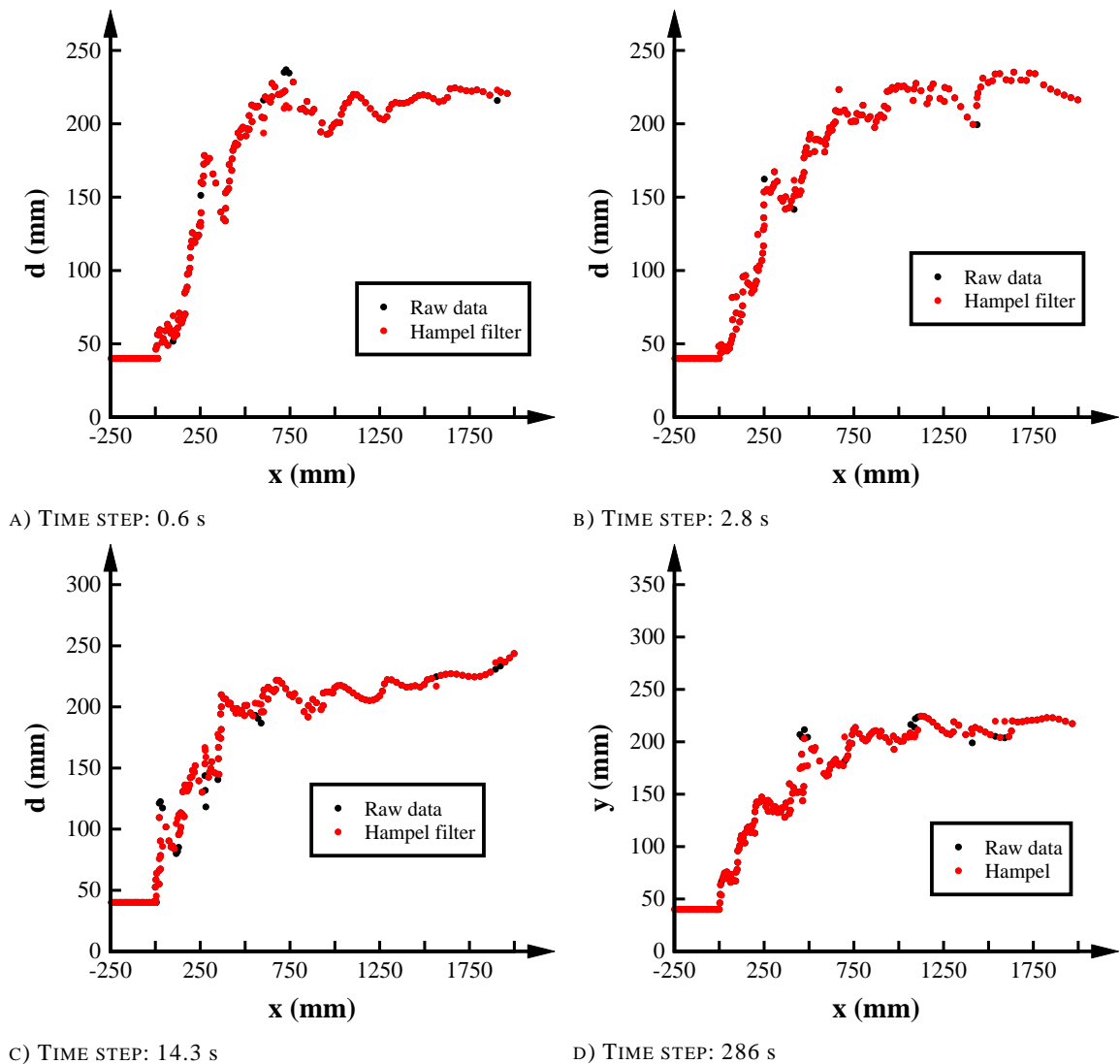


FIGURE C-3. SENSITIVITY ANALYSIS OF THE EFFECT OF HAMPSEL FILTER IN THE FREE-SURFACE PROFILES IN THE SPACE DOMAIN.

An additional sensitivity analysis of the Hampel filter effect into the raw data was conducted in the time domain. Figure C-4 presents a comparison of the raw data and the Hampel filtered data at different positions along the hydraulic jump. Large data was filtered in the upstream part of the hydraulic jump linked with the stronger fluctuations and larger water splashes while at the downstream end of the hydraulic jump, less than 5% of the data were replaced. For all the cross-sections analysed, most of the filtered data was replaced by lower free-surface values suggesting that most of the filtered data corresponded to high peaks in the free-surface profile. Since the space domain analysis suggested that the Hampel identifier was not strictly replacing outliers and instead, it replaced large peaks commonly observed in the free-surface features of the hydraulic jump. Therefore, the large data replacement of high peaks in the time domain suggested that the Hampel identifier method was removing a significant quantity of valid data points in the analysis of the hydraulic jump. In order to avoid the elimination of useful information, no outlier filtering technique was used in the present study.

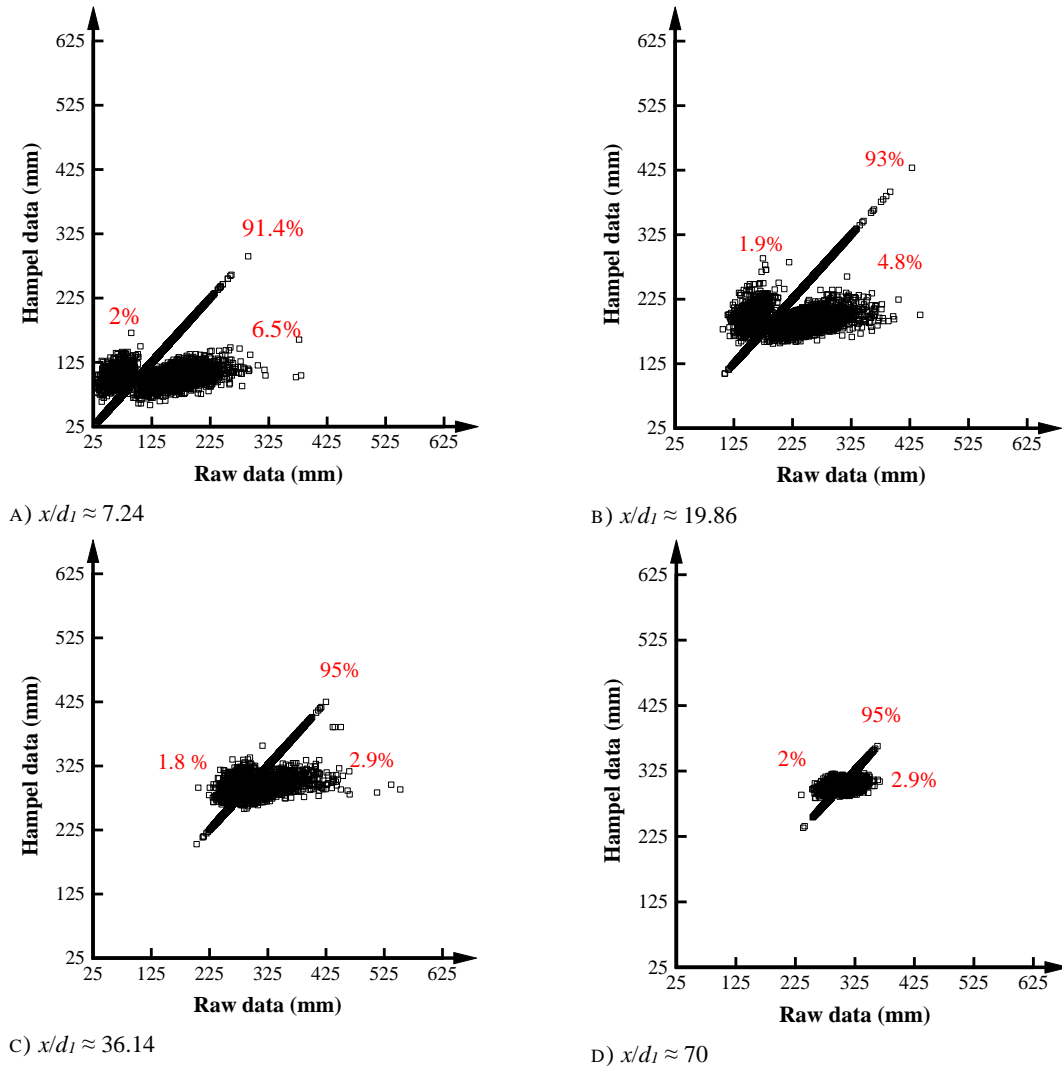


FIGURE C-4. SENSITIVITY ANALYSIS OF THE EFFECT OF HAMPSEL FILTER IN THE FREE-SURFACE PROFILES IN THE TIME DOMAIN.

C.3. LOAD CELL

The measurement of the internal forces in the hydraulic jump presented large data fluctuation and potential spikes. In order to obtain the most “pure” data in the analysis of the internal forces in the hydraulic jump, the Phase-Space Thresholding Method (PST) proposed by Goring and Nikora (2002) and modified by Wahl (2003) in ADVs was applied for all force raw data. The PST follows the three-dimensional Poincaré map including the variable of analysis with its corresponding first and second derivatives without dividing by the time step (Goring and Nikora 2002). A robust data estimator based on the median of the absolute deviations $\left| \frac{f_x - F_x}{\varphi MAD(f_x - F_x)} \right|$ is compared with an ellipsoid estimated based on the Universal criterion ($\zeta = \sqrt{2 \ln N}$) where f_x is the instantaneous streamwise force, F_x is the time-averaged streamwise force, φ is a factor equal to 1.483 for Gaussian distributions, ζ is the universal threshold and N is the number of data points (Goring and Nikora 2002; Wahl 2003; Valero 2018). If the robust data estimator is larger than the Universal criterion, the data will be replaced by the mean value of the two adjacent

points (Goring and Nikora 2002; Wahl 2003). The process will be repeated until the spikes are removed.

Figure C-5 presents the application of the PST method for the vertical force data at $y/d_l = 1.544$. Blue dots represent the raw data, red dots the filtered data and the black line represents the Normal distribution function. Figures C-5A, B and C include the three-dimensional analysis comprising F_y , the first derivative ΔF_y and the second derivative $\Delta^2 F_y$. All the raw data presented in Figure C-5 was enclosed between the ellipsoid defined by the Universal criterion suggesting no outliers for this position. Since the data was clean of outliers, no data replacement was conducted. Figure C-5D presents the Probability Mass Function (PMF) and the comparison with the normal distribution. Figure C-5D confirmed that the force data at $y/d_l = 1.544$ followed a Gaussian distribution.

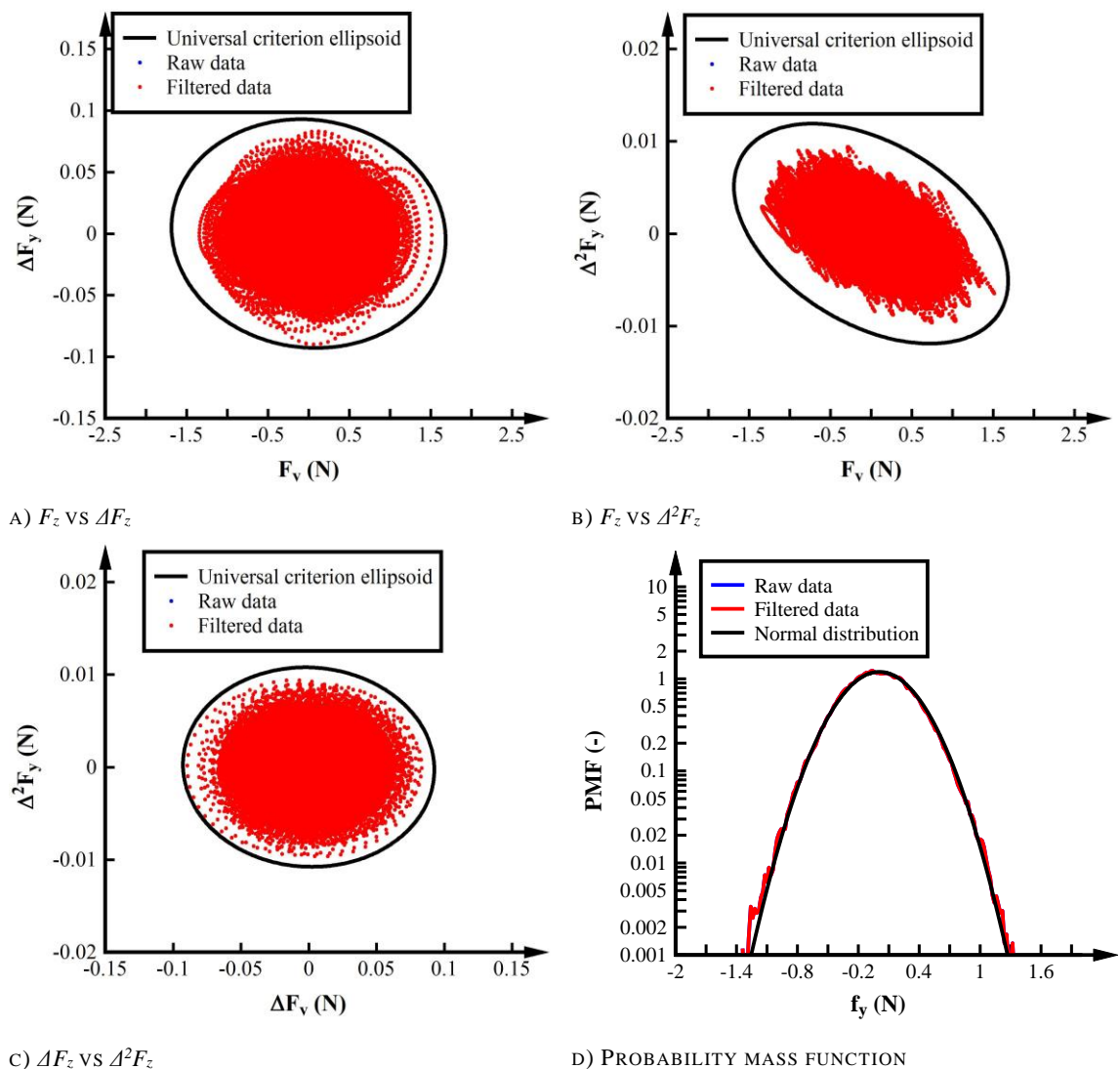


FIGURE C-5. PHASE-SPACE PLOT FOR CLEAN DATASET (EXPERIMENT H: $Fr_l = 3.8$, $Re = 6.2 \times 10^4$, $x/d_l = 5$, $y/d_l = 1.544$).

For larger Froude numbers, the hydraulic jump presented stronger instabilities and internal force fluctuations. Figure C-6 presents the PST method applied in the internal force measurements in a stronger hydraulic jump. Although most of the data were enclosed within the Universal threshold, a proportion of the data was located outside the ellipsoid resulting in data replacement (Figure C-6A). The data was replaced by the mean value of the two adjacent points resulting in modifications in the first and second derivatives (Figure C-6B and C). The modified data could be observed in the right side of the PMF graph highlighting outliers towards the positive force (Figure C-6D). Despite some small deviations, the force data followed a Gaussian distribution. For the example presented in Figure C-6, only 0.01% of the data was replaced suggesting that the overall force measurements with the load cell were minimally affected by outliers.

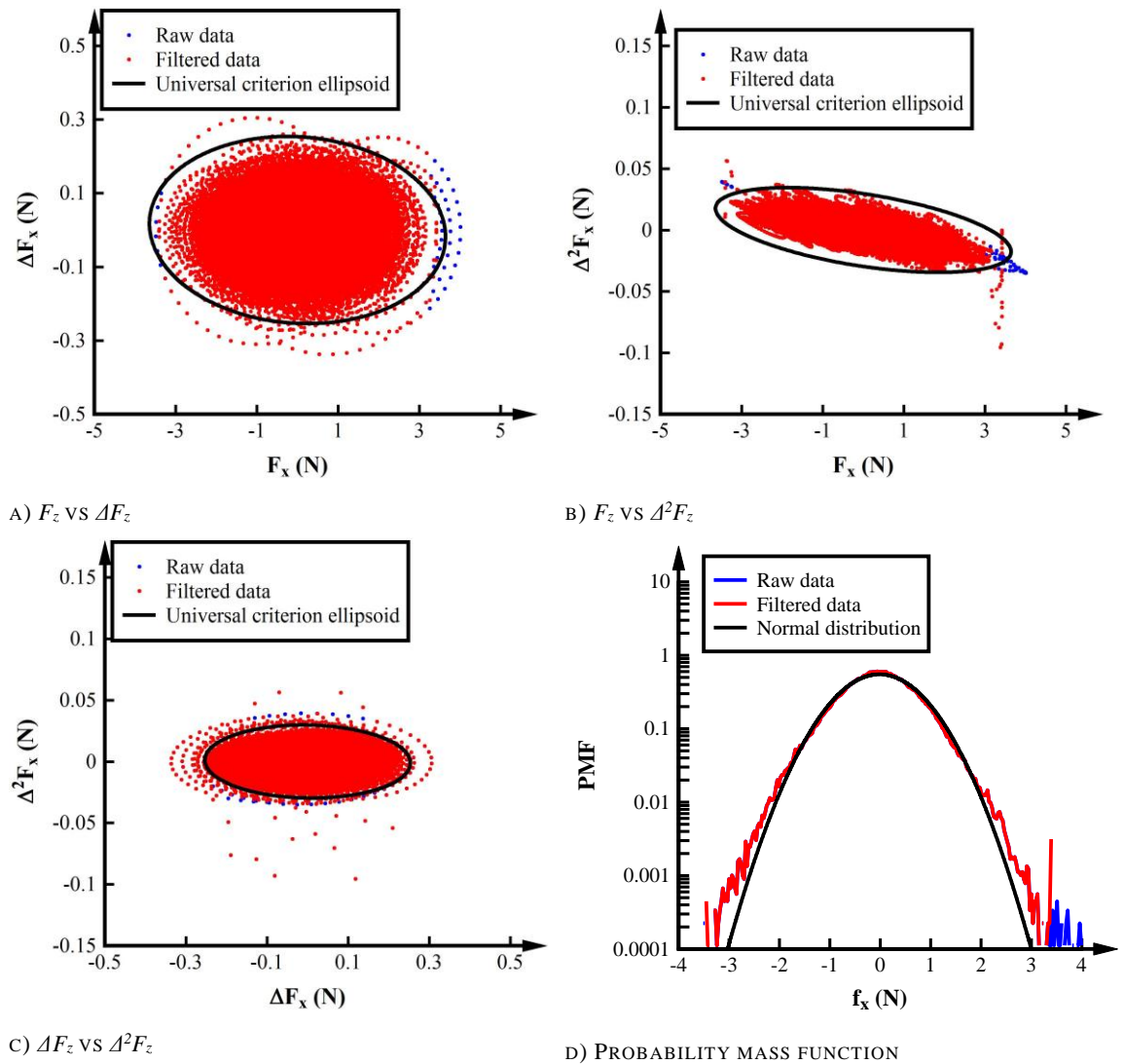


FIGURE C-6. PHASE-SPACE PLOT FOR DATASET WITH OUTLIERS (EXPERIMENT D: $Fr_1 = 7.0$, $Re = 1.1 \times 10^5$, $x/d_1 = 20$, $y/d_1 = 3.31$).

Table C-1 presents a summary of the maximum cross-sectional percentage of data replacement for all the experiments conducted in the present study. Overall, the data replaced

was of about 0.09% for F_x , 0.2% for F_z and 0.09% for F_y suggesting a larger number of outliers in the transverse forces. Nonetheless, the data replacement was minor with a maximum of 0.8% data replaced for experiments conducted with large Froude numbers. The low percentage of data replacements indicated good data quality and minor number of outliers in the measurement of the internal forces in the hydraulic jump.

TABLE C-1. PERCENTAGE OF FORCE MEASUREMENT DATA REPLACED BY THE PHASE-SPACE THRESHOLD METHOD .

Experiment	FD/PD	Fr_1	Re	x/d_1	% Data	% Data	% Data
					replaced	replaced	replaced
					F_x	F_z	F_y
H	FD	3.8	6.2×10^4	3	0.002	0.01	0
				5.5	0.02	0.1	0
				8	0.13	0.11	0.01
				13	0.02	0.16	0.03
				17	0.02	0.1	0.1
H	PD	3.8	6.2×10^4	3	0.03	0.02	0.003
				5.5	0.004	0.05	0.005
				8	0.008	0.1	0.003
				13	0.02	0.1	0.02
				17	0.02	0.10	0.02
I	FD	3.8	9.5×10^4	3	0.10	0.60	0
				5.5	0.005	0.06	0.006
				8	0.05	0.30	0.02
				13	0.08	0.20	0.10
				17	0.05	0.10	0.10
A	FD	5.1	8.3×10^4	3	0.20	0.20	0
				8	0.005	0.08	0.004
				13	0.10	0.20	0.01
				20	0.02	0.10	0.09
				30	0.03	0.05	0.10
A	PD	5.1	8.3×10^4	3	0.1	0.09	0
				8	0.009	0.20	0.01
				13	0.02	0.10	0.01
				20	0.07	0.20	0.04
				30	0.06	0.20	0.10
B	FD	5.1	6.2×10^4	3	0.10	0.02	0.001
				8	0.004	0.10	0.006
				13	0.04	0.10	0.02
				20	0.02	0.10	0.08
				30	0.07	0.03	0.20
B	PD	5.1	6.2×10^4	3	0.07	0.20	0
				8	0	0.06	0.003
				13	0.02	0.10	0.03

Experiment	FD/PD	Fr_1	Re	x/d_1	% Data	% Data	% Data
					replaced	replaced	replaced
					F_x	F_z	F_y
				20	0.03	0.10	0.07
				30	0.02	0.1	0.08
C	FD	7.0	6.2×10^4	8	0.01	0.06	0
				13	0.05	0.30	0.20
				20	0.04	0.20	0.03
				30	0.08	0.30	0.10
				40	0.08	0.40	0.20
C	PD	7.0	6.2×10^4	8	0.006	0.06	0.01
				13	0.02	0.10	0.008
				20	0.02	0.10	0.01
				30	0.06	0.20	0.08
				40	0.07	0.10	0.10
D	FD	7.0	1.1×10^5	8	0.02	0.30	0.20
				13	0.20	0.60	0.10
				20	0.10	0.50	0.08
				30	0.40	0.40	0.10
				40	0.30	0.30	0.30
D	FD	7.0	1.1×10^5	8	0.01	0.07	0.003
				13	0.10	0.50	0.08
				20	0.03	0.20	0.04
				30	0.20	0.30	0.09
				40	0.20	0.40	0.20
E	FD	8.2	7.5×10^4	8	0.02	0.20	0.05
				20	0.03	0.20	0.02
				30	0.20	0.30	0.07
				40	0.10	0.20	0.10
				50	0.10	0.20	0.50
E	PD	8.5	7.5×10^4	8	0.03	0.20	0.05
				20	0.02	0.15	0.01
				30	0.10	0.10	0.07
				40	0.15	0.30	0.10
				50	0.15	0.20	0.40
F	FD	8.0	1.2×10^5	8	0.30	0.80	0.20
				20	0.10	0.50	0.15
				30	0.20	0.40	0.15
				40	0.30	0.40	0.30
				50	0.10	0.30	0.40
F	PD	8.4	1.2×10^5	8	0.05	0.20	0.03
				20	0.08	0.30	0.06
				30	0.10	0.30	0.06
				40	0.40	0.50	0.20

Experiment	FD/PD	Fr_1	Re	x/d_1	% Data replaced	% Data replaced	% Data replaced
					F_x	F_z	F_y
G	FD	10	8.8×10^4	50	0.50	0.30	0.40
				8	0.03	0.25	0.05
				20	0.17	0.40	0.06
				30	0.10	0.30	0.05
				40	0.20	0.30	0.05
				50	0.10	0.30	0.40
G	PD	10	8.8×10^4	8	0.05	0.20	0.06
				20	0.04	0.20	0.03
				30	0.08	0.20	0.05
				40	0.20	0.20	0.20
				50	0.30	0.30	0.80

D. AIR-WATER FLOW PROPERTIES: DECAY AIR-WATER FLOW PARAMETERS

D.1. INTRODUCTION

The hydraulic jump is characterised by air entrapment at the impingement point and air entrainment in the recirculation region. Extensive studies have investigated the aeration features in hydraulic jumps providing a good understanding of the aeration processes (e.g. Resch et al. 1974; Chanson and Brattberg 2000; Chanson 2009b; Takahashi and Ohtsu 2017). Close to the jump toe, the hydraulic jump presents large aeration and number of bubbles linked with the air entrapped at the jump toe position. The dissipative and turbulent levels in the hydraulic jumps provoke breaking up of bubbles and bubble dispersion leading to a decay in the air-water flow properties with increasing distance from the jump toe. The present sub-chapter presents the decay of the main air-water flow parameters including the void fraction, bubble count rate and interfacial velocity and the comparison with previous literature.

D.2. VOID FRACTION

Figure D-1 presents the void fraction distribution for fully and partially developed inflow conditions for $x/d_1 = 8$ and 20 and the comparison with previous studies (Wang 2014; Takahashi and Ohtsu 2017). Overall, the experiments of the present study presented good agreement with the experiments conducted by Wang (2014) in partially developed inflow conditions (PD) and the experiments with undeveloped (UD) and fully developed (FD) inflow conditions of Takahashi and Ohtsu (2017). Slight larger data scatter could be observed in previous studies due to the shorter sampling time of previous studies (45 s).

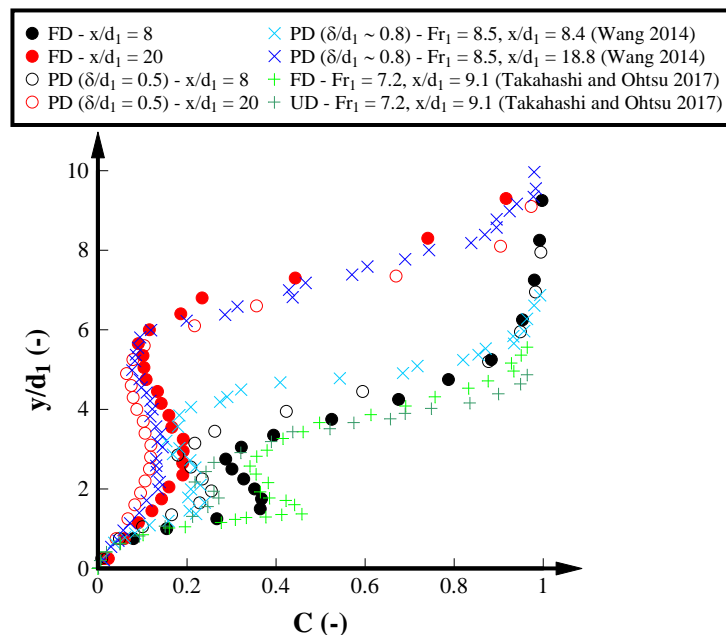


FIGURE D-1. VOID FRACTION DISTRIBUTION FOR EXPERIMENT E: $Fr_1 = 8.5$, $Re = 7.5 \times 10^4$ WITH FULLY (FD) AND PARTIALLY (PD) DEVELOPED INFLOW CONDITIONS; COMPARISON WITH THE EXPERIMENTS OF WANG (2014) AND TAKAHASHI AND OHTSU (2017) FOR SIMILAR FROUDE NUMBERS.

Figure D-2 presents the decay of C_{mean} as a function of x/d_1 for hydraulic jumps with fully and partially developed inflow conditions. Longer aeration was observed for experiments conducted with larger Froude numbers and no differences were observed between hydraulic jumps with different Reynolds numbers. The C_{mean} decay was compared with the experiments conducted by Wang (2014) and Chanson (2009b) with similar Froude and Reynolds numbers in hydraulic jumps with partially developed inflow conditions as well as with the empirical equation proposed by Wang (2014) for partially developed inflow conditions:

$$C_{mean} = 0.45 \times \exp\left(-\frac{1}{3.33 \times (Fr_1 - 1)} \times \frac{x}{d_1}\right) \quad (D.1) \text{ (Wang 2014)}$$

Overall, all previous experimental results were in agreement with the present study, although some deviations were identified from the empirical equation of Wang (2014) for larger Froude numbers.

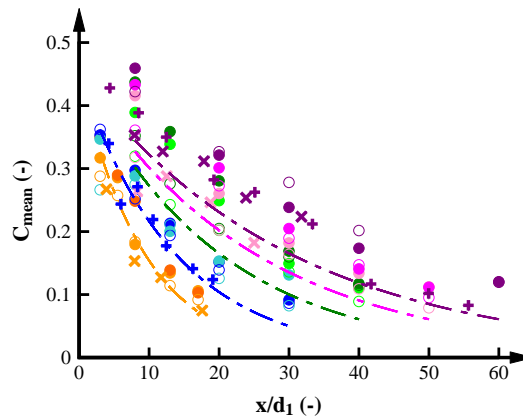
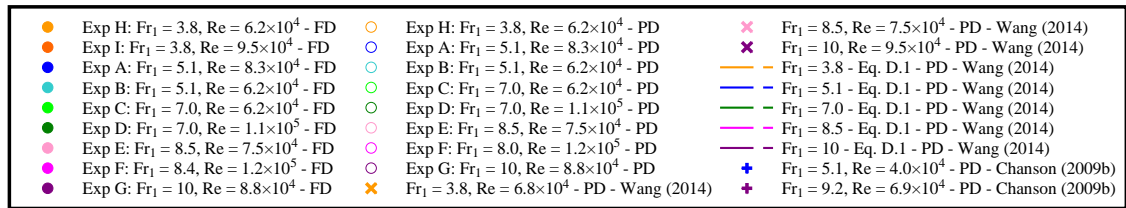


FIGURE D-2. C_{mean} AS FUNCTION OF x/d_1 FOR HYDRAULIC JUMPS WITH FULLY (FD) AND PARTIALLY (PD) DEVELOPED INFLOW CONDITIONS. COMPARISON WITH EXPERIMENTAL DATA FROM CHANSON (2009B) AND WANG (2014) AND EMPIRICAL EQUATION OF WANG (2014)

Figure D-3 presents the decay of C_{max} as a function of x/d_1 and a comparison with the experiments conducted by Wang (2014) and Takahashi and Ohtsu (2017). The experiments conducted with partially developed inflow conditions agreed with the experimental data of Wang (2014). Good agreement was also observed between the present study and the empirical equation proposed by Wang (2014) for $Fr_1 \leq 8.5$:

$$C_{max} = 0.5 \times \exp\left(-\frac{1}{1.8 \times (Fr_1 - 1)} \times \frac{x}{d_1}\right) \quad (D.2) \text{ (Wang 2014)}$$

Despite Takahashi and Ohtsu found larger C_{max} in fully developed hydraulic jumps in agreement with the findings of the present study, the maximum void fractions observed in their

study for fully and partially developed inflow conditions were consistently larger compared to the present study and the experiments conducted by Wang (2014). This difference may be linked with the smaller tip diameter used in their experiments, data processing techniques and smoother free-surface roughness upstream the hydraulic jumps while similar rough conditions and identical data processing were used between the experiments of Wang (2014) and the present study.

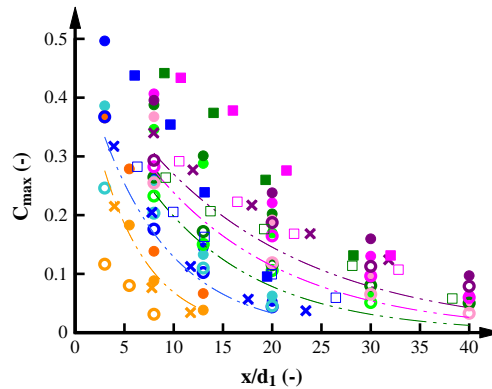
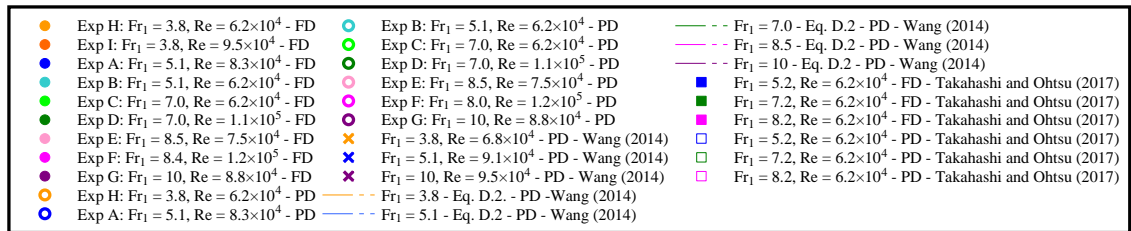


FIGURE D-3. C_{max} DECAY FOR FULLY (FD) AND PARTIALLY (PD) DEVELOPED INFLOW CONDITIONS. COMPARISON WITH EXPERIMENTAL DATA FROM WANG (2014) AND TAKAHASHI AND OHTSU (2017).

Figure D-4 presents the decays in C_{min} as a function of x/d_1 and a comparison with previous studies. Despite some data scatter, the decay in C_{min} was similar for hydraulic jumps with similar Froude numbers and significant larger C_{min} were observed for hydraulic jumps with fully developed inflow conditions. The values of C_{min} were in agreement with the experiments conducted by Chachereau and Chanson (2010) and Wang (2014) for hydraulic jumps with partially developed inflow conditions and similar Froude numbers.

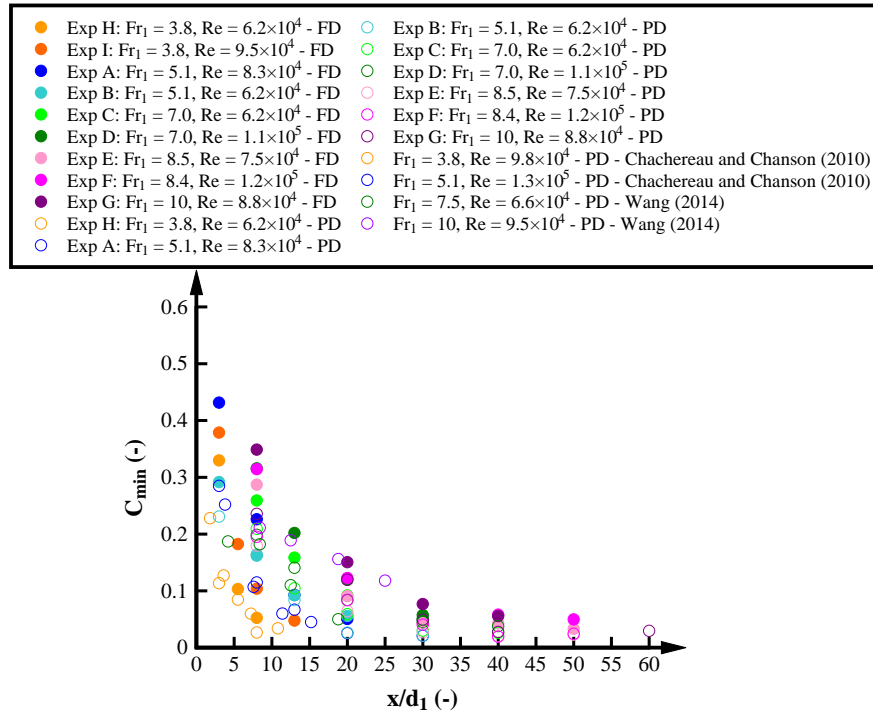


FIGURE D-4. C_{min} DECAY FOR FULLY (FD) AND PARTIALLY (PD) DEVELOPED INFLOW CONDITIONS. COMPARISON WITH EXPERIMENTAL DATA FROM CHACHEREAU AND CHANSON (2010) AND WANG (2014)

D.3. BUBBLE COUNT RATE

Figure D-5 presents the distribution of the bubble count rate for fully and partially developed inflow conditions and the comparison with the experiment of Wang (2014) for similar inflow Froude numbers and slight lower Reynolds numbers. Overall, the distribution of the bubble count rate for fully and partially developed inflow conditions presented good agreement with the experiments of Wang (2014). Likewise, the bubble count rates measured by Wang (2014) were lower compared with the experiments conducted with fully developed inflow conditions in the present study and slightly larger compared with the partially developed. The larger bubble count rate in partially developed inflow conditions may be linked with the larger Reynolds numbers and slight larger boundary layer development ($\delta/d_1 \approx 0.65$).

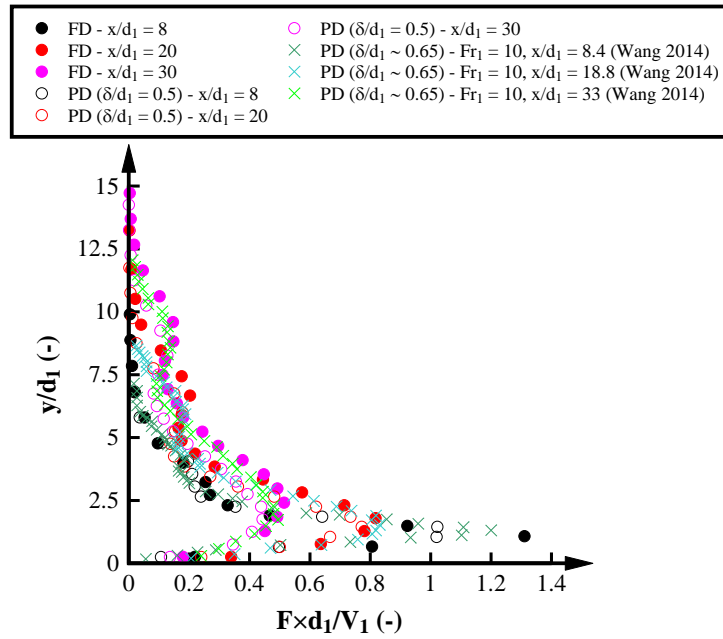


FIGURE D-5. BUBBLE COUNT RATE DISTRIBUTION FOR EXPERIMENT G: $Fr_1 = 10$, $Re = 8.8 \times 10^4$ AND HYDRAULIC JUMPS WITH FULLY (FD) AND PARTIALLY (PD) DEVELOPED INFLOW CONDITIONS; COMPARISON WITH THE EXPERIMENTS OF WANG (2014).

Figure D-6 presents the decay in the dimensionless maximum bubble count rate in the shear region $F_{maxSR} \times d_1 / V_1$ and the comparison with the experimental results of Chachereau and Chanson (2010) and Wang (2014) in partially developed inflow conditions. The decay in $F_{maxSR} \times d_1 / V_1$ for partially developed inflow conditions presented good agreement with previous studies and the experimental equation of Wang (2014):

$$\frac{F_{maxSR} \times d_1}{V_1} = \left(0.343 + 0.131 \times \frac{Re}{10^4} \right) \times \exp\left(-\frac{1}{2.67 \times (Fr_1 - 1)} \times \frac{x}{d_1} \right) \quad (D.3) \text{ (Wang 2014)}$$

In agreement with the study of Wang (2014), the maximum bubble count rate distribution in the shear region was dependent of the Froude and Reynolds numbers. Larger $F_{maxSR} \times d_1 / V_1$ were observed for larger Reynolds numbers linked with the larger turbulence levels and shear stress for larger Re . Hydraulic jumps with larger Froude and Reynolds numbers showed larger bubble count rate and remained a longer distance in the hydraulic jump.

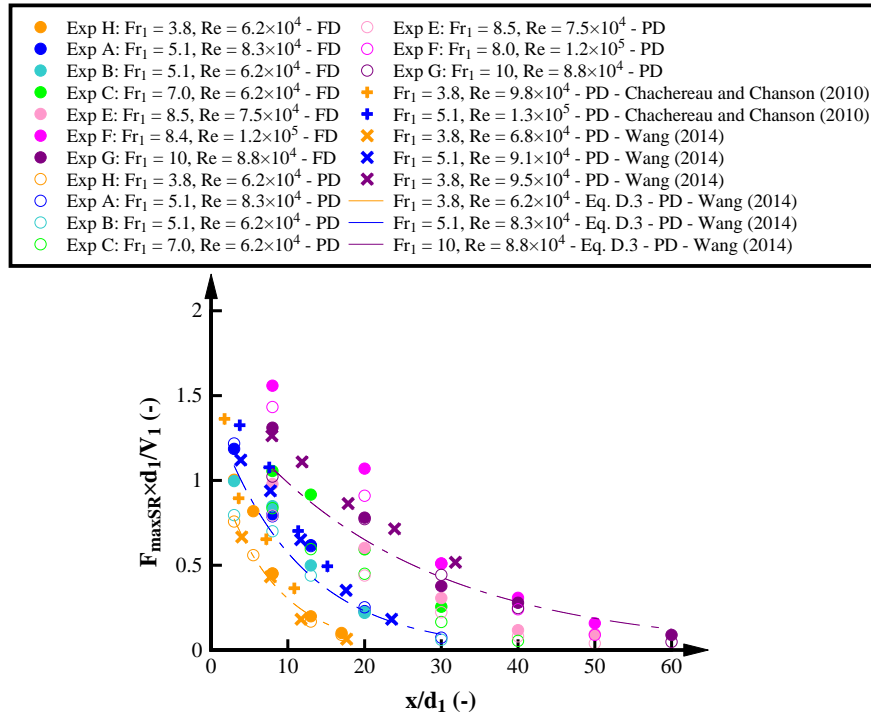


FIGURE D-6. F_{maxSR} AS FUNCTION OF x/d_I AND HYDRAULIC JUMPS WITH FULLY (FD) AND PARTIALLY (PD) DEVELOPED INFLOW CONDITIONS. COMPARISON WITH EXPERIMENTAL DATA FROM CHACHEREAU AND CHANSON (2010) AND WANG (2014) AND EMPIRICAL EQUATION OF WANG (2014)

D.4. INTERFACIAL VELOCITY

Figure D-7 illustrates the decay in V_{max} with increasing the distance from the jump toe. The decay in V_{max} showed good agreement with previous experiments conducted by Chanson (2009b) and Wang (2014) (Figure D-7). Despite some data scatter, especially at regions located close to the jump toe, the experimental data agreed with the empirical equation provided by Chanson (2009b):

$$\frac{V_{max}}{v_1} = \exp(-0.028 \times \frac{x}{d_1}) \quad (D.4) \text{ (Chanson 2009b)}$$

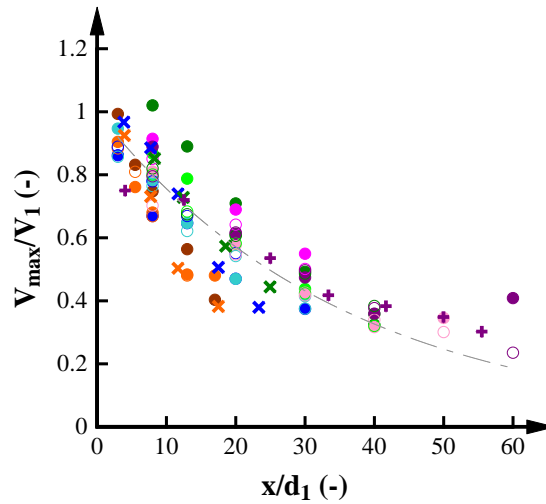
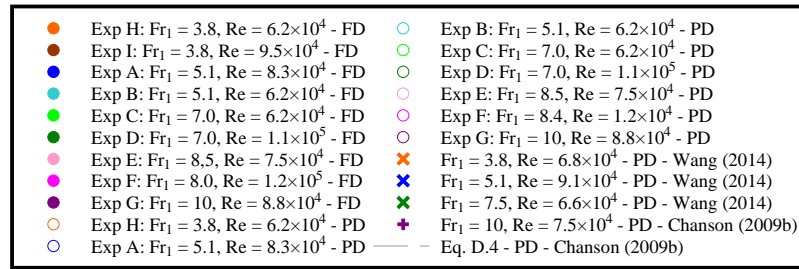


FIGURE D-7. V_{max}/V_1 AS FUNCTION OF x/d_1 FOR HYDRAULIC JUMPS WITH FULLY (FD) AND PARTIALLY (PD) DEVELOPED INFLOW CONDITIONS. COMPARISON WITH EXPERIMENTAL DATA FROM CHANSON (2009B) AND WANG (2014) AND EMPIRICAL EQUATION OF CHANSON (2009B).

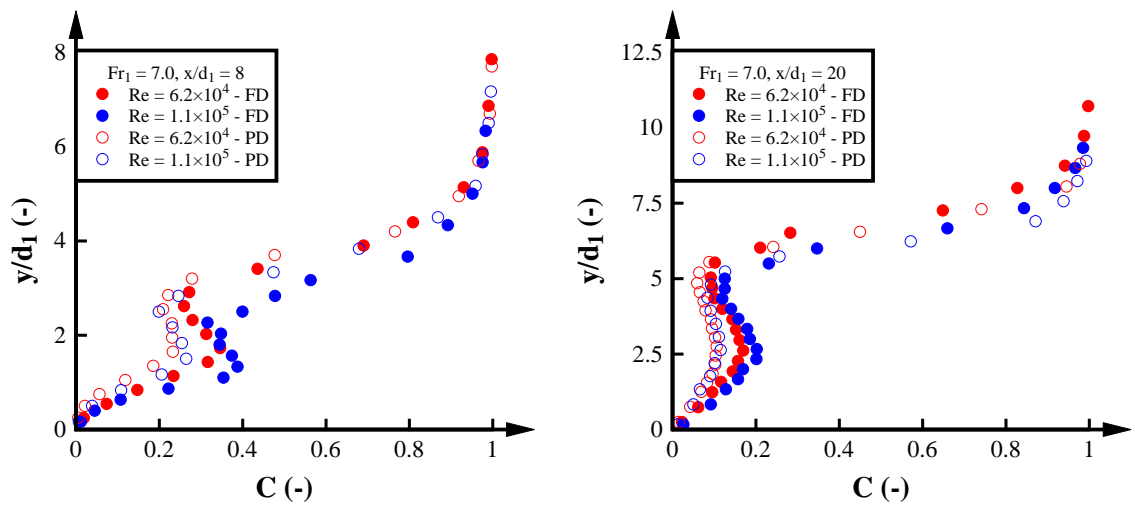
E. AIR-WATER FLOW PARAMETERS: SCALE EFFECTS

E.1. INTRODUCTION

The analysis of hydraulic jumps in laboratory models is limited by scale effects. The present Chapter includes the analysis of scale effects in the air-water flow properties in the hydraulic jump considering hydraulic jumps with fully and partially developed inflow conditions. The analysis was based upon a Froude similitude.

E.2. VOID FRACTION

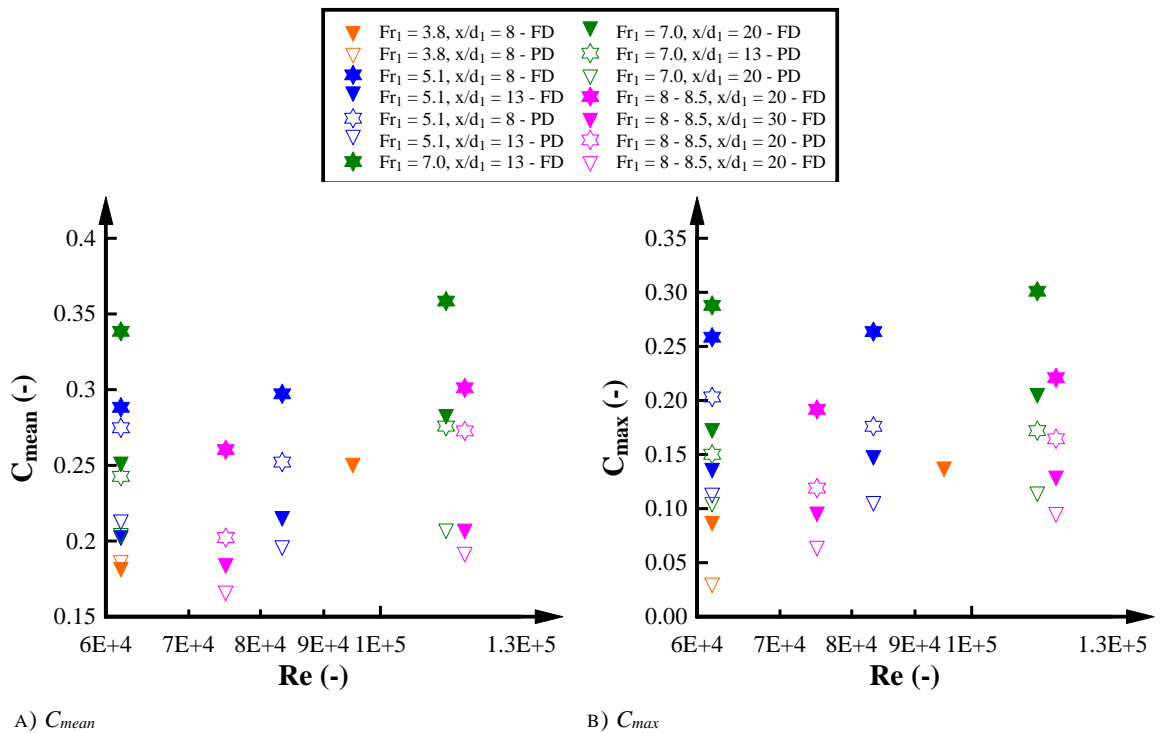
Figure E-1 presents the void fraction distribution for selected hydraulic jumps at two cross-sections. In solid symbols are included hydraulic jumps with fully developed inflow conditions while hollow symbols represent partially developed hydraulic jumps. Larger void fractions were consistently observed for hydraulic jumps with fully developed inflow conditions. However, for the same inflow condition and Froude number, the void fraction distribution showed no scale effects in terms of Froude similitude in agreement with previous studies in partially developed hydraulic jumps (Chanson and Chachereau 2013; Wang 2014). Figure E-2 presents the mean and maximum void fraction as a function of the Reynolds numbers for similar Froude numbers. Despite some data scatter, the void fraction parameters showed similar values at different Reynolds numbers suggesting no scale effects for the range of Reynolds numbers analysed ($6.2 \times 10^4 < Re < 1.2 \times 10^5$) for fully and partially developed inflow conditions.



A) $Fr_1 = 7.0, x/d_1 = 8$

B) $Fr_1 = 7.0, x/d_1 = 20$

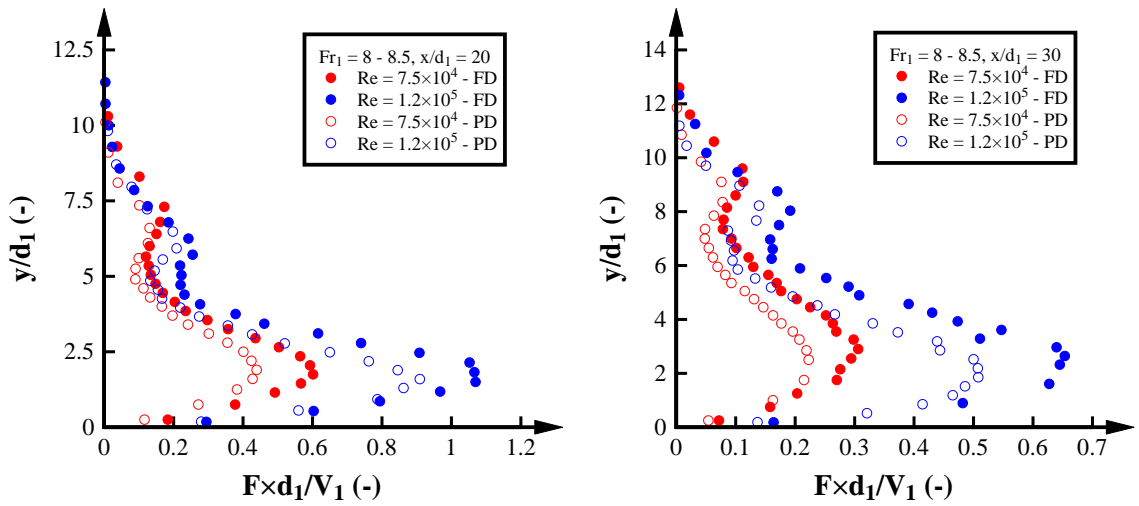
FIGURE E-1. COMPARATIVE ANALYSIS OF THE VOID FRACTION DISTRIBUTION BETWEEN HYDRAULIC JUMPS WITH FULLY (FD) AND PARTIALLY (PD) DEVELOPED INFLOW CONDITIONS UPON FROUDE SIMILITUDE.



A) C_{mean} B) C_{max}
FIGURE E-2. SCALE EFFECT COMPARISON IN THE VOID FRACTION PARAMETERS BETWEEN HYDRAULIC JUMPS WITH FULLY (FD) AND PARTIALLY (PD) DEVELOPED INFLOW CONDITIONS UPON FROUDE SIMILITUDE.

E.3. BUBBLE COUNT RATE

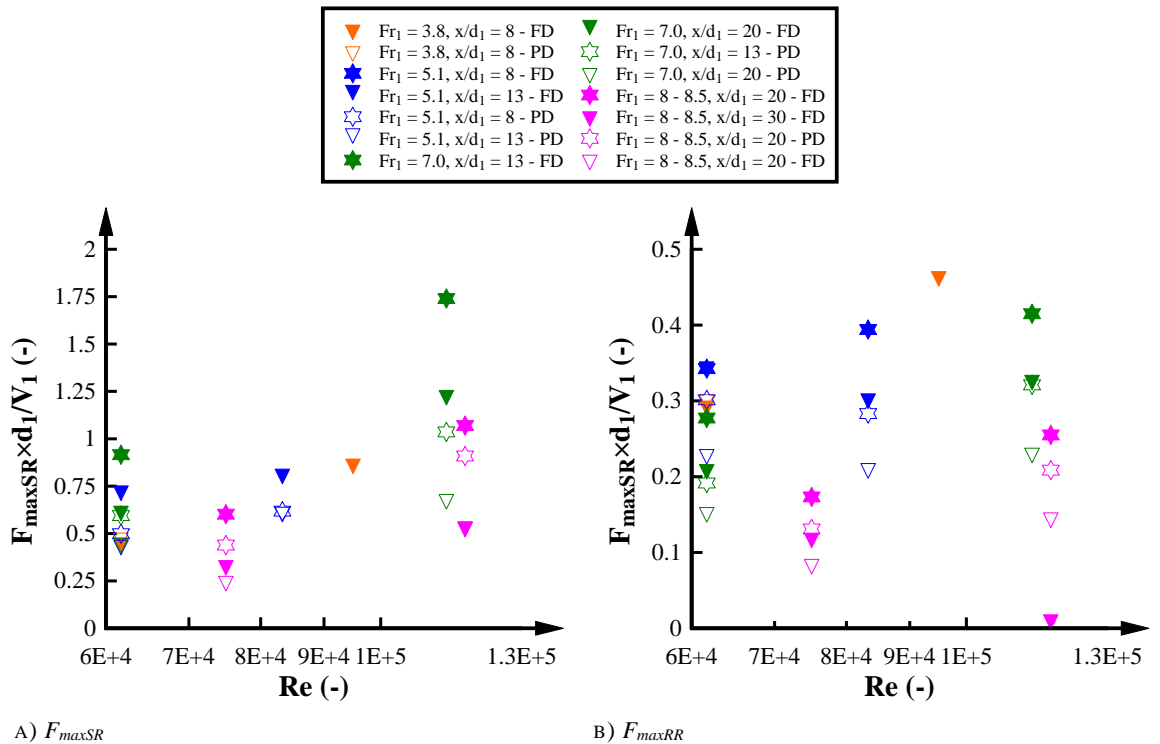
Figure E-3 presents the comparison in the bubble count rate distribution for selected hydraulic jumps at different cross-sections. Larger bubble count rates were observed for hydraulic jumps with fully developed inflow conditions indicating a larger number of bubbles when the boundary layer reaches the free-surface upstream the hydraulic jump. For similar Froude number, the bubble count rate in the shear and recirculation regions increased with the increase in the Reynolds numbers suggesting scale effects. The scaling was observed for hydraulic jumps with fully and partially developed inflow conditions. The results were also consistent with the increase in the bubble count rate parameters in the shear and recirculation regions with increasing Reynolds numbers (Figure E-4A and B) as well as with the scale effect analysis conducted under partially developed inflow conditions in previous studies (Murzyn and Chanson 2008; Chanson and Chachereau 2013; Wang 2014). Overall, scale effects were observed in the bubble count rate for hydraulic jumps with fully and partially developed inflow conditions.



A) $Fr_1 = 8 - 8.5, x/d_1 = 20$

B) $Fr_1 = 8 - 8.5, x/d_1 = 30$

FIGURE E-3. COMPARATIVE ANALYSIS OF THE BUBBLE COUNT RATE DISTRIBUTION BETWEEN HYDRAULIC JUMPS WITH FULLY (FD) AND PARTIALLY (PD) DEVELOPED INFLOW CONDITIONS UPON FROUDE SIMILITUDE.



A) F_{maxSR}

B) F_{maxRR}

FIGURE E-4. SCALE EFFECT COMPARISON IN THE BUBBLE COUNT RATE PARAMETERS BETWEEN HYDRAULIC JUMPS WITH FULLY (FD) AND PARTIALLY (PD) DEVELOPED INFLOW CONDITIONS UPON FROUDE SIMILITUDE.

E.4. INTERFACIAL VELOCITY

The interfacial velocity distribution was also analysed in terms of scale effects upon Froude similitude. Larger interfacial velocity distributions were consistently observed close to the jump toe for hydraulic jumps with fully developed inflow conditions. Apart from some data scatter in the shear region, slight larger interfacial velocities were observed for hydraulic jumps with larger Reynolds numbers close to the jump toe (Figure E-5). The differences were more obvious in hydraulic jumps with fully developed inflow conditions and larger Froude numbers. Nonetheless, the differences were not significant as observed in Figure E-6, where the

maximum interfacial velocity in the shear region V_{max} was almost constant with the increase in the Reynolds numbers. Further downstream, the interfacial velocity distribution showed no scale effects. In the recirculation region, the interfacial velocity distribution showed no differences with increasing Reynolds numbers suggesting no scale effects. The self-similarity observed in the velocity distribution was in agreement with the findings of Chanson and Chachereau (2013) and Wang (2014) in partially developed inflow conditions.

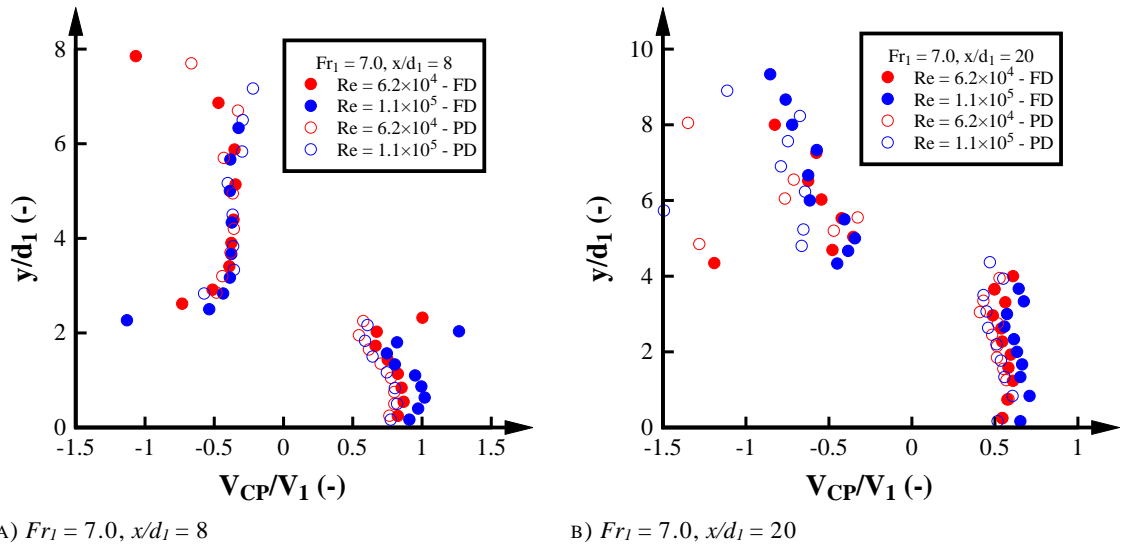


FIGURE E-5. COMPARATIVE ANALYSIS OF THE INTERFACIAL VELOCITY BETWEEN HYDRAULIC JUMPS WITH FULLY (FD) AND PARTIALLY (PD) DEVELOPED INFLOW CONDITIONS UPON FROUDE SIMILITUDE.

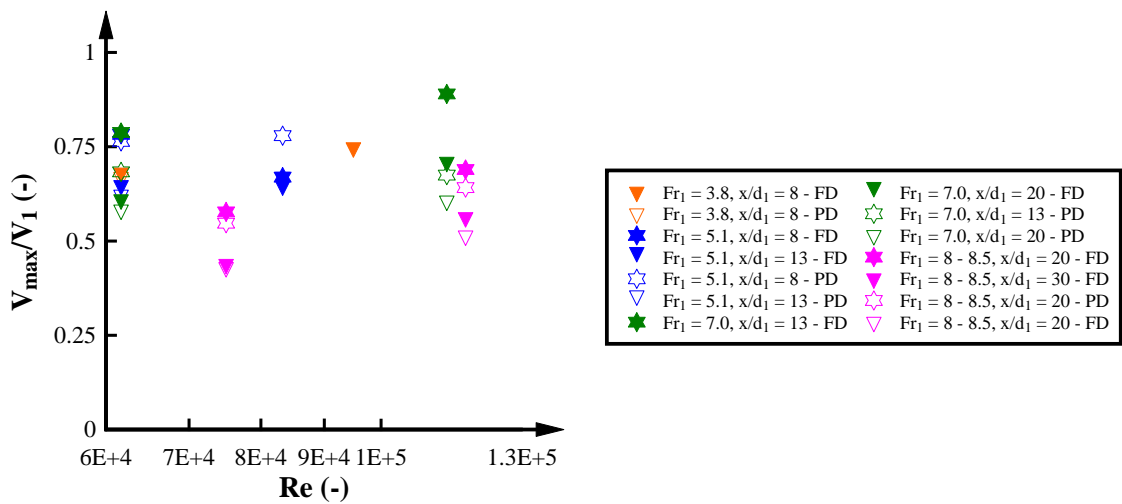
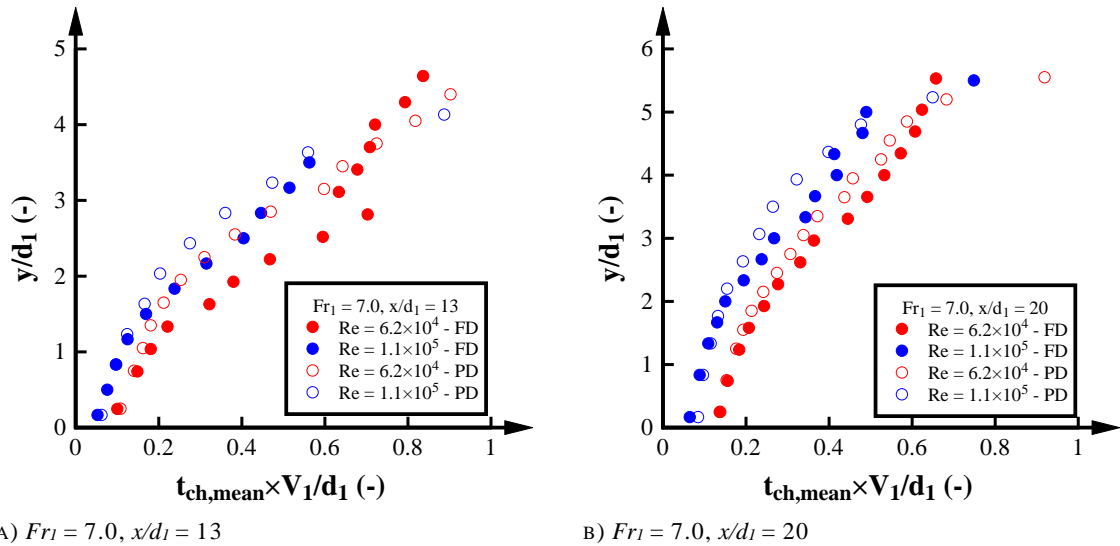


FIGURE E-6. SCALE EFFECT COMPARISON IN THE MAXIMUM INTERFACIAL VELOCITY BETWEEN HYDRAULIC JUMPS WITH FULLY (FD) AND PARTIALLY (PD) DEVELOPED INFLOW CONDITIONS UPON FROUDE SIMILITUDE.

E.5. CHORD TIME

The time-averaged chord time was also compared in terms of scale effects based upon Froude similitude. Figure E-7 presents the distribution of the chord time for similar Froude numbers at different locations along selected hydraulic jumps. Since the averaged chord time depends upon the void fraction and the bubble count rate, the chord time was subsequently affected by scale effects. For identical Froude numbers, larger mean chord times were observed for lower

Reynolds numbers. The results were observed for hydraulic jumps with fully and partially developed inflow conditions indicating scale effects independent of the inflow conditions and were consistent with the analysis of scale effects in partially developed inflow conditions (Chanson 2007a; Murzyn and Chanson 2008; Wang 2014).



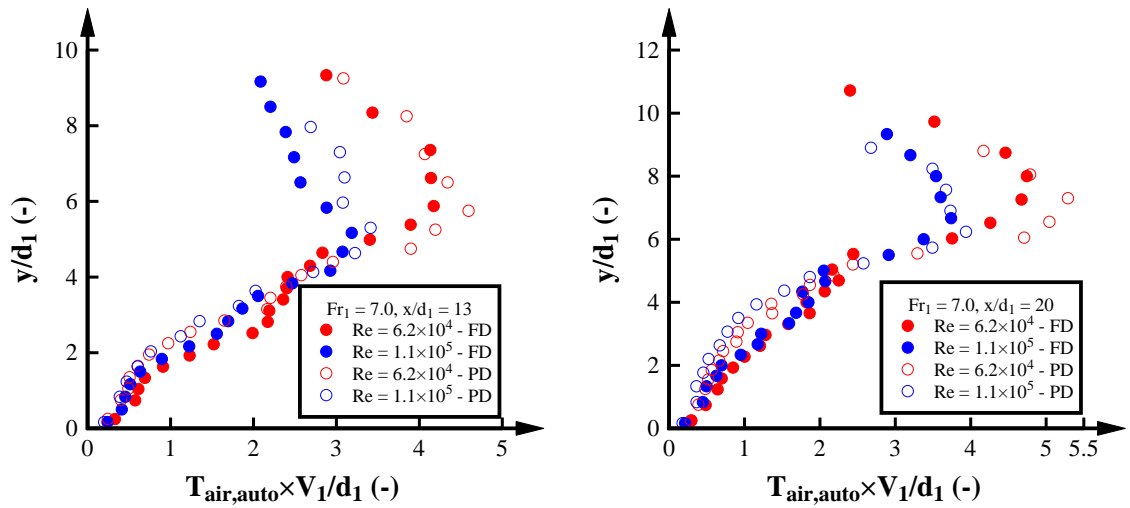
A) $Fr_1 = 7.0, x/d_1 = 13$

B) $Fr_1 = 7.0, x/d_1 = 20$

FIGURE E-7. COMPARATIVE ANALYSIS OF TIME-AVERAGED CHORD TIME BETWEEN HYDRAULIC JUMPS WITH FULLY (FD) AND PARTIALLY (PD) DEVELOPED INFLOW CONDITIONS UPON FROUDE SIMILITUDE.

E.6. AUTO- AND CROSS-CORRELATION TIME SCALES

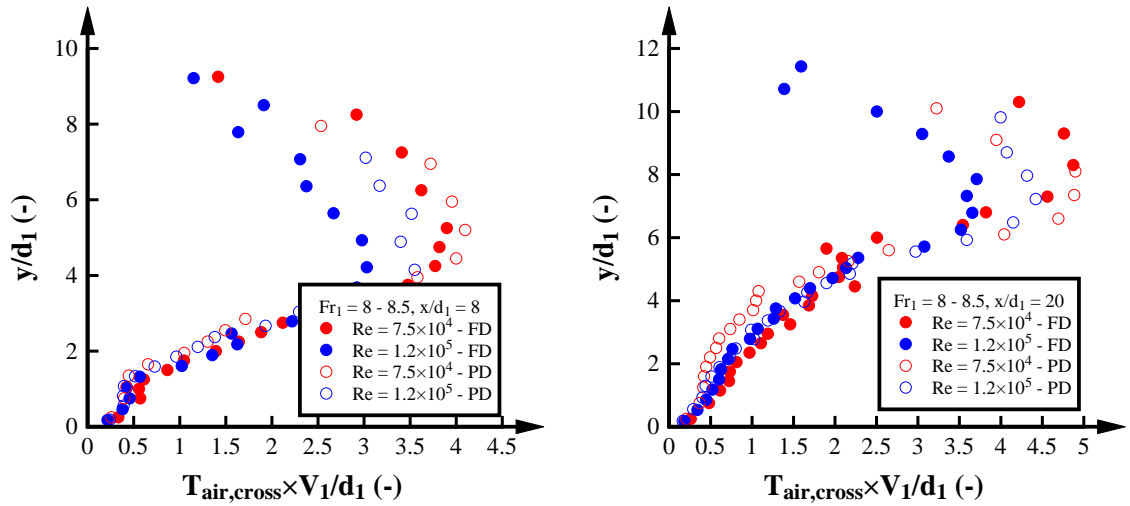
Scale effects were also evaluated in terms of the auto- and cross-correlation time scales. Figure E-8 and E-9 present the vertical distribution of the auto- and cross-correlation time scales respectively for hydraulic jumps with identical Froude numbers and different Reynolds numbers. For all the experiments, the correlation time scales showed a large increase in the recirculation region, highlighting similar flow patterns independent of the inflow conditions and the Froude or Reynolds numbers. With increasing the Reynolds numbers and under similar Froude numbers, the auto-correlation time scale in the recirculation region decreased (Figure E-8). Similar results were observed in terms of the cross-correlation time scales (Figure E-9). The results were consistently observed for all the experiments conducted suggesting scale effects in the auto- and cross-correlation time scales. The results were in agreement with the auto- and cross-correlation time scale analyses conducted in hydraulic jumps on channel bed with macroroughness (Felder and Chanson 2016a).



A) $Fr_1 = 7.0, x/d_1 = 13$

B) $Fr_1 = 7.0, x/d_1 = 20$

FIGURE E-8. COMPARATIVE ANALYSIS OF AUTO-CORRELATION TIME SCALE BETWEEN HYDRAULIC JUMPS WITH FULLY (FD) AND PARTIALLY (PD) DEVELOPED INFLOW CONDITIONS UPON FROUDE SIMILITUDE.



A) $Fr_1 = 8 - 8.5, x/d_1 = 8$

B) $Fr_1 = 8 - 8.5, x/d_1 = 20$

FIGURE E-9. COMPARATIVE ANALYSIS OF CROSS-CORRELATION TIME SCALE BETWEEN HYDRAULIC JUMPS WITH FULLY (FD) AND PARTIALLY (PD) DEVELOPED INFLOW CONDITIONS UPON FROUDE SIMILITUDE.

F. AIR-WATER FLOW PARAMETERS: HYDRAULIC JUMPS ON SLOPED CHANNELS

Some content of this chapter has been previously presented in the following publication:

Journal Publications

Montano, L., and Felder, S. 2019. ‘An experimental study of air-water flows in hydraulic jumps on flat slopes’, *Journal of Hydraulic Research* (in print, accepted for publication on 20/9/2019)

Conference Proceedings

Montano, L., and Felder, S 2017a, ‘Air-water flow properties in hydraulic jumps on a positive slope’, in *Proc., 37th IAHR World Congress*, Kuala Lumpur, Malaysia, 10 pages.

Montano, L., and Felder, S 2017b, ‘Measurements of air-water flow properties in hydraulic jumps in a sloping channel’, in *Proc., 13th Hydraulics in Water Engineering Conference*, Sydney, Australia, 9 pages.

F.1. INTRODUCTION

To date hydraulic jump research has mostly focused on Classical Hydraulic Jumps (CHJ) which are defined as hydraulic jumps in rectangular smooth horizontal channels (Rajaratnam 1967). Hydraulic jumps may however also occur in sloped channels, adverse channels, rough channels and in non-rectangular channels. Downstream of an inclined channel, the position of the hydraulic jump depends on the tailwater conditions and the jump toe may be on the horizontal channel downstream of the slope forming a CHJ; a special case is a Type A jump which occurs at the start of the horizontal channel (Bradley and Peterka 1957; Rajaratnam 1966). If the tailwater is sufficiently high, the hydraulic jump may occur on the slope forming a hydraulic jump Type B, C, D or E (Kindsvater 1944; Bradley and Peterka 1957; Rajaratnam 1966; Ohtsu and Yasuda 1991). These hydraulic jump types are defined depending upon the location of the jump toe and the end of the roller. Hydraulic jumps occurring partially in the horizontal section and partially in the sloped section are known as Type B jumps (Kindsvater 1944; Rajaratnam 1966; Bradley and Peterka 1957). If the end of the roller occurs at the end of the sloped section, the hydraulic jump is known as Type C jump (Kindsvater 1944; Rajaratnam 1966; Bradley and Peterka 1957). Type D and E jumps occur entirely on the sloped channel (Kindsvater 1944; Rajaratnam 1966; Bradley and Peterka 1957). Type E jumps occur in long, flat channels where the free-surface is parallel to the channel bed (Rajaratnam 1966, 1967). Figure F-1 illustrates the types of hydraulic jumps generated on sloped channels where d_1 is the inflow flow depth and d_2 the conjugate flow depth downstream the hydraulic jump.

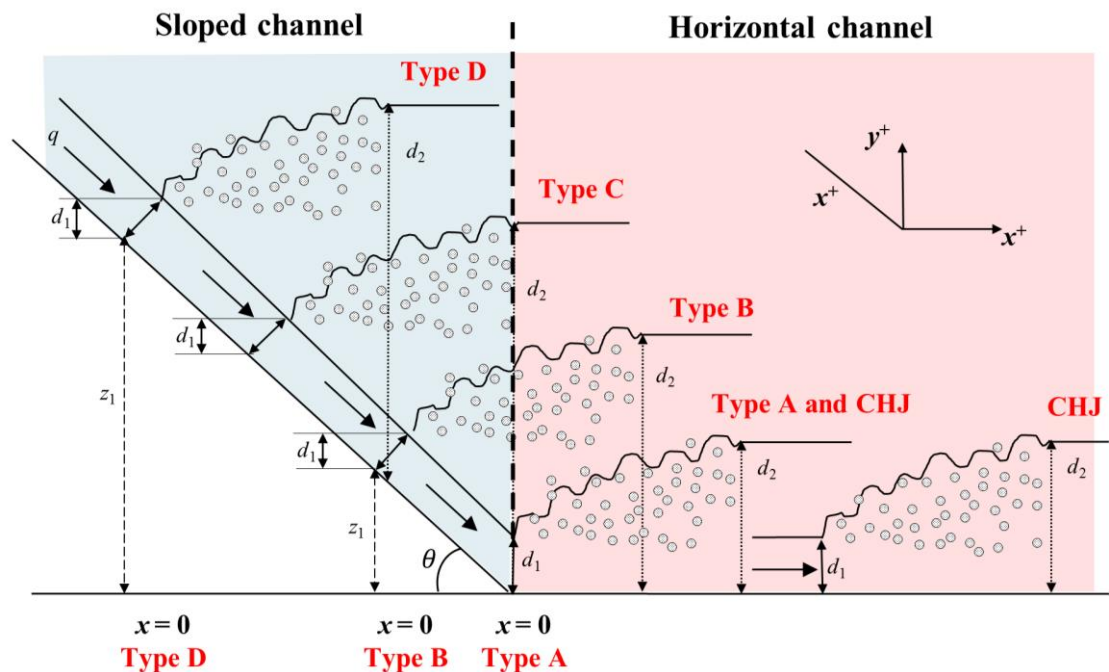
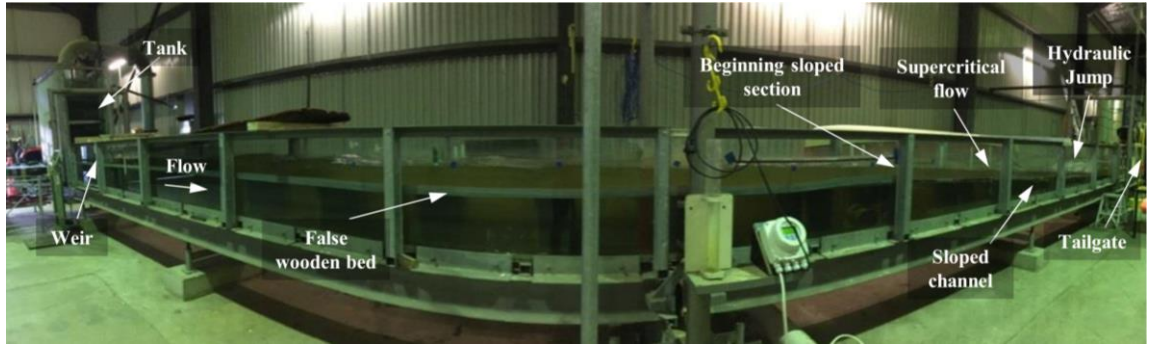


FIGURE F-1. DEFINITION SKETCH OF CLASSICAL HYDRAULIC JUMPS (CHJ) AND HYDRAULIC JUMPS ON SLOPED CHANNELS. THE CONJUGATE DEPTH d_1 AND d_2 ARE SHOWN AND THE ELEVATION OF THE JUMP TOE FROM THE HORIZONTAL BED z_1 IS PRESENTED WITH DASHED LINES.

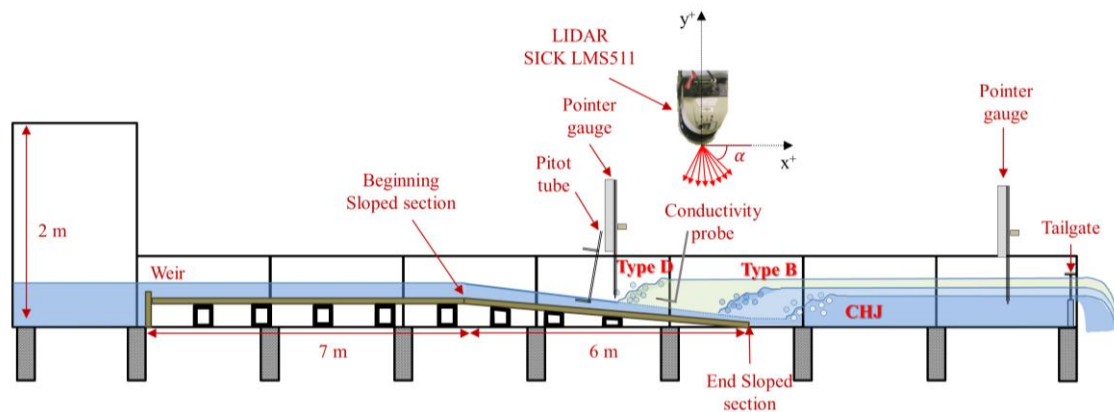
Past experiments in CHJs provided the conjugate depth relationships (e.g. Bélanger 1841; Bakhmeteff 1932; Hager and Bremen 1989), free-surface profiles and free-surface fluctuations (e.g. Hager 1993; Chachereau and Chanson 2011b; Wang and Chanson 2015), jump toe oscillations (e.g. Long et al. 1991; Mossa 1999; Mok 2004; Zhang et al. 2013; Wang and Chanson 2015), velocity distributions (e.g. Rajaratnam 1965; Hager and Bremen 1989; Wu and Rajaratnam 1995) and air-water flow properties (e.g. Resch and Leutheusser 1972a; Chanson and Brattberg 2000; Murzyn et al. 2005; Wang et al. 2014a). The latter one has been a key focus in recent decades documenting detailed air-water flow distributions in CHJs including void fractions, bubble count rate and interfacial velocities using conductivity probes (e.g. Chanson and Brattberg 2000; Chanson 2007b) and single tip fibre-optical probes (Murzyn et al. 2005; Zhang et al. 2014). For hydraulic jumps in sloped channels, experimental research has been limited to the conjugate depth relationship (e.g. Bakhmeteff and Matzke 1938; Kindsvater 1944; Bradley and Peterka 1957; Hager 1988), the energy dissipation efficiency (Hager 1988; Beirami and Chamani 2010), the roller length (Hager 1988; Ohtsu and Yasuda 1991) and the velocity distributions (Rajaratnam and Murahari 1974; Ohtsu and Yasuda 1990b; 1991; Gunal and Narayanan 1996). To date, no study has investigated the air-water flow properties in hydraulic jumps on sloped channels. Herein the present study investigated air-water flows in Type B and Type D jumps for three channel slopes $\theta = 1.25^\circ$, 2.5° and 5° providing novel information about the void fractions, bubble count rate, interfacial velocity, bubble chord sizes and turbulent scales.

F.2. EXPERIMENTAL CONFIGURATION

Experiments were undertaken at the UNSW Water Research Laboratory. Three sloped channels ($\theta = 1.25^\circ$, 2.5° and 5°) were tested in two flumes comprising a rectangular channel of width $W = 0.5$ m, 40 m length and 1 m height (Configuration I) and a channel with $W = 0.6$ m, 40 m length and 0.6 m height (Configuration II) (Figure F-2). Figure F-2A presents a skewed side view of the experimental setup of Configuration II for the analysis of hydraulic jumps on sloped channels. Figure F-2B shows a sketch of the experimental setup of Configuration II including the positioning of the hydraulic jumps and the instrumentation. The experimental setup was similar for Configuration I. The positive slopes of $\theta = 1.25^\circ$, 2.5° and 5° provided supercritical inflow conditions and the subcritical tail water was controlled by a weir at the downstream end of both flumes.



A) SKEWED SIDE VIEW. FLOW FROM LEFT TO RIGHT.



B) SKETCH OF THE EXPERIMENTAL SETUP (NOT TO SCALE)

FIGURE F-2. EXPERIMENTAL SETUP OF HYDRAULIC JUMPS ON A SLOPED CHANNEL – CONFIGURATION II.

Flows were provided directly from Manly Dam controlled with an ABB WaterMaster flow meter with $\pm 0.4\%$ accuracy. The conjugate depths d_1 and d_2 were measured with a pointer gauge within an accuracy of ± 0.5 mm. The velocities and the boundary layer properties upstream of the jump were measured with a pitot tube ($\varnothing = 3$ mm). Measurements of the air-water flow properties were conducted with a WRL double-tip conductivity probe with an inner electrode of $\varnothing = 0.125$ mm (Felder and Pfister 2017; Felder et al. 2019). The two probe tips were separated in streamwise direction by 5.01 mm and in transverse direction by 1.17 mm. Both tips were sampled simultaneously with 20 kHz and for 45 s as recommended by Felder and Chanson (2015). The air-water flow raw data were post-processed with the software of Felder (2018) providing a wide range of air-water flow properties. Continuous time-varying free-surface profiles in centre line were measured with a SICK LIDAR LMS511 with a sampling rate of 35 Hz and angular resolution of 0.25° for about 1 hour duration. Detailed information on the LIDAR setup and the post-processing can be found in Montano et al. (2018).

A total of 14 experimental flow conditions were investigated comprising CHJs, Type B and D jumps for a range of Froude numbers upstream of the hydraulic jump $1.8 < Fr_1 < 4.6$ and Reynolds numbers $5 \times 10^4 < Re < 4 \times 10^5$ (Table F-1). Comparative analyses of the hydraulic jumps were conducted for equal Froude or Reynolds numbers respectively. Note that d_1 was controlled by the sloped section upstream of the hydraulic jump limiting the range of Froude

and Reynolds numbers in the present study. Table F-1 summarises the experimental flow conditions including d_1 , θ , Fr_1 and Re , the flow rate per unit width q , and the hydraulic jump type.

TABLE F-1. FLOW CONDITIONS IN THE PRESENT STUDY

Config.	W (m)	θ (°)	Jump Type			q (m ² s ⁻¹)	d_1 (m)	Fr_1 (-)	Re (-)	Instruments					
			CHJ	B	D					PG	PT	CP	Lidar		
I	0.5	1.25	x			0.400	0.154	2.1	4.0×10 ⁵	x	x	x	x		
				x		0.400	0.152	2.1	4.0×10 ⁵	x	x	x			
					x	0.400	0.170	1.8	4.0×10 ⁵	x	x	x			
					x	0.230	0.115	1.9	2.4×10 ⁵	x	x	x			
II	0.6	2.5	x			0.113	0.046	3.6	1.1×10 ⁵	x	x	x	x		
				x		0.097	0.042	3.6	9.6×10 ⁴	x	x	x			
					x	0.113	0.049	3.3	1.1×10 ⁵	x	x	x			
					x	0.098	0.042	3.6	9.8×10 ⁴	x	x	x			
					x	0.113	0.052	3.0	1.1×10 ⁵	x	x	x			
			5	x			0.115	0.040	4.6	1.0×10 ⁵	x	x	x	x	
				x			0.084	0.032	4.7	8.4×10 ⁴	x	x	x	x	
					x			0.050	0.023	4.6	5.0×10 ⁴	x		x	
					x			0.115	0.047	3.6	1.2×10 ⁵	x	x	x	
					x			0.067	0.038	2.9	6.6×10 ⁴	x		x	
			x		0.115	0.058	2.6	1.1×10 ⁵	x	x	x				

F.3. FLOW PATTERNS

F.3.1. FLOW VISUALISATIONS

The comparison of flow visualisations was focussed on hydraulic jumps with similar Froude and Reynolds numbers. All hydraulic jump types showed typical features including the formation of a jump roller entraining air as well as free-surface and jump toe fluctuations. With increasing Fr_1 , the air entrainment and free-surface fluctuations increased as observed previously for CHJs (e.g. Chachereau and Chanson 2011b). These effects were more significant for CHJs and Type B jumps. These two jump types had visually similar aeration for all flow conditions in the present study while the Type D jump had lower aeration.

Figure F-3 shows typical photographs of the flow visualisations for the hydraulic jumps in the present study with similar Froude numbers. The CHJs and the Type B jump showed similar flow behaviour with strong air entrainment at the jump toe and free-surface disturbances (Figure F-3A and B). The flow features were consistent with observations of hydraulic jumps in previous studies for a similar range of Froude and Reynolds numbers (e.g. Hager 1989; Chachereau and Chanson 2011b). Larger oscillations and a slightly longer region of white water and turbulence were identified for the CHJ compared with the Type B jump (Figure F-3A and B). In contrast to the strong similarity between CHJ and Type B jump with similar Froude

numbers, Type D jump showed almost no air entrainment at the impingement point of the hydraulic jump and significant lower flow aeration (Figure F-3C). The free-surface oscillations and hydraulic jump toe fluctuations were also lower for the Type D jump. Overall, CHJs and Type B jumps presented similar flow instabilities and oscillations for all flow conditions, while the Type D jumps were less aerated and more stable. These observations were independent of the Froude and Reynolds numbers. The flow patterns were consistent for all flow conditions independent of Froude and Reynolds numbers and the upstream slope.

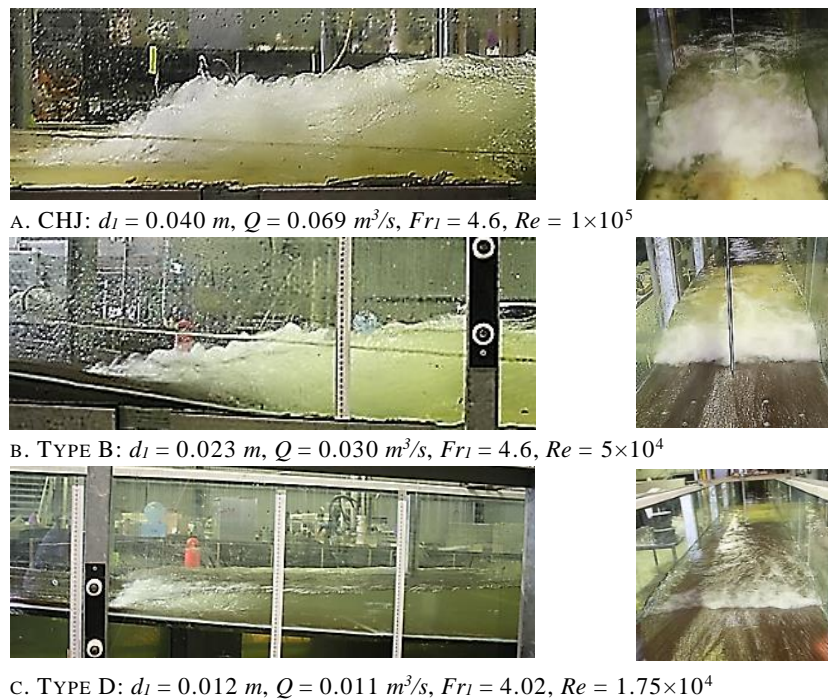


FIGURE F-3 –VISUAL OBSERVATION OF HYDRAULIC JUMPS IN SLOPED AND FLAT CHANNELS WITH SIMILAR FROUDE NUMBER. LEFT FIGURES REPRESENT THE HYDRAULIC JUMP PROFILE IN SIDE VIEW (FLOW FROM LEFT TO RIGHT) AND RIGHT FIGURES SHOW THE JUMP TOE BEHAVIOUR (FLOW FROM BOTTOM TO TOP).

F.3.2. CONJUGATE FLOW DEPTH

The conjugate depth relationship d_2/d_1 for all present configurations is shown in Figure F-3 as function of Fr_1 together with previous data on sloped channels. All present hydraulic jump types showed an increase in d_2/d_1 with increasing Fr_1 (Figure F-4). The hydraulic jumps on the slopes showed consistently larger conjugate depth ratios for the same Froude numbers (Type D > Type B > CHJ). For the mildest slope ($\theta = 1.25^\circ$), the differences in d_2/d_1 between the three hydraulic jump types were small while the differences increased with increasing slope. The present observations were consistent with observations by Bakhmeteff and Matzke (1938) and Bradley and Peterka (1957) for similar slopes. Large differences were observed with the data by Kawagoshi and Hager (1990) for Type B jumps on steeper slopes ($\theta = 30^\circ$ and 45°). The CHJ data were in good agreement with the Bélanger (1841) equation

$$\frac{d_2}{d_1} = \frac{1}{2} [(1 + 8 \times Fr_1^2)^{0.5} - 1] \quad (F.1)$$

Kawagoshi and Hager (1990) proposed an empirical equation for conjugate depths for Type B jumps for $Fr_1 < 10$, $\theta = 30^\circ$ and $0.1 < (d_2 - z_1)/d_2 < 1$:

$$\frac{d_2}{d_1} = \left[3.75 \times \left(\frac{d_2 - z_1}{d_2} \right)^{-0.575} \right] + \frac{\sqrt{2} \times (Fr_1 - 3)}{\tanh \left[3.5 \times \left(\frac{d_2 - z_1}{d_2} \right) \right]} \quad (F.2)$$

where z_1 is the vertical distance from the horizontal channel bed to the jump toe (Figure F-1). For all channel slopes, the present Type B jumps compared well with Equation F.2 with differences $< 8\%$ (Figure F-4).

Rajaratnam (1966) proposed a conjugate depth equation for Type D jumps based upon the experiments of Kindsvater (1944) and Bradley and Peterka (1957) considering $3^\circ < \theta < 15^\circ$ and $2 < Fr_1 < 18$:

$$\frac{d_2}{d_1} = \frac{1}{2} \left\{ \left[1 + 8 \times (10^{0.027\theta})^2 \times Fr_1^2 \right]^{0.5} - 1 \right\} \quad (F.3)$$

The present data for Type D jumps matched Equation F.3 well with differences $< 10\%$ (Figure F-4).

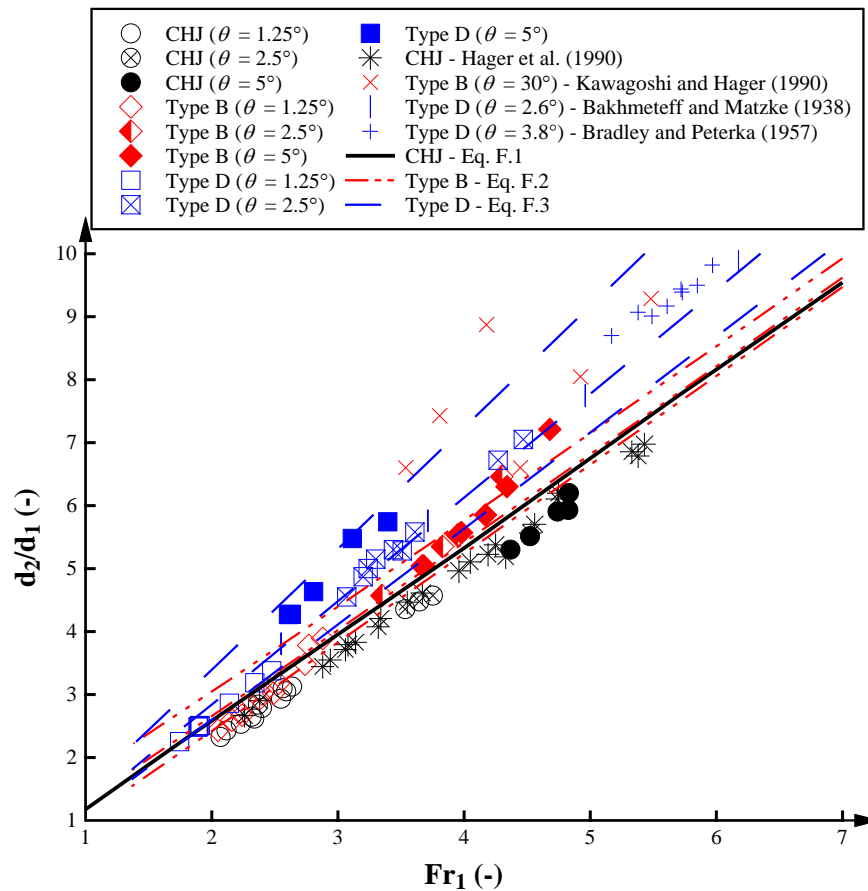


FIGURE F-4 - CONJUGATE DEPTH RELATIONSHIPS FOR HYDRAULIC JUMPS IN THE PRESENT STUDY; COMPARISON WITH PREVIOUS EXPERIMENTAL DATA AND EMPIRICAL EQUATIONS

F.3.3. ENERGY DISSIPATION EFFICIENCY OF HYDRAULIC JUMPS ON SLOPES

In hydraulic jumps on sloped channels, the energy dissipation efficiency $\eta = (H_1 - H_2)/H_1$ is

based upon differences in total head upstream H_1 and downstream H_2 of the hydraulic jump (Hager 1988). Figure F-5 shows the efficiency for the present data and a comparison with previous data for CHJs (Hager et al. 1990; Bradley and Peterka 1957) and for Type B jumps (Hager 1988; Beirami and Chamani 2010). For all hydraulic jumps, η increased with increasing Fr_1 . The efficiencies for CHJs and Type B jumps were similar in particular for larger Froude numbers suggesting little difference in energy dissipation. This observation was consistent with the visual observation of similar flow aeration. The efficiencies of CHJs and Type B jumps compared well with the Belanger equation (Equation F.1). Type D jumps were less efficient with 20% lower efficiency compared to CHJs (Figure F-5). Type D jump efficiencies compared well with the semi-theoretical approach of Palermo and Pagliara (2018) for hydraulic jumps in sloped channels (Figure F-5).

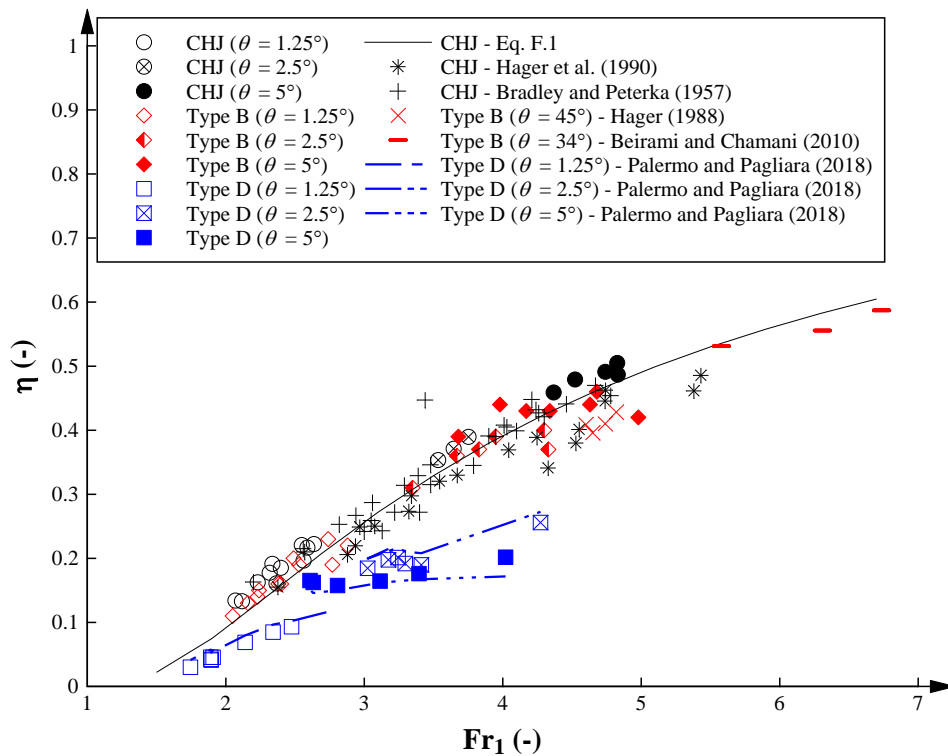


FIGURE F-5 - ENERGY DISSIPATION EFFICIENCY FOR HYDRAULIC JUMPS IN THE PRESENT STUDY; COMPARISON WITH PREVIOUS EXPERIMENTAL DATA, BÉLANGER EQUATION (EQUATION F.1) AND SEMI-EMPIRICAL APPROACH BY PALERMO AND PAGLIARA (2018)

F.3.4. FREE-SURFACE FLUCTUATIONS AND JUMP TOE OSCILLATIONS

Free-surface fluctuations and jump toe oscillations were measured with the LIDAR following the approach presented in Montano et al. (2018). Typical free-surface fluctuations d'/d_1 , where d' is the standard deviation of the free-surface elevations, are shown in Figure F-6 as function of the dimensionless distance from the jump toe x/d_1 . Independently of the hydraulic jump type, d'/d_1 increased close the mean jump toe position $x/d_1 = 0$ suggesting that the free-surface fluctuations were linked with the horizontal jump toe movements. While the CHJ had the largest fluctuations, the jumps on the slope showed lower small scale free-surface movements.. While

CHJs and Type B jumps had similar energy dissipation efficiencies, the differences in d'/d_1 suggested that the internal flow motions may have contributed more to the energy dissipation compared to the free-surface fluctuations.

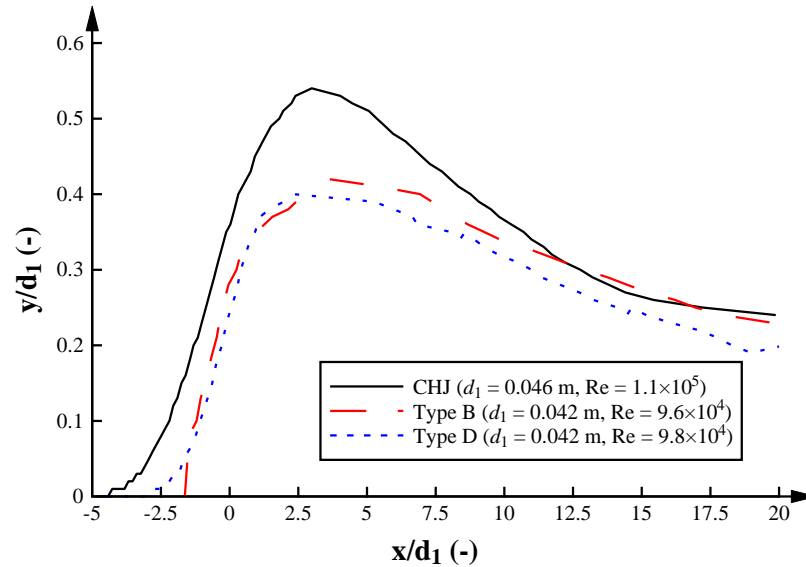
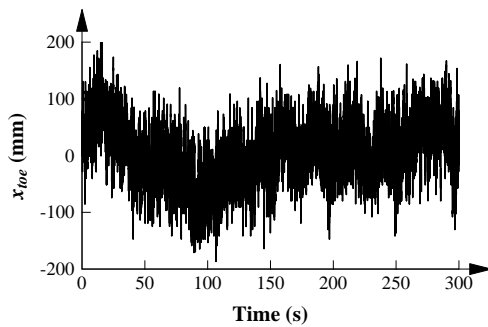
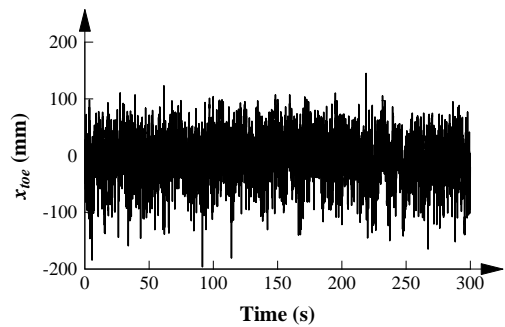


FIGURE F-6 - COMPARISON OF FREE-SURFACE FLUCTUATIONS FOR THE THREE JUMP TYPES: $\theta = 2.5^\circ$, $Fr_1 = 3.6$

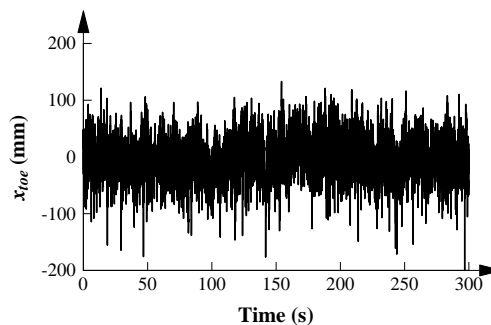
The jump toe oscillations were recorded with the LIDAR. Typical raw data of the jump toe positions x_{toe} are shown in Figure F-7 highlighting differences between CHJs and hydraulic jumps on the slope. While the data for CHJs showed large variations of x_{toe} and little uniformity in the signal, Type B and D jumps showed more uniform oscillations (Figure F-7). These results were consistent for all experiments suggesting increased stability for the jumps on the slope.



A) CHJ: $Re = 1.13 \times 10^5$



B) TYPE B: $Re = 1.16 \times 10^5$, $\theta = 5^\circ$



c) TYPE D: $Re = 9.8 \times 10^4$, $\theta = 2.5^\circ$

FIGURE F-7 - JUMP TOE OSCILLATIONS FOR DIFFERENT HYDRAULIC JUMP TYPES WITH $Fr_1 = 3.6$.

Figure F-8 illustrates the standard deviations of the jump toe oscillations x_{toe}'/d_1 as function of Fr_1 showing increasing standard deviations of the jump toe oscillations with increasing Fr_1 for all hydraulic jumps, which is consistent with observations on CHJs (Long et al. 1991; Wang 2014). For similar Froude numbers, CHJs showed consistently the largest standard deviations suggesting stronger longitudinal movements and less stability. Type B and D jumps showed similar oscillations (Figure F-8). The quantitative observations were in agreement with the visual observations indicating that the CHJ was the least stable jump type.

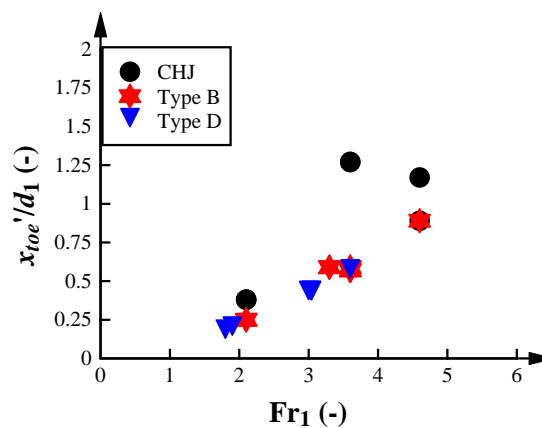


FIGURE F-8 - DIMENSIONLESS STANDARD DEVIATION OF THE JUMP TOE OSCILLATIONS AS FUNCTION OF THE INFLOW FROUDE NUMBER FOR THE THREE JUMP TYPES

F.4. VOID FRACTION

Figure F-9 shows typical void fraction C distributions for the three jump types as a function of the dimensionless elevation above the bed d/d_1 . Independent of hydraulic jump type and slope, all void fraction distributions showed typical shapes reflecting the shear region and the upper recirculation region as shown in Figure F-9. While the distributions were overall similar, some distinctive differences between the three hydraulic jump types were identified (Figure F-9). The largest void fractions were consistently observed for CHJ and Type B jumps with slightly larger air entrainment for CHJs. Both jump types had a peak in the shear region, while Type B jumps had lower void fraction in the recirculation region at the downstream end of the roller due to the larger flow depth (Figure F-9). Type D jumps had substantially lower void fractions with the largest difference in the shear region where no distinctive peak in maximum void fraction in the shear region C_{max} was observed in the second half of the jump. The close agreement between CHJs and Type B jumps highlighted similar aeration performances while the differences with Type D jumps indicated a reduction in flow aeration and an upwards shift of the jump roller. The differences in void fraction between CHJs and Type D jumps increased with increasing slope. Independent of the hydraulic jump type, all void fraction distributions were well

correlated with the advective diffusion equation.

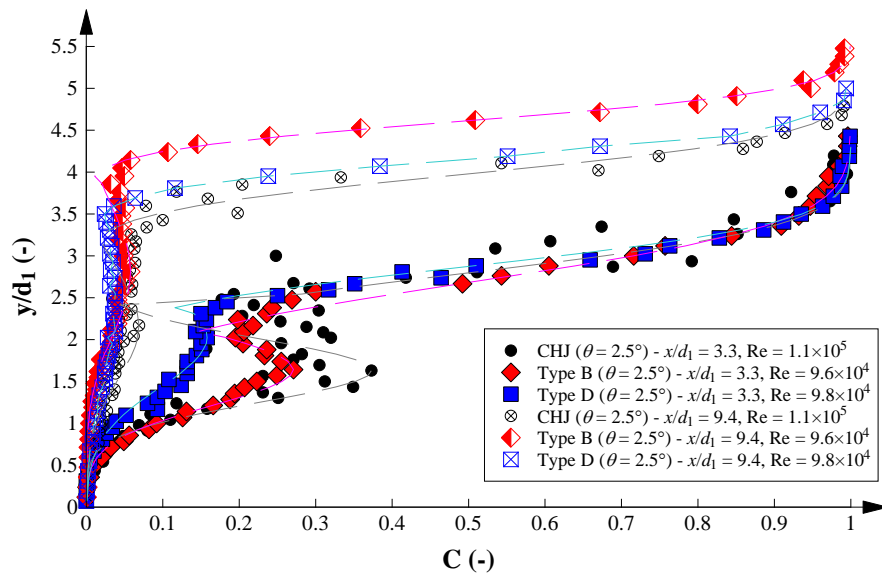
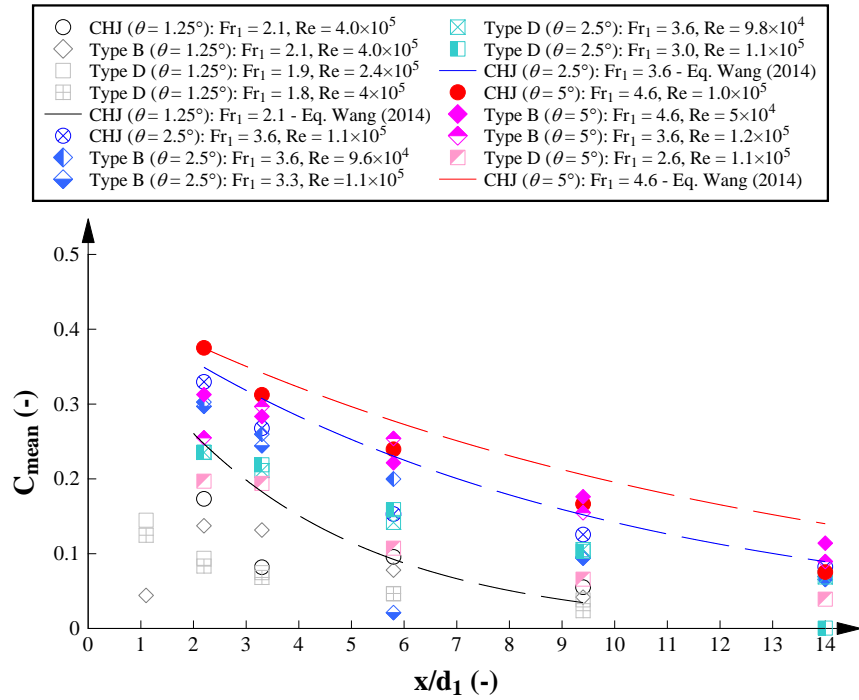
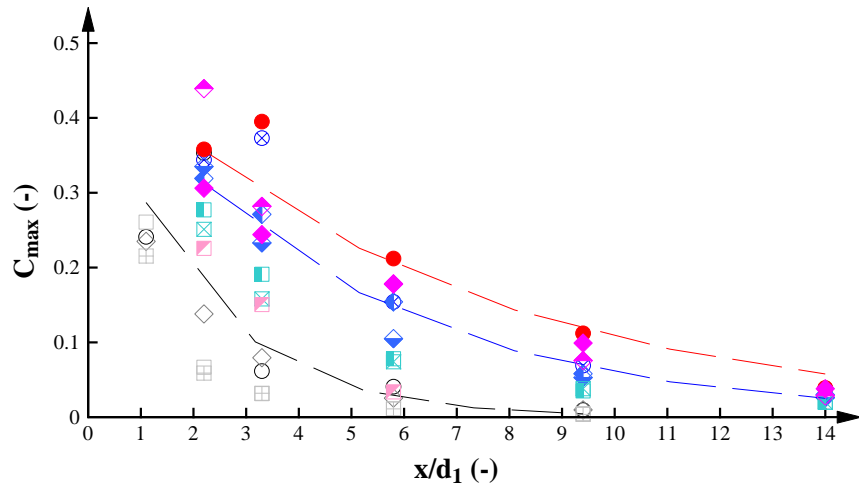


FIGURE F-9 –COMPARISON OF VOID FRACTION DISTRIBUTIONS: $\theta = 2.5^\circ$, $Fr_1 = 3.6$. DOTTED LINE REPRESENTS THE COMPARISON WITH THE ADVECTIVE DIFFUSION EQUATION FOR AIR BUBBLES IN HYDRAULIC JUMPS.

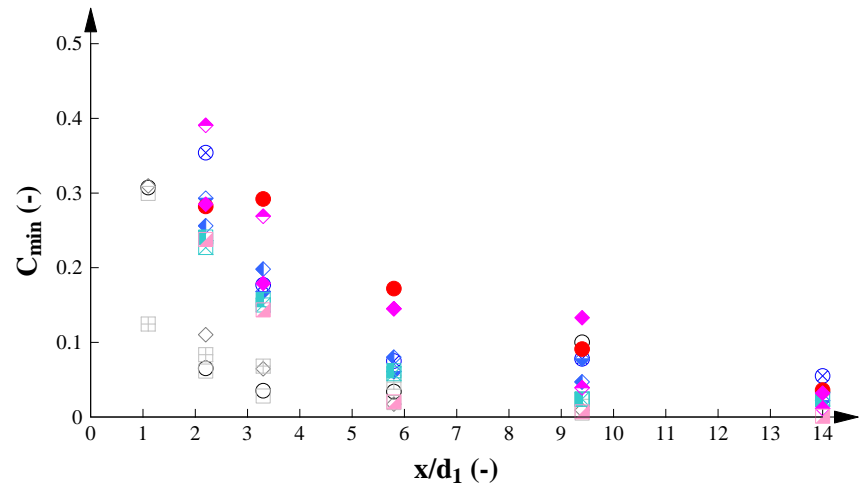
Figure F-10 shows a comparison of C_{mean} , C_{max} , C_{min} for the three jump types for identical Froude and Reynolds numbers as a function of x/d_1 . All the void fraction parameters decreased with increasing distance from the jump toe. C_{mean} , C_{max} , C_{min} values of CHJs and Type B jumps were similar for slopes of $\theta = 1.25^\circ$ and 2.5° while for $\theta = 5^\circ$, the CHJ had slightly larger values. Distinctively lower C_{mean} , C_{max} , C_{min} values were observed for Type D jumps confirming lower aeration. The data were also compared with the empirical equations by Wang (2014) for CHJs with partially developed inflow conditions. C_{mean} values were slightly lower compared with the empirical equation provided by Wang (2014) maybe related to smoother flows for hydraulic jumps downstream of the sloped section. The C_{max} data showed reasonable agreement with CHJs and Type B jumps (Figure F-10).



A) C_{mean} , COMPARISON EMPIRICAL EQUATION OF WANG (2014)



B) C_{max} , COMPARISON EMPIRICAL EQUATION OF WANG (2014)



C) C_{min}

FIGURE F-10 –COMPARISON OF MAXIMUM VOID FRACTIONS IN THE SHEAR REGION WITH SIMILAR FROUDE NUMBERS; COMPARISON WITH THE EMPIRICAL DECAY IN C_{mean} AND C_{max} FOR CHJs (WANG 2014).

F.5. BUBBLE COUNT RATE

Figure F-11 shows typical dimensionless bubble count rates $F \times d_1 / V_1$ as a function of d/d_1 . The bubble count rate distributions for CHJs and Type B jumps were almost identical apart from small differences in the recirculation region linked with the increase in flow depth for Type B jumps. Type D jumps showed significantly smaller numbers of entrained bubbles, i.e. a 50% reduction compared to CHJs (Figure F-11). Close to the jump toe, $x/d_1 \leq 2.2$, a peak in maximum bubble count rate in the shear region F_{max} was identified for all hydraulic jumps. Further downstream $x/d_1 > 3.3$, F_{max} was distinctive for CHJs, and Type B jumps, while for Type D jumps the peak in bubble count rate shifted into the recirculation region suggesting a shorter vortex region which was in agreement with visual observations and a reduction in energy dissipation efficiency. Differences in bubble count rate between the three jump types increased with increasing channel slope.

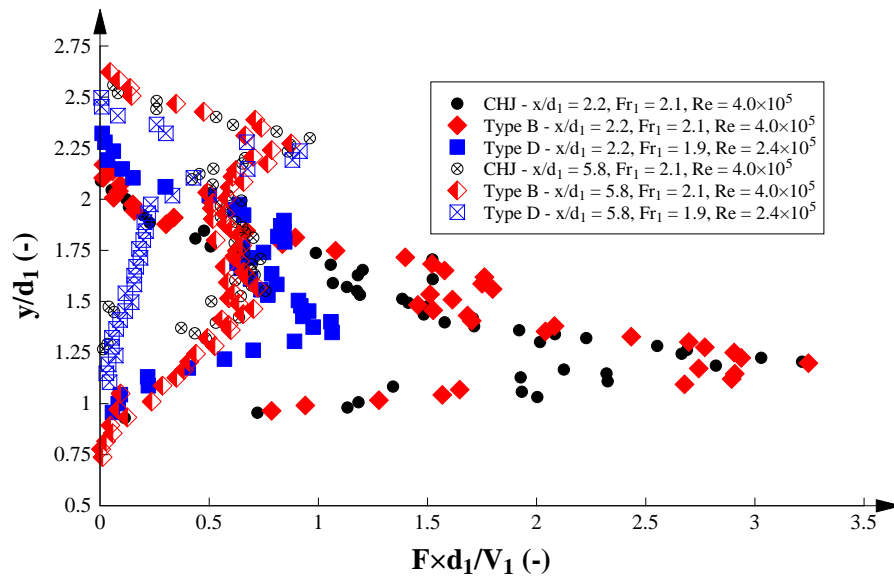
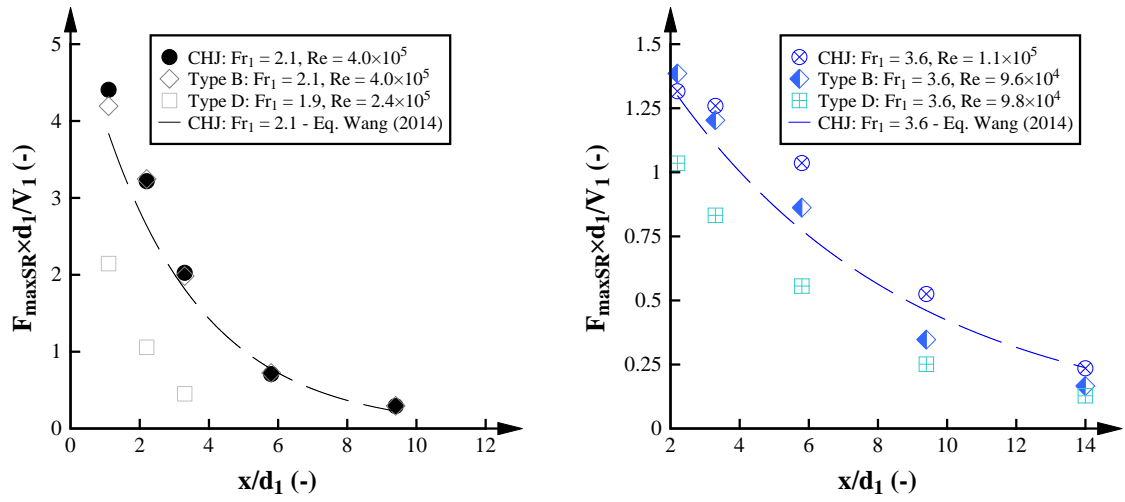


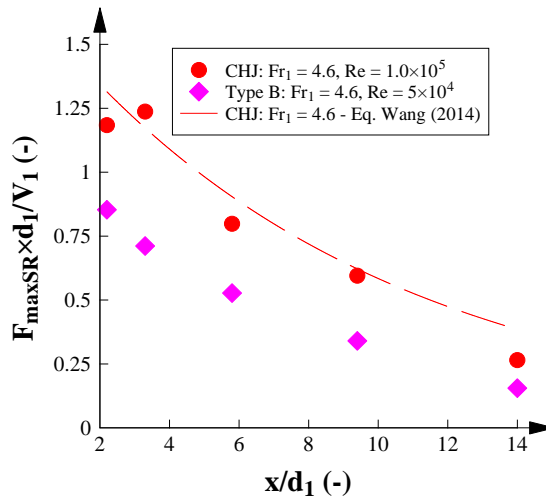
FIGURE F-11 –COMPARISON OF BUBBLE COUNT RATE DISTRIBUTIONS: $\theta = 1.25^\circ$.

Figure F-12 shows the maximum dimensionless bubble count rate in the shear region $F_{maxSR} \times d_1 / V_1$ as a function of x/d_1 . For the same Fr_1 and for CHJs and Type B jumps, $F_{maxSR} \times d_1 / V_1$ was similar for $\theta = 1.25^\circ$ while increasing differences were observed with increasing slope (Figure F-12). Type D jumps showed consistently lower values of $F_{maxSR} \times d_1 / V_1$ suggesting lower air-water interactions for this type of jump with differences above 40% respect to the CHJ. The present data were also compared with an empirical equation for CHJs by Wang (2014) showing good agreement for the CHJ data (Figure F-12).



A) $\theta = 1.25^\circ$

B) $\theta = 2.5^\circ$



C) $\theta = 5^\circ$

FIGURE F-12 –COMPARISON OF MAXIMUM BUBBLE COUNT IN THE SHEAR REGION FOR SIMILAR FROUDE NUMBERS, COMPARISON WITH EMPIRICAL DECAY IN F_{maxSR} FOR CHJs BY WANG (2014).

The decay in the dimensionless maximum bubble count rate distribution in the recirculation region $F_{maxRR} \times d_1 / V_1$ is presented in Figure F-13. In agreement with the bubble count rate in the shear region, stronger similarities were observed between CHJs and Type B jumps for $\theta \leq 2.5^\circ$. For $\theta = 5^\circ$, $F_{maxRR} \times d_1 / V_1$ in CHJs was more than 20% larger close to the jump toe. Type D jump showed consistently lower $F_{maxRR} \times d_1 / V_1$ values for the different slopes analysed highlighting the lesser air entrainment and number of bubbles for hydraulic jumps occurring entirely in the slope. The CHJ data was also compared with the empirical equation proposed by Wang (2014) in the recirculation region. The equation fitted well with the CHJ values for $\theta \leq 2.5^\circ$. Nonetheless, the empirical equation overestimated the $F_{maxRR} \times d_1 / V_1$ values for the slope of $\theta = 5^\circ$.

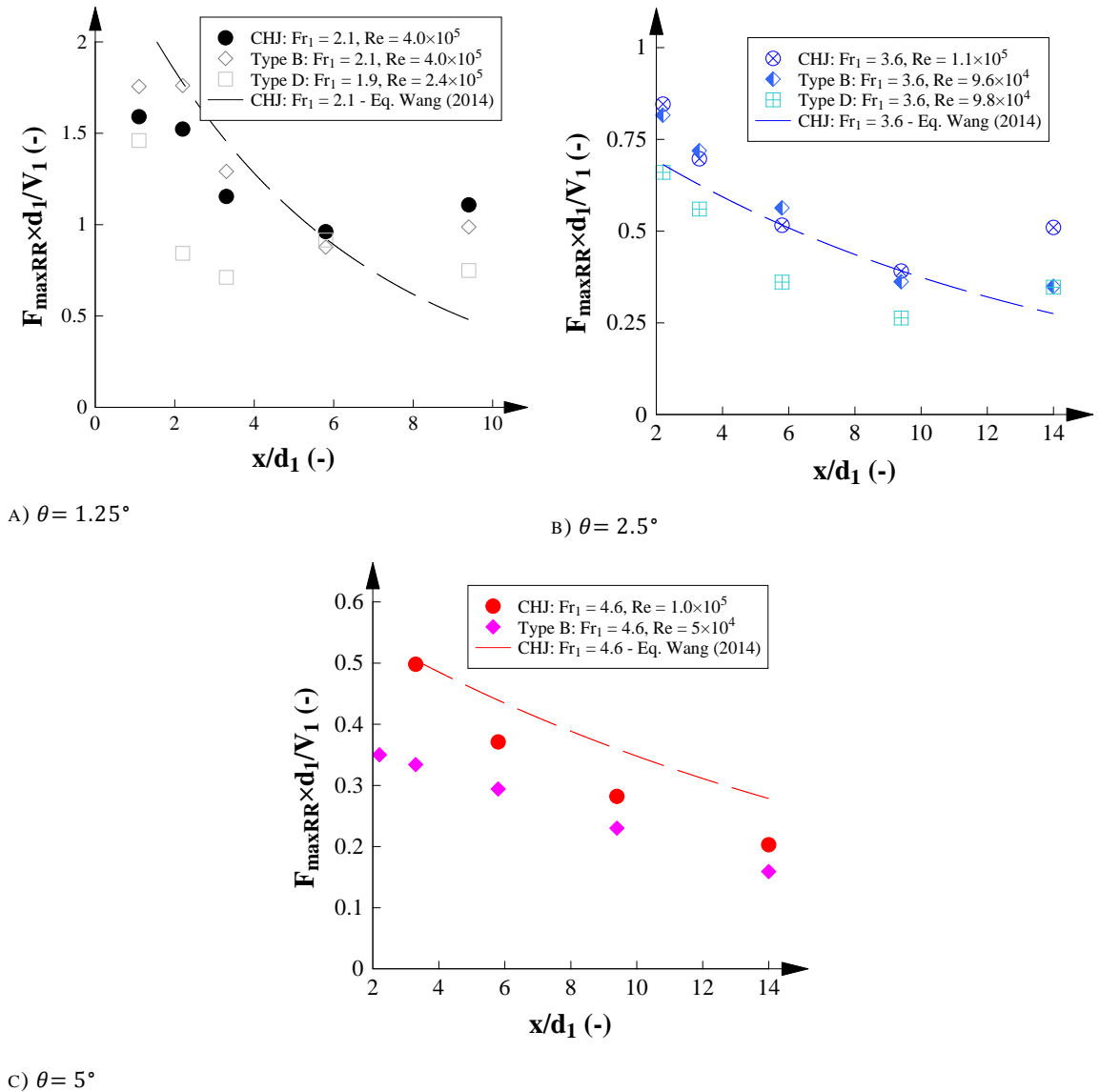


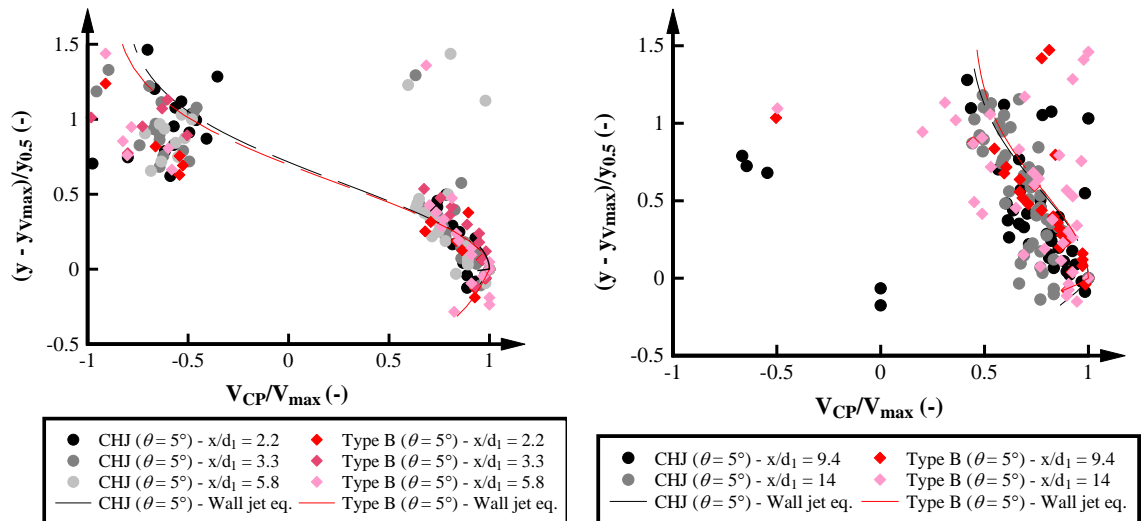
FIGURE F-13 – COMPARISON OF MAXIMUM BUBBLE COUNT IN THE RECIRCULATION REGION FOR SIMILAR FROUDE NUMBERS, COMPARISON WITH EMPIRICAL DECAY IN F_{maxRR} FOR CHJS BY WANG (2014).

F.6. INTERFACIAL VELOCITY

Figure F-14 presents typical dimensionless distributions of time-averaged interfacial velocity V_{CP}/V_1 as a function of y/d_1 for selected hydraulic jumps with the same Froude and Reynolds numbers. Overall, CHJ and Type B jump presented a similar trend in the shear region for all cross-sections, and the experimental data were well fitted by the wall jet theory despite some data scatter. Similar to the results obtained by Ohtsu and Yasuda (1990b; 1991), the velocity distribution in Type B jump was not affected by the change from sloped to horizontal section. In the recirculation region, higher data scatter and velocity fluctuations were identified for both hydraulic jump types. Since the conductivity probe was positioned in the flow direction, the data scatter was associated with the wake of the probe support, and the negative velocities in this region (e.g. Chanson and Brattberg 2000; Chanson 2010; Zhang et al. 2014). The velocity distributions in the recirculation region $x/d_1 \leq 5.8$ were characterised by negative velocities for

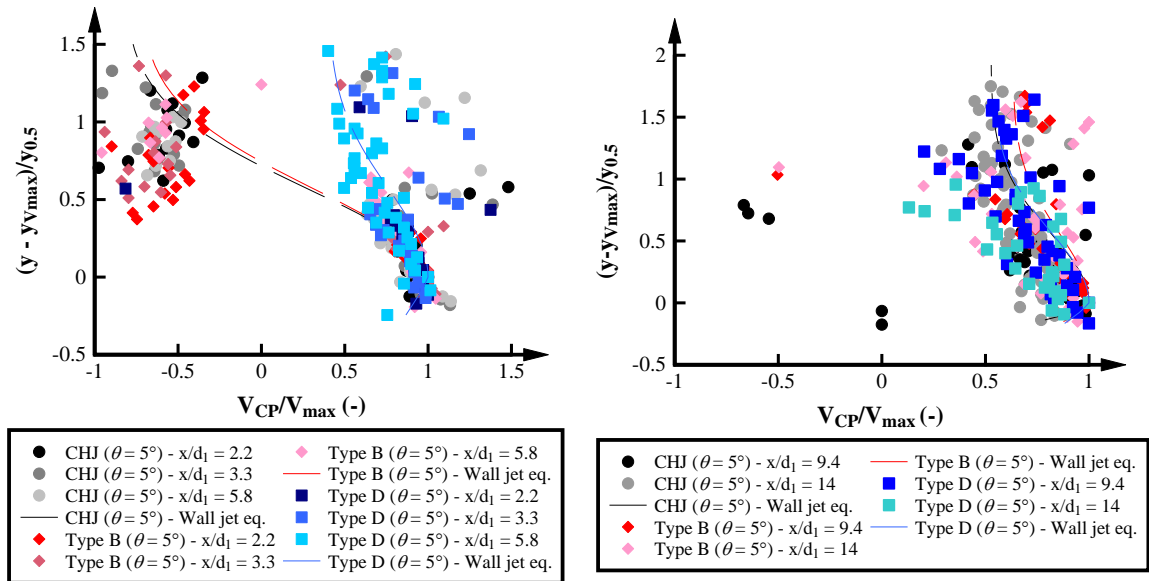
both jump types (Figure F-14A). For $x/d_1 > 5.8$, a negligible number of negative velocities were identified, and the velocity distributions were in the transition to a more uniform flow velocity profile (Figure F-14B). These observations were consistent with previous findings (Wu and Rajaratnam 1996). Overall for the same Froude number, no significant differences in the interfacial velocity distributions were identified between CHJ and Type B jumps.

Figures F-14C and D show the dimensionless interfacial velocity distribution for CHJ, Type B and D jumps with same Reynolds number ($Re = 1.1 \times 10^5$). Similar to the close agreement in velocity distributions with the same Froude number (Figures F-14A and B), no significant differences were observed in the shear region between the three hydraulic jump types (Figures F-14C and D). However, significant differences were observed in the recirculation region. For $x/d_1 \leq 5.8$, the CHJ and Type B jump presented similar velocity distributions in the recirculation region with negative velocity values whereas almost no negative velocities were observed for the Type D jump. In other words, while CHJ and Type B jump followed the wall jet velocity distribution in the region downstream of the jump toe, Type D jump showed a more uniform velocity distribution throughout the roller. This result suggested that the Type D jump presented a shorter roller region and a faster transition from wall jet velocity distribution to uniform flow velocity compared with Type B and CHJ. This result is in agreement with the lower air entrainment region and the rapid decrease in the number of bubbles in Type D jump. For $x/d_1 > 5.8$, all hydraulic jumps showed more uniform flow velocity distributions with some negligible negative velocities in the recirculation region for the Type B jump and the CHJ. Overall, the close agreement between all hydraulic jump types highlighted little effect of the slope upon the interfacial velocities.



A) VELOCITY DISTRIBUTION FOR $x/d_1 = 2.2, 3.3$ AND 5.8 WITH THE SAME FROUDE NUMBER ($Fr_1 = 4.6$).

B) VELOCITY DISTRIBUTION FOR $x/d_1 = 9.4$ AND 14 WITH THE SAME FROUDE NUMBER ($Fr_1 = 4.6$).



C) VELOCITY DISTRIBUTION FOR $x/d_1 = 2.2, 3.3$ AND 5.8 WITH THE SAME REYNOLDS NUMBER ($Re = 1.1 \times 10^5$).

D) VELOCITY DISTRIBUTION FOR $x/d_1 = 9.4$ AND 14 WITH THE SAME REYNOLDS NUMBER ($Re = 1.1 \times 10^5$).

FIGURE F-14 –COMPARISON OF DIMENSIONLESS INTERFACIAL VELOCITY DISTRIBUTIONS OF CHJ AND TYPE B AND D ($\theta = 5^\circ$). COMPARISON OF THE EXPERIMENTAL DATA WITH THE WALL JET THEORY.

Figure F-15 presents the decay in V_{max} as a function of the distance from the jump toe for CHJs and Type B and D jumps. For all the hydraulic jump types, the maximum velocity decreased with increasing the distance from the jump toe, suggesting lesser velocities at the downstream end of the hydraulic jumps. Despite some data scatter, V_{max} showed a slight increase with the increase in the Froude number. No differences were observed in V_{max} between hydraulic jumps occurring in the horizontal channel and the slope suggesting no slope effect in the advective velocity occurring in the shear region of the hydraulic jump. The velocity decay was in agreement with the empirical equation proposed by Chanson (2009b).

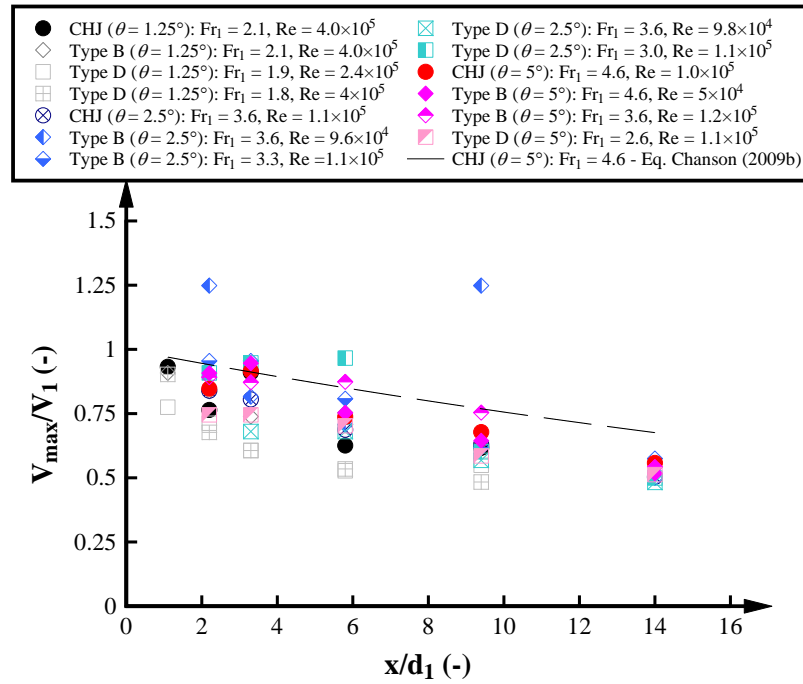
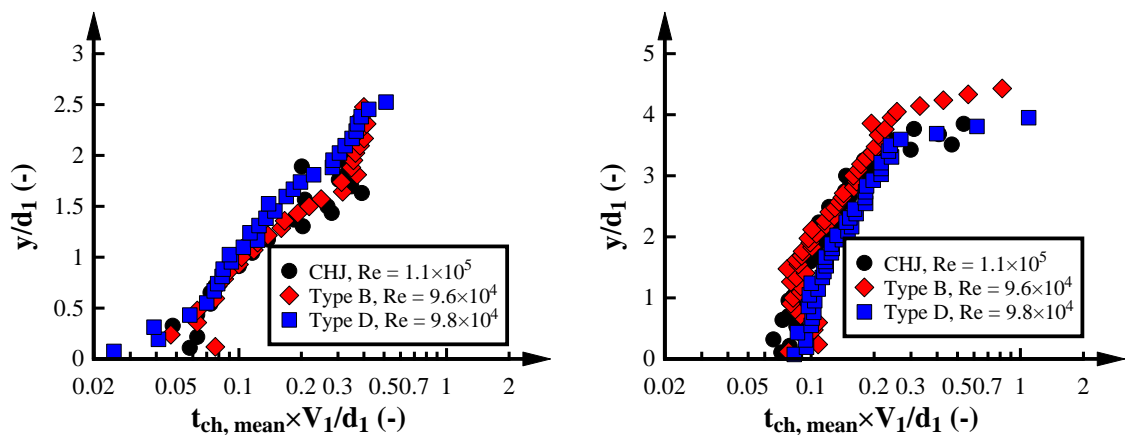


FIGURE F-15. V_{max} DECAY FOR HYDRAULIC JUMPS IN HORIZONTAL AND SLOPED CHANNELS AND COMPARISON WITH THE EMPIRICAL EQUATION BY CHANSON (2009B)

F.7. CHORD SIZES

Figure F-16 shows a comparison of typical dimensionless distributions of time-averaged chord times $t_{ch,mean} \times V_1/d_1$ in the shear region. For all jump types, the dimensionless chord times increased with increasing flow depth, and increasing distance from the jump toe suggesting on average smaller bubble sizes closer to the channel bed and closer to the jump toe respectively. The chord time distributions of CHJs and Type B jumps were similar while Type D jumps had larger average bubble sizes in the lower part of the shear region, and the differences increased with increasing distance from the jump toe. For the slope of $\theta = 5^\circ$, CHJs had smaller average chord times compared to Type B jumps in the lower shear region and these differences increased with increasing distance from the jump toe suggesting a potential effect of the slope on the chord times.



A) $x/d_1 = 3.3$

B) $x/d_1 = 9.4$

FIGURE F-16. DIMENSIONLESS TIME-AVERAGED CHORD TIMES: $\theta = 2.5^\circ$, $Fr_1 = 3.6$.

Figure F-17 shows typical probability distribution functions of the dimensionless chord times corresponding to C_{max} . Independent of the jump type and the position along the hydraulic jump, the probability distributions showed a comparatively larger number of smaller chord times and a gradual decrease for larger chord times as reported previously for CHJs (e.g. Chanson 2007b; Wang 2014). For all jump types, comparatively larger chord times were observed close to the jump toe while smaller chord times were observed downstream with the largest chord times for CHJs and Type B jumps (Figure F-17). Type D jumps had comparatively smaller dimensionless chord times. The result suggested that for C_{max} , the bubble sizes were comparatively largest for CHJs and smallest for Type D jumps.

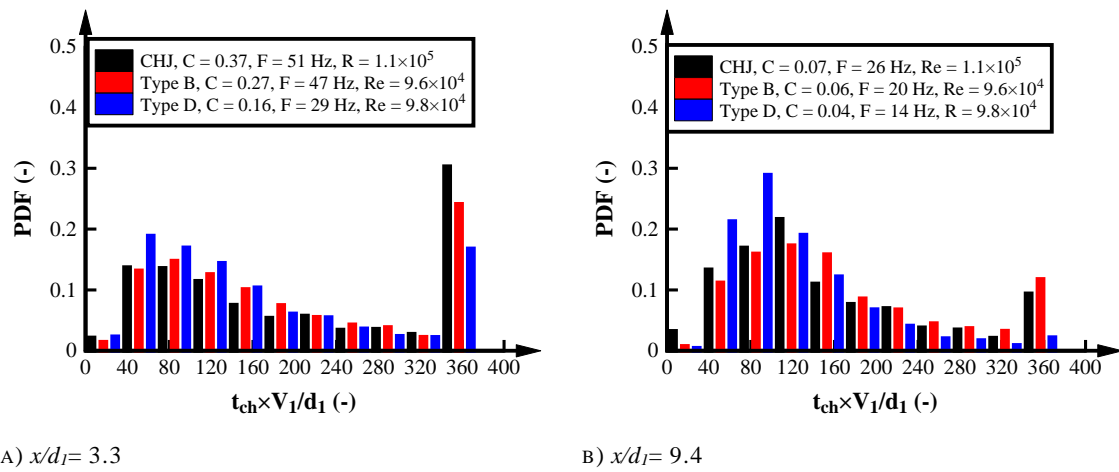
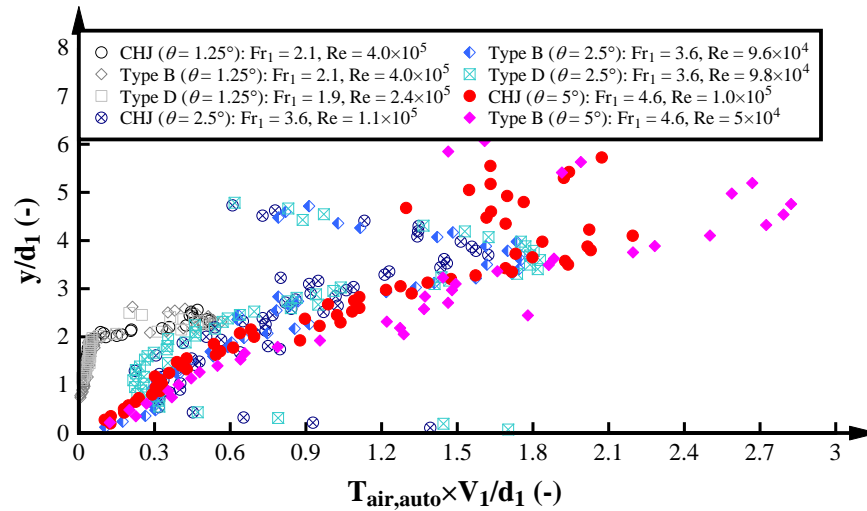


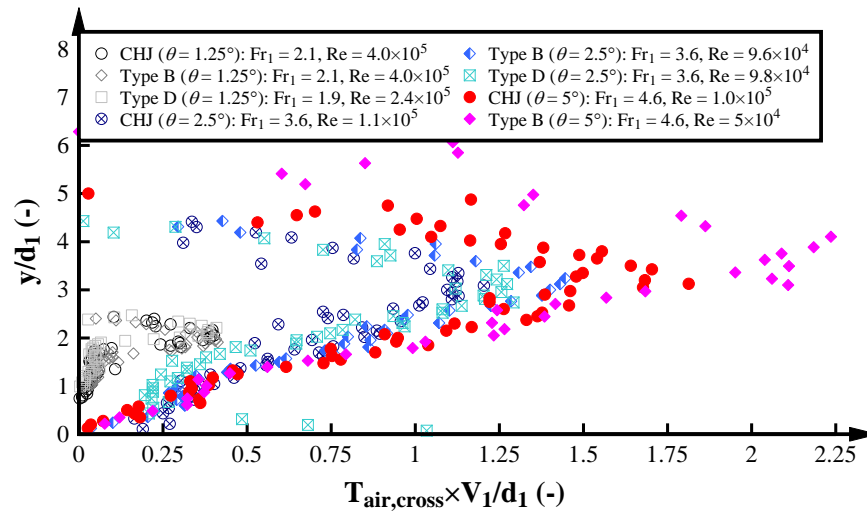
FIGURE F-17. PROBABILITY DISTRIBUTION FUNCTION OF AIR-BUBBLE CHORD TIMES AT C_{max} FOR $\theta = 2.5^\circ$, $Fr_1 = 3.6$.

F.8. AUTO- AND CROSS-CORRELATION TIME SCALES

Figure F-18A and B present a comparative analysis of the auto- and cross-correlation time scales respectively for hydraulic jumps on horizontal and sloped channels with identical dimensionless distance from the jump toe. All hydraulic jumps presented the typical auto- and cross-correlation time scale distribution with a slight increase with increasing the distance from the channel bed followed by a steeper increase in the recirculation region. Some data scatter could be observed in the lower part of the hydraulic jumps linked with low aeration in the bottom of the hydraulic jump. The analysis in the correlation time scales showed minimal effect of the slope on the turbulent scales for the lower slopes $\theta \leq 2.5^\circ$. The result suggested that all the hydraulic jumps presented the same turbulent scales in spite of the location of the hydraulic jump and the lesser air entrainment and bubble count rate observed in Type D jumps. For $\theta = 5^\circ$, Type B jump showed larger correlation in the recirculation region, indicating larger advective scales compared to hydraulic jumps on horizontal channels. Further research is required to identify the turbulent scales in larger slopes.



A) $T_{air,auto} - x/d_1 = 5.8$



B) $T_{air,cross} - x/d_1 = 3.3$

FIGURE F-18. COMPARISON OF THE CORRELATION TIME SCALES FOR HYDRAULIC JUMPS ON SLOPED CHANNELS.

F.9. DISCUSSION

CHJs, Type B and Type D jumps for three flat slopes $\theta = 1.25^\circ$, 2.5° and 5° were compared and differences in terms of free-surface fluctuations, jump toe oscillations and air-water flow properties were identified. Table F-2 summarises the differences of Type B and D jumps compared to the reference CHJs. For same Froude and Reynolds numbers, CHJs were found to be the most efficient, dissipative, aerated and turbulent hydraulic jumps. The flow properties for Type B jumps were mostly similar to CHJs for the smallest slopes ($\theta = 1.25^\circ$ and 2.5°) with key differences in terms of the stability of the jump toe. For the largest slope in the present study ($\theta = 5^\circ$), differences between CHJs and Type B jumps increased in terms of all flow properties. Further research with larger slopes ($\theta > 5^\circ$) is needed to confirm these observations. Independent of the slope, Froude and Reynolds numbers, Type D jumps differed substantially

from CHJs showing lesser aeration, and lesser efficiency while the stability of the jump toe was largest (Table F-2).

Stilling basin designs must account for strong jump toe oscillations and often additional elements are used to increase the stability of the jump toe including blocks and sills (Bradley and Peterka 1957; Hager and Damei 1992; Pagliara and Palermo 2015). Sloped stilling basin designs have rarely been used. The present observations suggest that Type B jumps on a flat sloped channel or stilling basin apron could be a preferred hydraulic jump type. While Type B jumps showed almost identical air-water flow properties, energy dissipation and conjugate depth relationships compared to CHJs, Type B jumps appeared to be more stable. Further research is required to investigate a wider range of slopes and to further explore the option of a positively sloped stilling basin design.

TABLE F-2. SUMMARY TABLE OF THE EFFECT OF THE INFLOW CONDITIONS AND SCALE EFFECTS IN THE AERATION FEATURES IN THE HYDRAULIC JUMP

Parameter	Type B	Type D
Flow visualizations	Similar	Lower
Efficiency	Similar	Lower
Free-surface fluctuations	More stable	More stable
Jump toe oscillations	More stable	More stable
Void fraction (C)	Similar	Lower
Mean void fraction (C_{mean})	Similar	Lower
Maximum void fraction (C_{max})	Similar	Lower
Bubble count rate (F)	Similar	Lower
Maximum bubble count rate in the shear region (F_{maxSR})	Similar	Lower
Maximum bubble count rate in the recirculation region (F_{maxRR})	Similar	Lower
Interfacial velocity (V_{CP})	Similar	Similar
Maximum interfacial velocity (V_{max})	Similar	Similar
Time-averaged bubble chord time $t_{ch,mean}$	Similar	Larger in the shear region
Auto-correlation time scale of the air-water flow properties ($T_{air,auto}$)	Similar	Similar
Cross-correlation time scale of the air-water flow properties ($T_{air,cross}$)	Similar	Similar

F.10. CONCLUSION

New experiments of CHJs and Type B and D jumps for several flat slopes $1.25^\circ \leq \theta \leq 5^\circ$ were conducted for comparative Froude and Reynolds numbers $1.8 \leq Fr_1 \leq 4.6$ and $5 \times 10^4 \leq Re \leq 4 \times 10^5$. Flow visualizations showed larger air entrainment and fluctuations in CHJs while Type D jumps had the lowest aeration. For similar Froude numbers, CHJs and Type B jumps had similar conjugate depths and similar dissipation efficiency while Type D jumps had a larger conjugate depths ratio and lower efficiencies. Analyses of jump toe oscillations and free-surface fluctuations showed a close agreement between Type B and D jumps, while CHJs were less stable quantified through larger jump toe oscillations and free-surface fluctuations. The

comparison of a wide range of air-water flow properties showed close agreement between CHJs and Type B jumps for $1.25^\circ \leq \theta \leq 2.5^\circ$ and increasing differences for the largest slope $\theta = 5^\circ$. Type D jumps had consistently lower flow aeration for comparable Froude and Reynolds numbers quantified by lower void fractions, bubble count rate and cluster count rate. Overall, the close similarities in energy dissipation and flow aeration for CHJs and Type B jumps combined with the larger jump toe stability for Type B jumps suggests that a Type B jump may be a preferable stilling basin design. The current results are limited to slopes between $1.25^\circ \leq \theta \leq 5^\circ$ and further research is needed to expand the results to a wider range of slopes as well as Froude and Reynolds numbers.

G. FREE-SURFACE PROPERTIES: TURBULENT SCALES

G.1. AUTO-CORRELATION FUNCTIONS AND FREE-SURFACE AUTO-CORRELATION TIME SCALES

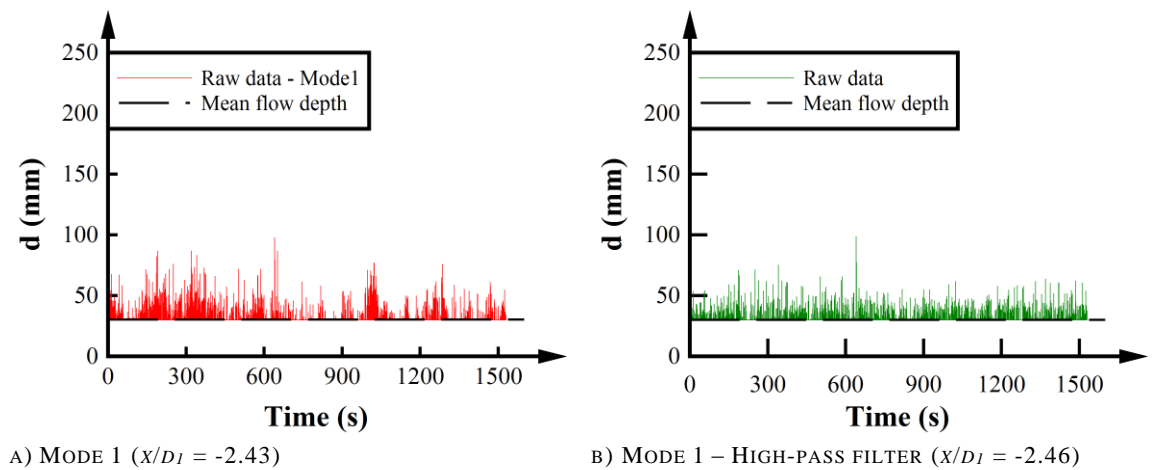
The free-surface turbulent time scales were estimated based on the correlation equation:

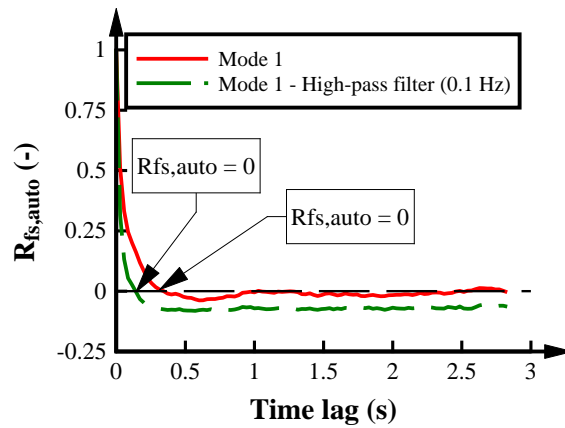
$$R_{fs,cross} = \frac{\sum(d(t)_i - \bar{d}_i) \times (d(t-\tau)_j - \bar{d}_j)}{\sqrt{\sum(d(t)_i - \bar{d}_i)^2 \times \sum(d(t-\tau)_j - \bar{d}_j)^2}} \quad (G.1)$$

where $R_{fs,cross}$ is the correlation function, d is an instantaneous value of the free-surface at time t , \bar{d} is the mean value of the total sampling time, i and j represent different positions along the hydraulic jump and τ is the time lag. For auto-correlation functions, i is equal to j .

G.1.1. EXPERIMENT A

The raw signal and auto-correlation functions were analysed for Experiment A ($Fr_1 = 5.1$, $Re = 8.3 \times 10^4$). Figure G-1 presents the raw signal and auto-correlation functions upstream the mean jump toe position at $x/D_1 = -2.43$. At this position, large number of raw signal data is equal to the inflow flow depth. Nonetheless, Mode 1 without filter showed larger fluctuations compared to Mode 1 with high-pass filter. The larger fluctuations in Mode 1 resulted in larger deviations from the mean in Equation G.1 leading to higher auto-correlation values. Figure G-1C is also highlighting the maximum integration limit of the free-surface auto-correlation time scale. For both Mode 1 and Mode 1 with high-pass filter, the maximum integration limit of Equation G.1 was equal to the time lag where $R_{fs,auto}$ was crossing the x-axis.

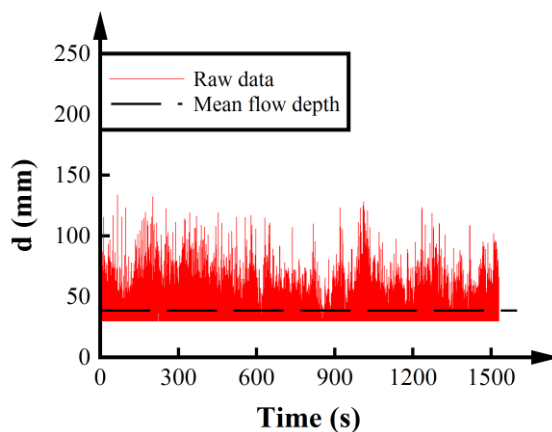




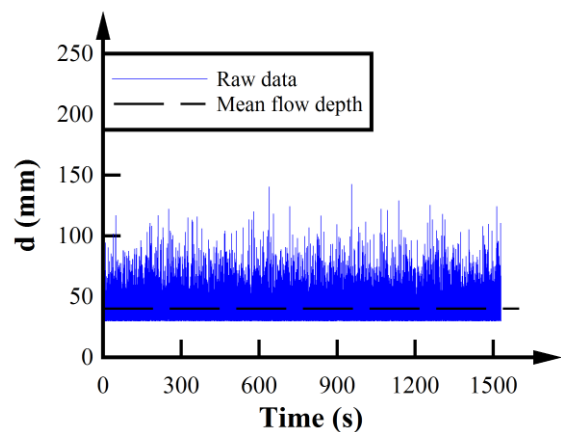
C) AUTO-CORRELATION FUNCTION ($x/d_l = -2.43$)

FIGURE G-1. AUTO-CORRELATION FUNCTIONS FOR EXPERIMENT A: $Fr_l = 5.1$, $Re = 8.3 \times 10^4$ ($x/d_l = -2.4$).

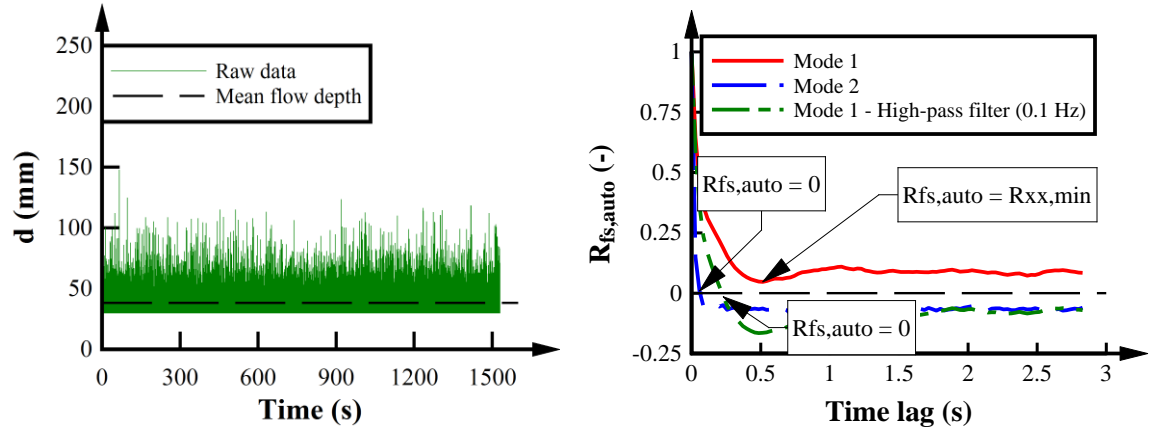
At $x/d_l = 0.18$, almost at the mean jump toe position, the raw data is presenting more number of fluctuations compared to $x/d_l = -2.43$ resulting in larger correlation. Likewise, Mode 1 presented larger correlations compared to Mode 2 and Mode 1 with a high-pass filter of 0.1 Hz. This result may be linked to the larger standard deviation in Mode 1 compared to the other conditions. Also, note that Mode 1 showed large number of data with $d = d_l$ suggesting a strong influence of d_l in the correlation function. In contrast, the minimum flow depth in Mode 2 was larger to d_l resulting in no influence of d_l in the correlation function leading to lower correlation. Figure G-2D is also presenting the maximum integration limit of Equation G.1. For Mode 1, the auto-correlation function is always positive suggesting an infinite auto-correlation time scale. Therefore, the maximum integration limit was established as the time lag where $R_{fs,auto} = R_{fs,auto_min}$. The maximum integration limits of Mode 2 and Mode 1 with high-pass filter were selected at the time lag of the first crossing with the x-axis.



A) MODE 1 ($x/d_l = 0.19$)



B) MODE 2 ($x/d_l = 0.19$)

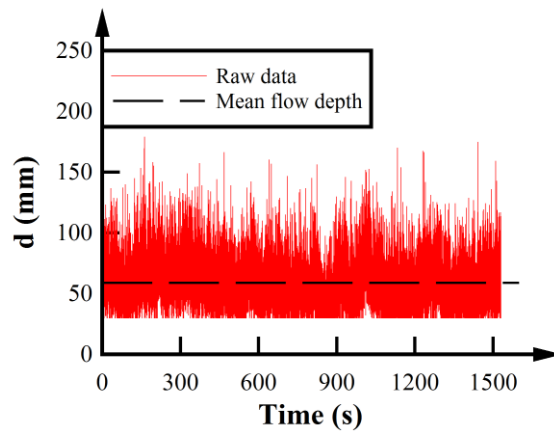


C) MODE 1 – HIGH-PASS FILTER ($x/d_1 = 0.21$)

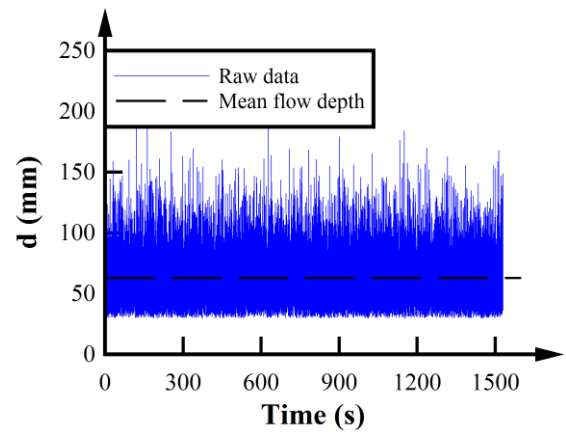
D) AUTO-CORRELATION FUNCTION ($x/d_1 = 0.19$)

FIGURE G-2. AUTO-CORRELATION FUNCTIONS FOR EXPERIMENT A: $Fr_1 = 5.1$, $Re = 8.3 \times 10^4$ ($x/d_1 = 0.19$).

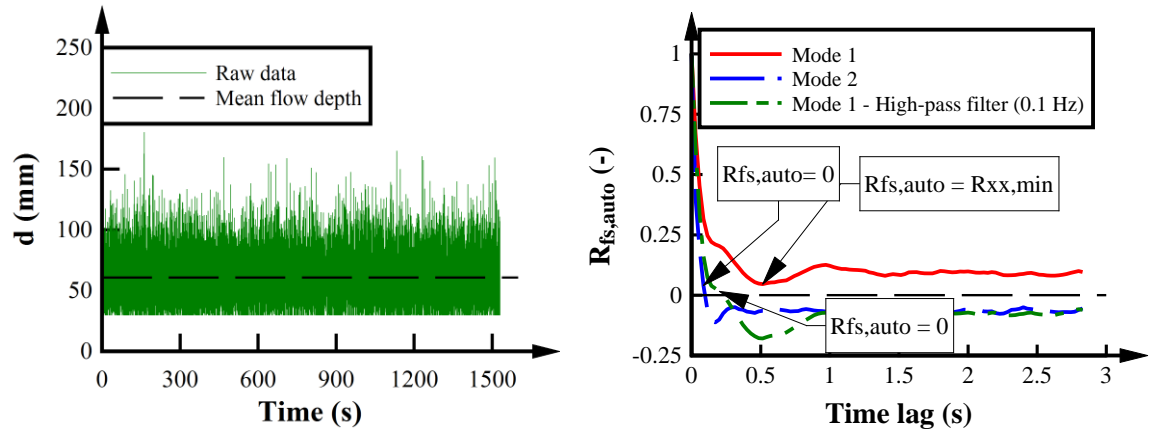
At $x/d_1 = 2.48$, the raw signal data for Mode 1 and Mode 1 with high-pass filter still presented a strong influence of the inflow flow depth in the raw signal. The repeatability of d_I in the raw signal resulted in larger correlation functions for Mode 1 compared to Mode 2. Likewise, Mode 1 showed larger standard deviations compared to Mode 1 with high-pass filter resulting in larger correlation for Mode 1. Similar to the behaviour observed at $x/d_1 = 0.19$, the auto-correlation function of Mode 1 was always positive leading to infinite auto-correlation time scales. Therefore, the maximum integration limit of equation 2.5 for Mode 1 was established as the time lag where $R_{fs,auto} = R_{fs,auto,min}$. The maximum integration limit for Mode 2 and Mode 1 with high-pass filter was selected as the time lag where the correlation function crossed the x-axis.



A) MODE 1 ($x/d_1 = 2.48$)



B) MODE 2 ($x/d_1 = 2.48$)

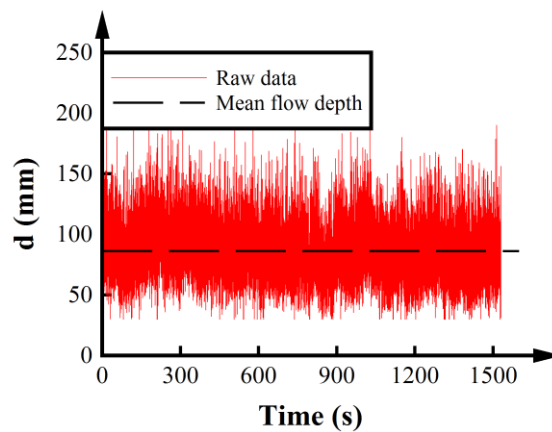


C) MODE 1 – HIGH-PASS FILTER ($x/d_1 = 2.55$)

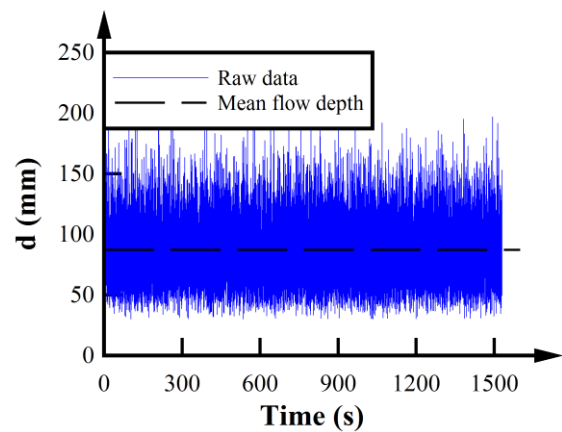
D) AUTO-CORRELATION FUNCTION ($x/d_1 = 2.48$)

FIGURE G-3. AUTO-CORRELATION FUNCTIONS FOR EXPERIMENT A: $Fr_1 = 5.1$, $Re = 8.3 \times 10^4$ ($x/d_1 = 2.48$).

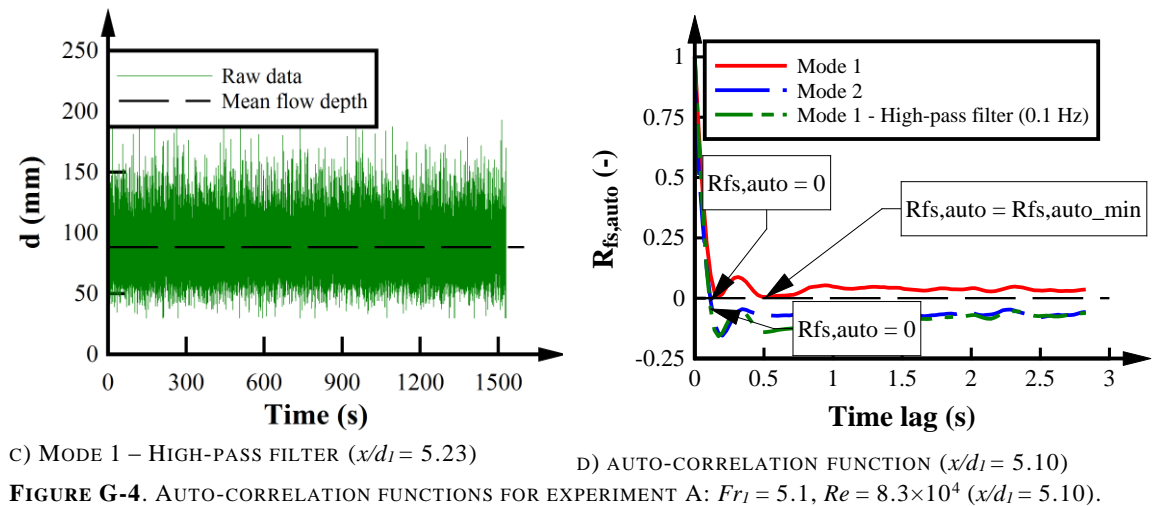
At $x/d_1 = 5.10$, the auto-correlation time scales showed a more similar behaviour compared to the upstream locations. Mode 1 presented a minor influence of the inflow depth with a small number of data with $d = d_1$. The remaining influence of the inflow flow depth resulted in larger correlations in Mode 1 compared to Mode 2. Likewise, Mode 1 showed larger fluctuations compared to Mode 1 with high-pass filter resulting in larger correlation functions. The maximum integration limit for Mode 2 and Mode 1 with high-pass filter corresponded to the time lag of the first crossing with the x-axis. As occurred in upstream positions, the auto-correlation function did not present a crossing with the x-axis for Mode 1 and the maximum integration limit was selected as the time lag of the minimum of the auto-correlation function. Note that the auto-correlation function in Mode 1 showed multiple minimum positions of similar values at different time lags. For the present study, the minimum was selected as the global minimum of the auto-correlation function. Further research may be needed to identify better approximations in the selection of the minimum point.



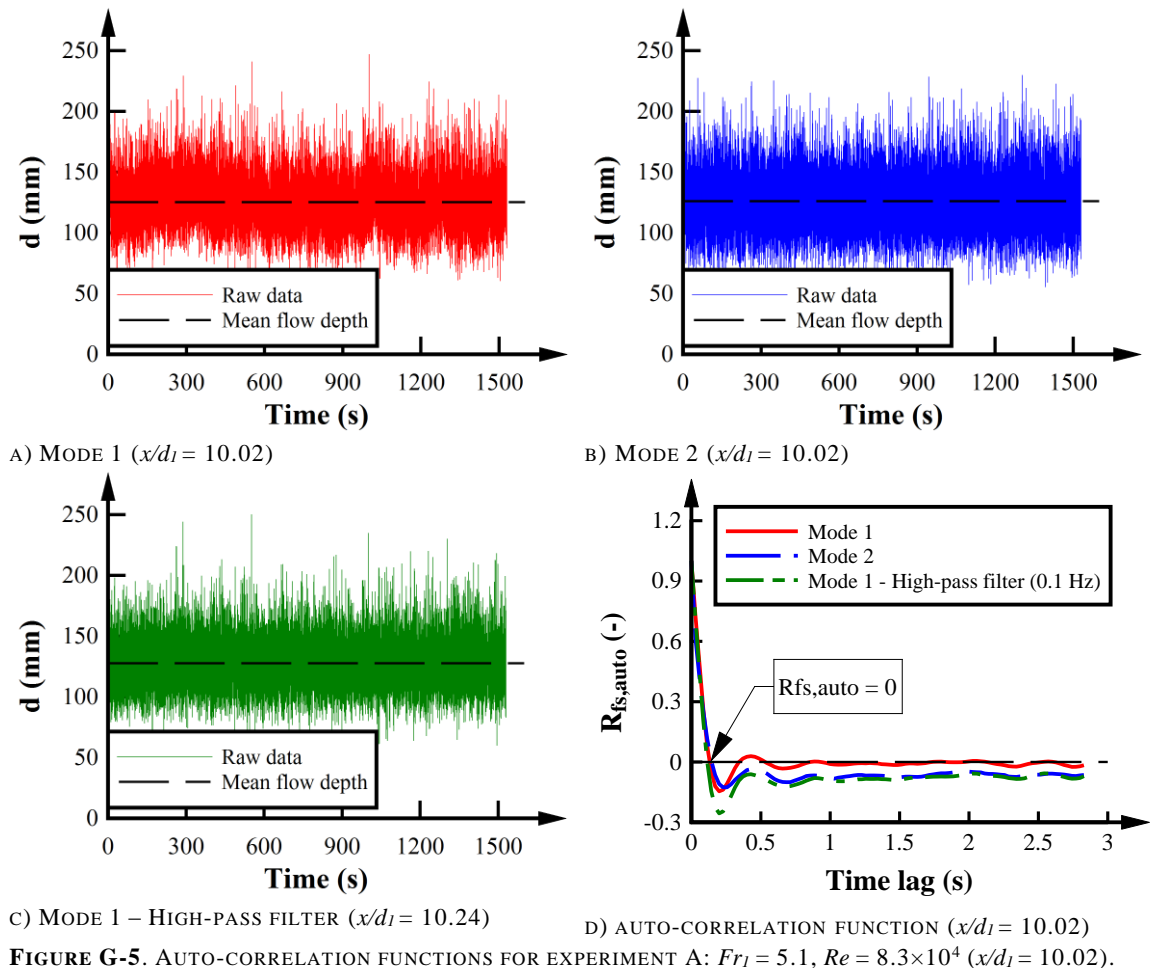
A) MODE 1 ($x/d_1 = 5.10$)



B) MODE 2 ($x/d_1 = 5.10$)



No influence of the inflow flow depths was observed at $x/d_1 = 10.02$. Therefore, the auto-correlation function showed a similar pattern between Mode 1, Mode 2, and Mode 1 with high-pass filter. Slight deviations in the auto-correlation time scales were related with small differences in the auto-correlation curve at small time lags related to different fluctuation patterns. Nonetheless, the differences were minor and the auto-correlation function and its resulting time scales were similar. At this position, the maximum integration limit was selected as the first crossing with the x-axis.



Similar to $x/d_I = 10.02$, the auto-correlation functions showed similar patterns between Mode 1, Mode 2, and Mode 1 with high-pass filter at $x/d_I = 15.27$. Mode 2 showed slightly larger deviations in the free-surface raw signal resulting in larger auto-correlation time scales. All the integration limits were selected as the first cross with the x-axis.

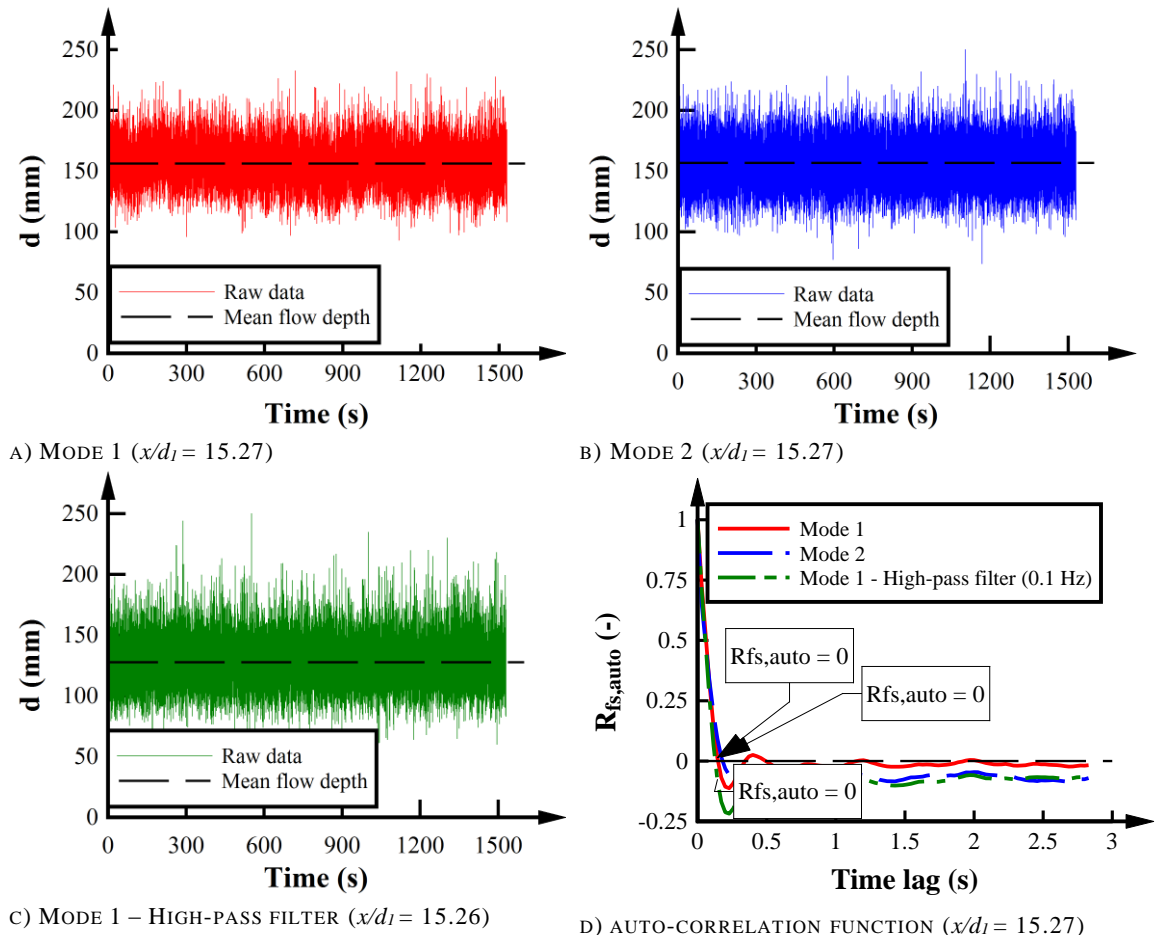


FIGURE G-6. AUTO-CORRELATION FUNCTIONS FOR EXPERIMENT A: $Fr_I = 5.1$, $Re = 8.3 \times 10^4$ ($x/d_I = 15.27$).

At the downstream end of the jump, at $x/d_I = 20.18$, the free-surface raw signal was similar between Mode 1, Mode 2 and Mode 1 with high-pass filter. Smaller auto-correlation time scales were observed for Mode 1 with high-pass filter because this mode showed slightly less fluctuations compared with the other conditions. All the correlation curves presented a crossing with the x-axis.

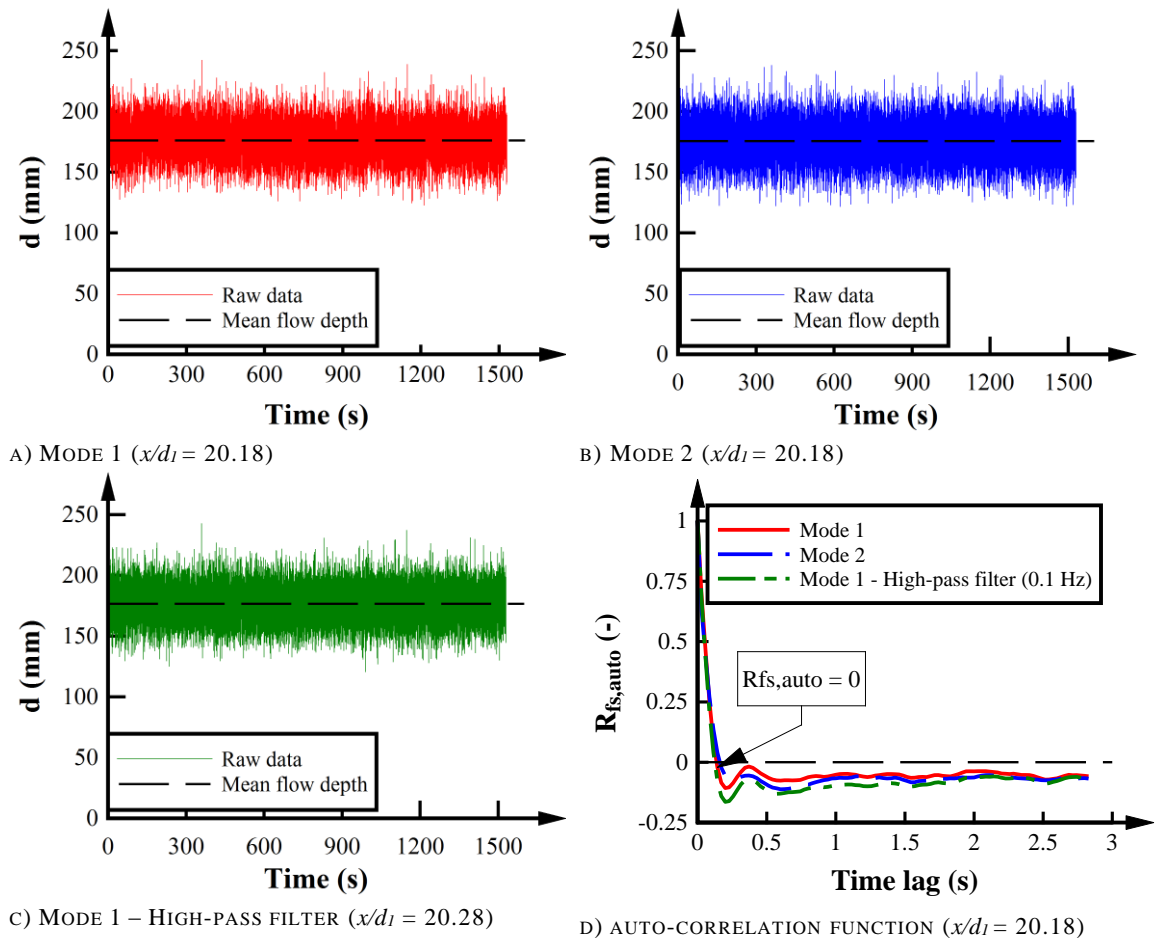
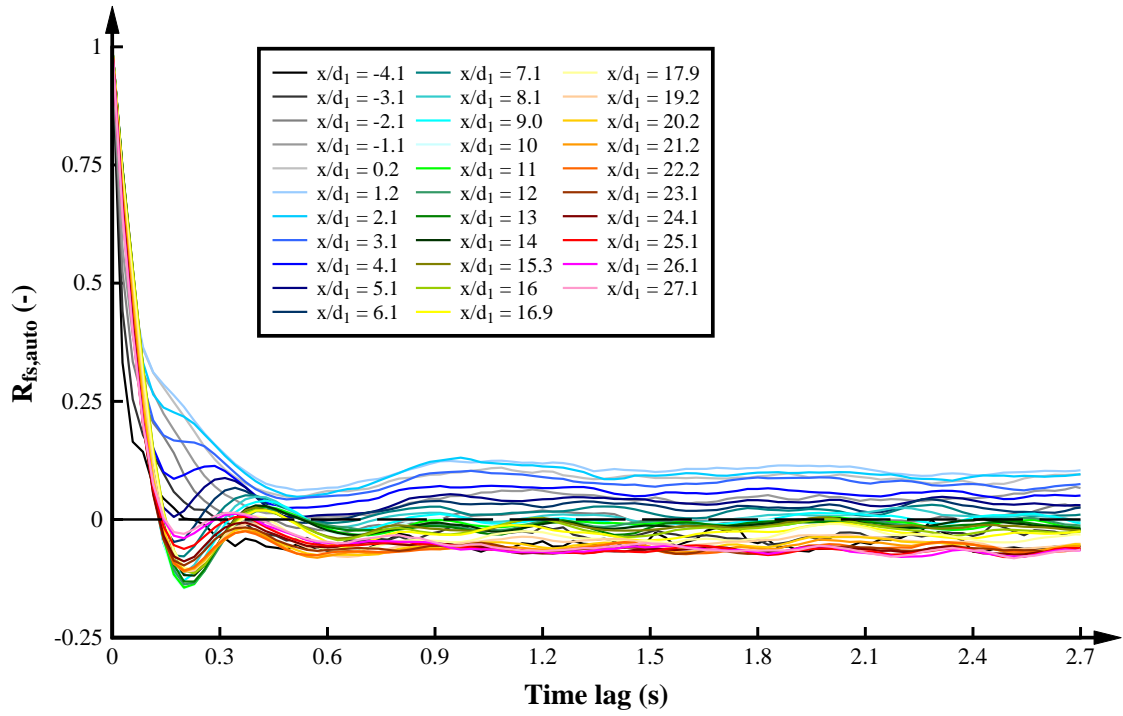
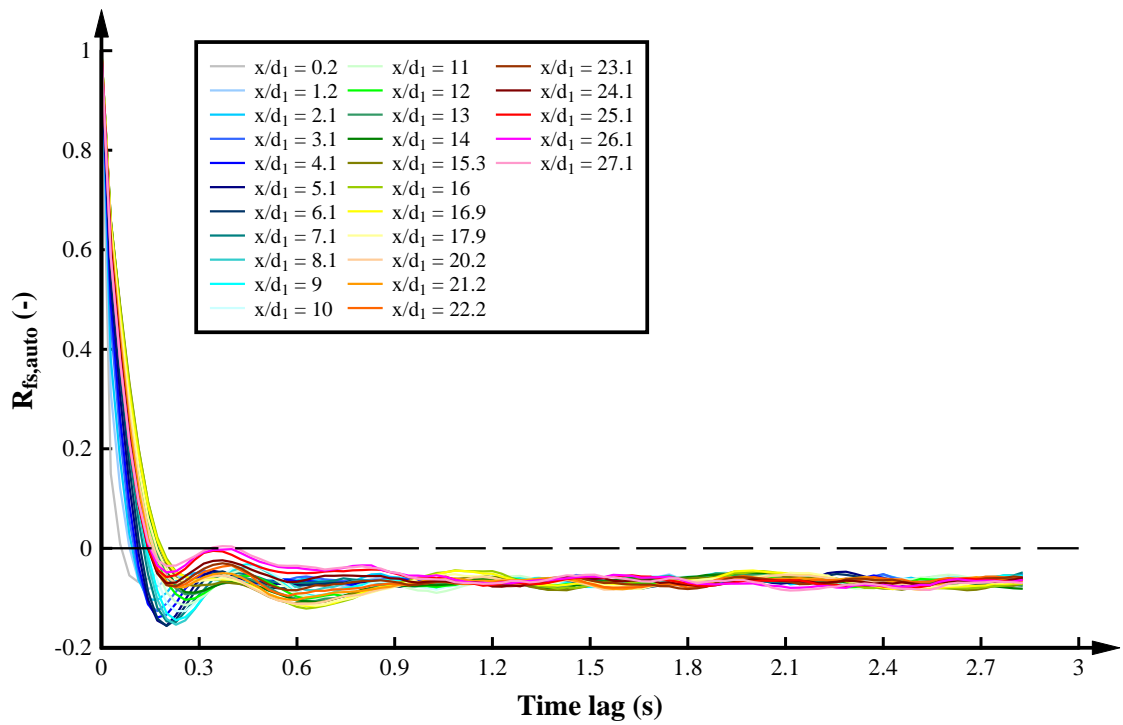


FIGURE G-7. AUTO-CORRELATION FUNCTIONS FOR EXPERIMENT A: $Fr_1 = 5.1$, $Re = 8.3 \times 10^4$ ($x/d_1 = 20.18$).

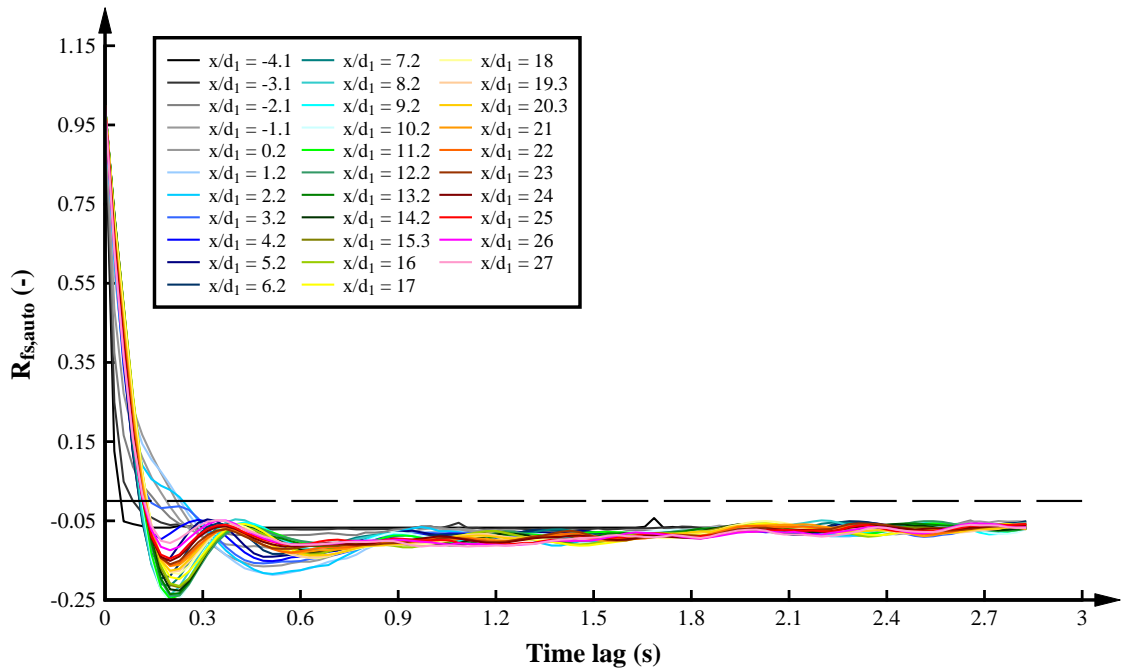
Figure G-8 illustrates typical auto-correlation functions along the hydraulic jump for Mode 1 (Figure G-8A), Mode 2 (Figure G-8B), and Mode 1 with high-pass filter (Figure G-8C). Large auto-correlation functions were observed close to the jump toe for Mode 1 with positive correlation for all the time lags analysed (blue lines). In contrast, Mode 2 and Mode 1 with high-pass filter showed a crossing with the x-axis for small time lags. The result suggested that the repeatability of d_i in Mode 1 may be creating strong positive correlations resulting in large auto-correlation time scales close to the jump toe. At positions that were not more affected by the jump toe oscillations, the auto-correlation functions were similar between the three mode conditions.



A) AUTO-CORRELATION FUNCTION FOR MODE 1



B) AUTO-CORRELATION FUNCTION FOR MODE 2

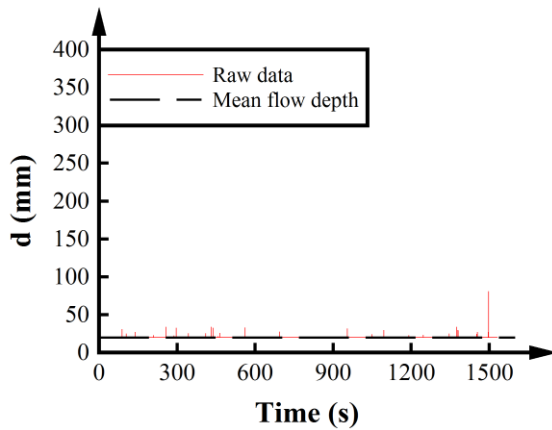


C) AUTO-CORRELATION FUNCTION FOR MODE 1 WITH HIGH-PASS FILTER OF 0.1 HZ.

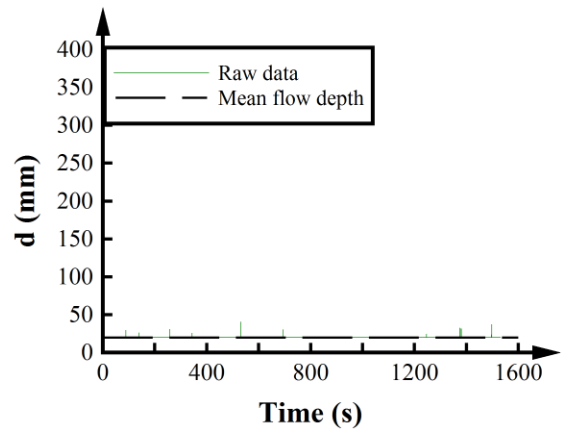
FIGURE G-8. AUTO-CORRELATION FUNCTIONS FOR EXPERIMENT A: $Fr_1 = 5.1$, $Re = 8.3 \times 10^4$.

C.6.2. EXPERIMENT G

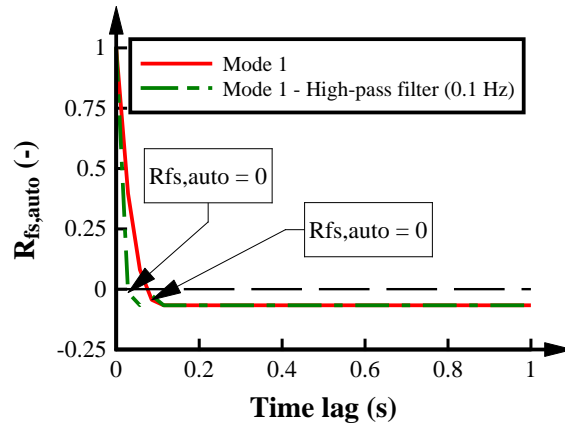
The raw signal and auto-correlation functions were analysed for Experiment G ($Fr_1 = 10$, $Re = 8.8 \times 10^4$). Figure G-9 presents the raw signal and the auto-correlation function for $x/d_1 = -9.96$ for Mode 1 and Mode 1 with high-pass filter of 0.1 Hz. At this cross-section, the majority of the raw signal data in Mode 1 is equal to the inflow flow depth where $d = d_1$. Hence, the auto-correlation function was strongly affected by any flow depth different to the inflow flow depth. Since the high-pass filtering reduced the number of flow depths different to the inflow flow depth, the auto-correlation function in the filtered mode was more sensitive and showed a faster drop compared with the analysis without filter. The auto-correlation functions for both modes crossed the x-axis indicating that $R_{fs,auto} = R_{fs,auto_{min}}$.



A) MODE 1 ($x/d_1 = -9.96$)



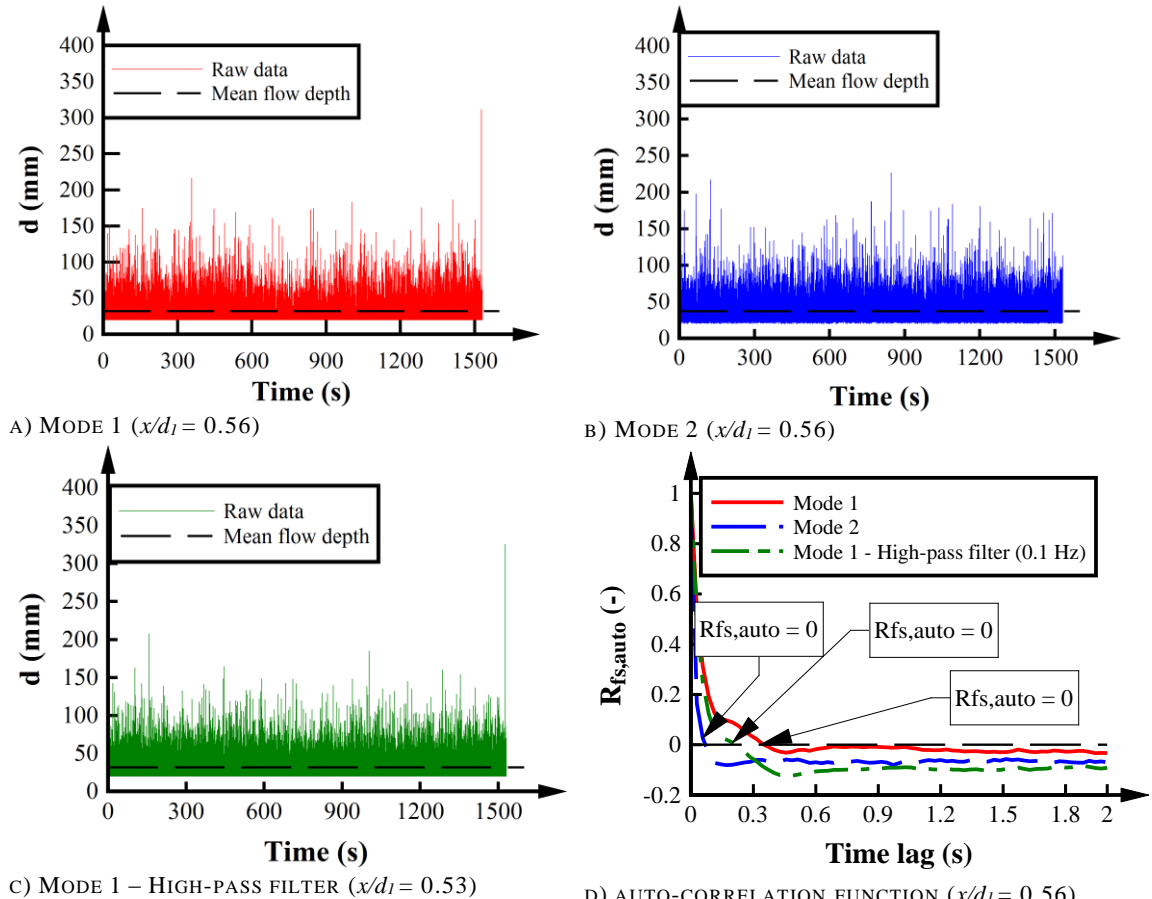
B) MODE 1 – HIGH-PASS FILTER ($x/d_1 = -9.96$)



C) AUTO-CORRELATION FUNCTION ($x/d_1 = -9.96$)

FIGURE G-9. AUTO-CORRELATION FUNCTIONS FOR EXPERIMENT G: $Fr_1 = 10$, $Re = 8.8 \times 10^4$ ($x/d_1 = -9.96$).

At $x/d_1 = 0.56$, the hydraulic jump fluctuations observed in Mode 1 with and without filter were still strongly affected by the influence of the inflow flow depth. Nonetheless, since the hydraulic jump showed larger number of fluctuations, it was larger correlation compared with $x/d_1 = -9.97$. On the other hand, Mode 2 was not influenced by the inflow flow depth since this analysis mode considered flow depths higher than the inflow flow depth. Because the values in the flow depth are not the same between time steps in Mode 2 (different to Mode 1 where the flow depth is being repeated), the auto-correlation function is lower in Mode 2 compared with Mode 1.



A) MODE 1 ($x/d_1 = 0.56$)

B) MODE 2 ($x/d_1 = 0.56$)

C) MODE 1 – HIGH-PASS FILTER ($x/d_1 = 0.53$)

D) AUTO-CORRELATION FUNCTION ($x/d_1 = 0.56$)

FIGURE G-10. AUTO-CORRELATION FUNCTIONS FOR EXPERIMENT G: $Fr_1 = 10$, $Re = 8.8 \times 10^4$ ($x/d_1 = 0.56$).

At $x/d_1 = 10.2$, the hydraulic jump was almost not influenced by the inflow flow depth. At this point, the auto-correlation functions were similar for Mode 1, Mode 1 with high-pass filter and Mode 2. Slight larger correlation was observed for Mode 1 which may be linked to the influence of the minor numbers of flow depths equal to the inflow flow depth. Note that the pattern of the raw data signal of Mode 1 and Mode 1 without filter is almost the same (showing the peaks in the same location) while Mode 2 presented a completely different pattern. This can be confirmed in the shape of the auto-correlation functions. Mode 1 and Mode 1 with high-pass filter are showing the same correlation shape but the curve of the filtered analysis is shifted down. In contrast, Mode 2 presented a different shape compared to Mode 1. For a time lag of 0.3 s, the correlation function of Mode 1 and Mode 2 is almost the same. For $x/d_1 = 10.2$, the auto-correlation function always crossed the x-axis for all the conditions.

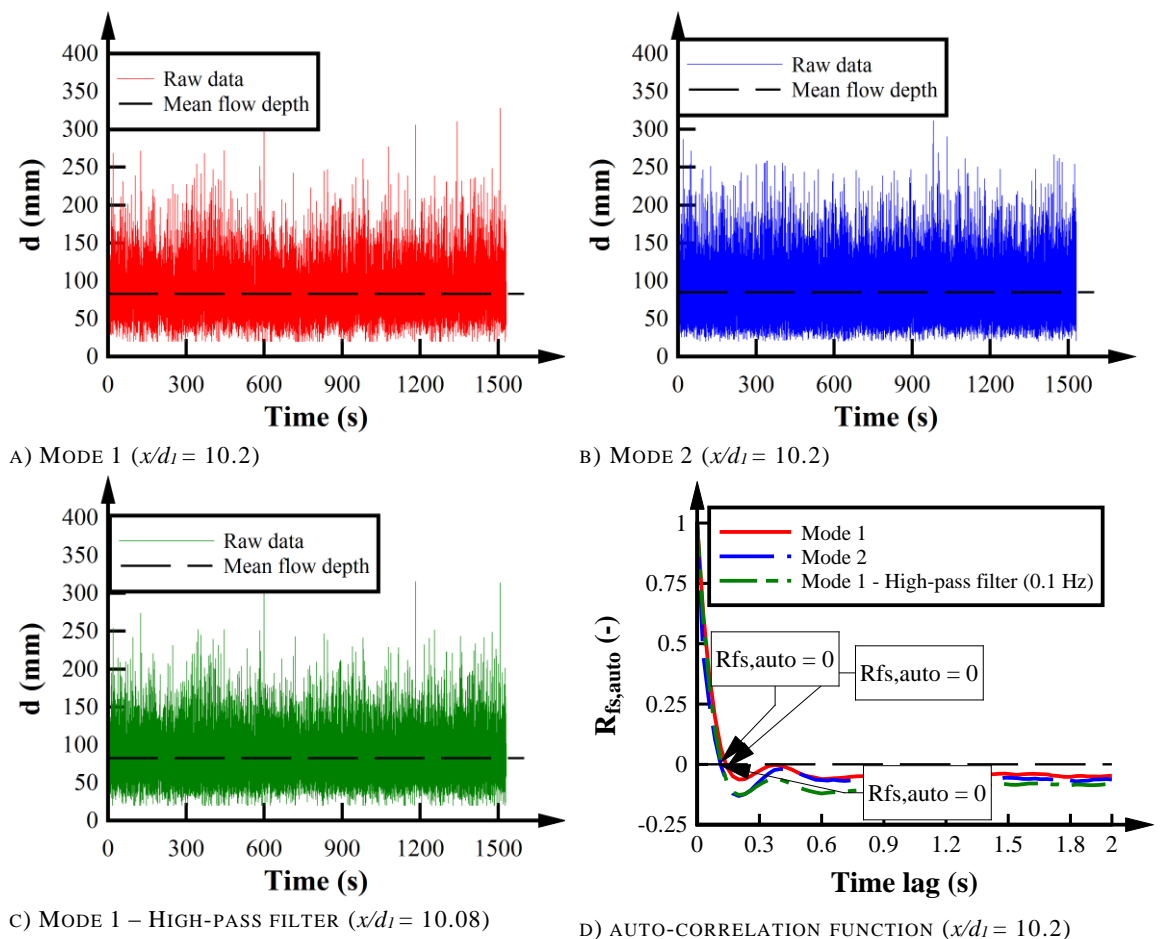


FIGURE G-11. AUTO-CORRELATION FUNCTIONS FOR EXPERIMENT G: $Fr_1 = 10$, $Re = 8.8 \times 10^4$ ($x/d_1 = 10.2$).

At $x/d_1 = 30.36$, the hydraulic jump was not influenced by the inflow flow depth. At this point, the auto-correlation functions were similar for Mode 1, Mode 1 with high-pass filter and Mode 2. Slight larger correlation was observed for Mode 1. Again, the correlation function of Mode 1 with high-pass filter showed the same shape as the correlation function of Mode 1 but shifted downwards. Mode 2 showed a similar shape to Mode 1 with similar values for time lags

larger to 0.5 s. For all conditions, the maximum integration limit of equation 2.5 was selected as the time lag of the first crossing with the x-axis.

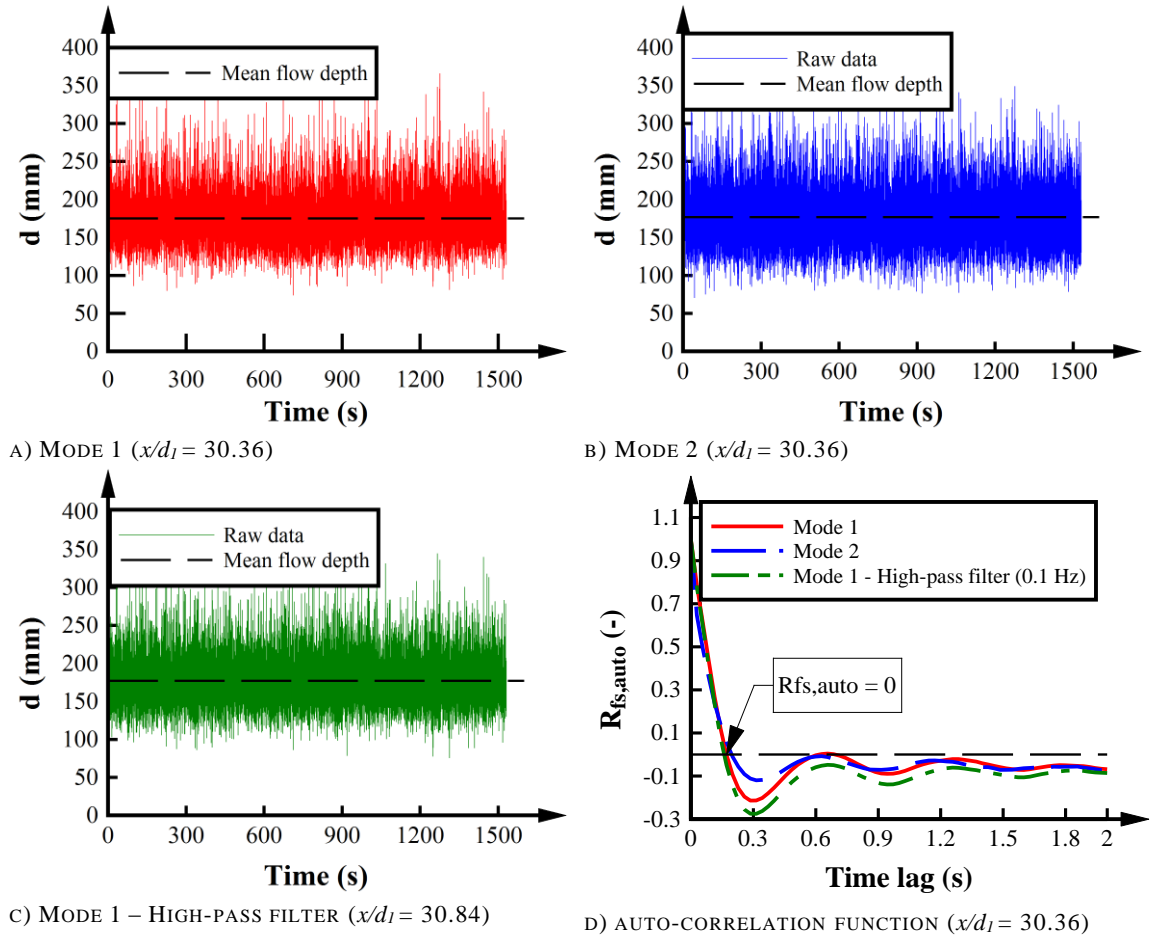
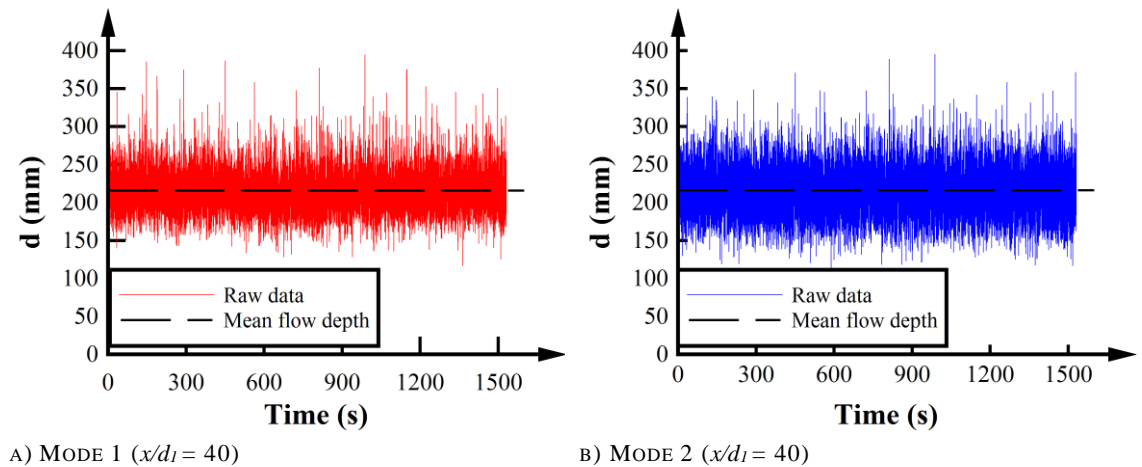


FIGURE G-12. AUTO-CORRELATION FUNCTIONS FOR EXPERIMENT G: $Fr_I = 10$, $Re = 8.8 \times 10^4$ ($x/d_I = 30.36$).

Larger fluctuations in the raw signal data of Mode 2 compared to Mode 1 can be observed at $x/d_I = 40$. Nonetheless, the correlation functions are similar between the three modes. In addition, for all the conditions, the correlation function was crossing the x-axis.



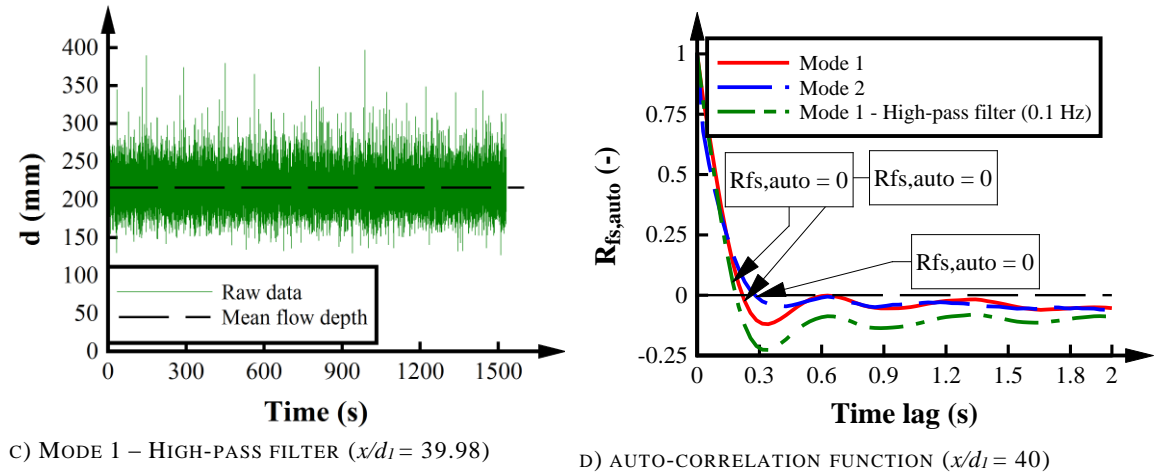


FIGURE G-13. AUTO-CORRELATION FUNCTIONS FOR EXPERIMENT G: $Fr_1 = 10$, $Re = 8.8 \times 10^4$ ($x/d_1 = 40$).

The correlation function of Mode 1 and Mode 2 is almost identical at this point. Slight larger correlations are observed in Mode 1 for small time lags. The maximum integration limit of equation 2.5 was selected as the time lag with the first cross with the x-axis.

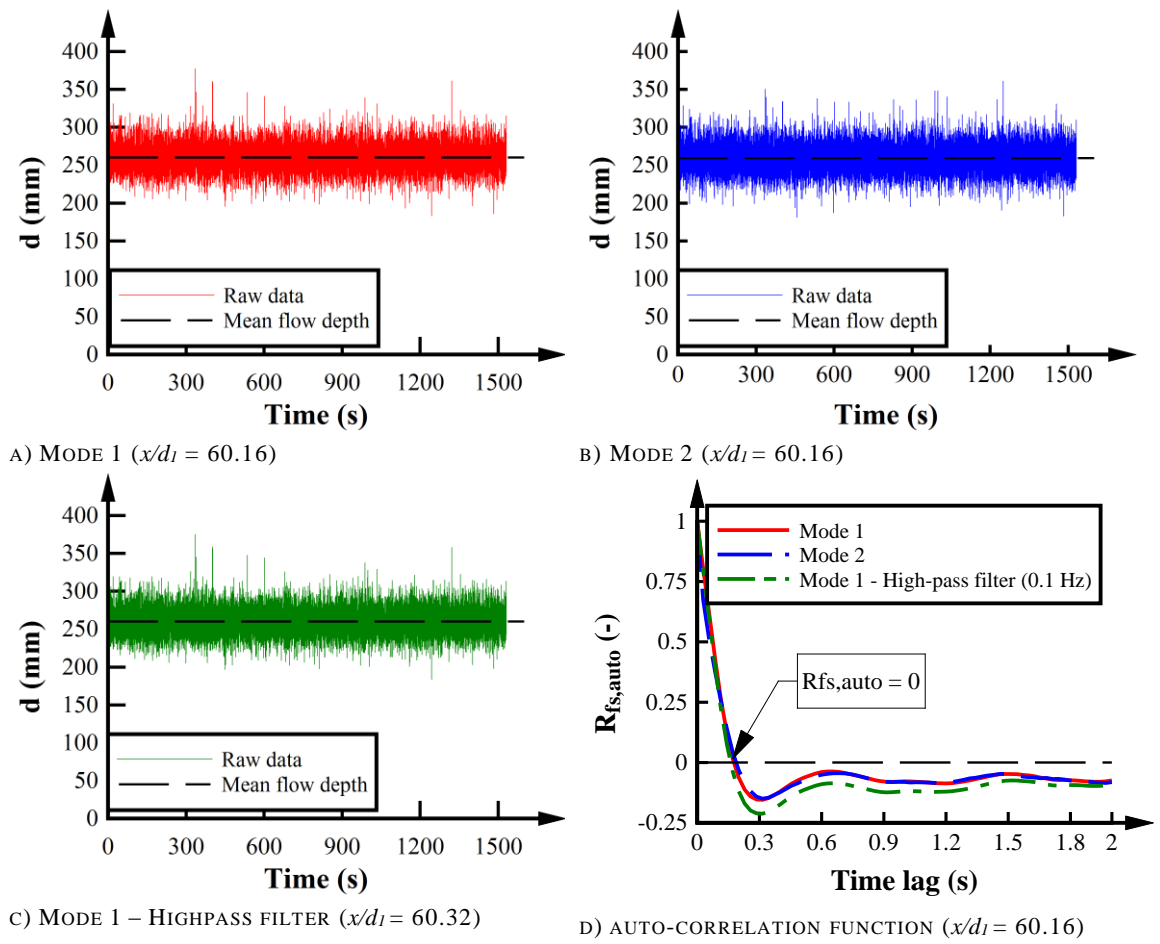


FIGURE G-14. AUTO-CORRELATION FUNCTIONS FOR EXPERIMENT G: $Fr_1 = 10$, $Re = 8.8 \times 10^4$ ($x/d_1 = 60.16$).

Similar to $x/d_1 = 60.16$, the correlation function of Mode 1 and Mode 2 is almost identical at this point. Slight larger correlations are observed in Mode 1 for small time lags. All the correlation curves showed a crossing with the x-axis.

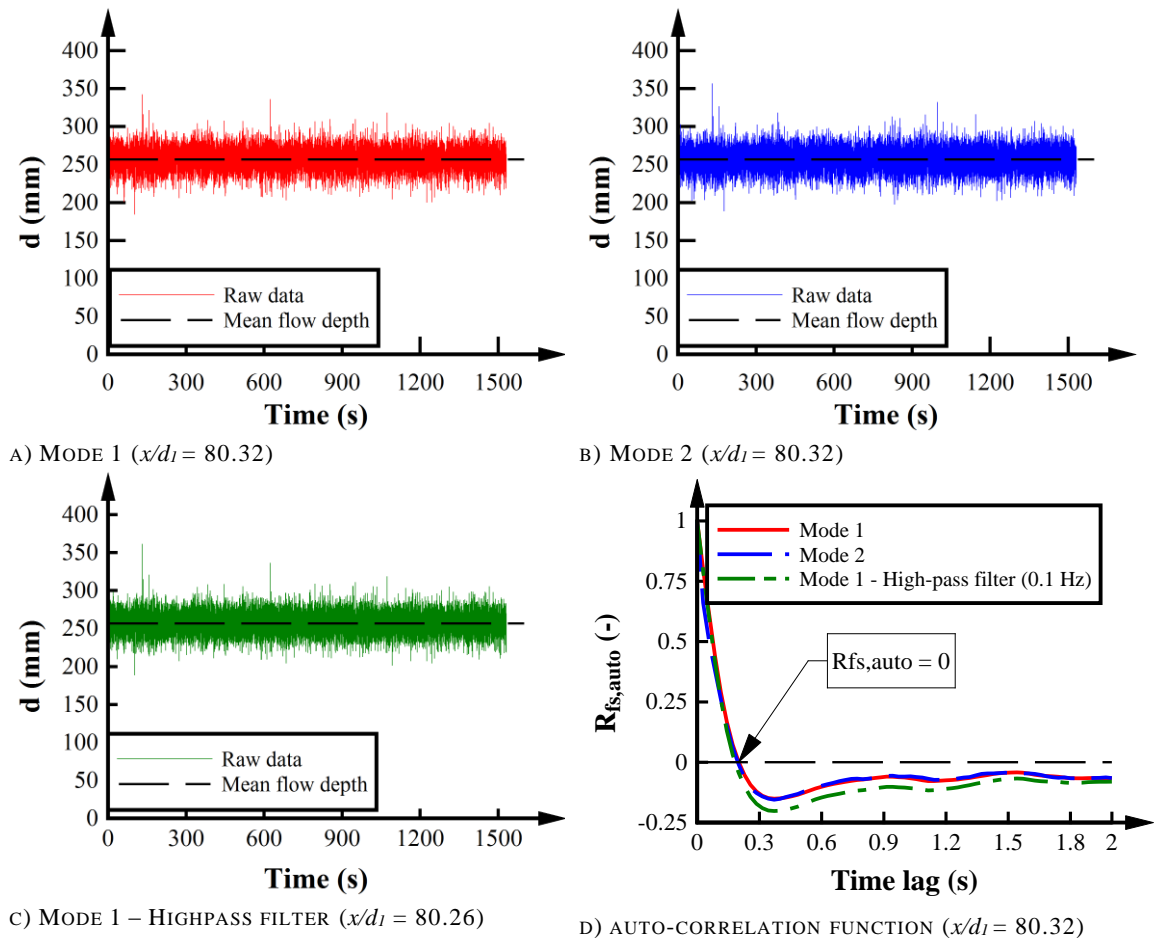
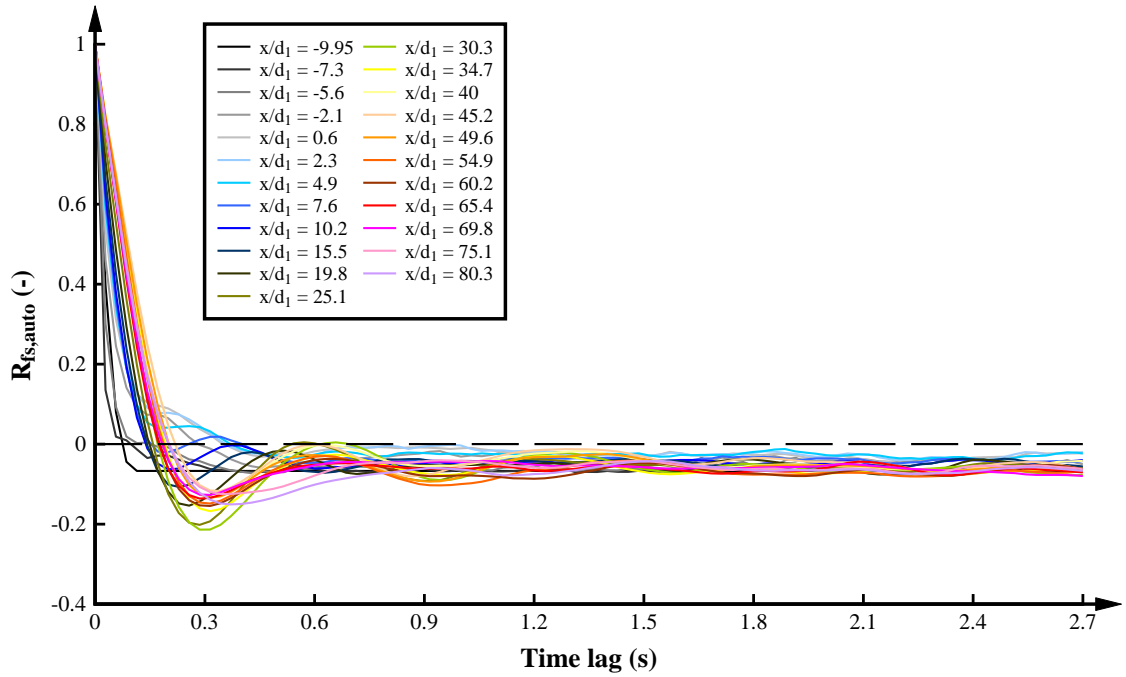
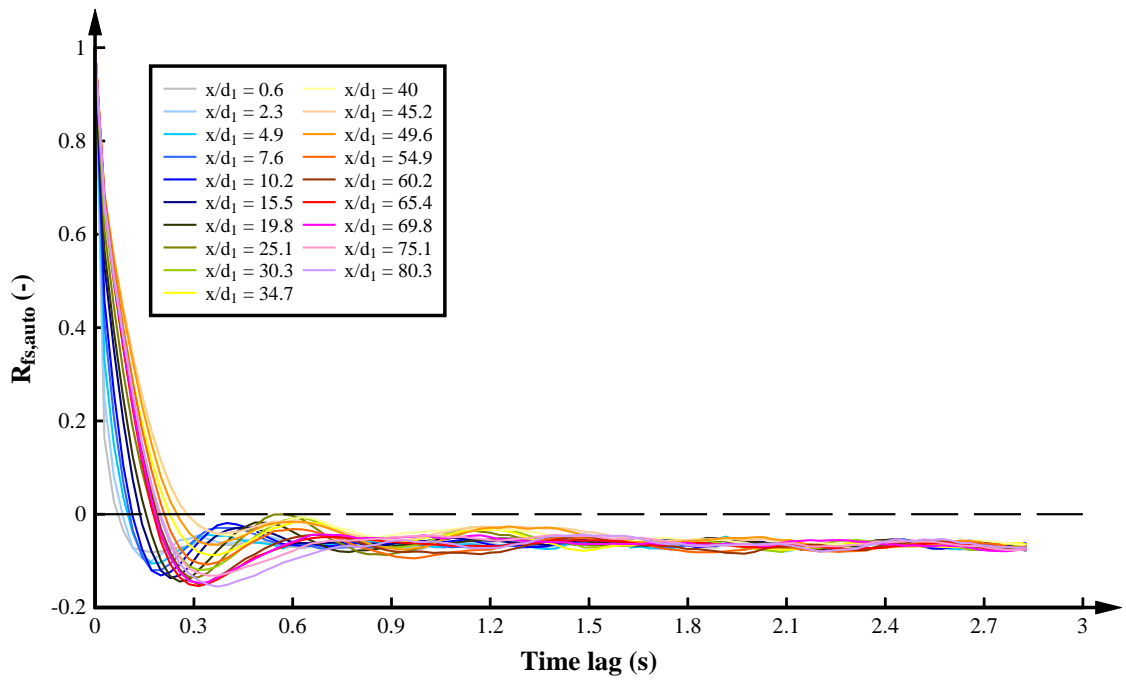


FIGURE G-15. AUTO-CORRELATION FUNCTIONS FOR EXPERIMENT G: $Fr_1 = 10$, $Re = 8.8 \times 10^4$ ($x/d_1 = 80.32$).

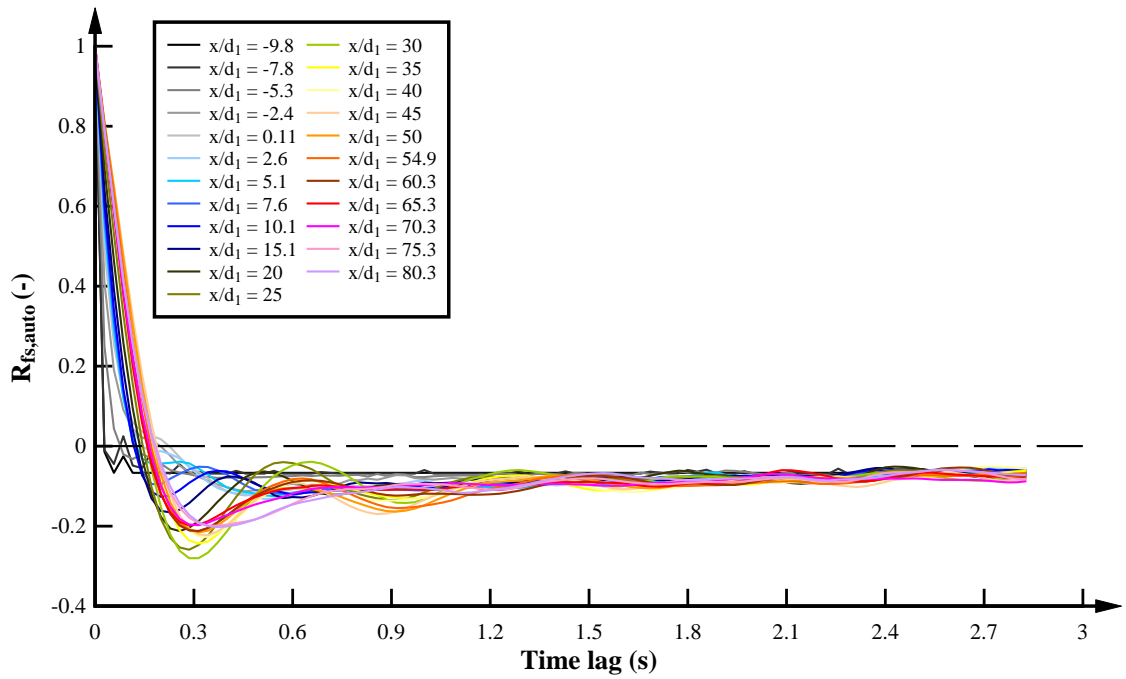
Figure G-16 illustrates the auto-correlation functions along the hydraulic jump for Experiment G and Mode 1 (Figure G-16A), Mode 2 (Figure G-16B), and Mode 1 with high-pass filter (Figure G-16C). Independent of the mode of analysis, all the auto-correlation functions showed a crossing with the x-axis for small time lags. Close to the jump toe, the auto-correlation function showed large deviations between Mode 1 and Mode 2. Further downstream, all the auto-correlation curves were similar. In comparison with Experiment A, Experiment G always showed a crossing with the x-axis suggesting that the strong deviations in Experiment G affected the correlation in the raw data close to the jump toe.



A) AUTO-CORRELATION FUNCTION FOR MODE 1



B) AUTO-CORRELATION FUNCTION FOR MODE 2



C) AUTO-CORRELATION FUNCTION FOR MODE 1 WITH HIGH-PASS FILTER OF 0.1 Hz.

FIGURE G-16. AUTO-CORRELATION FUNCTIONS FOR EXPERIMENT G: $Fr_l = 10$, $Re = 8.8 \times 10^4$.

H. INTERNAL FORCES: DEFINITION STRUCTURAL DESIGN

The design of the most suitable force measurement system was undertaken in a systematic process involving the testing of: i) several different rods with various length and thickness (Figure H-1), ii) various sphere diameters (i.e. $3 \leq \varnothing_{sphere} \leq 8$ cm) and iii) two support frames for the load cell. The present experiments were conducted with a sphere of $\varnothing_{sphere} = 54.64$ mm and the selection process in this section is based upon a sphere with this diameter. Figure H-1 illustrates the tested rods highlighting their diameters and lengths as well as the shape of the selected truss structure.



FIGURE H-1. DIFFERENT ROD DIAMETERS AND LENGTHS TESTED IN THE PRESENT STUDY.

The design of the force measurement system was guided by previously reported internal dominant streamwise frequencies of $freq_p \cong 2.6$ Hz and $freq_p = 8$ to 13 Hz (Wang et al. 2014). Similar characteristic frequencies were expected for the internal forces in the present hydraulic jump. The design of the system was therefore conducted to ensure that the natural frequency of the overall system was above $freq_{Fx,dom} = 13$ Hz. The natural frequency of the signal of the load cell (without any external loads) showed a characteristic signal peak at 50 Hz suggesting an influence of the electrical current. The electrical current frequency was consistently observed in all load cell tests.

The natural frequency for each configuration was tested experimentally using the load cell and exciting the sphere in one direction by hitting once the bottom of the structure above the top of the sphere. The raw force signals for each test were recorded and post processed with an FFT analysis which provided the dominant frequencies of the system (Table H-1). A detailed description of each test conducted is described below:

1. **Test 1:** The first series of experiments were conducted with the sphere attached to a rod of 6 mm. The load cell was attached to a plastic support which was directly connected to a digital height gauge of 60 cm. The gauge was located above a wood sheet of 2 cm

thickness clamped to the sides of the channel (Figure H-2). The natural frequency of the system on air was of about 6 Hz for F_x , F_y and F_z . This frequency was in the range of the characteristic frequencies expected inside the hydraulic jump.

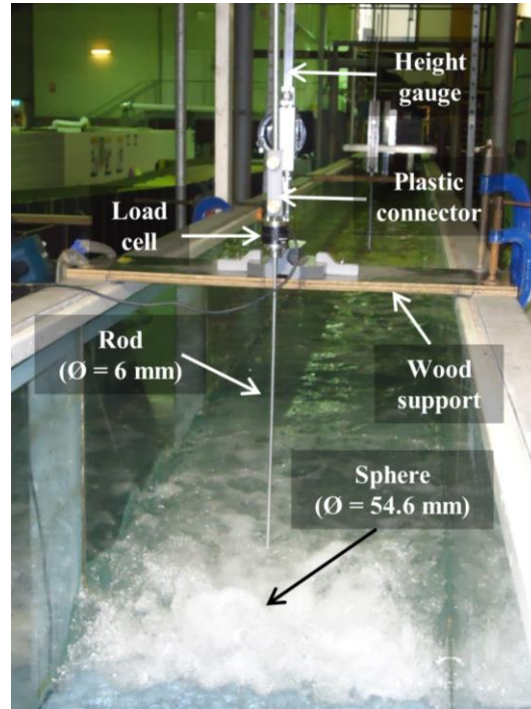


FIGURE H-2. EXPERIMENTAL CONFIGURATION OF THE SENSITIVITY ANALYSIS OF THE NATURAL FREQUENCY – TRIAL 1.

2. **Test 2:** To increase the natural frequency of the system, a thicker rod was analysed with a diameter of 10 mm. The rod had the same length as in Trial 1 and was mounted on the same configuration showed in Figure H-2. However, to increase the stiffness of the system, a wood frame was added at the back of the height gauge. The frame reduced the vibrations at the top of the height gauge resulting in larger natural frequencies in the system. The natural frequency of the system showed a slight increase of 2 Hz resulting in a natural frequency of 8 Hz. However, this frequency was still in the characteristic frequency range observed in hydraulic jumps.

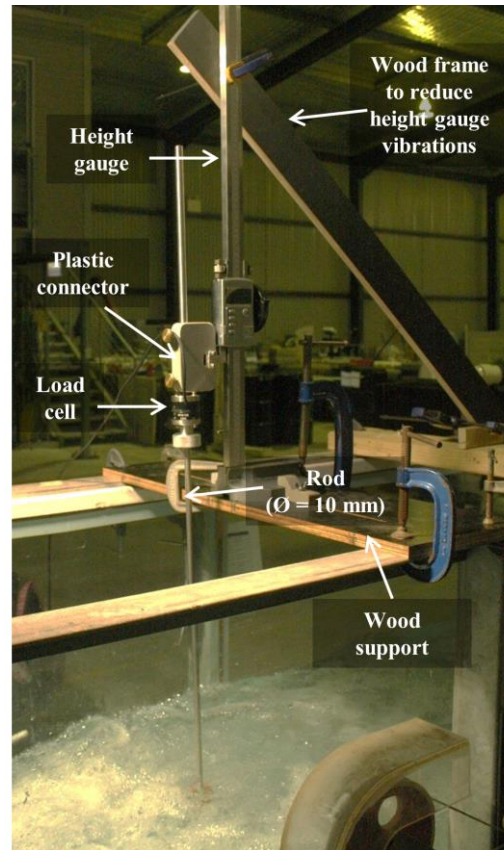


FIGURE H-3. EXPERIMENTAL CONFIGURATION OF THE SENSITIVITY ANALYSIS OF THE NATURAL FREQUENCY – TRIAL 2.

3. **Test 3:** Since the water can act as a dampener, another set of experiments were conducted to identify the natural frequency of the system showed in Trial 2 when the sphere and the rod were under water. To evaluate the effect of the water elevation, the sensitivity analysis was conducted at different elevations. The natural frequencies under water showed a reduction of about 2 Hz compared with the natural frequencies observed on air. The natural frequencies oscillated between 5.7 Hz for the sphere located 22 cm under water to 6.05 Hz when the sphere was submerged 3 cm.
4. **Test 4:** The next experiments were conducted with the same configuration showed in Figure H-3. However, to reduce the natural frequency of the system, the length of the rod was reduced to 40 cm. The natural frequency of the system increased significantly showing resonant frequencies of about 15 Hz for the three axes of the load cell. Despite the increase in the natural frequency, this frequency was still close to the characteristic frequencies observed in hydraulic jumps.
5. **Test 5:** Following the analysis observed in Trial 4, the next experiments evaluated the natural frequency of the system under water and air with rods of about 40 cm and diameters of 12 mm and 16 mm. This analysis did not include the sphere. The natural frequency remained similar to the frequencies observed in trial 4 with natural frequencies 7 – 8.5 Hz under water and 11 – 16 on air. The results suggested that an

increase in the rod diameter did not have a significant effect on the natural frequency of the system and further tests were required to be outside the characteristic frequencies of the hydraulic jump.

- Test 6:** A new system was proposed to increase the natural frequency of the system. The height gauge was changed for a shorter gauge of 40 cm and a truss structure was designed to increase the natural frequency of the system. Different combinations of shapes and diameters were considered in the analysis of the natural frequencies of the truss structure using the software RFEM®. The truss selected generated the largest natural frequencies of about 300 Hz with a $\phi_{truss} = 5$ mm. In addition, the wood support was located inside the channel to create a stiffer system. Figure H-4 presents the experimental configuration of the new system proposed. The natural frequency of the new system increased to 22 Hz. Since the natural frequency of the system was significantly lower than 300 Hz, the resonant frequency of the system was not governed by the truss natural frequency.

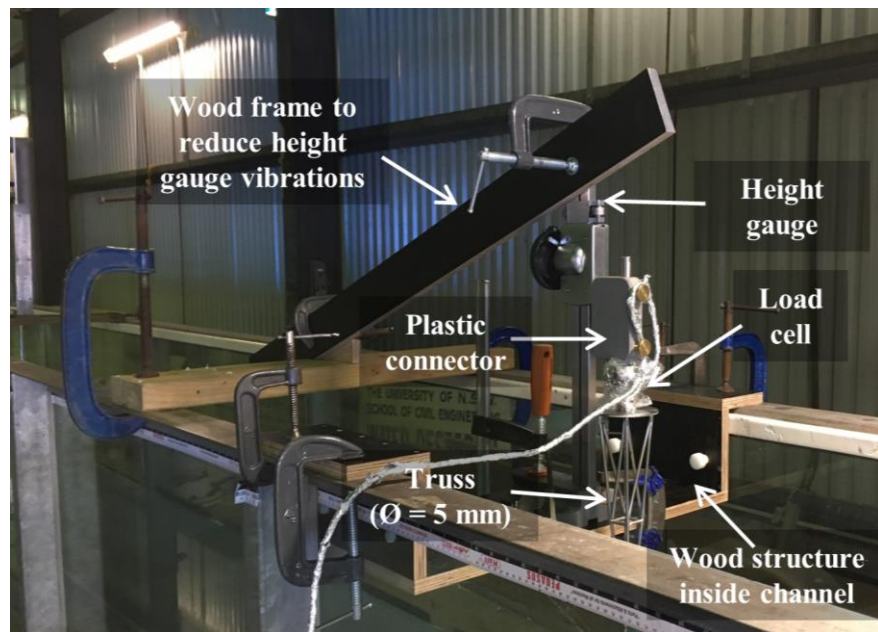


FIGURE H-4. EXPERIMENTAL CONFIGURATION OF THE SENSITIVITY ANALYSIS OF THE NATURAL FREQUENCY – TRIAL 6.

- Test 7:** Despite the truss connected to the sphere increased the natural frequency of the system, the frequency was still in a range close to the internal frequencies of the hydraulic jump. Therefore, since the wood can act as a dampening, Trial 7 proposed a metal support instead of the wood support used in previous trials (Figure H-5). However, the resonant frequency of the system remained almost constant with natural frequency values between 22 – 26 Hz.

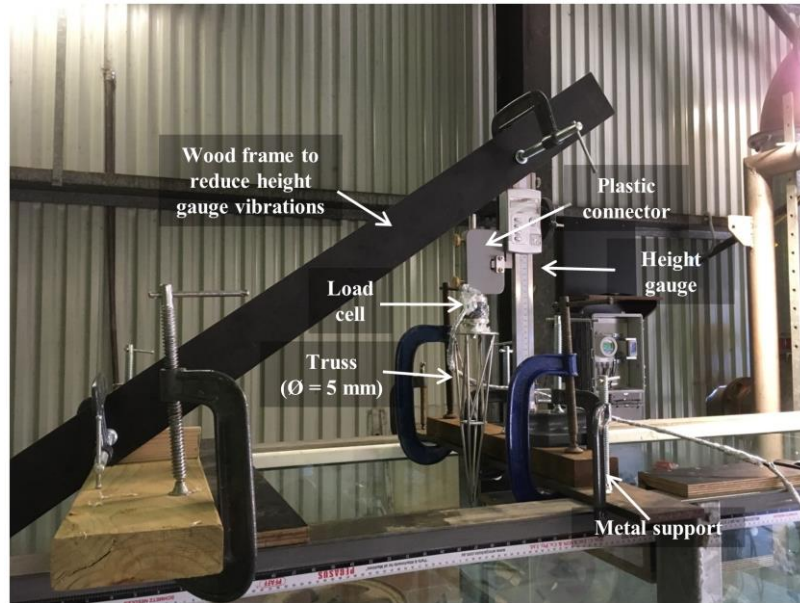


FIGURE E-5. EXPERIMENTAL CONFIGURATION OF THE SENSITIVITY ANALYSIS OF THE NATURAL FREQUENCY – TRIAL 7.

- Test 8:** Since the metal support did not show any effect on the natural frequency, the new setup proposed in Trial 8 considered the change of the digital height gauge for a metal support attached to the horizontal metal support shown in Figure H-5. Figure H-6 presents a preliminary configuration aiming to test the natural frequencies of the system without the digital height gauge. With the new configuration, the natural frequency of the system increased to 31 Hz.

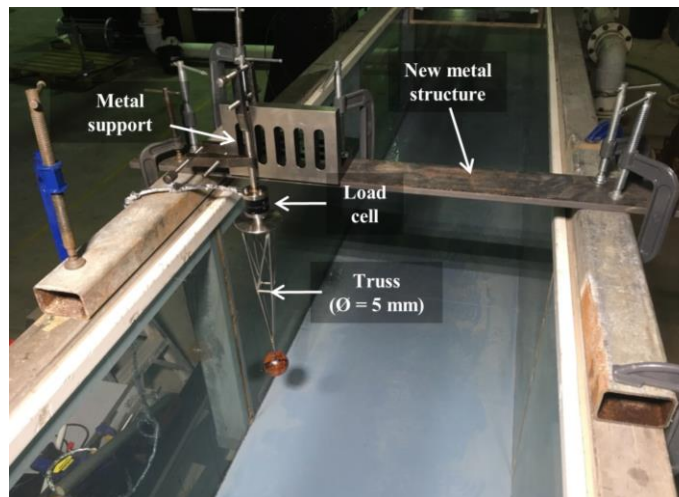


FIGURE H-6. EXPERIMENTAL CONFIGURATION OF THE SENSITIVITY ANALYSIS OF THE NATURAL FREQUENCY – TRIAL 8.

- Test 9:** A further analysis was conducted by hitting the channel side and recording the vibration frequency with the load cell. Unfortunately, the load cell was able to capture the vibrations occurring at the channel suggesting a strong effect of the natural frequency of the channel into the resonant frequency of the system. Based on the recordings, the channel natural frequencies were of about 12 Hz and 31 Hz. Since it was

not possible to increase the natural system of the channel itself, the design selected for the analysis of the forces in the hydraulic jump considered the preliminary setup showed in Figure H-6.

10. **Final design:** A final design was proposed considering the construction of the stiffest structure. The new structure consisted in thick metal connected to the channel sides. At the channel centreline, a thick metal rod allowed the change of the elevation of the load cell. This rod was connected to a 5 cm thick metal structure which held the load cell. The sphere was connected to the load cell with a truss of 5 mm which generated larger natural frequencies compared with the rods analysed. The natural frequencies in water with the present setup were of 30 Hz. Since the maximum internal frequency in the hydraulic jump was of about 13 Hz, the natural frequency of the system seemed valid to do not interfere with the force measurements.

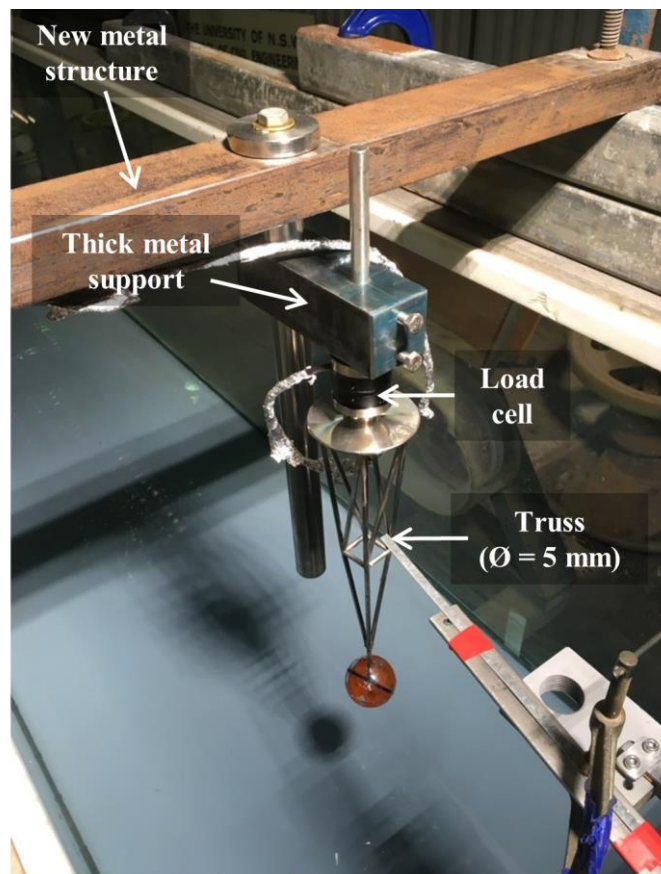


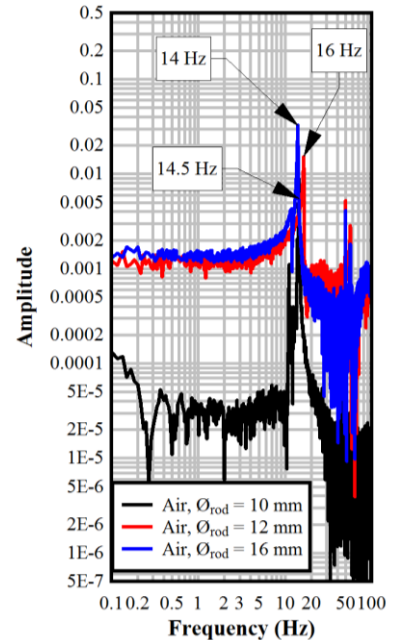
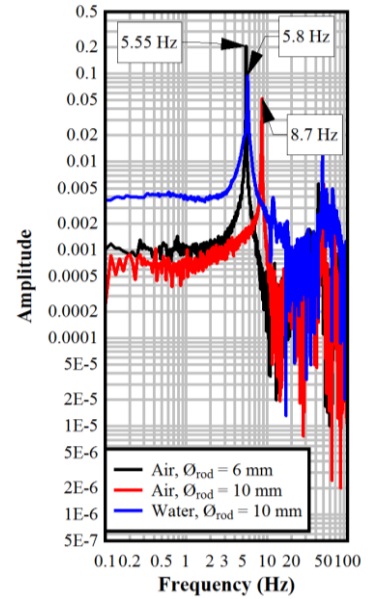
FIGURE H-7. EXPERIMENTAL CONFIGURATION OF THE SENSITIVITY ANALYSIS OF THE NATURAL FREQUENCY – TRIAL 9.

Table H-1 summarises the specifics of the tested rods including description of the structure, the rod diameter \varnothing_{rod} and rod length L_{rod} as well as characteristic resonant frequencies in x-direction of the tested configurations in air and in water respectively for three different truss systems(i.e. the connection between load cell and sphere), for different rod thicknesses and

lengths (Configuration 1 and 2) and for different support structures (Configuration 3). Similar results were observed for the natural frequency analyses in y- and z-directions

TABLE H-1. CHARACTERISTICS OF THE INVESTIGATED SPHERE HOLDING SYSTEMS IN THE PRESENT STUDY; $\varnothing_{sphere} = 54.64$ mm.

Config.	Description	Holding system	$\varnothing_{rod}, \varnothing_{truss}$ (mm)	L_{rod} (cm)	Resonant frequency (Hz)
1	Digital height gauge of 60 cm Support: Wood sheet	Rod	6	60	Air: 5.5
		Rod	10	60	Air: 9 / Water: 5.8
2	Digital height gauge of 60 cm Support: Wood sheet	Rod	10	40	Air: 14.5
		Rod	12	40	Air: 16
		Rod	16	40	Air: 14



Config.	Description	Holding system	$\varnothing_{rod}, \varnothing_{truss}$ (mm)	L_{rod} (cm)		Resonant frequency (Hz)
3	Digital height gauge of 40 cm Support: Wood sheet	Truss	5	30	Air: 25	
	Digital height gauge of 40 cm Support: Metal sheet	Truss	5	30	Air: 26	
	Sturdy metal structure + attached height scale Support: Thick metal sheet	Truss	5	30	Air: 34	

I. INTERNAL FORCES

I.1. INTRODUCTION

The hydraulic jump is characterised by three-dimensional motions within the transition region from supercritical to subcritical flow. Apart from some characterisation of the one-dimensional analysis of the internal motions in hydraulic jumps in the pressure fluctuations at the channel bed (e.g. Abdul Khader and Elango 1974; Fiorotto and Rinaldo 1992) and streamwise pressure fluctuations at different elevations (Wang et al. 2014b), the distribution of the three-dimensional motions along the hydraulic jump remains widely unclear. Herein, the present study measured the three-dimensional forces and interpreted motions in hydraulic jumps with a six-axis load cell connected to a sphere and its support structure.

I.2. STREAMWISE FORCES

The streamwise forces were measured with the load cell in the channel centreline at different elevations and cross-sections along the hydraulic jump. The streamwise forces on the sphere were susceptible to the positive and negative motions occurring insight the hydraulic jump in x-direction showing a periodic oscillation around the mean. Figure I-1 presents an example of a typical streamwise force raw signal close to the jump toe. The raw signal showed large streamwise force fluctuations f_x within a range of $-2.06 < f_x < 3.23$ N and a positive mean force of $F_x = 0.56$ N. Signal smoothing with 100 points (black line) and 1000 points (blue line) highlighted the periodic oscillation of the streamwise force fluctuation around the mean (Figure I-1). Overall, Figure I-1 shows the instability of the hydraulic jump and its dynamic behaviour with a large number of streamwise force fluctuations. The magnitude, amplitude and fluctuation patterns of the streamwise forces were dependant on the Froude and Reynolds numbers. This sections presents the distributions of the streamwise forces in hydraulic jumps.

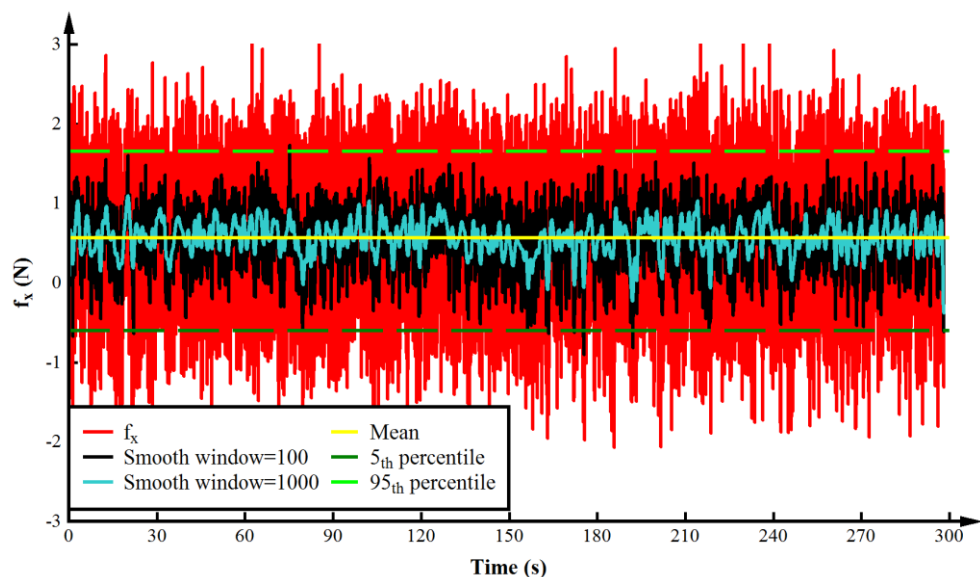


FIGURE I–1. STREAMWISE FORCES ON A SPHERE SUBMERGED INTO A HYDRAULIC JUMP; EXPERIMENT A: $Fr_1 = 5.1$, $Re = 8.3 \times 10^4$, FULLY DEVELOPED INFLOW CONDITIONS, $x/d_1 = 8$, $y/d_1 = 1.54$.

I.2.1. TIME-AVERAGED STREAMWISE FORCES

The time-averaged streamwise forces F_x were recorded for a period of 450 s close to the jump toe and 300 s further downstream. Figure I-2 shows the time-averaged dimensionless streamwise force $F_x/F_{u/s}$ as function of the dimensionless flow depth y/d_1 , where $F_{u/s}$ is the incoming total force on a width equal to the sphere diameter comprising the hydrostatic component F_I and the dynamic component ρQV_1 just upstream the hydraulic jump over the full inflow depth d_1 . F_x decreased with the increase in the distance from the jump toe x/d_1 . For all cross-sections, larger streamwise forces were recorded close to the channel bed at $y/d_1 \approx 1$ which may be related to the maxima in the wall jet-like velocities in hydraulic jumps close to the channel bed (Rajaratnam 1965; Ohtsu et al. 1990; Chanson and Brattberg 2000). For regions close to the jump toe, at $x/d_1 \leq 8$, $F_x/F_{u/s}$ decreased with increasing elevation reflecting the velocity distributions in hydraulic jump with larger flow velocities close to the channel bed and negative velocities in the recirculation region in the upper part of the jump. Further downstream, $x/d_1 > 8$, the forces became more uniform across the flow column linked with a more uniform velocity distribution (Figure I-2). For $x/d_1 \geq 13$, most of the forces on the sphere at different elevation agreed well with an estimated drag force $F_{D,d/s}$ based upon the cross-sectional average velocity at the downstream end of the hydraulic jump ($F_{D,d/s} = 0.5 \times C_d \times \rho \times A_s \times V_2^2$ where $C_d \approx 0.44$ based on the Reynolds number, A_s is the sphere area and V_2 is the average velocity at the downstream end of the hydraulic jump). The maximum time-averaged drag force on the sphere at $x/d_1 = 3$ was about 10% of the upstream net force, 7.5% at $x/d_1 = 5.5$, about 5% at $x/d_1 = 5.5$ and less than 2.5% for $x/d_1 > 8$. The forces on the partially submerged sphere in the upper part of the flow column were overall similar to the fully submerged sphere despite stronger data scatter. The overall shape of the streamwise force distributions were in agreement with the vertical profiles of the mean total pressure distributions recorded with the pressure sensor for comparable Froude numbers (Wang et al. 2014b).

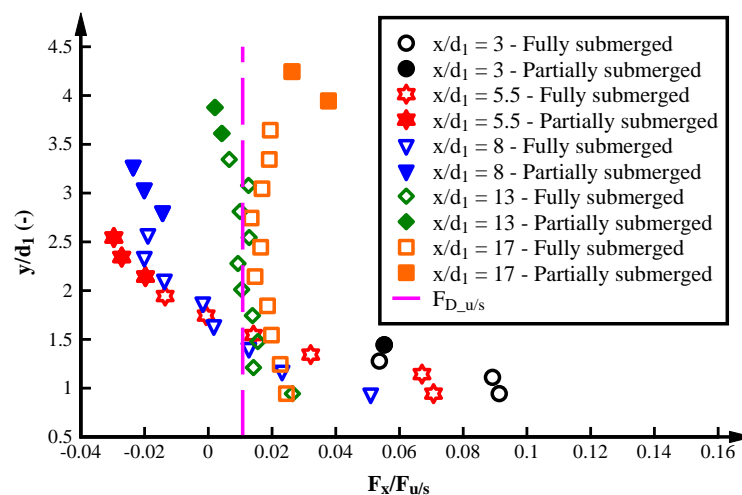
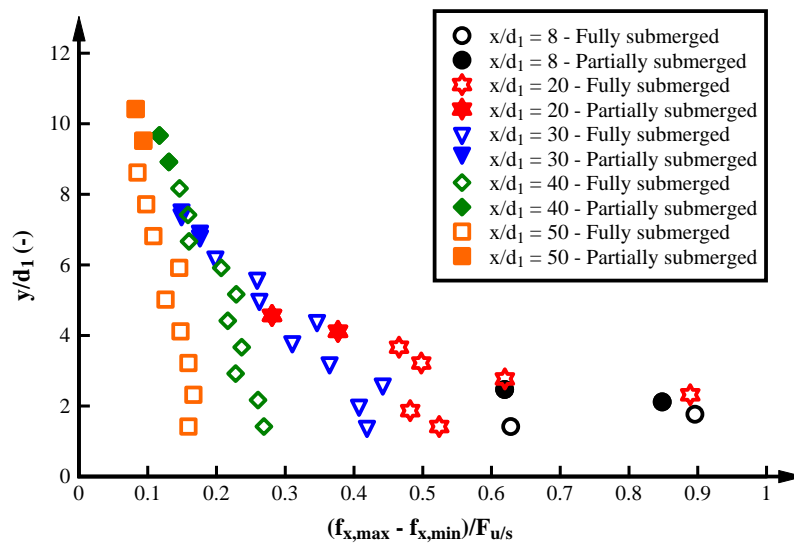


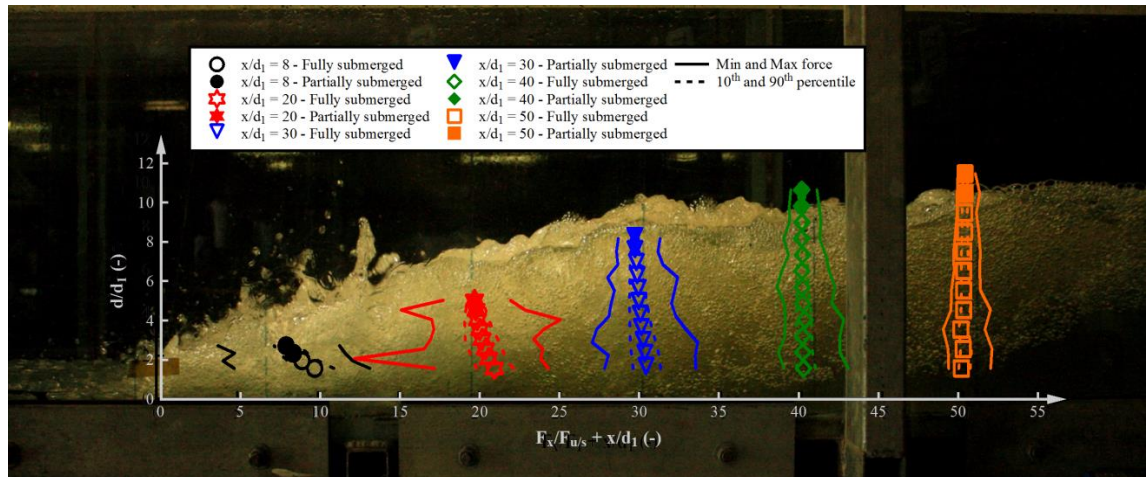
FIGURE I-2. DISTRIBUTION OF THE TIME-AVERAGED STREAMWISE FORCES AT DIFFERENT CROSS-SECTIONS ALONG THE HYDRAULIC JUMP. EXPERIMENT H: $Fr_I = 3.8$, $Re = 6.2 \times 10^4$, FULLY DEVELOPED INFLOW CONDITIONS.

I.2.2. AMPLITUDE OF STREAMWISE FORCES

The difference between the maximum and minimum streamwise forces is the streamwise force amplitude, i.e. $f_{x,max} - f_{x,min}$. The maximum and minimum values were estimated based upon the complete data set since any outlier was already filtered by the phase-space thresholding method. Figure I-3A presents typical vertical distributions of the streamwise force amplitudes. Larger amplitudes were observed close to the jump toe with decreasing amplitudes along the hydraulic jumps reflecting a reduction in flow motions. The amplitude had a maximum peak in a region equivalent to the local maximum in void fraction followed by a reduction with increasing the vertical distance from the channel bed. Overall, the largest force amplitudes and motions were recorded in the shear region of the hydraulic jump and close to the jump toe. Note that at the downstream end of the jump ($x/d_1 \geq 20$) and close to the free surface, the maximum amplitude reached an almost constant dimensionless value of 0.1 equivalent to 1.5 N (Figure I-3A). This value was similar for all experiments and may indicate an inherent oscillation pattern at the downstream end of the jump due to the remaining turbulence of the hydraulic jump itself and potentially some oscillations in the water body between the end of the hydraulic jump and the downstream tailgate. Figure I-3B overlaps a photography of the hydraulic jump and the respective distribution of the streamwise force parameters including the mean, minimum, maximum and 10th and 90th. The largest streamwise force amplitudes occurred in the most aerated areas close to the jump toe while smaller amplitudes were recorded in the least aerated regions. Figure I-3B provides an alternative visualization of the strongest motions inside hydraulic jumps including regions with largest streamwise motions and a decay in forces with increasing distance from the jump toe and the channel bed respectively.



A) DISTRIBUTION OF AMPLITUDES IN STREAMWISE FORCES



B) VISUALISATION OF STREAMWISE FORCES INCLUDING MINIMUM AND MAXIMUM FORCES AND 10TH AND 90TH PERCENTILES

FIGURE I-3. STREAMWISE FORCES IN A HYDRAULIC JUMP. EXPERIMENT E: $Fr_1 = 8.5$, $Re = 7.5 \times 10^4$, FULLY DEVELOPED INFLOW CONDITIONS.

I.2.3. STREAMWISE FORCE FLUCTUATIONS

The streamwise force fluctuations are represented by the standard deviations of the streamwise force signal. Figure I-4 shows typical distributions of the dimensionless streamwise force fluctuations F_x'/F_{u_s} at different cross-sections along the hydraulic jump as function of y/d_1 . The largest fluctuations in the streamwise force were observed close to the jump toe at $x/d_1 = 8$ (Figure I-4). Note that the largest force fluctuations did not occur in the cross-section immediately at the jump toe ($x/d_1 = 3$) which may be related to the large data uncertainty at this position due to the effect of the jump toe oscillations affecting the sphere submersion. The fluctuations decreased with increasing distance from the jump toe. For $x/d_1 \leq 13$, F_x'/F_{u_s} showed a maximum peak at $y/d_1 \approx 2$ within the shear region (Figure I-4). This peak occurred in a higher elevation compared to the peak observed in the time-averaged streamwise forces and agreed with the location of the maximum bubble count rate. The force fluctuations decreased with increasing elevation with lowest fluctuations in the recirculation region of the jump roller. At the downstream end of the jump ($x/d_1 = 30$), the streamwise force fluctuations were almost constant and independent of the elevation (Figure I-4). Overall, the streamwise force fluctuations were larger in the shear region and close to the jump toe while lower fluctuations were recorded close to the free-surface and at the downstream end of the hydraulic jump. The results agreed with the trends in pressure fluctuations in flow direction measured by Wang et al. (2014) for comparable Froude and Reynolds numbers.

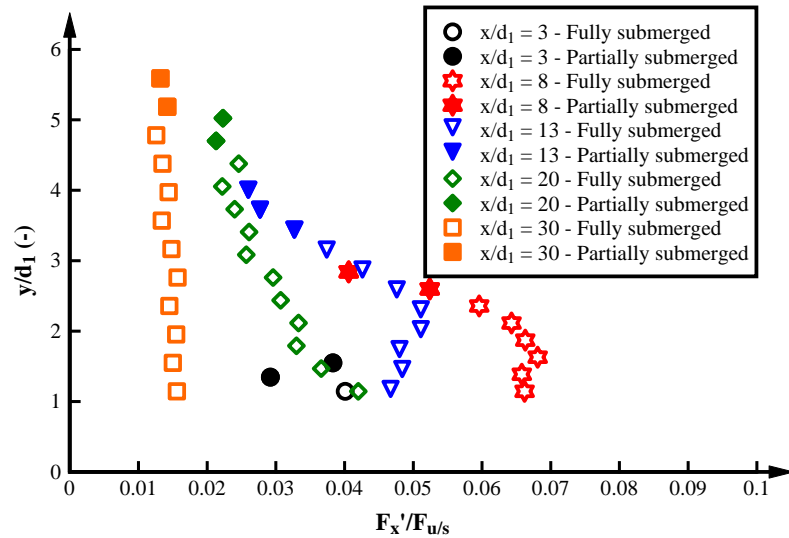


FIGURE I-4. DISTRIBUTION OF STREAMWISE FORCE FLUCTUATIONS AT DIFFERENT CROSS-SECTIONS ALONG THE HYDRAULIC JUMP. EXPERIMENT B: $Fr_1 = 5.1$, $Re = 6.2 \times 10^4$, FULLY DEVELOPED INFLOW CONDITIONS.

I.2.4. CHARACTERISTIC FREQUENCIES OF THE STREAMWISE FORCE FLUCTUATIONS

A spectral analysis of the streamwise forces was conducted for all experiments. Typical results are illustrated in Figure I-5 presenting the FFT and the characteristic frequencies at different locations along the hydraulic jump including the raw signal data without filtering (blue line), force data with a low-pass filter of 20 Hz (red line) and a smoothing of 100 points of the low-pass filter data (black line). The characteristic frequency peaks represented the largest energy density. Due to the type of internal flow motions in hydraulic jumps, the frequency spectrum showed high energy for a wide range of frequencies and the dominant characteristic frequency in the present study was selected as the frequency with the highest peak within the range of larger energy density. Close to the jump toe, the low-pass filtered data presented two characteristic peaks with frequencies of 0.3 Hz and 22 Hz. The first frequency was consistent with the jump toe oscillation frequency. The second peak represented the maximum limit of the low-pass filter suggesting that the characteristic peak was larger as observed in the raw data without filtering (blue line) and the system was self-excited by the internal frequency motions of the hydraulic jump. At $x/d_1 = 8$, the characteristic frequencies of the system were below the resonant frequency with two characteristic frequencies between 0.2-0.5 Hz and 5-8 Hz. The first range was similar to the characteristic frequency of the jump toe oscillations and the second range was similar to streamwise frequencies recorded with a pressure sensor by Wang et al. (2014b). At $x/d_1 = 20$, the frequency spectrum was different. A characteristic frequency of 0.2 Hz and a second peak at 6.25 Hz were observed. In contrast with previous locations, the second peak showed considerable lesser energy density compared with the first peak indicating that the contribution of the second peak was minor. Note that for $x/d_1 \geq 8$, the characteristic frequencies observed in the hydraulic jump were below the resonant frequency of the system of 27 to 29 Hz. Note that the resonant frequency of the system was self-excited by the internal motions in the

hydraulic jump for regions located close to the jump toe for $Fr_1 > 3.8$. Further research and structural design should be conducted to increase the resonant frequency of the system above the streamwise internal frequencies recorded in the hydraulic jump. Further downstream, at $x/d_1 > 8$, the system was not self-excited for most of the present experiments.

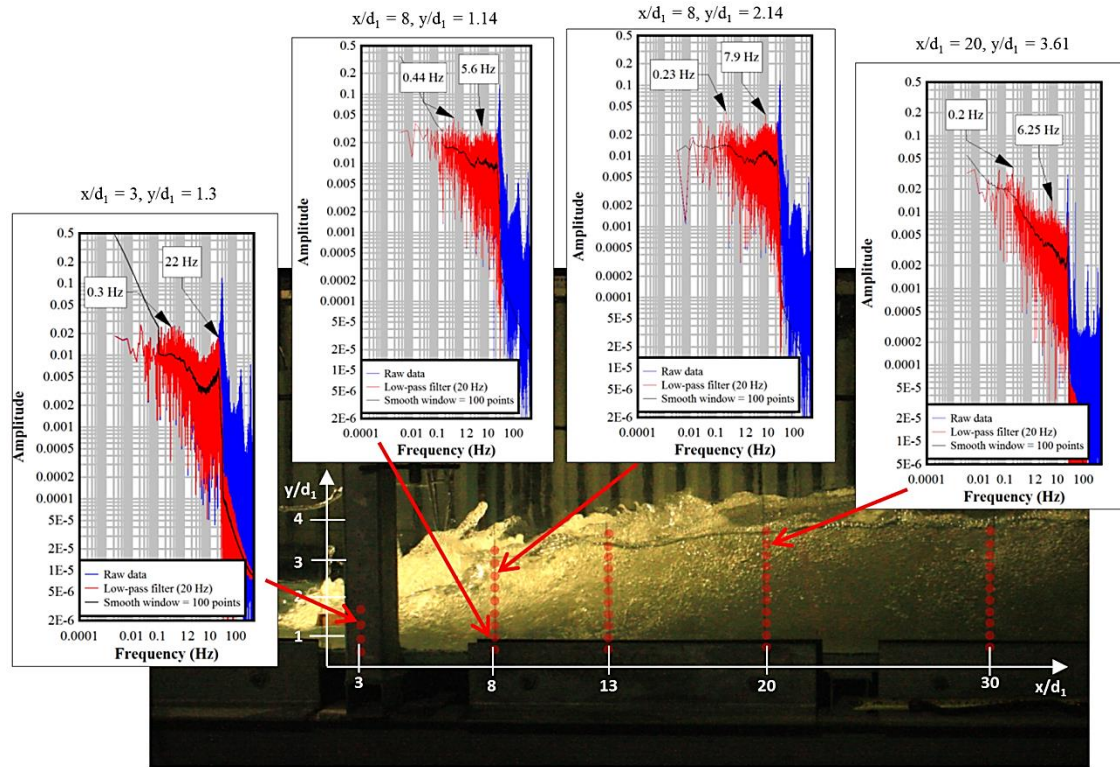


FIGURE I-5. SPECTRAL ANALYSIS AND CHARACTERISTIC FREQUENCIES OF THE STREAMWISE FORCES INSIDE A HYDRAULIC JUMP. EXPERIMENT B: $Fr_1 = 5.1$, $Re = 6.2 \times 10^4$, FULLY DEVELOPED INFLOW CONDITIONS.

Figure I-6 presents the dominant $freq_{Fx,dom}$ and secondary $freq_{Fx,sec}$ frequencies of the streamwise force fluctuations. Figure I-6A illustrates the dominant streamwise frequencies for four cross-sections and at various elevations while Figure I-6B shows the corresponding secondary frequencies. The data showed the most distinct peak in the frequency spectrum analysis as well as the range of frequencies with large energy density (vertical lines). No secondary frequencies were observed at $x/d_1 = 40$. This may be linked to the small streamwise force fluctuations towards the downstream end of the hydraulic jump.

Overall there was close agreement in terms of dominant and secondary streamwise frequencies for the four cross-sections ($x/d_1 \leq 40$) (Figure I-6). Independent of the cross-section and the elevation, the dominant frequency peaks were in the range of $0.3 \leq freq_{Fx,dom} \leq 1$ Hz (Figure I-6A), which was consistent with the frequencies observed in terms of jump toe oscillations (Mossa and Tolve 1998; Chanson and Gualtieri 2008; Murzyn and Chanson 2009a; Montano et al. 2018). Close to the jump toe, the frequency ranges were large with frequencies between 0.1 Hz to 6.5 Hz at most. This large frequency range may be linked with the strong turbulence and instability of the hydraulic jump in this region yielding in large number of frequencies with distinctive energy density. For some measurement locations, a secondary

frequency peak $freq_{Fx,sec}$ was also observed with most of the secondary frequencies between $3 \leq freq_{Fx,sec} \leq 12$ Hz; close to the jump toe, $freq_{Fx,sec} > 20$ Hz (Figure I-6B). These peaks were not considered in the analysis of characteristic frequencies in the hydraulic jump since they were close to the resonant frequency of the system. Further research is required to identify the characteristic frequency of the system close to the jump toe.

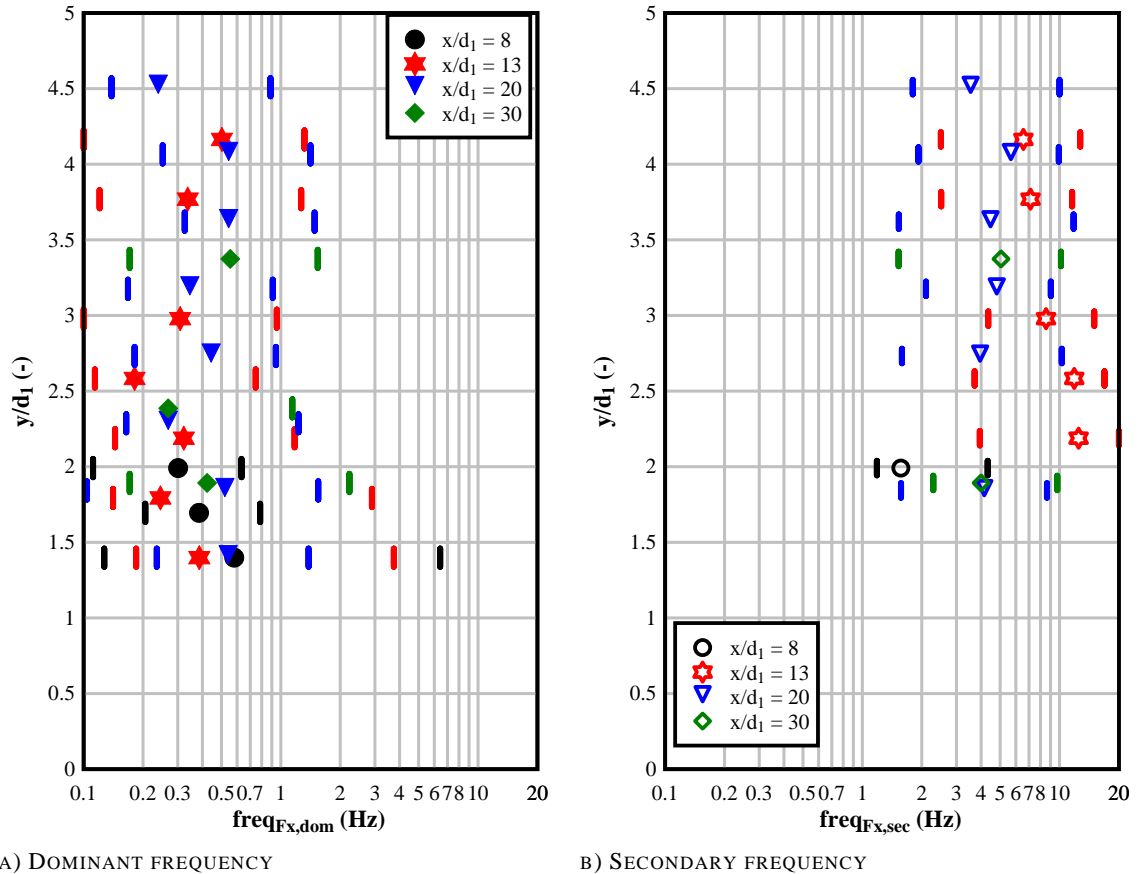


FIGURE I-6. CHARACTERISTIC FREQUENCIES OF THE STREAMWISE FORCES INSIDE THE HYDRAULIC JUMP; SYMBOLS INDICATE DISTINCTIVE PEAK IN FREQUENCIES AND VERTICAL LINES THE FREQUENCY RANGE OF THESE PEAKS. EXPERIMENT C: $Fr_1 = 7.0$, $Re = 6.2 \times 10^4$, FULLY DEVELOPED INFLOW CONDITIONS.

Figure I-7 presents $freq_{Fx,dom}$ and $freq_{Fx,sec}$ of the streamwise forces at different elevations and cross-sections for all present experiments with fully developed inflow conditions. Despite large data scatter, the characteristic frequencies could be grouped into two frequency ranges between 0.1 to 1.5 Hz and 1.5 to 20 Hz. The majority of the experiments showed dominant frequencies within the range of $0.15 < freq_{Fx,dom} < 1.5$ Hz (Figure I-7A). These frequencies are consistent with the characteristic frequencies of the jump toe motions suggesting a strong influence of the jump toe oscillations on the streamwise internal motions. Note that $freq_{Fx,dom}$ between 2 and 12 Hz could be observed for experiments with $Fr_1 \leq 5.1$, $x/L_r > 0.2$ and $y/d_1 > 1.5$ indicating that the jump toe motions were not the dominant streamwise frequency in the hydraulic jump at these locations and the streamwise force was dominated by faster motions. The faster dominant frequencies were only identified in weak hydraulic jumps ($Fr_1 < 5.1$) and further research is required to analyse the dominant frequency spectrum in stronger hydraulic

jumps without the influence of the system resonancy. Figure I-7B presents $freq_{Fx,sec}$ observed in the hydraulic jumps. Most of the frequencies were identified between 3 and 13 Hz. These frequencies may represent the frequency of the internal streamwise motions in hydraulic jumps. For $Fr_1 \leq 5.1$, $x/d_1 > 0.2$ and $y/d_1 > 1.5$, some secondary frequencies were observed between $0.2 < freq_{Fx,sec} < 1.5$, which were consistent with the dominant frequencies for hydraulic jumps with $Fr_1 > 5.1$ (Figure I-7A).

Overall, the streamwise characteristic frequencies were strongly dominated by the jump toe oscillations with dominant frequencies 0.15 to 1.5 Hz. The range was found for different Froude and Reynolds numbers, at different elevations and cross-sections along the hydraulic jump. A further frequency range of the internal streamwise motions was between 2 and 12 Hz. These frequencies were similar to the dominant frequencies observed in pressure fluctuations of 8 to 13 Hz and for $3.8 < Fr_1 < 8.5$ (Wang et al. 2014b).

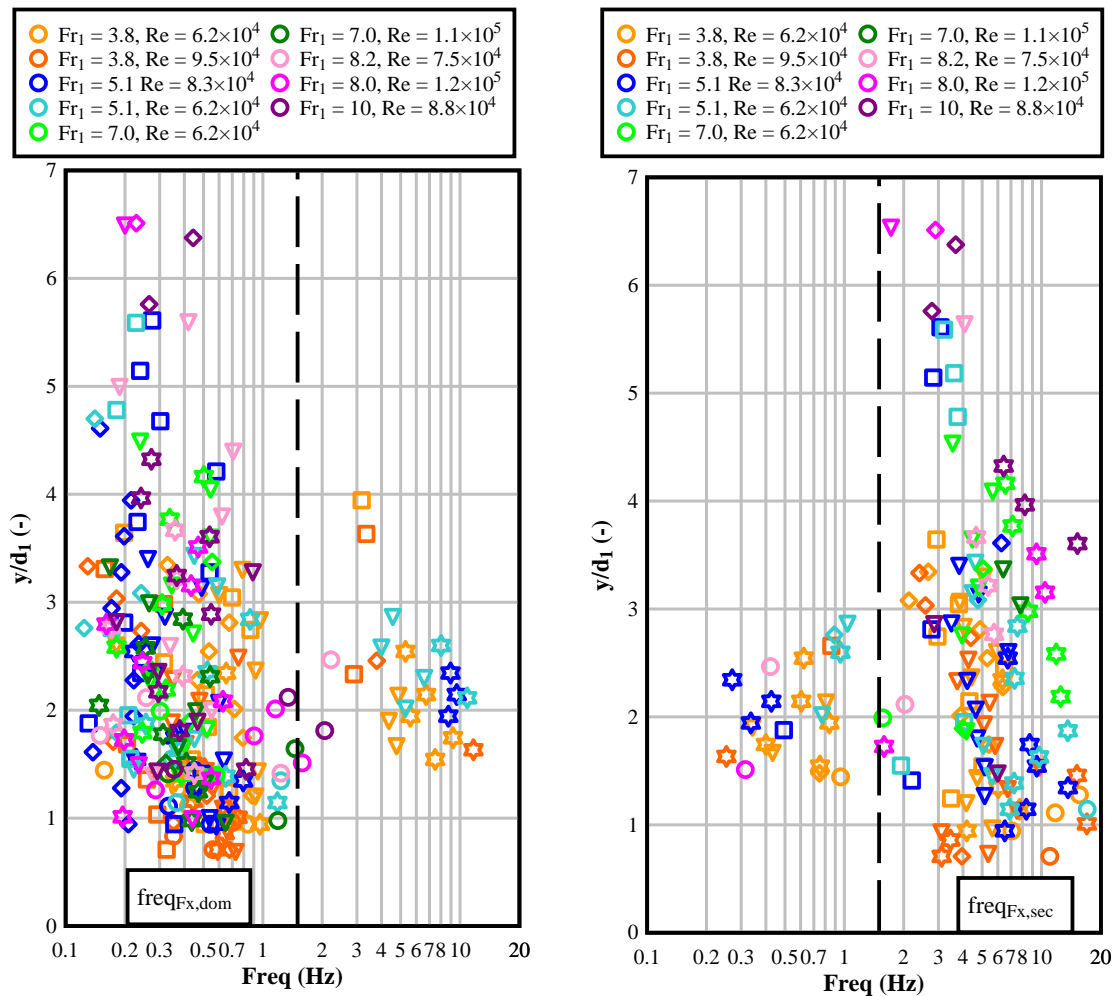


FIGURE I-7. SUMMARY OF THE CHARACTERISTIC FREQUENCIES OF THE STREAMWISE FORCES IN THE HYDRAULIC JUMPS WITH FULLY DEVELOPED INFLOW CONDITIONS; SYMBOLS INDICATE DISTINCTIVE PEAK FREQUENCIES AT DIFFERENT CROSS-SECTIONS: ● $x/L_r < 0.2$, ★ $0.2 < x/L_r < 0.45$, ▼ $0.45 < x/L_r < 0.68$, ◆ $0.67 < x/L_r < 0.9$ AND ■ $0.9 < x/L_r < 1.2$.

I.2.5. AUTO-CORRELATION TIME SCALE OF THE STREAMWISE FORCES

The auto-correlation time scale of the streamwise forces T_{Fx} estimated the longitudinal advective time of the internal turbulent structures. Note that the auto-correlation time scale is strongly dependant on the magnitude of the drag forces and sphere size ($\varnothing = 54.64$ mm in the present study). Figure I-8 presents the vertical distributions of $T_{Fx} \times V_1/d_1$ at different cross-sections along the hydraulic jump. The auto-correlation time scales were similar at elevations in the lower part of the hydraulic jump (Figure I-8). In the upper part, the auto-correlation time scales gradual increased indicating larger turbulent structures in the recirculation region (Figure I-8). This increase is consistent with observations of air-water auto-correlation time scales in the advective structures in hydraulic jumps (Wang 2014). In the present study, T_{Fx} also increased with increasing distance from the jump toe. This result indicated lower correlation and smaller ‘lifetime’ of the turbulent structures close to the jump toe while large structures were more persistent at the downstream end of the jump (Figure I-8). This result is in agreement with the findings of Long et al. (1991) highlighting growing vortices along the hydraulic jump. A local minimum in the auto-correlation time scales was observed in the shear region for most of the cross-sections suggesting the shortest lifetime of the large structures within the shear region. The minimum is located close to the maximum streamwise force fluctuations indicating large instability in this region which lead to a reduction in signal correlation. More prominent minima were observed with increasing Froude number. Note that unrealistically large time scales were observed at the downstream end of hydraulic jumps with large Froude numbers and they were not considered in the analysis since they may be linked with the slow wavy profile at the downstream end of the hydraulic jump instead of with the characteristic turbulent eddies observed within the hydraulic jump.

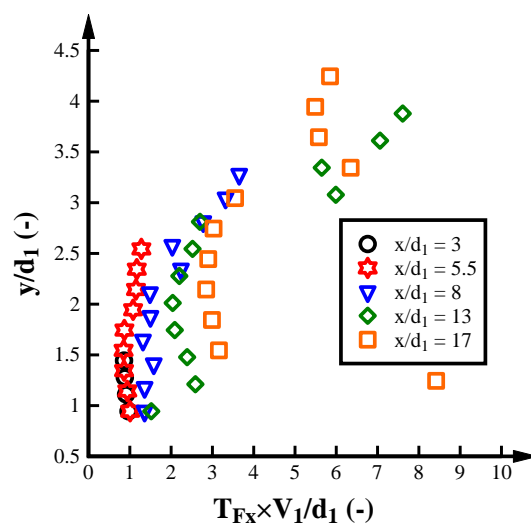


FIGURE I-8. AUTO-CORRELATION TIME SCALES OF THE STREAMWISE FORCES ON A SUBMERGED SPHERE INSIDE A HYDRAULIC JUMP. EXPERIMENT H: $Fr_1 = 3.8$, $Re = 6.2 \times 10^4$, FULLY DEVELOPED INFLOW CONDITIONS.

I.2. TRANSVERSE FORCES

The transverse forces on the submerged sphere inside the hydraulic jump provides some insights into the lateral motions. For the first time, these lateral internal forces were measured. The experiments were conducted in channel centreline and at different cross-sections along the hydraulic jump. The first observations of transverse motions inside a hydraulic jump provide novel information to better understand the three-dimensionality and the energy dissipation rates of hydraulic jumps. Figure I-9 shows a typical raw signal of the transverse forces on the submerged sphere f_z for the sampling duration of 300 s. The force raw signal showed a periodic oscillation around the mean of -0.05 N with a minimum force of -3.06 N and a maximum force of 2.95 N. Note that the mean transverse force was close to zero as expected from the transverse force measurements in the centreline of a symmetric hydraulic jump. The raw signal was smoothed with 100 points (black line) and 1000 points (blue line) respectively providing better illustration of the oscillatory pattern around the mean. The present chapter presents the distribution of the transverse forces along hydraulic jumps with different Froude and Reynolds numbers and different inflow conditions.

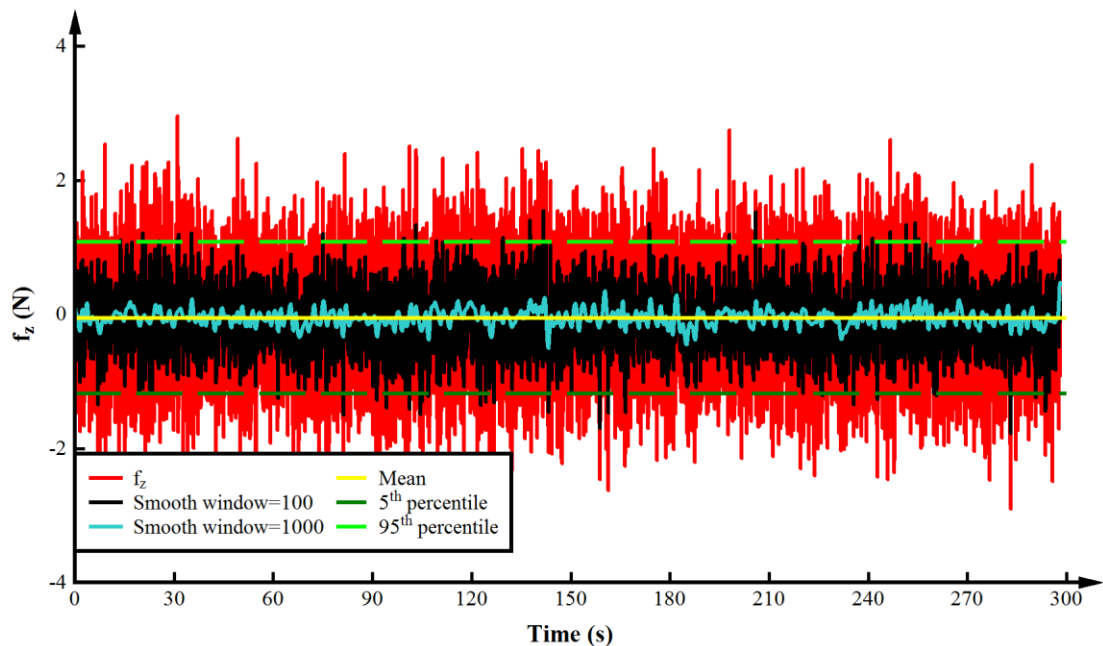


FIGURE I-9. TRANSVERSE FORCE ON A SUBMRGED SPHERE INSIDE A HYDRAULIC JUMP FOR EXPERIMENT B: $Fr_1 = 5.1$, $Re = 6.2 \times 10^4$, FULLY DEVELOPED INFLOW CONDITIONS, $x/d_1 = 8$, $y/d_1 = 1.63$.

I.5.1. TIME-AVERAGED TRANSVERSE FORCES

The time-averaged transverse forces F_z were recorded for a period of 450 s close to the jump toe and 300 s further downstream. Figure I-10 presents the time-averaged dimensionless transverse force $F_z/F_{u/s}$ as function of y/d_1 . The mean transverse force were overall close to zero in channel centreline for all experiments. This result highlighted the symmetry of the present experiments. Small deviation of about 0.1 N were observed for data near the channel bed and close to the jump toe which may be linked with strong fluctuations in this region, instrument

accuracy and potential non-symmetric inflow conditions. Similar trends were observed for all present hydraulic jumps. No differences were identified between the partially and fully submerged sphere in the upper part of the flow column.

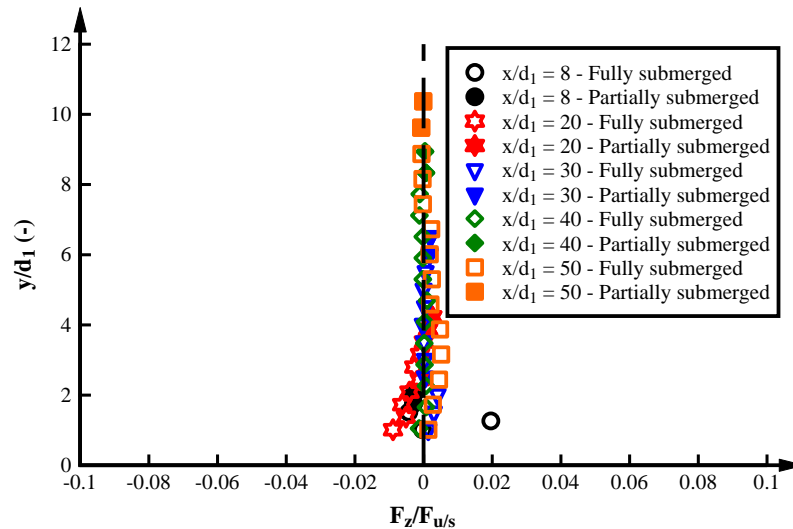


FIGURE I-10. VERTICAL DISTRIBUTION OF TIME-AVERAGED TRANSVERSE FORCES ALONG THE HYDRAULIC JUMP. EXPERIMENT F: $Fr_1 = 8.0$, $Re = 1.2 \times 10^5$, FULLY DEVELOPED INFLOW CONDITIONS.

I.5.2. AMPLITUDE OF TRANSVERSE FORCES

The amplitude of the minimum and maximum transverse forces ($f_{z,max} - f_{z,min}$) was estimated for all hydraulic jumps. Figure I-11 illustrates an example of the vertical distributions of the dimensionless amplitudes at different cross-sections along the hydraulic jump. The transverse force amplitudes decreased with increasing distance from the jump toe in agreement with the dissipative process observed in hydraulic jumps. For regions close to the jump toe ($x/d_1 \leq 13$), the transverse force amplitude had a local peak close to the channel bed and the amplitude decreased linearly with increasing elevation above this peak. The peak in amplitude indicated large transverse fluctuations close to the jump toe. The vertical position of the peak increased with increasing distance from the jump toe, which was consistent with the overall direction of the roller movement. Note that the peak occurred below the locations of maximum void fraction and bubble count rates in the shear region suggesting no direct correlation between the amplitude of the transverse forces and the air-water flow properties in the streamwise direction. For $x/d_1 > 13$, the transverse force amplitudes were almost constant independent of the elevation suggesting similar transverse motions at the downstream end of hydraulic jumps. Overall, the transverse force amplitudes highlighted strong movements for $x/d_1 \leq 13$ for all present the experiments.

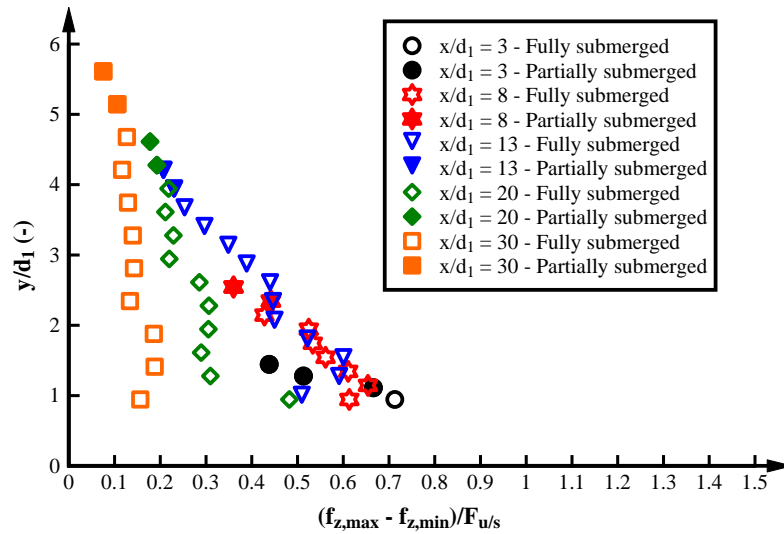


FIGURE I-11. DIMENSIONLESS DISTRIBUTIONS OF THE TRANSVERSE FORCE AMPLITUDES ALONG A HYDRAULIC JUMP. EXPERIMENT A: $Fr_1 = 5.1$, $Re = 8.3 \times 10^4$, FULLY DEVELOPED INFLOW CONDITIONS.

I.5.3. TRANSVERSE FORCE FLUCTUATIONS

The transverse force fluctuations F_z' showed a maximum fluctuation close to the jump toe followed by a linear decay with increasing elevation indicating maximum transverse fluctuations near the channel bed and smaller movements near the free-surface (Figure I-12). This result was consistent along the hydraulic jump even in regions located far from the jump toe ($x/d_1 = 20$). Overall F_z' tended to decrease along the hydraulic jump suggesting lesser force fluctuations at the downstream end of the jump. The lower fluctuations close to the jump toe at $x/d_1 = 8$ (Figure I-12) may be associated with the proximity to the oscillating jump toe and the low flow depth affecting the overall force measurements. Close similarity in the shapes of the transverse force fluctuation profiles were found in the upper part of the hydraulic jump suggesting similar transverse fluctuations in the recirculation region. The transverse force fluctuations were largest close to the bed and close to the jump toe highlighting the regions of larger motions which may be linked with the dissipative processes occurring in the hydraulic jump.

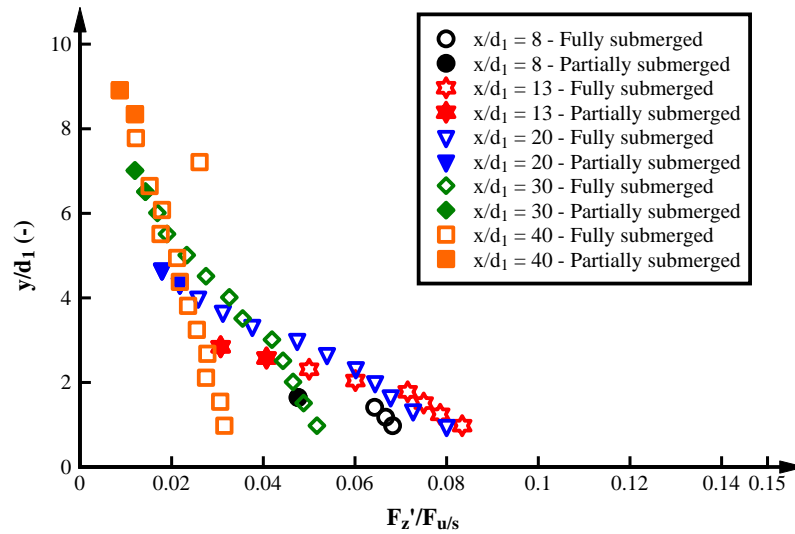


FIGURE I-12. DIMENSIONLESS DISTRIBUTIONS OF THE TRANSVERSE FORCE FLUCTUATIONS ALONG A HYDRAULIC JUMP. EXPERIMENT D: $Fr_1 = 7.0$, $Re = 1.1 \times 10^5$, FULLY DEVELOPED INFLOW CONDITIONS.

I.5.4. CHARACTERISTIC FREQUENCIES OF THE TRANSVERSE FORCE FLUCTUATIONS

Figure I-13 presents a typical frequency spectrum and characteristic frequencies of the transverse forces. The frequency spectrum showed distinctive peaks at different locations along the hydraulic jump. Close to the jump toe, the filtered frequency spectrum showed two peaks at 0.27 Hz and 20 Hz (Figure I-13). The first peak was similar to the jump toe oscillation frequencies while the latter represents the maximum limit of the low-pass filter suggesting self-excitation of the system (As observed in the streamwise frequency spectrum). Further downstream ($x/d_1 = 20$), dominant frequencies of 4 to 7 Hz were observed and a secondary frequency of 0.3 Hz was identified. The former frequencies may be related with the internal periodic motions inside the hydraulic jump. For $x/d_1 = 30$, one single characteristic frequency of 4.8 Hz was observed. Note that for $Fr_1 \geq 7.0$ the transverse forces were affected by the system's self-excitation in particular at locations close to the jump toe.

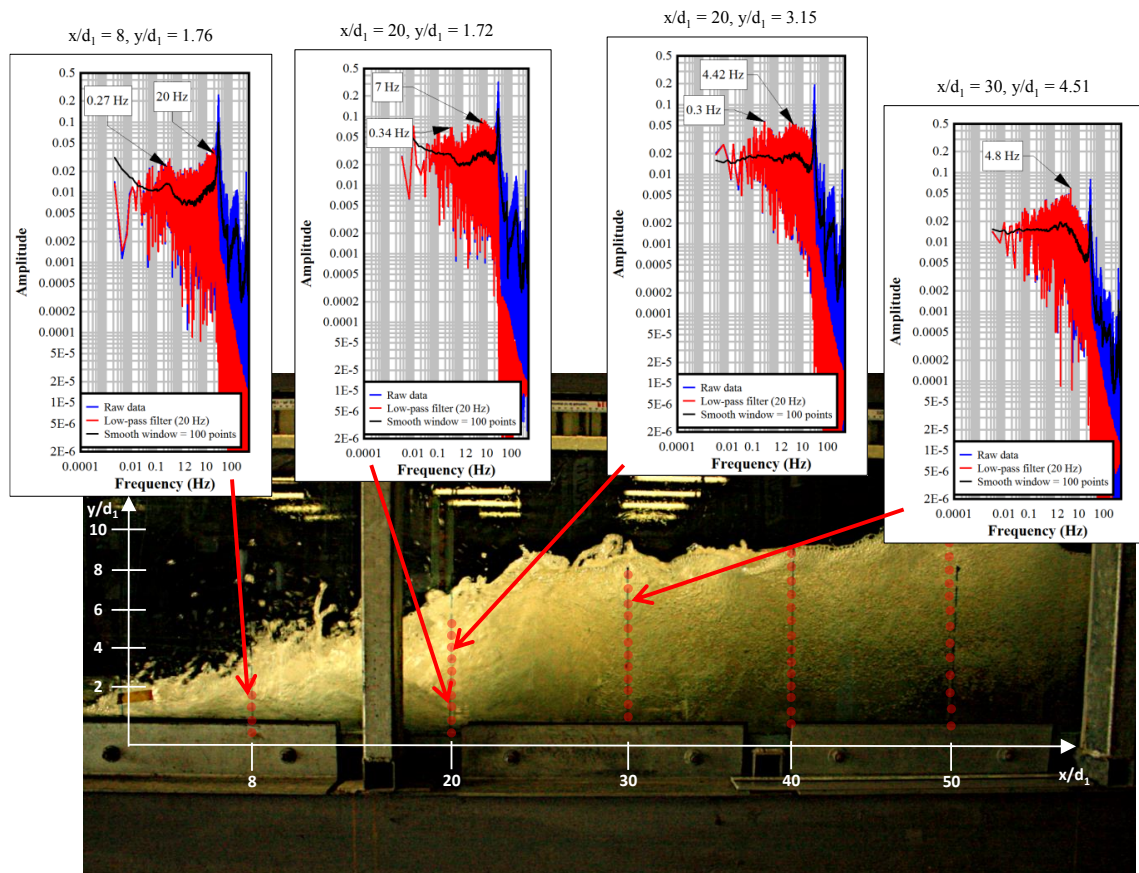
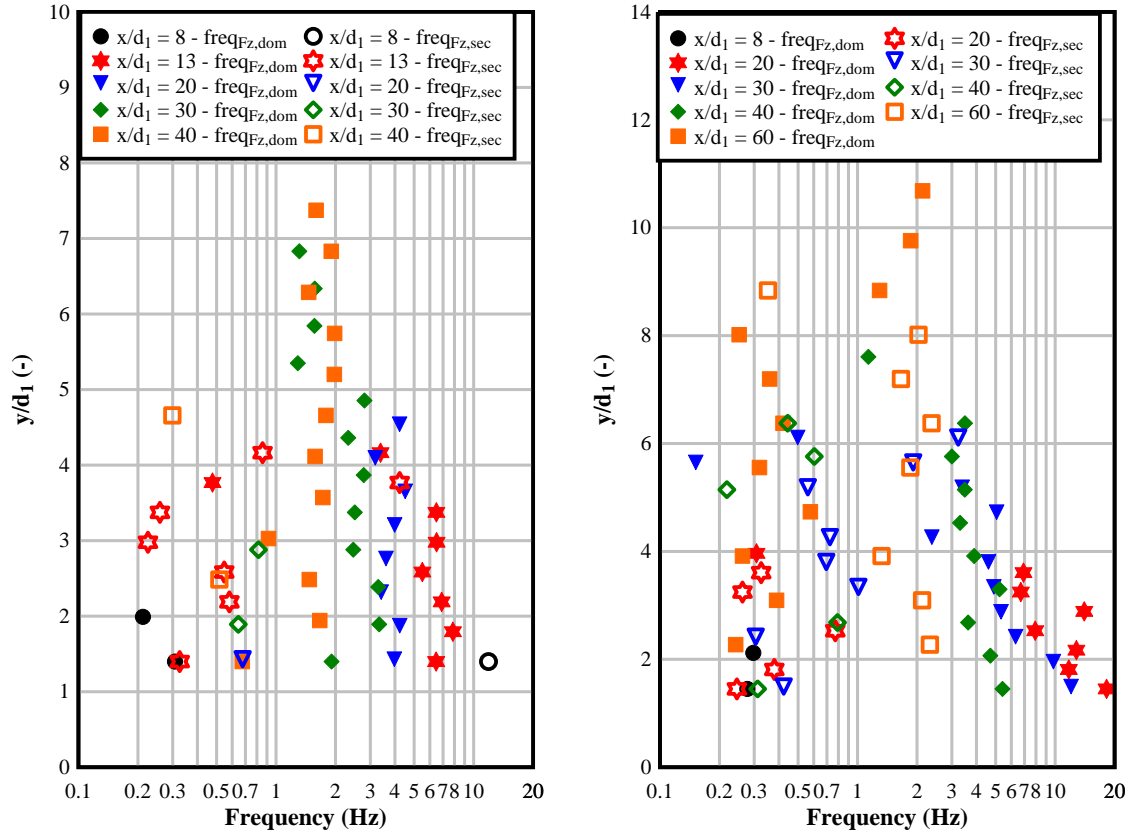


FIGURE I-13. SPECTRAL ANALYSIS AND CHARACTERISTIC FREQUENCIES OF THE TRANSVERSE FORCES ON A SUBMERGED SPHERE INSIDE A A HYDRAULIC JUMP. EXPERIMENT F: $Fr_1 = 8.0$, $Re = 1.2 \times 10^5$, FULLY DEVELOPED INFLOW CONDITIONS.

Figure I-14 shows the vertical distribution of the dominant and secondary frequencies of the transverse forces for three experiments with different Froude number. For all experiments, $0.2 < freq_{Fz,dom} < 1$ were observed close to the jump toe highlighting the strong influence of the jump toe oscillations in this region. Further downstream, dominant frequencies between $2 < freq_{Fz,dom} < 20$ were observed with larger frequencies observed close to the jump toe and lower frequencies at the downstream end of the jump. For experiments with $Fr_1 \leq 7.0$, the dominant frequencies were similar at difference elevations independent of the location within the hydraulic jump. In contrast, $freq_{Fz,dom}$ for $Fr_1 = 10$ at $x/d_1 = 20$ and 30 decreased with elevation highlighting stronger motions close to the channel bed. The dominant frequency at the downstream end of a hydraulic jump with $Fr_1 = 10$ was $0.3 < freq_{Fz,dom} < 1$ highlighting significant influence of the jump toe motions along strong hydraulic jumps. Generally most of the secondary frequencies were similar to the jump toe oscillation frequency indicating an influence of the jump toe oscillations on the internal motions of hydraulic jumps.



A) EXPERIMENT C: $Fr_1 = 7.0$, $Re = 6.2 \times 10^4$ – FULLY DEVELOPED

B) EXPERIMENT G: $Fr_1 = 10$, $Re = 8.8 \times 10^4$ – FULLY DEVELOPED

FIGURE I-14. VERTICAL DISTRIBUTIONS OF CHARACTERISTIC FREQUENCIES OF THE TRANSVERSE FORCES ON A SUBMERGED SPHERE IN HYDRAULIC JUMPS.

I.5.5. AUTO-CORRELATION TIME SCALES OF THE TRANSVERSE FORCE

The auto-correlation time scales of the transverse forces on the submerged sphere ($\phi = 54.64$ mm) T_{F_z} represent a characteristic time of the transverse motions. Figure I-15 presents the vertical distributions of $T_{F_z} \times V_1 / d_1$ at different cross-sections along the hydraulic jump. $T_{F_z} \times V_1 / d_1$ increased with increasing distance from the jump toe. This result suggested smaller lifetime of the large vortical turbulent structures close to the jump toe linked with faster fluctuations and instabilities in this region. Three regions could be distinguished in terms of $T_{F_z} \times V_1 / d_1$. Close to the jump toe, $T_{F_z} \times V_1 / d_1$ remained almost constant at different elevations indicating a similar structure of the large transverse vortices. Further downstream, the auto-correlation time scales gradually increased with increasing elevation. At the downstream end of the jump, the transverse auto-correlation time scales decreased with increasing elevation up to a minimum in the upper part of the shear region followed by an increase in the recirculation region (Figure I-15). Overall, the transverse auto-correlation time scales indicated small internal motions close to the jump toe which increased along the downstream direction and with increasing elevation. Herein the auto-correlation times were consistent with the visual observations of the development of large vortical structures inside hydraulic jumps (Long et al. 1991).

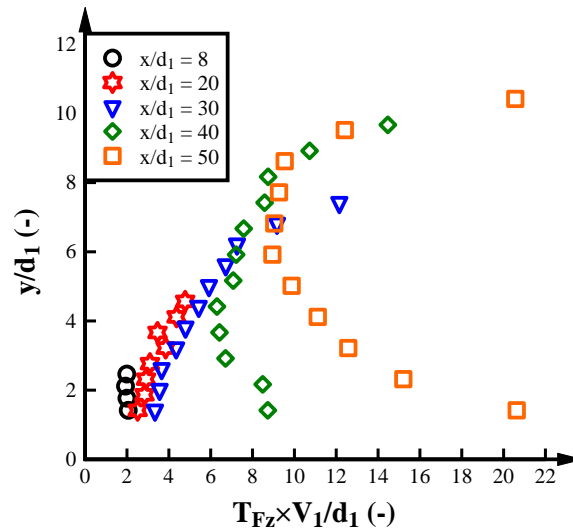


FIGURE I-15. AUTO-CORRELATION TIME SCALES OF THE TRANSVERSE FORCES ON A SUBMERGED SPHERE. EXPERIMENT E: $Fr_1 = 8.2$, $Re = 6.2 \times 10^4$, FULLY DEVELOPED INFLOW CONDITIONS.

I.3. VERTICAL FORCES

The vertical forces on the submerged load cell represented upwards or downwards movements of the flows around the sphere. While previous studies have recorded the vertical pressure fluctuations at the channel bed below hydraulic jumps with pressure transducers (e.g. Schiebe and Bowers 1971; Abdul Khader and Elango 1974; Fiorotto and Rinaldo 1992), only the total pressure above the channel bed was measured. There is currently no information about the vertical motions inside hydraulic jumps. Herein, the present study measured profiles of the vertical forces on a submerged sphere along the hydraulic jumps providing new insights into the vertical motions inside hydraulic jumps.

Figure I-16 presents a typical raw signal of the vertical motions f_y inside a hydraulic jump. The instantaneous force signal showed large force fluctuations around the mean. The negative mean force as well as a large number of negative force peaks indicating an overall downwards motion of the submerged sphere. Signal smoothing indicated some oscillatory pattern in instantaneous forces.

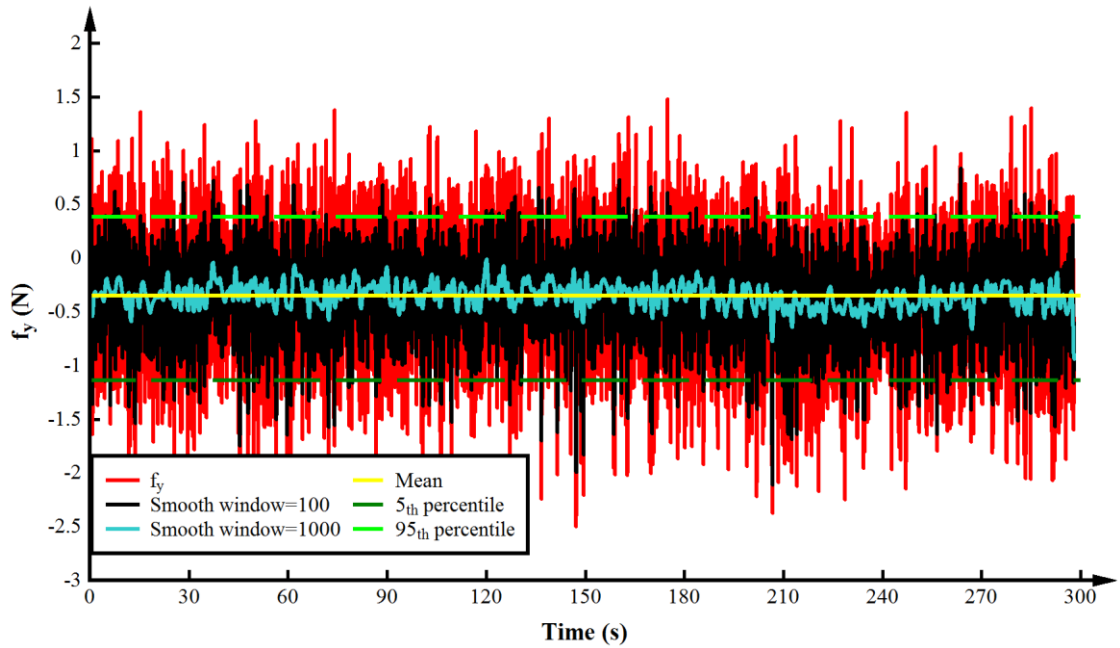


FIGURE I-16. RAW SIGNALS OF VERTICAL FORCES ON A SUBMERGED SPHERE INSIDE A HYDRAULIC JUMP FOR EXPERIMENT C: $Fr_1 = 7.0$, $Re = 6.2 \times 10^4$, FULLY DEVELOPED INFLOW CONDITIONS, $x/d_1 = 20$, $y/d_1 = 2.73$.

I.6.1. TIME-AVERAGED VERTICAL FORCES

The measured average vertical forces on the submerged sphere F_y represented the sum of the buoyancy forces $F_{buoyancy}$ and the dynamic drag force F_{Dy} (Equation I.1). While $F_{buoyancy}$ estimates the upward force due to the volume displaced by the sphere in the two-phase fluid and was strongly dependent of the local void fraction, F_{Dy} characterises the dynamic vertical motions and flow direction in the hydraulic jump. Therefore, the total vertical force comprised the sum of the vertical forces linked with the void fraction and the dynamic motions of the hydraulic jump:

$$F_y = F_{buoyancy} + F_{Dy} = \rho_{air_water} g \nabla + F_{Dy} \quad (I.1)$$

Figure I-17 presents profiles of the vertical forces F_y at different cross-sections along the hydraulic jump together with the contributions of $F_{buoyant}$ and F_{Dy} . For example, Figure I-17B, presents the vertical forces at $x/d_1 = 20$ and $y/d_1 = 1.42$, indicating that $F_{buoyant}$ represented 67% of F_y and F_{Dy} 33%. The total vertical force was positive at this location $F_y/F_{ws} = 0.073$ (Figure I-17B). At $y/d_1 = 1.87$, F_y was negative representing a split up of the contribution of $F_{buoyant}$ of 61% while F_{Dy} accounted for 39%. Further downstream, $x/d_1 \geq 30$ (Figures I-17C, D and E), the contribution of the buoyancy force over the total vertical force represented more than 80% suggesting a minor influence of the vertical flow motions in the hydraulic jump at the downstream end. Despite $F_{buoyancy} > F_y$, the shape of F_y was strongly influenced by F_{Dy} along the hydraulic jump since $F_{buoyant}$ was almost constant. Overall, the understanding of the buoyancy and drag force contribution on the total vertical force provided a better understanding of the vertical force distribution at different locations throughout the hydraulic jump.

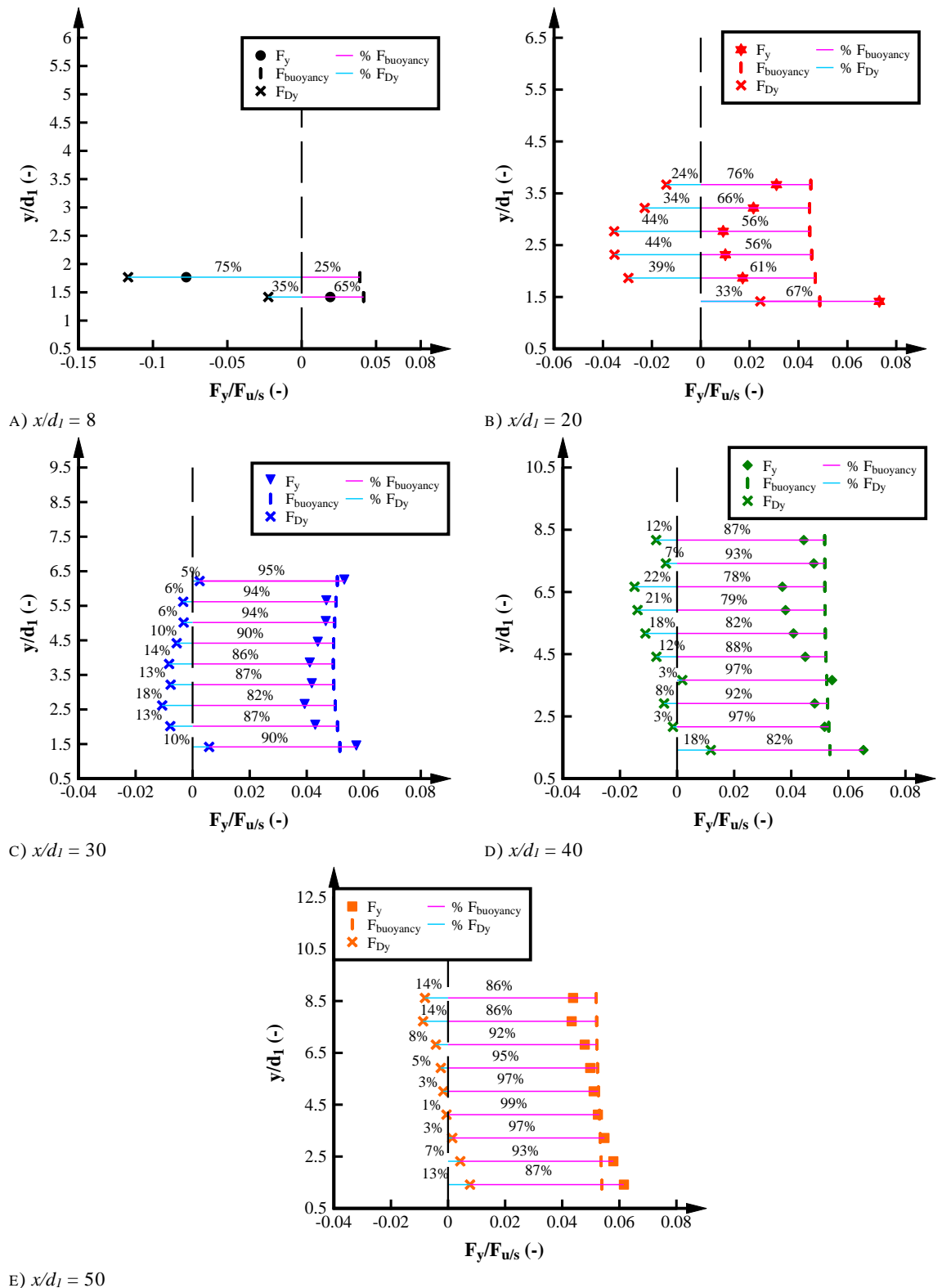


FIGURE I-17. CONTRIBUTION OF THE BUOYANT AND DRAG FORCES TO THE TOTAL VERTICAL FORCE ON A SUBMERGED SPHERE INSIDE A HYDRAULIC JUMP. EXPERIMENT E: $Fr_1 = 8.2$, $Re = 7.5 \times 10^4$, FULLY DEVELOPED INFLOW CONDITIONS.

Figure I-18 presents typical distributions of $F_{buoyancy}$, F_{Dy} and F_y at different cross-sections downstream of the jump toe (Figures I-18A, B and C respectively). For $x/d_1 \leq 20$, F_y had a distinct minimum in the shear region at a location similar to the local maxima in void fraction

and bubble count rate. This minimum corresponded to low $F_{buoyancy}$ due to low ρ_{air_water} surrounding the sphere (Figure I-18A). A local maximum in F_{Dy} was also observed which indicated a strong upwards motions generated by the unsteady vortex shedding process (Figure I-18B). Above this minimum, F_y increased with increasing elevation due to a decrease in flow aeration (increase in average density and buoyant force) and a decrease in F_{Dy} . For $x/d_1 > 30$, F_y decreased with increasing elevation from the channel bed linked with buoyancy effects. In this region, the drag forces had only minor contributions.

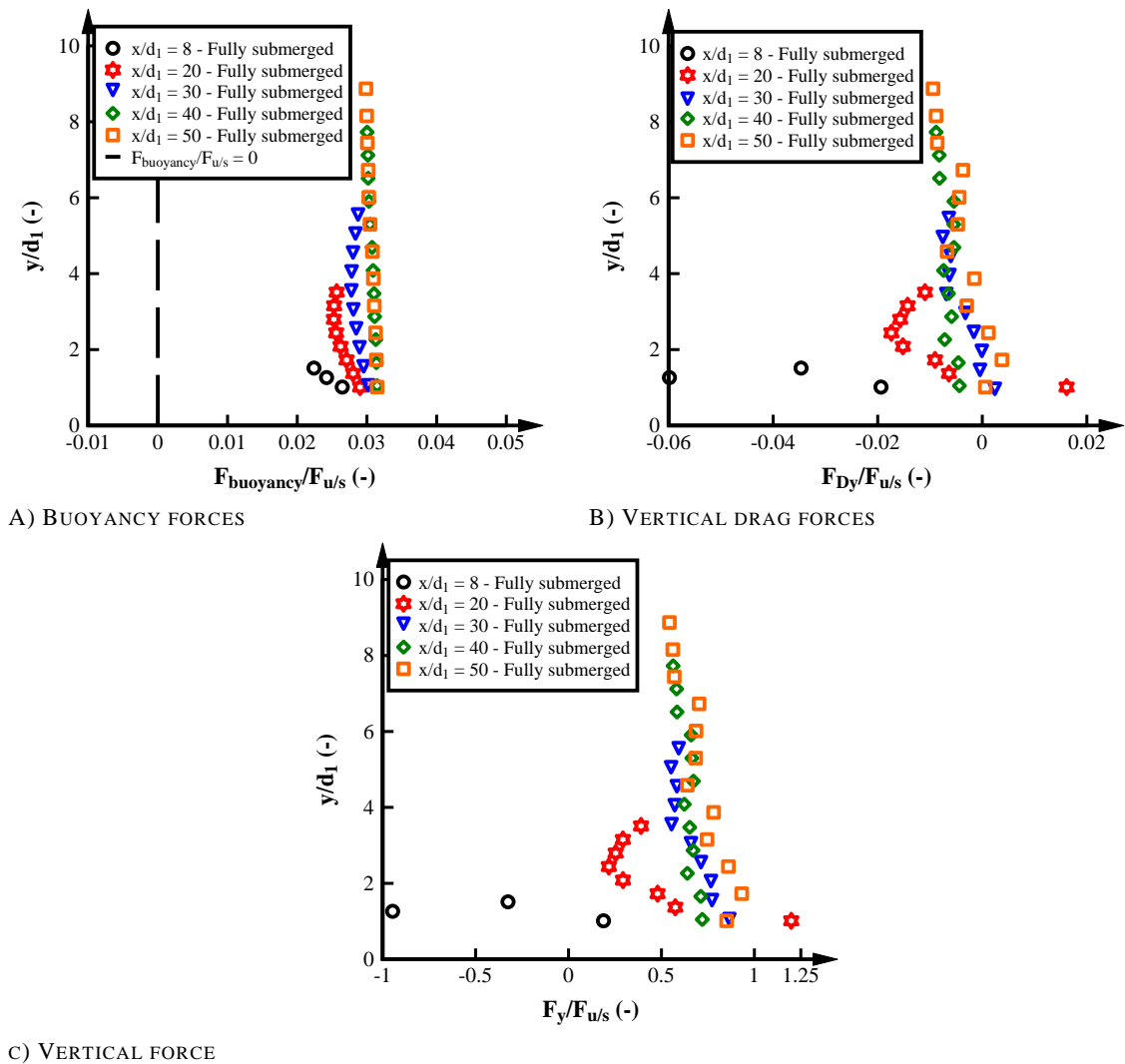


FIGURE I-18. VERTICAL FORCE ON A SUBMERGED SPHERE INSIDE A HYDRAULIC JUMP. EXPERIMENT F: $Fr_1 = 8.0$, $Re = 1.2 \times 10^5$, FULLY DEVELOPED INFLOW CONDITIONS.

I.6.2. AMPLITUDE OF VERTICAL FORCES

Figure I-19 presents the vertical distribution of the amplitude of the vertical force fluctuations ($f_{y,max} - f_{y,min}$), as function of the distance from the jump toe. Note that the amplitude of the vertical fluctuations comprises the influence of $F_{buoyancy}$ and F_{Dy} and therefore, the variation in ($f_{y,max} - f_{y,min}$) is dependent of the variation in the void fraction surrounding the sphere and the variation in the vertical flow motions. The amplitude was decreasing with increasing distance

from the jump toe indicating lower vertical movements at the downstream end of the jump. Maximum amplitude peaks were observed close to the jump toe and close to the channel bed indicating regions of larger force fluctuations. This result may be related with large void fraction variation and stronger vortex shedding in this area. For $x/d_1 = 30$, the vertical force amplitude was almost constant at different elevations linked with an almost constant void fraction with increasing distance from the channel bed and minor drag forces.

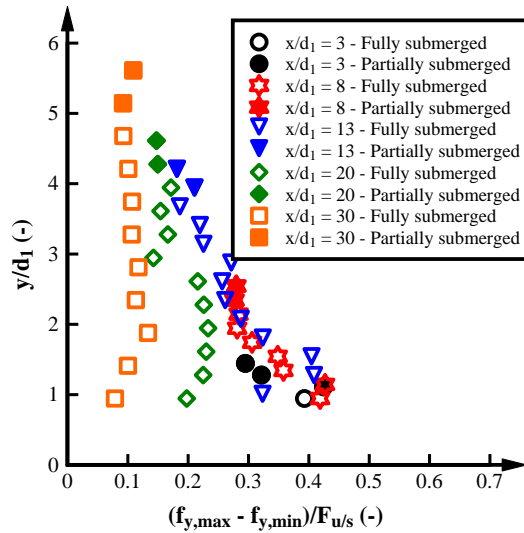


FIGURE I-19. LONGITUDINAL DISTRIBUTION OF THE VERTICAL FORCE AMPLITUDE. EXPERIMENT A: $Fr_1 = 5.1$, $Re = 8.3 \times 10^4$, FULLY DEVELOPED INFLOW CONDITIONS.

I.6.3. VERTICAL FORCE FLUCTUATIONS

The vertical force fluctuations comprised the fluctuations of the buoyancy force linked with the local void fraction and the vertical drag force linked with the fluid motions. Based upon the time-averaged analysis (Figure I-17), regions located close to the jump toe showed time-averaged vertical forces equally represented by F_{Dy} and $F_{buoyancy}$ while $F_{buoyancy}$ became more significant at the downstream end of the hydraulic jump. Since the present experiments did not perform a simultaneous analysis of the void fraction distribution with the force measurements, there is no clear information of the influence of the void fraction fluctuations in the vertical force fluctuations in the hydraulic jump. Therefore, while at some regions of the hydraulic jumps the force fluctuations may be more influenced by the buoyancy force or the drag force, the present study considered the vertical distribution of the force fluctuations based upon the combined influence of the buoyancy and vertical drag forces. Figure I-20 presents a typical distribution of the vertical force fluctuations inside a hydraulic jump. In consistency with the streamwise and transverse force fluctuations, the vertical fluctuations were larger close to the channel bed and decreased with increasing the elevation suggesting stronger vortex shedding and larger variation in the void fraction surrounding the sphere. Close to the jump toe ($x/d_1 \leq 13$), the vertical fluctuation distributions were similar at different cross-sections suggesting similar oscillation patterns considering fluid motions and void fraction variations. Further

downstream ($x/d_1 > 13$), at regions with lesser air entrainment and lesser visual motions, F_y' decreased with increasing the distance from the jump toe. For regions close to the jump toe ($x/d_1 < 30$), the vertical fluctuation showed an increase in the fluctuation close to the free-surface region where the sphere was partially submerged. This increase may be linked with the sphere exposure to non-submerged conditions increasing the data deviation. At the downstream end of the jump ($x/d_1 = 40$), similar vertical fluctuations were observed at different elevations with $F_y'/F_{u/s} \approx 0.1$.

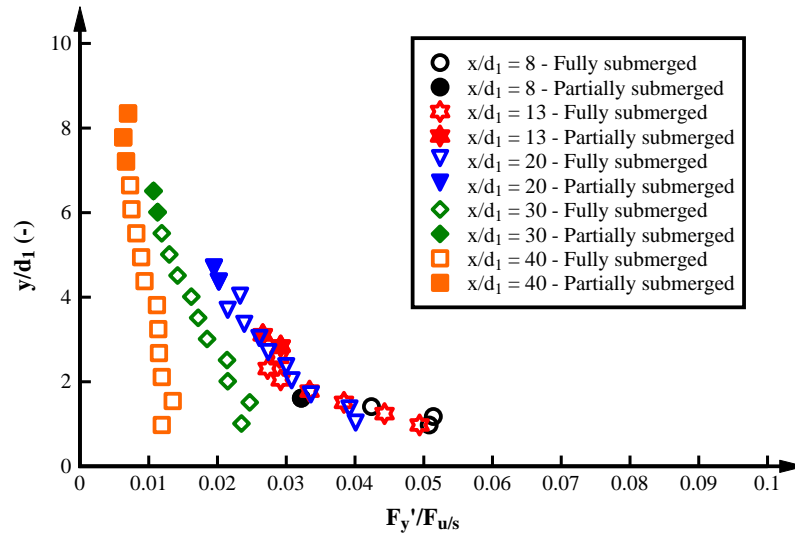


FIGURE I-20. VERTICAL DISTRIBUTION OF THE VERTICAL FORCE FLUCTUATIONS AT DIFFERENT CROSS-SECTIONS ALONG THE HYDRAULIC JUMP. EXPERIMENT D: $Fr_1 = 7.0$, $Re = 1.1 \times 10^5$, PARTIALLY DEVELOPED INFLOW CONDITIONS.

1.6.4. CHARACTERISTIC FREQUENCIES OF THE VERTICAL FORCE FLUCTUATIONS

Figure I-21 shows typical frequency spectra and characteristic frequencies of the vertical force fluctuations in hydraulic jumps at four different locations. The frequency spectrum at the cross-section located close to the jump toe ($x/d_1 = 8$) showed a dominant frequency of 0.96 Hz in agreement with typical jump toe oscillations frequencies. Further downstream ($x/d_1 > 8$), the dominant frequencies ranged between $1.5 < freq_{F_y, dom} < 4$. This frequency range was typical of dominant frequencies observed in the free-surface fluctuations in hydraulic jumps (Murzyn and Chanson 2009a; Chachereau and Chanson 2011b; Montano et al. 2018). For the frequency spectra presented in Figure I-21, no secondary frequencies were identified suggesting that the free-surface fluctuations mainly dominate the vertical force fluctuation in hydraulic jumps. Note that the resonant frequency of the system was above the characteristic frequency of the vertical forces indicating no system self-excitation.

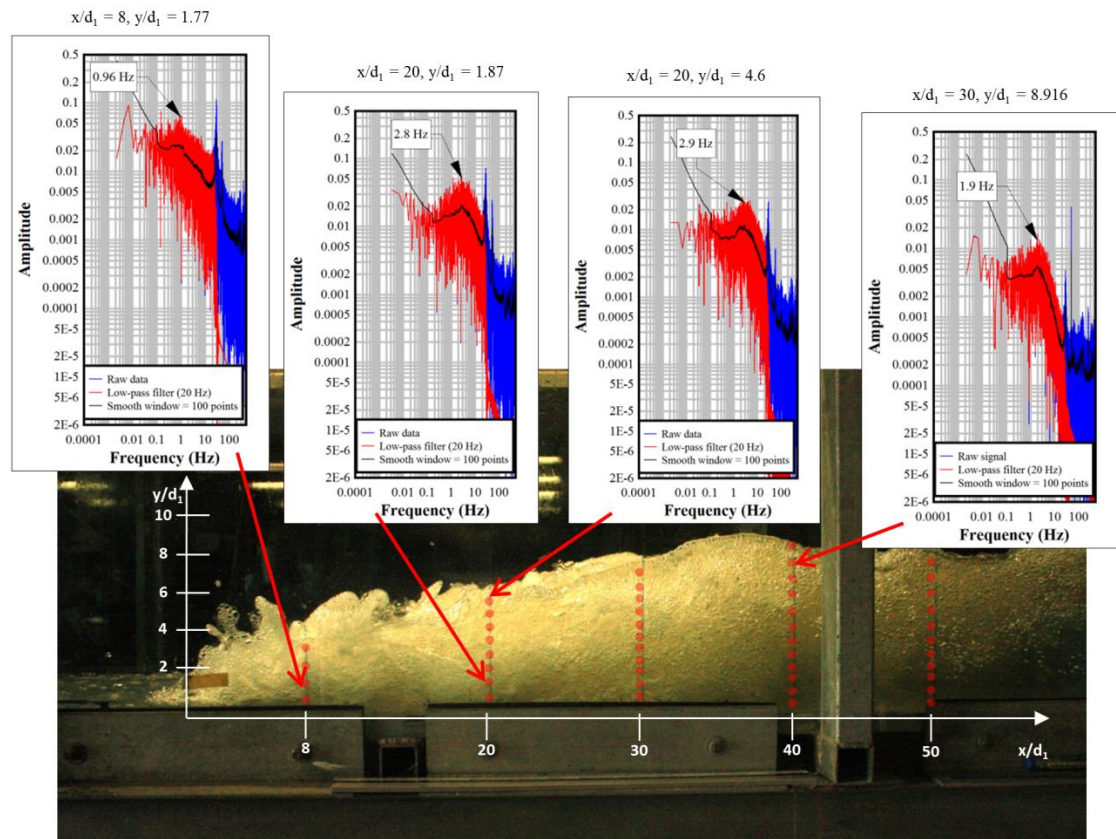
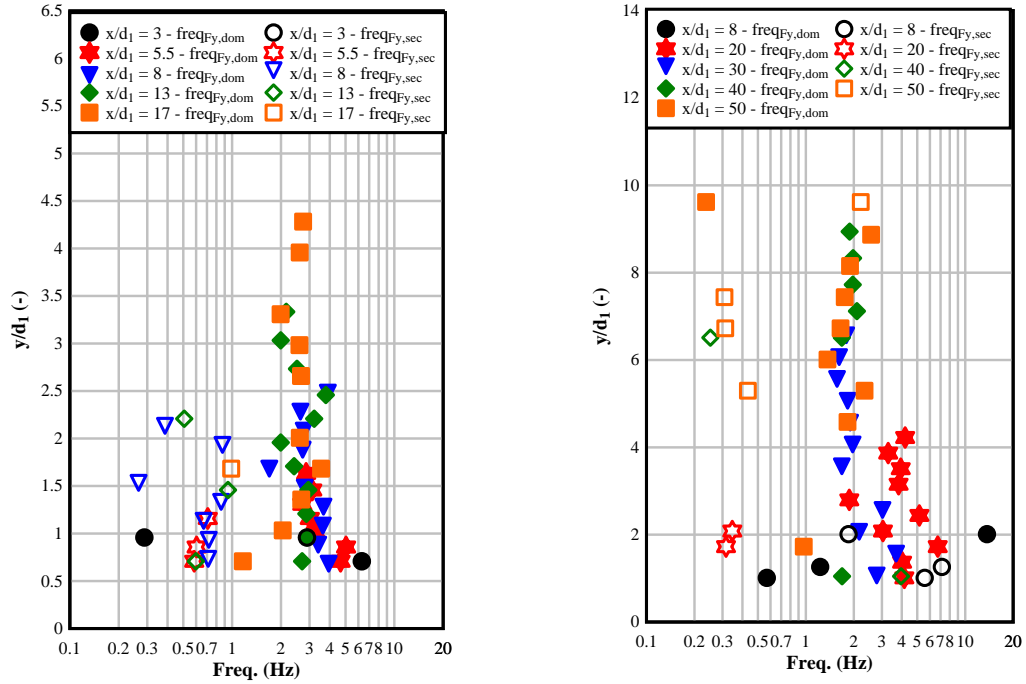


FIGURE I-21. SPECTRAL ANALYSIS AND CHARACTERISTIC FREQUENCIES OF THE TRANSVERSE FORCE MEASUREMENTS IN A HYDRAULIC JUMP. EXPERIMENT F: $Fr_1 = 8.0$, $Re = 1.2 \times 10^5$, FULLY DEVELOPED INFLOW CONDITIONS.

Figure I-22 illustrates the vertical distribution of the characteristic frequencies of the vertical force fluctuations for two Froude numbers. Jump toe oscillation frequencies between $0.2 < freq_{F_y, dom} < 1.5$ were observed close to the jump toe highlighting the strong influence of the jump toe oscillations at this region. Further downstream, most of the dominant frequencies were found between $1.5 < freq_{F_z, dom} < 4$ with similar frequencies at different elevations. These frequencies were in agreement with typical free-surface frequencies in the hydraulic jump. Some larger frequencies between $4 < freq_{F_z, dom} < 7$ were observed close to the jump toe for experiments with $Fr_1 \geq 7$ and $Re > 8 \times 10^4$ which was linked with the large turbulence and instabilities for the strongest hydraulic jumps.

For hydraulic jumps with $Fr_1 < 7$, the dominant frequencies showed a minor decrease with increasing the distance from the jump toe (Figure I-22A) suggesting that the oscillation frequency was almost independent of the position along the hydraulic jump. For $Fr_1 \geq 7$, the dominant frequency showed a more significant decrease with increasing the distance from the jump toe (Figure I-22B) indicating faster vertical fluctuations close to the jump toe. Apart from experiments conducted with $Fr_1 < 5.1$, a minor number of secondary frequencies were identified in the vertical force fluctuations suggesting that the vertical force motions in the hydraulic jump were only dominated by the periodic free-surface fluctuations. For $Fr_1 < 5.1$, a group of

secondary frequencies ranged between $0.3 < freq_{Fy,dom} < 1.5$ highlighting the strong influence of the jump toe oscillation in the weakest hydraulic jumps analysed. Overall, the analysis of the characteristic frequencies of the vertical force fluctuations at different elevations and longitudinal positions along the hydraulic jump were strongly linked with the free-surface fluctuations in the hydraulic jump



A) EXPERIMENT I: $Fr_1 = 3.8$, $Re = 9.5 \times 10^4$ – FULLY DEVELOPED B) EXPERIMENT F: $Fr_1 = 8.0$, $Re = 1.2 \times 10^5$ – FULLY DEVELOPED

FIGURE I-22. VERTICAL DISTRIBUTION OF THE CHARACTERISTIC FREQUENCIES OF THE TRANSVERSE FORCES IN THE HYDRAULIC JUMP.

1.6.5. AUTO-CORRELATION TIME SCALE OF THE TRANSVERSE FORCE

The auto-correlation time scale of the vertical forces in the hydraulic jump T_{Fy} indicate the advective lifetime of the vertical motions. To the knowledge of the author, no previous study has attempted to measure the internal vertical scales at different positions along the hydraulic jump. Figure I-23 presents the vertical distribution of the dimensionless auto-correlation time scales of the vertical forces in the hydraulic jump at different cross-sections. $T_{Fy} \times V_1/d_1$ increased with increasing the distance from the jump toe, suggesting smaller turbulent scales closer to the jump toe position of the hydraulic jump. The results were in agreement with the visual observations in hydraulic jumps by Long et al. (1991). The vertical auto-correlation time scales were similar at different elevations close to the jump toe and in the lower part of the hydraulic jump. In the upper part of the hydraulic jump and at regions far from the jump toe, the auto-correlation time scales of the vertical forces showed a gradual increase with increasing the elevations indicating an increase in the lifetime of the vertical structures at the free-surface region. At the downstream end of the jump, similar auto-correlation time scales were observed at different elevations.

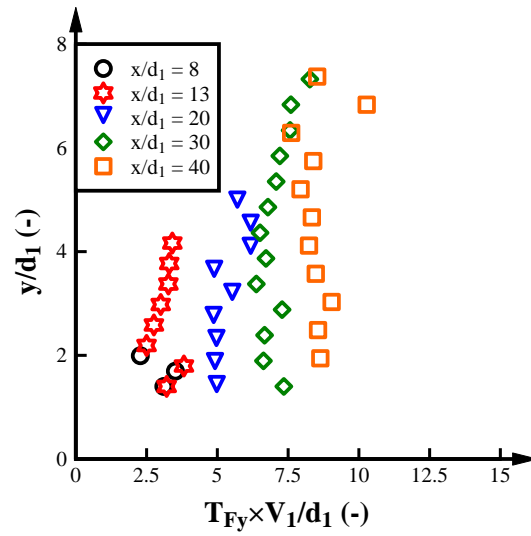


FIGURE I-23. AUTO-CORRELATION TIME SCALE OF THE VERTICAL FORCES: EXPERIMENT C: $Fr_1 = 7.0$, $Re = 6.2 \times 10^4$, FULLY DEVELOPED INFLOW CONDITIONS

DIGITAL APPENDIX

Digital Appendix A. INTRODUCTION

The present thesis aimed to provide a better understanding of the energy dissipation processes in hydraulic jumps combining novel experimental results of a) air-water flow properties, b) free-surface fluctuations and jump toe oscillations and c) the internal three-dimensional forces on a submerged sphere inside hydraulic jumps. The digital appendix comprises the full data results of all the experiments conducted in the present study and which were not included in the main document. Table A-1 summarizes the experimental flow conditions including d_1 , Fr_1 , Re , the ratio of the boundary layer depth at the jump toe position (δ), the inflow gate height h_0 , the distance from the sluice gate to the jump toe x_{sg} .

DIGITAL APPENDIX A-1. EXPERIMENTAL FLOW CONDITION IN THE PRESENT STUDY.

Test	d_1 (m)	Q ($m^3 s^{-1}$)	Fr_1	Re	h_0 (m)	x_{sg} (m)	δ/d_1
H_PD	0.03	0.037	3.8	6.17×10^4	0.026	0.68	0.5
H_FD	0.03	0.037	3.8	6.17×10^4	0.022	2.28	1.5
I_FD	0.04	0.057	3.8	9.50×10^4	0.0275	2.85	1.5
A_PD	0.03	0.05	5.1	8.33×10^4	0.027	0.50	0.4
A_FD	0.03	0.05	5.1	8.33×10^4	0.025	2.44	1.4
B_PD	0.0248	0.037	5.1	6.17×10^4	0.022	0.58	0.5
B_FD	0.0248	0.037	5.1	6.17×10^4	0.018	1.87	1.5
C_PD	0.02	0.037	7.0	6.17×10^4	0.0175	0.46	0.5
C_FD	0.02	0.037	7.0	6.17×10^4	0.014	1.45	1.5
D_PD	0.03	0.068	7.0	1.13×10^5	0.027	0.71	0.5
D_FD	0.03	0.068	7.0	1.13×10^5	0.019	1.97	1.5
E_PD	0.02	0.045	8.5	7.50×10^4	0.019	0.50	0.5
E_FD	0.02	0.045	8.5	7.50×10^4	0.016	1.66	1.5
F_PD	0.027	0.07	8.4	1.17×10^5	0.024	0.63	0.5
F_FD	0.028	0.07	8.0	1.17×10^5	0.020	2.07	1.5
G_PD	0.02	0.053	10.0	8.83×10^4	0.017	0.45	0.5
G_FD	0.02	0.053	10.0	8.83×10^4	0.014	1.45	1.5

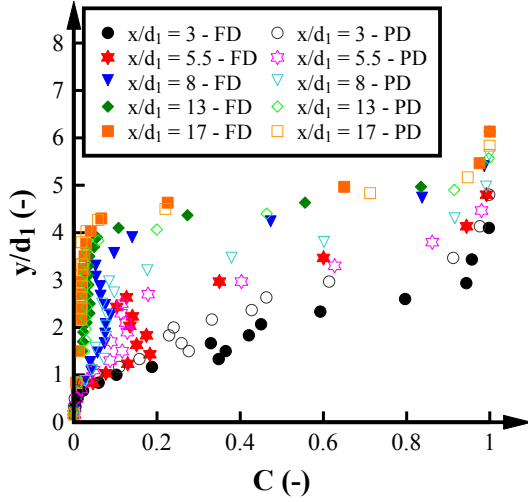
This digital appendix document is organised in the three main sections of the thesis document: a) Air-water flow properties, b) Free-surface features, c) Internal forces:

INTRODUCTION	2
AIR-WATER FLOW PROPERTIES	2
VOID FRACTION DISTRIBUTIONS	4
BUBBLE COUNT RATE	6
INTERFACIAL VELOCITY	8
TIME-AVERAGED CHORD TIME	10
FREE-SURFACE FEATURES	12
JUMP TOE CHARACTERISTIC FREQUENCIES	12
FREE-SURFACE CHARACTERISTIC FREQUENCIES	18

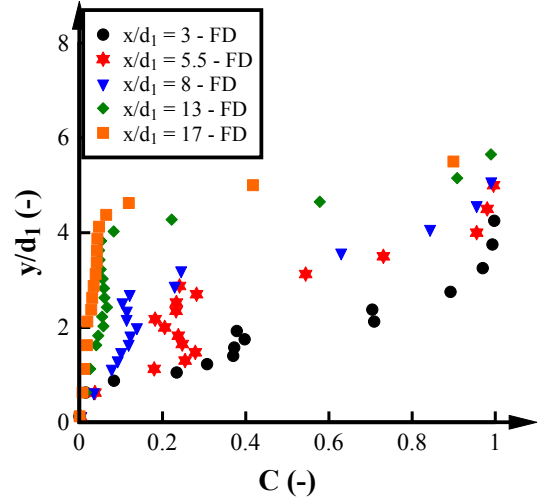
AUTO-CORRELATION TIME SCALES	26
INTEGRAL LENGTH SCALES	32
INTERNAL FORCES	38
TIME-AVERAGED STREAMWISE FORCES	38
STREAMWISE FORCE FLUCTUATIONS	41
STREAMWISE FORCE CHARACTERISTIC FREQUENCIES	44
TIME-AVERAGED TRANSVERSE FORCES	49
TRANSVERSE FORCE FLUCTUATIONS	52
TRANSVERSE FORCE CHARACTERISTIC FREQUENCIES	55
TIME-AVERAGED BUOYANCY FORCES	60
TIME-AVERAGED VERTICAL DRAG FORCES	63
VERTICAL FORCE FLUCTUATIONS	66
VERTICAL FORCE CHARACTERISTIC FREQUENCIES	69

Digital Appendix B. AIR-WATER FLOW PROPERTIES

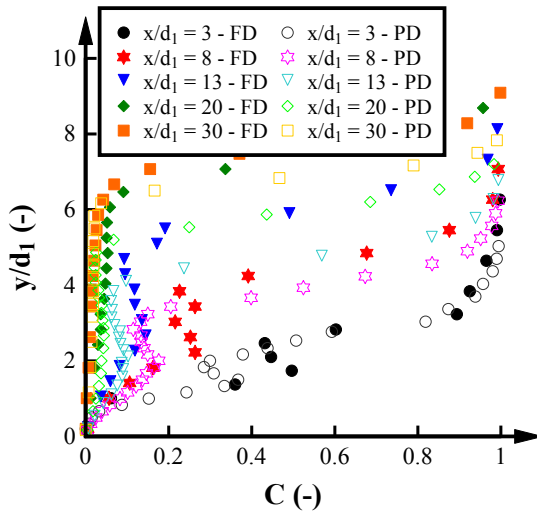
DIGITAL APPENDIX. B.1. VOID FRACTION



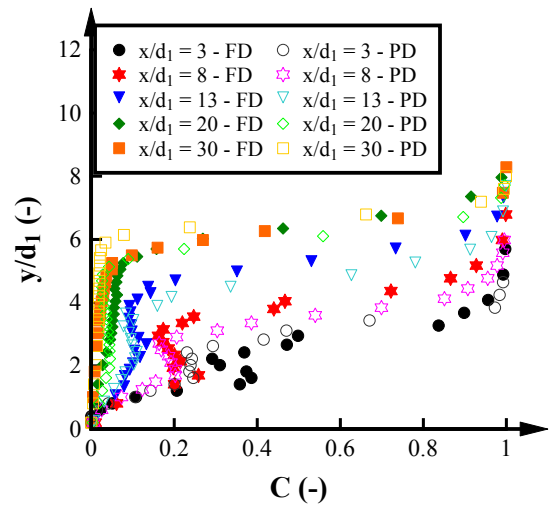
A) EXPERIMENT H: $Fr_1 = 3.8$, $Re = 6.2 \times 10^4$



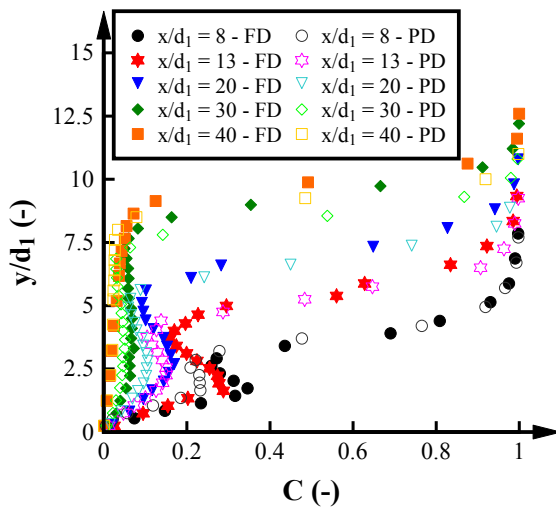
B) EXPERIMENT I: $Fr_1 = 3.8$, $Re = 9.5 \times 10^4$



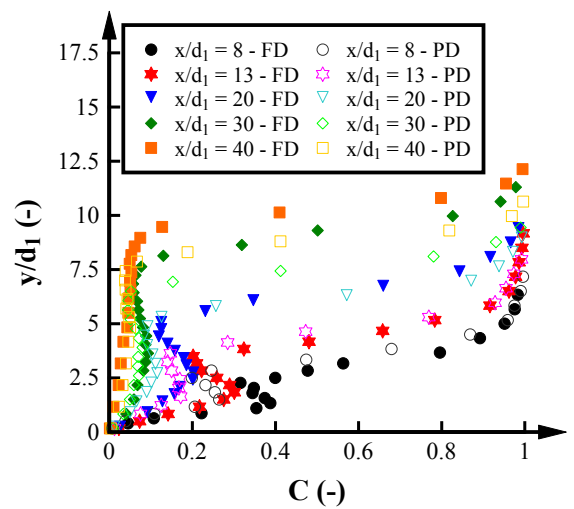
C) EXPERIMENT A: $Fr_1 = 5.1$, $Re = 8.3 \times 10^4$



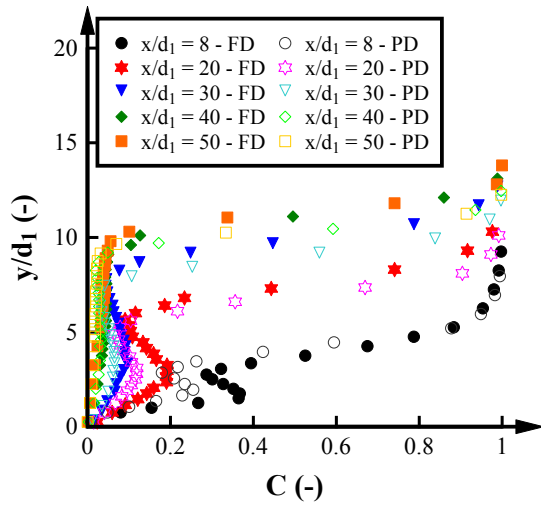
D) EXPERIMENT B: $Fr_1 = 5.1$, $Re = 6.2 \times 10^4$



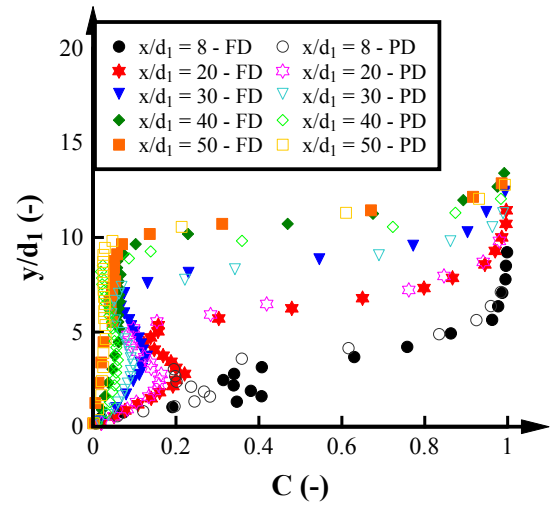
E) EXPERIMENT C: $Fr_1 = 7.0$, $Re = 6.2 \times 10^4$



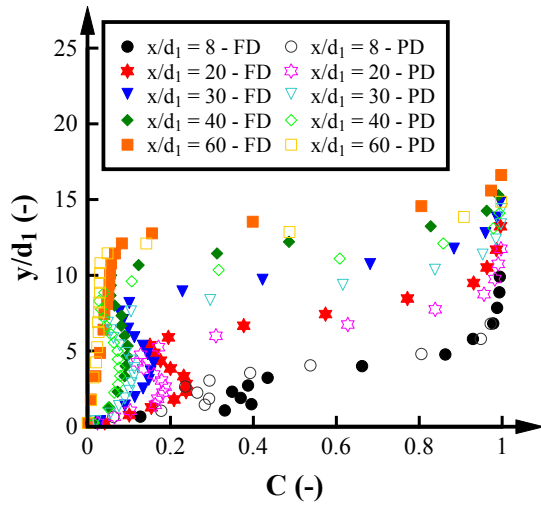
F) EXPERIMENT D: $Fr_1 = 7.0$, $Re = 1.1 \times 10^5$



G) EXPERIMENT E: $Fr_1 = 8.5$, $Re = 7.5 \times 10^4$



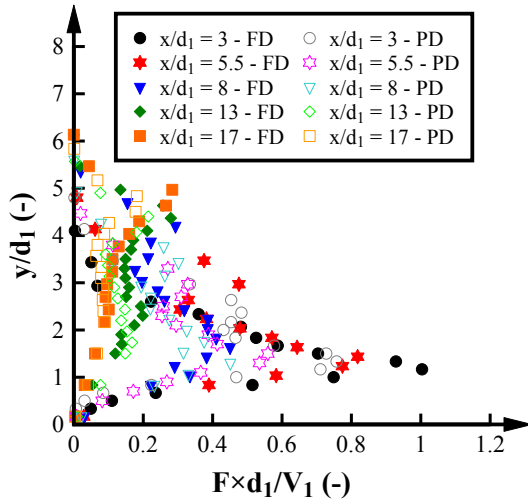
G) EXPERIMENT F: $Fr_1 = 8.5$, $Re = 1.2 \times 10^5$



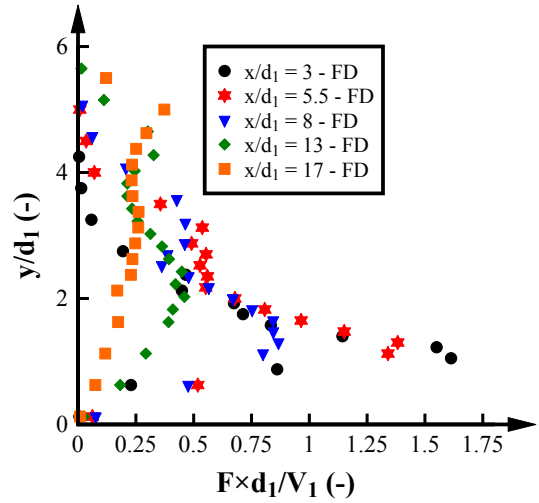
H) EXPERIMENT G: $Fr_1 = 10$, $Re = 8.8 \times 10^4$

DIGITAL APPENDIX B-1. VOID FRACTION DISTRIBUTIONS.

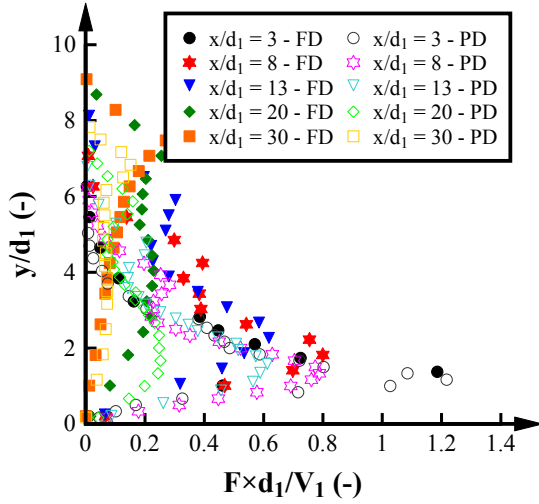
DIGITAL APPENDIX. B.2. BUBBLE COUNT RATE



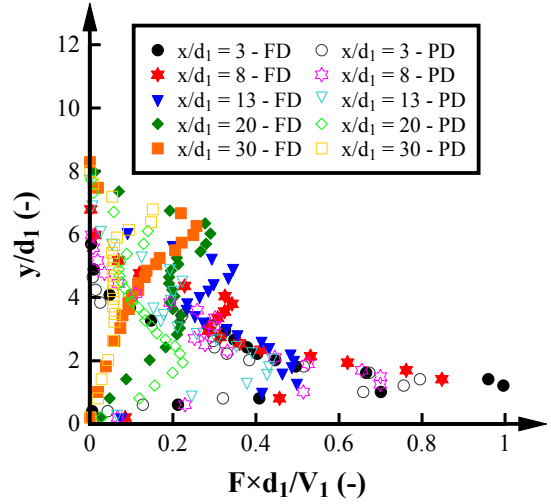
A) EXPERIMENT H: $Fr_1 = 3.8$, $Re = 6.2 \times 10^4$



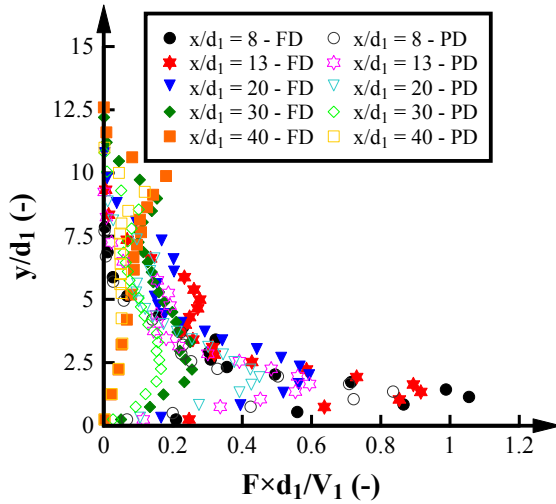
B) EXPERIMENT I: $Fr_1 = 3.8$, $Re = 9.5 \times 10^4$



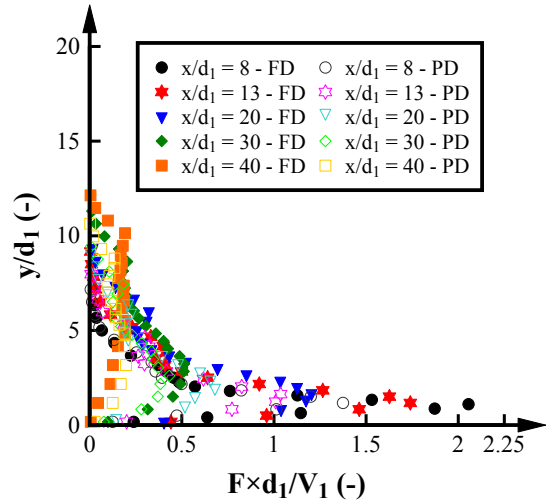
C) EXPERIMENT A: $Fr_1 = 5.1$, $Re = 8.3 \times 10^4$



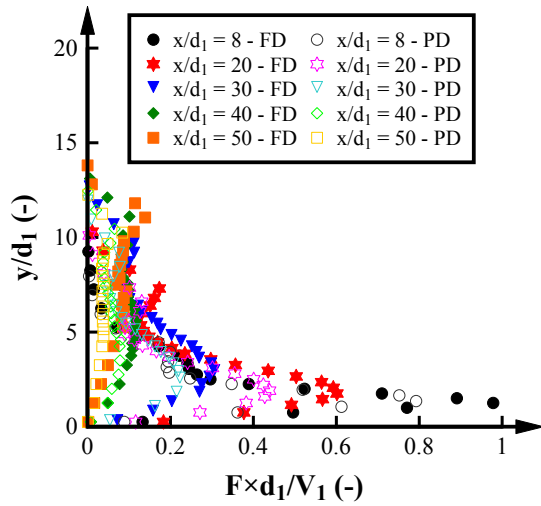
D) EXPERIMENT B: $Fr_1 = 5.1$, $Re = 6.2 \times 10^4$



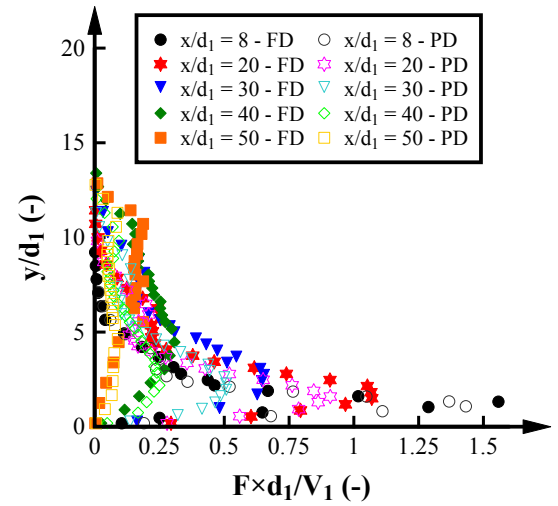
E) EXPERIMENT C: $Fr_1 = 7.0$, $Re = 6.2 \times 10^4$



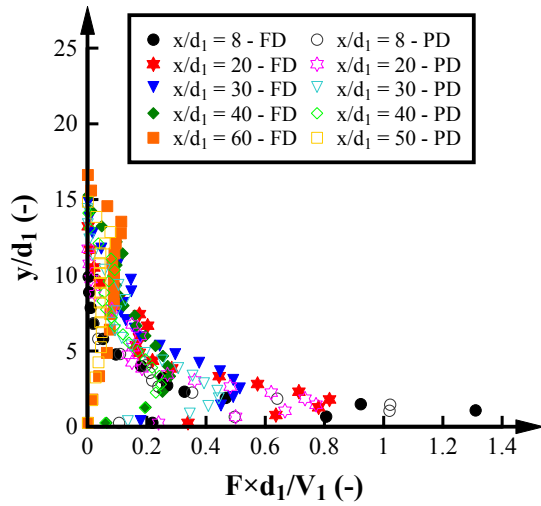
F) EXPERIMENT D: $Fr_1 = 7.0$, $Re = 1.1 \times 10^5$



G) EXPERIMENT E: $Fr_1 = 8.5$, $Re = 7.5 \times 10^4$



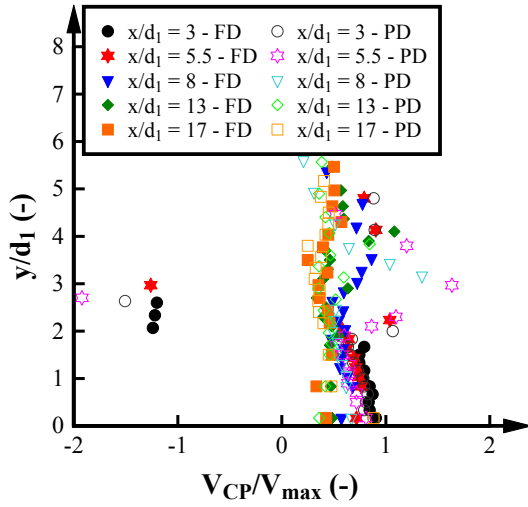
G) EXPERIMENT F: $Fr_1 = 8.5$, $Re = 1.2 \times 10^5$



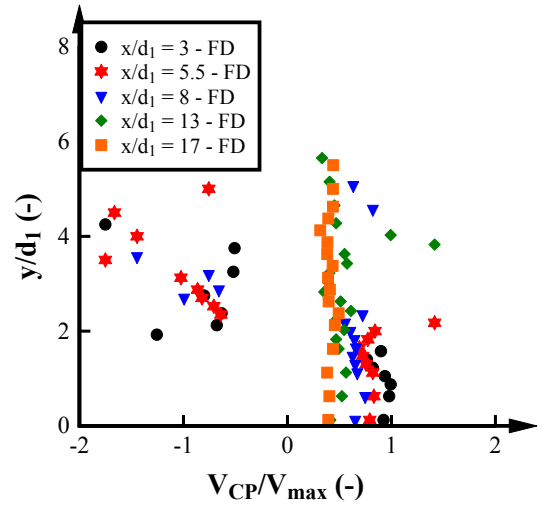
H) EXPERIMENT G: $Fr_1 = 10$, $Re = 8.8 \times 10^4$

DIGITAL APPENDIX B-2. BUBBLE COUNT RATE DISTRIBUTIONS.

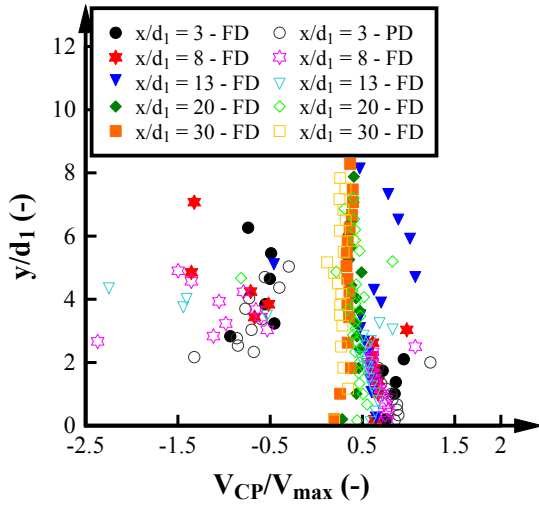
DIGITAL APPENDIX. B.3. INTERFACIAL VELOCITY



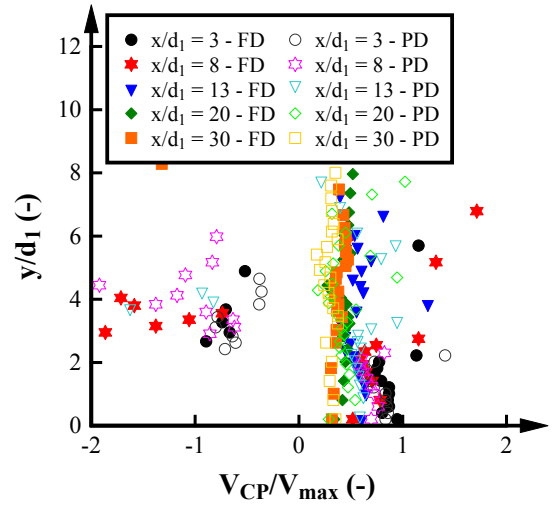
A) EXPERIMENT H: $Fr_1 = 3.8$, $Re = 6.2 \times 10^4$



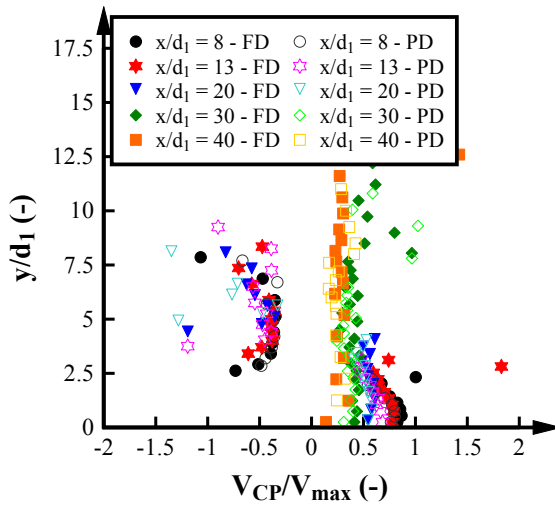
B) EXPERIMENT I: $Fr_1 = 3.8$, $Re = 9.5 \times 10^4$



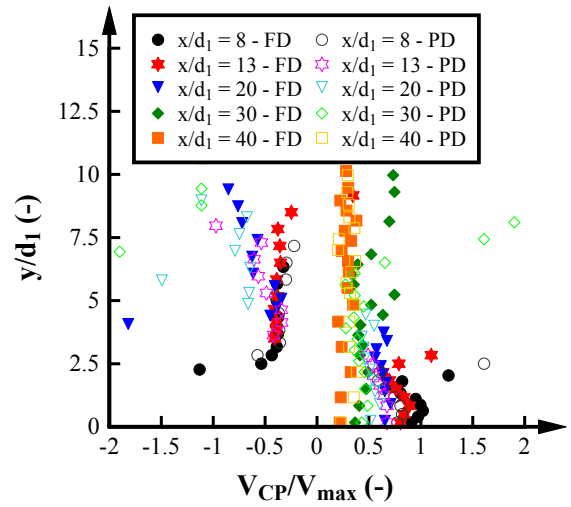
C) EXPERIMENT A: $Fr_1 = 5.1$, $Re = 8.3 \times 10^4$



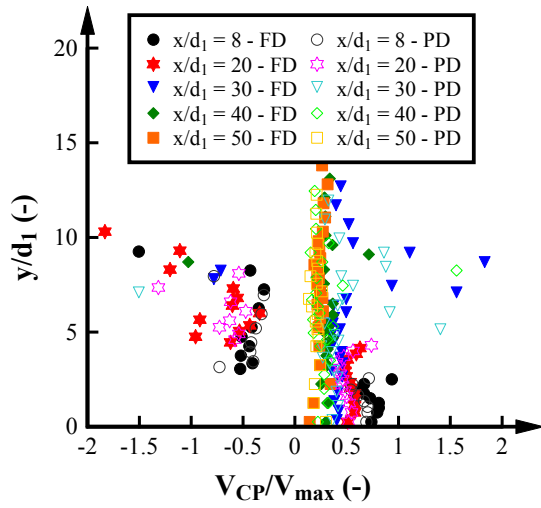
D) EXPERIMENT B: $Fr_1 = 5.1$, $Re = 6.2 \times 10^4$



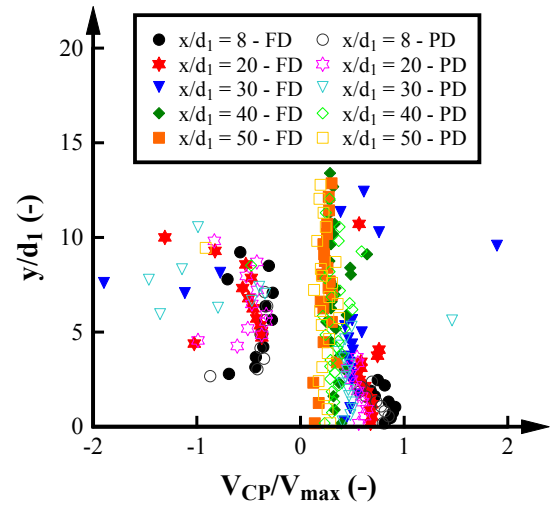
E) EXPERIMENT C: $Fr_1 = 7.0$, $Re = 6.2 \times 10^4$



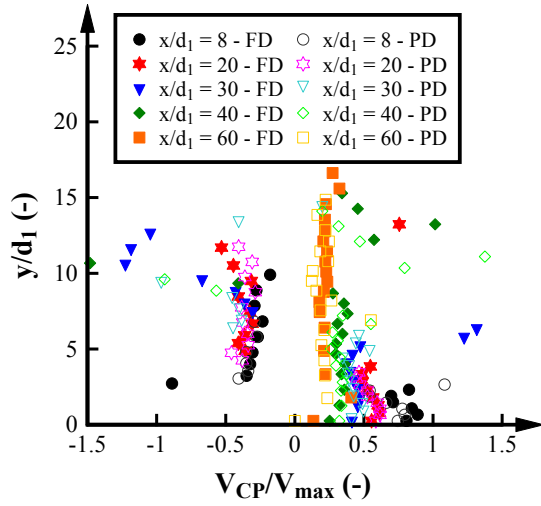
F) EXPERIMENT D: $Fr_1 = 7.0$, $Re = 1.1 \times 10^5$



G) EXPERIMENT E: $Fr_1 = 8.5$, $Re = 7.5 \times 10^4$



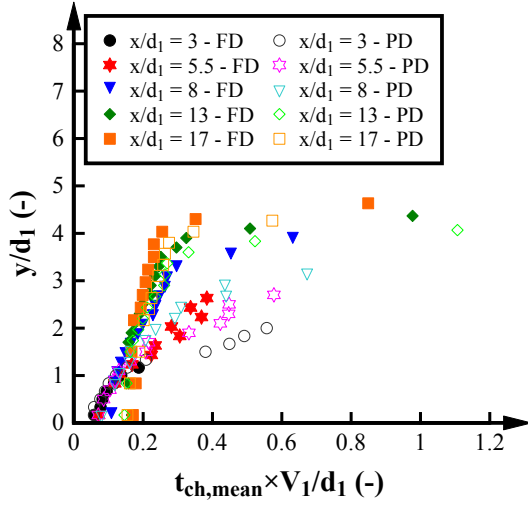
G) EXPERIMENT F: $Fr_1 = 8.5$, $Re = 1.2 \times 10^5$



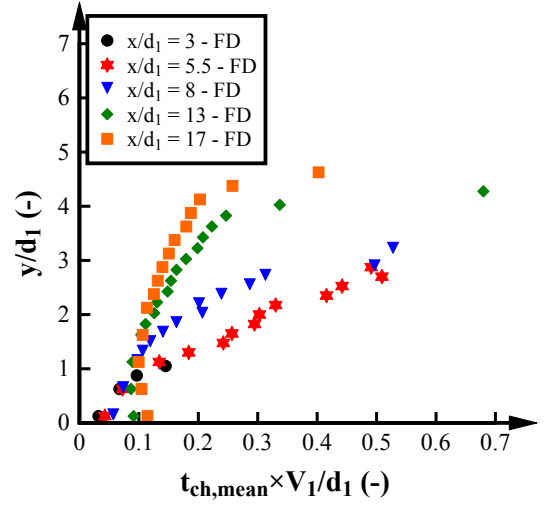
H) EXPERIMENT G: $Fr_1 = 10$, $Re = 8.8 \times 10^4$

DIGITAL APPENDIX B-3. INTERFACIAL VELOCITY DISTRIBUTIONS.

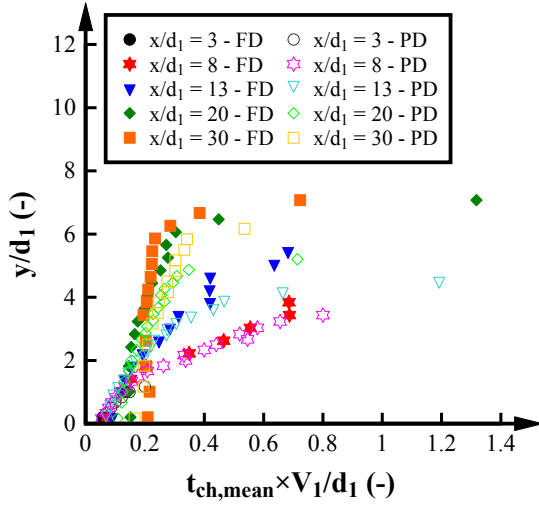
DIGITAL APPENDIX. B.4. TIME-AVERAGED CHORD TIME



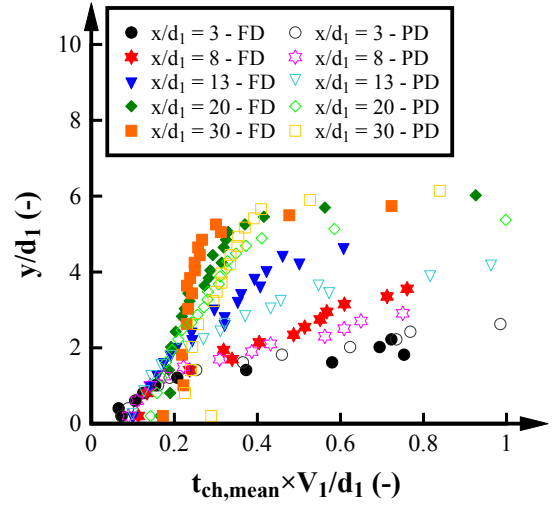
A) EXPERIMENT H: $Fr_1 = 3.8$, $Re = 6.2 \times 10^4$



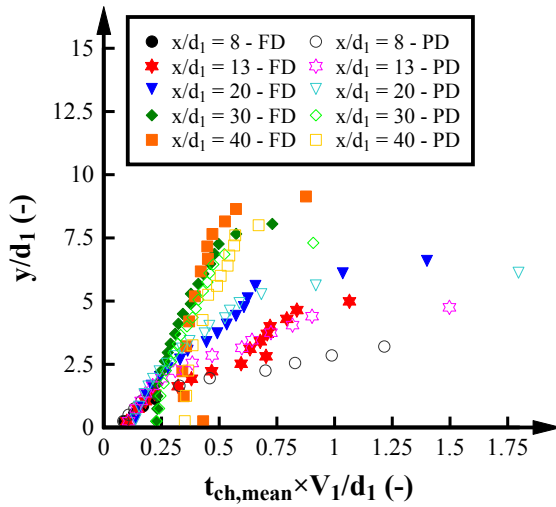
B) EXPERIMENT I: $Fr_1 = 3.8$, $Re = 9.5 \times 10^4$



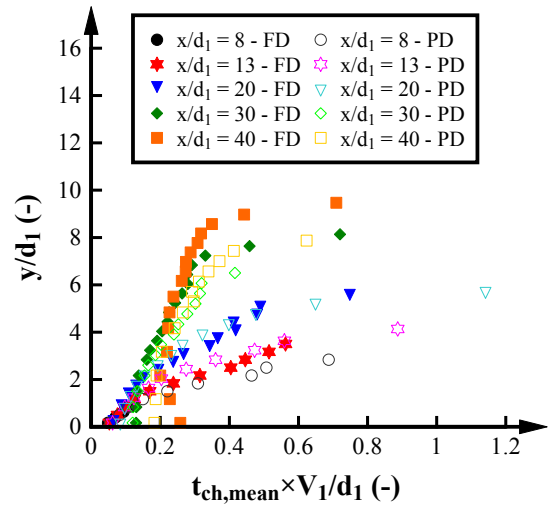
C) EXPERIMENT A: $Fr_1 = 5.1$, $Re = 8.3 \times 10^4$



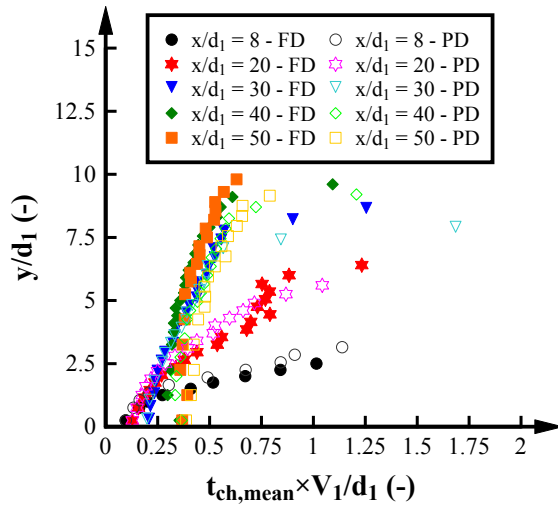
D) EXPERIMENT B: $Fr_1 = 5.1$, $Re = 6.2 \times 10^4$



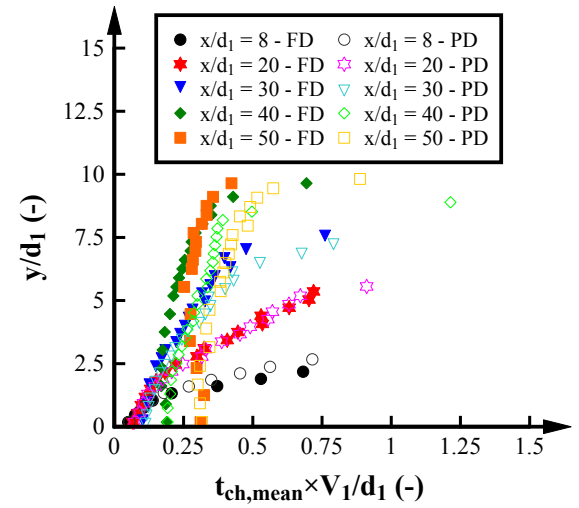
E) EXPERIMENT C: $Fr_1 = 7.0$, $Re = 6.2 \times 10^4$



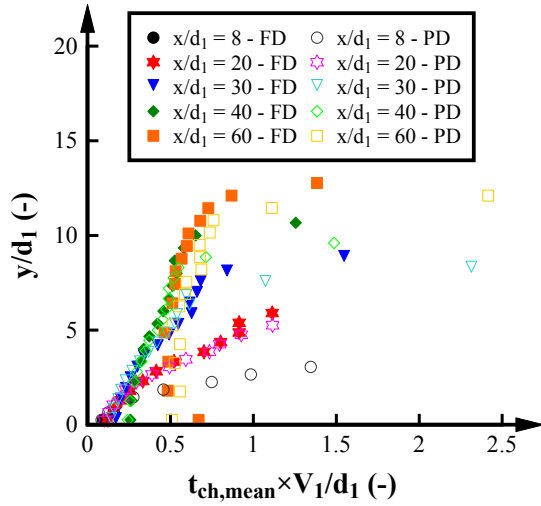
F) EXPERIMENT D: $Fr_1 = 7.0$, $Re = 1.1 \times 10^5$



G) EXPERIMENT E: $Fr_1 = 8.5$, $Re = 7.5 \times 10^4$



G) EXPERIMENT F: $Fr_1 = 8.5$, $Re = 1.2 \times 10^5$



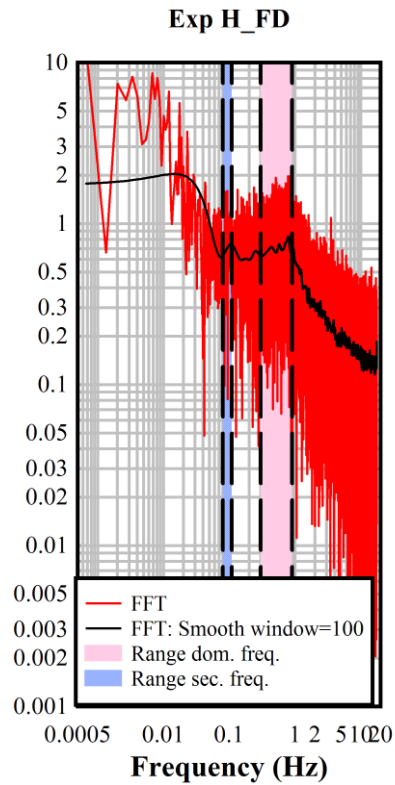
H) EXPERIMENT G: $Fr_1 = 10$, $Re = 8.8 \times 10^4$

DIGITAL APPENDIX B-4. TIME-AVERAGED CHORD TIME DISTRIBUTIONS.

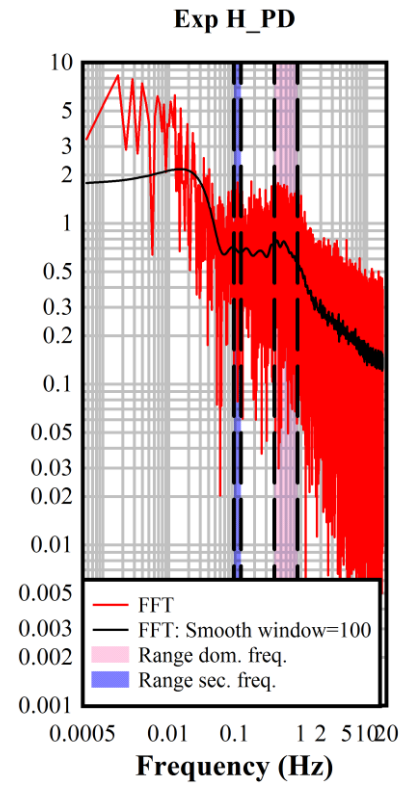
Digital Appendix C. FREE-SURFACE FEATURES

DIGITAL APPENDIX. C.1. JUMP TOE CHARACTERISTIC FREQUENCIES

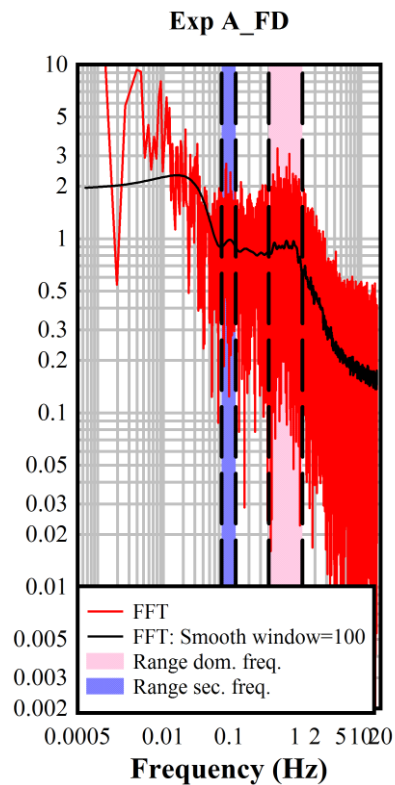
A FFT analysis of the raw jump toe oscillation signal was conducted to identify the characteristic frequencies of the jump toe oscillations. Digital Appendix C-1 shows the FFT analysis for the present experiments including the raw FFT signal, and a smoothed signal of 100 data points respectively to assist with the identification of the most relevant frequency peaks. For all experiments, three characteristic frequency ranges were identified. Note that due to the large data fluctuation, the characteristic frequencies were identified in terms of ranges instead of a single value. The dominant frequency range was observed for frequency ranges between 0.2 – 1.6 Hz in close agreement with previous studies which identified a dominant jump toe frequency in the range of 0.5 to 2 Hz (Mossa and Tolve 1998; Chanson and Gualtieri 2008; Murzyn and Chanson 2009). Secondary frequency peaks were observed for a range of 0.04 to 0.4 Hz. This frequency has not been reported before and may be linked with the channel configuration itself. In addition, a slow frequency was observed for all the hydraulic jumps with a frequency range between 0.001 – 0.01 Hz. These frequencies were consistent with the study of Wang and Chanson (2015). Wang and Chanson (2015) observed jump toe oscillations for a sampling duration of 160 minutes identifying a further characteristic frequency of about 0.004 Hz for his experiments of a hydraulic jump with $Fr_l = 5.1$. This frequency is very similar to the present frequency between 0.001 – 0.01 Hz which was observed for all present experiments for $3.6 < Fr_l < 10$. Overall, the present experiments were consistent with previous studies indicating that a LIDAR is a suitable instrument to measure the characteristic features of the jump toe oscillations.



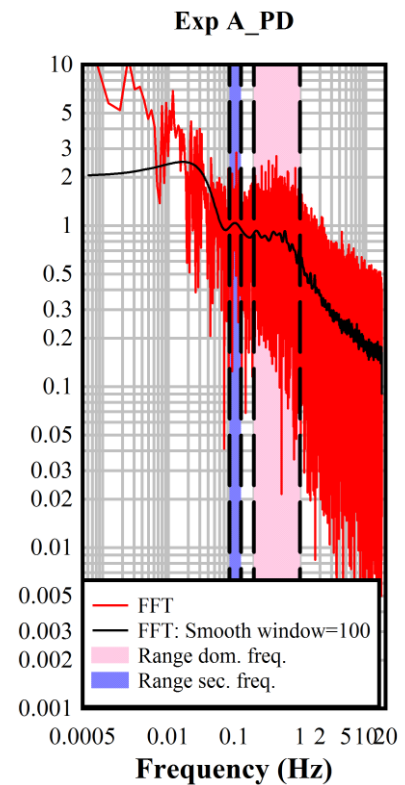
A) EXPERIMENT H ($Fr_1 = 3.8$, $Re = 6.2 \times 10^4$, FD)



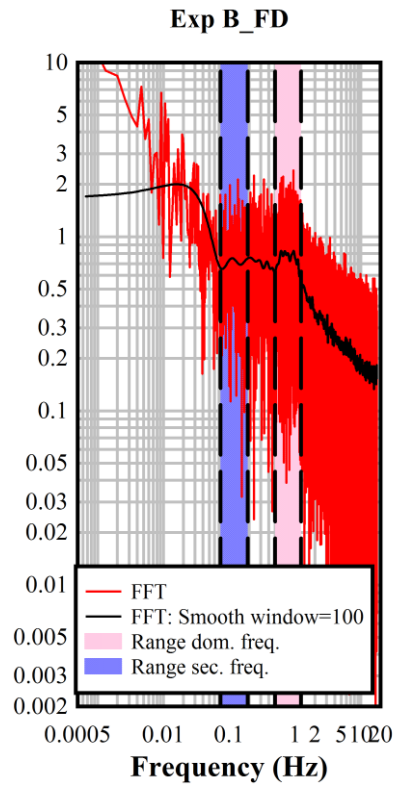
B) EXPERIMENT H ($Fr_1 = 3.8$, $Re = 6.2 \times 10^4$, PD)



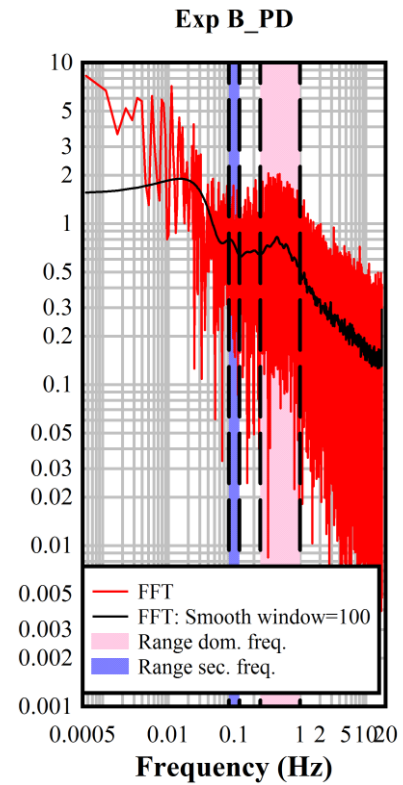
C) EXPERIMENT A ($Fr_1 = 5.1$, $Re = 8.3 \times 10^4$, FD)



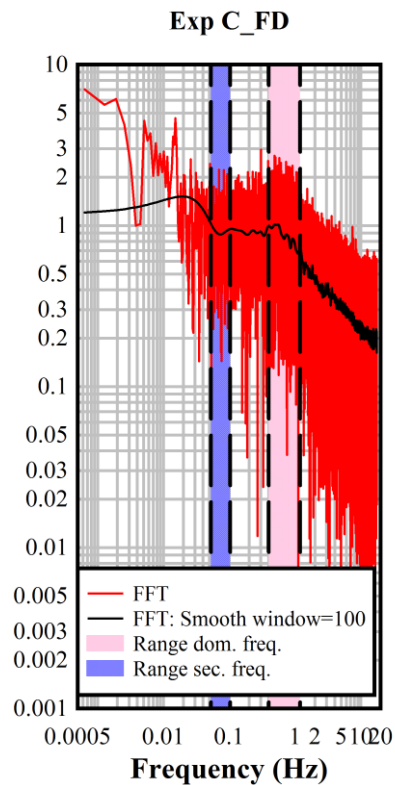
D) EXPERIMENT A ($Fr_1 = 5.1$, $Re = 8.3 \times 10^4$, PD)



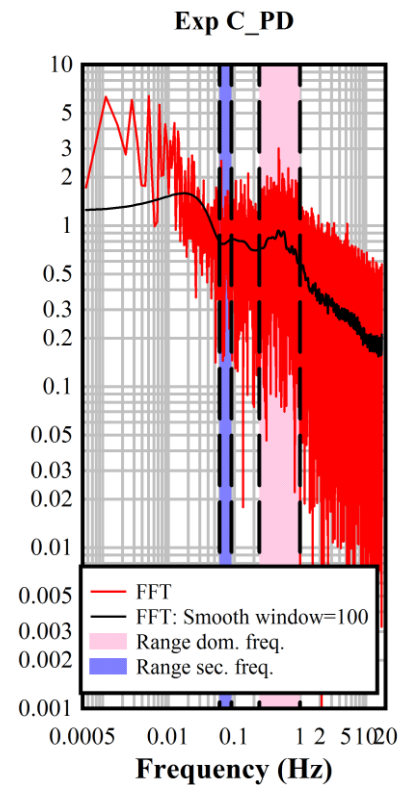
E) EXPERIMENT B ($Fr_1 = 5.1, Re = 6.2 \times 10^4$, FD)



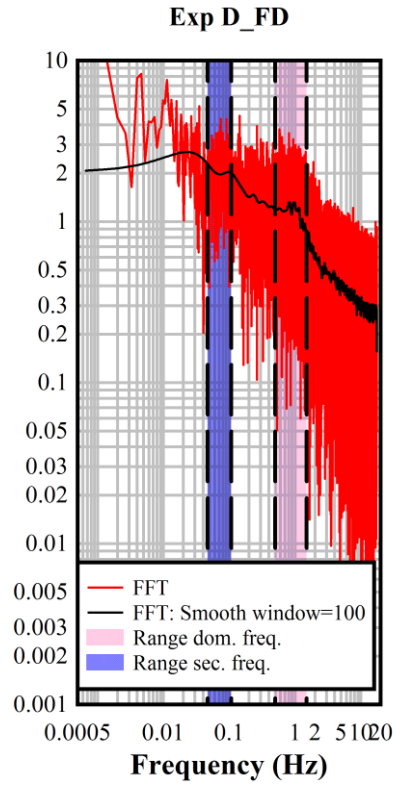
F) EXPERIMENT B ($Fr_1 = 5.1, Re = 6.2 \times 10^4$, PD)



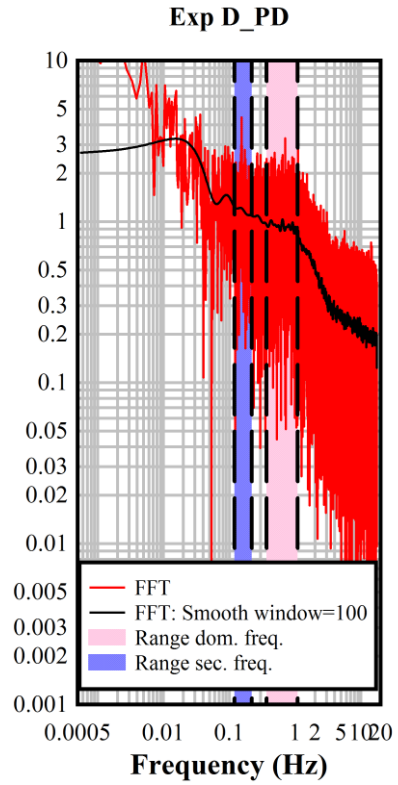
G) EXPERIMENT C ($Fr_1 = 7.0, Re = 6.2 \times 10^4$, FD)



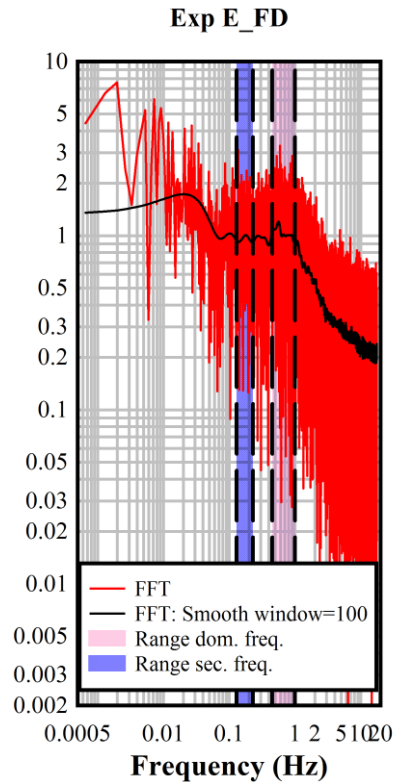
H) EXPERIMENT C ($Fr_1 = 7.0, Re = 6.2 \times 10^4$, PD)



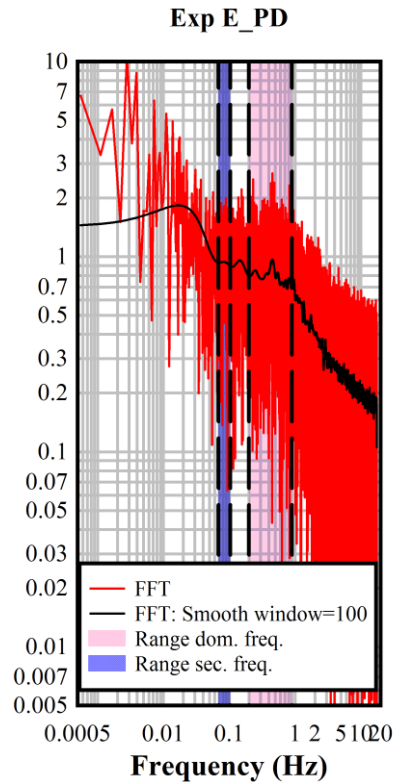
i) EXPERIMENT D ($Fr_1 = 7.0$, $Re = 1.1 \times 10^5$, FD)



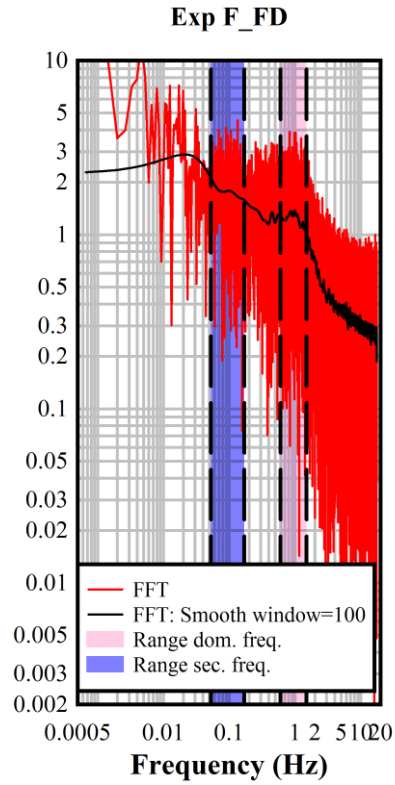
j) EXPERIMENT D ($Fr_1 = 7.0$, $Re = 1.1 \times 10^5$, PD)



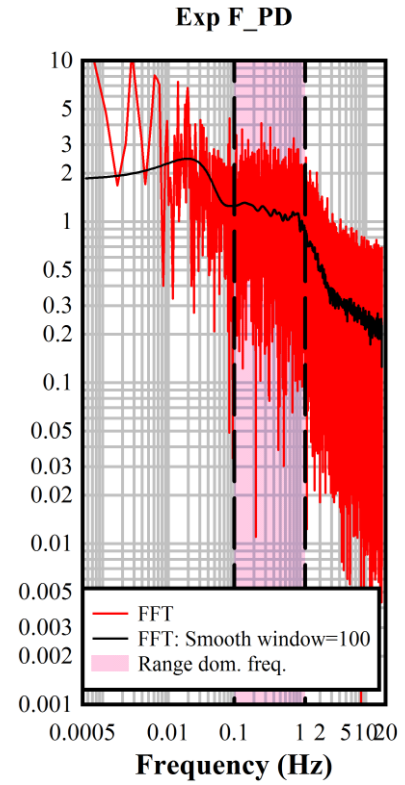
k) EXPERIMENT E ($Fr_1 = 8.2$, $Re = 7.5 \times 10^4$, FD)



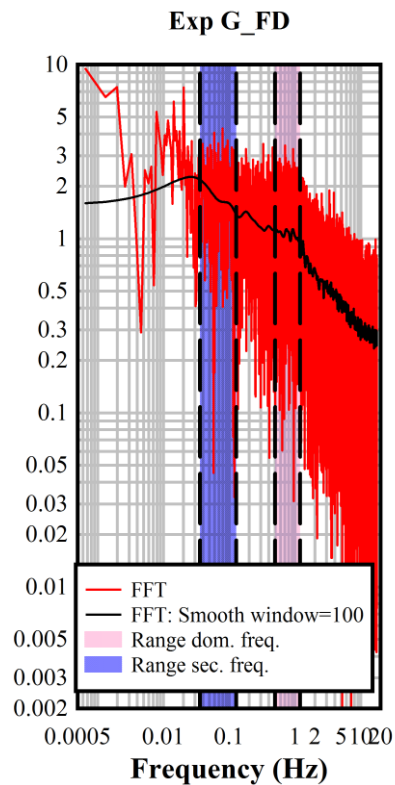
l) EXPERIMENT E ($Fr_1 = 8.5$, $Re = 7.5 \times 10^4$, PD)



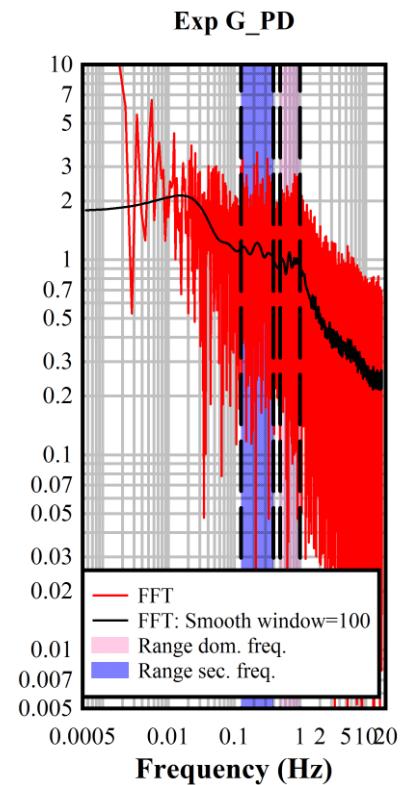
M) EXPERIMENT F ($Fr_1 = 8.0$, $Re = 1.2 \times 10^5$, FD)



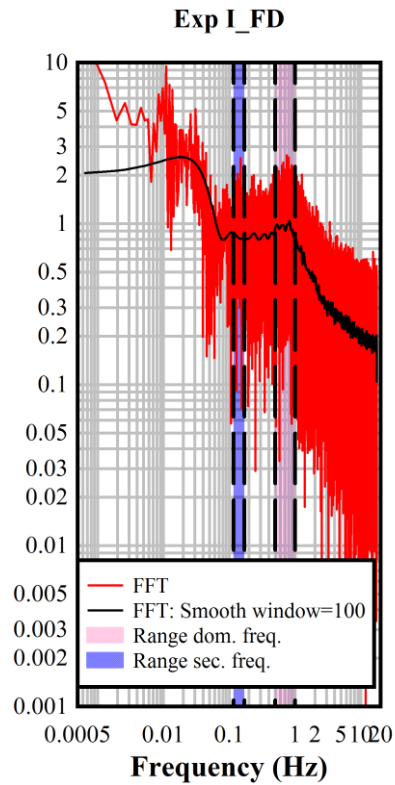
N) EXPERIMENT F ($Fr_1 = 8.4$, $Re = 1.2 \times 10^5$, PD)



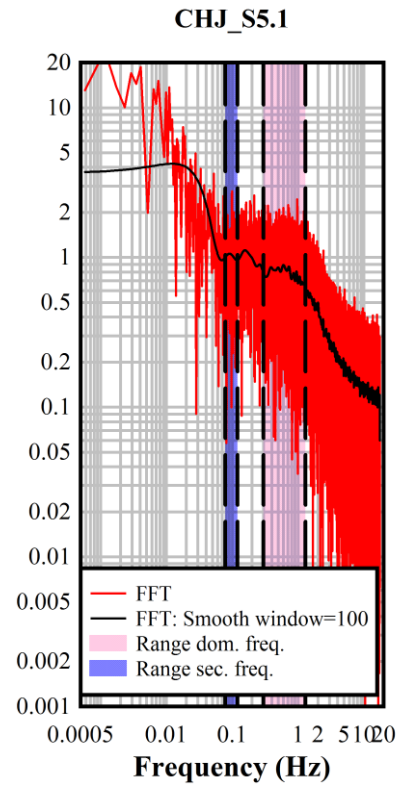
O) EXPERIMENT G_FD



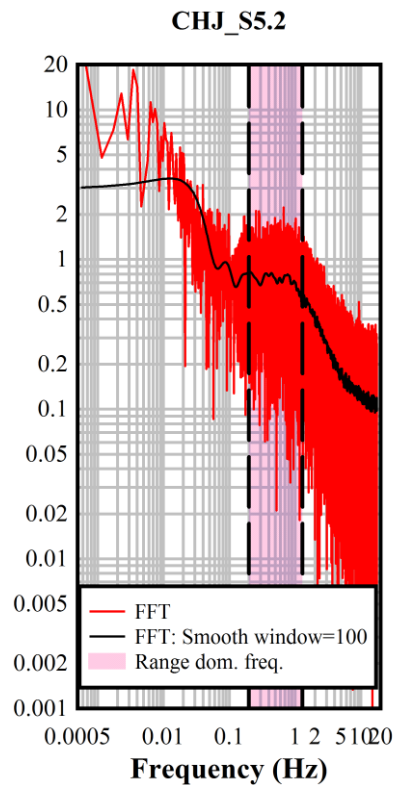
P) EXPERIMENT G_PD



Q) EXPERIMENT I ($Fr_l = 3.8, Re = 9.5 \times 10^4$, FD)



R) EXPERIMENT CHJ_S5.1 ($Fr_l = 4.6 Re = 1 \times 10^5$)

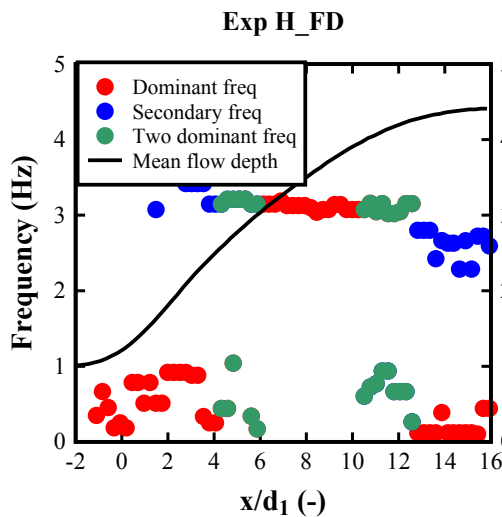


S) EXPERIMENT CHJ ($Fr_l = 4.7 Re = 8.4 \times 10^4$)

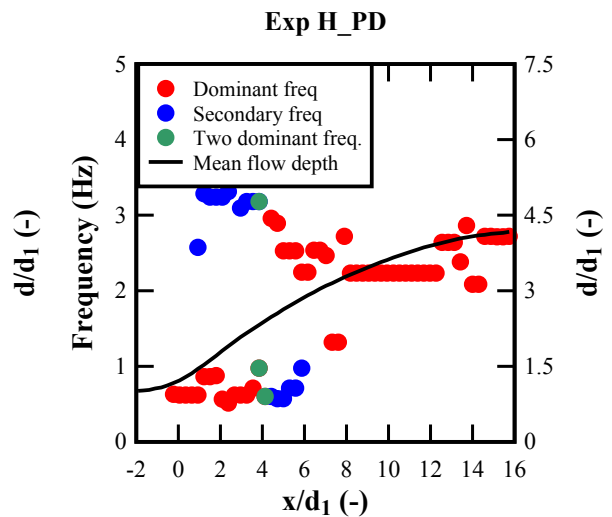
DIGITAL APPENDIX C-1. SPECTRAL ANALYSIS AND CHARACTERISTIC FREQUENCIES OF THE JUMP TOE OSCILLATIONS IN THE PRESENT STUDY.

DIGITAL APPENDIX. C.2. FREE-SURFACE CHARACTERISTIC FREQUENCIES

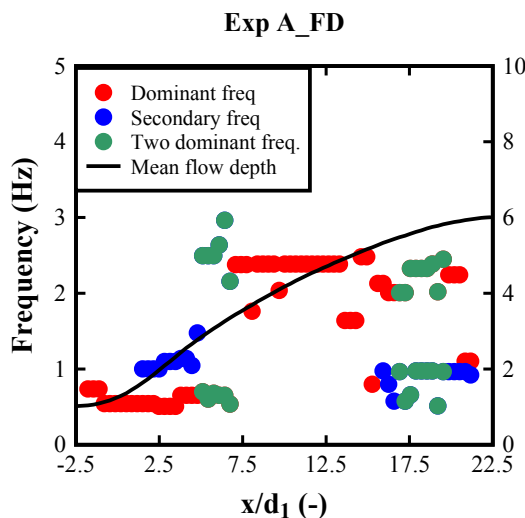
Digital appendix C-2 present the frequency patterns for the free-surface fluctuations of all the experiments conducted under free-jump toe movement (Mode 1). A frequency classification between dominant and secondary frequencies was conducted manually and Digital appendix C-2 shows the dominant frequencies in red, secondary frequencies in blue and in cases where two frequencies were equally dominant green symbols were used. The mean flow depth was included as reference (Black line). Close to the jump toe, the characteristic frequencies observed were between 0.2 – 1.5 Hz and 1.5 - 4 Hz, within the jump roller the frequencies were in the range of 1.5 – 4 Hz and at the end of the jump a range of frequencies were observed within 0.1 – 3 Hz. Large data scatter was observed for larger Froude numbers associated with larger free-surface fluctuations and instabilities. However, despite the data scatter, the three regions are clearly observed in all the experiments conducted i.e. Jump toe region, roller region and conjugate flow depth region.



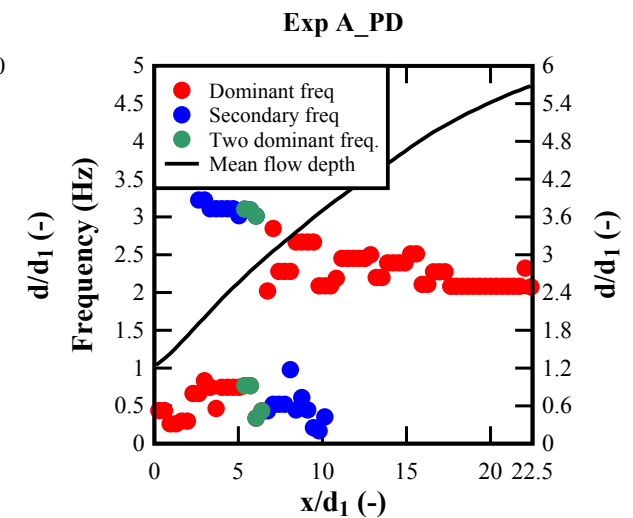
A) EXPERIMENT H ($Fr_1 = 3.8$, $Re = 6.2 \times 10^4$, FD)



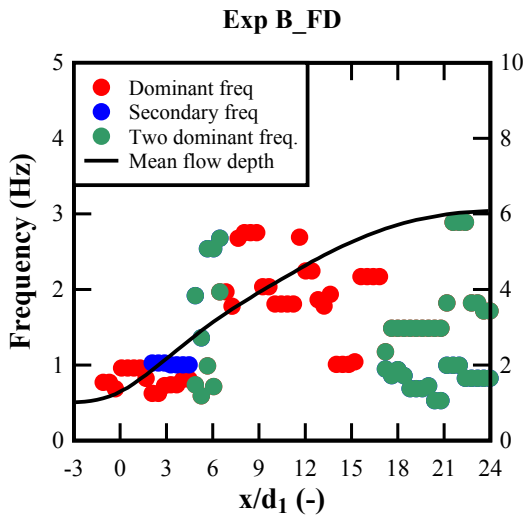
B) EXPERIMENT H ($Fr_1 = 3.8$, $Re = 6.2 \times 10^4$, PD)



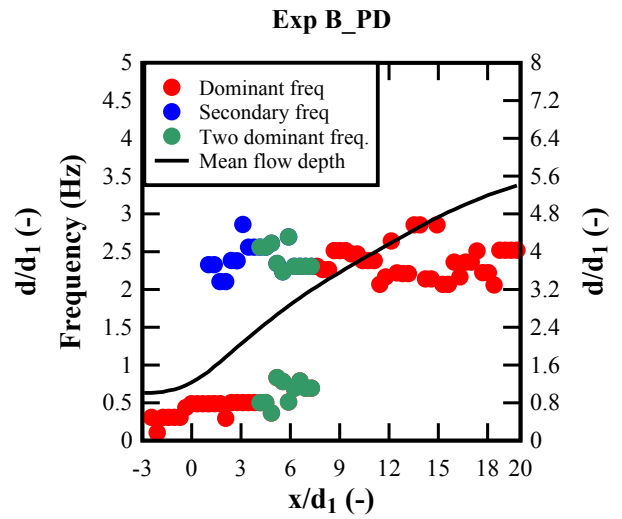
C) EXPERIMENT A ($Fr_1 = 5.1$, $Re = 8.3 \times 10^4$, FD)



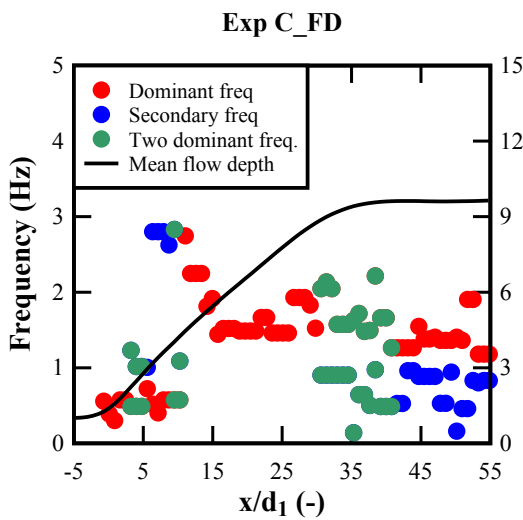
D) EXPERIMENT A ($Fr_1 = 5.1$, $Re = 8.3 \times 10^4$, PD)



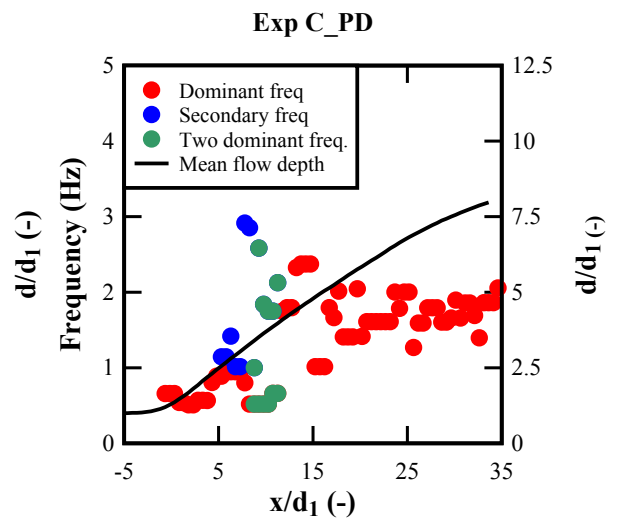
E) EXPERIMENT B ($Fr_1 = 5.1$, $Re = 6.2 \times 10^4$, FD)



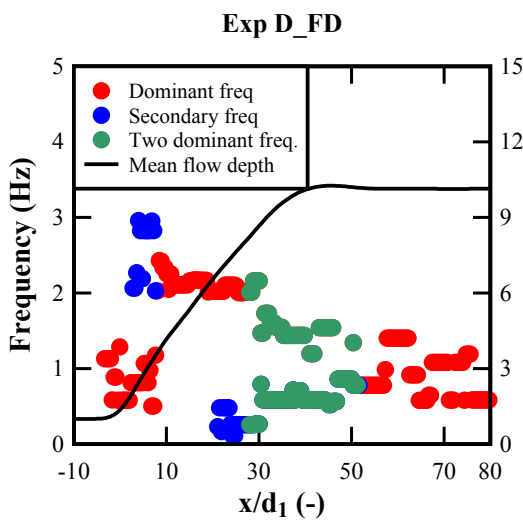
F) EXPERIMENT B ($Fr_1 = 5.1$, $Re = 6.2 \times 10^4$, PD)



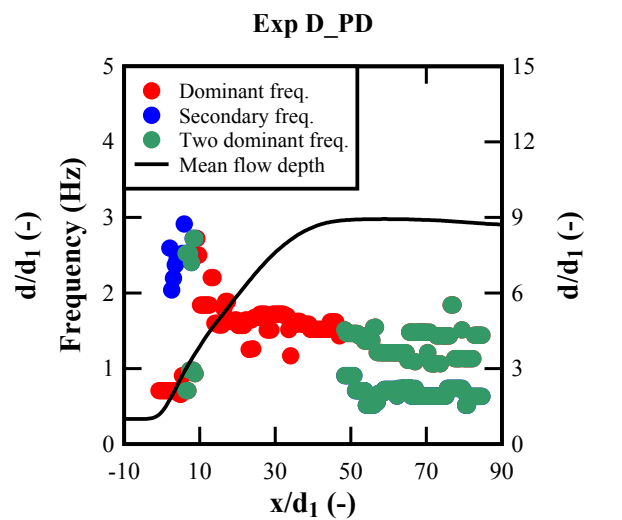
G) EXPERIMENT C ($Fr_1 = 7.0$, $Re = 6.2 \times 10^4$, FD)



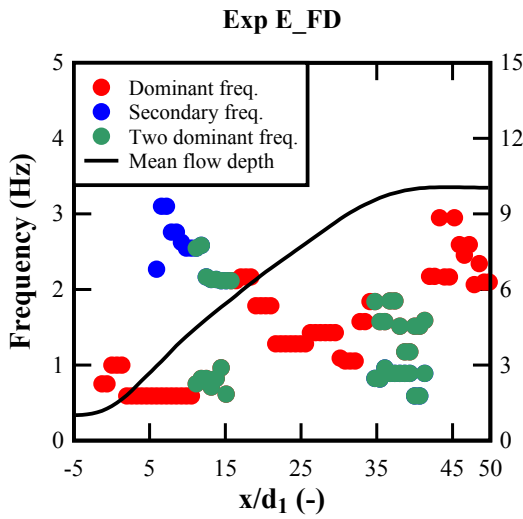
H) EXPERIMENT C ($Fr_1 = 7.0$, $Re = 6.2 \times 10^4$, PD)



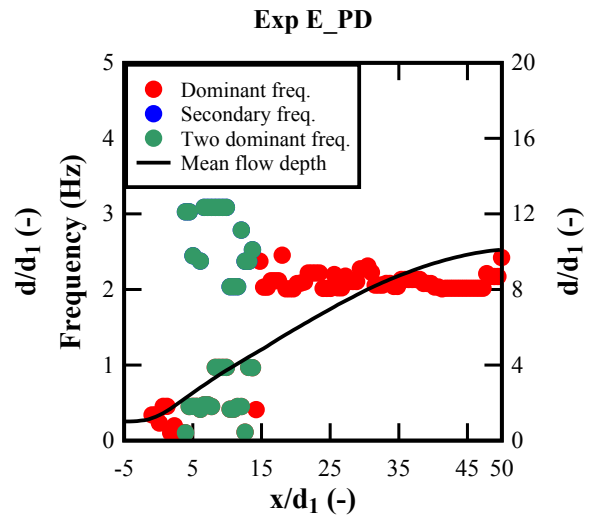
I) EXPERIMENT D ($Fr_1 = 7.0$, $Re = 1.1 \times 10^5$, FD)



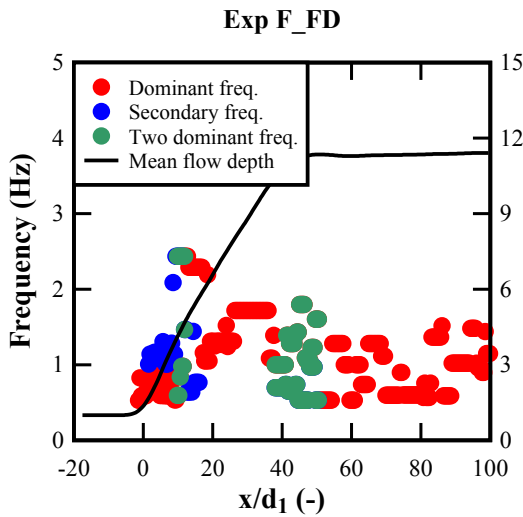
J) EXPERIMENT D ($Fr_1 = 7.0$, $Re = 1.1 \times 10^5$, PD)



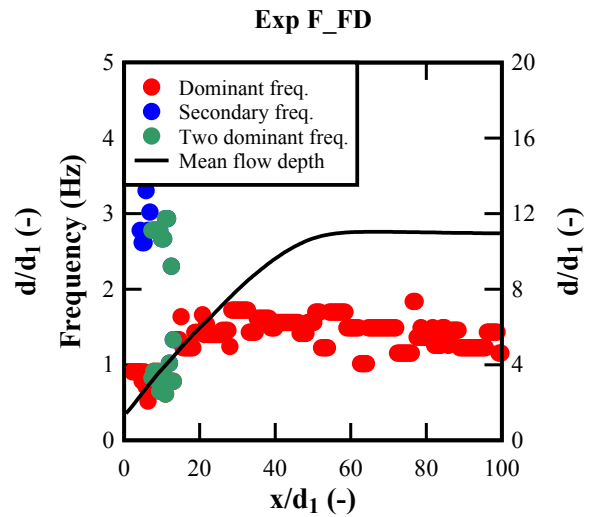
K) EXPERIMENT E ($Fr_1 = 8.2, Re = 7.5 \times 10^4$, FD)



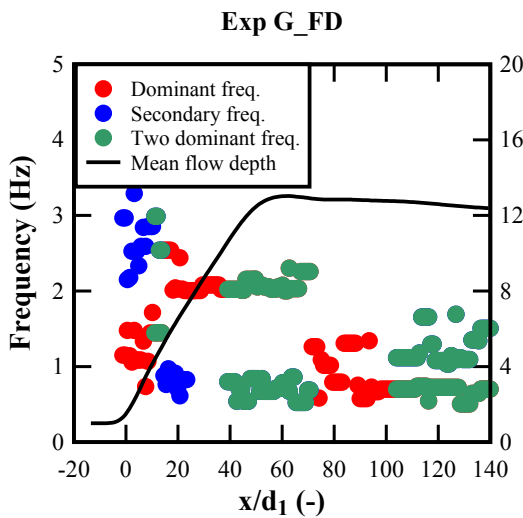
L) EXPERIMENT E ($Fr_1 = 8.5, Re = 7.5 \times 10^4$, PD)



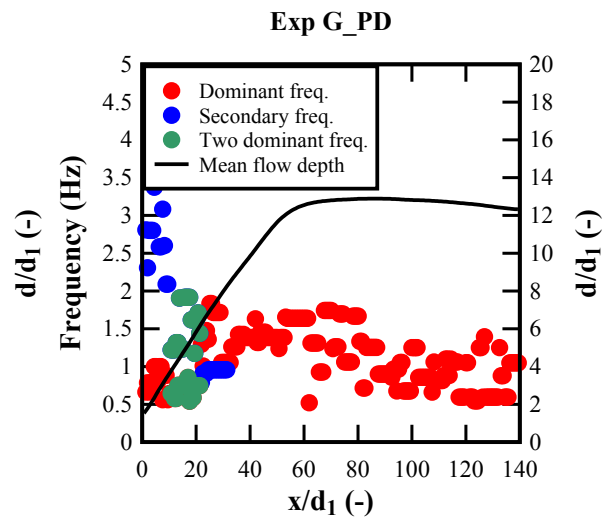
M) EXPERIMENT F ($Fr_1 = 8.0, Re = 1.2 \times 10^5$, FD)



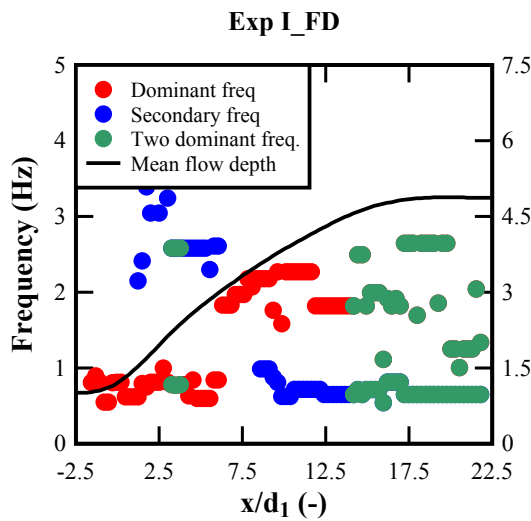
N) EXPERIMENT F ($Fr_1 = 8.4, Re = 1.2 \times 10^5$, PD)



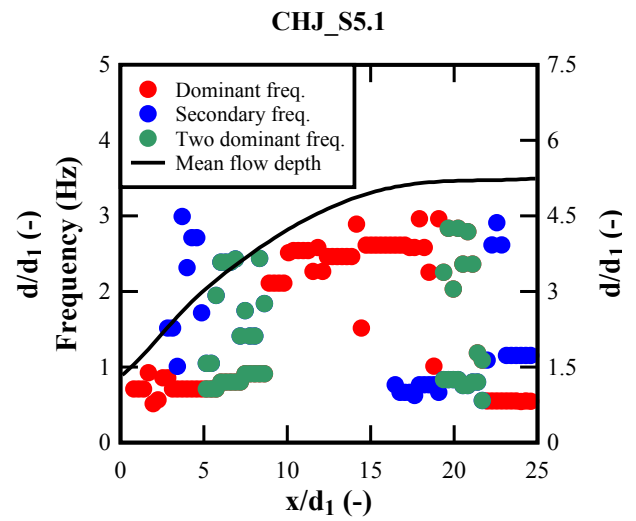
O) EXPERIMENT G ($Fr_1 = 10, Re = 8.8 \times 10^4$, FD)



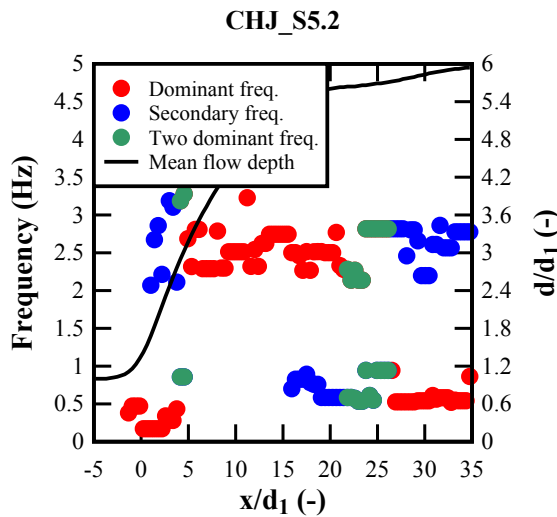
P) EXPERIMENT G ($Fr_1 = 10, Re = 8.8 \times 10^4$, PD)



Q) EXPERIMENT I ($Fr_1 = 3.8, Re = 9.5 \times 10^4$, FD)



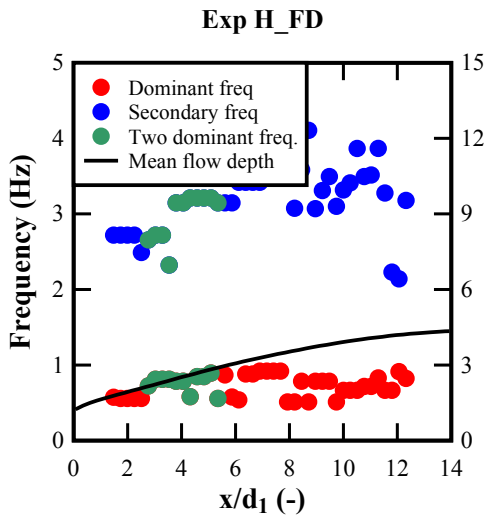
R) EXPERIMENT CHJ_S5.1 ($Fr_1 = 4.6, Re = 1 \times 10^5$)



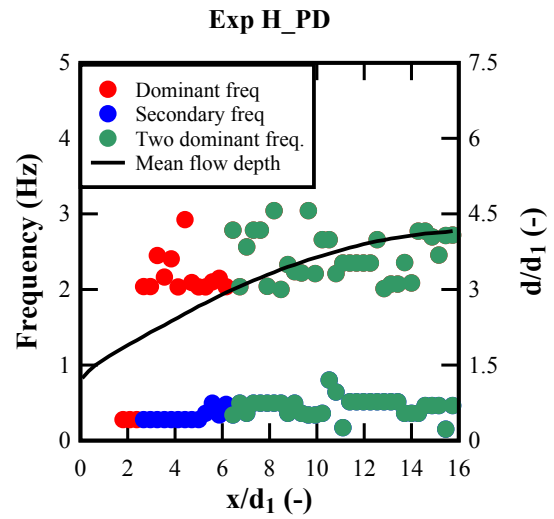
S) EXPERIMENT CHJ_S5.2 ($Fr_1 = 4.7, Re = 8.4 \times 10^4$)

DIGITAL APPENDIX C-2. CHARACTERISTIC FREQUENCIES FOR THE PRESENT HYDRAULIC JUMPS WITH FREE-MOVING JUMP TOE (MODE 1). RED SYMBOLS: DOMINANT FREQUENCY; BLUE SYMBOLS: SECONDARY FREQUENCY; GREEN SYMBOLS: TWO DOMINANT FREQUENCIES. BLACK LINE: MEAN FLOW DEPTH d/d_1 .

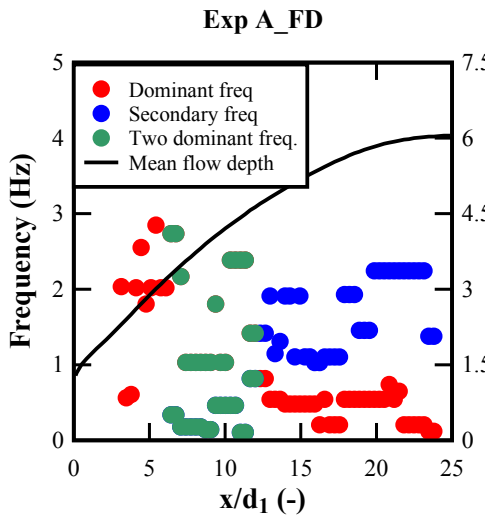
Digital appendix C-3 presents the frequency patterns for the free-surface fluctuations of all the experiments conducted under fixed jump toe condition (Mode 2). Despite some scatter in the frequency values, different frequency regions were identified near the jump toe, within the jump roller and towards the downstream end of the roller. Near the jump toe, the dominant frequencies were in the range of 1 – 3 Hz. In the jump roller, the frequency range presented large data scatter showing two dominant frequencies is some of the experiments with frequency ranges between 0.5 – 3 Hz with the majority of dominant frequencies within the range of 0.5 – 1 Hz. Towards the downstream end of the roller, a dominant frequency of about 0.1 – 1.5 Hz was observed for the majority of the cases and a range of secondary frequencies of 1.5 – 3 Hz. Mode 2 was acting as a filter analysis of Mode 1 by the addition of jump toe oscillation frequencies in areas without the effect of the jump toe oscillation and the reduction of the jump toe frequencies close to the jump toe .



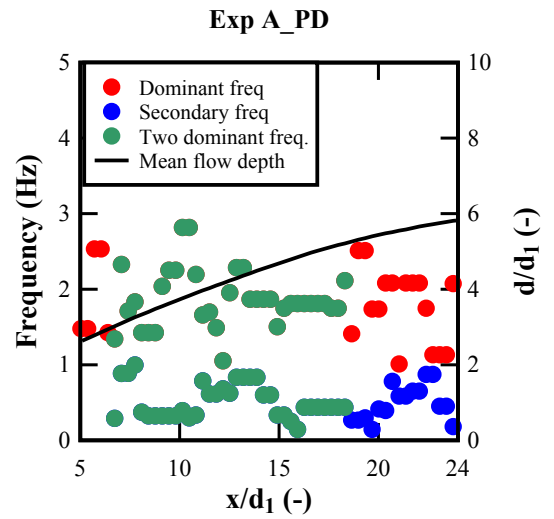
A) EXPERIMENT H ($Fr_1 = 3.8$, $Re = 6.2 \times 10^4$, FD)



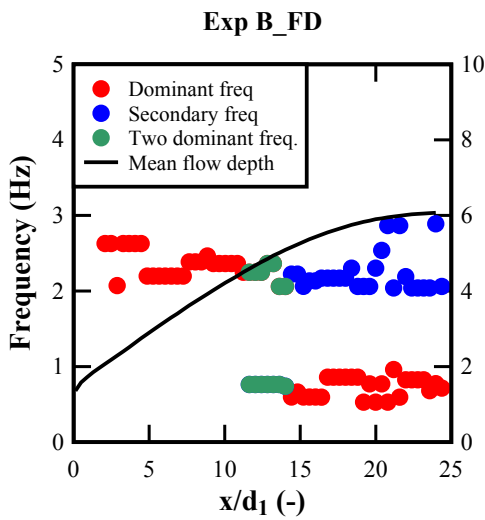
B) EXPERIMENT H ($Fr_1 = 3.8$, $Re = 6.2 \times 10^4$, PD)



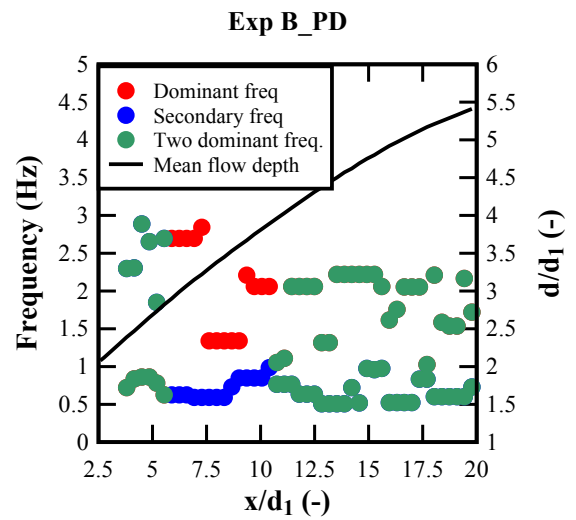
C) EXPERIMENT A ($Fr_1 = 5.1$, $Re = 8.3 \times 10^4$, FD)



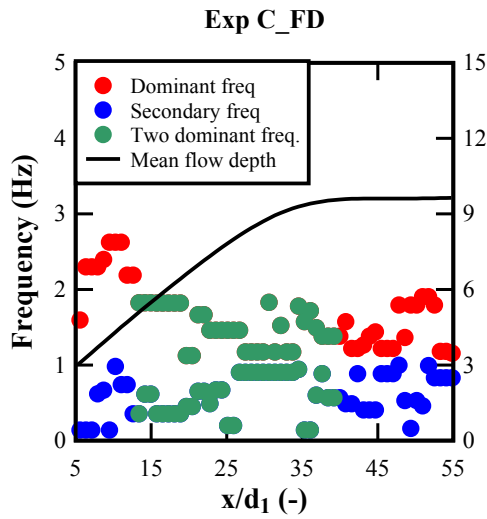
D) EXPERIMENT A ($Fr_1 = 5.1$, $Re = 8.3 \times 10^4$, PD)



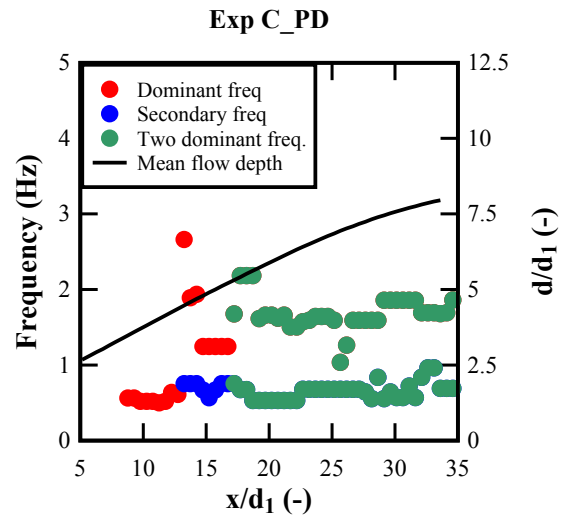
E) EXPERIMENT B ($Fr_1 = 5.1$, $Re = 6.2 \times 10^4$, FD)



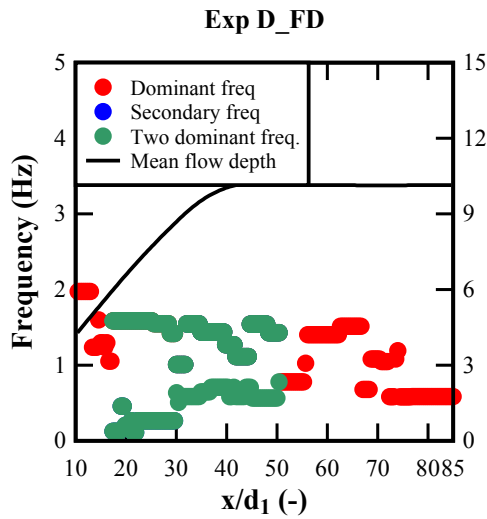
F) EXPERIMENT B ($Fr_1 = 5.1$, $Re = 6.2 \times 10^4$, PD)



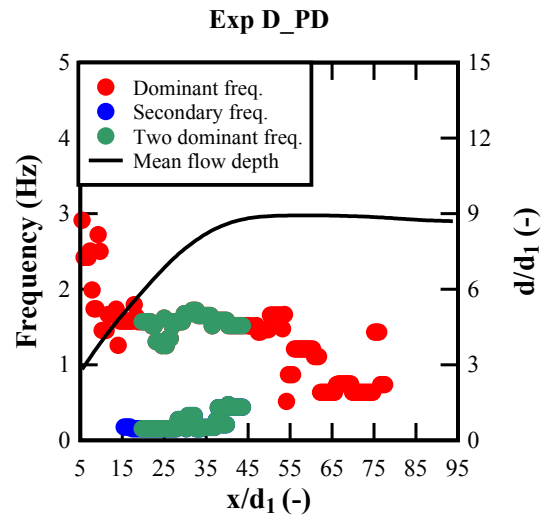
G) EXPERIMENT C ($Fr_1 = 7.0$, $Re = 6.2 \times 10^4$, FD)



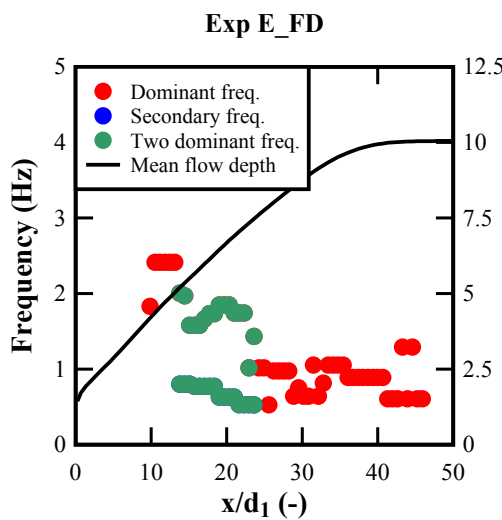
H) EXPERIMENT C ($Fr_1 = 7.0$, $Re = 6.2 \times 10^4$, PD)



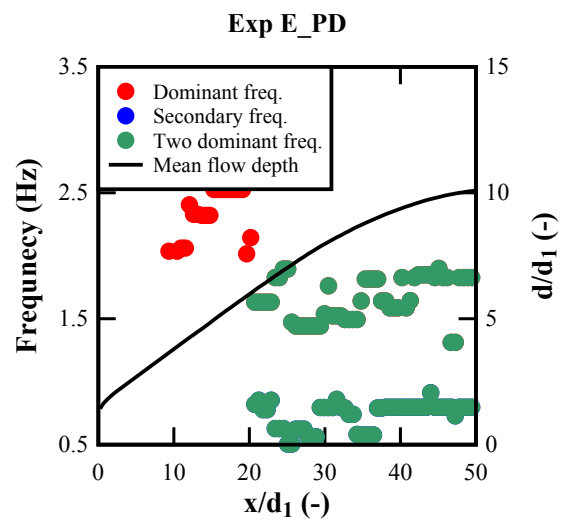
I) EXPERIMENT D ($Fr_1 = 7.0$, $Re = 1.1 \times 10^5$, FD)



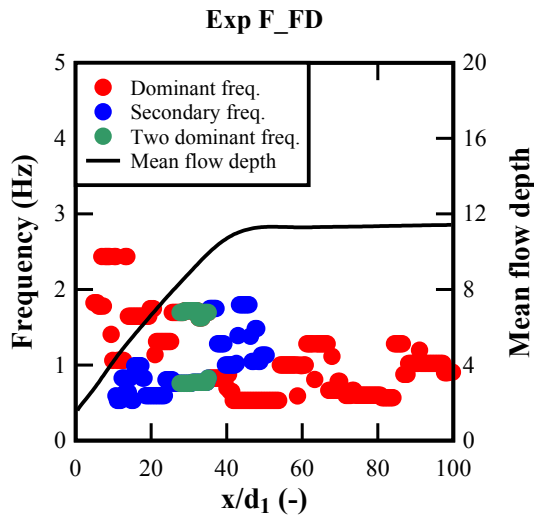
J) EXPERIMENT D ($Fr_1 = 7.0$, $Re = 1.1 \times 10^5$, PD)



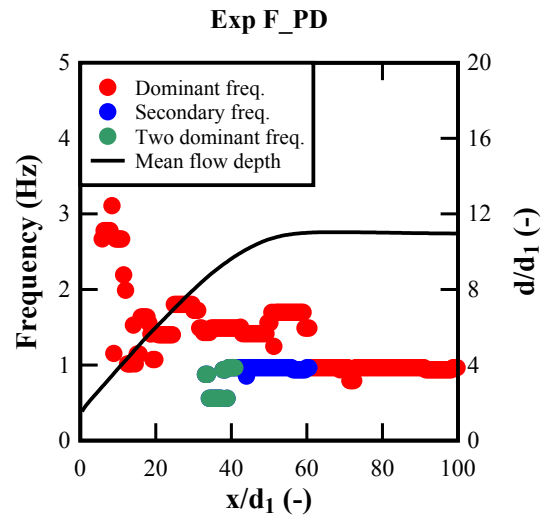
K) EXPERIMENT E ($Fr_1 = 8.2$, $Re = 7.5 \times 10^4$, FD)



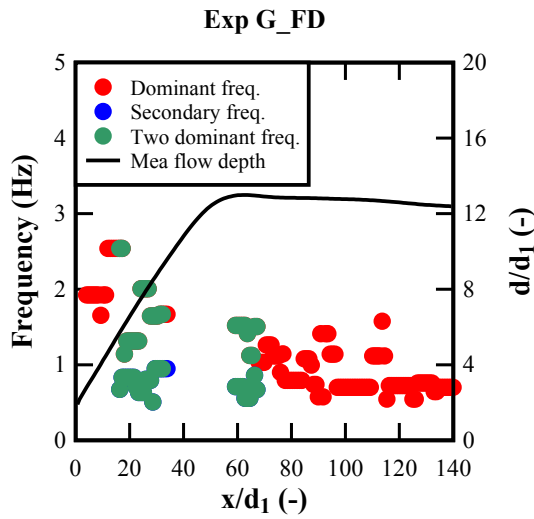
L) EXPERIMENT E ($Fr_1 = 8.5$, $Re = 7.5 \times 10^4$, PD)



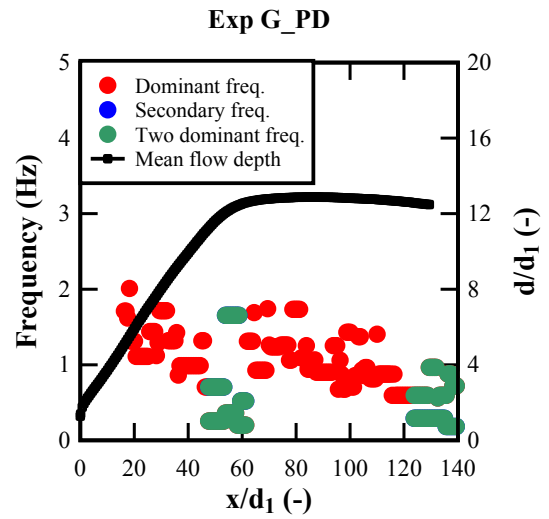
M) EXPERIMENT F ($Fr_1 = 8.0, Re = 1.2 \times 10^5$, FD)



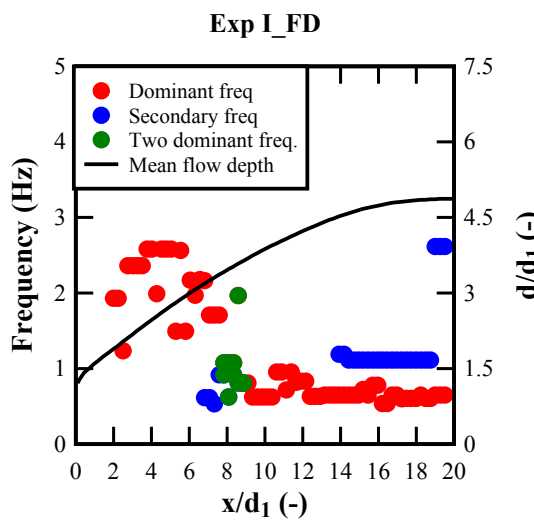
N) EXPERIMENT F ($Fr_1 = 8.4, Re = 1.2 \times 10^5$, PD)



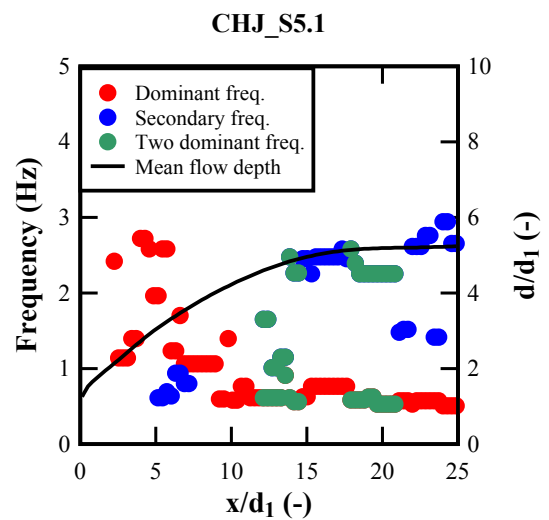
O) EXPERIMENT G ($Fr_1 = 10, Re = 8.8 \times 10^4$, FD)



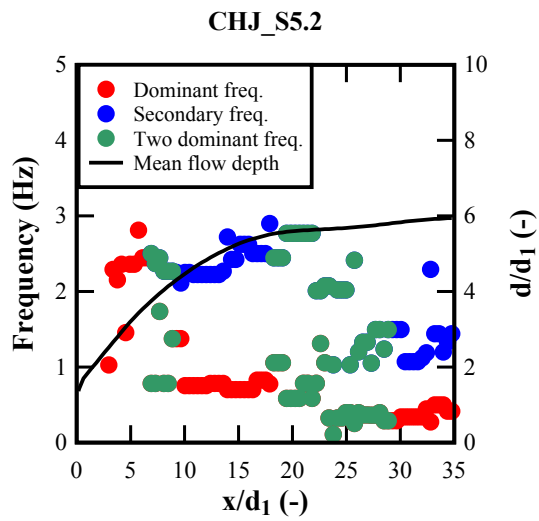
P) EXPERIMENT G ($Fr_1 = 10, Re = 8.8 \times 10^4$, PD)



Q) EXPERIMENT I ($Fr_1 = 3.8, Re = 9.5 \times 10^4$, FD)



R) EXPERIMENT CHJ_S5.1 ($Fr_1 = 4.6, Re = 1 \times 10^5$)



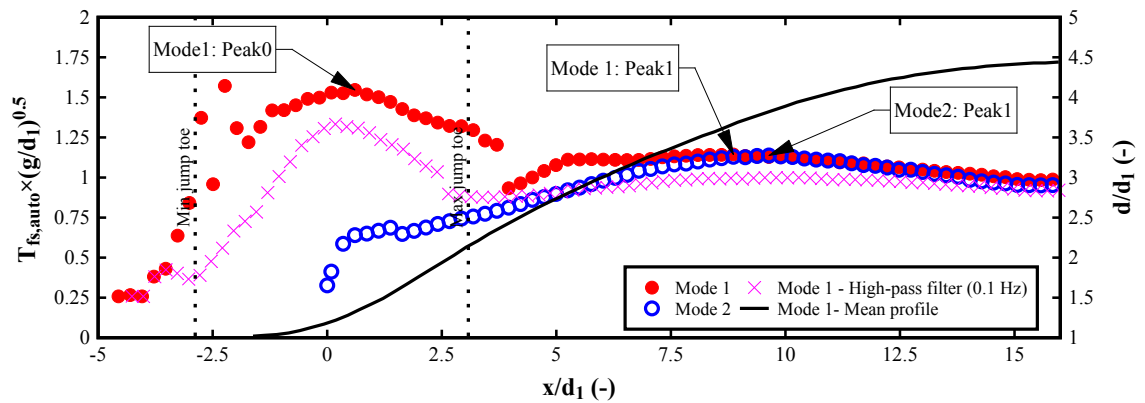
s) EXPERIMENT CHJ_S5.2 ($Fr_1 = 4.7$ $Re = 8.4 \times 10^4$)

DIGITAL APPENDIX C-3. CHARACTERISTIC FREQUENCIES FOR THE PRESENT HYDRAULIC JUMPS WITH FIXED JUMP TOE (MODE 2). RED SYMBOLS: DOMINANT FREQUENCY; BLUE SYMBOLS: SECONDARY FREQUENCY; GREEN SYMBOLS: TWO DOMINANT FREQUENCIES. BLACK LINE: MEAN FLOW DEPTH d/d_1 .

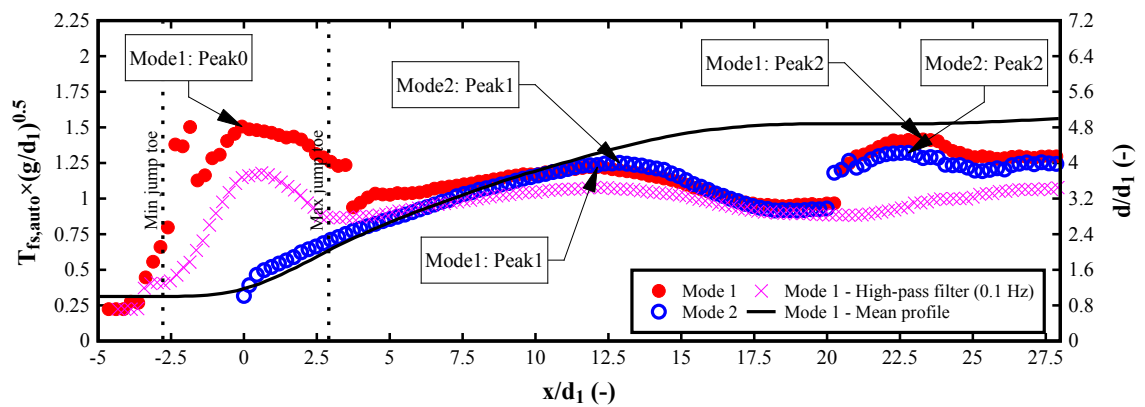
DIGITAL APPENDIX. C.3. AUTO-CORRELATION TIME SCALES

DIGITAL APPENDIX. C.3.1. FULLY DEVELOPED INFLOW CONDITIONS

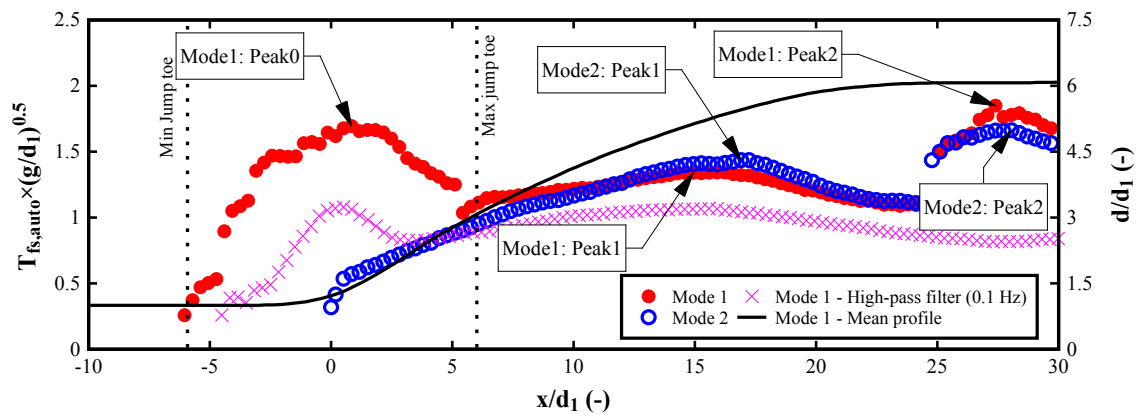
Digital appendix C-4 presents the auto-correlation time scales for Mode 1, Mode 2 and Mode 1 with a high-pass filter of 0.1 Hz as function of the distance from the jump toe for all the experiments conducted with fully developed inflow conditions.



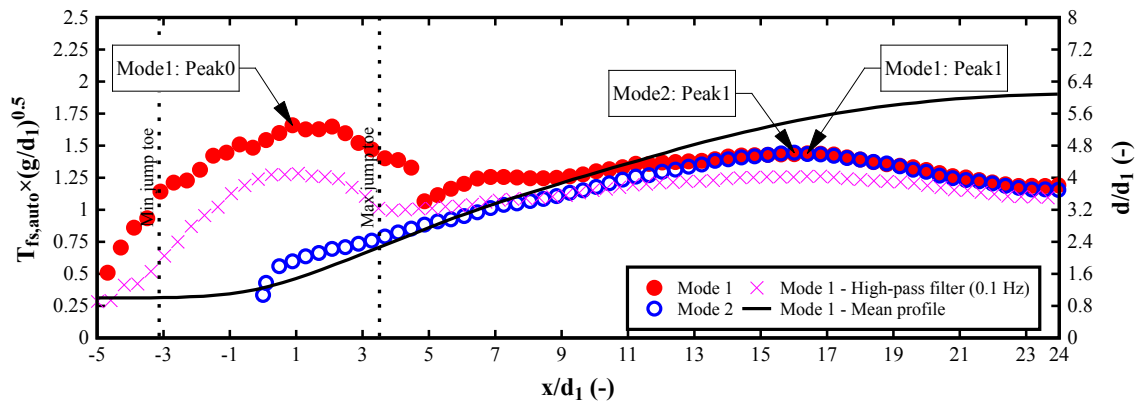
A) EXPERIMENT H ($Fr_1 = 3.8$, $Re = 6.2 \times 10^4$, FD)



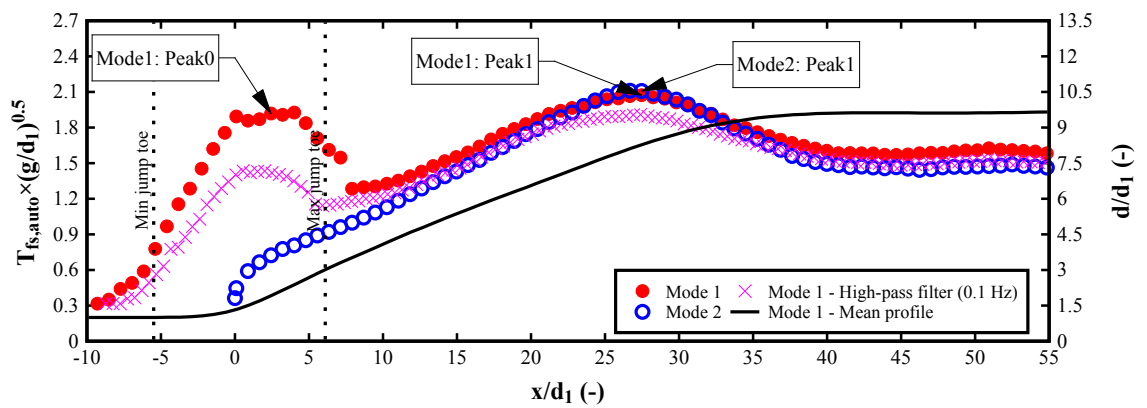
B) EXPERIMENT I ($Fr_1 = 3.8$, $Re = 9.5 \times 10^4$, FD)



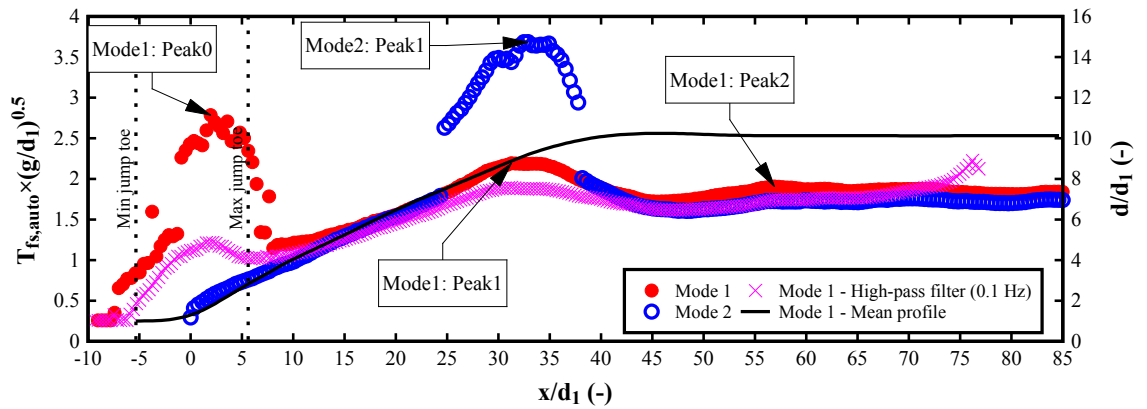
C) EXPERIMENT A ($Fr_1 = 5.1$, $Re = 8.3 \times 10^4$, FD)



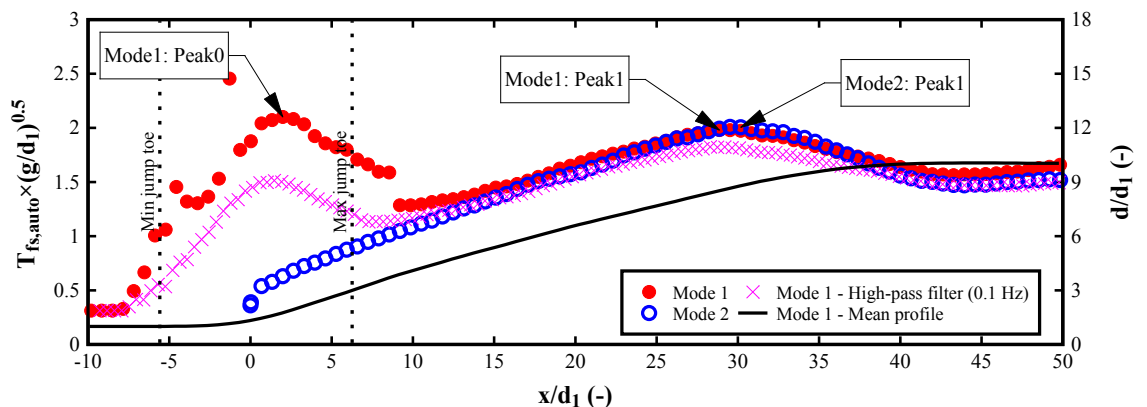
D) EXPERIMENT B ($Fr_1 = 5.1$, $Re = 6.2 \times 10^4$, FD)



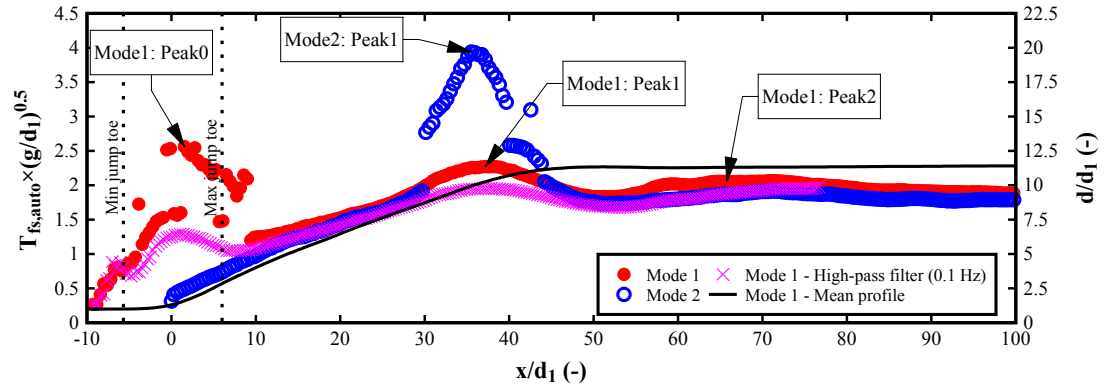
F) EXPERIMENT C ($Fr_1 = 7.0$, $Re = 6.2 \times 10^4$, FD)



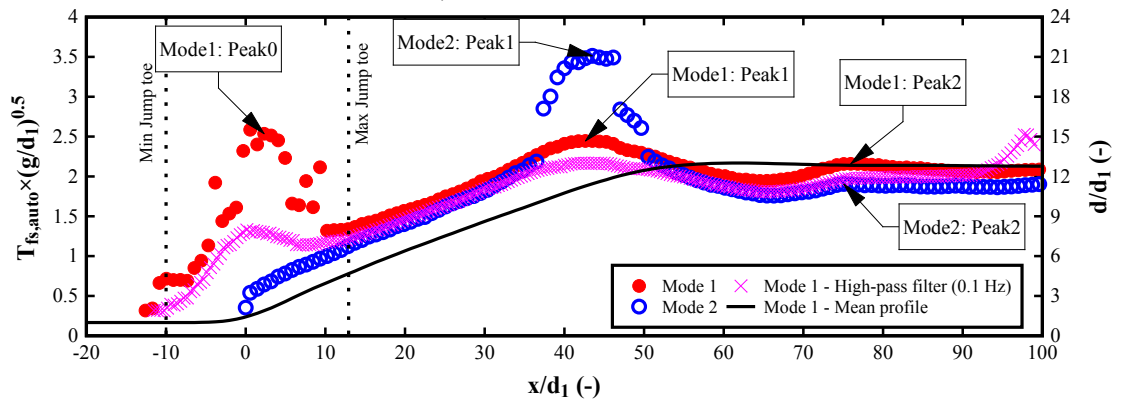
G) EXPERIMENT D ($Fr_1 = 7.0$, $Re = 1.1 \times 10^5$, FD)



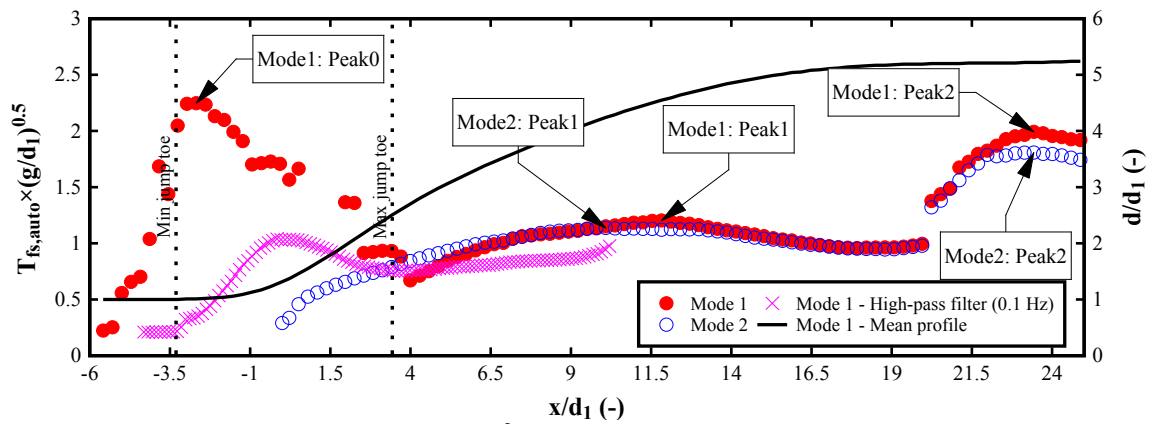
H) EXPERIMENT E_FD ($Fr_1 = 8.2$, $Re = 7.5 \times 10^4$, FD)



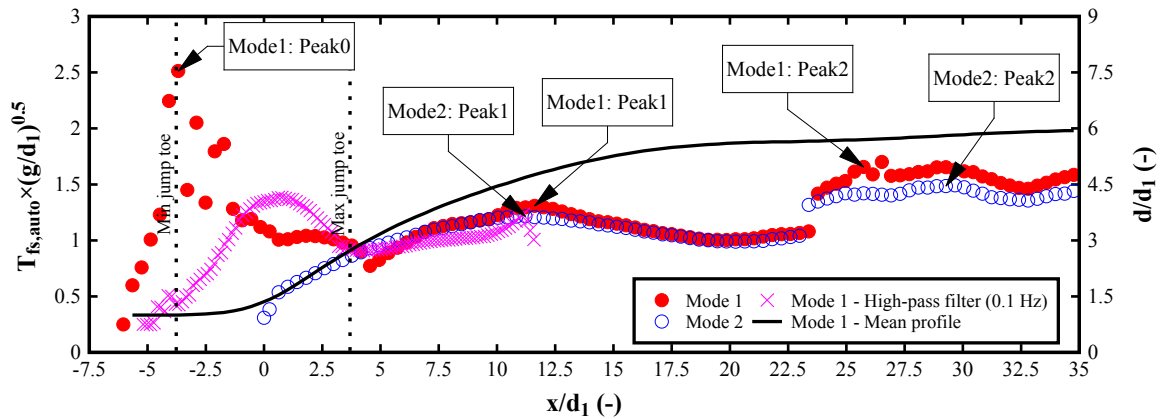
I) EXPERIMENT F ($Fr_1 = 8.0$, $Re = 1.2 \times 10^5$, FD)



J) EXPERIMENT G ($Fr_1 = 10$, $Re = 8.8 \times 10^4$, FD)



L) EXPERIMENT CHJ_S5.1 ($Fr_1 = 4.6$, $Re = 1 \times 10^5$)

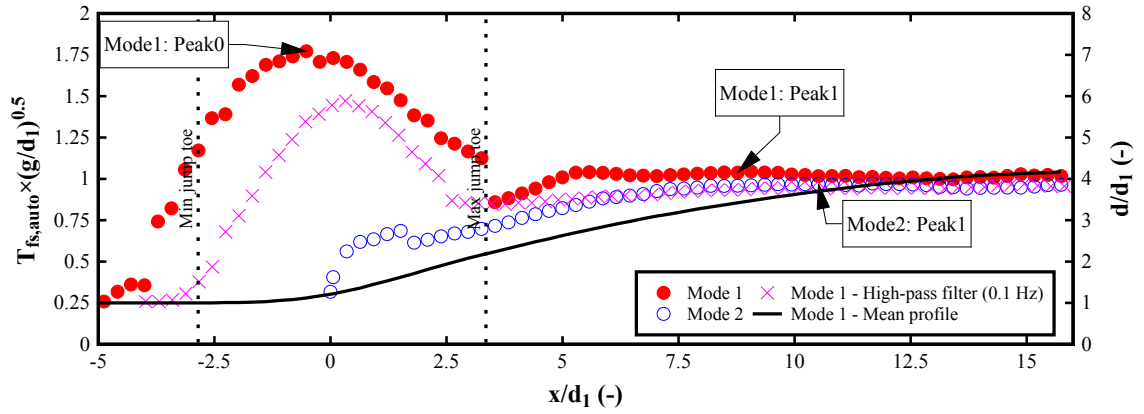


M) EXPERIMENT CHJ_S5.2 ($Fr_1 = 4.7$, $Re = 8.4 \times 10^4$)

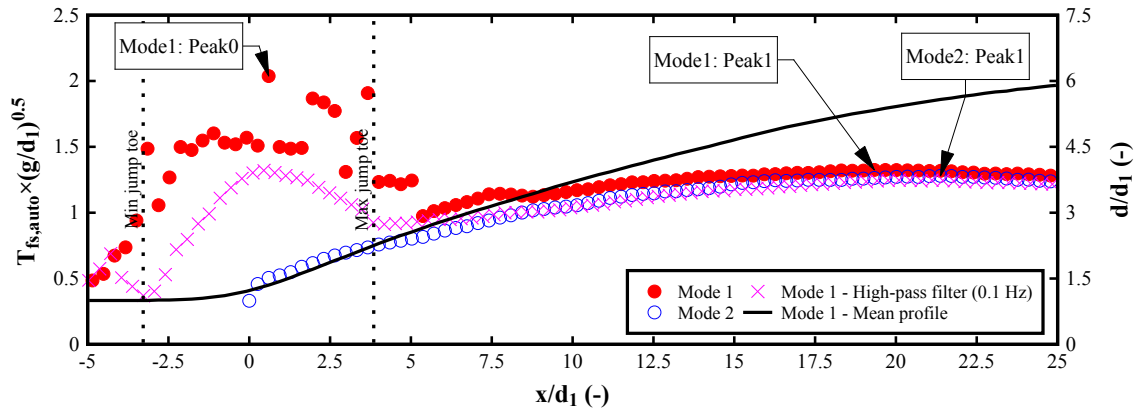
DIGITAL APPENDIX C-4. FREE-SURFACE AUTO-CORRELATION TIME SCALES ALONG THE HYDRAULIC JUMP WITH FULLY DEVELOPED INFLOW CONDITIONS.

DIGITAL APPENDIX. C.3.2. PARTIALLY DEVELOPED INFLOW CONDITIONS

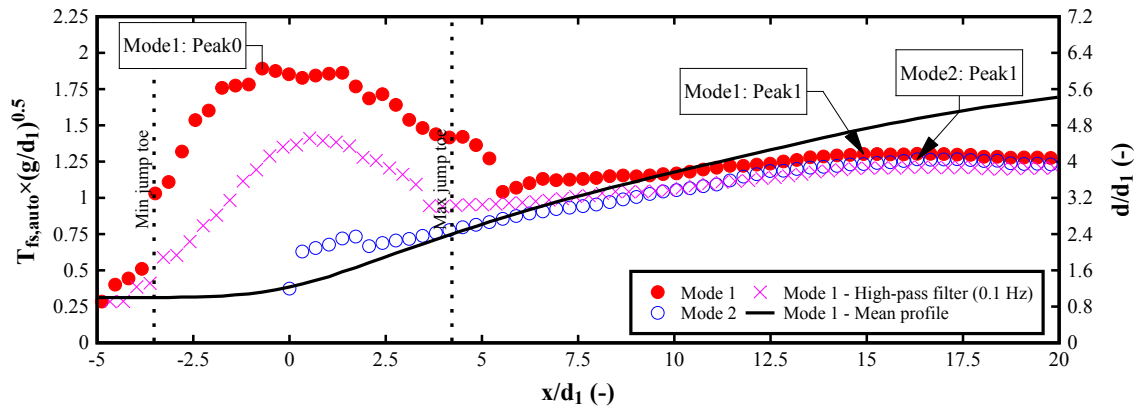
Digital appendix C-5 presents the auto-correlation time scales for Mode 1, Mode 2 and Mode 1 with a high-pass filter of 0.1 Hz as function of the distance from the jump toe for all the experiments conducted with partially developed inflow conditions.



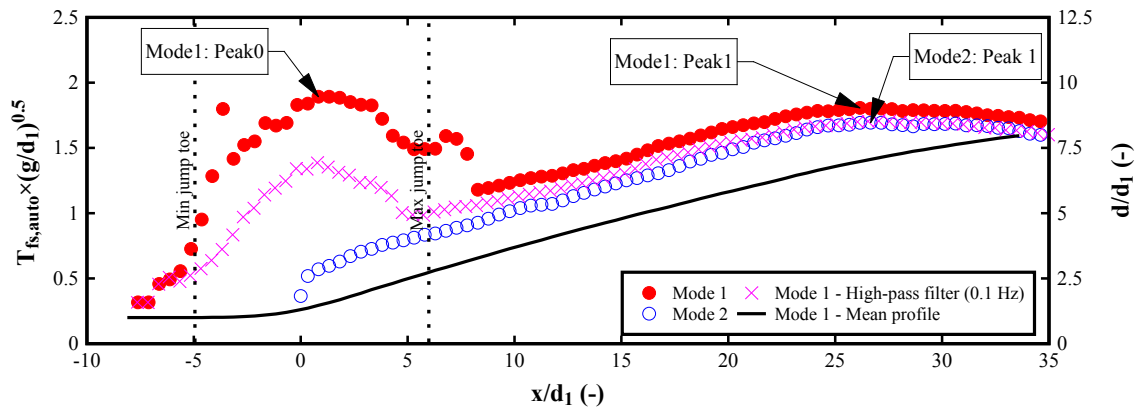
A) EXPERIMENT H ($Fr_1 = 3.8$, $Re = 6.2 \times 10^4$, PD)



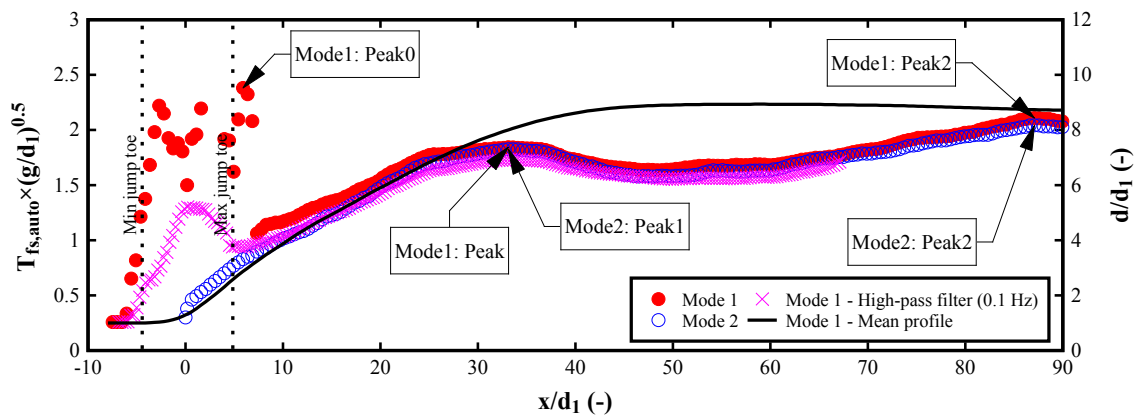
B) EXPERIMENT A ($Fr_1 = 5.1$, $Re = 8.3 \times 10^4$, PD)



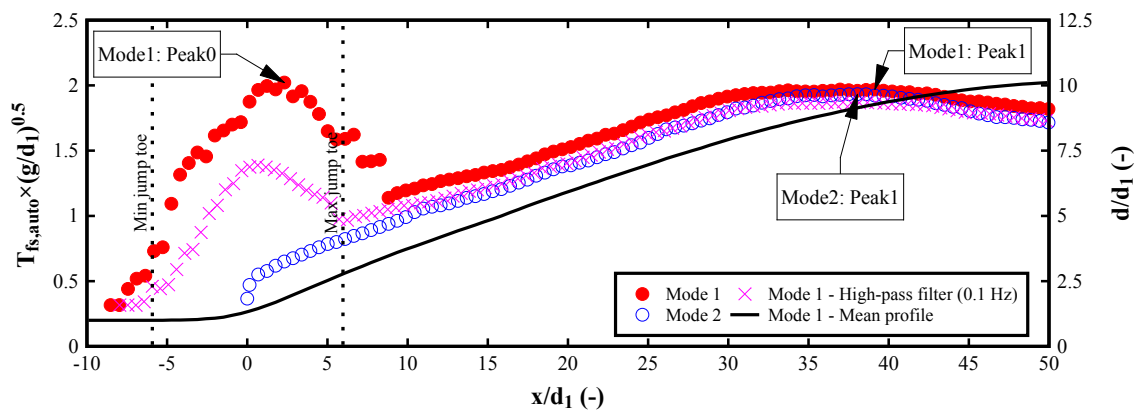
C) EXPERIMENT B ($Fr_1 = 5.1$, $Re = 6.2 \times 10^4$, PD)



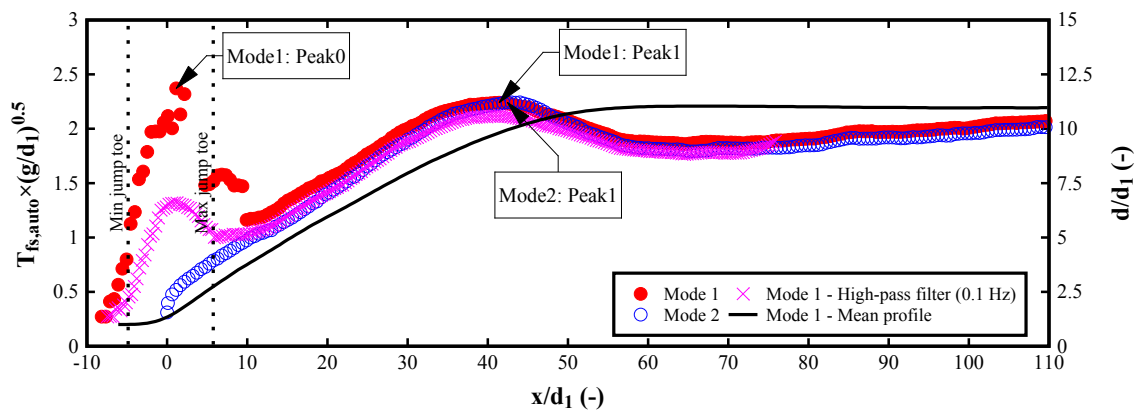
D) EXPERIMENT C ($Fr_1 = 7.0$, $Re = 6.2 \times 10^4$, PD)



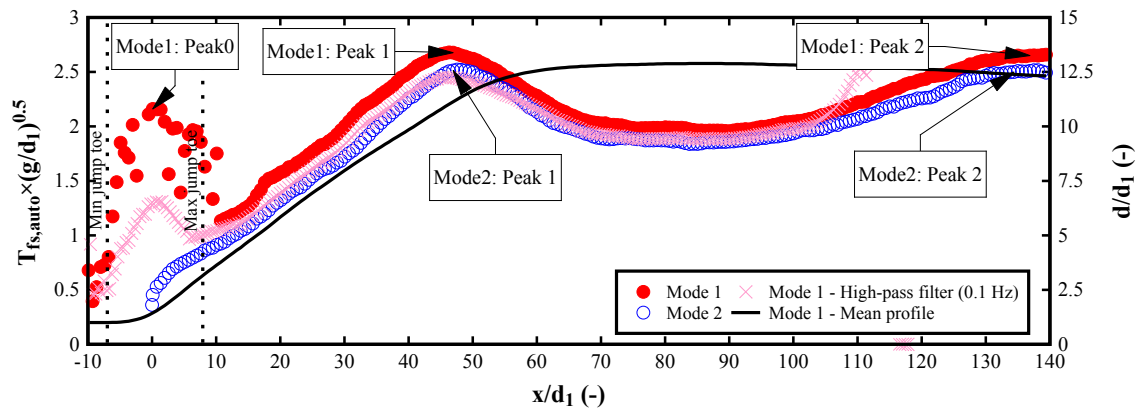
E) EXPERIMENT D ($Fr_1 = 7.0$, $Re = 1.1 \times 10^5$, PD)



F) EXPERIMENT E ($Fr_1 = 8.5$, $Re = 7.5 \times 10^4$, PD)



G) EXPERIMENT F ($Fr_1 = 8.4$, $Re = 1.2 \times 10^5$, PD)



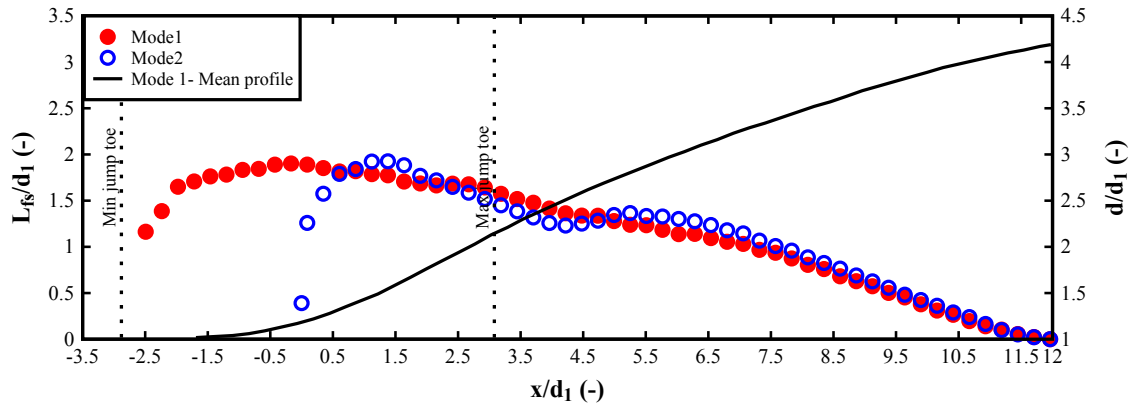
H) EXPERIMENT G ($Fr_1 = 10$, $Re = 8.8 \times 10^4$, PD)

DIGITAL APPENDIX C-5. FREE-SURFACE AUTO-CORRELATION TIME SCALES ALONG THE HYDRAULIC JUMP WITH PARTIALLY DEVELOPED INFLOW CONDITIONS.

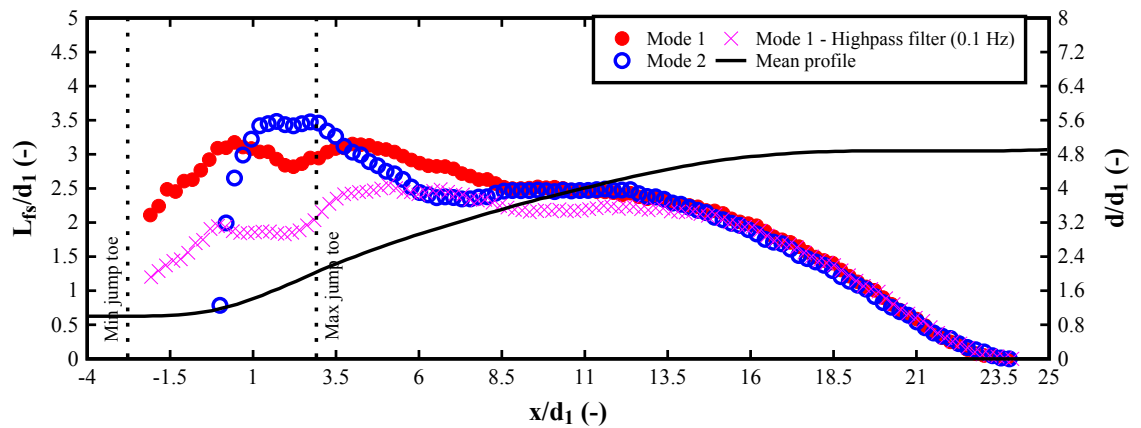
DIGITAL APPENDIX. C.4. INTEGRAL LENGTH SCALES

DIGITAL APPENDIX. C.4.1. FULLY DEVELOPED INFLOW CONDITIONS

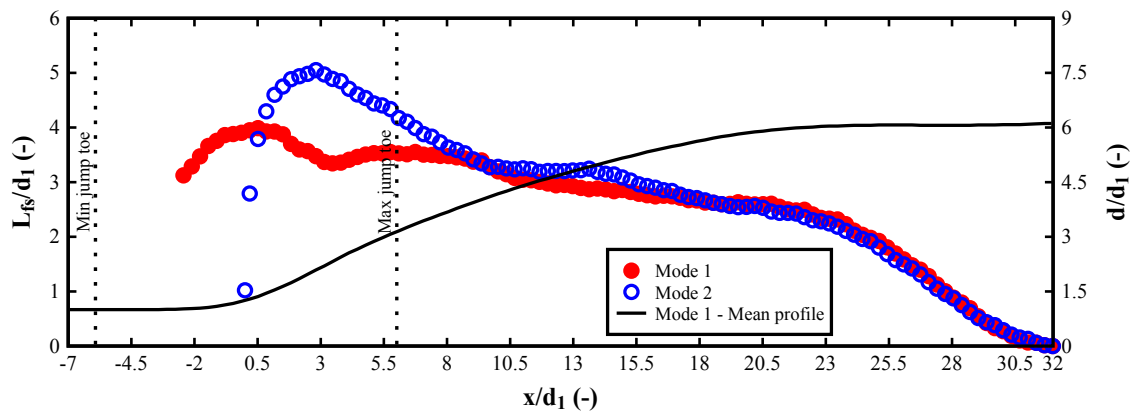
Digital appendix C-6 presents the integral free-surface length scales for Mode 1, Mode 2 and Mode 1 with a high-pass filter of 0.1 Hz as function of the distance from the jump toe for all the experiments conducted with fully developed inflow conditions.



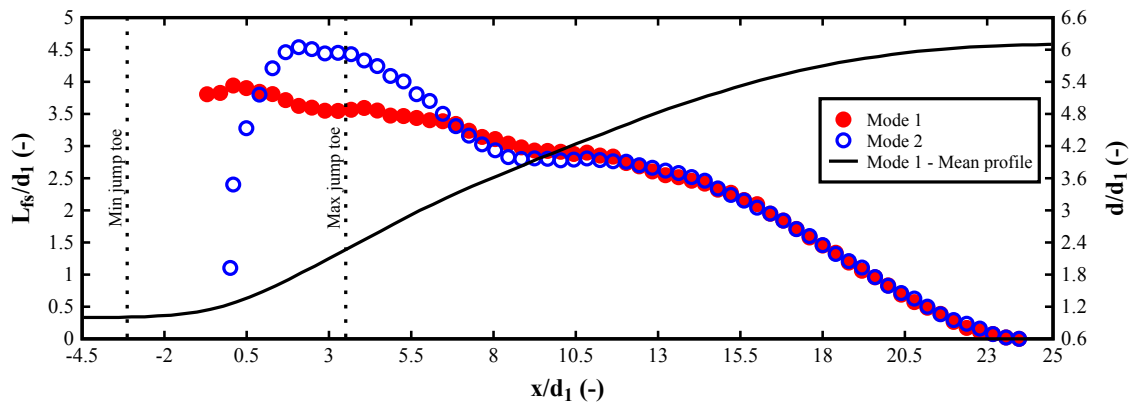
A) EXPERIMENT H ($Fr_1 = 3.8$, $Re = 6.2 \times 10^4$, FD)



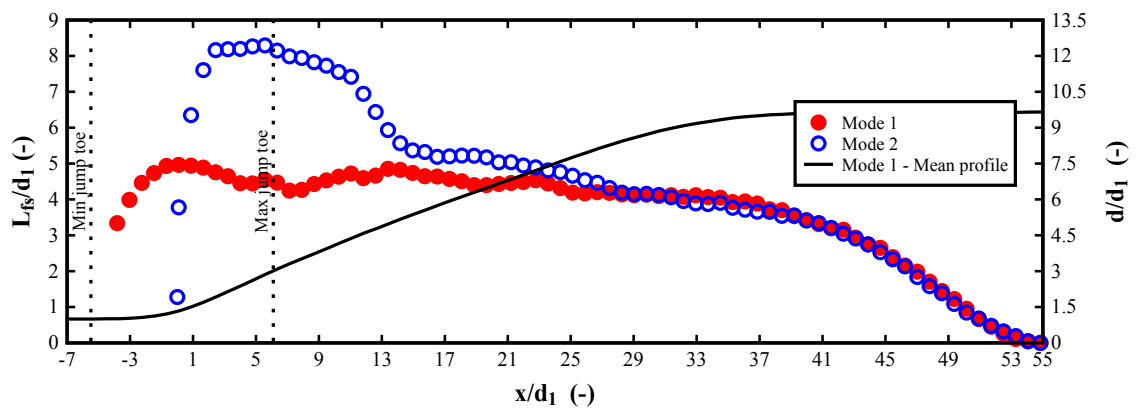
B) EXPERIMENT I ($Fr_1 = 3.8$, $Re = 9.5 \times 10^4$, FD)



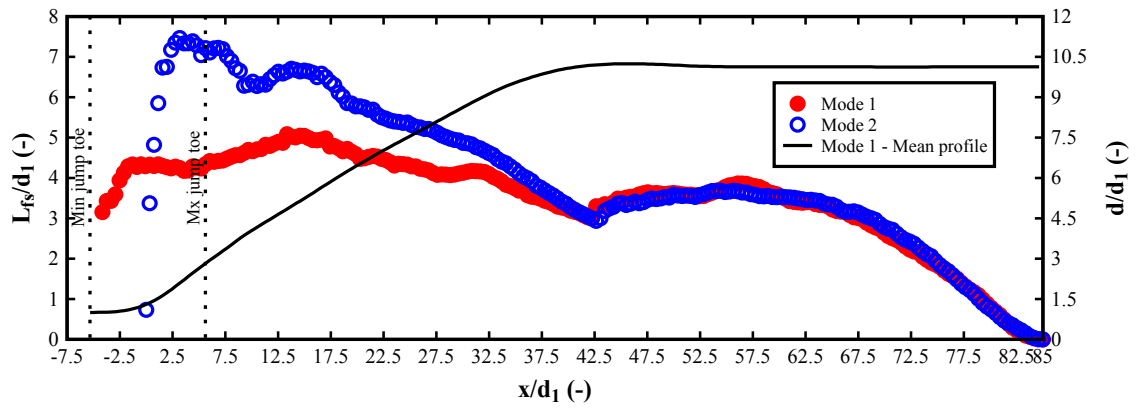
C) EXPERIMENT A ($Fr_1 = 5.1$, $Re = 8.3 \times 10^4$, FD)



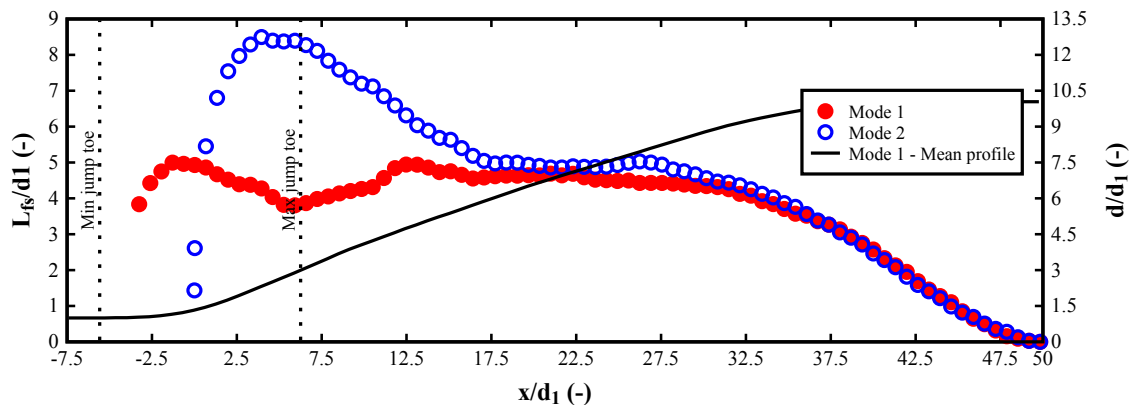
D) EXPERIMENT B ($Fr_1 = 5.1$, $Re = 6.2 \times 10^4$, FD)



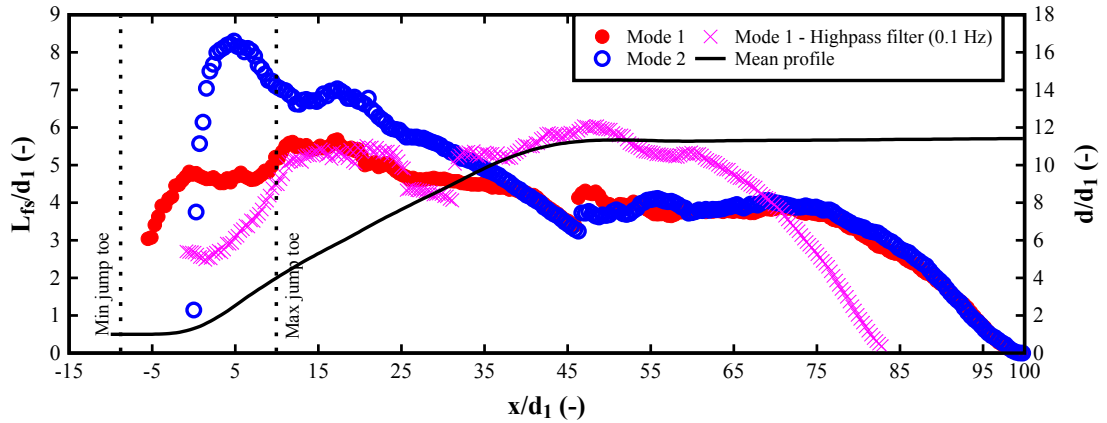
E) EXPERIMENT C ($Fr_1 = 7.0$, $Re = 6.2 \times 10^4$, FD)



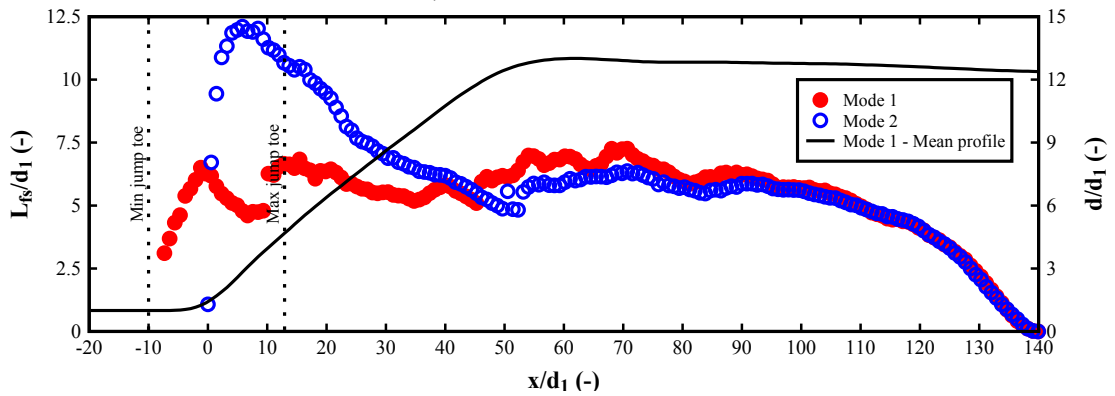
F) EXPERIMENT D ($Fr_1 = 7.0$, $Re = 1.1 \times 10^5$, FD)



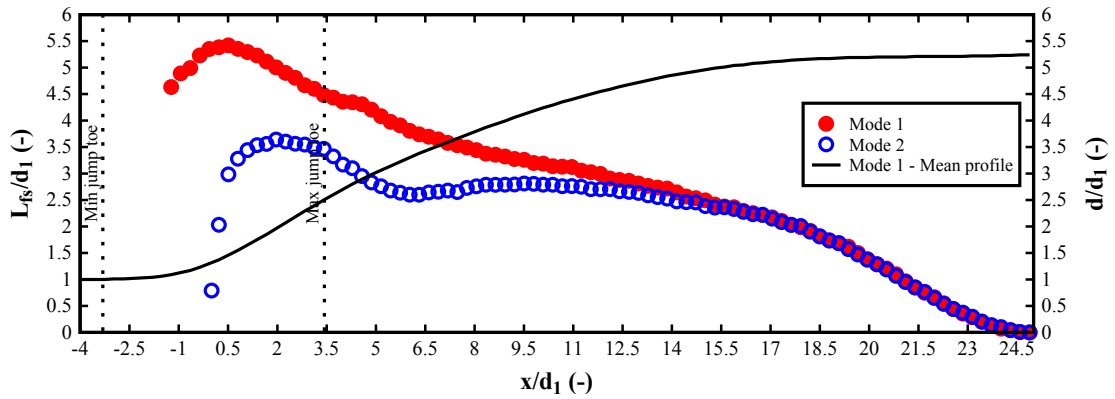
G) EXPERIMENT E_FD ($Fr_1 = 8.2$, $Re = 7.5 \times 10^4$, FD)



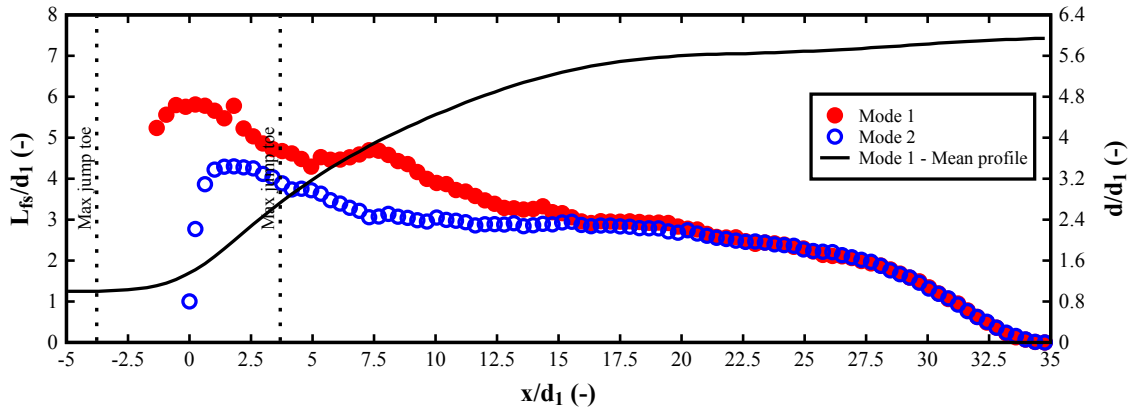
H) EXPERIMENT F ($Fr_1 = 8.0$, $Re = 1.2 \times 10^5$, FD)



I) EXPERIMENT G ($Fr_1 = 10$, $Re = 8.8 \times 10^4$, FD)



J) EXPERIMENT CHJ_S5.1 ($Fr_1 = 4.6$, $Re = 1 \times 10^5$)

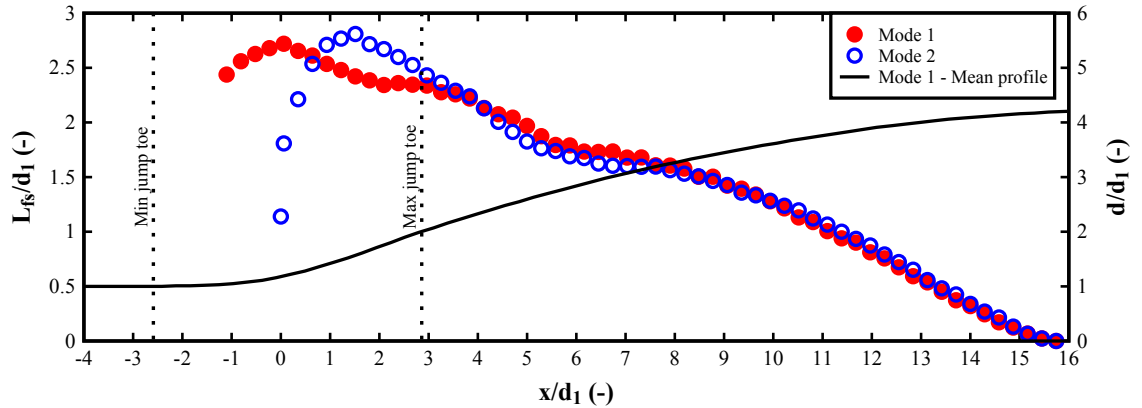


K) EXPERIMENT CHJ_S5.2 ($Fr_1 = 4.7$, $Re = 8.4 \times 10^4$)

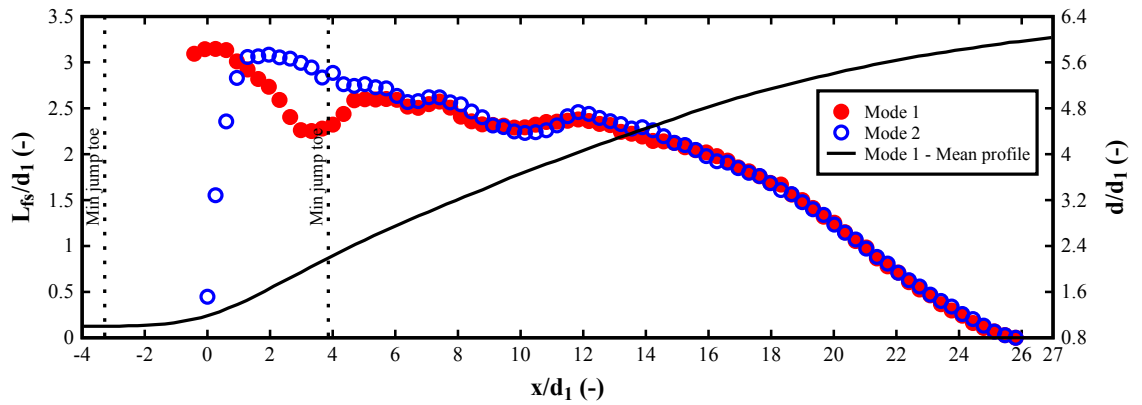
DIGITAL APPENDIX C-6. INTEGRAL FREE-SURFACE LENGTH SCALES ALONG THE HYDRAULIC JUMP WITH FULLY DEVELOPED INFLOW CONDITIONS.

DIGITAL APPENDIX. C.4.2. PARTIALLY DEVELOPED INFLOW CONDITIONS

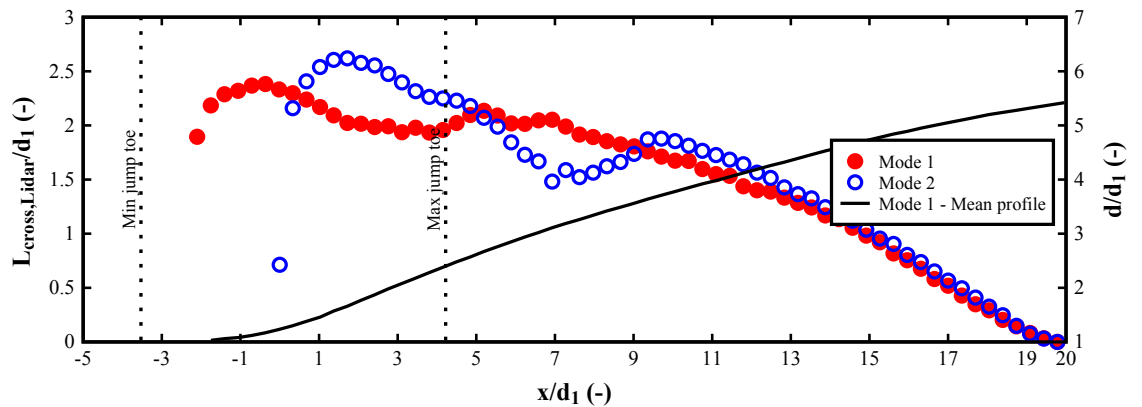
Digital appendix C-7 presents the integral free-surface length scales for Mode 1, Mode 2 and Mode 1 with a high-pass filter of 0.1 Hz as function of the distance from the jump toe for all the experiments conducted with partially developed inflow conditions.



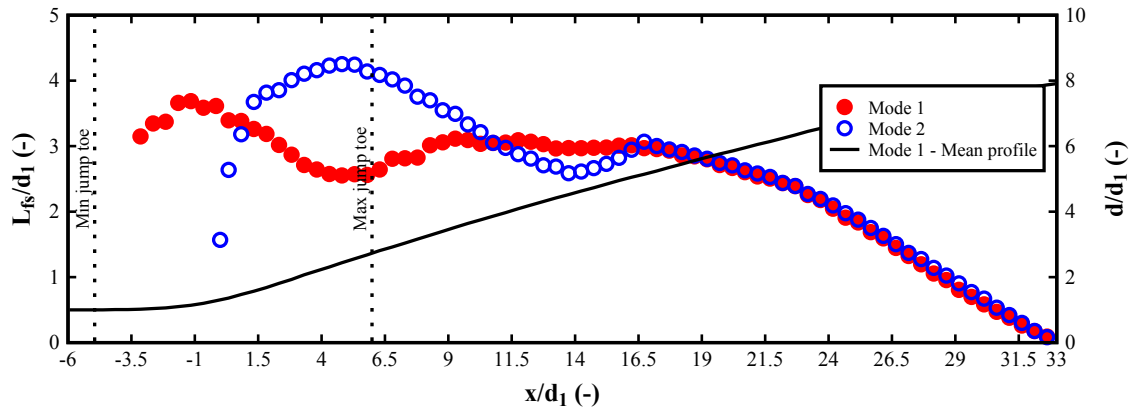
A) EXPERIMENT H ($Fr_1 = 3.8$, $Re = 6.2 \times 10^4$, PD)



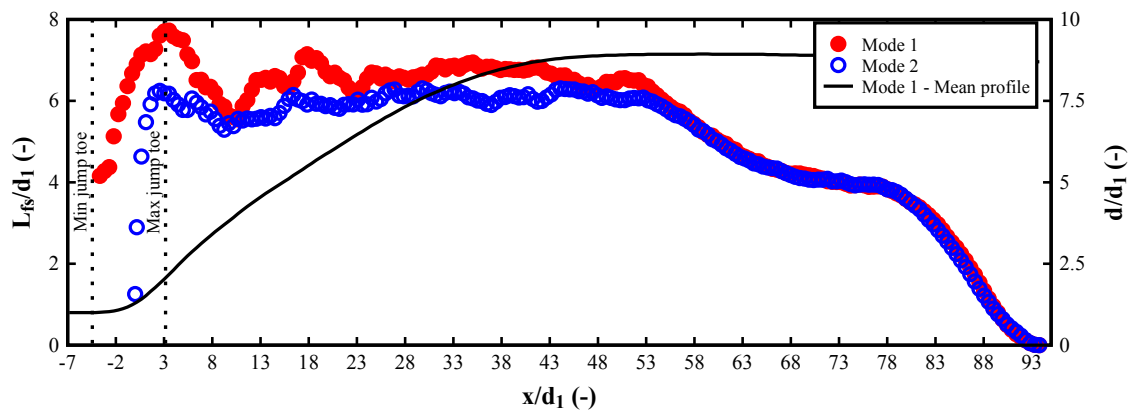
B) EXPERIMENT A ($Fr_1 = 5.1$, $Re = 8.3 \times 10^4$, PD)



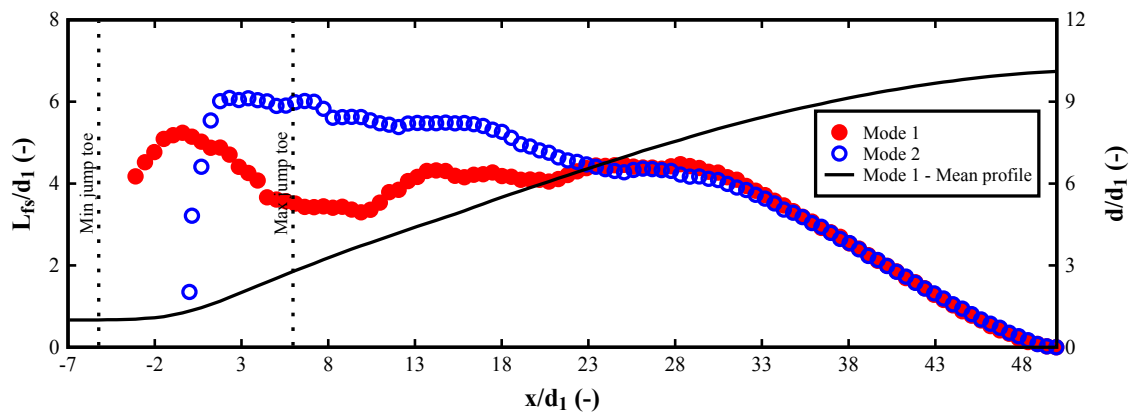
C) EXPERIMENT B ($Fr_1 = 5.1$, $Re = 6.2 \times 10^4$, PD)



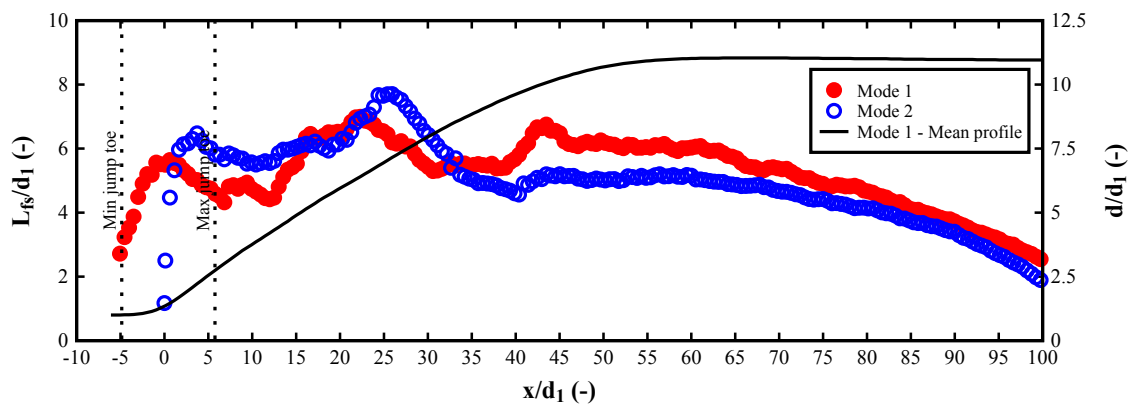
D) EXPERIMENT C ($Fr_1 = 7.0$, $Re = 6.2 \times 10^4$, PD)



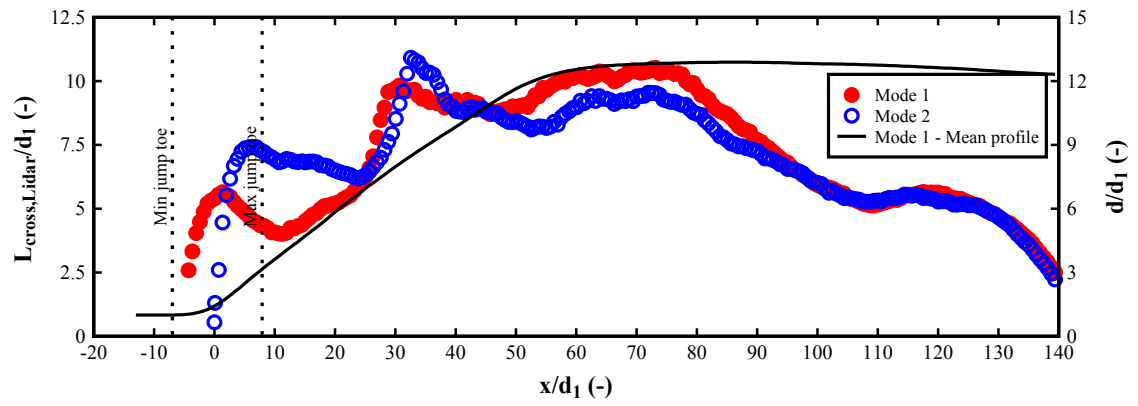
E) EXPERIMENT D ($Fr_1 = 7.0$, $Re = 1.1 \times 10^5$, PD)



F) EXPERIMENT E ($Fr_1 = 8.5$, $Re = 7.5 \times 10^4$, PD)



G) EXPERIMENT F ($Fr_1 = 8.4$, $Re = 1.2 \times 10^5$, PD)



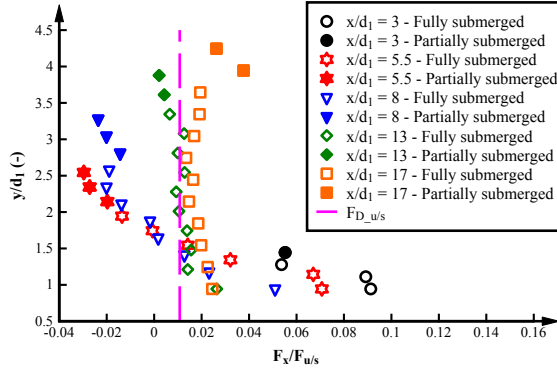
H) EXPERIMENT G ($Fr_1 = 10$, $Re = 8.8 \times 10^4$, PD)

FIGURE C-7. INTEGRAL FREE-SURFACE LENGTH SCALES ALONG THE HYDRAULIC JUMP WITH PARTIALLY DEVELOPED INFLOW CONDITIONS.

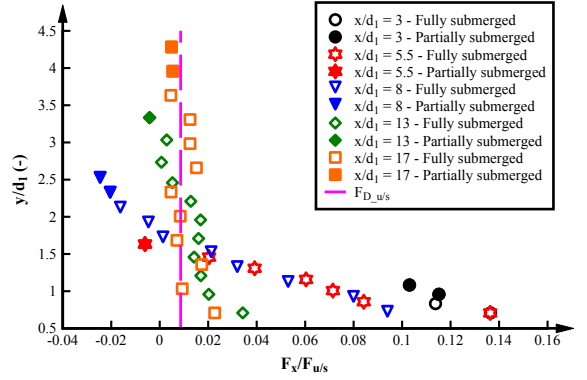
Digital Appendix D. INTERNAL FORCES

DIGITAL APPENDIX. D.1. TIME-AVERAGED STREAMWISE FORCES

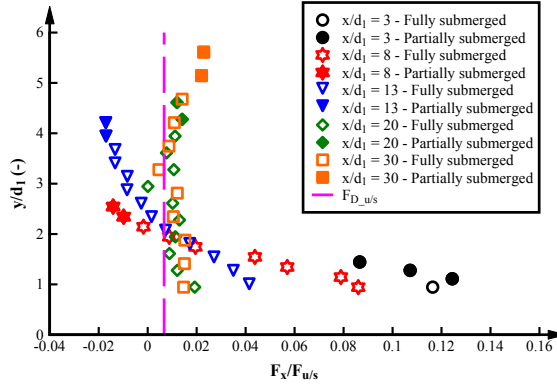
DIGITAL APPENDIX. D.1.1. FULLY DEVELOPED INFLOW CONDITIONS



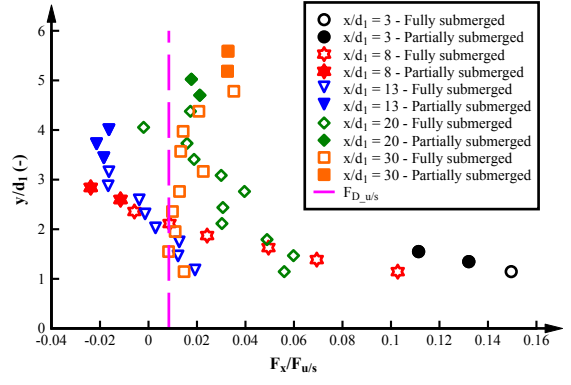
A) EXPERIMENT H: $Fr_1 = 3.8$, $Re = 6.2 \times 10^4$



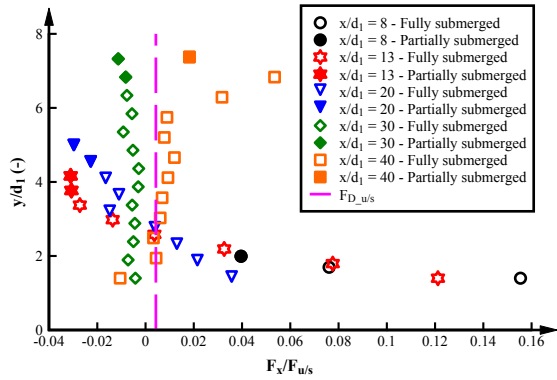
B) EXPERIMENT I: $Fr_1 = 3.8$, $Re = 9.5 \times 10^4$



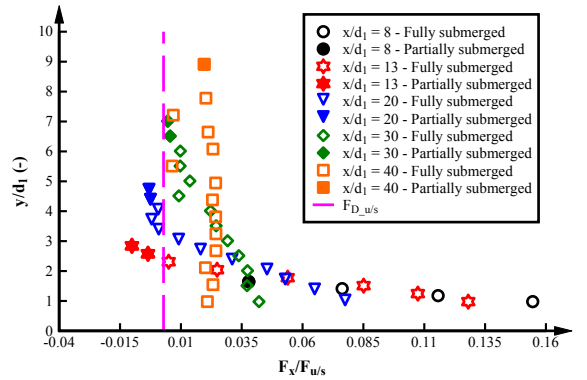
C) EXPERIMENT A: $Fr_1 = 5.1$, $Re = 8.3 \times 10^4$



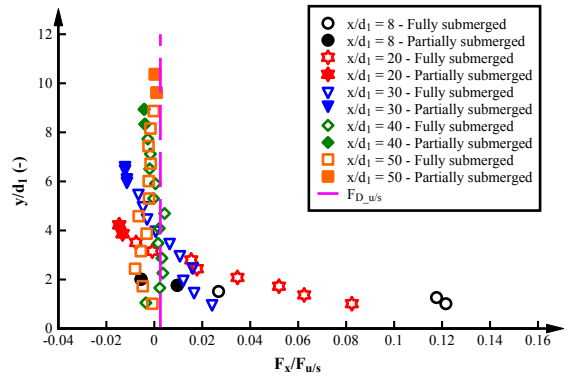
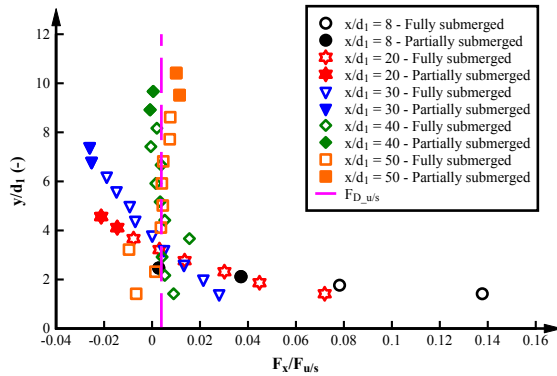
D) EXPERIMENT B: $Fr_1 = 5.1$, $Re = 6.2 \times 10^4$



E) EXPERIMENT C: $Fr_1 = 7.0$, $Re = 6.2 \times 10^4$

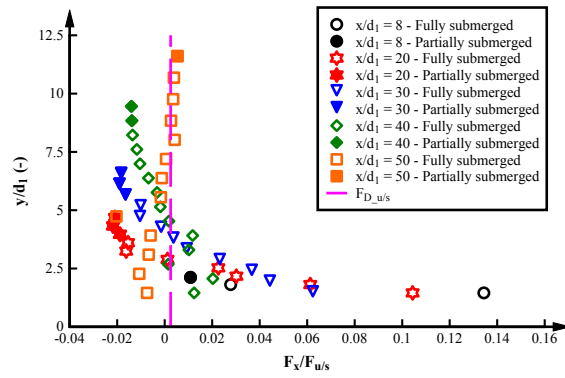


F) EXPERIMENT D: $Fr_1 = 7.0$, $Re = 1.1 \times 10^5$



G) EXPERIMENT E: $Fr_1 = 8.5$, $Re = 7.5 \times 10^4$

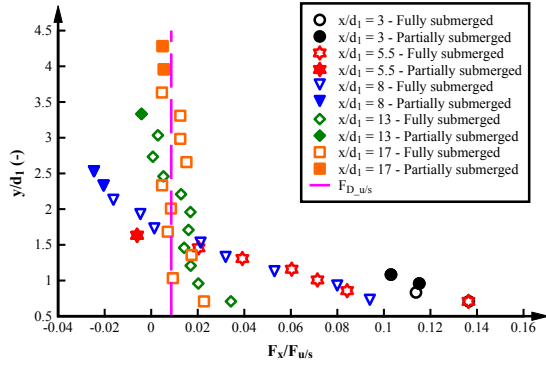
G) EXPERIMENT F: $Fr_1 = 8.5$, $Re = 1.2 \times 10^5$



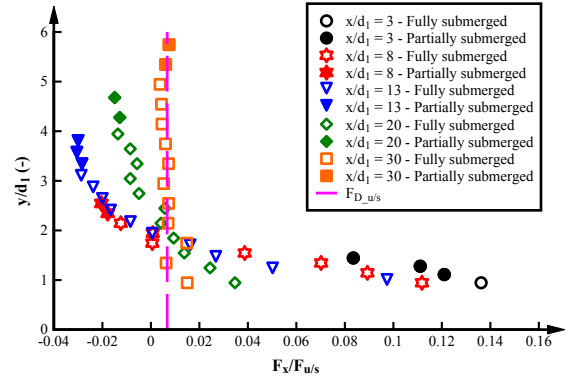
H) EXPERIMENT G: $Fr_1 = 10$, $Re = 8.8 \times 10^4$

DIGITAL APPENDIX D-1. TIME-AVERAGED STREAMWISE FORCES, FULLY DEVELOPED INFLOW CONDITIONS.

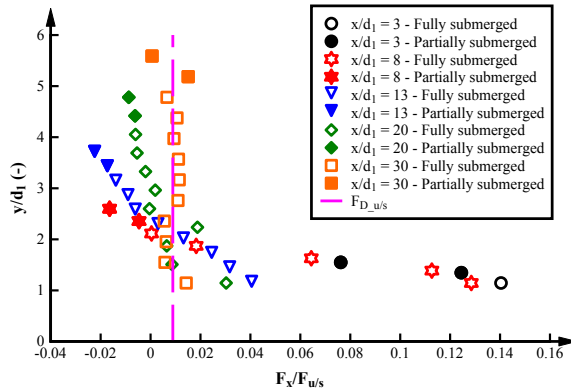
DIGITAL APPENDIX. D.1.2. PARTIALLY DEVELOPED INFLOW CONDITIONS



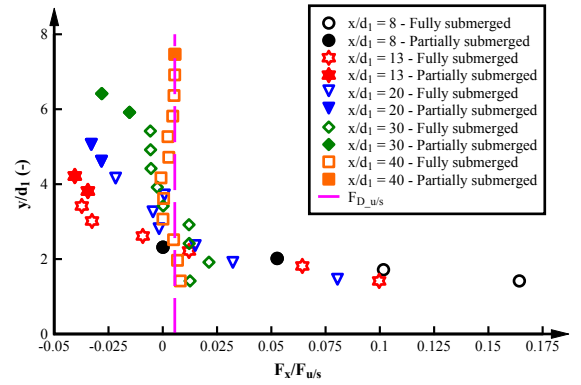
A) EXPERIMENT H: $Fr_1 = 3.8$, $Re = 6.2 \times 10^4$



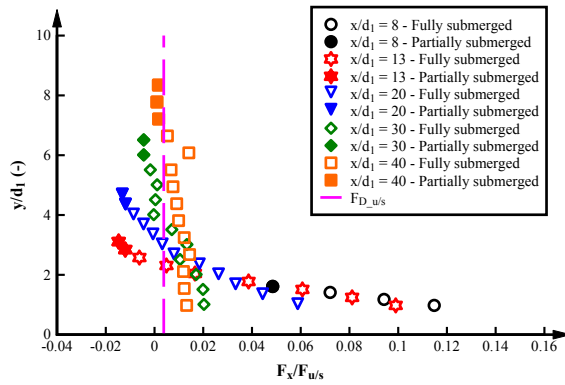
B) EXPERIMENT A: $Fr_1 = 5.1$, $Re = 8.3 \times 10^4$



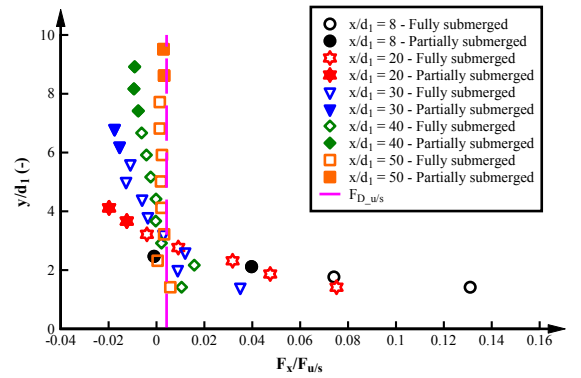
C) EXPERIMENT B: $Fr_1 = 5.1$, $Re = 6.2 \times 10^4$



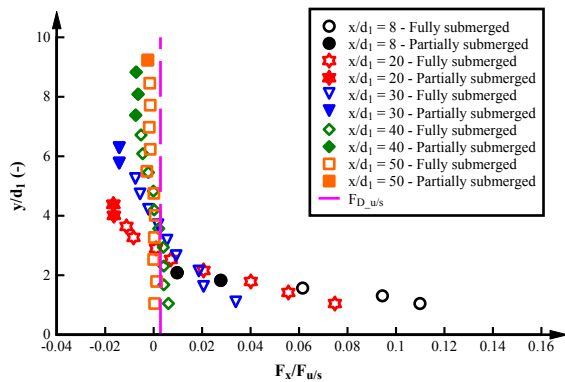
D) EXPERIMENT C: $Fr_1 = 7.0$, $Re = 6.2 \times 10^4$



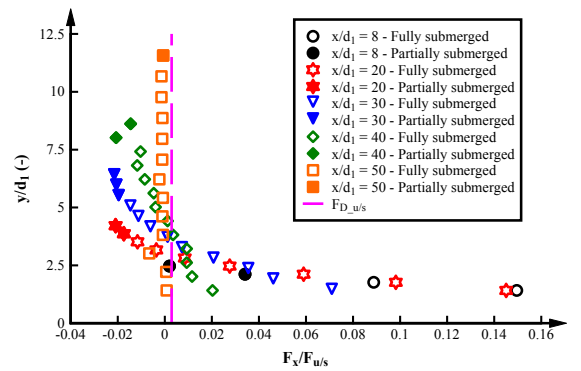
E) EXPERIMENT D: $Fr_1 = 7.0$, $Re = 1.1 \times 10^5$



F) EXPERIMENT E: $Fr_1 = 8.5$, $Re = 7.5 \times 10^4$



G) EXPERIMENT F: $Fr_1 = 8.5$, $Re = 1.2 \times 10^5$

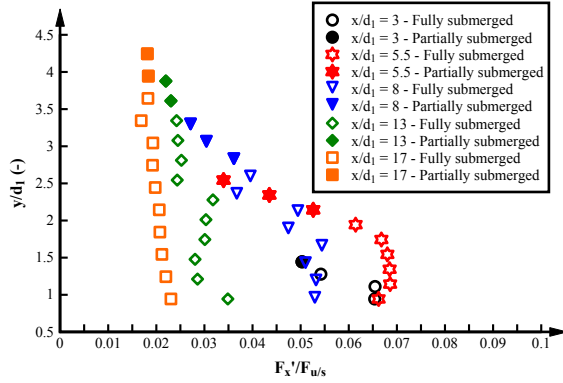


G) EXPERIMENT G: $Fr_1 = 10$, $Re = 8.8 \times 10^4$

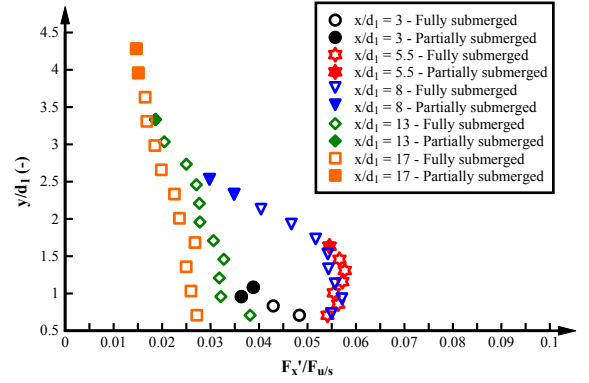
DIGITAL APPENDIX D-2. TIME-AVERAGED STREAMWISE FORCES, PARTIALLY DEVELOPED INFLOW CONDITIONS

DIGITAL APPENDIX. D.2. STREAMWISE FORCE FLUCTUATIONS

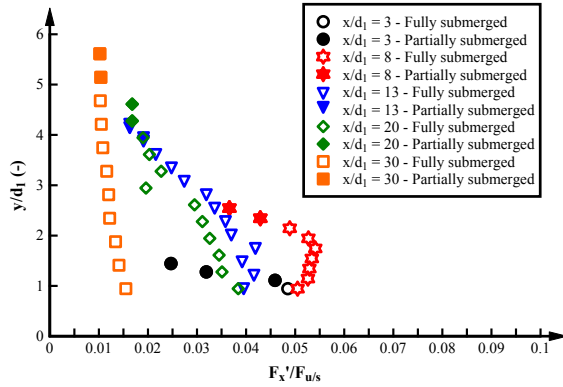
DIGITAL APPENDIX. D.2.1. FULLY DEVELOPED INFLOW CONDITIONS



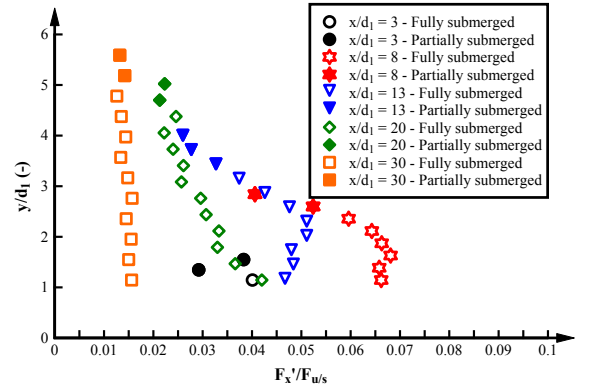
A) EXPERIMENT H: $Fr_1 = 3.8$, $Re = 6.2 \times 10^4$



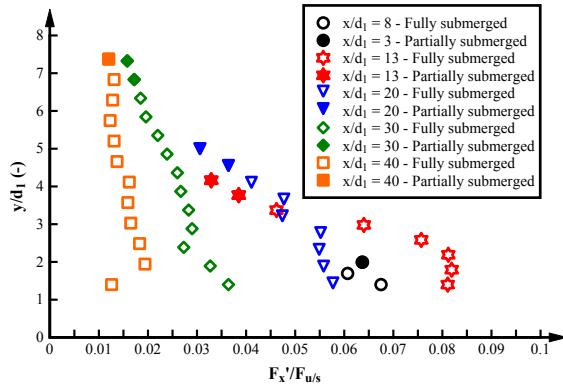
B) EXPERIMENT I: $Fr_1 = 3.8$, $Re = 9.5 \times 10^4$



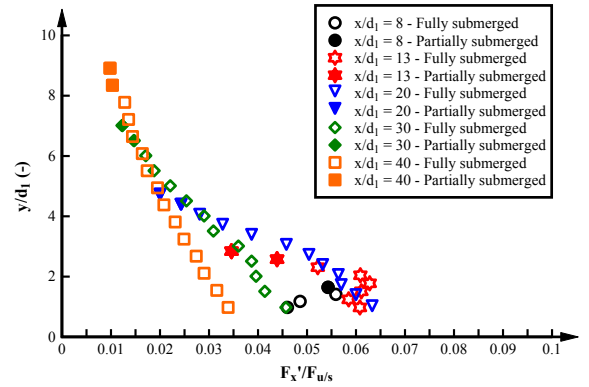
C) EXPERIMENT A: $Fr_1 = 5.1$, $Re = 8.3 \times 10^4$



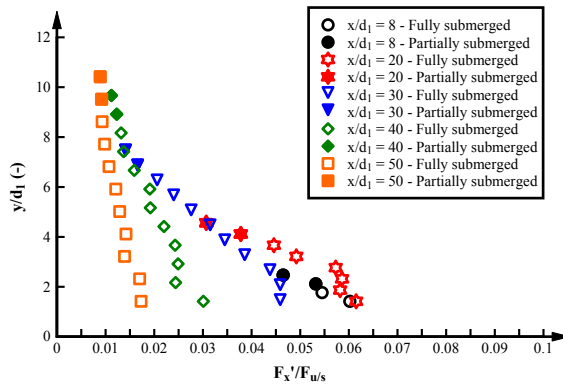
D) EXPERIMENT B: $Fr_1 = 5.1$, $Re = 6.2 \times 10^4$



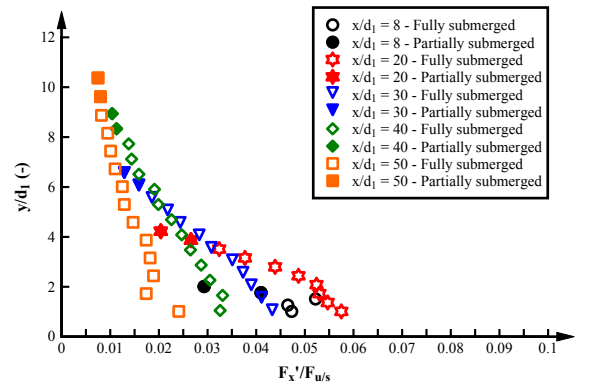
E) EXPERIMENT C: $Fr_1 = 7.0$, $Re = 6.2 \times 10^4$



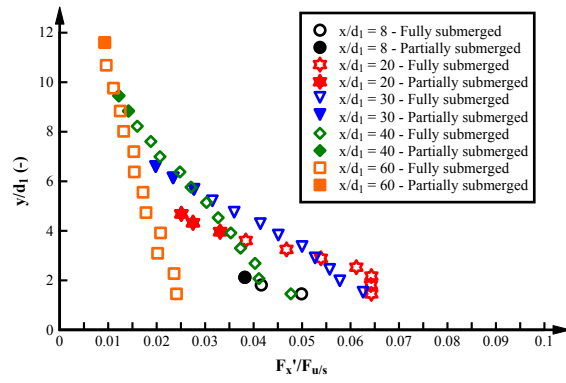
F) EXPERIMENT D: $Fr_1 = 7.0$, $Re = 1.1 \times 10^5$



G) EXPERIMENT E: $Fr_1 = 8.5$, $Re = 7.5 \times 10^4$



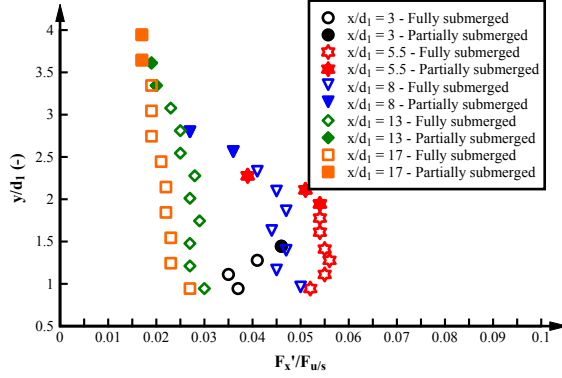
G) EXPERIMENT F: $Fr_1 = 8.5$, $Re = 1.2 \times 10^5$



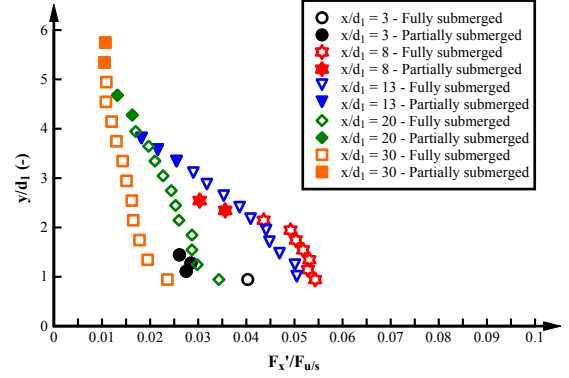
H) EXPERIMENT G: $Fr_1 = 10$, $Re = 8.8 \times 10^4$

DIGITAL APPENDIX D-3. TIME-AVERAGED STREAMWISE FORCES, FULLY DEVELOPED INFLOW CONDITIONS.

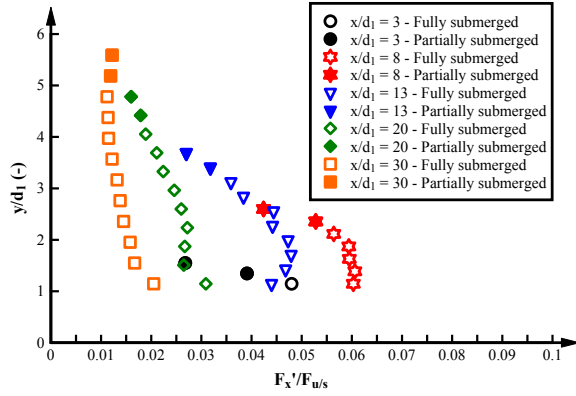
DIGITAL APPENDIX. D.2.2. PARTIALLY DEVELOPED INFLOW CONDITIONS



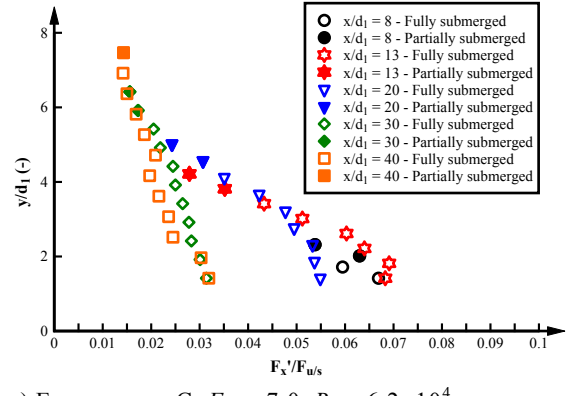
A) EXPERIMENT H: $Fr_1 = 3.8$, $Re = 6.2 \times 10^4$



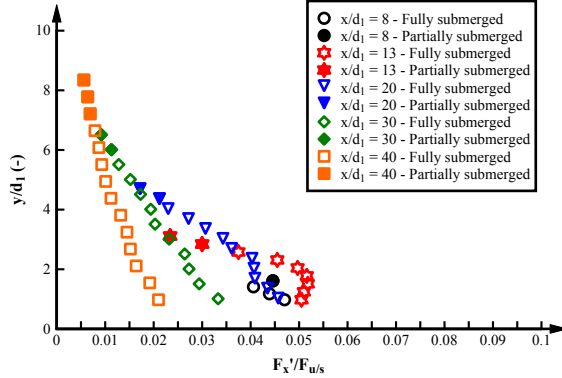
B) EXPERIMENT A: $Fr_1 = 5.1$, $Re = 8.3 \times 10^4$



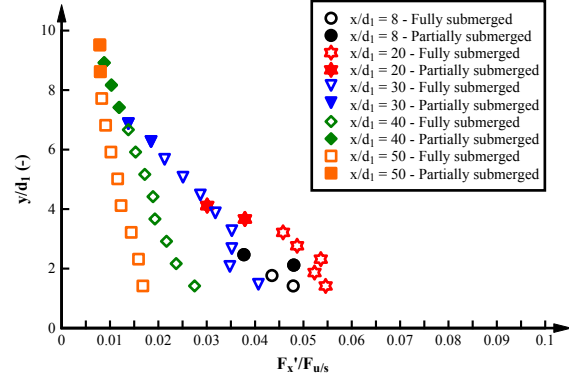
C) EXPERIMENT B: $Fr_1 = 5.1$, $Re = 6.2 \times 10^4$



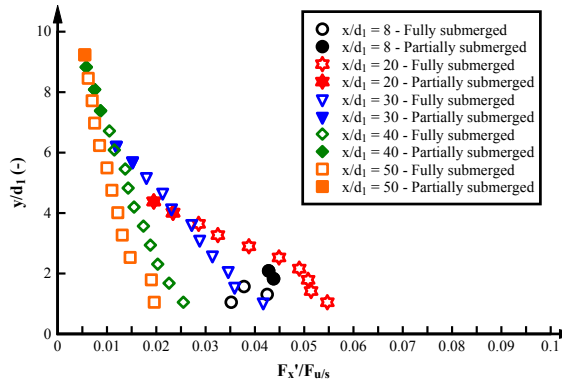
D) EXPERIMENT C: $Fr_1 = 7.0$, $Re = 6.2 \times 10^4$



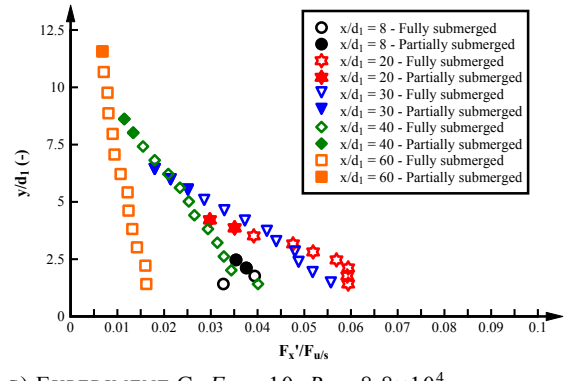
E) EXPERIMENT D: $Fr_1 = 7.0$, $Re = 1.1 \times 10^5$



F) EXPERIMENT E: $Fr_1 = 8.5$, $Re = 7.5 \times 10^4$



G) EXPERIMENT F: $Fr_1 = 8.5$, $Re = 1.2 \times 10^5$

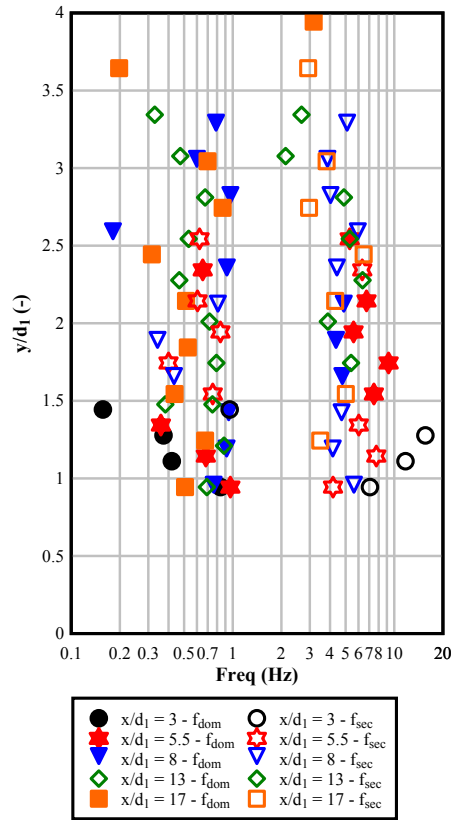


G) EXPERIMENT G: $Fr_1 = 10$, $Re = 8.8 \times 10^4$

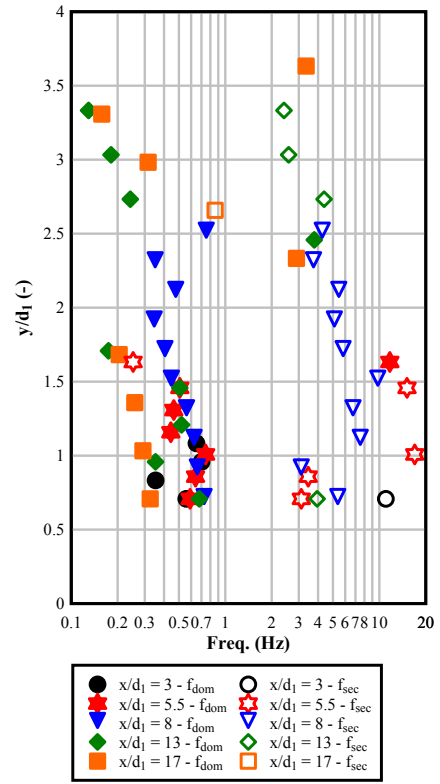
DIGITAL APPENDIX D-4. TIME-AVERAGED STREAMWISE FORCES, PARTIALLY DEVELOPED INFLOW CONDITIONS

DIGITAL APPENDIX. D.3. STREAMWISE FORCE CHARACTERISTIC FREQUENCIES

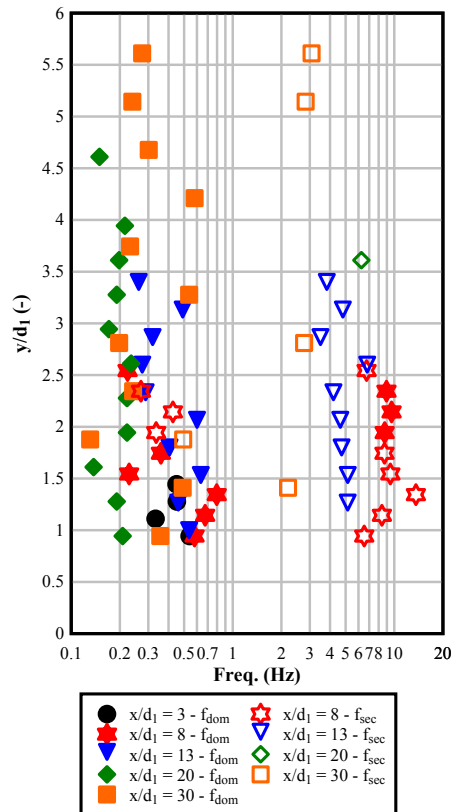
DIGITAL APPENDIX. D.3.1. FULLY DEVELOPED INFLOW CONDITIONS



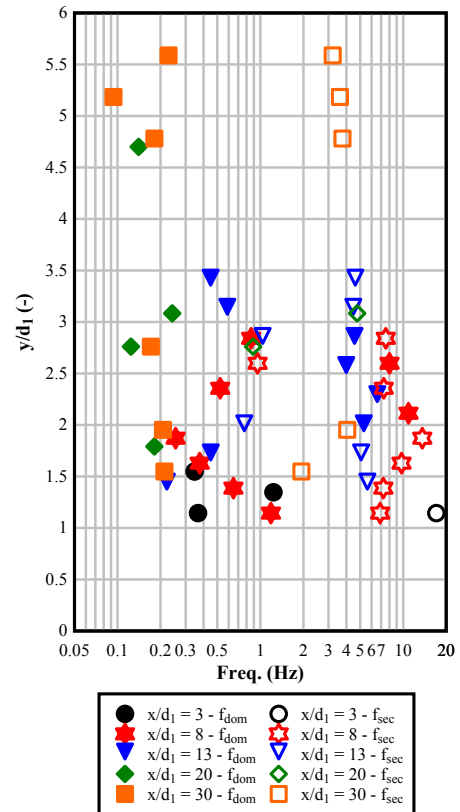
A) EXPERIMENT H: $Fr_1 = 3.8$, $Re = 6.2 \times 10^4$



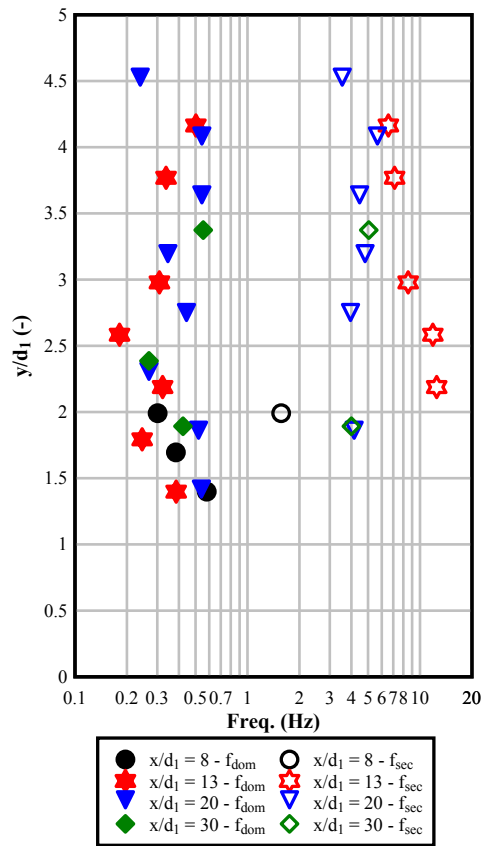
B) EXPERIMENT I: $Fr_1 = 3.8$, $Re = 9.5 \times 10^4$



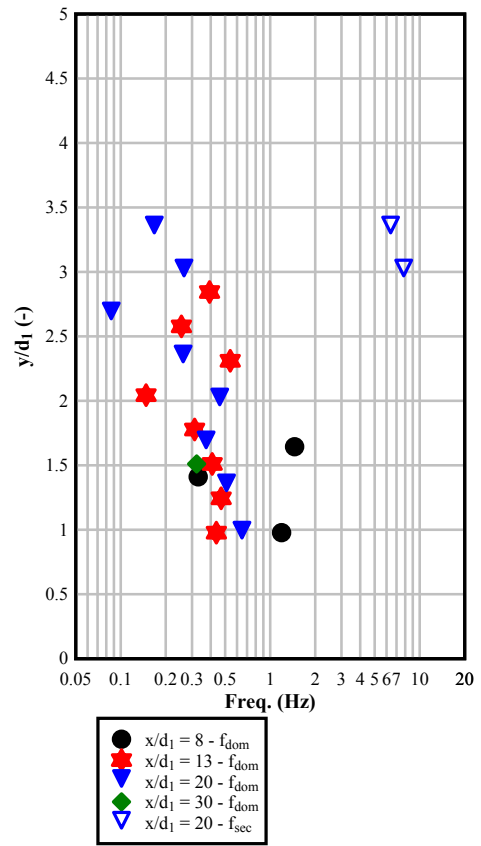
C) EXPERIMENT A: $Fr_1 = 5.1$, $Re = 8.3 \times 10^4$



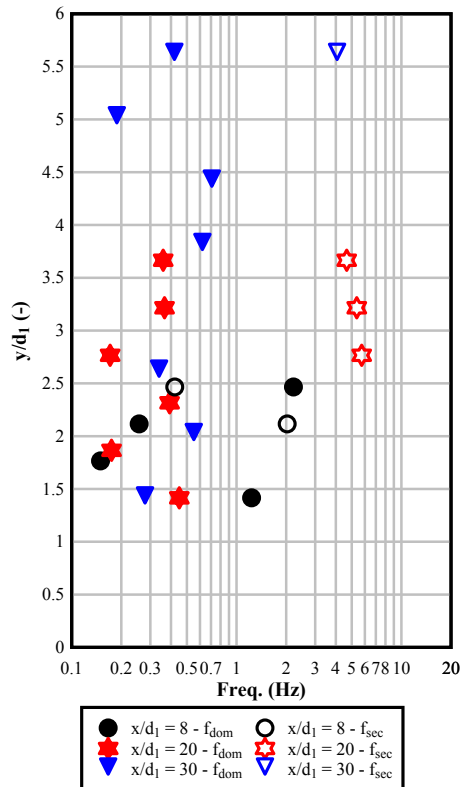
D) EXPERIMENT B: $Fr_1 = 5.1$, $Re = 6.2 \times 10^4$



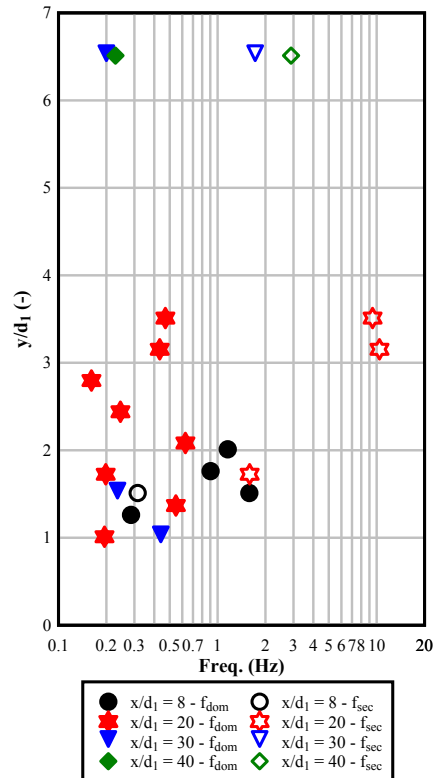
E) EXPERIMENT C: $Fr_1 = 7.0$, $Re = 6.2 \times 10^4$



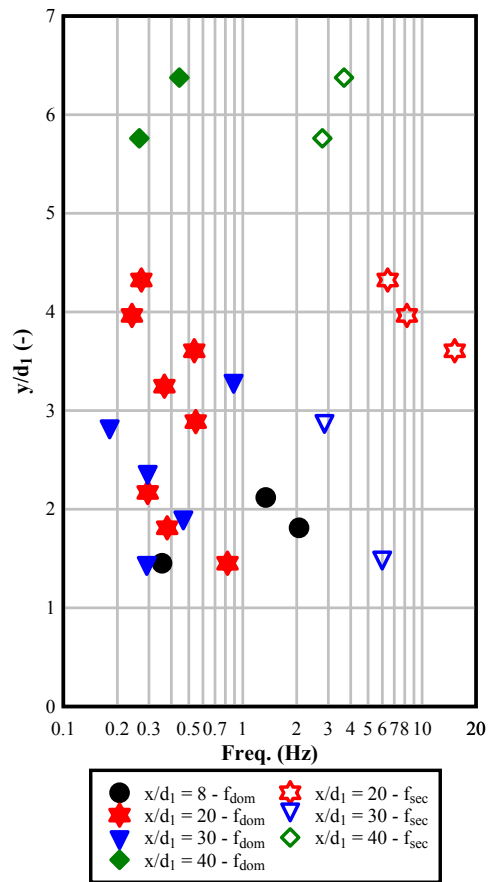
F) EXPERIMENT D: $Fr_1 = 7.0$, $Re = 1.1 \times 10^5$



G) EXPERIMENT E: $Fr_1 = 8.5$, $Re = 7.5 \times 10^4$



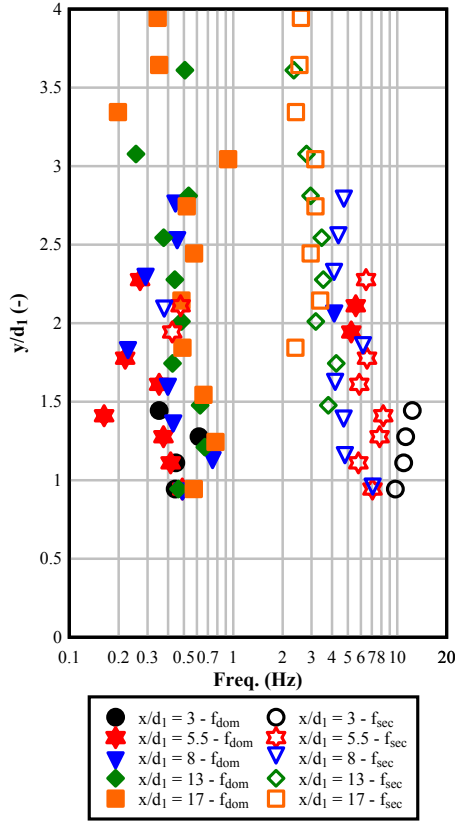
G) EXPERIMENT F: $Fr_1 = 8.5$, $Re = 1.2 \times 10^5$



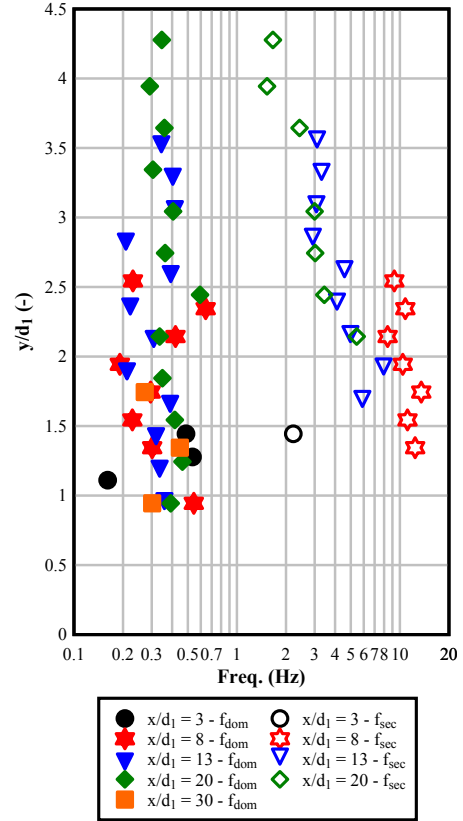
H) EXPERIMENT G: $Fr_1 = 10$, $Re = 8.8 \times 10^4$

DIGITAL APPENDIX D-5. CHARACTERISTIC FREQUENCIES OF THE STREAMWISE FORCES, FULLY DEVELOPED INFLOW CONDITIONS.

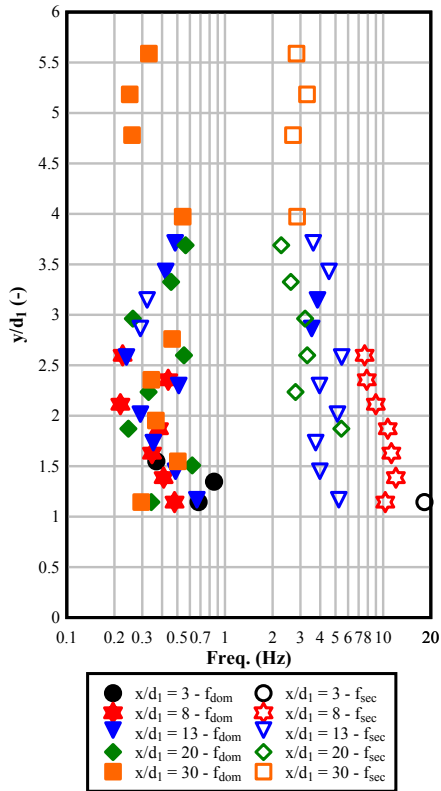
DIGITAL APPENDIX. D.3.2. PARTIALLY DEVELOPED INFLOW CONDITIONS



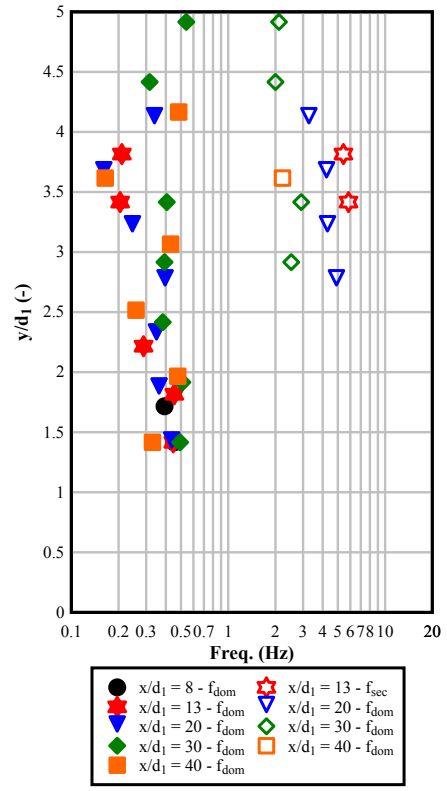
A) EXPERIMENT H: $Fr_1 = 3.8$, $Re = 6.2 \times 10^4$



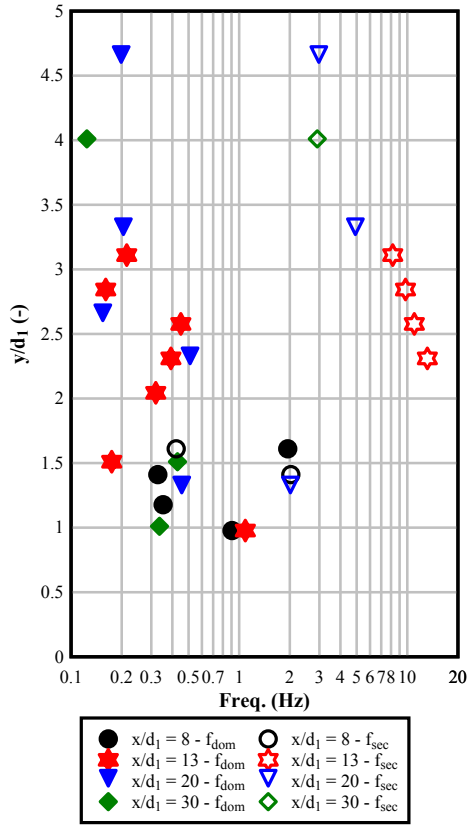
B) EXPERIMENT A: $Fr_1 = 5.1$, $Re = 8.3 \times 10^4$



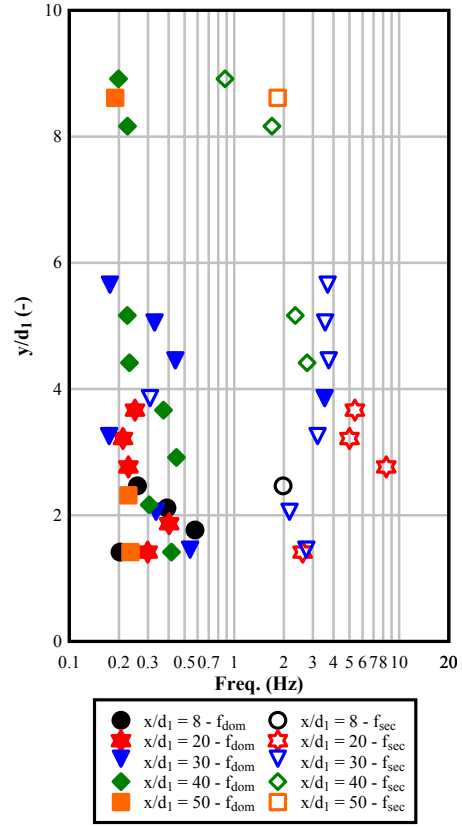
C) EXPERIMENT B: $Fr_1 = 5.1$, $Re = 6.2 \times 10^4$



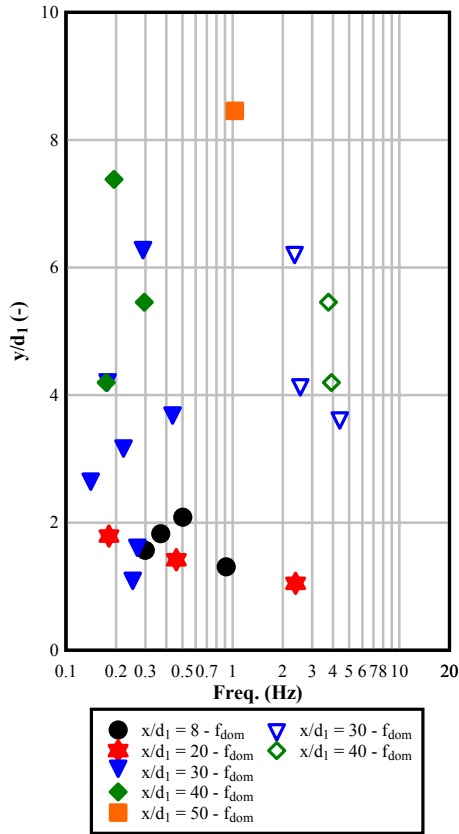
D) EXPERIMENT C: $Fr_1 = 7.0$, $Re = 6.2 \times 10^4$



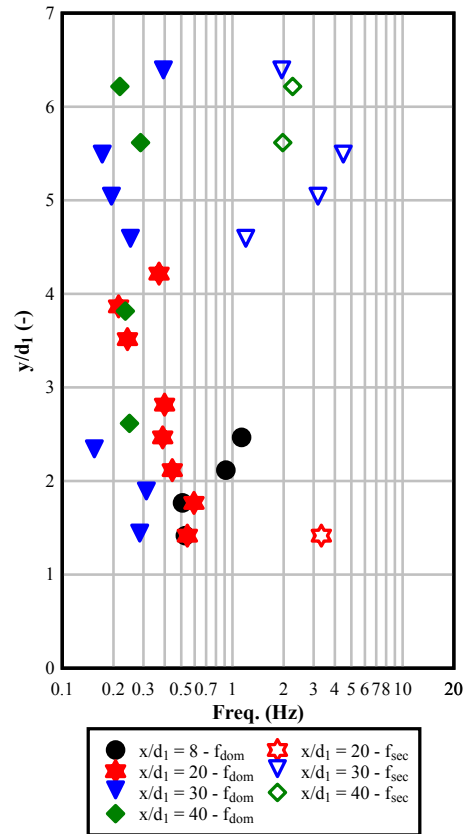
E) EXPERIMENT D: $Fr_1 = 7.0$, $Re = 1.1 \times 10^5$



F) EXPERIMENT E: $Fr_1 = 8.5$, $Re = 7.5 \times 10^4$



G) EXPERIMENT F: $Fr_1 = 8.5$, $Re = 1.2 \times 10^5$

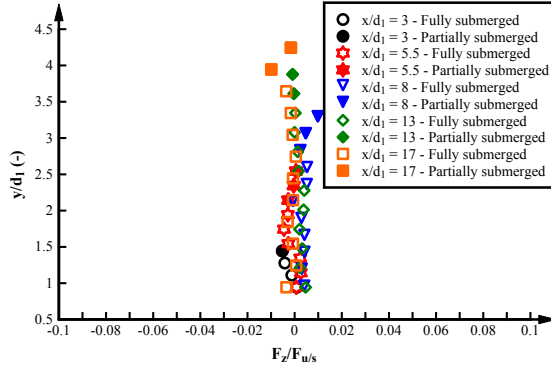


G) EXPERIMENT G: $Fr_1 = 10$, $Re = 8.8 \times 10^4$

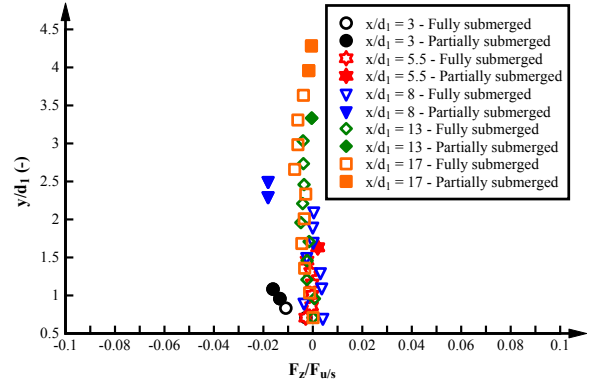
DIGITAL APPENDIX D-6. TIME-AVERAGED STREAMWISE FORCES, PARTIALLY DEVELOPED INFLOW CONDITIONS

DIGITAL APPENDIX. D.4. TIME-AVERAGED TRANSVERSE FORCE

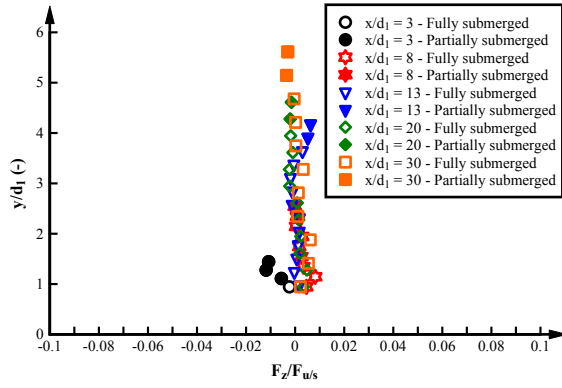
DIGITAL APPENDIX. D.4.1. FULLY DEVELOPED INFLOW CONDITIONS



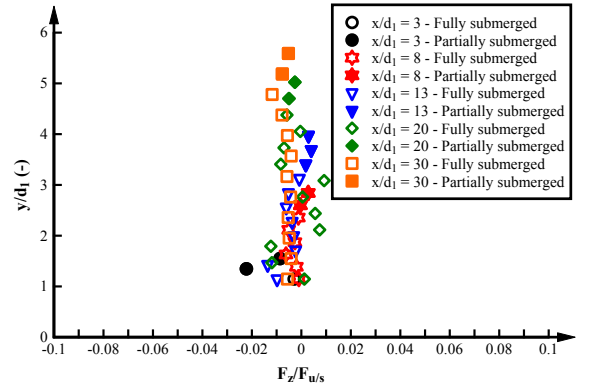
A) EXPERIMENT H: $Fr_1 = 3.8$, $Re = 6.2 \times 10^4$



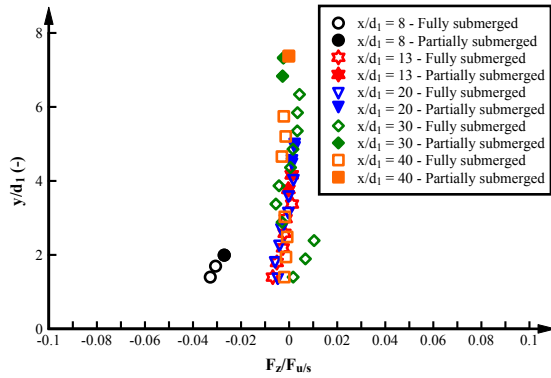
B) EXPERIMENT I: $Fr_1 = 3.8$, $Re = 9.5 \times 10^4$



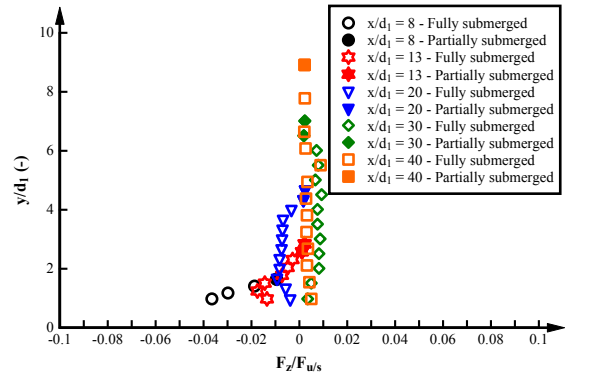
C) EXPERIMENT A: $Fr_1 = 5.1$, $Re = 8.3 \times 10^4$



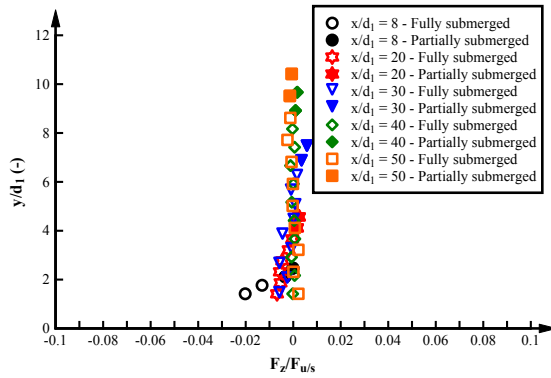
D) EXPERIMENT B: $Fr_1 = 5.1$, $Re = 6.2 \times 10^4$



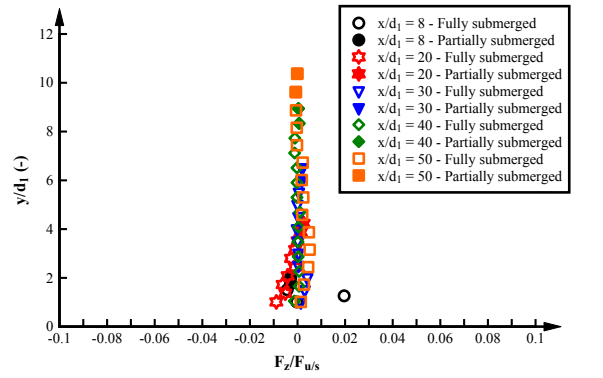
E) EXPERIMENT C: $Fr_1 = 7.0$, $Re = 6.2 \times 10^4$



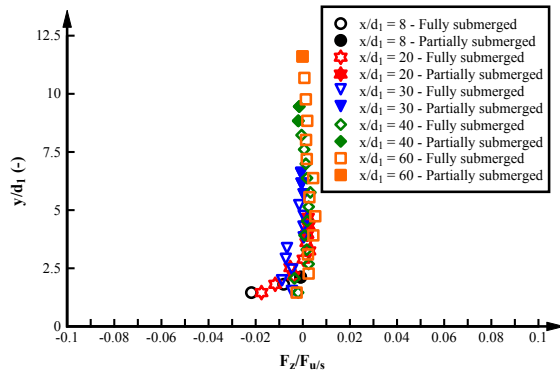
F) EXPERIMENT D: $Fr_1 = 7.0$, $Re = 1.1 \times 10^5$



G) EXPERIMENT E: $Fr_1 = 8.5$, $Re = 7.5 \times 10^4$



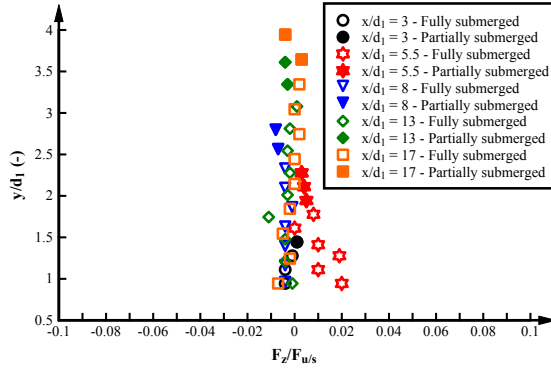
G) EXPERIMENT F: $Fr_1 = 8.5$, $Re = 1.2 \times 10^5$



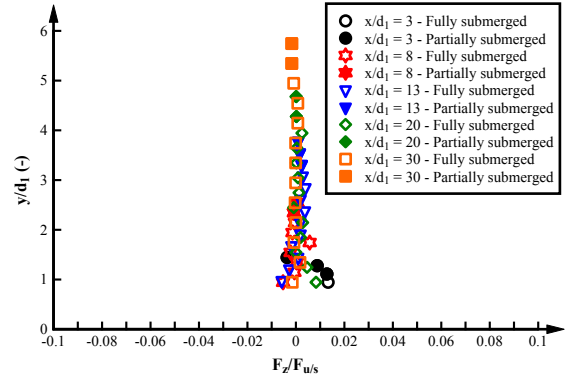
H) EXPERIMENT G: $Fr_I = 10$, $Re = 8.8 \times 10^4$

DIGITAL APPENDIX D-7. TIME-AVERAGED STREAMWISE FORCES, FULLY DEVELOPED INFLOW CONDITIONS.

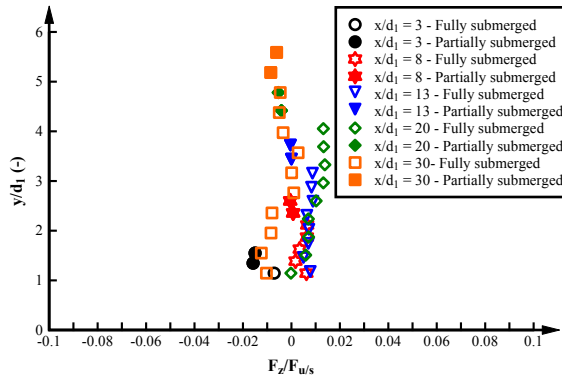
DIGITAL APPENDIX. D.4.2. FULLY DEVELOPED INFLOW CONDITIONS



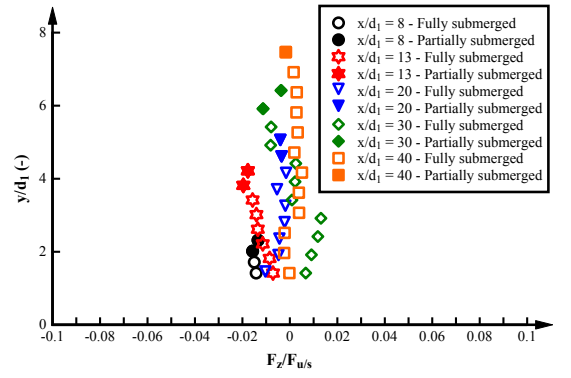
A) EXPERIMENT H: $Fr_1 = 3.8$, $Re = 6.2 \times 10^4$



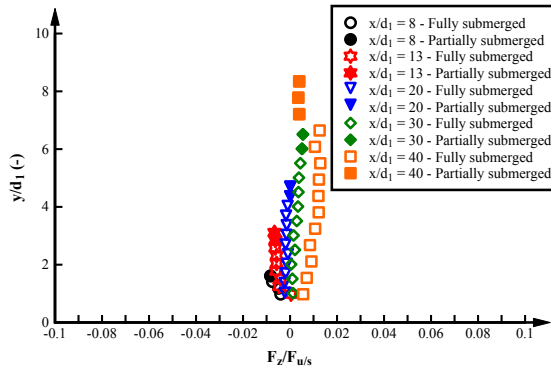
B) EXPERIMENT A: $Fr_1 = 5.1$, $Re = 8.3 \times 10^4$



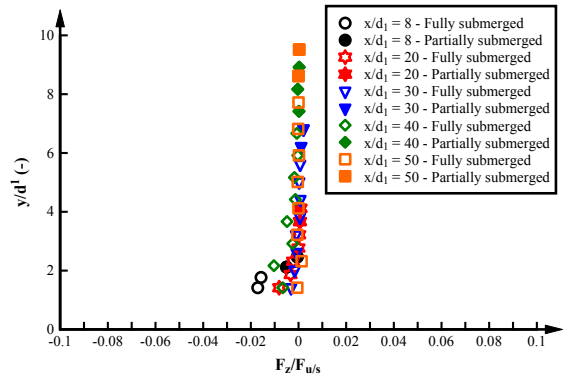
C) EXPERIMENT B: $Fr_1 = 5.1$, $Re = 6.2 \times 10^4$



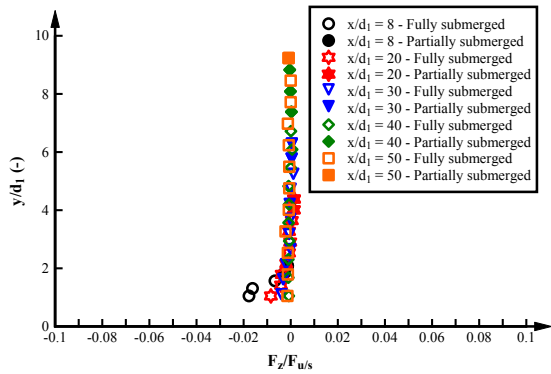
D) EXPERIMENT C: $Fr_1 = 7.0$, $Re = 6.2 \times 10^4$



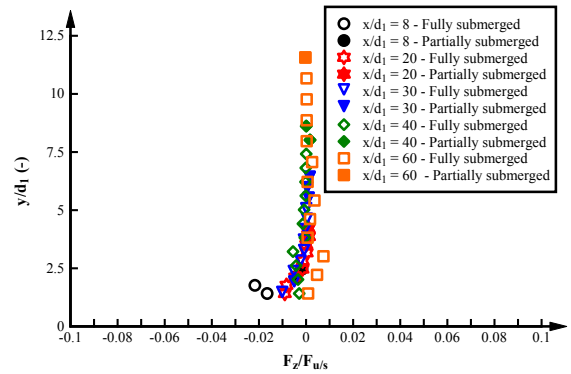
E) EXPERIMENT D: $Fr_1 = 7.0$, $Re = 1.1 \times 10^5$



F) EXPERIMENT E: $Fr_1 = 8.5$, $Re = 7.5 \times 10^4$



G) EXPERIMENT F: $Fr_1 = 8.5$, $Re = 1.2 \times 10^5$

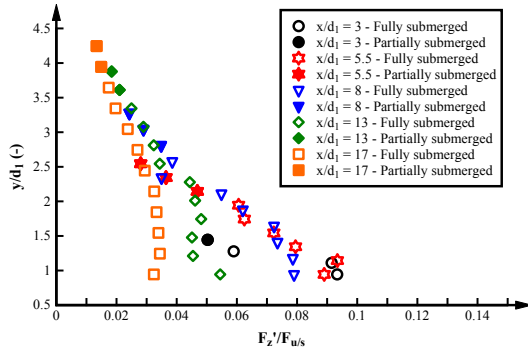


G) EXPERIMENT G: $Fr_1 = 10$, $Re = 8.8 \times 10^4$

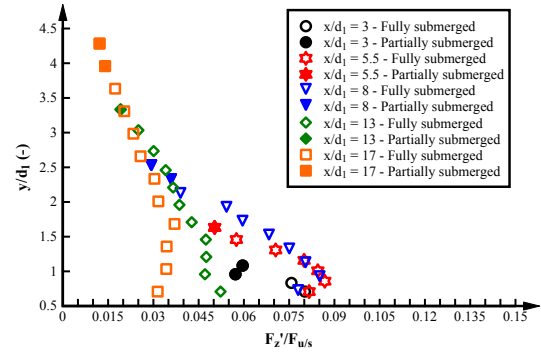
DIGITAL APPENDIX D-8. TIME-AVERAGED STREAMWISE FORCES, PARTIALLY DEVELOPED INFLOW CONDITIONS

DIGITAL APPENDIX. D.5. TRANSVERSE FORCE FLUCTUATIONS

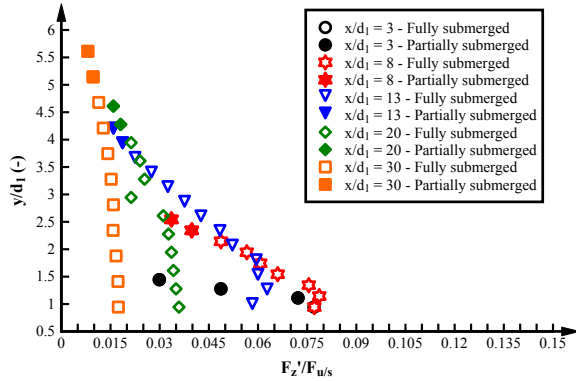
DIGITAL APPENDIX. D.5.1. FULLY DEVELOPED INFLOW CONDITIONS



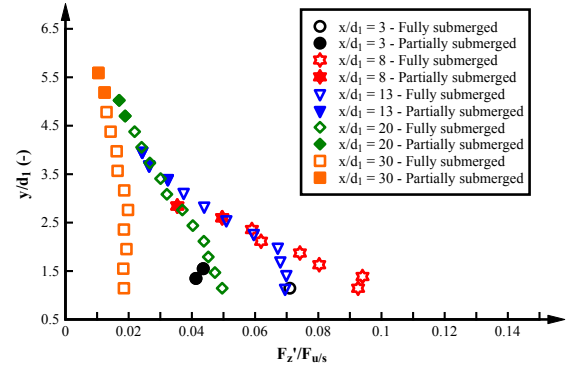
A) EXPERIMENT H: $Fr_1 = 3.8$, $Re = 6.2 \times 10^4$



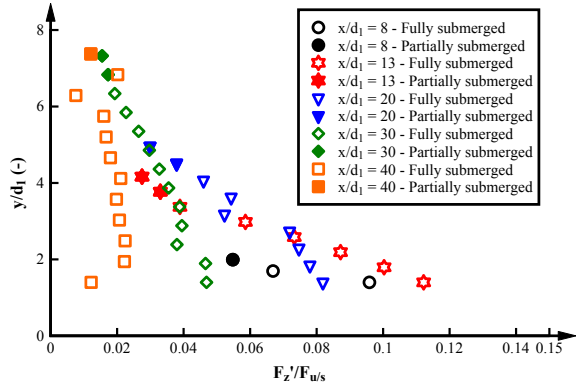
B) EXPERIMENT I: $Fr_1 = 3.8$, $Re = 9.5 \times 10^4$



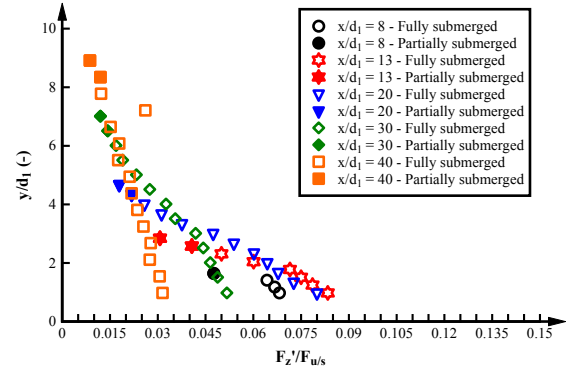
C) EXPERIMENT A: $Fr_1 = 5.1$, $Re = 8.3 \times 10^4$



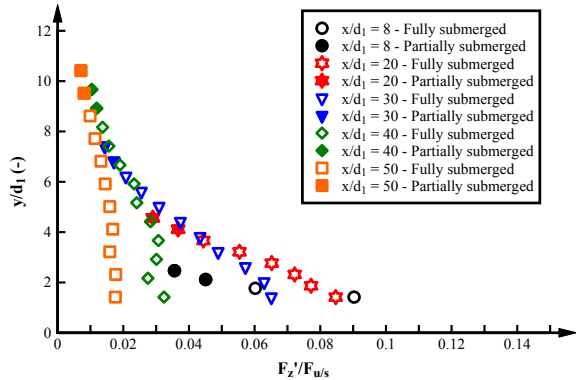
D) EXPERIMENT B: $Fr_1 = 5.1$, $Re = 6.2 \times 10^4$



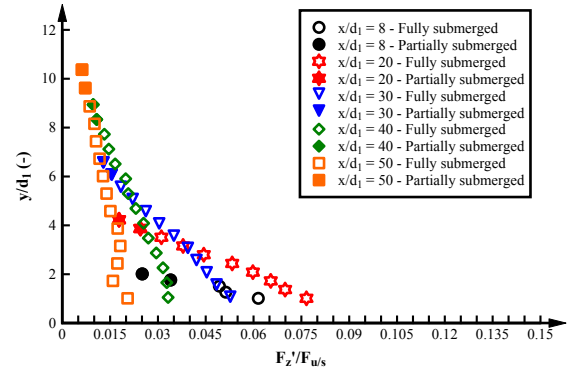
E) EXPERIMENT C: $Fr_1 = 7.0$, $Re = 6.2 \times 10^4$



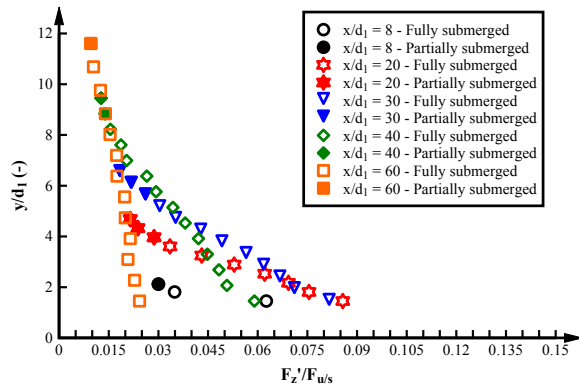
F) EXPERIMENT D: $Fr_1 = 7.0$, $Re = 1.1 \times 10^5$



G) EXPERIMENT E: $Fr_1 = 8.5$, $Re = 7.5 \times 10^4$



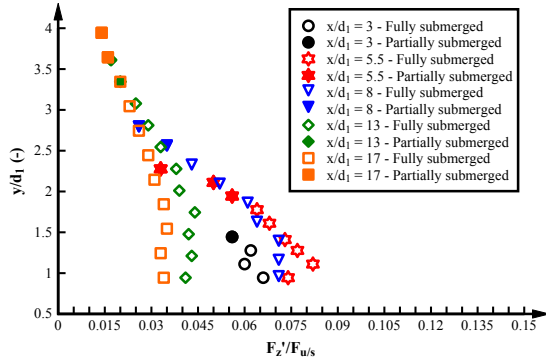
G) EXPERIMENT F: $Fr_1 = 8.5$, $Re = 1.2 \times 10^5$



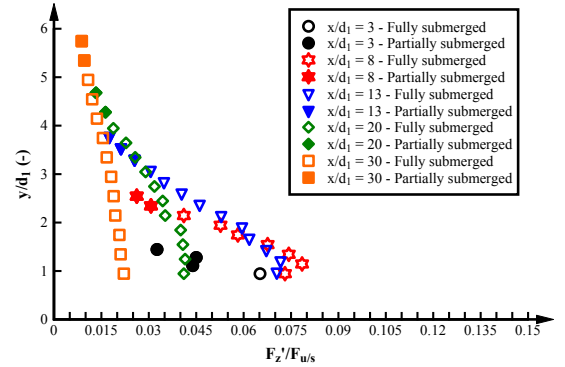
H) EXPERIMENT G: $Fr_1 = 10$, $Re = 8.8 \times 10^4$

DIGITAL APPENDIX D-9. TIME-AVERAGED STREAMWISE FORCES, FULLY DEVELOPED INFLOW CONDITIONS.

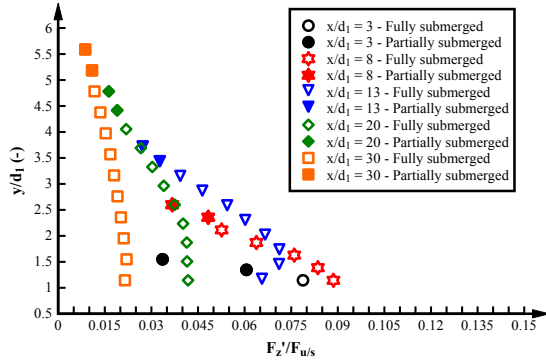
DIGITAL APPENDIX. D.5.2. PARTIALLY DEVELOPED INFLOW CONDITIONS



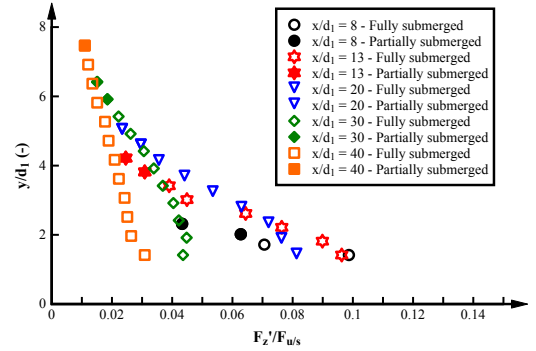
A) EXPERIMENT H: $Fr_1 = 3.8$, $Re = 6.2 \times 10^4$



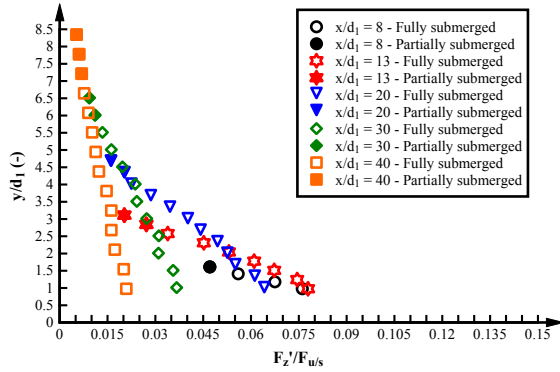
B) EXPERIMENT A: $Fr_1 = 5.1$, $Re = 8.3 \times 10^4$



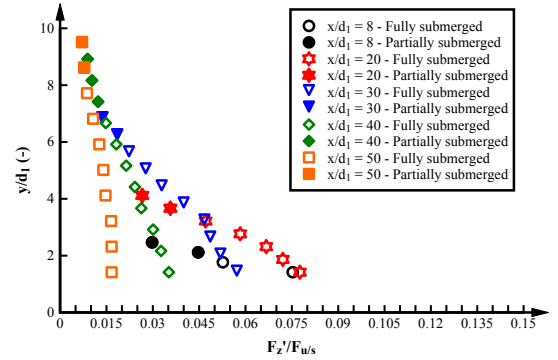
C) EXPERIMENT B: $Fr_1 = 5.1$, $Re = 6.2 \times 10^4$



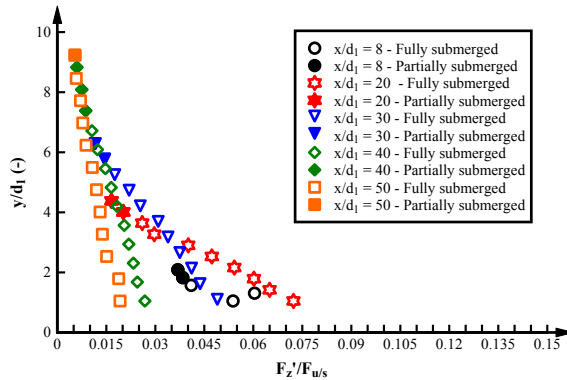
D) EXPERIMENT C: $Fr_1 = 7.0$, $Re = 6.2 \times 10^4$



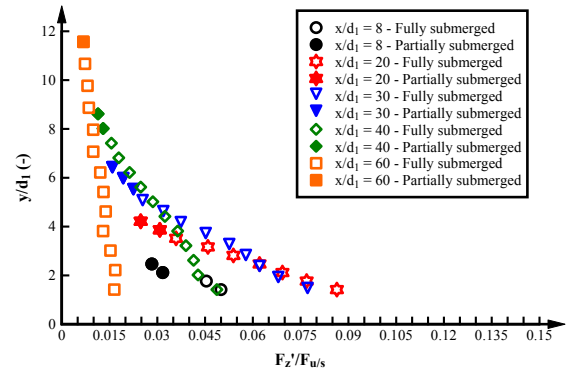
E) EXPERIMENT D: $Fr_1 = 7.0$, $Re = 1.1 \times 10^5$



F) EXPERIMENT E: $Fr_1 = 8.5$, $Re = 7.5 \times 10^4$



G) EXPERIMENT F: $Fr_1 = 8.5$, $Re = 1.2 \times 10^5$

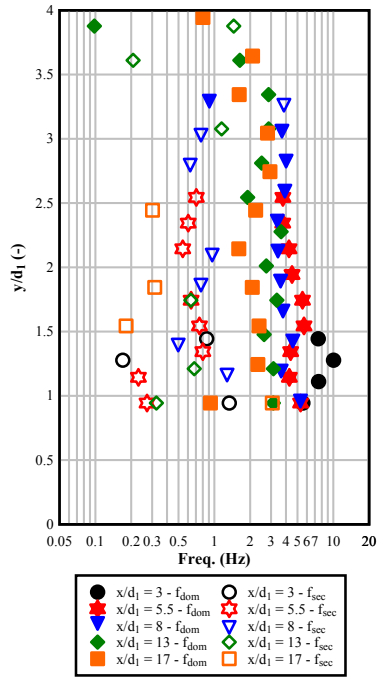


G) EXPERIMENT G: $Fr_1 = 10$, $Re = 8.8 \times 10^4$

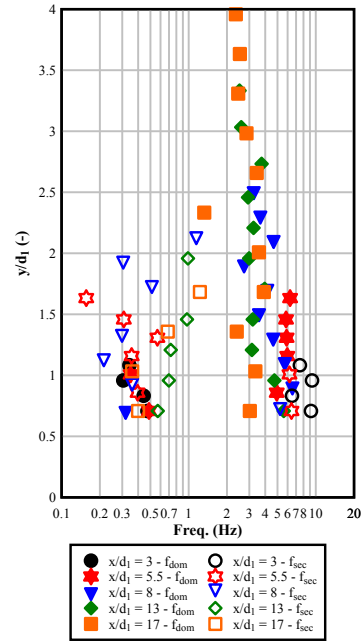
DIGITAL APPENDIX D-10. TIME-AVERAGED STREAMWISE FORCES, PARTIALLY DEVELOPED INFLOW CONDITIONS

DIGITAL APPENDIX. D.6. TRANSVERSE FORCE CHARACTERISTIC FREQUENCIES

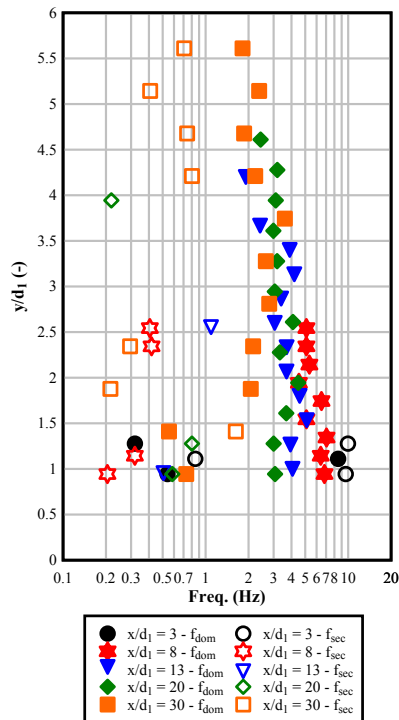
DIGITAL APPENDIX. D.6.1. FULLY DEVELOPED INFLOW CONDITIONS



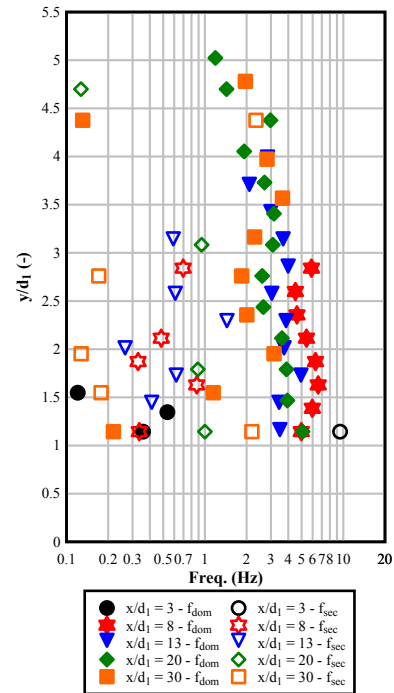
A) EXPERIMENT H: $Fr_1 = 3.8$, $Re = 6.2 \times 10^4$



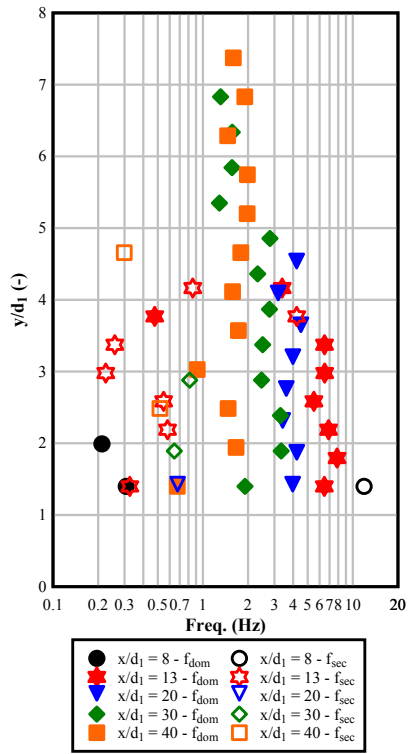
B) EXPERIMENT I: $Fr_1 = 3.8$, $Re = 9.5 \times 10^4$



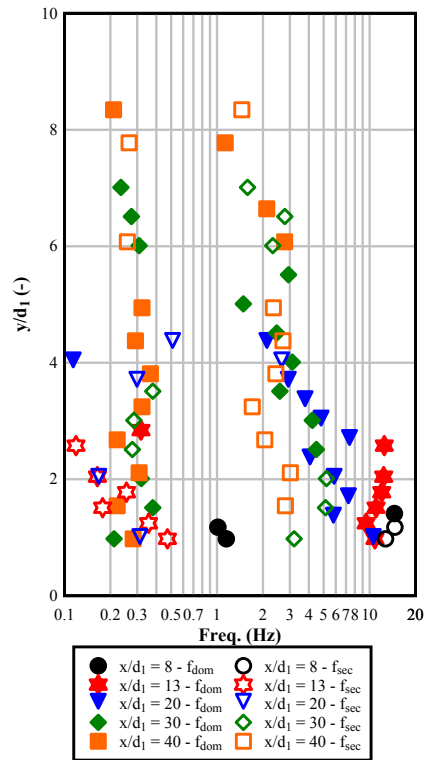
C) EXPERIMENT A: $Fr_1 = 5.1$, $Re = 8.3 \times 10^4$



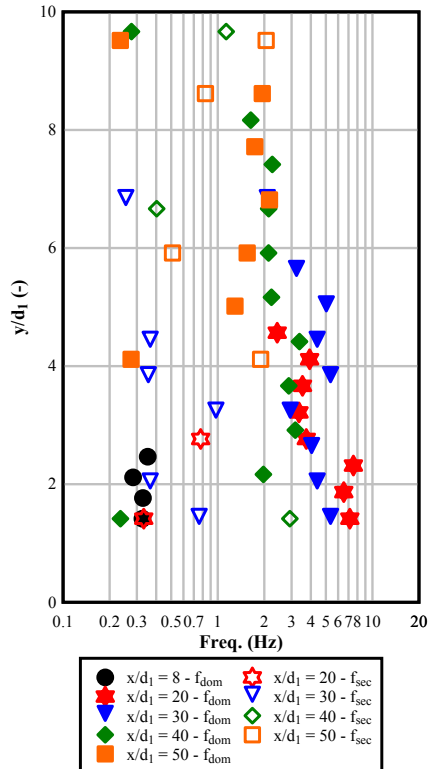
D) EXPERIMENT B: $Fr_1 = 5.1$, $Re = 6.2 \times 10^4$



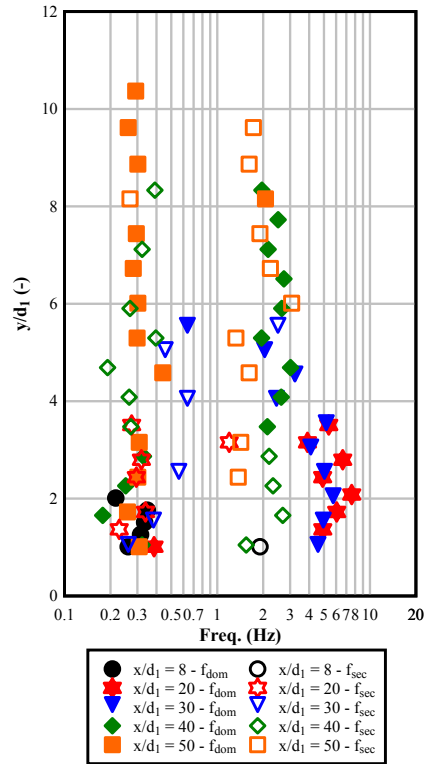
E) EXPERIMENT C: $Fr_1 = 7.0$, $Re = 6.2 \times 10^4$



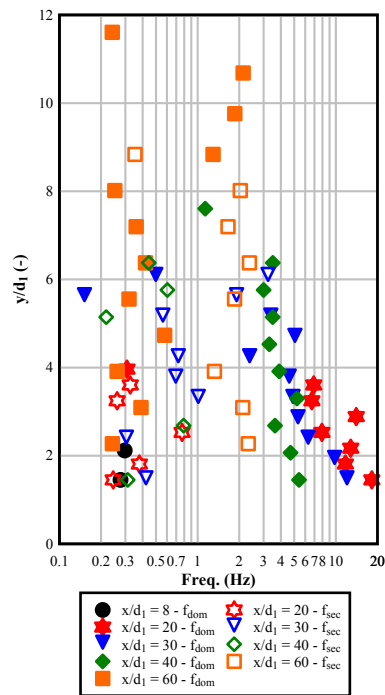
F) EXPERIMENT D: $Fr_1 = 7.0$, $Re = 1.1 \times 10^5$



G) EXPERIMENT E: $Fr_1 = 8.5$, $Re = 7.5 \times 10^4$



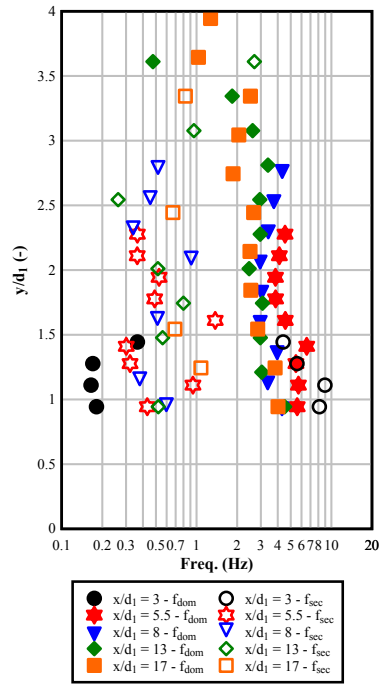
G) EXPERIMENT F: $Fr_1 = 8.5$, $Re = 1.2 \times 10^5$



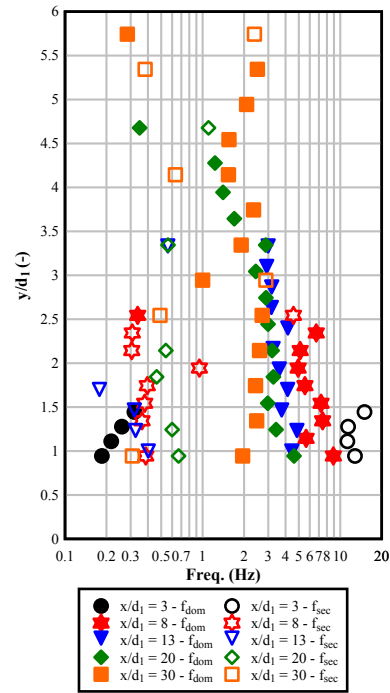
H) EXPERIMENT G: $Fr_1 = 10$, $Re = 8.8 \times 10^4$

DIGITAL APPENDIX D-11. TIME-AVERAGED STREAMWISE FORCES, FULLY DEVELOPED INFLOW CONDITIONS.

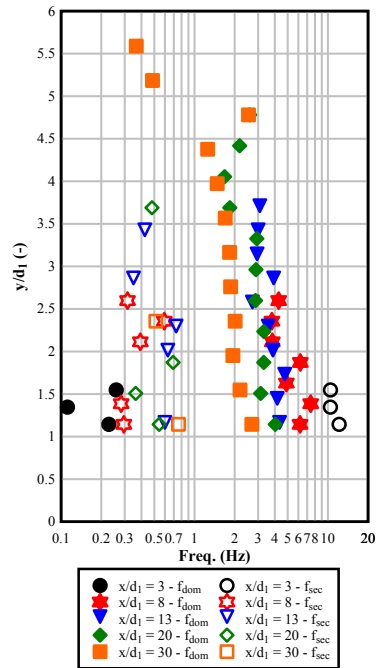
DIGITAL APPENDIX. D.6.2. PARTIALLY DEVELOPED INFLOW CONDITIONS



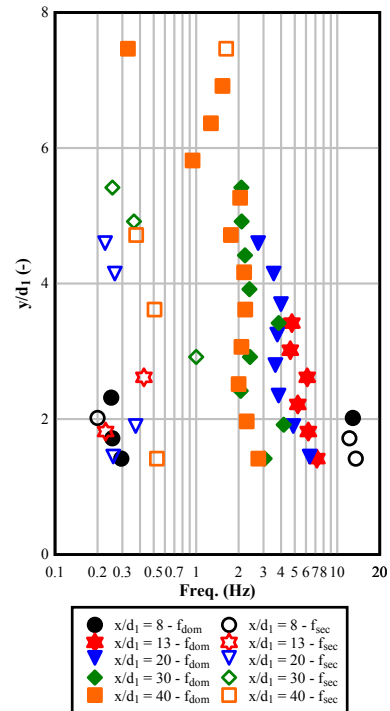
A) EXPERIMENT H: $Fr_1 = 3.8$, $Re = 6.2 \times 10^4$



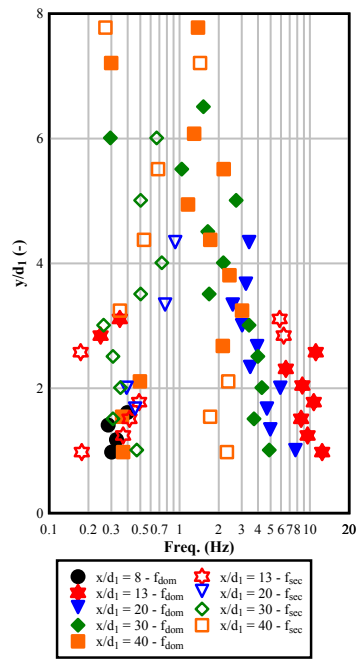
B) EXPERIMENT A: $Fr_1 = 5.1$, $Re = 8.3 \times 10^4$



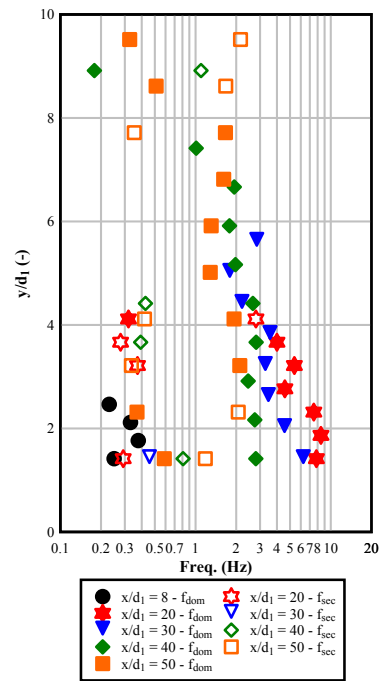
C) EXPERIMENT B: $Fr_1 = 5.1$, $Re = 6.2 \times 10^4$



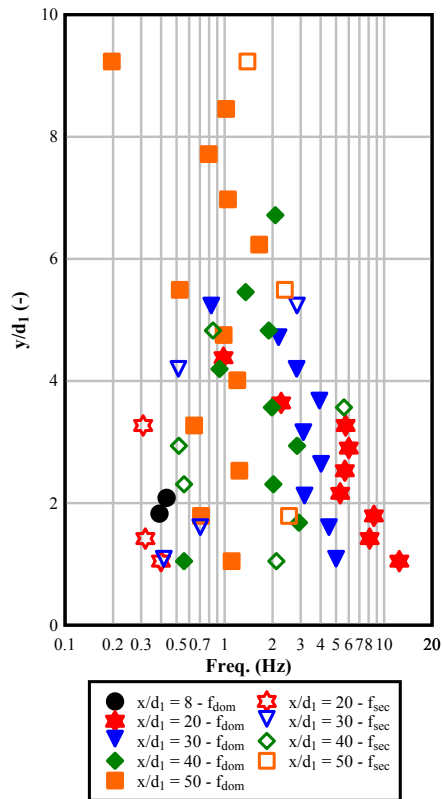
D) EXPERIMENT C: $Fr_1 = 7.0$, $Re = 6.2 \times 10^4$



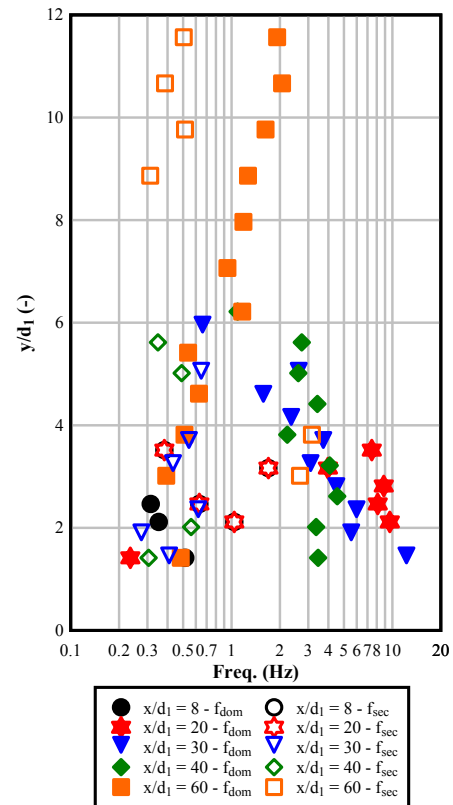
E) EXPERIMENT D: $Fr_1 = 7.0$, $Re = 1.1 \times 10^5$



F) EXPERIMENT E: $Fr_1 = 8.5$, $Re = 7.5 \times 10^4$



G) EXPERIMENT F: $Fr_1 = 8.5$, $Re = 1.2 \times 10^5$

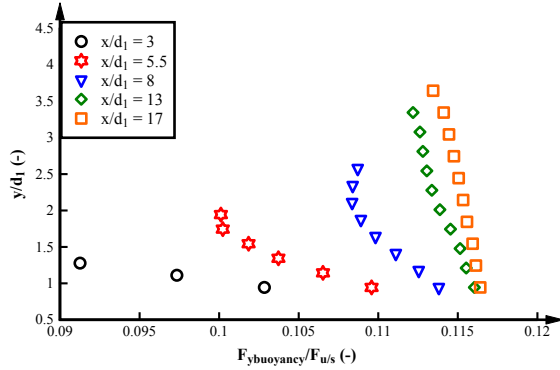


G) EXPERIMENT G: $Fr_1 = 10$, $Re = 8.8 \times 10^4$

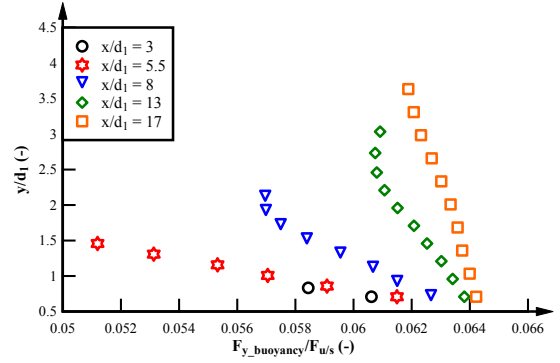
DIGITAL APPENDIX D-12. TIME-AVERAGED STREAMWISE FORCES, PARTIALLY DEVELOPED INFLOW CONDITIONS

DIGITAL APPENDIX. D.7. TIME-AVERAGED BUOYANCY FORCES

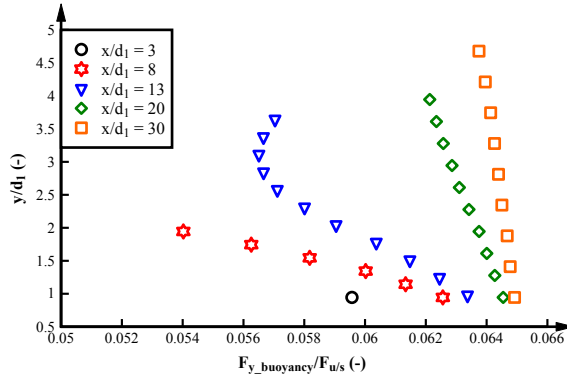
DIGITAL APPENDIX. D.7.1. FULLY DEVELOPED INFLOW CONDITIONS



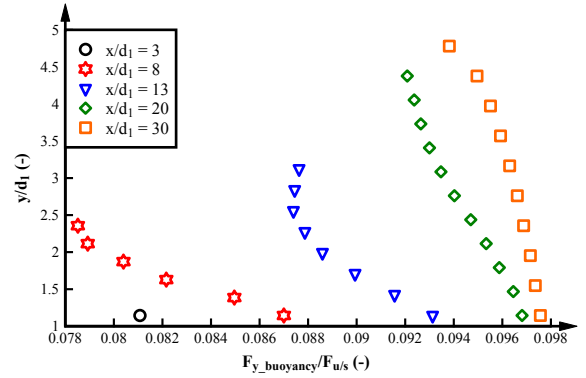
A) EXPERIMENT H: $Fr_I = 3.8$, $Re = 6.2 \times 10^4$



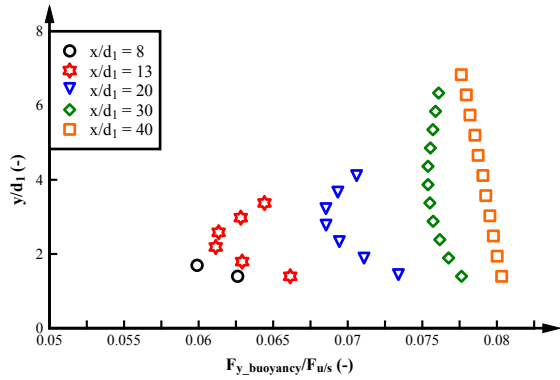
B) EXPERIMENT I: $Fr_I = 3.8$, $Re = 9.5 \times 10^4$



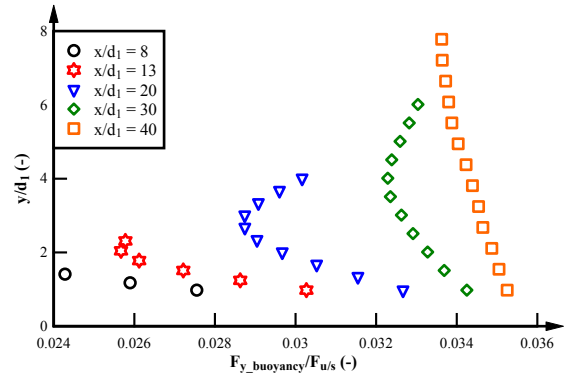
C) EXPERIMENT A: $Fr_I = 5.1$, $Re = 8.3 \times 10^4$



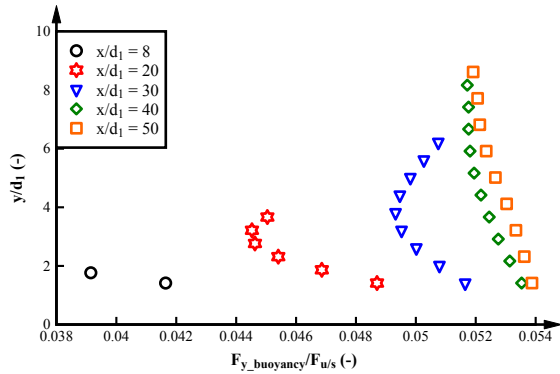
D) EXPERIMENT B: $Fr_I = 5.1$, $Re = 6.2 \times 10^4$



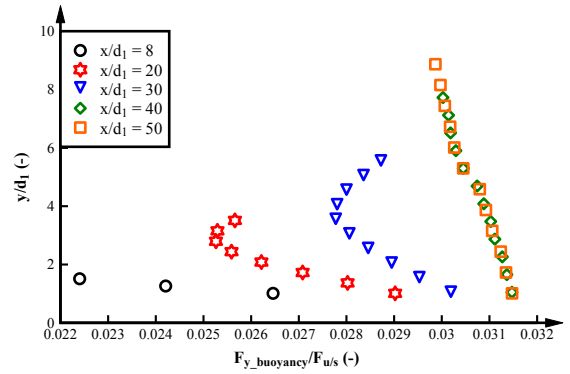
E) EXPERIMENT C: $Fr_I = 7.0$, $Re = 6.2 \times 10^4$



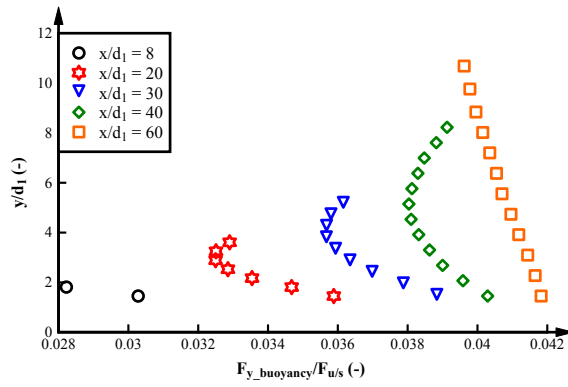
F) EXPERIMENT D: $Fr_I = 7.0$, $Re = 1.1 \times 10^5$



G) EXPERIMENT E: $Fr_I = 8.5$, $Re = 7.5 \times 10^4$



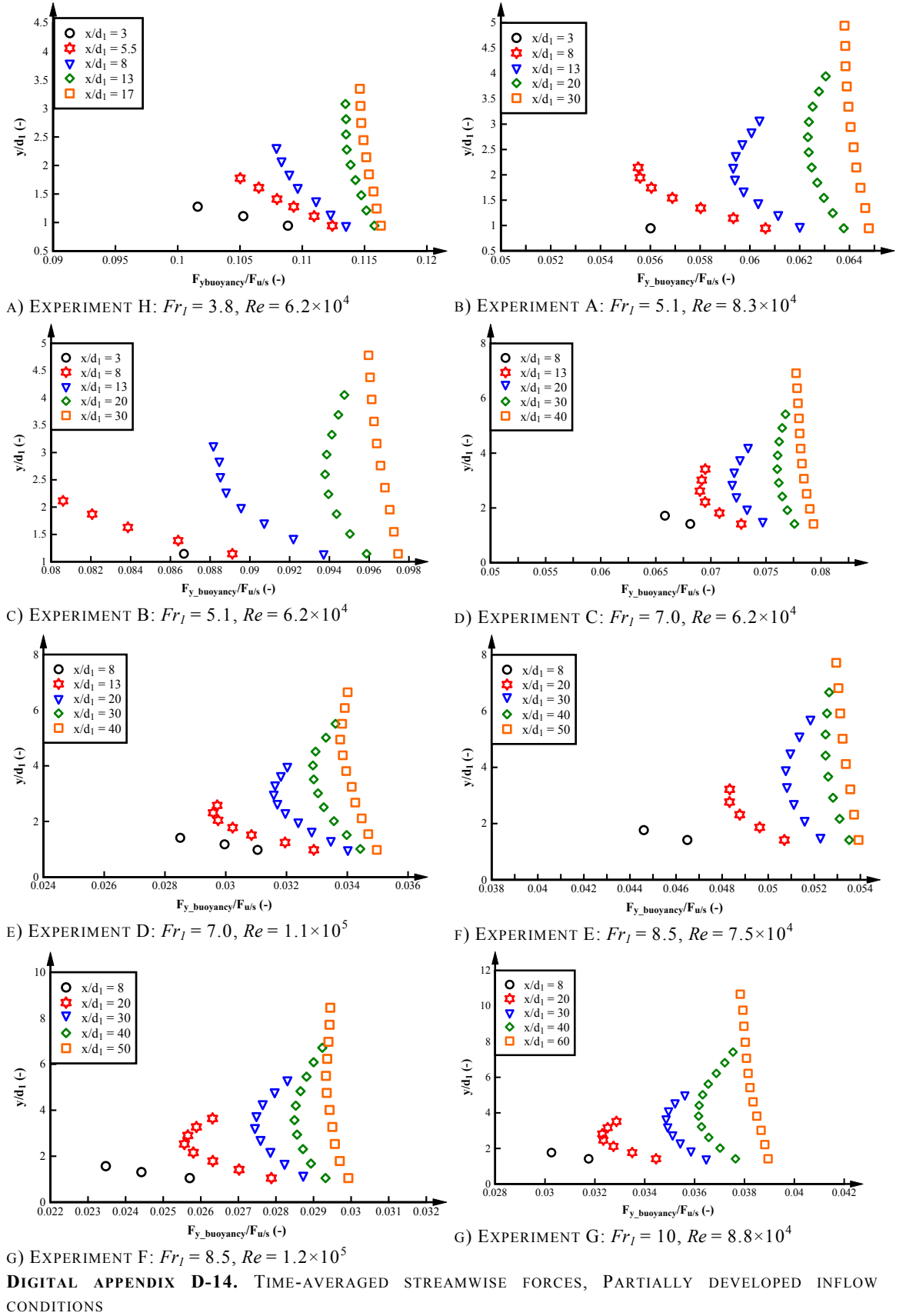
G) EXPERIMENT F: $Fr_I = 8.5$, $Re = 1.2 \times 10^5$



H) EXPERIMENT G: $Fr_I = 10$, $Re = 8.8 \times 10^4$

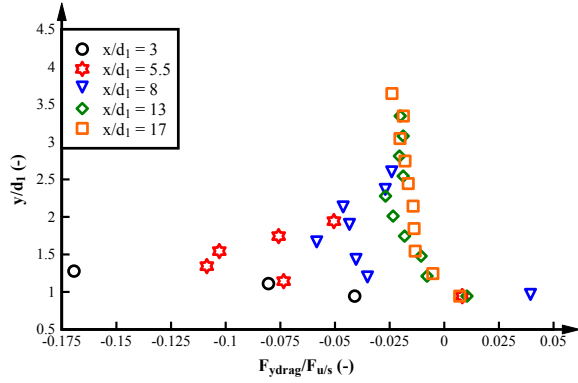
DIGITAL APPENDIX D-13. TIME-AVERAGED STREAMWISE FORCES, FULLY DEVELOPED INFLOW CONDITIONS.

DIGITAL APPENDIX. D.7.2. PARTIALLY DEVELOPED INFLOW CONDITIONS

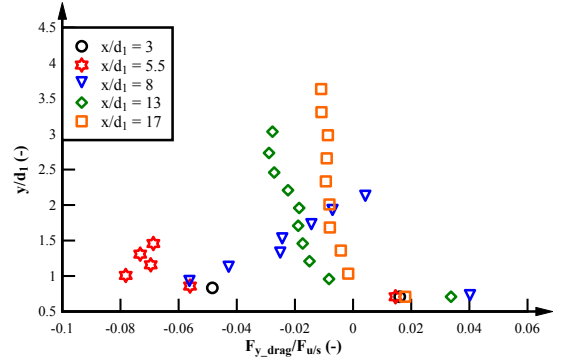


DIGITAL APPENDIX. D.8. TIME-AVERAGED VERTICAL DRAG FORCES

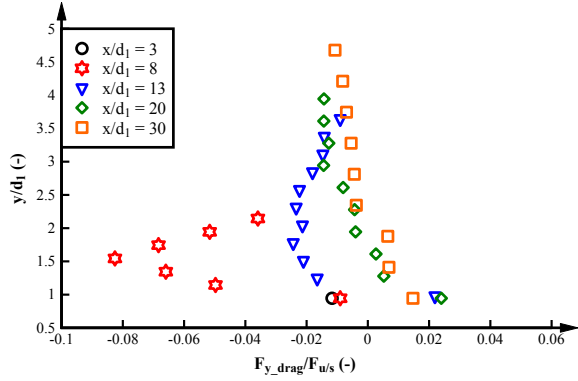
DIGITAL APPENDIX. D.8.1. FULLY DEVELOPED INFLOW CONDITIONS



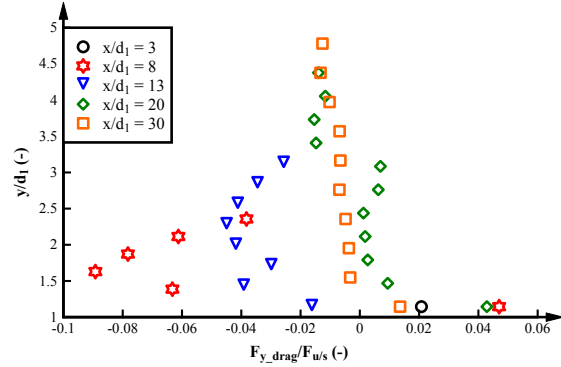
A) EXPERIMENT H: $Fr_1 = 3.8$, $Re = 6.2 \times 10^4$



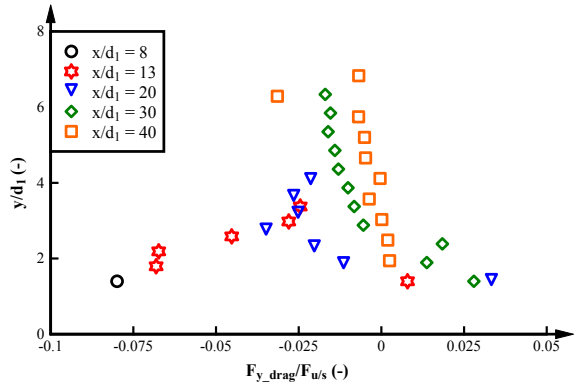
B) EXPERIMENT I: $Fr_1 = 3.8$, $Re = 9.5 \times 10^4$



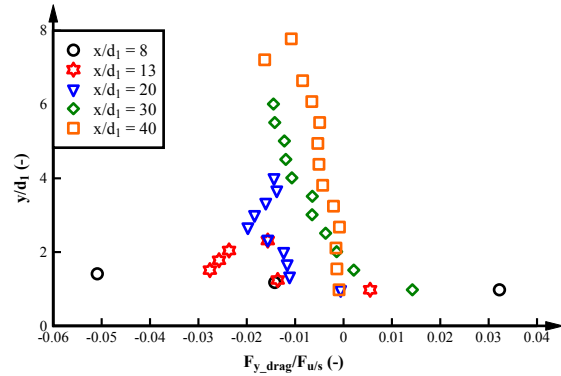
C) EXPERIMENT A: $Fr_1 = 5.1$, $Re = 8.3 \times 10^4$



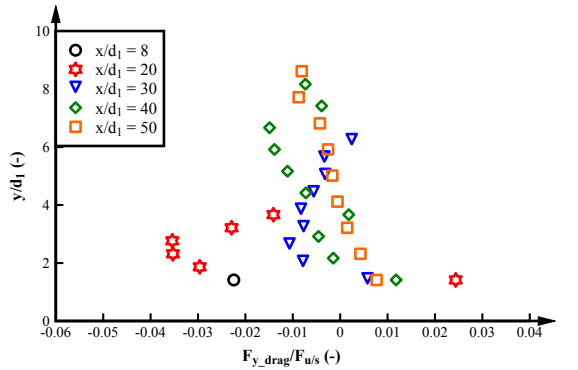
D) EXPERIMENT B: $Fr_1 = 5.1$, $Re = 6.2 \times 10^4$



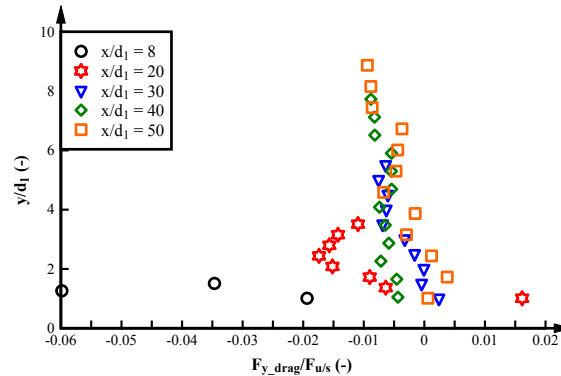
E) EXPERIMENT C: $Fr_1 = 7.0$, $Re = 6.2 \times 10^4$



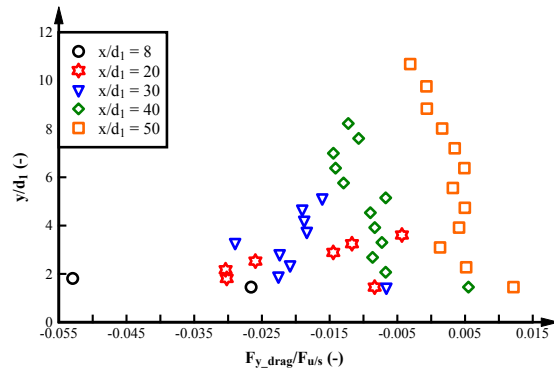
F) EXPERIMENT D: $Fr_1 = 7.0$, $Re = 1.1 \times 10^5$



G) EXPERIMENT E: $Fr_1 = 8.5$, $Re = 7.5 \times 10^4$



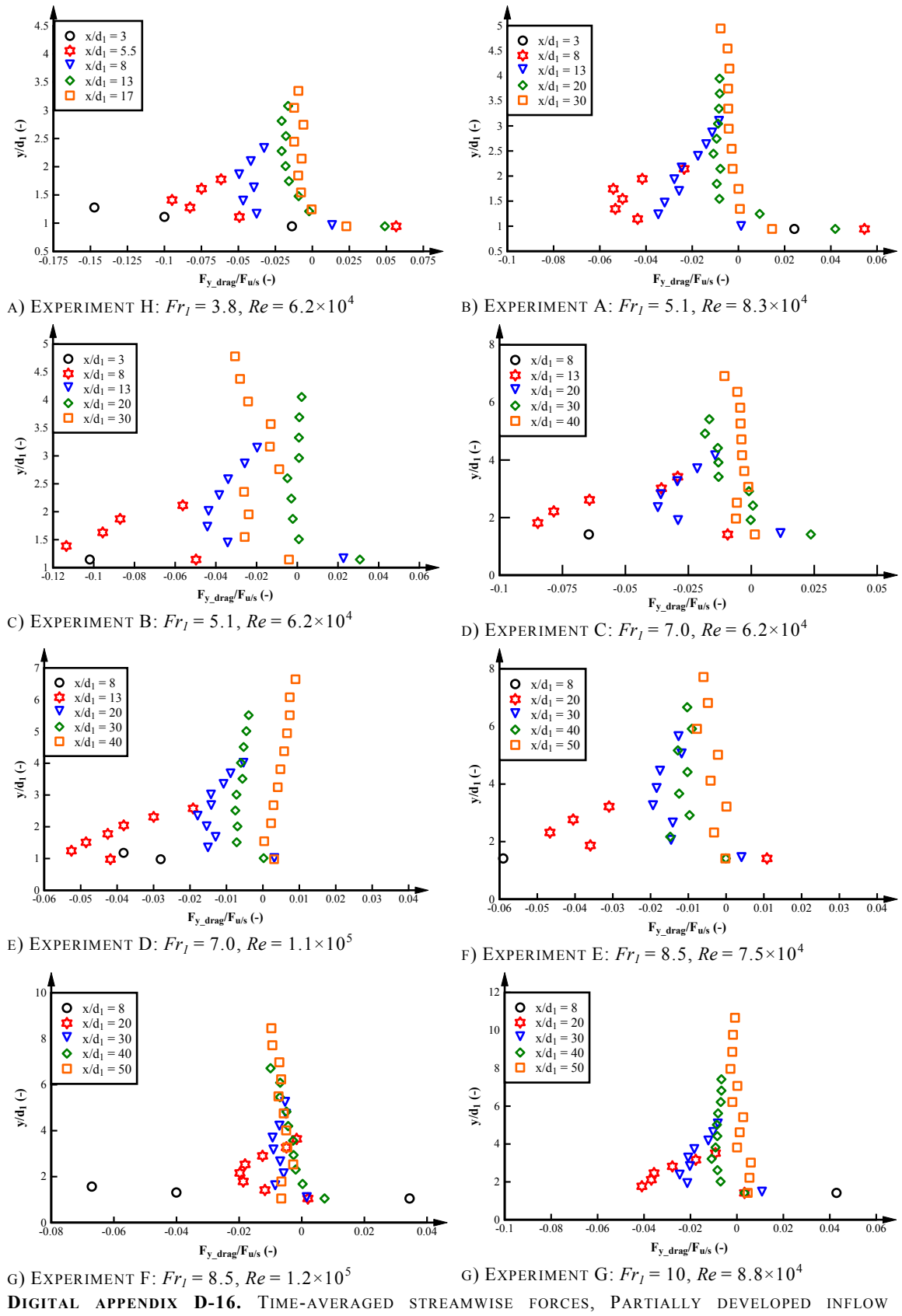
G) EXPERIMENT F: $Fr_1 = 8.5$, $Re = 1.2 \times 10^5$



H) EXPERIMENT G: $Fr_1 = 10$, $Re = 8.8 \times 10^4$

DIGITAL APPENDIX D-15. TIME-AVERAGED STREAMWISE FORCES, FULLY DEVELOPED INFLOW CONDITIONS.

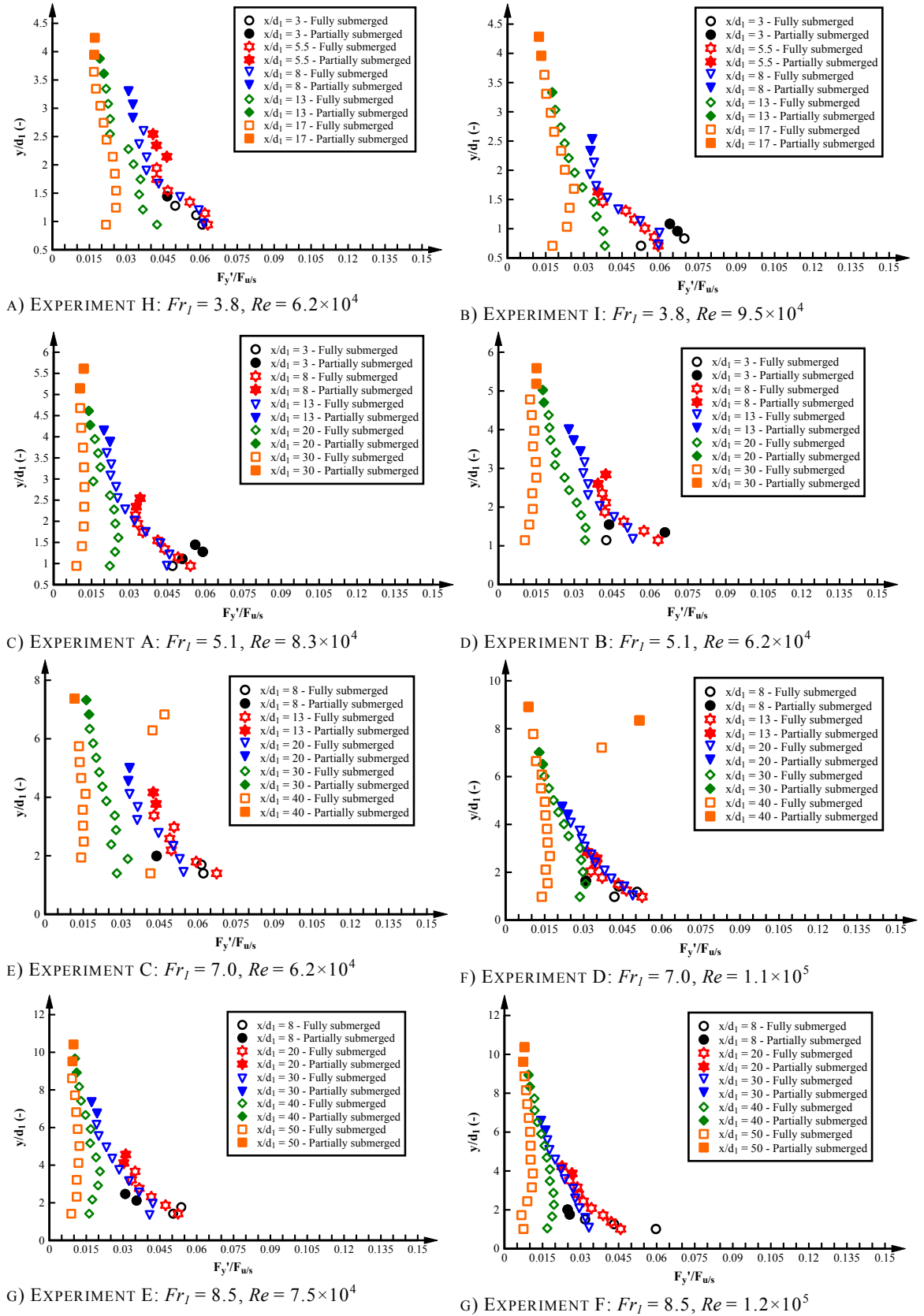
DIGITAL APPENDIX. D.8.2. FULLY DEVELOPED INFLOW CONDITIONS

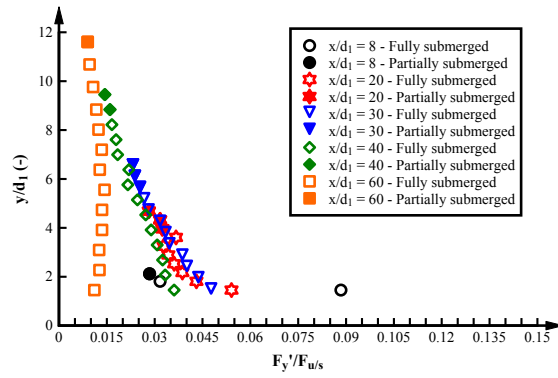


DIGITAL APPENDIX D-16. TIME-AVERAGED STREAMWISE FORCES, PARTIALLY DEVELOPED INFLOW CONDITIONS

DIGITAL APPENDIX. D.9. VERTICAL FORCE FLUCTUATIONS

DIGITAL APPENDIX. D.9.1. FULLY DEVELOPED INFLOW CONDITIONS

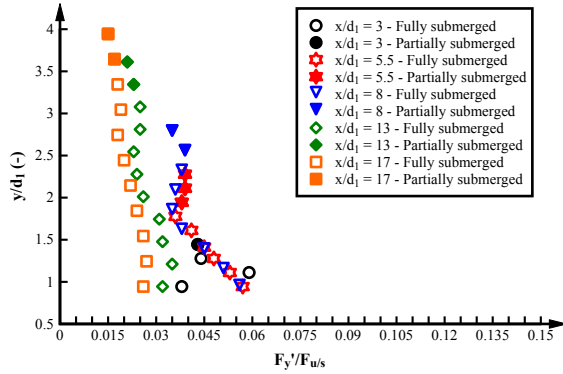




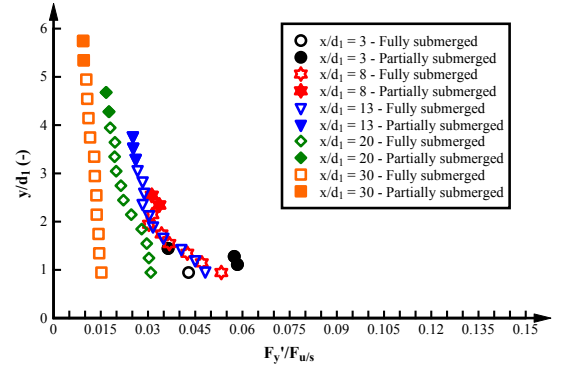
H) EXPERIMENT G: $Fr_1 = 10$, $Re = 8.8 \times 10^4$

DIGITAL APPENDIX D-17. TIME-AVERAGED STREAMWISE FORCES, FULLY DEVELOPED INFLOW CONDITIONS.

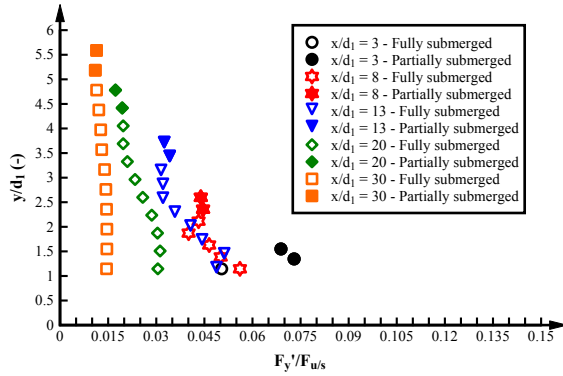
DIGITAL APPENDIX. D.9.2. PARTIALLY DEVELOPED INFLOW CONDITIONS



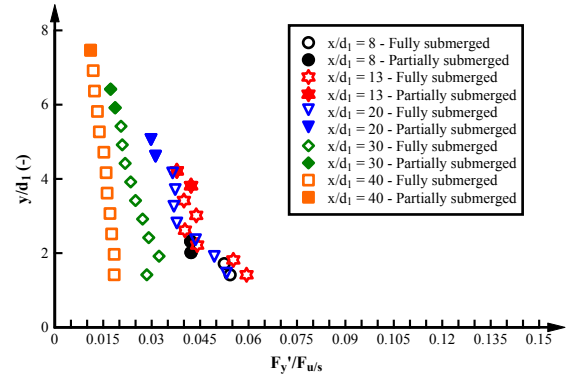
A) EXPERIMENT H: $Fr_1 = 3.8$, $Re = 6.2 \times 10^4$



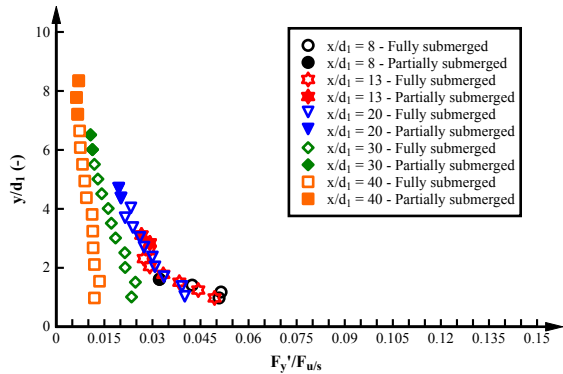
B) EXPERIMENT A: $Fr_1 = 5.1$, $Re = 8.3 \times 10^4$



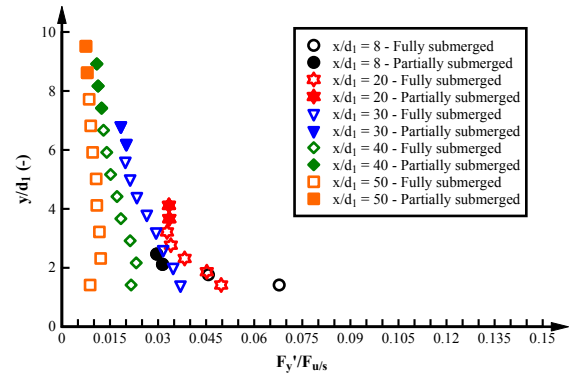
C) EXPERIMENT B: $Fr_1 = 5.1$, $Re = 6.2 \times 10^4$



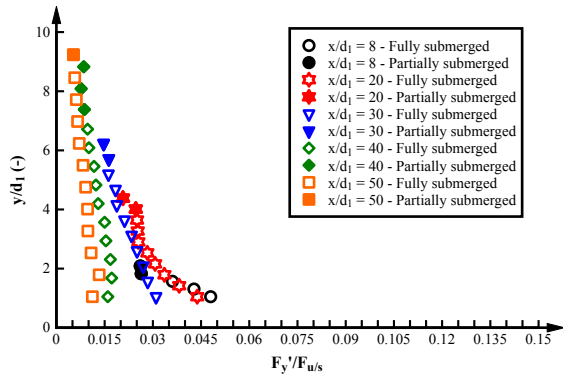
D) EXPERIMENT C: $Fr_1 = 7.0$, $Re = 6.2 \times 10^4$



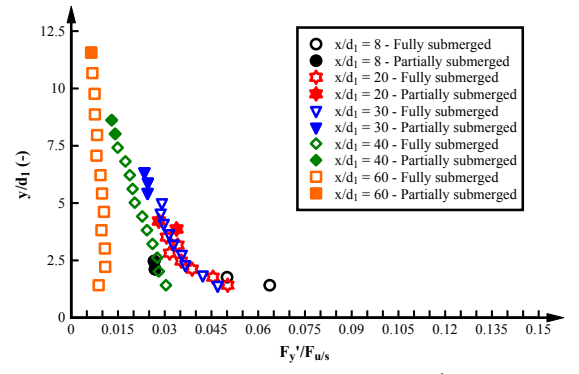
E) EXPERIMENT D: $Fr_1 = 7.0$, $Re = 1.1 \times 10^5$



F) EXPERIMENT E: $Fr_1 = 8.5$, $Re = 7.5 \times 10^4$



G) EXPERIMENT F: $Fr_1 = 8.5$, $Re = 1.2 \times 10^5$

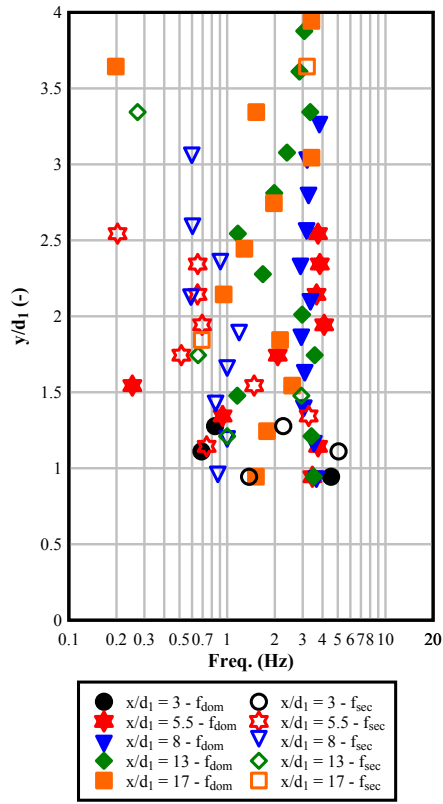


G) EXPERIMENT G: $Fr_1 = 10$, $Re = 8.8 \times 10^4$

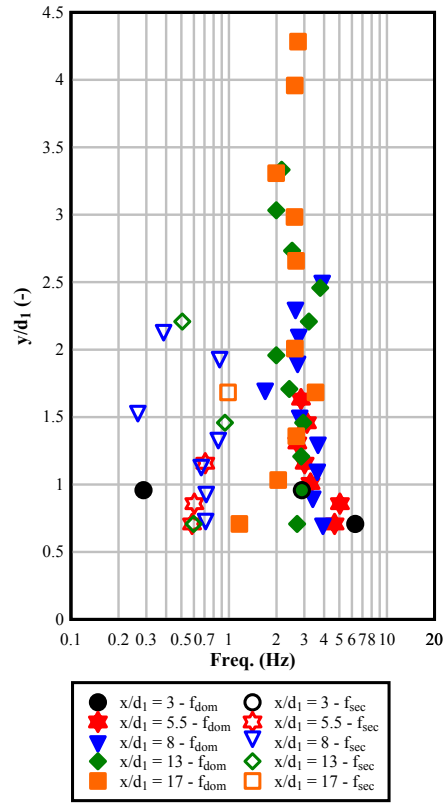
DIGITAL APPENDIX D-18. TIME-AVERAGED STREAMWISE FORCES, PARTIALLY DEVELOPED INFLOW CONDITIONS

DIGITAL APPENDIX. D.10. VERTICAL FORCE CHARACTERISTIC FREQUENCIES

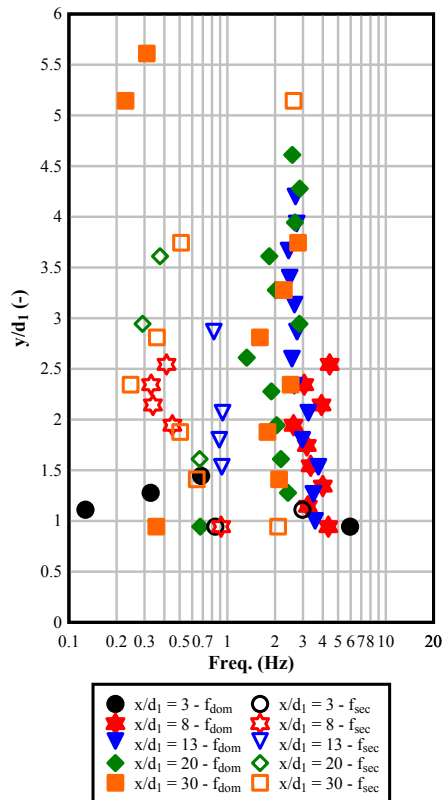
DIGITAL APPENDIX. D.10.1. FULLY DEVELOPED INFLOW CONDITIONS



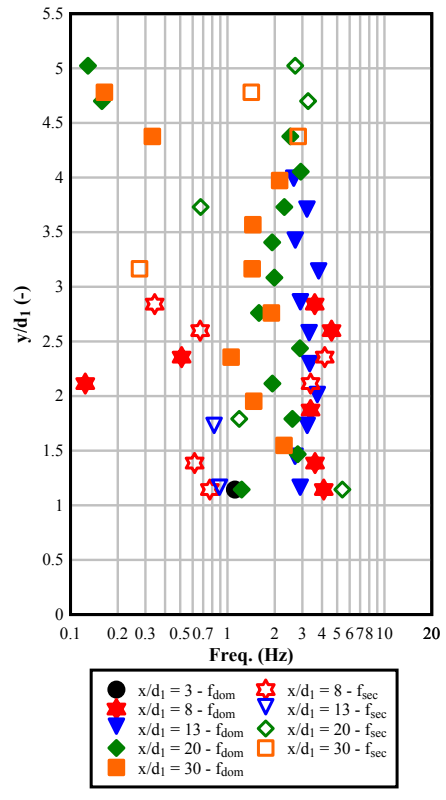
A) EXPERIMENT H: $Fr_1 = 3.8$, $Re = 6.2 \times 10^4$



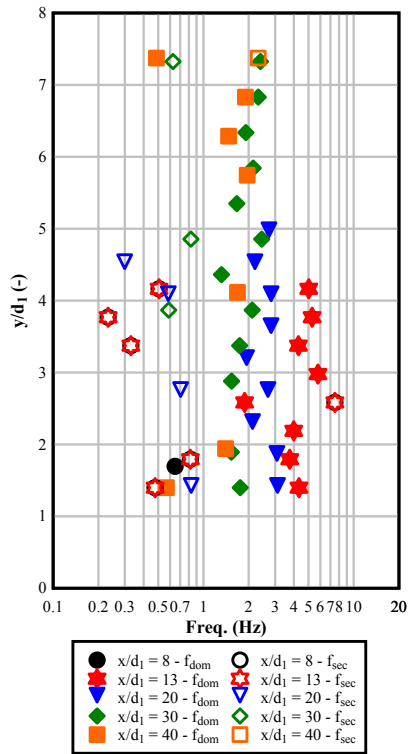
B) EXPERIMENT I: $Fr_1 = 3.8$, $Re = 9.5 \times 10^4$



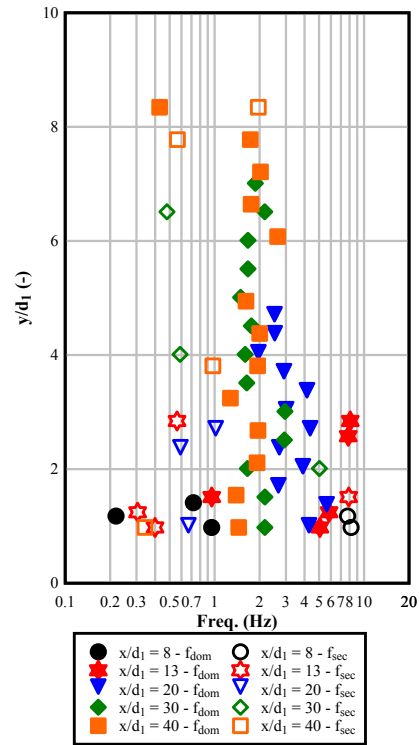
C) EXPERIMENT A: $Fr_1 = 5.1$, $Re = 8.3 \times 10^4$



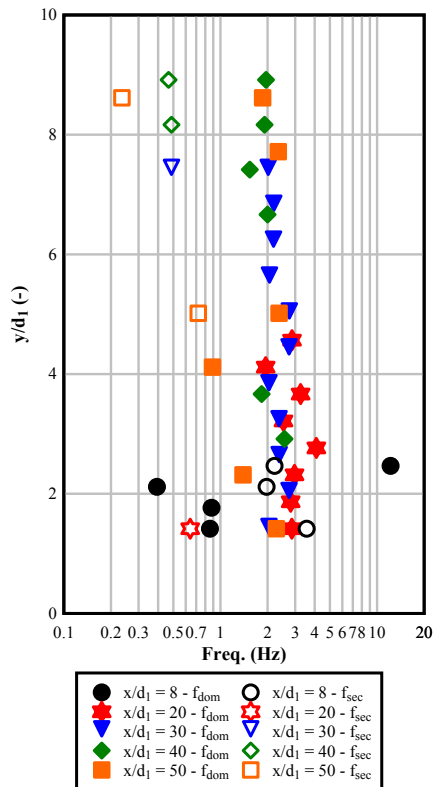
D) EXPERIMENT B: $Fr_1 = 5.1$, $Re = 6.2 \times 10^4$



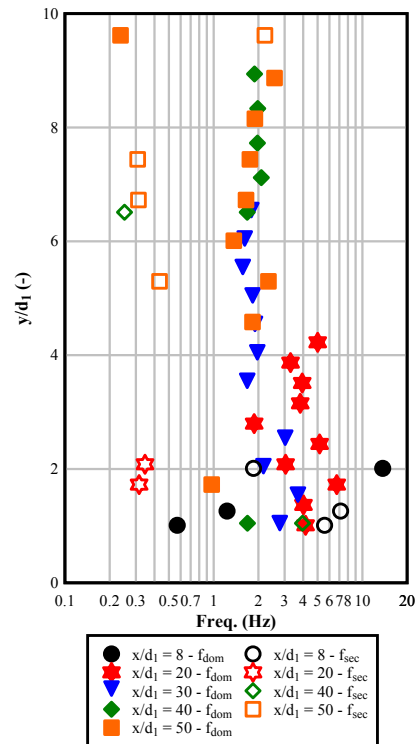
E) EXPERIMENT C: $Fr_1 = 7.0$, $Re = 6.2 \times 10^4$



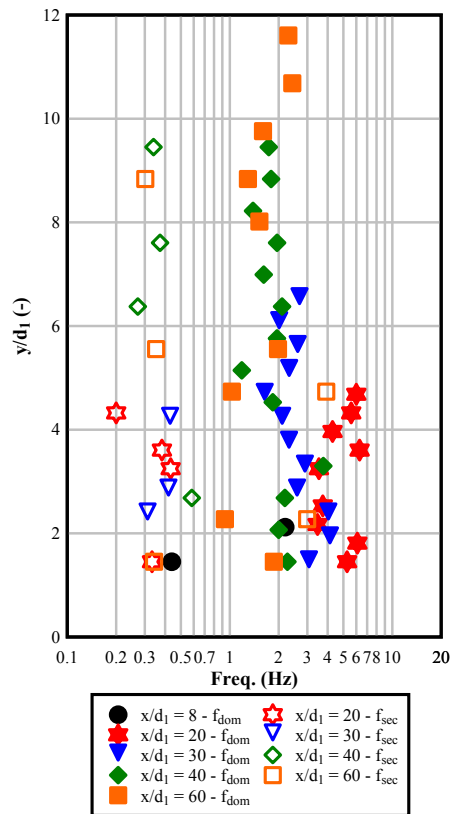
F) EXPERIMENT D: $Fr_1 = 7.0$, $Re = 1.1 \times 10^5$



G) EXPERIMENT E: $Fr_1 = 8.5$, $Re = 7.5 \times 10^4$



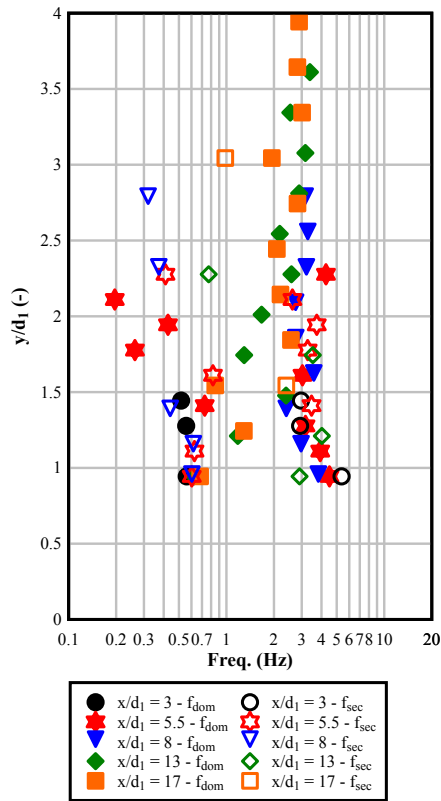
G) EXPERIMENT F: $Fr_1 = 8.5$, $Re = 1.2 \times 10^5$



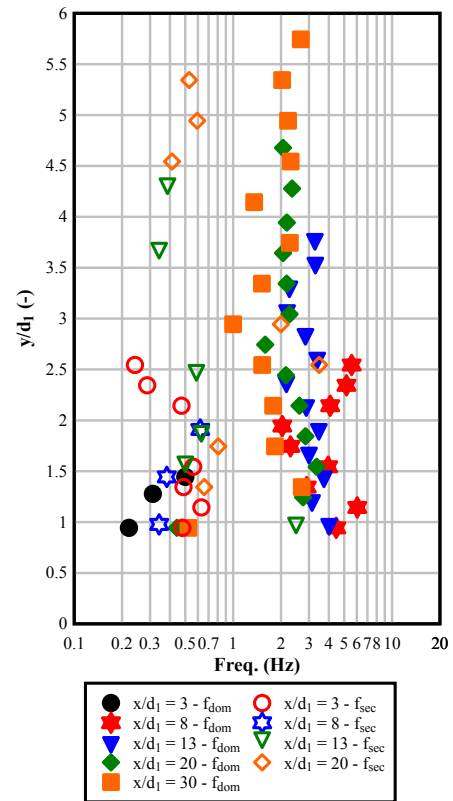
H) EXPERIMENT G: $Fr_1 = 10$, $Re = 8.8 \times 10^4$

DIGITAL APPENDIX D-19. TIME-AVERAGED STREAMWISE FORCES, FULLY DEVELOPED INFLOW CONDITIONS.

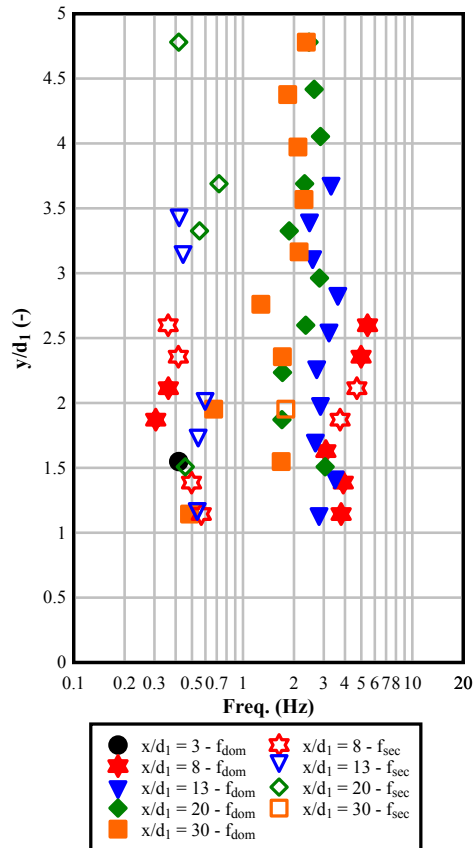
DIGITAL APPENDIX. D.10.2. PARTIALLY DEVELOPED INFLOW CONDITIONS



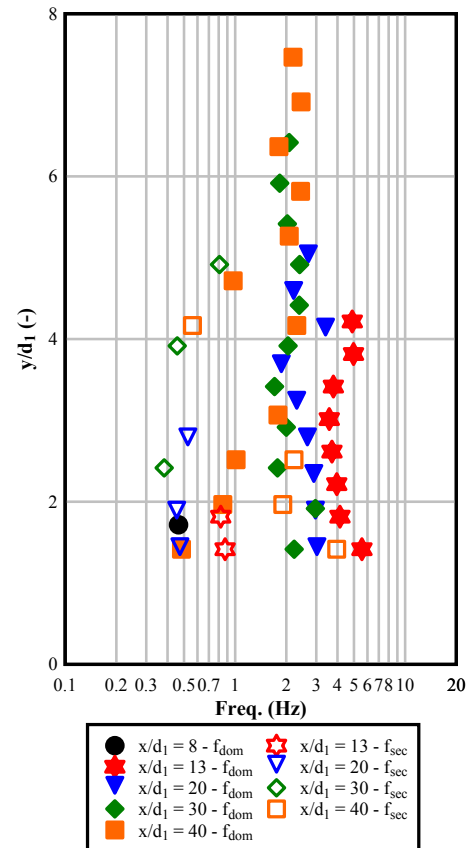
A) EXPERIMENT H: $Fr_1 = 3.8$, $Re = 6.2 \times 10^4$



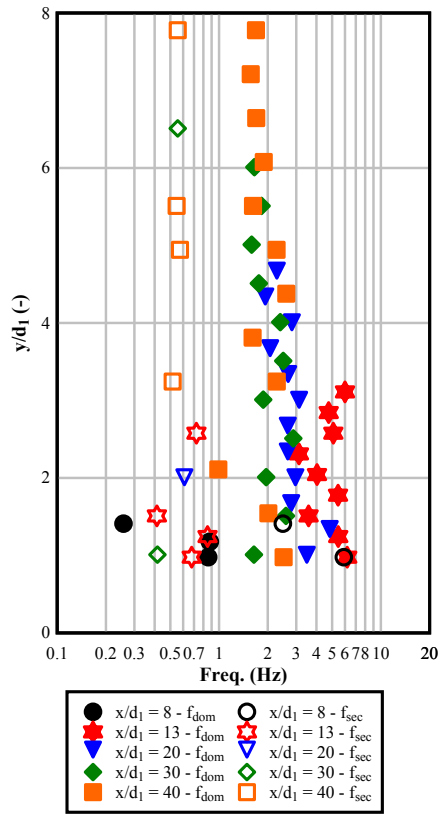
B) EXPERIMENT A: $Fr_1 = 5.1$, $Re = 8.3 \times 10^4$



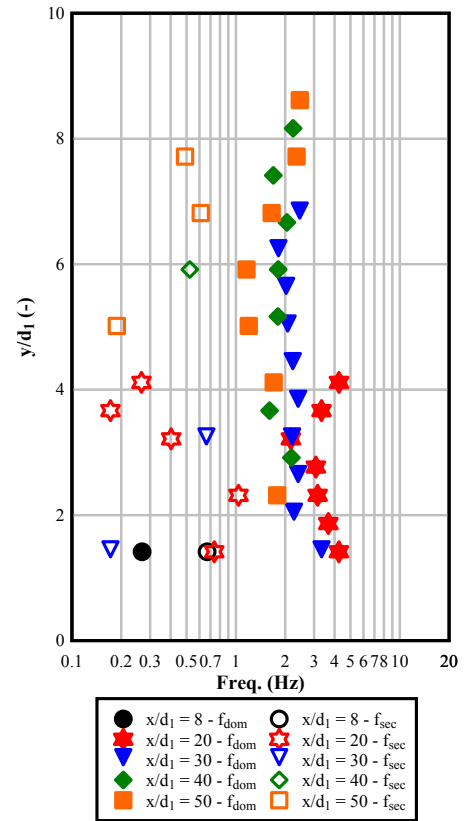
C) EXPERIMENT B: $Fr_1 = 5.1$, $Re = 6.2 \times 10^4$



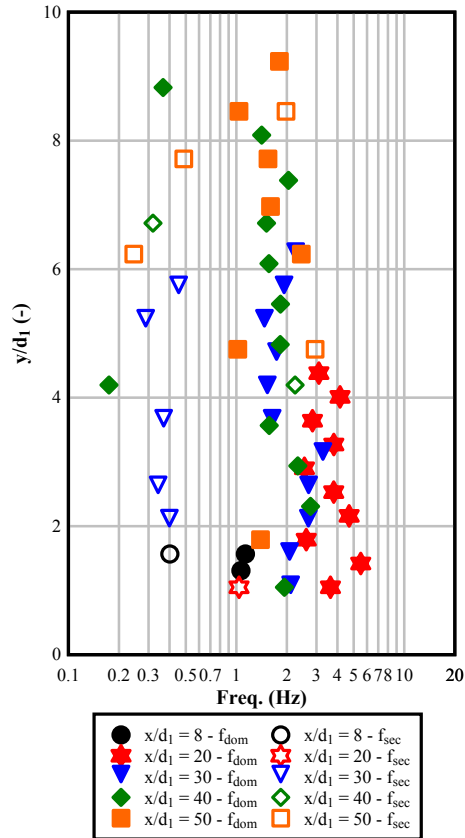
D) EXPERIMENT C: $Fr_1 = 7.0$, $Re = 6.2 \times 10^4$



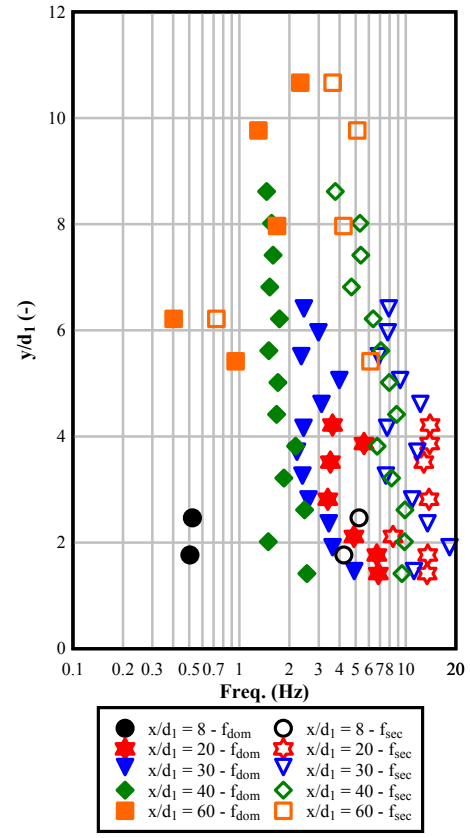
E) EXPERIMENT D: $Fr_1 = 7.0$, $Re = 1.1 \times 10^5$



F) EXPERIMENT E: $Fr_1 = 8.5$, $Re = 7.5 \times 10^4$



G) EXPERIMENT F: $Fr_1 = 8.5$, $Re = 1.2 \times 10^5$



G) EXPERIMENT G: $Fr_1 = 10$, $Re = 8.8 \times 10^4$

DIGITAL APPENDIX D-20. TIME-AVERAGED STREAMWISE FORCES, PARTIALLY DEVELOPED INFLOW CONDITIONS